

NONGRAY GAS AND NONGRAY PARTICLE EFFECTS IN MODELING  
FLUIDIZED BED COMBUSTORS

A THESIS SUBMITTED TO  
THE GRADUATE SCHOOL OF NATURAL AND APPLIED SCIENCES  
OF  
MIDDLE EAST TECHNICAL UNIVERSITY

BY

CİHAN ATEŞ

IN PARTIAL FULFILLMENT OF THE REQUIREMENTS  
FOR  
THE DEGREE OF DOCTOR OF PHILOSOPHY  
IN  
CHEMICAL ENGINEERING

AUGUST 2018



Approval of the thesis:

**NONGRAY GAS AND NONGRAY PARTICLE EFFECTS IN MODELING  
FLUIDIZED BED COMBUSTORS**

submitted by **CİHAN ATEŞ** in partial fulfillment of the requirements for the degree  
of **Doctor of Philosophy in Chemical Engineering Department, Middle East  
Technical University** by,

Prof. Dr. Halil Kalıpçılar  
Dean, Graduate School of **Natural and Applied Sciences** \_\_\_\_\_

Prof. Dr. Pınar Çalık  
Head of Department, **Chemical Engineering** \_\_\_\_\_

Assoc. Prof. Dr. Görkem Külah  
Supervisor, **Chemical Engineering Dept., METU** \_\_\_\_\_

Prof. Dr. Nevin Selçuk  
Co-Supervisor, **Chemical Engineering Dept., METU** \_\_\_\_\_

**Examining Committee Members:**

Prof. Dr. Murat Köksal  
Mechanical Engineering Dept., Hacettepe Uni. \_\_\_\_\_

Assoc. Prof. Dr. Görkem Külah  
Chemical Engineering Dept., METU \_\_\_\_\_

Assoc. Prof. Dr. Nimeti Döner  
Mechanical Eng. Dept., Kütahya Dumlupınar Uni. \_\_\_\_\_

Asst. Prof. Dr. Harun Koku  
Chemical Engineering Dept., METU \_\_\_\_\_

Asst. Prof. Dr. İnci Ayrancı  
Chemical Engineering Dept., METU \_\_\_\_\_

**Date:** 27.08.2018

**I hereby declare that all information in this document has been obtained and presented in accordance with academic rules and ethical conduct. I also declare that, as required by these rules and conduct, I have fully cited and referenced all material and results that are not original to this work.**

Name, Last name: Cihan ATEŞ

Signature:

## **ABSTRACT**

### **NONGRAY GAS AND NONGRAY PARTICLE EFFECTS IN MODELING FLUIDIZED BED COMBUSTORS**

Ateş, Cihan  
Ph.D., Department of Chemical Engineering  
Supervisor: Assoc. Prof. Dr. Görkem Kùlah  
Co-Supervisor: Prof. Dr. Nevin Selçuk

August 2018, 489 pages

Thermal radiation accounts for the majority of the heat transferred in combusting systems where it is constituted of the contributions from both participating gases and solid particles; hence gas and particle radiative properties play an important role. In spite of the lower operating temperatures (750-950 °C), radiation is still the predominant mode of heat transfer in fluidized bed combustors (FBCs) due to the presence of higher particle loads in the flue gas. Therefore, modeling of radiative heat transfer in such systems is of considerable importance and necessitates not only accurate but also computationally efficient methods for radiative property estimation of particle-laden combustion gases. Although extensive research has been carried out for non-gray behaviour of the flue gas, non-gray behaviour of particles has been investigated in limited number of studies, where only few involved both non-gray gas and non-gray particle properties. Therefore, the ultimate objective of this study is to develop CPU efficient, accurate and compatible non-gray gas and non-gray particle radiative property models such that the outcome will provide guidelines when choosing radiation models for combustion related investigations.

For that purpose, several multi-dimensional radiation codes have been developed, which can simultaneously take into consideration non-gray gas and non-gray particle property estimation techniques in conjunction with the radiative transfer equation

(RTE) for the determination of radiative heat flux and source term distributions. Predictive accuracy and computational efficiency of different radiative property estimation techniques for both participating combustion gases and particles are tested in one comprehensive study by benchmarking their predictions against reference solutions and measurements for the conditions relevant to combusting systems, particularly FBCs.

Comparisons reveal that non-gray particle radiation is of significant importance for accurate calculation of radiative heat transfer in combusting systems and it originates from the spectral nature of the complex index of refraction. Furthermore, it is shown that chemical composition has a significant effect on non-gray particle absorption properties as well as heat flux/source term predictions. It is also demonstrated that the dominance of particle radiation in total radiative heat exchange is strongly dependent on particle chemical composition. Accordingly, particle radiation does not necessarily dominate total radiation even at high particle loads. Therefore, negligence of the non-gray behavior of either combustion gases or particles can lead to significant errors in both heat flux and source term predictions even at high particle loads.

**Keywords:** Radiative heat transfer, non-gray gas radiation, non-gray particle radiation, fluidized bed combustors, coal combustion

## ÖZ

### GRİ-OLMAYAN GAZ VE GRİ-OLMAYAN PARÇACIK ETKİLERİNİN AKIŞKAN YATAKLI YAKICILARDA MODELLENMESİ

Ateş, Cihan  
Doktora, Kimya Mühendisliği Bölümü  
Tez Yöneticisi: Doç. Dr. Görkem Külah  
Ortak Tez Yöneticisi: Prof. Dr. Nevin Selçuk

Ağustos 2018, 489 sayfa

Yanma sistemlerinde gerçekleşen ısı transferinin büyük kısmını yanma gazları ve katı taneciklerin katılımı ile oluşan ısı ışınım oluşturmaktadır; bu nedenle gaz ve taneciklerin ışınım özellikleri önemli bir rol oynamaktadır. Düşük operasyonel sıcaklıklarına (750-950 °C) karşın yüksek tanecik yükleri nedeni ile akışkan yataklı yakıcılarda (AYY) da ışınım hala baskın ısı transferi modu olmaktadır. Bu nedenle, benzer sistemlerde ışınım ısı transferinin modellenmesi yüksek önem arz etmekte olup bu modeller tanecik yüklü baca gazları için kesinliği ve CPU verimi yüksek özellik modellerine gereksinim duymaktadır. Gri-olmayan gaz davranışı, baca gazları için detaylıca çalışılmış olmakla birlikte gri-olmayan davranış tanecikler için sayıca çok az çalışmada incelenmiştir ve gaz ve taneciklerin gri-olmayan davranışlarının birlikte incelendiği çalışma sayısının daha da az olduğu görülmektedir. Bu nedenle, bu çalışmanın amacı, yanma ile ilgili incelemelere ışınım modelleri seçerken rehberlik edebilecek çıktılar sağlanmak üzere gri-olmayan gaz ve tanecikler için CPU verimliliği yüksek, kesinliği yüksek ve uyumlu ışınım özellik modelleri geliştirmek olarak belirlenmiştir.

Bu amaç doğrultusunda, birkaç çok boyutlu ışınım kodu geliştirilmiştir. Bu kodlar gri-olmayan gaz ve tanecik özelliklerini aynı anda hesaplayabilme özelliğine sahip olup özellik modellerini ışınım ısı akısı ve enerjisinin tespiti için ışınım transfer

denklemlerine (ITD) entegre edebilmektedir. Yanma gazları ve tanecikleri için farklı ışı nım özellikleri hesaplama yöntemlerinin yanma sistemleri koşullarında, özellikle AYY koşullarında, tahmin başarısı ve hesaplama verimliliği, referans çözümler ve deneysel verilerle kapsamlı bir çalıřma içerisinde test edilmiştir.

Karşılařtırmalar, gri-olmayan tanecik özelliklerinin karmařık kırılma indeksinin tayfsal deęişiminden kaynaklandığını ortaya koymuş ve gri-olmayan tanecik özelliklerinin yanma sistemlerinde ışı nım ısı transferinin doęru hesaplanabilmesi için gerekli olduğunu göstermiştir. Ayrıca, kimyasal kompozisyonun gri-olmayan taneciklerin emme özellikleri, ısı akısı ve enerjisi üzerinde önemli bir etkisinin olduğu sonucuna varılmıştır. Taneciklerin toplam ışı nım ısı transferi üzerindeki baskın etkisinin de tanecik kimyasal kompozisyonuna baęlı olduğu tespit edilmiş ve bu durumun yüksek tanecik yüklerinde dahi geçerli olduğu görülmüştür. Buna baęlı olarak, yanma gazlarının veya taneciklerinin gri-olmayan davranışlarının ihmalinin, yüksek tanecik yüklerinde dahi ışı nım ısı akı ve ışı nım enerjisi tahminlerinde önemli hatalara yol açabileceęi sonucuna varılmıştır.

**Anahtar Kelimeler:** ışı nım ısı transferi, gri-olmayan gaz ışı nımını, gri-olmayan tanecik ışı nımını, akışkan yataklı yakıcı, kömür yanması



to Ceren  
&  
to life  
we will live  
to the fullest  
together

## ACKNOWLEDGMENTS

First and foremost, I would like to express my sincerest gratitude to Prof. Dr. Nevin Selçuk for her continuous support, encouragement, suggestions, wisdom, and trust on me. It has been a privilege and a great honor to study with such an outstanding, caring, and exceptional professor. Her invaluable advises have not only enlightened the path of this dissertation, but also become precious guidelines for the years ahead of me. She has shown me, by her own personality, how a good researcher, teacher and person should be. I am grateful to her for always supporting me.

I also owe my gratitude to my thesis supervisor Assoc. Prof. Dr. Görkem Külâh for her support, encouragement and guidance throughout this challenging process. It has been a pleasure to work with you, and a fortune to be guided by your precious experience.

I want to thank all former members of my research group for their irreplaceable contributions. I wish to express my greatest appreciations to Hakan Harmandar, Dr. Yusuf Göğebakan, Dr. Zuhâl Göğebakan and Dr. Aykan Batu, whom contributed my work through their measurements. I would like to give special thanks to Dr. Güzide Özen for her excellent support and guidance. Your criticism, suggestions and contributions were very valuable to me.

I would like to show my gratitude to my dear friends who were beyond being colleagues, Atalay Çalıřan, Necip Berker Üner, Mustafa Yasin Aslan, Deniz Kaya, Merve Özkutlu, Onur Dođu, Zeynep Karakař, Soner Yařar, Seda Sivri and Ezgi Yavuzylmaz. I would like to express my special thanks to Berrak Erkmen, Özge Batır and Burak Akdeniz, with whom I wish I had more time to spend together. It is hard to imagine finishing this study without your friendship and without our breakfast sessions. I also wish to express my thanks to my precious friends, Seren Ođuz and Nilay Tam, who have always been a family to me and supported me through good and bad times.

I especially thank my mom, dad, and sister for their love, endless trust and support. I would not have made it this far without them. I am also truly and deeply indebted to Ahmet Servet Özcan and Müzeyyen Özcan, my parents-in-law, for their love, care and selfless support throughout this long process.

And, I owe the most to my other half, my wife, Ceren, who has been there for me since the very beginning. I am so fortunate to be blessed with a someone like you. Thank you for relieving my tiredness with your warm smile, knowing how to make me smile, being the one whom I shared the best moments in my life, standing with me when I am in need, being strong when I am weak, and making me feel my best self. Thank you for being in my life, and for loving me the way you do. None of this could have happened without your care and support.

## TABLE OF CONTENTS

ABSTRACT.....	v
ÖZ.....	vi
ACKNOWLEDGMENTS.....	x
TABLE OF CONTENTS.....	xii
LIST OF TABLES.....	xvii
LIST OF FIGURES.....	xxi
LIST OF SYMBOLS.....	xxiii
CHAPTERS	
1 INTRODUCTION .....	1
1.1 Research Objectives .....	16
2 SOLUTION METHOD FOR RADIATIVE TRANSFER EQUATION (RTE) 19	
2.1 Radiative Transfer Equation (RTE) .....	19
2.1.1 RTE in Cylindrical Coordinate System .....	20
2.1.2 RTE in Rectangular Coordinate System .....	24
2.1.3 Radiative Heat Flux and Source Term.....	25
2.2 Discrete Ordinates Method (DOM).....	26
2.2.1 Parameters Affecting the Accuracy of DOM.....	32
2.3 Method of Lines (MOL) Solution of Discrete Ordinates Method (DOM) .35	
2.3.1 Parameters Affecting the Accuracy of MOL Solution DOM .....	37

2.4	Structure and Operation of the In-House Developed Code.....	40
3	RADIATIVE PROPERTY MODELS FOR GASES.....	47
3.1	Gas Property Models .....	47
3.2	Gray Gas Model based on Leckner’s Correlations.....	49
3.3	Gray Wide Band (GWB) Approximation .....	51
3.4	Gray Narrow Band (GNB) Approximation.....	53
3.5	Spectral Line-Based Weighted Sum of Gray Gases (SLW).....	54
3.5.1	Calculation of Absorption Coefficients .....	56
3.5.2	Calculation of Gray Gas Weights .....	57
3.5.3	Treatment of Non-Isothermal and Non-Homogeneous Media in SLW.....	64
3.5.4	Treatment of Binary Gas Mixtures in SLW.....	66
3.6	Banded Spectral Line-Based Weighted Sum of Gray Gases (banded SLW) .....	69
3.7	One-Gas Spectral Line-Based Weighted Sum of Gray Gases (SLW-1).....	73
4	RADIATIVE PROPERTY MODELS FOR PARTICLES .....	75
4.1	Radiative Properties of a Single Spherical Particle.....	77
4.1.1	Limiting Solutions of Maxwell Equations .....	79
4.1.2	Geometric Optics Approximation (GOA).....	80
4.1.3	Mie Theory.....	86
4.2	Radiative Properties of Polydisperse Particle Clouds .....	90
4.3	Scattering Phase Function Simplifications.....	94
4.4	Complex Index of Refraction Models .....	97
5	DESCRIPTION OF THE TEST CASES.....	101
5.1	300 kW <sub>t</sub> Atmospheric Bubbling Fluidized Bed Combustor Test Rig.....	101
5.1.1	Coal Combustion Tests .....	106
5.1.2	Coal Combustion Tests with Limestone and Biomass Addition .....	113

5.1.3	Treatment of the Freeboard in Radiative Heat Transfer Calculations .	122
5.2	150 kW <sub>t</sub> Circulating Fluidized Bed Combustor Test Rig .....	125
5.2.1	Coal Combustion Test.....	128
5.2.2	Treatment of the Dilute Zone in Radiative Heat Transfer Calculations .....	134
6	RESULTS AND DISCUSSIONS .....	143
6.1	Directional Nature of Particle Radiation.....	144
6.1.1	Benchmarking the Predictive Accuracy of In-House Developed Code .....	147
6.1.2	Selection of Gas Radiative Property Estimation Model .....	148
6.1.3	Selection of Particle Radiative Property Estimation Model .....	150
6.1.4	Spatial and Angular Discretization Refinement .....	152
6.1.5	Effect of Particle Scattering on Radiative Heat Transfer.....	157
6.2	Effect of Particle Size on Radiative Heat Transfer Calculations .....	162
6.2.1	Comparison between Geometric Optics Approximations for Particle Properties .....	163
6.2.2	Accuracy of GOA in Radiative Heat Transfer Predictions.....	164
6.3	Effect of Particle Size Distribution on Radiative Heat Transfer Calculations .....	172
6.4	Effect of Particle Load Distribution on Radiative Heat Transfer.....	179
6.4.1	Spatial Discretization Refinement .....	180
6.4.2	Effect of Particle Load Distribution on Radiative Heat Transfer .....	186
6.5	Effect of Limestone Addition on Radiative Heat Transfer .....	193
6.5.1	Effect of Limestone Addition on Radiative Properties of the Particle Cloud .....	194
6.5.2	Effect of Limestone Addition on Radiative Heat Transfer .....	201
6.6	Effect of Changing Biomass Source on Radiative Heat Transfer.....	205

6.6.1	Effect of Changing Biomass Source on Radiative Properties of the Particle Cloud.....	207
6.6.2	Effect of Changing Biomass Source on Radiative Heat Transfer.....	216
6.7	Investigation of the Spectral Nature of Particle Radiation.....	227
6.7.1	Banded Solution of RTE for Spectral Particle Radiation .....	228
6.7.1.1	Banded Particle Properties.....	229
6.7.1.2	Banded Solution of RTE for Spectral Particle Radiation and its Validation .....	240
6.7.2	Origins of the Spectral Nature of Particle Radiation .....	246
6.7.2.1	Selection of Spectral Complex Index of Refraction Models .....	249
6.7.2.2	Effect of Complex Index of Refraction on Spectral Particle Properties .....	253
6.7.2.3	Effect of Refractive Index on Heat Flux and Source Term Predictions.....	272
6.7.2.4	Sensitivity of Heat Flux and Source Term Predictions on Temperature Dependency of the Absorption Index (k) .....	275
6.7.2.5	Influence of Wall Temperature on Heat Flux and Source Term Predictions.....	278
6.7.2.6	Comparison between Spectrally-Averaged and Spectral Properties: Effect on Heat Flux and Source Term Predictions.....	283
6.7.2.7	Concluding Remarks on the Spectral Nature of Particle Radiation .....	286
6.7.3	Spectral Dependency of Phase Function Simplifications .....	287
6.8	Investigation of the Gas Property Models Compatible with Spectral Particle Radiation .....	295
6.8.1	Benchmarking the predictive accuracy of the radiation code .....	296
6.8.2	Spatial and Angular Discretization for ABFBC Test Rig.....	299
6.8.3	Testing the Predictive Accuracy of Proposed Gas Property Models ...	305
6.8.4	Accuracy of GWB Approximation in the Presence of Non-gray Particles .....	311
6.9	Influence of Spectral Particle Radiation on Predictive Accuracy of Gas Property Approximations .....	316

6.9.1	Comparison of Gas and Particle Absorption Bands .....	321
6.9.2	Sensitivity of Gas Property Approximations to Spectral Particle Radiation .....	324
6.10	Assessment of SLW-1 Model in the Presence of Gray / Non-Gray Particles .....	329
6.10.1	Benchmarking the predictive accuracy of MOL solution of DOM with SLW-1 .....	333
6.10.2	Testing the Predictive Accuracy of SLW-1 in ABFBC Test Rig .....	336
6.10.2.1	Testing the Predictive Accuracy of SLW-1 without Particles....	336
6.10.2.2	Testing the Predictive Accuracy of SLW-1 in the Presence of Gray Particles .....	340
6.10.2.3	Testing the Predictive Accuracy of Banded SLW-1 in the Presence of Non-Gray Particles .....	344
7	CONCLUSIONS.....	351
7.1	Suggestions for Future Work .....	354
8	REFERENCES .....	357
APPENDICES		
A.	ORDINATES AND WEIGHTS FOR SN APPROXIMATION.....	375
B.	BANDED SLW PARAMETERS.....	377
C.	COMPLEX INDEX OF REFRACTIONS MODELS FOR ASH PARTICLES.....	391
D.	RADIOMETER CALIBRATION CURVE.....	411
E.	PSD MEASUREMENTS FOR THE COMBUSTION TESTS.....	413
F.	CALCULATION OF PLANCK MEAN PROPERTIES .....	437
G.	SPECTRAL MIE SOLUTIONS FOR ASH I-V.....	441
	CURRICULUM VITAE.....	487



## LIST OF TABLES

Table 2.1 Total number of discrete directions specified by order of approximation .	33
Table 2.2 Spatial differencing schemes with FDM [90, 91] .....	38
Table 3.1 Fitting constants of Leckner's Correlations ( $c_{ij}$ ) for H <sub>2</sub> O (M=2, N=2).....	50
Table 3.2 Fitting constants of Leckner's Correlations ( $c_{ij}$ ) for CO <sub>2</sub> (M=3, N=4).....	50
Table 3.3 $blmn$ coefficients used in Eq. (3.16) for H <sub>2</sub> O [28].....	61
Table 3.4 $clmn$ coefficients used in Eq. (3.18) for H <sub>2</sub> O [28] .....	62
Table 3.5 $dlmn$ coefficients used in Eq. (3.20) for CO <sub>2</sub> [28].....	63
Table 4.1 Input Parameters for Goodwin's Model Equations.....	99
Table 5.1 Fuel characteristics of the Beypazarı Lignite.....	107
Table 5.2 Fuel ash analysis of the lignite used in SET I.....	107
Table 5.3 Operating conditions for the combustion tests in ABFBC .....	108
Table 5.4 Polynomials for temperature profiles.....	109
Table 5.5 Fly ash compositions and densities.....	112
Table 5.6 Characteristics of Çan lignite, olive residue and hazelnut shell .....	115
Table 5.7 Operating conditions of the combustion tests .....	116
Table 5.8 Polynomials for temperature profiles.....	118
Table 5.9 Fly ash compositions.....	121
Table 5.10 Characteristics of Çan lignite.....	128
Table 5.11 Çan lignite ash composition.....	129
Table 5.12 Operating parameters of the combustion test in CFBC .....	129
Table 5.13 Polynomials for temperature profiles.....	131
Table 5.14 CO <sub>2</sub> and H <sub>2</sub> O Concentration profiles .....	132
Table 5.15 Fly ash compositions.....	134
Table 6.1 Effect of gray gas model on predictive accuracy and CPU efficiency ....	148

Table 6.2 Effect of particle radiation model on predictive accuracy and CPU efficiency .....	152
Table 6.3 Effect of angular scheme refinement on predictive accuracy and CPU efficiency for the source term predictions .....	155
Table 6.4 Effect of grid refinement on predictive accuracy and CPU efficiency....	157
Table 6.5 Effect of scattering phase function simplifications on incident heat fluxes and sources terms.....	159
Table 6.6 Effect of angular discretization refinement on predictive accuracy and CPU efficiency of transport approximation.....	161
Table 6.7 Comparison of geometric optics approximations for various complex index of refraction values .....	164
Table 6.8 Gray gas and gray particle properties for Test 1-3 .....	165
Table 6.9 Effect of GOA on incident heat fluxes and sources terms.....	170
Table 6.10 Effect of PSD on radiative properties of particles .....	173
Table 6.11 Effect of PSD on incident heat flux and source term predictions.....	178
Table 6.12 Effect of grid refinement on predictive accuracy and CPU efficiency..	185
Table 6.13 Effect of particle load on incident heat fluxes .....	187
Table 6.14 Absolute percentage relative errors in the source terms at various axial and radial positions .....	192
Table 6.15 Radiative properties of particle laden combustion gases.....	199
Table 6.16 Radiative properties of particle laden combustion gases.....	214
Table 6.17 Differences in heat flux and source term predictions when OR is replaced by HS .....	226
Table 6.18 Effect of spectral discretization on predictive accuracy and CPU efficiency for the incident wall heat flux and source term predictions.....	244
Table 6.19 Fly ash compositions .....	247
Table 6.20 Average relative percentage errors in spectral refractive (n) and absorption (k) indices.....	252
Table 6.21 Average relative percentage errors in absorption efficiencies (Q <sub>a</sub> ), scattering efficiencies (Q <sub>s</sub> ) and asymmetry factor (g) for 10, 50 and 250 μm particles .....	263

Table 6.22 Average relative percentage errors in absorption coefficient ( $\kappa_p$ ), scattering coefficient ( $\sigma_p$ ) and asymmetry factor ( $g$ ) of Ash-IV for three particle clouds .....	269
Table 6.23 Average relative percentage errors in absorption coefficient ( $\kappa_p$ ), scattering coefficient ( $\sigma_p$ ) and asymmetry factor ( $g$ ) of Ash-I to V for BFBC particle cloud .	271
Table 6.24 Average relative percentage errors in incident wall heat fluxes ( $q_w$ ) and source terms along the centerline ( $\nabla q$ ) of Ash-I to V for BFBC combustion test ...	273
Table 6.25 Average relative percentage errors in incident wall heat fluxes ( $q_w$ ) and source terms along the centerline ( $\nabla q$ ) of Ash-I to V for the parametric study with panel tube walls (537 K) .....	280
Table 6.26 Average relative percentage errors in incident wall heat fluxes ( $q_w$ ) and source terms along the centerline ( $\nabla q$ ) of Ash-I to V for Planck mean property models .....	284
Table 6.27 Effect of phase function simplifications on incident heat fluxes and sources terms in the presence of non-gray particles.....	293
Table 6.28 Effect of phase function simplifications on incident heat fluxes and sources terms with gray Mie particles.....	294
Table 6.29 Input data for the benchmark problems .....	297
Table 6.30 Effect of spatial grid refinement on predictive accuracy and CPU efficiency .....	302
Table 6.31 Effect of angular grid refinement on predictive accuracy and CPU efficiency.....	304
Table 6.32 Effect of number of gray gases on predictive accuracy and CPU efficiency .....	304
Table 6.33 Predictive accuracy and CPU efficiency of gas models .....	310
Table 6.34 Effect of gas property approximations on incident heat fluxes and sources terms in the presence of non-gray particles.....	315
Table 6.35 Effect of gray particle assumption on the predictive accuracy of GWB model.....	326
Table 6.36 Maximum and average absolute percentage relative errors in total net heat flux ( $q_x$ ) and total divergence of the net heat flux ( $\text{div}q_x$ ) predictions.....	336
Table 6.37 Predictive accuracy and CPU efficiency of gas models .....	340

Table 6.38 Predictive accuracy and CPU efficiency of gas models in the presence of gray particles .....	343
Table 6.39 Predictive accuracy and CPU efficiency of gas model in the presence of non-gray particles.....	347
Table 6.40 Predictive accuracy of banded SLW-1 for each spectral band in the presence of non-gray particles .....	349

## LIST OF FIGURES

Figure 2.1 Directional cosines for cylindrical geometries .....	23
Figure 2.2 Directional cosines for rectangular geometries .....	24
Figure 2.3 Schematic representation of discrete directions represented by $m, \ell$ in one octant of a unit sphere for $S_4$ order of approximation.....	28
Figure 2.4 Orders of approximation.....	33
Figure 2.5 Schematic representation of MOL solution of DOM .....	37
Figure 2.6 Flowchart for MOLSDOM - AESM.....	44
Figure 2.7 Algorithm of the subroutine DERV_RAD .....	45
Figure 3.1 Spectral absorption cross-section of H <sub>2</sub> O at 1500 K generated from HITEMP 2010 database [93] .....	48
Figure 3.2 Spectral absorption cross-section of CO <sub>2</sub> at 1500 K generated from HITEMP 2010 database [93] .....	48
Figure 3.3 Approximation of a real spectrum by grouping into 4 gray gases [28] ....	54
Figure 3.4 Spectrum involving a few representative absorption lines and corresponding fraction of blackbody energy.....	58
Figure 3.5 Portions of the spectrum where absorption cross-section ( $C_{abs}$ ) is between two supplemental absorption cross sections ( $C_{abs,j}$ and $C_{abs,j + 1}$ ).....	59
Figure 3.6 Idealized gas temperature dependence of high-resolution spectrum resulting in equivalent blackbody fractions .....	65
Figure 3.7 Portions of the spectrum where the absorption-line blackbody distribution function for H <sub>2</sub> O-CO <sub>2</sub> mixture is calculated [28] .....	68
Figure 4.1 Dependent and independent scattering regimes [37].....	77
Figure 4.2 Scattering of incident radiation by a particle .....	79
Figure 4.3 Emissivity of different materials as a function of $\theta_1$ [37].....	82

Figure 4.4 (a) Diffraction phase function in GOA limit and (b) its demonstration in polar coordinates .....	84
Figure 4.5 (a) Reflection phase function in GOA limit (b) its demonstration in polar coordinates .....	85
Figure 4.6 Henyey-Greenstein phase function for several g values in polar coordinates .....	95
Figure 5.1 METU 300 kW <sub>t</sub> ABFBC Test Rig .....	103
Figure 5.2 Flow sheet of METU 300 kW <sub>t</sub> ABFBC Test Rig.....	104
Figure 5.3 Temperature profiles along the freeboard for (a) Test 1 and (b) Test 2 ..	110
Figure 5.4 (a) Differential and (b) cumulative particle size distributions in the freeboard for Test 1 and Test 2 .....	111
Figure 5.5 Temperature profiles along the freeboard for (a) Test 1-5 and (b) Test 1, 2, 6-8 .....	117
Figure 5.6 Cumulative particle size distributions for the particles collected from the cyclone for (a) olive residue and (b) hazelnut shell co-firing experiments .....	119
Figure 5.7 Cumulative particle size distributions for the particles collected from the baghouse filter for (a) olive residue and (b) hazelnut shell co-firing experiments ..	120
Figure 5.8 Treatment of freeboard as a 3-D enclosure [48].....	124
Figure 5.9 METU 150 kW <sub>t</sub> CFBC Test Rig .....	126
Figure 5.10 Process diagram of the CFBC test rig .....	127
Figure 5.11 Temperature profiles along the dilute zone .....	131
Figure 5.12 Gas concentration profiles along the dilute zone .....	132
Figure 5.13 Measured particle size distributions for CFBC combustion test .....	133
Figure 5.14 Treatment of the dilute zone as a 3-D enclosure .....	136
Figure 5.15 Particle load (a) and wall layer thickness (b) profiles along the riser in 1D model.....	139
Figure 5.16 Variations in particle load in (a) radial and (b) axial directions in 2D model .....	141
Figure 6.1 Effect of anisotropic scattering on the net radial radiative heat distribution .....	147
Figure 6.2 Effect of particle radiation on (a) incident wall heat flux and (b) source term predictions.....	149

Figure 6.3 Effect of particle radiation model on (a) incident wall heat flux and (b) source term predictions .....	151
Figure 6.4 Angular discretization for the incident wall heat flux predictions with (a) forward scattering and (b) isotropic scattering.....	153
Figure 6.5 Angular discretization for the source term predictions with (a) forward scattering and (b) isotropic scattering .....	154
Figure 6.6 Effect of spatial discretization for (a) incident wall heat flux and (b) source term predictions.....	156
Figure 6.7 Effect of scattering phase function simplifications on radiative (a) heat fluxes and (b) source terms .....	158
Figure 6.8 Sensitivity of transport approximation to angular discretization in (a) incident heat fluxes and (b) source terms calculations.....	160
Figure 6.9 Effect of GOA on incident heat fluxes for (a) Test 1, (b) Test 2 and (c)Test 3.....	166
Figure 6.10 Effect of GOA on source terms for (a) Test 1, (b) Test 2 and (c)Test 3 .....	168
Figure 6.11 Demonstration of the applicability of GOA limit based on cumulative cross sectional area distribution .....	171
Figure 6.12 Effect of particle size on the extinction, scattering and absorption efficiencies .....	174
Figure 6.13 Effect of particle size on the asymmetry factor .....	175
Figure 6.14 Effect of PSD on source term predictions for (a) Test 1 (b) Test 2 and (c) Test 3.....	177
Figure 6.15 Effect of spatial discretization on incident wall heat fluxes for (a) 0D, (b) 1D and (c) 2D particle load distribution models.....	181
Figure 6.16 Effect of spatial discretization on source terms for (a) 0D, (b) 1D and (c) 2D particle load distribution models.....	183
Figure 6.17 Effect of particle load distribution on incident wall heat fluxes.....	186
Figure 6.18 Effect of particle load on radial source term distributions .....	189
Figure 6.19 Effect of particle load on axial source term distributions.....	190
Figure 6.20 Spectral refractive indices for (a) cyclone and (b)baghouse filter particles .....	195

Figure 6.21 Spectral absorption indices for (a) cyclone and (b) baghouse filter particles .....	196
Figure 6.22 (a) Cumulative cross sectional area distribution and (b) particle number densities for Test 1-4.....	200
Figure 6.23 Effect of limestone share on (a) radiative incident wall heat fluxes and (b) heat fluxes averaged over the entire freeboard .....	202
Figure 6.24 Effect of limestone share on (a) source terms averaged in cross sectional planes and (b) source terms averaged over the entire freeboard.....	204
Figure 6.25 Spectral refractive indices for (a) cyclone and (b) baghouse filter particles .....	208
Figure 6.26 Spectral absorption indices for (a-c) cyclone and (d-f) baghouse filter particles .....	210
Figure 6.27 (a) Cumulative cross sectional area and (b) particle number density distributions.....	215
Figure 6.28 Effect of changing the biomass source on radiative incident wall heat fluxes for about (a) 15, (b) 35 and (c) 50 % biomass shares on thermal basis .....	218
Figure 6.29 Effect of changing the biomass source on source terms for about (a) 15, (b) 35 and (c) 50 % biomass shares on thermal basis .....	220
Figure 6.30 Effect of changing the biomass source on heat fluxes with cold wall assumption for (a) 15, (b) 35 and (c) 50 % biomass shares .....	222
Figure 6.31 Effect of changing the biomass source on source terms with cold wall assumption for (a) 15, (b) 35 and (c) 50 % biomass shares .....	224
Figure 6.32 Cumulative (f) and differential ( $\Delta f$ ) blackbody emissive power distributions under FBC conditions .....	230
Figure 6.33 Spectral particle (a) absorption coefficient, (b) scattering coefficient and (c) asymmetry factor with their banded representations for Test 1 .....	232
Figure 6.34 Spectral particle (a) absorption coefficient, (b) scattering coefficient and (c) asymmetry factor with their banded representations for Test 2 .....	234
Figure 6.35 Spectral particle (a) absorption coefficient, (b) scattering coefficient and (c) asymmetry factor with their banded representations for Test 3 .....	236
Figure 6.36 Distribution of radiant energy in spectral bands for Test 1 .....	238



Figure 6.37 (a) 4 banded and (b) 8 banded representations of spectral particle absorption coefficients for Test 1 .....	239
Figure 6.38 Effect of spectral discretization in heat flux predictions for (a) Test 1, (b) Test 2 and (c) Test 3 .....	240
Figure 6.39 Effect of spectral discretization in source term predictions for (a) Test 1, (b) Test 2 and (c) Test 3 .....	242
Figure 6.40 Validation of banded RTE solution for (a) Test 1 and (b) Test 2 .....	245
Figure 6.41 Particle size distributions used in the evaluation of non-gray particle properties .....	248
Figure 6.42 Spectral refractive indices calculated by using different RI models for (a) Ash-I to (e) Ash-V .....	250
Figure 6.43 Spectral absorption indices calculated by using different RI models for (a) Ash-I to (e) Ash-V .....	251
Figure 6.44 Comparison of absorption efficiencies (Q <sub>a</sub> ) for (a-c) Ash-I, (d-f) Ash-III and (g-i) Ash-V .....	255
Figure 6.45 Comparison of scattering efficiencies (Q <sub>s</sub> ) for (a-c) Ash-I, (d-f) Ash-III and (g-i) Ash-V .....	258
Figure 6.46 Comparison of asymmetry factors (g) for (a-c) Ash-I, (d-f) Ash-III and (g-i) Ash-V .....	260
Figure 6.47 Comparison of representative (a-c) particle absorption coefficients, (d-f) scattering coefficients and (g-i) asymmetry factors for PC-Fired furnace, BFBC and CFBC for Ash-IV .....	267
Figure 6.48 Comparison of (a) heat flux and (b) source term predictions for Ash-IV .....	274
Figure 6.49 Comparison of (a) absorption indices, (b) particle absorption coefficients, (c) heat flux and (d) source term distributions for Ash-IV at 295 K and 1163 K....	276
Figure 6.50 Comparison of heat flux (a) and source term predictions (b) for Ash-IV in the parametric study with panel tube walls (537 K) .....	281
Figure 6.51 Comparison of heat flux (a) and source term predictions (b) of Planck mean approximations for Ash-II in the parametric study with panel tube walls (537 K) .....	285

Figure 6.52 Effect of phase function simplifications on incident heat fluxes for (a) Test 1, (b) Test 2 and (c) Test 3 in the presence of non-gray particles.....	289
Figure 6.53 Effect of phase function simplifications on sources terms for (a) Test 1, (b) Test 2 and (c) Test 3 in the presence of non-gray particles.....	291
Figure 6.54 Comparison between in-house developed radiation codes and MC solution for (a) Test Problem 1 and (b, c) Test Problem 2 .....	298
Figure 6.55 Effect of spatial discretization on (a) incident wall heat fluxes and (b) source terms .....	301
Figure 6.56 Effect of angular discretization on (a) wall heat fluxes and (b) source terms.....	303
Figure 6.57 (a) Comparison of spectral gas absorption coefficients ( $\kappa_{g,\lambda}$ ) calculated from HITRAN and HITEMP databases and (b) their banded representations .....	307
Figure 6.58 Comparison between (a) heat flux and (b) source term predictions of different gas models.....	308
Figure 6.59 Measured and predicted incident radiative heat fluxes for (a) Test 1 and (b) Test 2 .....	312
Figure 6.60 Effect of GWB approximation on source term predictions for (a) Test 1 and (b) Test 2 .....	313
Figure 6.61 Spectral (a) refractive index and (b) absorption index data for Ash I-III .....	319
Figure 6.62 (a, b) Particle absorption coefficients, (c, d) scattering coefficients and (e, f) asymmetry factors for (a, c, e) Test 1 and (b, d, f) Test 2 .....	320
Figure 6.63 Ratio of gas absorption coefficient to total absorption coefficient predicted with gray and non-gray particles for Test 1 (a-c) and Test 2 (d-f) .....	323
Figure 6.64 Comparison of heat flux predictions with non-gray (a-c) and gray particles (d) for Test 2 in the parametric study with panel tube walls (537 K).....	327
Figure 6.65 Comparison of source term predictions with non-gray (a-c) and gray particles (d) for Test 2 in the parametric study with panel tube walls (537 K) .....	328
Figure 6.66 Non-gray (a) absorption coefficients, (b) scattering coefficients and (c) asymmetry factors for the polydisperse fly ash particles with their gray representations .....	332

Figure 6.67 Comparison between (a) total net heat flux and (b) total divergence of the net heat flux predictions of the present study and reference solutions .....	335
Figure 6.68 Effect of gray gas and SLW-1 models on incident radiative heat fluxes for (a) Test 1 and (b) Test 2 .....	338
Figure 6.69 Effect of gray gas and SLW-1 models on source terms for (a) Test 1 and (b) Test 2 .....	339
Figure 6.70 Comparisons between measurements and model predictions in the presence of gray particles for (a) Test 1 and (b) Test 2 .....	341
Figure 6.71 Comparison between source term predictions of gray gas, SLW-1, and SLW models in the presence of gray particles for (a) Test 1 and (b) Test 2 .....	342
Figure 6.72 Comparisons between measurements and model predictions in the presence of non-gray particles for (a) Test 1 and (b) Test 2 .....	345
Figure 6.73 Comparison between source term predictions of gray gas, banded SLW-1, and banded SLW models in the presence of non-gray particles for (a) Test 1 and (b) Test 2 .....	346
Figure 6.74 Comparison between source term predictions of banded SLW-1 approximations in the presence of non-gray particles for band 4 .....	350

## LIST OF SYMBOLS

$a$	gray gas weight, (-)
$a$	particle load decay constant
$a_n$	Mie scattering coefficient, (-)
$A$	forward scattering normalization factor
$A_c$	total cross sectional area of the particles, (m <sup>2</sup> )
$B$	particle load, (kg m <sup>-3</sup> )
$B$	backward scattering normalization factor
$B_i$	mass retained in sieve $i$ , (kg)
$b_n$	Mie scattering coefficient, (-)
$c$	clearance between particles, (m)
$c$	speed of light, (m/s)
$C$	absorption cross-section
$C_{abs}$	absorption cross section of participating gases
$\tilde{C}_{abs}$	supplemental absorption cross section of participating gases
$D$	logarithmic derivative
$d_p$	particle diameter, (m)
$e_i$	unit vector in the coordinate direction $i$ , (-)
$E_s$	scattered energy
$F$	blackbody distribution function, (-)
$g$	asymmetry factor, (-)

$g'$	expansion coefficient, (-)
$G$	incident radiation, ( $\text{Wm}^{-2}$ )
$H_{\text{exit}}$	height of the combustor, (m)
$H_x$	height of the dense bed, (m)
$I$	radiative intensity, ( $\text{Wm}^{-2}\text{sr}^{-1}$ )
$I_b$	blackbody intensity, ( $\text{Wm}^{-2}\text{sr}^{-1}$ )
$J_1$	1 <sup>st</sup> order Bessel function, (-)
$k$	imaginary part of complex refractive index, absorption index (-)
$K$	particle load decay constant
$k_t$	time constant, ( $\text{m/s}$ ) <sup>-1</sup>
$L$	total number of directions in an ordinate, (-)
$L_m$	mean beam length, (m)
$m$	complex index of refraction, (-)
$M$	total number of ordinates, (-)
$\mathbf{n}$	unit normal vector, (-)
$n$	order of accuracy of the chosen spatial differencing scheme, (-)
$n$	real part of complex refractive index, refractive index, (-)
$N$	order of approximation of $S_N$ angular quadrature scheme, (-)
$N_i$	molar density of gas $i$ , ( $\text{mole m}^{-3}$ )
$N(d_p)$	particle size distribution function
NB	number of wide bands for particles, (-)
ND	number of octants, (-)
NM	number of ordinates specified by the order of angular quadrature, (-)
NX, NY, NZ	number of nodes along x, y and z directions, (-)
NR	number of nodes along r direction, (-)
NGW, NGC	number of gray gases for water vapour and carbon dioxide, (-)
P	pressure, (bar)
$P_n$	Legendre polynomial of degree $n$ , (-)

$q$	radiative heat flux, ( $\text{Wm}^{-2}$ )
$q^+$	incoming wall heat flux, ( $\text{Wm}^{-2}$ )
$q^-$	leaving wall heat flux, ( $\text{Wm}^{-2}$ )
$Q_a$	absorption efficiency, (-)
$Q_e$	extinction efficiency, (-)
$Q_s$	scattering efficiency, (-)
$\mathbf{r}$	position vector, (-)
$R$	radius of the spherical particle, (m)
$\mathbf{r}_w$	position vector at the boundary, (-)
$r, \phi, z$	cylindrical coordinates
$s$	direction of intensity (-)
$t$	time
$T$	total number of particle sizes under consideration, (-)
$T$	temperature, (K)
TF	final time of integration, (s)
TP	print interval, (s)
$u_g$	gas velocity, ( $\text{m s}^{-1}$ )
$u_t$	terminal velocity, ( $\text{m s}^{-1}$ )
$u_0$	superficial air velocity, ( $\text{m s}^{-1}$ )
$w$	quadrature weight, (-)
$x$	size parameter, (-)
$x, y, z$	cartesian coordinates, (m)

### **Greek symbols**

$\alpha$	absorptivity, (-)
$\beta$	extinction coefficient, ( $\text{m}^{-1}$ )
$\gamma$	angular differencing coefficient, (-)
$\delta$	wall layer thickness, (m)
$\varepsilon$	emissivity, (-)

$\varepsilon$	local voidage, (-)
$\varepsilon_{Av}$	cross-section averaged voidage at any given height, (-)
$\varepsilon_{mf}$	voidage of the bed at minimum fluidization velocity, (-)
$\varepsilon$	error tolerance, (-)
$\eta$	direction cosine, (-)
$\theta$	polar angle, (rad)
$\Theta$	scattering angle, (rad)
$\kappa$	absorption coefficient, ( $m^{-1}$ )
$\lambda$	wavelength, ( $\mu m$ )
$\mu$	direction cosine, (-)
$\xi$	direction cosine, (-)
$\xi_n$	Ricatti-Bessel function
$\psi_n$	Ricatti-Bessel function
$\rho$	reflectivity, (-)
$\rho$	particle load (concentration), ( $kg\ m^{-3}$ )
$\rho_{\perp}$	normal reflectivity, (-)
$\bar{\rho}$	average reflectivity, (-)
$\bar{\rho}$	average particle load (concentration), ( $kg\ m^{-3}$ )
$\rho_{exit}$	particle load at the top of the combustor, ( $kg\ m^{-3}$ )
$\rho_x$	particle load at the top of the dense bed, ( $kg\ m^{-3}$ )
$\rho_p$	particle density, ( $kgm^{-3}$ )
$\sigma$	Stefan-Boltzmann constant = $5.67 \times 10^{-8}$ ( $Wm^{-2}K^{-4}$ )
$\sigma$	scattering coefficient, ( $m^{-1}$ )
$\tau$	optical thickness, (-)
$\tau$	transmissivity, (-)
$\phi$	azimuthal angle, (rad)
$\Phi$	scattering phase function, ( $sr^{-1}$ )
$\omega$	single scattering albedo, (-)

$\Omega$	direction vector of radiation intensity, (-)
$\Omega'$	direction vector of incident radiation intensity, (-)
$d\Omega$	solid angle, (sr)
$\Omega_m$	ordinate direction, (-)

### Subscripts

a	absorption
c	carbon dioxide index
e	extinction
g	gas
HG	Henyey – Greenstein function
j	wide band index
k	water vapour index in SLW model
l	carbon dioxide index in SLW model
$\ell'$	incoming discrete direction
$\ell$	index for a discrete direction
$\ell'$	index for a discrete incoming direction
$\ell'^-$	discrete backward direction
m	medium
m	ordinate index
$m'$	incoming ordinate
p	particle
r	radiative
s	scattering
tr	modified parameter in transport approximation
w	wall
w	water vapour index
'	incoming direction index



## Superscripts

m	ordinate index
m'	incoming ordinate
'	incoming

## Abbreviations

1D	One-Dimensional
2D	Two-Dimensional
3D	Three-Dimensional
8D	Eight-Dimensional
ABFBC	Atmospheric Bubbling Fluidized Bed Combustor
CFBC	Circulating Fluidized Bed Combustor
CFD	Computational Fluid Dynamics
DDS	Diamond Differencing Scheme
DOM	Discrete Ordinates Method
DSS012	Two-Point Upwind Differencing Scheme
DSS014	Three-Point Upwind Differencing Scheme
FBC	Fluidized Bed Combustion
FC	Fixed Carbon
FDM	Finite Difference Method
GG	Gray Gas
GNB	Gray Narrow Band Model
GOA	Geometric Optics Approximation
GWB	Gray Wide Band Model
HG	Henyey-Greenstein
LHV	Lower Heating Value
MC	Monte Carlo
MOL	Method of Lines
NSTOP	terminating step in Mie solution

ODE	Ordinary Differential Equation
PDE	Partial Differential Equation
PSD	Particle Size Distribution
RI	Complex Index of Refraction
RTE	Radiative Transfer Equation
SLW	Spectral Line-Based Weighted Sum of Gray Gases
VM	Volatile Matter
WSGG	Weighted sum of Gray Gases

# CHAPTER 1

## INTRODUCTION

Due to increase in population, industrialization and development in technology, electrical energy requirement of the world is increasing rapidly. To meet this demand, coal, which offers the greatest proven reserves, is utilized as a major energy source for electricity production today (9707 TWh) and share of coal in electricity production is estimated to be around 15305 TWh by 2040, which indicates about 60 % increase in coal based electricity generation [1]. Furthermore, coal is available in more than 100 countries distributed over all continents with high reserve/consumption ratio (127 years with 985 billion tons of proven reserves) compared to other types of fuels, which secures continuous supply at low price [1]. There exist geographically well spread lignite reserves in Turkey with an estimated total quantity of 15.6 billion tons [2]. A major proportion of this quantity is low quality lignite, which is characterized by its high moisture, sulfur and ash contents and low heating values. These heating values are reported to vary between 1000 and 4200 kcal/kg where about 90 % of the lignite has a gross calorific value lower than 3000 kcal/kg [2, 3].

Despite low heating value and high ash content of indigenous lignites, it has been used, with various degrees of success, in large pulverized coal-fired (PC-fired) utility power boilers to provide energy source for electricity generation, which is a technology developed for burning high quality coals. The ash constituents have posed significant design and operational problems due to their low ash fusion temperatures compared to

typical operating temperatures of PC-fired furnaces (1200-1500 °C) and necessitated special countermeasures such as reducing the operating temperatures to minimize slagging and fouling of heat transfer surfaces. Although acceptable results have eventually been achieved in some cases, these have been at the cost of considerable delays in project start-up, high capital investment, stringent operational vigilance, and frequent and expensive maintenance and repair [4].

Fluidized bed combustion technology is usually indicated to be the best choice within the available technologies for combusting low quality fuels like Turkish lignite due to its fuel flexible feature, high combustion efficiency and uniform and low combustion temperature (750-950°C) [5-7]. Due to these low operating temperatures, fluidized bed combustion technology offers the industry and utilities an alternative method to alleviate the slagging / fouling problems, reduce NO<sub>x</sub> formation and decrease SO<sub>x</sub> emissions with in-situ desulfurization with limestone addition [8, 9]. With these advantages, applications of fluidized bed combustion technology in Turkey have been steadily increasing in both capacity and number over the past decades.

Heat transfer in fluidized beds has been an important issue in the design, operation and optimization of industrial combustors and utility boilers [10, 11]. It is well known that thermal radiation accounts for the majority of the heat transferred in combusting systems and the share of radiation has been shown to exceed 70 % in fluidized bed combustors (FBCs) [12]. Therefore, modelling of radiative heat transfer in such systems is of considerable importance and necessitates not only accurate but also computationally efficient methods for (i) solution of the radiative transfer equation (RTE) in conjunction with the time-dependent conservation equations for mass, momentum, energy, and chemical species and (ii) radiative property estimation of particle laden combustion gases.

Previous work regarding the search for the most accurate and computationally efficient solution method in the freeboard of fluidized bed combustors revealed that Method of Lines (MOL) solution of Discrete Ordinates Method (DOM) meets all the requirements [13-15]. Assessment of the accuracy of this solution method was previously validated against exact solutions, Monte Carlo and zone method solutions, as well as measurements on a wide range of one-dimensional and multidimensional problems in rectangular and

cylindrical coordinates including absorbing, emitting, strongly anisotropically scattering media bounded by gray, diffuse walls [16-20].

With respect to radiative property modelling, which is the focus of this work, one of the most difficult aspects is the spectral dependence of those properties. For gas radiation, a wide variety of gas spectral radiative property models with different degrees of complexity and accuracy are available in the literature [21]. The line-by-line (LBL) method, which is an exact treatment of spectral properties, is extremely computationally intensive for practical engineering applications and requires the solution of radiative transfer equation (RTE) for over  $10^6$  wavelengths hence serves only as a benchmark to test the accuracy of other approximate models. Narrow band models such as statistical narrow band (SNB) and exponential wide band (EWB) models are designed to approximate this complex non-gray gas behavior over wave number intervals [21]. A drawback of these models is that they provide gas transmissivities or absorptivities instead of absorption coefficients, which are required for the differential solution of the RTE. Hence, there has been an increasing effort toward the development of gas spectral radiative property models which yield absorption coefficients and therefore are suitable for incorporation into any RTE solution technique. The correlated-k (CK) distribution model, originally developed by Goody et al. [22] and Lacis and Oinas [23] for atmospheric radiation, is one of these models. This model neglects the variation of blackbody intensity over a band and therefore enables the replacement of spectral integration over the wave number within a band by a quadrature over the absorption coefficient. Nevertheless, CK model utilizes prescribed quadrature and fixed wavenumber subdivisions and it is not possible to change or refine the spectral resolution of the RTE solution (23 and 46 semi wide bands for  $\text{CO}_2$  and  $\text{H}_2\text{O}$  respectively) [24]. These constraints can be alleviated by deploying a hybrid method called statistical narrow band CK (SNBCK), which enables the user to select any spectrum intervals for solution of RTE. This method has been shown to lead to very accurate results and considered to be as a reference solution [25], although it is computationally very demanding if narrow bands are utilized. Global models offer a solution for this high CPU requirement of banded models by approximating the radiative properties of the gases over the entire spectrum instead of wave number intervals. The most commonly used global model is the weighted

sum of gray gases (WSGG) model, which was originally developed by Hottel and Sarofim [26] within the framework of the zone method. Later, Denison and Webb improved this model to the spectral line-based weighted sum of gray gases (SLW) model by expressing the gray gas weights in terms of an absorption-line blackbody distribution function [27-29] derived from the high resolution HITRAN and HITEMP database [28, 30]. SLW has been validated against reference solutions on a wide variety of problems including absorbing-emitting and scattering media and shown to be the best choice with regard to computational time and accuracy [24, 27-29, 31, 32]. Furthermore, implementation of SLW into CFD software packages such as Fluent [33, 34] or OpenFoam [35] is also available in the literature.

Unlike participating gases, particles continuously emit and absorb radiation in the entire spectrum and may also scatter radiation depending on their size. Despite the fact that spectral properties of particles demonstrate a less complex behaviour contrary to that of gas radiation [21], modelling of particle radiation involves other challenges. Particle radiation depends on its absorption coefficient, scattering coefficient and scattering phase function, which in turn depend on composition, density, temperature, load, size and size distribution of particles. Chemical composition, particle density and temperature are also the major factors which determine the complex index of refraction (RI) of particles [36]. RI ( $m = n - ik$ ;  $i$  is the solution of the equation  $x^2 = -1$ ) is one of the fundamental parameters defining particle-radiation interactions [37] and it was shown to be a strong function of wavelength [36]. Nevertheless, wavelength dependency of RI of particles (hence the particle properties) is often neglected in the majority of the relevant literature as it is common to use a gray approach by deploying representative RI values for different particle types such as coal, char and ash particles [37]. Owing to the important role of particles in radiative heat transfer, however, there are some studies where spectral properties of particles have been considered.

In one of the early works on spectral particle properties, Mengüç and Viskanta [38] investigated the effect of spectral fly ash particle properties on an idealized cold (0 K) 1D slab problem. In this parametric work, monodisperse fine particles (1, 5, 10  $\mu\text{m}$ ) at low volume fraction ( $10^{-6}$ ) is assumed to be present between 1D parallel plates and effect of

spectral RI on scattered radiation is investigated without gas radiation. Comparisons revealed that distribution of radiant energy may be strongly dependent on the spectral complex index of refraction data of fly ash particles [38].

Goodwin and Mitchner [39] experimentally investigated the effect of spectrally dependent optical properties (RI) on particle properties. They took the optical constants from their own measurements [36] and calculated spectral absorption ( $\overline{Q_a}$ ) and scattering efficiencies ( $\overline{Q_s}$ ) and asymmetry factors ( $\overline{g}$ ) averaged over particle size distribution (PSD). They also evaluated total emissivities and transmissivities within an idealized 1D slab containing combustion gases and fly ash particles. Their calculations reveal that presence of fly ash particles increases the medium emissivity about 20 % compared to the case where only gas radiation is considered. Their study also revealed that radiative particle properties averaged over PSD ( $\overline{Q_a}$ ,  $\overline{Q_s}$ ,  $\overline{g}$ ) is highly non-gray for particle sizes relevant to PC-fired furnaces.

Mengüç et al. further extended their previous work [38] to an idealized 1D slab problem involving absorbing, emitting, and anisotropically scattering (linear anisotropy) medium [40]. In this problem, temperature profile was assumed to be non-uniform and particle properties were calculated by using local temperatures. Spectral RI values were taken from a previous measurement [36]. Nevertheless, particle size was still kept uniform (1, 5, 10  $\mu\text{m}$ ) as in their previous work and all other variables were selected arbitrarily [38]. They solved the radiative transfer equation (RTE) for 8 different wavelengths and compared the radiative heat flux and source terms predictions obtained by using spectral and gray particle properties. These comparisons showed that source terms calculated with spectral radiative properties are about 50% larger than those calculated from gray particle properties.

Effect of spectral optical constants on radiative heat transfer was also tested in several other parametric studies in the following years. Bhattacharya [41] presented a sensitivity analysis on the influence of spectral RI on wall emittance and particle cloud properties. He tested 16 different gray / non-gray RI values selected parametrically for two PSDs, which correspond to mean sizes of 3 and 15  $\mu\text{m}$ , respectively. He calculated spectral and total emissivities for (i) an ash slag layer deposited on the wall and (ii) particle cloud in

an idealized 1D slab containing absorbing, emitting, anisotropically scattering particles. His investigations revealed that wall/particle cloud emissivities are strongly influenced by the variation in absorption indices ( $k$ ) while they are much less sensitive to variations in refractive indices ( $n$ ). He also showed that particle size distribution can be more important than the emissivity of the ash particle cloud in radiative heat transfer calculations. It should be noted at this point that particle size and RI range investigated in this study was limited hence these outcomes should be considered within the limits of those parameters.

In another parametric study, Caliot et al. [42] investigated the influence of RI on particle radiative properties in an idealized 1D plane problem containing participating gases ( $H_2O$  and  $CO_2$ ) and monodisperse particles. Particle size was varied between 0.1-200  $\mu m$  for a volume fraction range of  $10^{-7}$ - $10^{-3}$ . Refractive ( $n$ ) and absorption ( $k$ ) indices of particles were changed between 1.7-2.5 and  $10^{-4}$ -20, respectively. Although particle absorption ( $Q_a$ ) and scattering ( $Q_s$ ) efficiencies were evaluated spectrally, only spectrally averaged (Planck mean) quantities ( $\overline{Q_a}$ ,  $\overline{Q_s}$ ) were compared for a wide range of particle size and volume fractions. These comparisons showed that particle absorption efficiencies increase with increasing absorption index ( $k$ ). Furthermore, contribution of gas radiation to total radiative heat transfer was found to be insignificant when particle volume fraction becomes greater than  $10^{-6}$  for large ( $k$ ) values ( $k > 0.1$ ).

Liu and Swithenbank [43] reported the first investigation regarding to the effect of spectral RI on particle absorption, scattering and extinction coefficients for polydisperse particle clouds, which were collected from a small scale PC-Fired furnace. They compared spectrally averaged particle properties (Planck mean) with gray particle properties and concluded that negligence of the spectral nature of particle properties lead to unacceptable results. It should be noted that their work is based on RI measurements for a specific ash composition taken from [36] and they formulated simple model equations to represent the spectral RI of ash particles.

Marakis et al. [44] extended the work of Liu and Swithenbank [43] in a parametric study and investigated the effect of optical properties on the overall heat transfer in a PC-Fired furnace. Different from the previous work, they also included coal and char particles in addition to ash particles and compared the relative magnitudes of radiative heat fluxes due



to gas, coal, char and ash radiation in a 2D enclosure representing PC-fired furnaces. Nevertheless, they neglected the spectral variations in particle radiative properties and used Planck mean properties in radiative heat transfer calculations. It should also be noted that Marakis et al. modified the spectral RI model equations derived by Liu and Swithenbank in their calculations (hence they also neglected the chemical composition dependency of RI) to include the effect of temperature variations on the RI values. Their investigations revealed that majority of wall heat fluxes are due to coal and char particles and contributions of combustion gases / ash particles to wall heat fluxes are small. The reason behind the dominance of coal/char particles is considered to be due to the fact that coal/char particle loads were assumed to be three orders of magnitude higher than that of ash particles [44].

Bahador and Sunden [45] investigated effect of fly ash particles on a biomass-fired boiler in a 3D enclosure. They modified the RI model equations given by [43] and evaluated radiative properties of particle clouds by averaging over Planck distribution. Particle volume fraction was the focus of this study and they investigated the radiative heat transfer within the boiler by changing the particle volume fraction between  $10^{-6}$  and  $10^{-5}$ . Comparison between radiative heat fluxes and source terms reveal that particle radiation becomes much more dominant with increasing particle volume fraction.

In the work of Butler and co-workers [46], they measured radiative and total heat fluxes in a 100 kW<sub>t</sub> PC-fired furnace. They also modelled the radiative heat transfer within the combustor by using both gray and spectral particle properties. In spectral solutions, Edward's wide band model was used for gas radiation while Mie theory was utilized for particle radiation. In spectral Mie solutions, spectral RI was taken from one of Goodwin's measurements [36]. In gray solutions, gas radiative properties were represented with an effective emissivity while gray particle properties were found by averaging the spectral properties via Planck and Patch mean averaging. Comparison between predicted radiative heat fluxes obtained from spectral and gray calculations with experimental data revealed that RTE solution with spectral properties gives the best agreement with the measurements. Furthermore, predictions obtained with Planck mean properties were found to be close to those of spectral solutions.

There are also some studies which highlights the discrepancy between Planck mean and spectral particle properties. Mischler and Steinfeld [47] worked on the radiative heat transfer in an idealized 1D slab problem containing absorbing emitting anisotropically scattering magnetite ( $\text{Fe}_2\text{O}_3$ ) particles. They compared the transmitted incident radiation through the  $\text{Fe}_2\text{O}_3$  particle cloud and calculated the temperature distribution within the slab by using spectral and Planck mean particle properties. Their comparisons revealed that Planck mean averaging of the spectral particle properties leads to 27 % errors in temperature field predictions. Ruan et al. [48] further extended the work of [47] for ash particles by comparing the predictions of Planck mean and Rosseland mean particle properties with those of spectral particle properties for an idealized 1D slab. They compared medium transmissivity, emissivity and reflectivity as well as emissive power and heat fluxes. These comparisons showed that predictive accuracy of Rosseland mean particle properties are acceptable while Planck mean particle properties can lead to significant errors depending on the particle volume fraction and size of the particles.

Recently, Hofgren and Sunden [49] investigated the effect of using Planck mean particle properties for ash particles for two different PSDs representing biomass and coal combustion. They calculated the radiative heat fluxes and source terms in an idealized 1D plane for four different arrangements with different temperatures, particle loads and wall emissivities. They compared the predictions obtained with Planck mean solutions with LBL calculations. These detailed investigations showed that average percentage errors in heat flux predictions due to Planck mean averaging of particle properties can be as high as 70 % while the average errors in source term predictions were found to be around 100 %.

Johansson et al. [50] investigated the radiative heat flux and source term distributions in 1D infinitely long cylinder (i.e., RTE is solved in only radial direction) for the conditions relevant to oxy-fired coal combustion. In the calculations, they used spectral gas (SNB) and particle properties (Mie theory). For particle radiation, they utilized chemical composition independent RI model equations. They parametrically investigated the influence of RI and particle load on heat flux predictions. These comparisons demonstrated that both RI and particle load has a large impact on the predicted wall heat

fluxes. They also compared the relative magnitudes of gas and particle radiation and showed that particle radiation dominates the total radiation even under oxy-fired conditions.

In particle radiation, another equally important challenge is the scattering. In particle radiation, knowing the amount of absorbed and scattered radiation by the particles is not enough to fully describe particle radiation interactions. Scattering phase function, which gives the probability that light incident on a particle in a given direction to be scattered into any other direction, is also required. In general, scattering phase function can be calculated numerically from Mie theory for simple geometries. However, solution of Mie theory is oscillatory in nature and numerical solutions for the scattering phase function become impractical especially for large particles. This is why approximate phase functions are usually preferred in the community. Isotropic scattering and nonscattering assumptions are the most commonly used approximations to simplify the solution of RTE as well as to reduce the computational effort for particle property evaluations. In isotropic scattering, equal amounts of radiation are assumed to be scattered into all directions while nonscattering assumption simply states that particles do not scatter thermal radiation. In fact, use of isotropic scattering assumption has been found to lead to fairly accurate results for combusting systems involving low particle loads such as pulverized fuel and bubbling fluidized bed furnaces although there is also some contradictory evidence.

Pallarez et al. [51] worked on CFD modelling of co-firing coal and biomass in a 350 MW<sub>e</sub> utility boiler. In the radiation model, particles are assumed to be gray and scatter radiation isotropically. Validation of the simulations is done by using measured temperatures and gas concentrations at the inlet section of the superheater, where the predictions obtained by using isotropically scattering particles were found to be in very good agreement with the measurements. In a similar study, Kangwanpongpan et al. [52] investigated oxy-fired coal combustion in 100 kW<sub>t</sub> pilot scale PC-fired furnace in ANSYS FLUENT. RTE is solved by using DOM with non-gray (WSGG) and isotropically scattering gray particles. Validation of the results are provided by comparing the predictions of temperature and velocity distributions against measurements. Similar to previous work, predictions obtained by using isotropically scattering particles were found to be in very good

agreement with the measurements. Crnomarkovic et al. [53] investigated the effect of non/isotropic scattering assumptions on temperature and radiative heat transfer predictions with a CFD study in a 210 MW<sub>e</sub> PC-fired furnace. In the radiation model, RTE is solved by using six-flux method. Both participating gases and particles are assumed to be gray. Incident heat flux and temperature measurements are used to validate the CFD model predictions. It is found that the difference between incident radiative heat fluxes obtained by using isotropic scattering and nonscattering can become as large as 70 % (average difference in heat fluxes obtained by using isotropic and nonscattering assumptions was found to be 16 %). Based on the comparisons between measurements and model predictions, isotropic scattering phase function was recommended for PC-fired furnaces. Use of isotropic scattering assumption is also found to lead to fairly accurate results in the recent CFD literature for coal combustion [54-59].

In addition to above mentioned CFD studies, effect of phase function simplifications was also tested in isolated radiative heat transfer studies, that is, radiation models were tested in isolation from the modelling of other physical processes (conservation equations for mass, momentum, energy and chemical species) by using prescribed input data, which eliminates the inaccuracies in the models used for the prediction of flow, reaction, other heat transfer mechanisms. One of the earliest isolated radiative heat transfer studies on phase function simplification was carried out by Yuen and Wong in an idealized 1D slab containing gray, absorbing, emitting and anisotropically scattering particles surrounded by isothermal, gray and diffuse walls [60]. They compared the heat flux predictions obtained by isotropic scattering with those of forward scattering. Comparisons showed that accurate representation of forward scattering peak is important and discrepancy between isotropic scattering and forward scattering increases with increasing optical thickness. However, it should be noted that forward scattering was represented by considering only two terms in the series solution of phase function, which is a very crude approximation.

Mengüç and Viskanta [61] investigated the effect of phase function simplifications on radiative heat fluxes in an axisymmetric cylindrical enclosure representing PC-fired furnaces. Radiative properties of gases and particles are assumed to be gray and RTE is

solved by using spherical harmonics method. Anisotropic scattering was represented by Delta-Eddington phase function, which is a more accurate method compared to the one used by Yuen and Wong [60]. They found that isotropic scattering assumption under-predicts the wall heat fluxes by about 35 % while nonscattering assumption over-predicts the heat fluxes up to 100 %, especially in the burnout region.

These large differences, however, were claimed to be unreliable by a later study of Truelove [62]. He solved the same problem with DOM and compared the predictions of both spherical harmonics and DOM with those of zone method, which is accepted as one of the most accurate solution methods in the literature [37]. These comparisons show that predictions obtained with the spherical harmonics method are incorrect and there exists little difference between the heat fluxes obtained by isotropic scattering and nonscattering assumptions for the simple problem under consideration.

Liu and Swithenbank [63] also utilized the Delta-Eddington phase function in order to investigate effect of phase function simplifications in a 3D rectangular enclosure. Input data necessary for the radiation model was taken from Selçuk [64]. They found that heat flux distribution obtained with forward scattering lies between the heat flux distributions of isotropic scattering and nonscattering assumptions, where the forward scattering heat flux profile is closer to that of nonscattering assumption. Furthermore, it was shown that source term distributions are not much sensitive to phase function simplifications along the centreline of the enclosure.

Marakis et al. [44] studied the effect of isotropic scattering and nonscattering assumptions on heat flux predictions by comparing their predictions with those of Delta-Eddington phase function in a 2D axisymmetric cylindrical enclosure containing coal, char and fly ash particles. Particle properties are evaluated parametrically for various particle size distributions and particle loads. Discrepancy between the heat flux predictions are found to be increasing with increasing particle load and decreasing particle size. Similar to Liu's results [63], they found that predictions obtained with nonscattering assumption is closer to those of anisotropic scattering.

Selçuk et al. [14] also performed a parametric investigation to assess the influence of phase function simplifications and particle load on incident wall heat fluxes along the

freeboard of METU 0.3 MW<sub>t</sub> ABFBC by comparing model predictions with those of zone method and measurements. In the radiation models, freeboard was considered as a 3-D rectangular enclosure containing gray, absorbing, emitting gas with gray absorbing, emitting and isotropically/anisotropically scattering particles. In this study, experimental data required for the radiation model and its validation were taken from a single combustion test and all calculations are based on measured parameters unlike the previously presented investigations. Experimental conditions with the isotropic scattering assumption were set as the base case and three parametric cases were investigated by increasing the particle load along the combustor and/or incorporating the anisotropic scattering into the calculations. Anisotropic scattering was represented by using linear anisotropic phase function, which includes only the first two terms of the series Mie solution for the scattering phase function. Comparisons revealed that heat flux distribution obtained by using isotropic assumption agrees very well with both measured radiative heat fluxes and the reference solution with anisotropically scattering particles. Furthermore, even 1000-fold increase in particle load does not lead to any discrepancies in wall heat fluxes calculated by using isotropically and anisotropically scattering particles. In other words, it was found that anisotropy has a negligible effect on radiative fluxes irrespective of the particle load. However, this outcome may be attributed to the smoothness of the linear anisotropic phase function utilized in this study, which may not be able to represent the actual strong forward scattering by the particles.

Bäckström et al. [65] investigated the influence of different particle types on radiative heat transfer in a 77 kW<sub>t</sub> swirling flame. Similar to [64], input data required for the radiation models were taken from measurements and model predictions were benchmarked against radiative intensity measurements. Radiative properties of combustion gases and particles (coal, char, ash) were calculated from SNB model and Mie theory, respectively. Coal, char and ash particles are assumed to scatter radiation isotropically. Comparisons revealed that radiative heat transfer is dominated by coal/char particles rather than ash particles/combustion gases in the flame region. Furthermore, modelled radiative intensities were found to be noticeably less than measured radiative intensities, which may be due to isotropic scattering assumption. In another study, Bäckström et al. [66] worked on a 400 kW<sub>t</sub> rotary kiln burner. They investigated the

radiative heat transfer within the flames of 11 different fuel blends composed of heavy fuel oil, natural gas, 2 different coals and 3 different biomass sources. Similar to their previous work, radiative properties of combustion gases and particles were calculated from SNB model and Mie theory, respectively. In all cases, particle radiation dominated total radiative heat transfer within flames. Interestingly, modelled radiative intensities were again found to be noticeably less than measured radiative intensities for these fuel blends, which makes the isotropic scattering assumption more questionable in modelling particle-radiation interactions.

Granate et al. [67] recently presented a detailed investigation on accurate representation of scattering phase function in different RTE solution methods. They used DOM with three different normalization methods, finite volume method (FVM), spherical harmonics discrete ordinates method (SHDOM) and Monte Carlo simulations (MC) in three multi-dimensional idealized test problems for various optical thicknesses (1-25) and asymmetry factors (0.2-0.95). In all cases (DOM, FVM, SHDOM), predictions obtained with Henyey–Greenstein phase function was found to be in very good agreement with MC solutions, which is accepted to be one of the most accurate solution methods. They also tested Delta-Eddington, transport and Delta-M scattering phase function approximations by comparing their predictions with those of Henyey–Greenstein phase function. Comparisons revealed that transport and Delta-Eddington approximations are quite accurate for asymmetry factors up to 0.90 while they lead to some discrepancies for asymmetry factors between 0.90-0.95, although the difference is not very large. In the case of transient problems with collimated irradiation as in laser applications, however, these simplifying assumptions were found to be incorrect. On the other hand, Delta-M phase function was found to be successful in all cases including the collimated irradiation. It should be noted that Delta-M model depends on a parameter called “M” and model predictions are very sensitive to the value of “M”. Considering the fact that its selection is rather arbitrary [67], ensuring the accuracy of this approximation is very difficult and it requires much more effort than other scattering phase function approximations.

As can be seen from the above-mentioned studies focusing on the “scattering challenge”, there are still many uncertainties and disagreements on scattering phase function and its

simplifications. Majority of these studies were performed on either idealized simple problems or the input data for the radiation models were not based on measurements but selected parametrically / arbitrarily. In other words, there is a lack of studies based on measured input data required for the application of radiation model and its validation in multidimensional enclosures. Furthermore, effect of phase function simplifications has only been investigated with gray particles in combusting systems and no numerical study involving the effect of phase function simplifications in conjunction with spectral particle properties have been reported in literature.

Another challenge in particle radiation is its dependency on particle size, load and density although these dependencies are not investigated as detailed as spectral nature of particle radiation or the effect of scattering on particle-radiation interactions. Study of Wall et al. [68] presented one of the earliest works on the effect of particle size. They investigated the absorption and scattering efficiencies of ash particles for a size range of 0.1-100  $\mu\text{m}$  by using several RI data available at that time. Their comparisons revealed that projected area of particles are mainly constituted by fine ash particles ( $<10 \mu\text{m}$ ), for which particle absorption and scattering efficiencies were found to be strongly dependent on both particle size and RI. In the following work of the same authors [69], they compared the relative influences of particle size, temperature and RI on radiative heat transfer for two idealized test problems, where the RTE was solved by using Monte Carlo method. They investigated three PSDs for a temperature range of 1200-1800 K and for an absorption index ( $k$ ) range of 0.001-1.0. In all cases, refractive index ( $n$ ) was assumed to be 1.5. Comparisons revealed that particle properties are much more affected from the variations in absorption index of the particles compared to the variations in particle size. However, it should be noted that all three PSDs were related to PC-fired furnaces with  $d_{50}$ <sup>1</sup> of 24, 20 and 11  $\mu\text{m}$ , respectively, which were not much different from one another.

Liu and Swithenbank [43] also addressed the effect of particle size distribution on radiative heat transfer in PC-fired furnaces. They investigated spectral absorption, scattering and extinction coefficient for a measured PSD, from which they evaluated Planck mean particle properties for a temperature range of 1200-2000 K. They represented

---

<sup>1</sup> 50% of the total mass of particles has a particle size below the specified value,  $d_{50}$ .



the same discrete PSD measurement with four different continuous functions and used these functions to evaluate particle radiative properties. It was found that even slight differences in the representation of measured PSD can cause more than 10% variations in the predicted Planck mean absorption and scattering coefficients. Based on these comparisons, they emphasized on the significance of the accurate representation of PSD in radiative property calculations.

Mengüç et al. [70] studied effective particle radiative properties in PC-fired furnaces both theoretically and experimentally. They compared particle radiative properties for two PSDs and three single particle diameters (6, 12, 18  $\mu\text{m}$ ) for a range of refractive (1.5, 1.7, 1.9) and absorption (0.001-10) indices. They found that particle radiative properties are more sensitive to particle size and size distribution than the RI of particles. They also presented the first investigation on the effect of particle size on the scattering phase function. It was demonstrated that scattering phase function is a strong function of particle size if it is calculated from a single particle diameter. However, this dependency is found to be weakened noticeably in the presence of a PSD.

Hua et al. [10] investigated the effect PSD on radiative heat transfer coefficient in a CFBC. They showed that heat transfer coefficient can increase up to 25 % with decreasing particle size. Furthermore, comparisons presented in the study revealed that surface mean diameter (Sauter mean diameter) can be utilized to evaluate radiative heat transfer coefficient of a polydisperse particle cloud if most particles are larger than 100  $\mu\text{m}$  and have similar optical properties. In other words, they found that radiative properties of the particle cloud are not a strong function of particle size if majority of the PSD is constituted by large particles.

In a recent study, relative influences of particle size and RI on radiative heat transfer are compared for conditions relevant to PC-fired furnaces [71]. Radiative heat transfer was modelled in a 1D infinitely long cylinder for non-gray, absorbing, emitting gases and non-gray, absorbing, emitting, anisotropically scattering particles. Radiative properties of combustion gases and particles were calculated from SNB method and Mie theory, respectively. In Mie solutions, two different chemical composition independent spectral RI models were selected for ash particles. Comparison between spectral absorption and

scattering efficiencies revealed that particle size is a more important parameter than RI on radiative properties of particles. On the other hand, comparison between radiative heat fluxes and source terms predictions obtained with different RI models indicated that RI model for ash particles can lead to 40 % and 10 % differences in heat flux and source term predictions, respectively. Furthermore, using a surface area mean diameter for the evaluation of particle properties was found to cause less than 7 % error in source term predictions.

There are also some studies where the effect of particle load / particle volume fraction on radiative heat transfer is investigated parametrically [14, 42, 44, 45, 65]. They all agree that increasing the particle load / particle volume fraction increases the share of particle radiation in total heat transfer. On the other hand, there is only one study available in the literature that specifically tested the sensitivity of radiative heat transfer predictions to particle density, which revealed that change in the density may lead to significant variation in predicted radiative intensities [65].

## **1.1 Research Objectives**

As briefly described in the previous section, radiation is the predominant mode of heat transfer in fluidized bed combustors (FBCs) hence accurate modelling of radiative heat transfer is of considerable importance and necessitates not only accurate but also computationally efficient methods for (i) the solution of the radiative transfer equation (RTE) and (ii) radiative property estimation of particle-laden combustion gases. Previous work regarding to the search for the most accurate and computationally efficient solution method for the solution of RTE already revealed that MOL solution of DOM meets all the requirements in combusting systems. With respect to radiative property modeling, however, there are still many uncertainties and disagreements on the effects of parameters determining spectral gas and particle properties and their influence on radiative heat transfer. Furthermore, sub-models used in estimation of gas and particle radiative properties determine the computational cost of the global model as number of radiative

intensity equations included in the solution of RTE is directly related to these property models.

Therefore, ultimate objective of this study is to develop CPU efficient and accurate gas and particle radiative property models, which are compatible with differential solution of RTE such as MOL solution DOM, DOM, FEM and FVM. For that purpose, present work focuses on developing and comparing methods to quantify the effect of participating combustion gases and particles on radiative heat transfer by using measurements for input data to the radiation models and for the validation of model predictions such that the outcome will provide guidelines when choosing radiation models for combustion related investigations.

To achieve this objective, main tasks of the present study have been set as follows:

1. Developing a multidimensional radiation code based on MOL solution of DOM for the simulation of radiative transfer with non-gray gas and non-gray particles.
2. Extending the code for incorporation of anisotropic scattering.
3. Testing the predictive accuracy of the developed codes on benchmark problems.
4. Quantifying the contribution of an accurate spectral gas radiation model to radiative heat transfer predictions.
5. Quantifying the contribution of particle radiation to total radiation under FBC conditions.
6. Investigating the effect of particle scattering and assessing the predictive accuracy and computational efficiency of phase function simplifications.
7. Investigating the effect of particle size and size distribution on particle radiation.
8. Incorporating the particle load distribution into the radiation model.
9. Creating a benchmark solution which involves spectral particle properties.
10. Identifying the origins of the spectral nature of particle radiation.

11. Evaluating the predictive accuracy and computational economy of gray particle approximations available in the literature.
12. Investigating the spectral dependency of phase function simplifications.
13. Developing CPU efficient gas property models compatible with spectral particle property models.
14. Investigating the influence of spectral particle properties on the predictive accuracy of gas property approximations.

## **CHAPTER 2**

### **SOLUTION METHOD FOR RADIATIVE TRANSFER EQUATION**

In this chapter, method of lines (MOL) solution of discrete ordinates method (DOM) is described for mathematical modeling of radiative heat transfer in multidimensional enclosures containing non-gray, absorbing, emitting and scattering media bounded by black / gray diffuse walls. Values of blackbody emissive power are assumed to be known at all points within the medium and at all points on the interior bounding surfaces. Equations representing MOL solution of DOM are derived starting from the radiative transfer equation (RTE) for both axisymmetric cylindrical and three-dimensional rectangular coordinate systems. This is followed by the numerical solution procedure utilized for the MOL solution of DOM.

#### **2.1 Radiative Transfer Equation (RTE)**

The starting point of all methods for the solution of radiation problems is the radiative transfer equation (RTE), which is derived by writing a balance equation for radiant energy passing in a specified direction ( $ds$ ) through a small volume element of non-gray, absorbing, emitting, scattering uniform media and can be written in the following form:

$$\begin{aligned}
\frac{dI_\lambda}{ds} &= (\mathbf{\Omega} \cdot \nabla) I_\lambda(\mathbf{r}, \mathbf{\Omega}) \\
&= -(\kappa_\lambda + \sigma_\lambda) I_\lambda(\mathbf{r}, \mathbf{\Omega}) + (\kappa_\lambda) I_{\lambda_b}(\mathbf{r}) + \frac{\sigma_\lambda}{4\pi} \int_{4\pi} \Phi_\lambda(\mathbf{\Omega}', \mathbf{\Omega}) I_\lambda(\mathbf{r}, \mathbf{\Omega}') d\mathbf{\Omega}' \quad (2.1)
\end{aligned}$$

where  $I_\lambda(\mathbf{r}, \mathbf{\Omega})$  is the spectral radiation intensity at position  $\mathbf{r}$  in the direction  $\mathbf{\Omega}$  defined as the quantity of radiant energy passing in a specified direction  $\mathbf{\Omega}$  along a path  $s$  per unit solid angle  $d\mathbf{\Omega}$  about the direction  $\mathbf{\Omega}$ , per unit area normal to the direction of travel, per unit time.  $\kappa_\lambda$  and  $\sigma_\lambda$  are the spectral absorption and spectral scattering coefficients of the medium, respectively.  $I_{\lambda_b}$  is the spectral black-body radiation intensity and  $\Phi_\lambda(\mathbf{\Omega}', \mathbf{\Omega})$  is the spectral phase function for scattering which describes the fraction of energy scattered from incoming direction  $\mathbf{\Omega}'$  to the outgoing direction  $\mathbf{\Omega}$ .  $\mathbf{\Omega}$  denotes the direction of solid angle. The term on the left - hand side represents the change of intensity in the specified direction  $s$  and solid angle  $\mathbf{\Omega}$ . The terms on the right - hand side stand for absorption and out-scattering, emission and in-scattering, respectively.

### 2.1.1 RTE in Cylindrical Coordinate System

In axisymmetric cylindrical geometry  $(r, z)$ , the directional derivative of radiation intensity can be expressed as follows from the chain rule,

$$\frac{dI_\lambda}{ds} = \frac{\partial I_\lambda}{\partial r} \frac{dr}{ds} + \frac{\partial I_\lambda}{\partial \phi} \frac{d\phi}{ds} + \frac{\partial I_\lambda}{\partial z} \frac{dz}{ds} \quad (2.2)$$

where

$$\frac{dr}{ds} = \mathbf{\Omega} \cdot \mathbf{e}_r = \mu \quad (2.3)$$

$$\frac{d\phi}{ds} = \mathbf{\Omega} \cdot \mathbf{e}_\phi = -\eta/r \quad (2.4)$$

$$\frac{dz}{ds} = \mathbf{\Omega} \cdot \mathbf{e}_z = \xi \quad (2.5)$$

In Eqs. (2.3-2.5),  $\mathbf{e}_r$ ,  $\mathbf{e}_\phi$ , and  $\mathbf{e}_z$  are the unit vectors and  $\mu(= \sin(\theta) \cos(\phi))$ ,  $\eta(= \sin(\theta) \sin(\phi))$  and  $\xi(= \cos(\theta))$  are direction cosines in  $r$ ,  $\phi$  and  $z$  directions, respectively (see Figure 2.1). Hence, the derivative of radiation intensity can be written as,

$$\frac{dI_\lambda}{ds} = \mu \frac{\partial I_\lambda}{\partial r} - \frac{\eta}{r} \frac{\partial I_\lambda}{\partial \phi} + \xi \frac{\partial I_\lambda}{\partial z} \quad (2.6)$$

In Eq. (2.6), directional derivative ( $d/ds$ ) is written in so-called conservation form to ensure that approximation to the RTE retain conservation properties. In other words, resulting coefficients of any differential term does not contain the variable of differentiation upon multiplying the differential equation by a volume element. Equation (2.6) is not yet in conservative form due to the presence of  $-\eta/r$  as a multiplier of  $\partial I_\lambda / \partial \phi$ . This difficulty is easily remedied by adding and subtracting the term  $(\mu/r)I_\lambda$  to Eq. (2.6),

$$\frac{dI_\lambda}{ds} = \mu \frac{\partial I_\lambda}{\partial r} - \frac{\eta}{r} \frac{\partial I_\lambda}{\partial \phi} + \xi \frac{\partial I_\lambda}{\partial z} + \frac{\mu}{r} I_\lambda - \frac{\mu}{r} I_\lambda \quad (2.7)$$

$$\frac{dI_\lambda}{ds} = \frac{\mu}{r} \left( r \frac{\partial I_\lambda}{\partial r} + \frac{\partial r}{\partial r} I_\lambda \right) - \frac{1}{r} \left( \eta \frac{\partial I_\lambda}{\partial \phi} + \frac{\partial \eta}{\partial \phi} I_\lambda \right) + \xi \frac{\partial I_\lambda}{\partial z} \quad (2.8)$$

where

$$\frac{\partial \eta}{\partial \phi} = \frac{\partial}{\partial \phi} (\sin(\theta) \sin(\phi)) = \sin(\theta) \cos(\phi) = \mu \quad (2.9)$$

Consequently, in conservative form, RTE (Eq. (2.1)) in axisymmetric cylindrical coordinates takes the following form,

$$\begin{aligned} \frac{dI_\lambda}{ds} &= \frac{\mu}{r} \frac{\partial (rI_\lambda)}{\partial r} - \frac{1}{r} \frac{\partial (\eta I_\lambda)}{\partial \phi} + \xi \frac{\partial I_\lambda}{\partial z} \\ &= -(\kappa_\lambda + \sigma_\lambda) I_\lambda(\mathbf{r}, \boldsymbol{\Omega}) + (\kappa_\lambda) I_{\lambda b}(\mathbf{r}) + \frac{\sigma_\lambda}{4\pi} \int_{4\pi} \Phi_\lambda(\boldsymbol{\Omega}', \boldsymbol{\Omega}) I_\lambda(\mathbf{r}, \boldsymbol{\Omega}') d\boldsymbol{\Omega}' \end{aligned} \quad (2.10)$$

If the surfaces bounding the medium are black / gray diffuse surfaces at specified temperatures, Eq. (2.1) is subjected to the following boundary condition,

$$I_\lambda(\mathbf{r}_w, \boldsymbol{\Omega}) = \varepsilon_w I_{\lambda_{b,w}}(\mathbf{r}_w) + \frac{(1 - \varepsilon_w)}{\pi} \int_{\mathbf{n}_w \cdot \boldsymbol{\Omega}' < 0} |\mathbf{n}_w \cdot \boldsymbol{\Omega}'| I_\lambda(\mathbf{r}_w, \boldsymbol{\Omega}') d\boldsymbol{\Omega}' \quad \mathbf{n} \cdot \boldsymbol{\Omega} > 0 \quad (2.11)$$

where  $I_\lambda(\mathbf{r}_w, \boldsymbol{\Omega})$  and  $I_\lambda(\mathbf{r}_w, \boldsymbol{\Omega}')$  are the spectral radiative intensities leaving and incident on the surface at a boundary location,  $\varepsilon_w$  is the surface emissivity,  $I_{\lambda_{b,w}}(\mathbf{r}_w)$  is the spectral blackbody radiation intensity at the surface temperature,  $\mathbf{n}_w$  is the local outward surface normal and  $\mathbf{n}_w \cdot \boldsymbol{\Omega}'$  is the cosine of the angle between incoming direction  $\boldsymbol{\Omega}'$  and the surface normal  $\mathbf{n}_w$ . The first and second term on the right-hand side of Eq. (2.11) stand for the contribution to the leaving intensity due to emission from the surface and reflection of the incoming radiation, respectively.



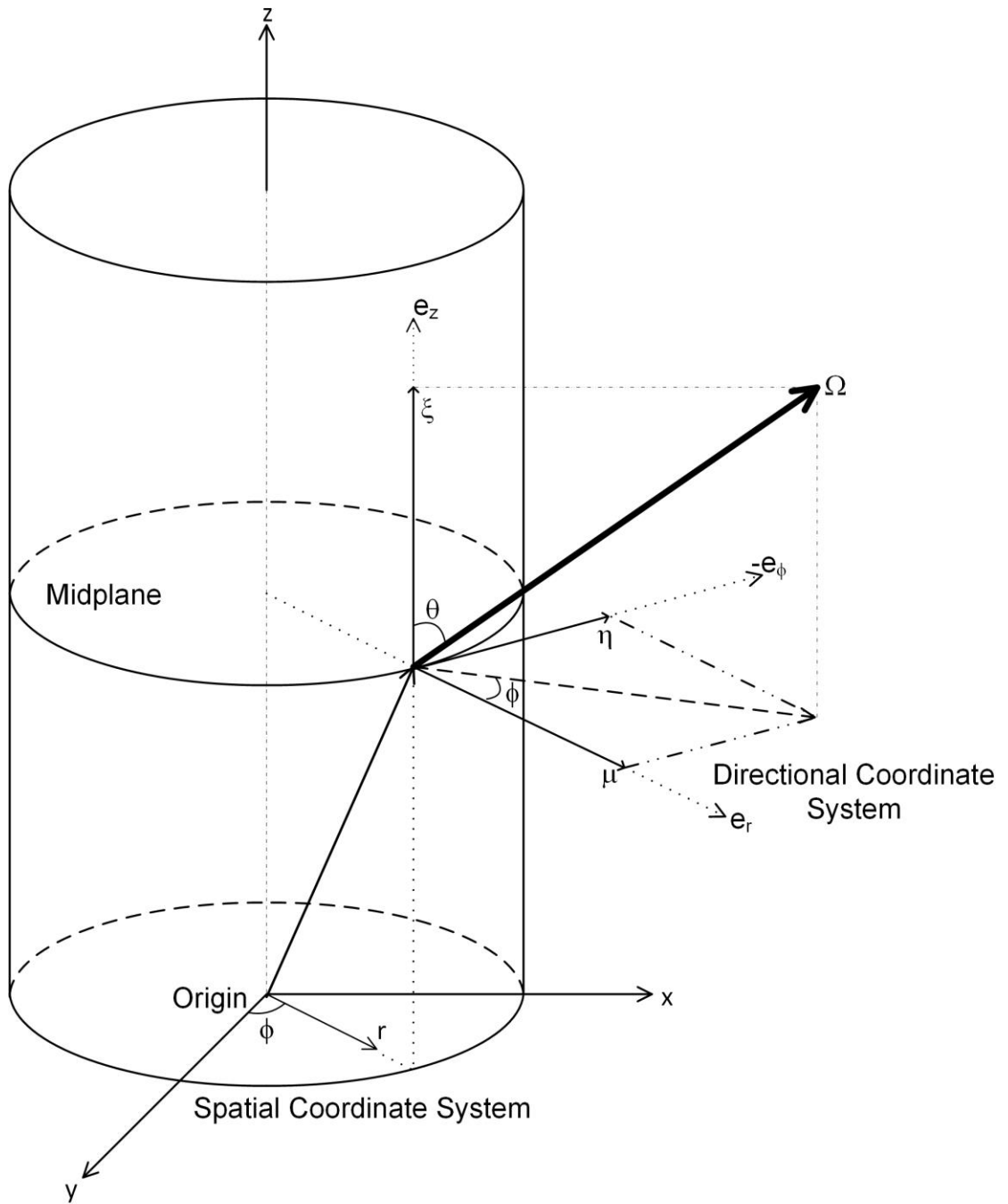


Figure 2.1 Directional cosines for cylindrical geometries

### 2.1.2 RTE in Rectangular Coordinate System

For rectangular coordinate system, gradient of intensity can be expressed in terms of derivatives with respect to space coordinates  $x$ ,  $y$ , and  $z$ . In that case, RTE becomes,

$$\begin{aligned} \frac{dI_\lambda}{ds} &= \mu \frac{\partial I_\lambda}{\partial x} + \eta \frac{\partial I_\lambda}{\partial y} + \xi \frac{\partial I_\lambda}{\partial z} \\ &= -(\kappa_\lambda + \sigma_\lambda)I_\lambda(\mathbf{r}, \boldsymbol{\Omega}) + (\kappa_\lambda)I_{\lambda_b}(\mathbf{r}) + \frac{\sigma_\lambda}{4\pi} \int_{4\pi} \Phi_\lambda(\boldsymbol{\Omega}', \boldsymbol{\Omega})I_\lambda(\mathbf{r}, \boldsymbol{\Omega}')d\boldsymbol{\Omega}' \end{aligned} \quad (2.12)$$

where directional cosines can be expressed in terms of polar angle  $\theta$  and azimuthal angle  $\phi$  as  $\mu = \cos(\theta)$ ,  $\eta = \sin(\theta) \sin(\phi)$  and  $\xi = \sin(\theta) \cos(\phi)$  (see Figure 2.2). If the surfaces bounding the medium are black / gray diffuse at specified temperatures, Eq. (2.11) is also valid for rectangular geometries.

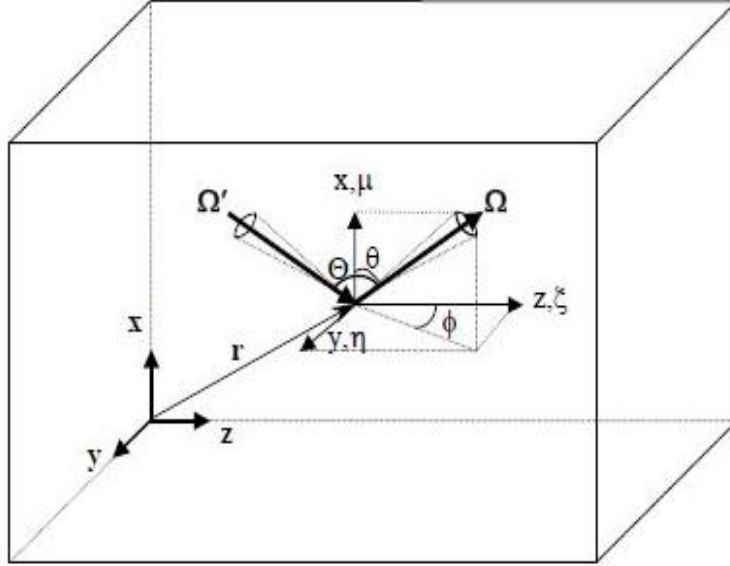


Figure 2.2 Directional cosines for rectangular geometries

### 2.1.3 Radiative Heat Flux and Source Term

Once the radiation intensities are evaluated by solving either Eq. (2.10) or Eq. (2.12) together with its boundary condition (Eq. 2.11), quantities of interest such as radiative flux and energy source term can be readily evaluated. The net radiative heat flux on a surface element is defined as,

$$q_{\text{net}\lambda} = q_{\lambda}^{+} - q_{\lambda}^{-} \quad (2.13)$$

where  $q_{\lambda}^{+}$  and  $q_{\lambda}^{-}$  are incident and leaving wall heat fluxes at a specified wavelength,  $\lambda$ , respectively. For a diffuse and gray wall,  $q_{\lambda}^{+}$  and  $q_{\lambda}^{-}$  are evaluated from,

$$q_{\lambda}^{+} = \int_{\mathbf{n} \cdot \boldsymbol{\Omega} < 0} |\mathbf{n} \cdot \boldsymbol{\Omega}| I_{\lambda} d\boldsymbol{\Omega} \quad (2.14)$$

$$q_{\lambda}^{-} = \int_{\mathbf{n} \cdot \boldsymbol{\Omega} > 0} |\mathbf{n} \cdot \boldsymbol{\Omega}| I_{\lambda} d\boldsymbol{\Omega} \quad (2.15)$$

The coordinate component of radiative heat flux vector is given by,

$$\mathbf{q}_{\lambda} = \int_{4\pi} (\mathbf{e}_i \cdot \boldsymbol{\Omega}) I_{\lambda} d\boldsymbol{\Omega} \quad (2.15)$$

where  $\mathbf{e}_i$  is the unit normal vector in the coordinate direction  $i$ .

The spectral radiative energy source term (i.e., divergence of the total radiative heat flux), is expressed as,

$$\nabla \cdot \mathbf{q}_{\lambda} = \kappa_{\lambda} \left( 4\pi I_{\lambda_b}(\mathbf{r}) - G_{\lambda}(\mathbf{r}) \right) \quad (2.16)$$

where  $G_{\lambda}$  is the incident spectral radiation defined as,

$$G_{\lambda}(\mathbf{r}) = \int_{4\pi} I_{\lambda}(\mathbf{r}, \boldsymbol{\Omega}) d\boldsymbol{\Omega} \quad (2.17)$$

It should be noted that RTE (Eqs. 2.10, 2.12) and its boundary conditions (Eq. 2.11) are closed if the temperature field throughout the medium is specified. Otherwise, coupling

between overall energy conservation equation with the RTE is required in order to solve for the temperature field.

## 2.2 Discrete Ordinates Method (DOM)

Discrete Ordinates Method (DOM) is based on representation of the continuous angular domain by a discrete set of equations for a finite number of directions spanning the total solid angle of  $4\pi$  steradians. With this approach, integral terms in Eqs. (2.10) and (2.12) representing the in-scattered spectral radiation are replaced by a quadrature summed over the ordinate directions. In other words, integro-differential form of RTE is transformed into a set of simultaneous PDEs containing only spatial coordinates as independent variables. Spatial discretization may be accomplished by using a variety of methods including finite volume, finite element or finite difference techniques. In the classical DOM applications [72-81], spatial differencing is carried out by using standard cell-centered, finite volume technique. In this approach, the discrete ordinates equations are integrated over a typical control volume and interpolation schemes are defined to relate face intensities with cell-centered intensities. An iterative, ordinate sweeping technique [77] is applied to solve for the intensities at each ordinate and at each control volume.

In axisymmetric cylindrical coordinate system, DOM representation of spectral RTE takes the following form,

$$\left( \frac{\mu_m}{r} \frac{\partial (rI_\lambda^m)}{\partial r} - \frac{1}{r} \frac{\partial (\eta_m I_\lambda^m)}{\partial \phi} + \xi_m \frac{\partial I_\lambda^m}{\partial z} \right) = -(\kappa_\lambda + \sigma_\lambda) I_\lambda^m + (\kappa_\lambda) I_{b\lambda} + \frac{\sigma_\lambda}{4\pi} \sum_{m'=1}^M \Phi_\lambda(\mathbf{\Omega}_{m'}, \mathbf{\Omega}_m) w_{m'} I_\lambda^{m'} \quad (2.18)$$

where  $I_\lambda^m [\equiv I_\lambda(\mathbf{r}; \mu_m, \eta_m, \xi_m)]$  is the spectral radiation intensity at position  $\mathbf{r}$  ( $r, z$ ) in the discrete direction  $\mathbf{\Omega}_m$  which is defined in terms of polar angle  $\theta$  and azimuthal angle  $\phi$  between  $\mathbf{r}$  and projection of  $\mathbf{\Omega}_m$  on the x-y plane.  $M$  is the total number of discrete directions. The components of direction  $\mathbf{\Omega}_m$  along the  $\mu, \eta$  and  $\xi$  axes are

$\mu_m (= \sin(\theta) \cos(\phi))$ ,  $\eta_m (= \sin(\theta) \sin(\phi))$  and  $\xi_m (= \cos(\phi))$ , which are the direction cosines of  $\Omega_m$  giving  $\mu_m^2 + \eta_m^2 + \xi_m^2 = 1$ . The direction  $\Omega_m$  can be pictured as a point on the surface of a unit sphere with which a surface area,  $w_m$  is associated.  $w_m$  has the role of angular quadrature weights, with the requirement that the weights sum to the total surface area of the unit sphere, i.e.,  $\sum w_m = 4\pi$ .

The solution of DOM equations in axisymmetric cylindrical geometry are complicated by the presence of the angular derivative in the transfer equation (Eq. 2.18). In Cartesian geometries, spectral RTE contains only spatial derivatives and the angles are independent from spatial coordinates so that angular decomposition is straightforward. For curvilinear geometries, however, spectral RTE includes both spatial and angular derivatives. The reason is that the local direction cosines change while traveling along the straight line of sight through the enclosure e.g., the azimuthal angle  $\phi$  steadily decreases in cylindrical enclosures. This is why angular decomposition of curvilinear geometries is not straightforward.

Carlson and Lathrop [82] have proposed a direct differencing technique for calculating the angular derivatives at the quadrature points. By introducing angular differencing coefficient ( $\gamma_{m,\ell\pm 1/2}$ ), angular derivative term on the left hand side of Eq. (2.18) is finite-differenced as

$$\left[ \frac{\partial(\eta_m I_\lambda^m)}{\partial \phi} \right]_{\Omega_m = \Omega_{m,\ell}} = \frac{(\gamma_{m,\ell+1/2} I_\lambda^{m,\ell+1/2} - \gamma_{m,\ell-1/2} I_\lambda^{m,\ell-1/2})}{w_{m,\ell}} \quad (2.19)$$

where  $I_\lambda^{m,\ell+1/2} (= (I_\lambda^{m,\ell} + I_\lambda^{m,\ell+1})/2)$  and  $I_\lambda^{m,\ell-1/2} (= (I_\lambda^{m,\ell-1} + I_\lambda^{m,\ell})/2)$  are radiation intensities in directions  $(m, \ell + 1/2)$  and  $(m, \ell - 1/2)$  which define the edges of angular range of  $w_{m,\ell}$ .  $\gamma_{m,\ell\pm 1/2}$  denotes the angular differencing coefficient. The two terms on the right hand side of Eq. (2.19) represent the flow out of and into the angular range, respectively. The pair of indices  $m$  and  $\ell$  in Eq. (2.19) denotes the constant polar angle  $\theta$  and the variation of azimuthal angle,  $\phi$ , respectively.

Direction cosines in standard quadrature sets are ordered in latitudes so that for each  $\xi_m (= \cos(\phi))$  level, there will be several  $\mu_m$  values. A sketch of discrete directions,

represented by pair of indices  $m, \ell$  in one octant of a unit sphere for  $S_4$  order of approximation, is shown in Figure 2.3. As can be seen from the figure, for  $S_4$  order of approximation, there are two latitudes and one value of  $\mu_m$  for the first latitude and two values of  $\mu_m$  for the second latitude. In order to avoid physically unrealistic directional coupling, discrete directions for a given  $\xi_m (= \cos(\phi))$  should be ordered according to the values of  $\phi (= \tan^{-1}(\eta/\mu))$ .

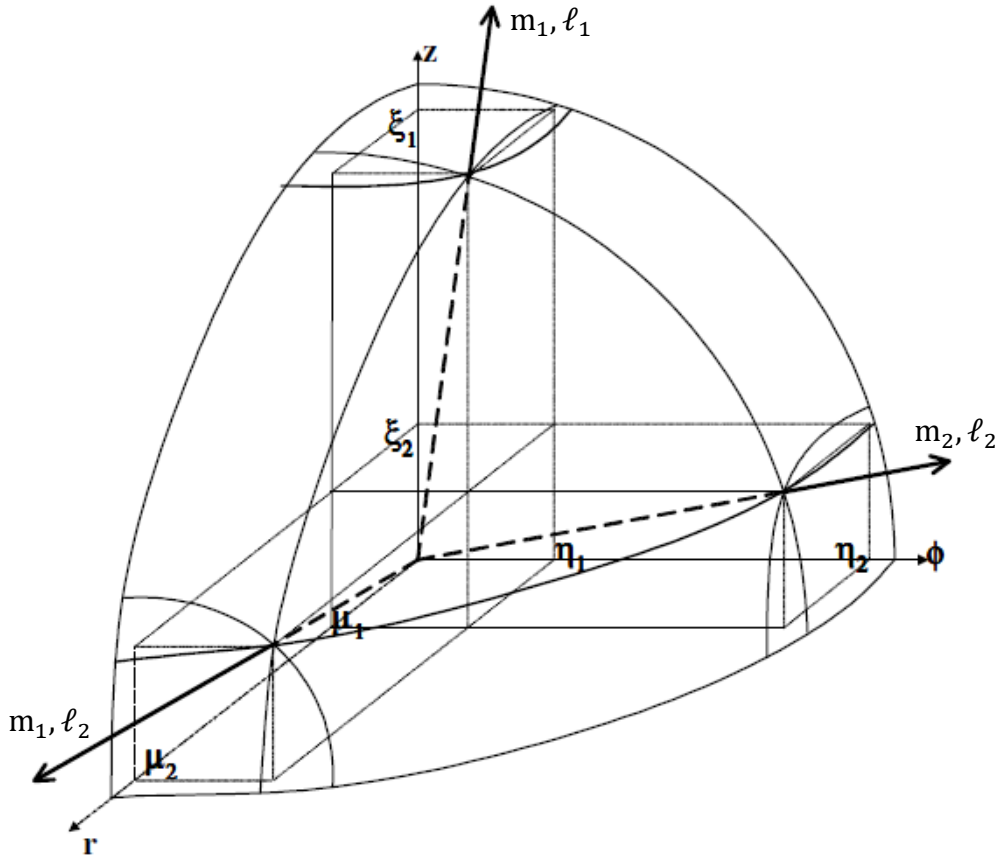


Figure 2.3 Schematic representation of discrete directions represented by  $m, \ell$  in one octant of a unit sphere for  $S_4$  order of approximation

By moving through the directions along the constant  $\xi_m$  level, the angular differencing coefficients,  $\gamma_{m, \ell \pm 1/2}$ , are evaluated from the following recurrence formula [82],

$$\gamma_{m, \ell+1/2} = \gamma_{m, \ell-1/2} + \mu_{m, \ell} w_{m, \ell} \quad \ell = 1, 2, 3, \dots L, \text{ for fixed } \xi_m \quad (2.20)$$

When Eq.(2.19) is integrated over all angles (multiplied by  $w_{m,\ell}$  and summed over  $m, \ell$ ) the result is,

$$\sum_m \left( \gamma_{m,L+1/2} I_\lambda^{m,L+1/2} - \gamma_{m,1/2} I_\lambda^{m,1/2} \right) \quad (2.21)$$

It should be noted that the second term on the left hand side of Eq (2.18) vanishes when integrated over all angles. In order to satisfy energy conservation, any representation of the angular derivative term should preserve this property. Therefore, Eq. (2.21) has to vanish as a requirement for energy conservation by setting

$$\gamma_{m,1/2} = \gamma_{m,L+1/2} = 0; \quad \text{for all } m \quad (2.22)$$

where  $L$  is the maximum value of  $\ell$  for a particular  $m$ . For instance, in  $S_4$  order of approximation,  $L = 4$  for  $m = 2$  with two octants in the range of  $0 \leq \phi \leq \pi$ .

Intensities at the edges of  $w_{m,\ell}$  and  $I_\lambda^{m,\ell \pm 1/2}$  are approximated in terms of discrete intensities  $I_\lambda^{m,\ell}$  by linear relations,

$$I_\lambda^{m,\ell+1/2} = \frac{I_\lambda^{m,\ell} + I_\lambda^{m,\ell+1}}{2}, \quad I_\lambda^{m,\ell-1/2} = \frac{I_\lambda^{m,\ell-1} + I_\lambda^{m,\ell}}{2} \quad (2.23)$$

Equations (2.18) and (2.19), and the recurrence relations (Eqs. (2.20) and (2.23)) yield discrete ordinates equations for axisymmetric cylindrical geometries. The final form of discrete ordinates equation for axisymmetric cylindrical geometry takes the following form,

$$\begin{aligned} & \left( \frac{\mu_{m,\ell}}{r} \frac{\partial (r I_\lambda^{m,\ell})}{\partial r} - \frac{1}{r} \frac{(\gamma_{m,\ell+1/2} I_\lambda^{m,\ell+1/2} - \gamma_{m,\ell-1/2} I_\lambda^{m,\ell-1/2})}{w_{m,\ell}} \right) + \xi_{m,\ell} \frac{\partial I_\lambda^{m,\ell}}{\partial z} \\ & = -(\kappa_\lambda + \sigma_\lambda) I_\lambda^{m,\ell} + (\kappa_\lambda) I_{b\lambda} + \frac{\sigma_\lambda}{4\pi} \sum_{m'=1}^M \sum_{\ell'=1}^L \Phi_\lambda(\boldsymbol{\Omega}_{m'\ell'}, \boldsymbol{\Omega}_{m,\ell}) w_{m'\ell'} I_\lambda^{m'\ell'} \end{aligned} \quad (2.24)$$

Boundary conditions required for the solution of Eq. (2.24) on the surface of the enclosure take the following forms for black / diffuse gray surfaces,

$$\text{at } r = R, \quad I_\lambda^{m,\ell} = \varepsilon_w I_{b\lambda,w} + \frac{(1 - \varepsilon_w)}{\pi} \sum_{m',\ell'} w_{m',\ell'} \mu_{m',\ell'} I_\lambda^{m',\ell'} \quad ; \mu_{m,\ell} < 0 \quad (2.25)$$

$$\text{at } z = 0, \quad I_{\lambda}^{m,\ell} = \varepsilon_w I_{b\lambda,w} + \frac{(1 - \varepsilon_w)}{\pi} \sum_{m',\ell'} w_{m',\ell'} |\xi_{m',\ell'}| I_{\lambda}^{m',\ell'} ; \xi_{m,\ell} > 0 \quad (2.26)$$

$$\text{at } z = H, \quad I_{\lambda}^{m,\ell} = \varepsilon_w I_{b\lambda,w} + \frac{(1 - \varepsilon_w)}{\pi} \sum_{m',\ell'} w_{m',\ell'} \xi_{m',\ell'} I_{\lambda}^{m',\ell'} ; \xi_{m,\ell} < 0 \quad (2.27)$$

On the axis of symmetry ( $r = 0$ ) the exact boundary condition is given by,

$$\left( \frac{\partial I_{\lambda}}{\partial \phi} \right)_{\theta=\text{constant}} = 0 \quad (2.28)$$

In discrete terms this is equivalent to  $I_{\lambda}^{m,\ell}$  being independent of  $\ell$  for a fixed  $m$ . With a finite quadrature this condition is generally not satisfied exactly for all values of  $\ell$ . In order to overcome this difficulty, conservation of heat flux on the axis of symmetry for the radial component of the net heat flux ( $q_r(r = 0) = 0$ ), is suggested by Hyde and Truelove [83]. This condition is satisfied if the axis of symmetry is treated as a fictitious, perfectly specular reflecting boundary ( $I_{\lambda}(r = 0; \theta, \phi) = I_{\lambda}'(r = 0; \theta, \pi - \phi)$ ). Consequently, boundary condition in discrete terms at the axis of symmetry can be written as,

$$\text{at } r = 0, \quad I_{\lambda}^{m,\ell} = I_{\lambda}^{m',\ell'} \quad \mu_{m',\ell'} = -\mu_{m,\ell} ; \mu_{m,\ell} > 0 \quad (2.29)$$

In Eqs. (2.25-2.27) and (2.29),  $m, \ell$  and  $m', \ell'$  denote outgoing and incoming directions respectively.

Once the intensity distribution is determined by solving Eq. (2.24) together with its boundary conditions, incident radiative flux and radiative source term can be obtained from the following equations,

$$\mathbf{q}_{\lambda} = \sum_m \sum_{\ell} w_{m,\ell} \bar{\xi} I_{\lambda}^{m,\ell} \quad (2.30)$$

$$\nabla \cdot \mathbf{q}_{\lambda} = \kappa_{\lambda} \left( 4\pi I_{\lambda,b} - \sum_m \sum_{\ell} w_{m,\ell} I_{\lambda}^{m,\ell} \right) \quad (2.31)$$

For 3-D rectangular coordinate system, DOM representation of spectral RTE is much simpler and takes the following form,



$$\begin{aligned}
& \mu_m \frac{\partial I_\lambda^{m,\ell}}{\partial x} + \eta_m \frac{\partial I_\lambda^{m,\ell}}{\partial y} + \xi_m \frac{\partial I_\lambda^{m,\ell}}{\partial z} \\
& = -(\kappa_\lambda + \sigma_\lambda) I_\lambda^{m,\ell} + (\kappa_\lambda) I_{\lambda_b} + \frac{\sigma_\lambda}{4\pi} \sum_{m'=1}^M \sum_{\ell'=1}^L \Phi_\lambda(\mathbf{\Omega}_{m'\ell'}, \mathbf{\Omega}_{m,\ell}) w_{m'} I_\lambda^{m'\ell'} \quad (2.32)
\end{aligned}$$

where  $I_\lambda^m [\equiv I_\lambda(\mathbf{r}; \mu_m, \eta_m, \xi_m)]$  is the spectral radiation intensity at position  $\mathbf{r}$  ( $x, y, z$ ) in the discrete direction  $\mathbf{\Omega}_m$ ,  $m$  denotes the discrete ordinate ( $m = 1, 2, \dots, M$ ),  $M$  is the total number of ordinates used in the approximation,  $\mu_m$ ,  $\eta_m$ , and  $\xi_m$  are the direction cosines of  $\mathbf{\Omega}_m$  with  $x, y, z$  axis, respectively and  $w_{m'}$  is the angular quadrature weight associated with the incoming direction  $\mathbf{\Omega}_{m'}$ .

The boundary conditions at the two opposite, black / gray diffuse surfaces with normal vectors parallel to  $x$  axis can be written as,

$$I_\lambda^m = \varepsilon_w I_{\lambda_{b,w}} + \frac{(1 - \varepsilon_w)}{\pi} \sum_{\mu_{m'} < 0} w_{m'} |\mu_{m'}| I_\lambda^{m'} \quad x = 0, \quad \mu_m > 0 \quad (2.33)$$

$$I_\lambda^m = \varepsilon_w I_{\lambda_{b,w}} + \frac{(1 - \varepsilon_w)}{\pi} \sum_{\mu_{m'} > 0} w_{m'} |\mu_{m'}| I_\lambda^{m'} \quad x = L, \quad \mu_m < 0 \quad (2.34)$$

where  $I_\lambda^m$  is the spectral intensity of radiation leaving the surface,  $\varepsilon_w$  is the surface emissivity,  $I_{\lambda_{b,w}}$  is the spectral black-body radiation intensity at the temperature of the surface. Similar expressions hold for boundaries in other coordinate directions ( $y$  and  $z$ ).

Once the intensity distribution is determined by solving Eq. (2.32) together with Eqs. (2.33) and (2.34), incident radiative flux along the direction  $i$  and source term can be obtained from,

$$\mathbf{q}_\lambda = \sum_{m'=1}^M w_{m'} \ell_{m',i} I_\lambda^{m'} \quad (2.35)$$

$$\nabla \cdot \mathbf{q}_\lambda = \kappa_\lambda \left( 4\pi I_{\lambda_b} - \sum_m w_m I_\lambda^m \right) \quad (2.36)$$

where  $\ell_{m',i}$  is the direction cosine of ordinate  $\Omega_{m'}$  with respect to unit vector  $\mathbf{e}_i$ ,  $w_{m'}$  is the angular quadrature weight associated with the incoming direction  $\Omega_{m'}$  and  $I_\lambda^{m'}$  is the intensity of radiation incident on the surface.

### 2.2.1 Parameters Affecting the Accuracy of DOM

The accuracy of discrete ordinates method is affected by the accuracy of angular quadrature scheme, order of approximation and spatial differencing scheme adopted for the solution.

Order of approximation of DOM determines the total number of discrete directions, “ $M$ ”. A representative sketch of the directions used in one octant of a unit sphere for  $S_2$ ,  $S_4$ ,  $S_6$  and  $S_8$  order of approximations is shown in Figure 2.4. As can be seen from the figure, discrete directions are ordered in levels with different number of directions. Table 2.1 summarizes the total number of discrete directions, total number of levels for each order of approximation and number of discrete directions on each level in one octant of a unit sphere for 1-D and 3-D problems.

It should be noted that ray effect is unavoidable in DOM since discrete number of directions is used to approximate the continuous angular variations. In order to alleviate this problem, number of discrete directions can be increased to have a better angular resolution. However, increasing number of rays not only necessitates additional computational time and memory requirement, but also leads to stability problems for a fixed spatial grid resolution [73]. Therefore, ray effect can only be minimized if finer angular discretization is accompanied by finer spatial discretization [84].

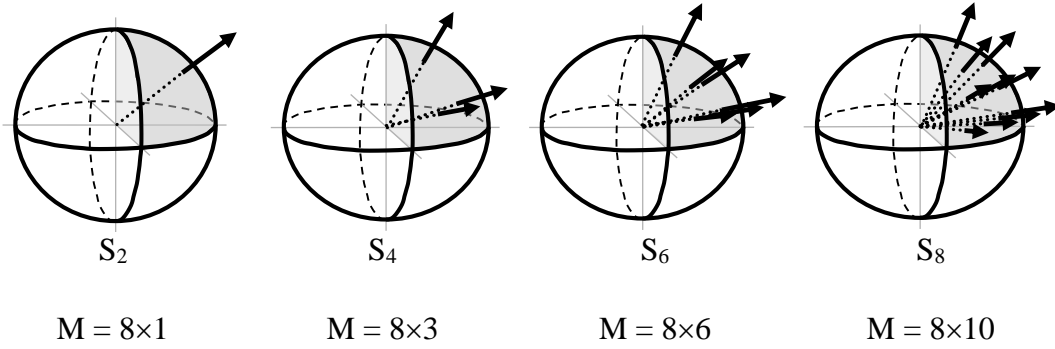


Figure 2.4 Orders of approximation

Table 2.1 Total number of discrete directions specified by order of approximation

Order of approximation	1-D	3-D	Number of levels	Number of points at $i^{\text{th}}$ level
Formula	$M = N$	$M = 2^D N(N+2)/8$	$N/2$	$N/2 - i + 1$
$S_2$	2	8	1	$2-i$
$S_4$	4	24	2	$3-i$
$S_6$	6	48	3	$4-i$
$S_8$	8	80	4	$5-i$

The second parameter affecting the accuracy of the DOM is the angular quadrature scheme, which defines the specifications of ordinates  $\Omega_m(\mu_m, \eta_m, \xi_m)$  and corresponding weights  $w_m$  used for the solution of RTE. The choice of quadrature scheme is arbitrary although restrictions on the directions and weights arise from the need to preserve symmetries and invariance properties of the physical system. Completely symmetric angular quadrature schemes (symmetry of the point and surface about the center of the unit sphere, also about every coordinate axis as well as every plane containing two coordinate axes) are preferred because of their generality and to avoid directional biasing solutions. In other words, description of the points in one octant becomes sufficient to describe the points in all octants. The quadrature sets are constructed to satisfy the key moments of the spectral RTE and its boundary conditions. These are the zeroth

( $\sum_{m=1}^M w_m = 4\pi$ ), first ( $\sum_{m=1}^M \xi w_m = 0$ ) and second ( $\sum_{m=1}^M \xi^2 w_m = 4\pi/3$ ) moments, corresponding to incident energy, heat flux and diffusion condition, respectively. It should be noted that scattering of radiant energy is anisotropic in practical heat transfer applications and angular quadrature schemes should satisfy as many moments as possible (even higher moments) to accurately integrate the phase function.

The most frequently used angular quadrature scheme is  $S_N$ , originally developed by Carlson and Lathrop [82] and extended to higher order of approximations by Fiveland [85] and El Wakil and Sacadura [86]. Therefore, in this study, DOM calculations will be based on  $S_N$  angular quadrature scheme. The quadrature ordinates and weights for  $S_N$  approximations are listed in the relevant appendices.

The third parameter affecting the accuracy of DOM is the spatial differencing scheme. The conventional spatial discretization technique used in DOM is the finite volume method, which makes use of face interpolation schemes that provide assumptions on the form of radiative intensity variation in a control volume. They are based on expressing the downstream (exit) cell boundary intensity as a function of a number of adjacent cell-center or face intensities depending upon the order of the scheme. The spatial differencing schemes can be basically classified as step (upwind), diamond differencing (DDS, central), variable weight differencing and exponential schemes. Detailed description of these schemes is presented in Kayakol [87]. Descriptions of higher order, high resolution, bounded schemes such as MINMOD, MUSCL, CALM and SMART and their applications to DOM can be found in Jessee et al. [88] and Liu et al. [89].

It must be highlighted that effect of order of approximation, angular quadrature schemes and spatial differencing schemes was previously assessed by Selçuk and Kayakol [78] by benchmarking the predictive accuracy of DOM with different approximations against exact solutions. Comparisons reveal that the order of approximation plays a more significant role than both angular quadrature schemes and spatial differencing schemes in radiative heat flux and source term predictions and the order of approximation is the main factor determining the predictive accuracy of DOM.

### 2.3 Method of Lines (MOL) Solution of Discrete Ordinates Method (DOM)

The solution of discrete ordinates equations with Method of Lines (MOL) is carried out by adaptation of the false-transients approach which involves incorporation of a pseudo-time derivative of intensity into the discrete ordinates equations.

MOL solution of DOM provides efficient and flexible computation using various higher order approximations for temporal and spatial discretization. As described in the previous section, DOM is based on representation of the continuous angular domain by a discrete set of equations for a finite number of directions and each integral is replaced by a quadrature summed over the ordinate directions, which converts the integro-differential form of RTE to PDEs. The solution of discrete ordinates equations with MOL is carried out by adoption of the false-transients approach which involves incorporation of a pseudo-time derivative of intensity into the discrete ordinate equation for each direction.

Application of this false-transients approach to Eqs. (2.24) and (2.32) yields the following equations for 2-D axisymmetric cylindrical and 3-D Cartesian coordinate systems, respectively,

$$k_t \frac{\partial I_\lambda^{m,\ell}}{\partial t} = - \left( \frac{\mu_{m,\ell}}{r} \frac{\partial (r I_\lambda^{m,\ell})}{\partial r} - \frac{1}{r} \frac{(Y_{m,\ell+1/2} I_\lambda^{m,\ell+1/2} - Y_{m,\ell-1/2} I_\lambda^{m,\ell-1/2})}{w_{m,\ell}} + \xi_{m,\ell} \frac{\partial I_\lambda^{m,\ell}}{\partial z} \right) - (\kappa_\lambda + \sigma_\lambda) I_\lambda^{m,\ell} + (\kappa_\lambda) I_{b\lambda} + \frac{\sigma_\lambda}{4\pi} \sum_{m'=1}^M \sum_{\ell'=1}^L \Phi_\lambda(\boldsymbol{\Omega}_{m'\ell'}, \boldsymbol{\Omega}_{m,\ell}) w_{m'} I_\lambda^{m'\ell'} \quad (2.37)$$

$$k_t \frac{\partial I_\lambda^{m,\ell}}{\partial t} = - \left( \mu_{m,\ell} \frac{\partial I_\lambda^{m,\ell}}{\partial x} + \eta_{m,\ell} \frac{\partial I_\lambda^{m,\ell}}{\partial y} + \xi_{m,\ell} \frac{\partial I_\lambda^{m,\ell}}{\partial z} \right) - (\kappa_\lambda + \sigma_\lambda) I_\lambda^{m,\ell} + (\kappa_\lambda) I_{b\lambda} + \frac{\sigma_\lambda}{4\pi} \sum_{m'=1}^M \sum_{\ell'=1}^L \Phi_\lambda(\boldsymbol{\Omega}_{m'\ell'}, \boldsymbol{\Omega}_{m,\ell}) w_{m'} I_\lambda^{m'\ell'} \quad (2.38)$$

where  $t$  is the pseudo-time variable and  $k_t$  is a time constant with dimension s/m which is introduced to make the equation dimensionally consistent and is taken as unity. The

system of partial differential equations (PDEs) with initial and boundary conditions is then transformed into an initial-value problem (ODE) by using the method of lines approach. The transformation is carried out by representation of the spatial derivatives with algebraic finite-difference approximations.

Figure 2.5 shows the flow diagram of the MOL solution, which consists of two main stages. In the first stage, spatial derivatives appearing in Eqs. (2.37) and (2.38) are discretized at each node for each ordinate of each octant by using the readily available spatial discretization methods such as finite difference. This yields a set of ODEs to be integrated by means of readily available explicit and implicit solvers, which constitutes the second step. In this step, ODE solver is called to integrate the system of ODEs by using a time adaptive method. The ODE solver takes the burden of time discretization and chooses the time steps in such a way that accuracy and stability of the evolving solution is ensured. Any initial condition can be chosen to start the integration, as its effect on the steady-state solution decays to insignificance. The ODE propagates in time by solving for the intensities at a time step, “n”, calculating the time derivatives and integrating again to solve for intensities at the new time step, “n+1”. If the intensities at all nodes and ordinates satisfy the condition given in Eq. (2.39), the solution at current time (n) is considered to be the steady-state solution and integration is terminated;

$$\frac{|I_n - I_{n-1}|}{I_{n-1}} < \epsilon \quad (2.39)$$

where  $\epsilon$  is the error tolerance and subscript (n-1) indicates solutions at a previous time.

Once the steady-state intensities at all grid points are available, incident radiative heat fluxes on enclosure boundaries and source terms at interior grid points are evaluated.

In the present work, for the implementation of the DOM,  $S_N$  angular quadrature scheme proposed by Carlson and Lathrop [82] is selected. The choice is based on an assessment study carried out by Selçuk and Kayakol [78]. For the difference relations of spatial derivatives, two-point and three-point upwind differencing schemes (DSS012, DSS014) are employed. The ODE solver utilized is ROWMAP which is based on the ROW-methods of order 4 and uses Krylov techniques for the solution of linear systems.

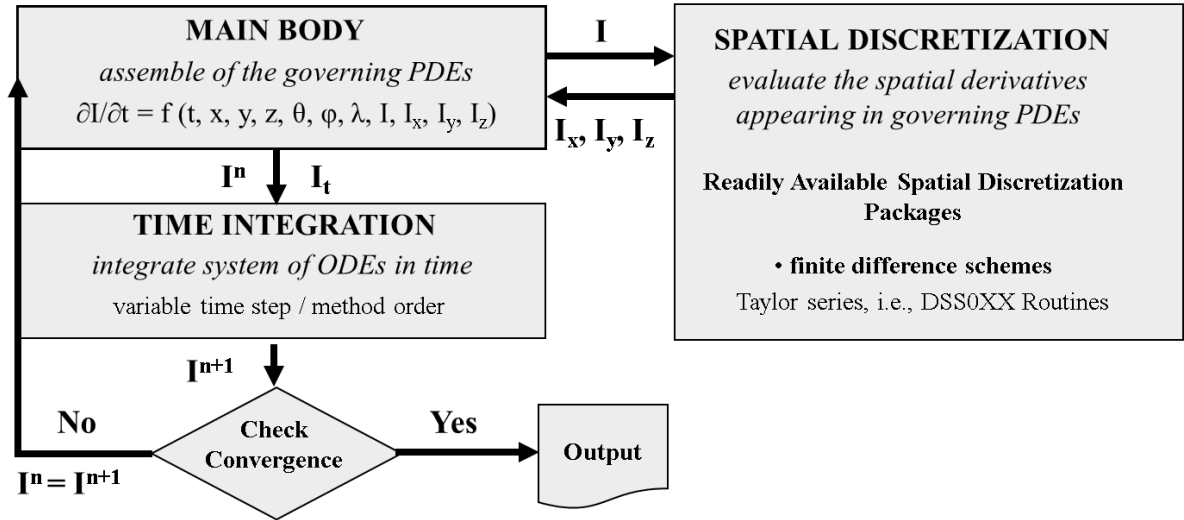


Figure 2.5 Schematic representation of MOL solution of DOM

### 2.3.1 Parameters Affecting the Accuracy of MOL Solution DOM

Accuracy and CPU efficiency of MOL solution of DOM is determined by the following parameters:

- ⊗ Accuracy of the angular discretization
- ⊗ Accuracy of the spatial discretization
- ⊗ Selection of time steps in the solution of initial value problem
- ⊗ Solution method used for the system of ODEs


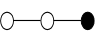
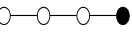
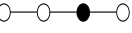
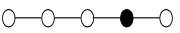
The accuracy of angular discretization depends on the angular quadrature scheme and the order of approximation selected for the implementation of DOM. Therefore, dependence of the accuracy of MOL solution of DOM on the angular approximation is the same as that of DOM (see Section 2.2.1).

The spatial discretization method used in MOL solution of DOM is finite-difference method (FDM) while finite-volume method (FVM) is utilized in DOM. In FVM, differential equation is integrated over a control volume and the resultant equation is discretized using spatial differencing scheme. The spatial discretization schemes used in

this study are two- and three-point upwind schemes (DSS012 and DSS014) [90, 91]. The reasons behind this choice are as follows; (i) after the implementation of false-transients approach, discrete ordinates equations take the form of first-order hyperbolic PDEs, for which upwind schemes eliminate the numerical oscillations caused by central differencing, as the direction of propagation of the dependent variables are taken into account in upwind schemes [90, 91], (ii) higher order upwind schemes (DSS016-DSS020) has been shown to lead to numerical oscillations in the solution of RTE [19].

Formulation and order of accuracy of the selected schemes, DSS012 and DSS014, are presented in Table 2.2 together with higher order of approximations. First two columns of the table show the name of the scheme and stencil, respectively. Formulation of first derivatives with selected schemes for grid spacing of  $\Delta\lambda$  is presented in the third column. Last column of the table shows the order of truncation error.

Table 2.2 Spatial differencing schemes with FDM [90, 91]

Name of the scheme	Stencil	Formulation $dI(\lambda)/d\lambda \approx$	Order of accuracy
<b>2-point upwind (DSS012)</b>		$(I_i - I_{i-1}) / \Delta\lambda$	$O(\Delta\lambda)$
<b>3-point upwind (DSS014)</b>		$(3I_i - 4I_{i-1} + I_{i-2}) / 2\Delta\lambda$	$O(\Delta\lambda^2)$
<b>4-point upwind (DSS016)</b>		$(11I_i - 18I_{i-1} + 9I_{i-2} - 2I_{i-3}) / 6\Delta\lambda$	$O(\Delta\lambda^3)$
<b>4-point biased upwind (DSS018)</b>		$(2I_{i+1} + 3I_i - 6I_{i-1} + I_{i-2}) / 6\Delta\lambda$	$O(\Delta\lambda^3)$
<b>5-point biased upwind (DSS020)</b>		$(3I_{i+1} + 10I_i - 18I_{i-1} + 6I_{i-2} - I_{i-3}) / 12\Delta\lambda$	$O(\Delta\lambda^4)$



Last factor affecting the predictive accuracy of MOL solution of DOM approach is the selection of time step for the initial value problem and ODE solver. In this study, solution method used for the system of ODEs is ROWMAP, which is based on the ROW-methods of order 4 and uses Krylov techniques for the solution of linear systems. By a special multiple Arnoldi process, order of the basic method is preserved with small Krylov dimensions. Step size control is done by embedding with a method of order 6. Detailed description of ROWMAP can be found elsewhere [92].

## 2.4 Structure and Operation of the In-House Developed Code

Figure 2.6 and Figure 2.7 show the flow diagram of the computer code Method of Lines Solution of Discrete Ordinates Method for non-gray absorbing, emitting and scattering medium (MOLSDOM - NGAESM). The general steps of the computer code are as follows:

1. Define the subdivision of the enclosure, number of wide bands, order of approximation and number of equations in the system of ODEs.
2. Declare 8D arrays to store intensities, position derivatives, and time derivatives at each ordinate of each grid point. The 8D arrays are of dimensions  $[NX \times NY \times NZ \times ND \times NM \times NB \times NW \times NC]$  where  $NX$ ,  $NY$  and  $NZ$  are the number of nodes along  $x$ ,  $y$  and  $z$ -axes respectively. In case of cylindrical coordinates,  $NX \times NY \times NZ$  becomes  $NR \times NZ$ , which are the number of nodes  $r$  and  $z$ -axes respectively.  $ND$  is the number of octants considered in the calculation ( $ND=8$ ),  $NM$  is the number of ordinates specified by the order of angular quadrature and  $NB$  is the number of spectral bands for gases/particles (if  $NB=1$ , medium is gray).  $NW$  and  $NC$  are the number of gray gases used in SLW model. If any other gas property model is used,  $NW$  and  $NC$  dimensions become 1.
3. Specify parameters for the ODE integrator which are the initial time, final time, print interval and the error tolerance.
4. Specify initial condition for the intensities.
5. Read in input data specifying the physics of the problem which are, the dimensions of the enclosure, emissivities of the walls, gas composition of the medium, temperatures and temperature profiles of the medium and the walls.
6. Specify direction cosines and corresponding weights.
7. Initialize the intensities at all ordinates at all grid points.
8. Print interpolated temperature profiles of the medium and side wall.
9. Read in input data related to radiative properties of the medium which are gas and particle absorption coefficients, particle scattering coefficient and coefficients of the scattering phase function.

10. Calculate the scattering phase function for each incoming and outgoing ordinates.
11. Set boundary conditions for the intensities leaving the boundary surfaces.

**Calculation of the Approximations for the Spatial Derivatives in Rectangular Coordinates:**

12. Specify the spatial discretization scheme (DSS012 or DSS014).
13. Specify an octant and ordinate.
14. Specify a discrete location on the y, z plane.
15. Store the values of the intensities (at this direction and location) along x – axis in a 1D array.
16. Call for spatial discretization subroutine which accepts the 1D array of intensities as an input and computes the derivative with respect to x – axis as an output over the grid of NX points.
17. Transfer the 1D array of spatial derivatives into 8D array of x – derivatives.
18. Repeat steps 13-17 for all discrete locations on y-z plane, all ordinates and all octants.
19. Repeat steps 13-18 for derivative terms with respect to y and z-axes, forming 1D arrays along y and z – axes.

**Calculation of the Approximations for the Spatial Derivatives in Cylindrical Coordinates:**

12. Specify the spatial discretization scheme (DSS012 or DSS014).
13. Specify an octant, number of level and an ordinate at specified level.
14. Specify a discrete location at the r direction.
15. Store the values of the intensities (at this direction and location) along r-axis in a 1D array.
16. Call for spatial discretization subroutine which accepts the 1D array of intensities as an input and computes the derivative with respect to r-axis as an output over the grid of NR points.
17. Transfer the 1D array of spatial derivatives into the 8D array of r-derivatives.

18. Repeat steps 11-15 for all discrete locations at r direction, all ordinates and all octants.
19. Repeat steps 11-16 for derivative terms with respect to z-axes, forming 1D arrays along z-axes.

### **Calculation of the Time Derivatives:**

20. Set the signs of the direction cosines for each octant.
21. Calculate the time derivative of intensity at each node for each ordinate of each octant to form a 8D array of time derivatives.
22. Set boundary conditions for the intensities leaving the boundary surfaces.
23. Transform the 8D arrays of intensities and time derivatives into 1D arrays to be sent to the ODE solver.

### **Integration of the system of ODEs:**

24. Set the initial conditions required for the ODE integrator.
25. Set parameters for the ODE integrator.
26. Call the ODE solver subroutine to integrate the system of ODEs by using a time adaptive method. The ODE propagates in time by solving for the intensities at a time step  $j$ , calculating the time derivatives by performing steps 11 to 23 and integrating again to solve for intensities at the new time step  $j+1$ .
27. Return to the main program at pre-specified time intervals.
28. Check if ODE integration has proceeded satisfactorily.
29. Transfer the solution at current print point from the 1D array to a 8D array.
30. Set the boundary conditions at current time step.
31. Check for convergence by comparing the solutions at current time step with those at previous three time steps. If current solution is within the specified range of the previous solution, convergence is established go to step 35.
32. If convergence is not established, save the solution for convergence check.
33. Check end of the run time if final time is not reached go back to step 13.
34. If convergence is established or final time is reached, calculate the parameters of interest such as incident radiative heat flux and radiative energy source term.

35. Print output.

36. Stop.

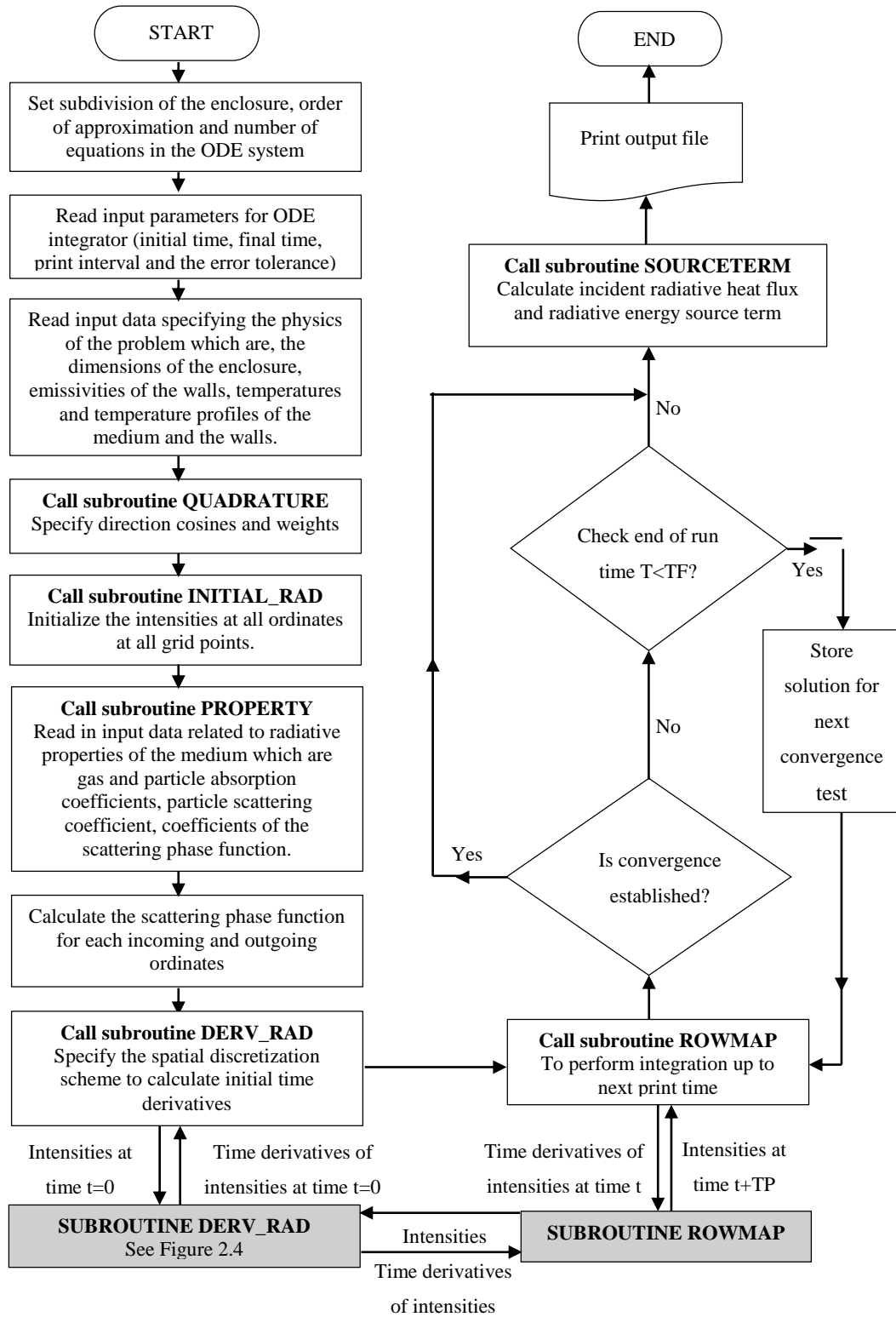


Figure 2.6 Flowchart for MOLSDOM - NGAESM

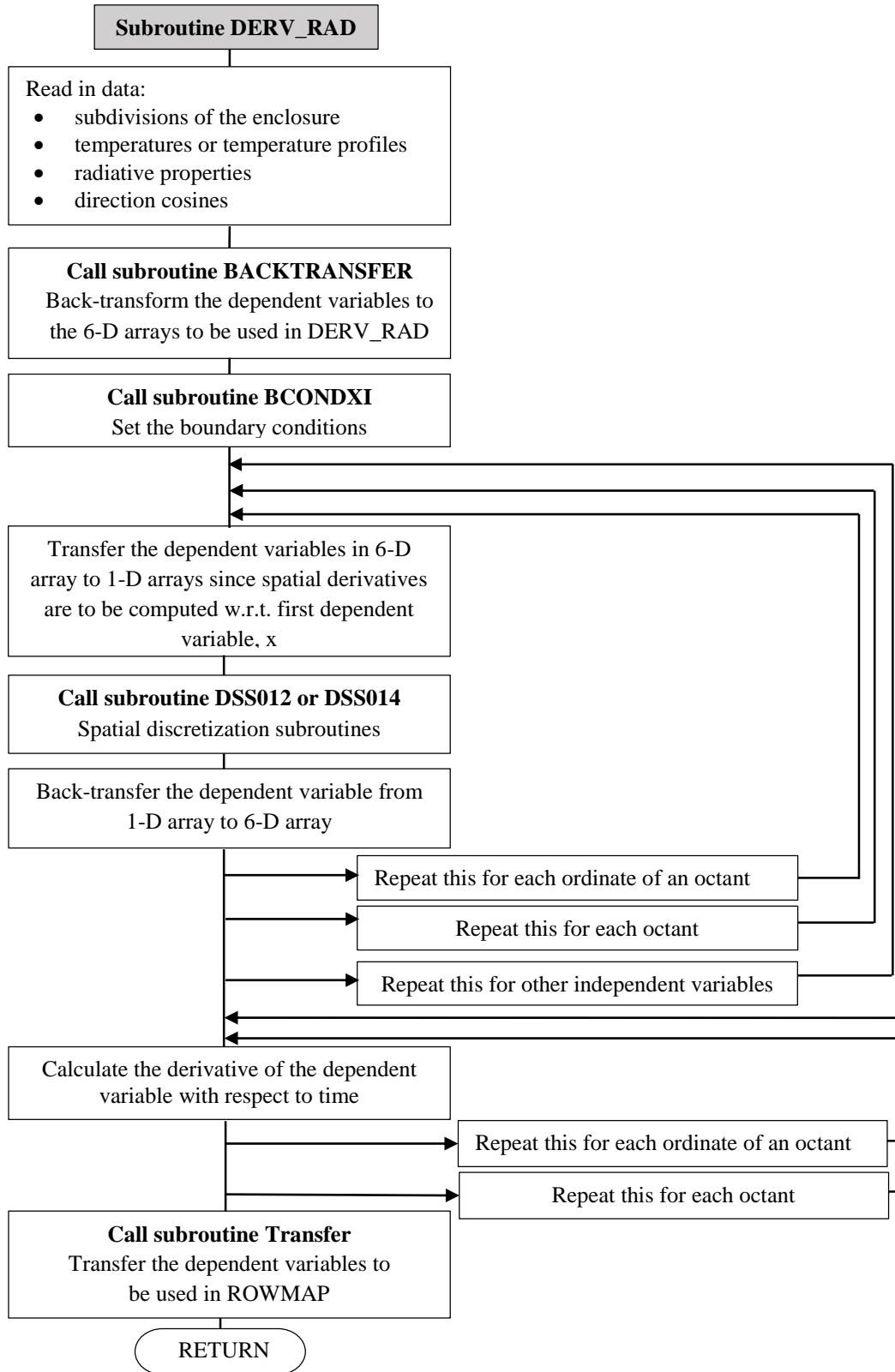


Figure 2.7 Algorithm of the subroutine DERV\_RAD





## CHAPTER 3

### RADIATIVE PROPERTY MODELS FOR GASES

Modeling of radiative heat transfer necessitates not only accurate but also computationally efficient methods for (i) solution of the radiative transfer equation (RTE) in conjunction with the time-dependent conservation equations for mass, momentum, energy, and chemical species and (ii) radiative properties of the medium. In the previous chapter, MOL solution of DOM has been explained as an accurate and CPU efficient technique for the solution of RTE. In this chapter, gas property models used in this study are described in detail.

#### 3.1 Gas Property Models

The most fundamental radiative property of participating gases is absorption coefficient or absorption cross-section, which is the absorption coefficient normalized by the molar density. The variation of absorption coefficient or absorption cross-section of a gas with wave number / wavelength is called a spectrum, and it consists of millions of spectral lines, which are produced by the vibrational-rotational transitions in molecular energy levels. Spectral absorption cross section of H<sub>2</sub>O and CO<sub>2</sub> generated from HITEMP 2010 database [30] at 1500 K is demonstrated for several gas pressures in Figure 3.1 and Figure

3.2, respectively. As can be clearly seen from these figures, spectral dependency of both H<sub>2</sub>O and CO<sub>2</sub> absorption coefficients are highly nonlinear and strongly wave number dependent. This is why modeling of radiative heat transfer is a formidable task when medium involves participating gases as in the case of combusting systems.

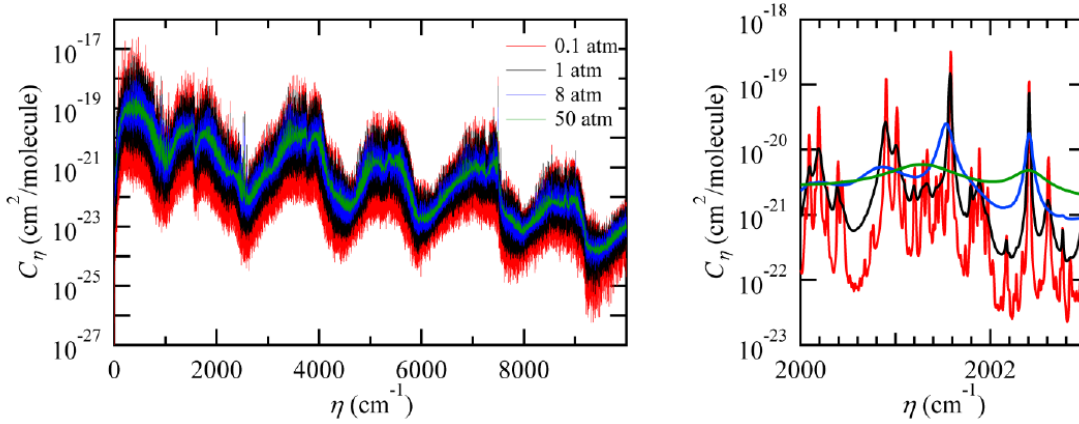


Figure 3.1 Spectral absorption cross-section of H<sub>2</sub>O at 1500 K generated from HITEMP 2010 database [93]

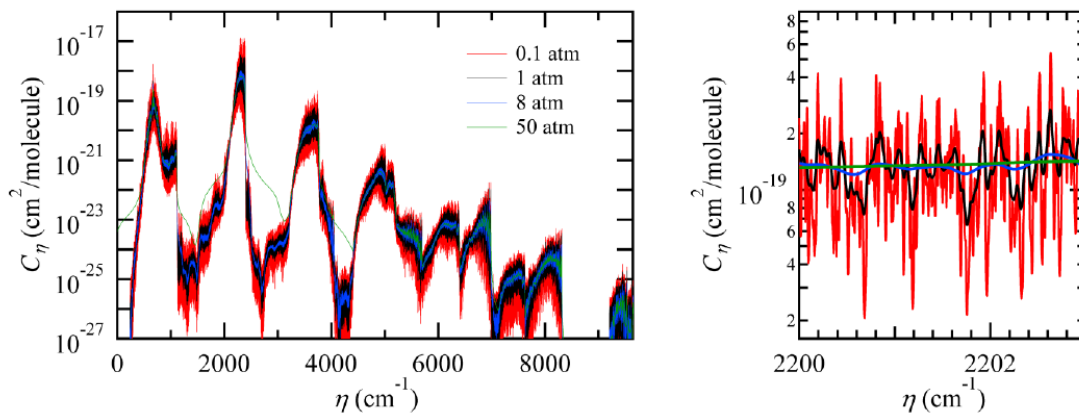


Figure 3.2 Spectral absorption cross-section of CO<sub>2</sub> at 1500 K generated from HITEMP 2010 database [93]

A wide variety of gas spectral radiative property models with different degrees of complexity and accuracy are available in the literature for the evaluation of radiative properties of gases. These models can be classified into two main groups, namely gray and non-gray gas radiative property models. Gray gas models are the crudest yet most CPU efficient models, in which gas absorption coefficient is assumed to be independent of wave number. Non-gray gas radiative property models, on the other hand, include the spectral dependency at various forms. In the present study, 2 gray and 5 non-gray gas property models are utilized. Details of these models are described in the following sections.

### 3.2 Gray Gas Model based on Leckner's Correlations

The first gray gas model used in this study is based on Leckner's correlations. In this model, a single gas absorption coefficient is evaluated for a gas mixture of H<sub>2</sub>O and CO<sub>2</sub> for the entire spectrum. Although this approach simplifies the radiative transfer calculations significantly and offers the best CPU economy, it brings the largest errors in the solution of RTE due to its crude gray gas assumption and its old database for gas absorption bands [94].

In this model, gas absorption coefficient is calculated from the emissivity of the gas mixture and mean beam length of the enclosure ( $=3.6\text{Volume}/\text{Surface Area}$ ),

$$\kappa_g = -(1/L_m)\ln(1 - \varepsilon_g) \quad (3.1)$$

where emissivity of the gas mixture ( $\varepsilon_g$ ) is calculated by using Leckner's correlations, which require emissivities of individual gaseous species,

$$\varepsilon_g = \varepsilon_{\text{H}_2\text{O}} + \varepsilon_{\text{CO}_2} - \varepsilon_{\text{H}_2\text{O}}\varepsilon_{\text{CO}_2} \quad (3.2)$$

where  $\varepsilon_{\text{H}_2\text{O}}$  and  $\varepsilon_{\text{CO}_2}$  are calculated from the gas temperature, partial pressures of water vapor and carbon dioxide and the mean beam length,

$$\varepsilon_k = \exp \left( \sum_{j=0}^M \sum_{i=0}^N c_{ij} \left( \frac{T}{1000} \right)^j (\log_{10}(P_k L_m))^i \right) \quad (3.2)$$

where T is the gas temperature,  $P_k$  is partial pressure of the participating gas k and  $c_{ij}$  are fitting constants for H<sub>2</sub>O and CO<sub>2</sub>. These constants are given in Table 3.1 and Table 3.2 for H<sub>2</sub>O and CO<sub>2</sub>, respectively [94].

Table 3.1 Fitting constants of Leckner's Correlations ( $c_{ij}$ ) for H<sub>2</sub>O (M=2, N=2)

i	$c_{0i}$	$c_{1i}$	$c_{2i}$
0	-2.2118	-1.1987	0.035596
1	0.85667	0.93048	-0.14391
2	-0.10838	-0.17156	0.045915
Deviation from values calculated with spectral data is max $\pm$ 5%			

Table 3.2 Fitting constants of Leckner's Correlations ( $c_{ij}$ ) for CO<sub>2</sub> (M=3, N=4)

i	$c_{0i}$	$c_{1i}$	$c_{2i}$	$c_{3i}$	$c_{4i}$
0	-3.9781	2.7353	-1.9882	0.31054	0.015719
1	1.9326	-3.5932	3.7247	-1.4535	0.20132
2	-0.35366	0.61466	-0.84207	0.39859	-0.063356
3	-0.080181	0.31466	0.19973	0.046532	-0.0033086
Deviation from values calculated with spectral data is max $\pm$ 5%					

### 3.3 Gray Wide Band (GWB) Approximation

Gray wide band approximation (GWB) is a method proposed within the scope of this study, which is based on the database of the well-known statistical narrow band (SNB) model [21, 95].

In the SNB model, gas transmissivity over an isothermal and homogeneous path is given as [95],

$$\bar{\tau}_\lambda(L) = \left[ -\frac{\pi B}{2} \left( \sqrt{1 + \frac{4SL}{\pi B}} - 1 \right) \right] \quad (3.3)$$

where  $B = 2\bar{\beta}_v/\pi^2$ ,  $S = \bar{k}_v X p$ ,  $L$  is the path length,  $X$  is the mole fraction of the radiating gas,  $p$  is the pressure,  $\bar{k}_v$  is the mean line-intensity to spacing ratio,  $\bar{\beta}_v = 2\pi\bar{\gamma}/\bar{\delta}_v$  is the mean line width to spacing ratio,  $\bar{\gamma}$  is the mean collision half-width of an absorption line and  $\bar{\delta}_v$  is the equivalent line spacing. In this study,  $\bar{k}_v$  and  $\bar{\delta}_v$  are taken from Soufiani and Taine [96] and from Riviere and Soufiani [97].  $\bar{\gamma}$  for  $H_2O$  and  $CO_2$ , are given by [23],

$$\bar{\gamma}_{H_2O} = \frac{p}{p_s} \left\{ 0.462 X_{H_2O} \left( \frac{T_s}{T} \right) + \left( \frac{T_s}{T} \right)^{0.5} \left[ 0.079(1 - X_{CO_2} - X_{O_2}) + 0.106 X_{CO_2} + 0.036 X_{O_2} \right] \right\} \quad (3.4)$$

$$\bar{\gamma}_{CO_2} = \frac{p}{p_s} \left( \frac{T_s}{T} \right)^{0.7} \left\{ 0.07 X_{CO_2} + 0.058(1 - X_{CO_2} - X_{H_2O}) + 0.1 X_{H_2O} \right\} \quad (3.5)$$

where  $p_s$  and  $T_s$  are equal to 1 atm and 296 K, respectively.

After obtaining the spectral transmissivity distribution with  $25 \text{ cm}^{-1}$  intervals, spectral absorption coefficients are found from:

$$\kappa_{g\lambda} = \left( -\frac{1}{L_m} \right) \ln(1 - \varepsilon_{g\lambda}) \quad (3.6)$$

where  $\varepsilon_{g\lambda} = 1 - \bar{\tau}_\lambda$  is the spectral gas emissivity.

After obtaining the spectral database as in the case of the SNB model, in the proposed approach (GWB approximation), spectrum is divided into wide spectral bands, in which gas absorption coefficient are assumed to be gray (constant). Then, for each band, gray gas absorption coefficient is evaluated from spectral absorption coefficients ( $\kappa_{g\lambda}$ ) by averaging over Planck distribution according to Eq. (3.7), where NB' represents the total number of spectral points within the  $j^{\text{th}}$  gray wide band<sup>2</sup>,

$$\kappa_{g,j} = \frac{\sum_{j'=1}^{\text{NB}'} \kappa_{g\lambda,j'} (F_{0-j'+1} - F_{0-j'})}{\sum_{j'=1}^{\text{NB}'} (F_{0-j'+1} - F_{0-j'})} \quad (3.7)$$

In order to utilize these gas absorption coefficients ( $\kappa_{g,j}$ ), spectral RTEs for non-gray absorbing, emitting and scattering media (Eqs. 2.37 and 2.38) are also written in a banded form as shown below,

$$\begin{aligned} k_t \frac{\partial I_j^{m,\ell}}{\partial t} = & - \left( \frac{\mu_{m,\ell}}{r} \frac{\partial (r I_j^{m,\ell})}{\partial r} - \frac{1}{r} \frac{(\gamma_{m,\ell+1/2} I_j^{m,\ell+1/2} - \gamma_{m,\ell-1/2} I_j^{m,\ell-1/2})}{w_{m,\ell}} \right) + \xi_{m,\ell} \frac{\partial I_j^{m,\ell}}{\partial z} \\ & - (\kappa_{g_j} + \kappa_{p_j} + \sigma_{p_j}) I_j^{m,\ell} + (\kappa_{p_j} + \kappa_{g_j}) (F_{0-j+1} - F_{0-j}) I_b \\ & + \frac{\sigma_{p_j}}{4\pi} \sum_{m',\ell'} \Phi_j(\boldsymbol{\Omega}_{m',\ell'}, \boldsymbol{\Omega}_{m,\ell}) w_{m',\ell'} I_j^{m',\ell'} \end{aligned} \quad (3.8)$$

$$\begin{aligned} k_t \frac{\partial I_j^{m,\ell}}{\partial t} = & -\mu_{m,\ell} \frac{\partial I_j^{m,\ell}}{\partial x} - \eta_{m,\ell} \frac{\partial I_j^{m,\ell}}{\partial y} - \xi_{m,\ell} \frac{\partial I_j^{m,\ell}}{\partial z} - (\kappa_{g_j} + \kappa_{p_j} + \sigma_{p_j}) I_j^{m,\ell} \\ & + (\kappa_{p_j} + \kappa_{g_j}) (F_{0-j+1} - F_{0-j}) I_b \\ & + \frac{\sigma_{p_j}}{4\pi} \sum_{m',\ell'} \Phi_j(\boldsymbol{\Omega}_{m',\ell'}, \boldsymbol{\Omega}_{m,\ell}) w_{m',\ell'} I_j^{m',\ell'} \end{aligned} \quad (3.9)$$

where  $(F_{0-j+1} - F_{0-j})$  is the fraction of the energy emitted from a blackbody in the  $j^{\text{th}}$  spectral band, g and p denote the gas mixture and particles, respectively.

---

<sup>2</sup> In this notation,  $j^{\text{th}}$  gray band refers to spectral region between (j) and (j+1). For example, "Band 3" refers to the spectral band between point "3" and "4".

It should be noted that gray wide band approximation (GWB) can be deployed as a gray gas approximation or a crude non-gray gas property model. If the width of the spectral band is selected as the entire spectrum, then only one gas absorption coefficient is calculated with Eq. (3.7) and  $(F_{0-j+1} - F_{0-j})$  in Eq. (3.8) or Eq. (3.9) becomes 1.0. In this case, GWB approximation becomes a gray gas property model. If the spectrum is divided into 10 wide bands, then 10 gas absorption coefficients are calculated with Eq. (3.7) and summation of fractions of blackbody emissions  $(F_{0-j+1} - F_{0-j})$  becomes 1.0. In this case, GWB approximation can be considered as a non-gray gas property model.

### 3.4 Gray Narrow Band (GNB) Approximation

Gray Narrow Band (GNB) model is an improved version of GWB approximation. In GWB approximation, this spectrum is divided into several wide bands by Planck mean averaging so that banded form of RTE (Eqs. (3.8) and (3.9)) is needed to be solved for only several times. However, this approximation may not capture the nonlinear behaviour of the gas spectrum.

In order to have a more refined model, the same approach is utilized with the narrowest band available in the database. Spectral database used in SNB model [97] is available for wave numbers between 25 and 11250  $\text{cm}^{-1}$ , with 25  $\text{cm}^{-1}$  intervals, which covers the entire thermal radiation spectrum. In GNB model, band width used in Eq. (3.7) is taken as 25  $\text{cm}^{-1}$  and gas absorption coefficient is taken as constant within each band width ( $\kappa_{g,j} = \kappa_{g\lambda}$ ). It should be noted that 25  $\text{cm}^{-1}$  intervals are indeed very narrow considering the variation of blackbody emissive power with wavenumber. To illustrate, average value of  $(F_{0-j+1} - F_{0-j})$  between 25 and 11250  $\text{cm}^{-1}$  becomes less than 0.002 with a maximum value 0.007 if band width is selected as 25  $\text{cm}^{-1}$ .

### 3.5 Spectral Line-Based Weighted Sum of Gray Gases (SLW)

The line-by-line (LBL) treatment of the gas spectrum is extremely computationally intensive for practical engineering applications and requires the solution of spectral RTE for over  $10^6$  wave numbers. These high CPU requirements can be alleviated by deploying accurate narrow band models such as SNBCK, which has been shown to lead to very accurate results and considered to be as a reference solution [25]. Nevertheless, dividing the spectrum into small wave number intervals consisting of a sufficient number of spectral lines and solving the RTE for each of these intervals is still computationally very intensive. Fortunately, it was observed that approximately the same values of the absorption cross-sections are repeated in many wave number intervals within a certain range delineated by two consecutive supplemental absorption cross-sections,  $\tilde{C}_{abs,j}$ . Therefore, it was considered that these repeated absorption cross sections can be combined in groups and treated as separate gray gases with constant absorption cross-sections,  $C_{abs,j}$ . Figure 3.3 schematically illustrates how the real spectrum can be approximated by grouping into 4 gray gases.

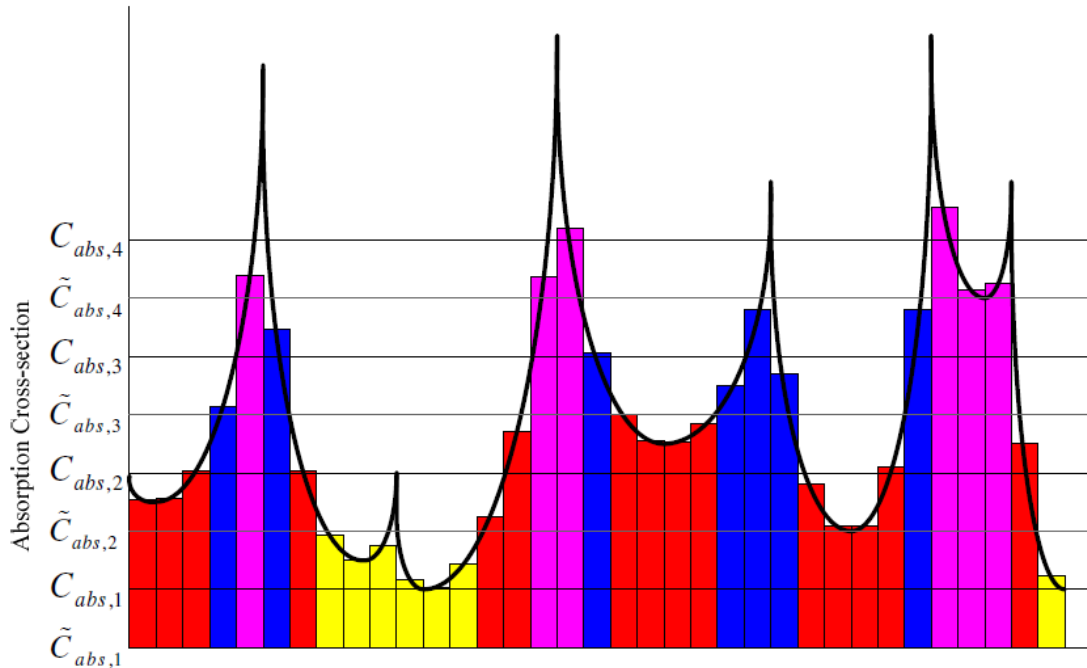


Figure 3.3 Approximation of a real spectrum by grouping into 4 gray gases [28]



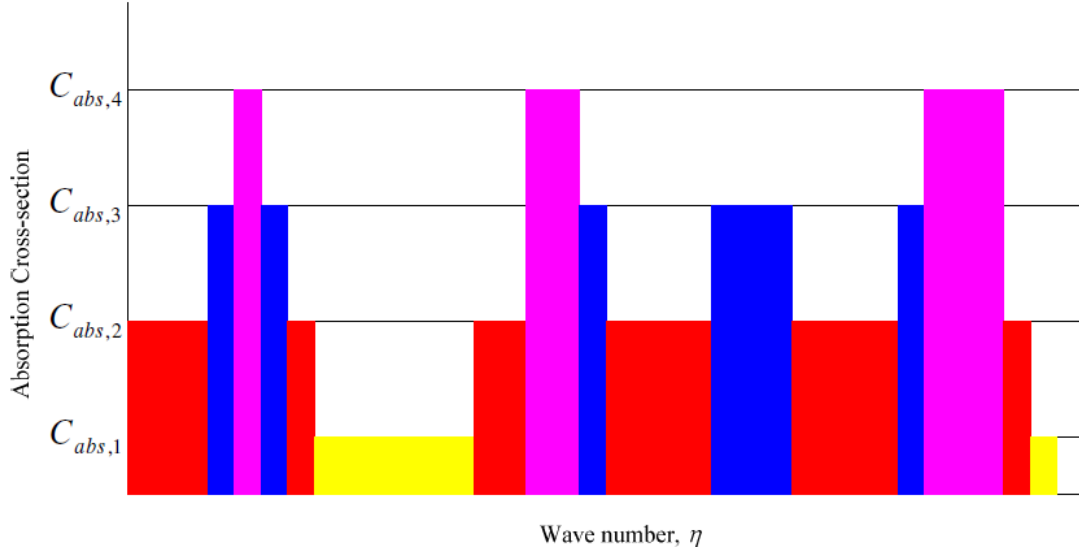


Figure 3.3 Approximation of a real spectrum by grouping into 4 gray gases [28] (cont'd)

This idea of replacing a non-gray (real) gas by a set of gray gases forms the basis of one of the most commonly used gas property model, Weighted Sum of Gray Gases (WSGG), which was first introduced by Hottel and Sarofim [26] for the approximation of gas total emissivity,

$$\varepsilon = \sum_j a_j (1 - \exp(-C_{abs,j}NL)) \quad (3.10)$$

where  $C_{abs,j}$  is the discrete gray gas absorption cross-section,  $N$  is the molar density,  $L$  is the path length and  $a_j$  is the associated gray gas weight. The gray gas weights can be physically interpreted as the fraction of the blackbody energy in the spectral regions where the absorption cross-section is  $C_{abs,j}$  [26].

Denison and Webb improved this model to the spectral line-based weighted sum of gray gases (SLW) model by expressing the gray gas weights in terms of an absorption-line blackbody distribution function [27-29] derived from the high resolution HITRAN and HITEMP database. SLW is accepted as a modern, state-of-the-art gas property model [21] and is utilized as the reference gas property model in this study.

In SLW, WSGG approach is extended by introducing an “absorption-line blackbody distribution function”, which incorporates the local value of the blackbody distribution function together with the local absorption cross-sections. The procedure of the SLW model consists of two main stages and they are described in detail in the following subsections.

### 3.5.1 Calculation of Absorption Coefficients

The primary variable used in the calculation of absorption coefficients is the absorption cross-section, which is defined as the ratio absorption coefficient to the molar density,  $N$ . In order to calculate the absorption coefficients, first, a set of logarithmically spaced absorption cross-sections are selected to span the gas spectrum. In this study, non-gray gas mixture is replaced by 3-25 absorption cross-sections, which are logarithmically spaced between  $3 \times 10^{-5}$  and  $60 \text{ m}^2/\text{mole}$  for  $\text{H}_2\text{O}$  and  $3 \times 10^{-5}$  and  $120 \text{ m}^2/\text{mole}$  for  $\text{CO}_2$  as recommended [28, 29]. These logarithmically spaced absorption cross-sections are called supplemental absorption cross-sections ( $\tilde{C}_{abs,j}$ ) and they are used to determine the boundaries of absorption cross sections ( $C_{abs,j}$ ) and to evaluate blackbody weights ( $a_j$ ).

Each space between two consecutive supplemental absorption cross sections ( $\tilde{C}_{abs,j}$  and  $\tilde{C}_{abs,j+1}$ ) is considered as a separate gray gas associated with a constant absorption cross section ( $C_{abs,j}$ ) and calculated as follows,

$$C_{abs,j} = \exp\left(\frac{\ln(\tilde{C}_{abs,j}) + \ln(\tilde{C}_{abs,j+1})}{2}\right) \quad (3.11)$$

Once the absorption cross-sections for each gray gas are determined, absorption coefficients of each gray gas are evaluated from,

$$\kappa_j = NC_{abs,j} \quad (3.12)$$

where molar density ( $N$ ) can be found from any equation of state by using local temperature, pressure and composition. In the present study, gas mixture is assumed to be

ideal due to high temperatures and low pressures of the gas mixtures in the test case problems (see Chapter 5).

It should be noted that one gray gas is associated with “zero absorption coefficient” and used to represent transparent regions in the spectrum.

### 3.5.2 Calculation of Gray Gas Weights

Absorption-line blackbody distribution function ( $F_s$ ), which was proposed by Denison and Webb to improve WSGG model [27], provides an efficient way for the evaluation of blackbody weights ( $a_j$ ). It is defined as the fraction of the blackbody energy ( $E_{b,\eta}$ ) within the spectrum, in which spectral absorption cross-section ( $C_{abs,\eta}$ ) is less than the prescribed value  $C_{abs}$ . A representative demonstration of blackbody distribution function is illustrated in Figure 3.4, where portions of the spectrum over which Planck’s function is integrated are represented by the shaded segments in the figure [28].

This blackbody distribution function is defined as follows for specie  $s$ ,

$$F_s(C_{abs}, T_b, T_g, P_T, Y_s) = \frac{1}{\sigma T_b^4} \sum_i \int_{\Delta\eta_i(C_{abs}, T_b, T_g, P_T, Y_s)} E_{b,\eta}(\eta, T_b) d\eta \quad (3.13)$$

where  $E_{b,\eta}$  is Planck’s function evaluated at the wave number of interest ( $\eta$ ) and blackbody temperature,  $T_b$ . Subscript  $i$  denotes the  $i^{\text{th}}$  spectral band and summation is performed over all bands covering the entire spectrum. The dependence of the function on the spectrum is through the spectral integration of each segment  $\Delta\eta_i$ , which is dependent on the absorption cross-section ( $C_{abs}$ ), gas temperature ( $T_g$ ), total pressure ( $P_T$ ) and mole fraction of specie  $s$  ( $Y_s$ ).

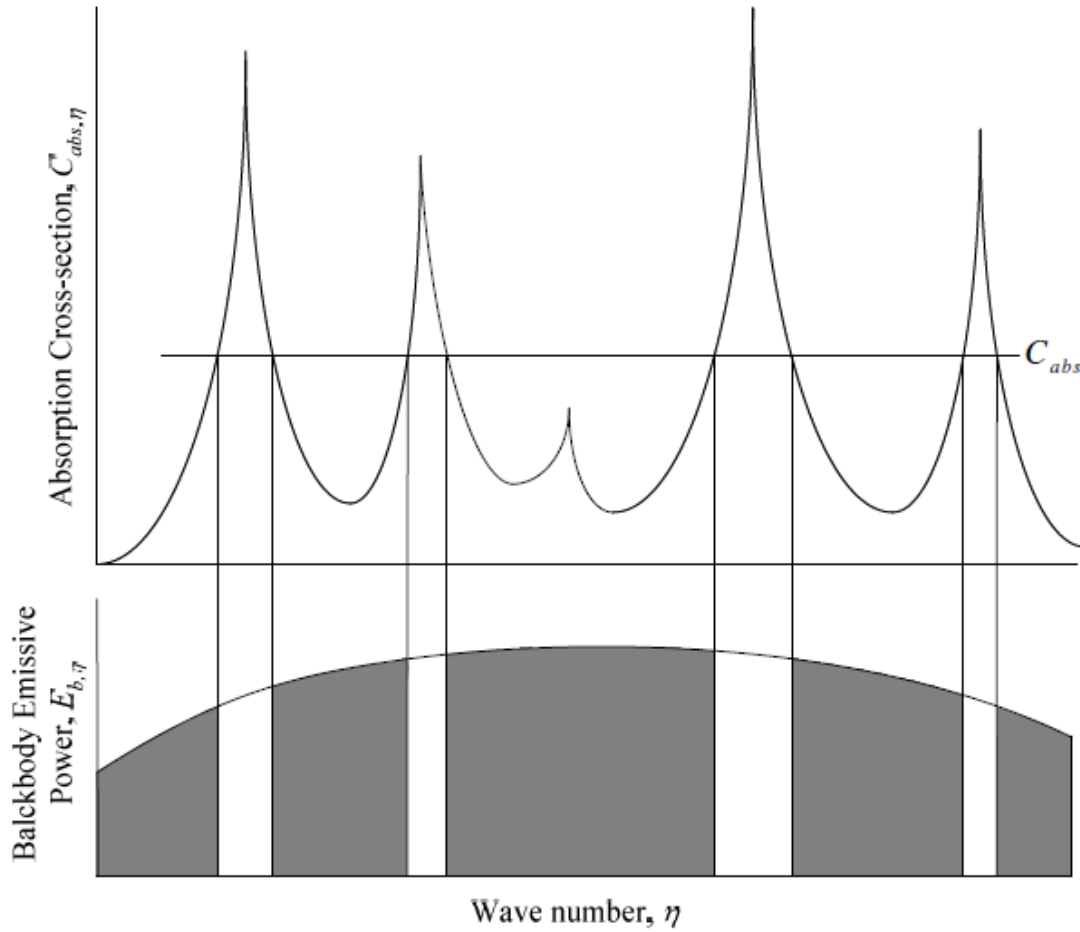


Figure 3.4 Spectrum involving a few representative absorption lines and corresponding fraction of blackbody energy

The blackbody weights ( $a_j$ ) are expressed as the fractions of the blackbody energy at local gas temperatures in the spectral regions where the absorption cross-section is between  $\tilde{C}_{abs,j}$  and  $\tilde{C}_{abs,j+1}$  (orange zones), which corresponds to gray shaded areas on blackbody emissive power distribution (see Figure 3.5). Therefore, blackbody weights ( $a_j$ ) can be calculated from the difference between absorption-line blackbody distribution functions ( $F_s$ ) evaluated at these two consecutive supplemental absorption cross-sections ( $\tilde{C}_{abs,j}$  and  $\tilde{C}_{abs,j+1}$ ),

$$a_j = F_s(\tilde{C}_{abs,j+1}, T_b, T_g, P_T, Y_s) - F_s(\tilde{C}_{abs,j}, T_b, T_g, P_T, Y_s) \quad (3.14)$$

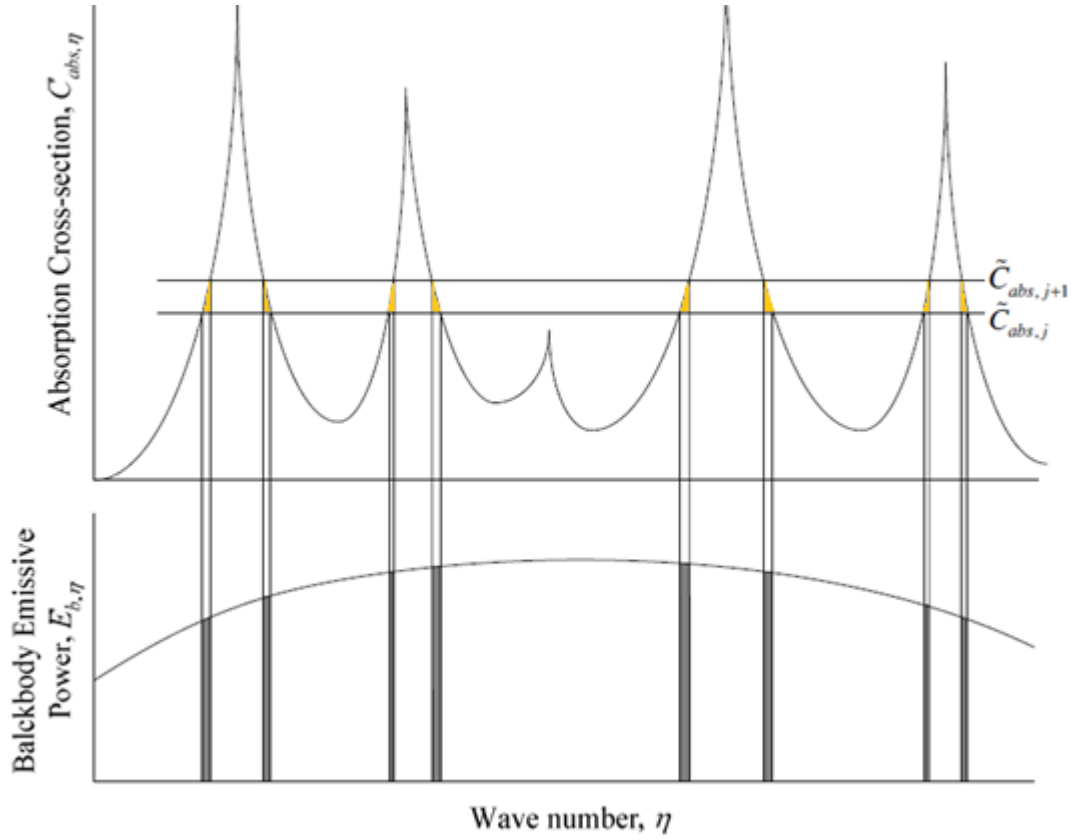


Figure 3.5 Portions of the spectrum where absorption cross-section ( $C_{abs}$ ) is between two supplemental absorption cross sections ( $\tilde{C}_{abs,j}$  and  $\tilde{C}_{abs,j+1}$ )

Denison and Webb [27-29] provided simple mathematical correlations for the absorption-line blackbody distribution function for H<sub>2</sub>O and CO<sub>2</sub>. For water vapor, absorption-line blackbody distribution function is given as,

$$F_w = \frac{1}{2} \tanh \left( P_w(T_g, T_b, \xi - \xi_{sb}) \right) + \frac{1}{2} \quad (3.15)$$

where  $P_w$  is found from,

$$P_w(T_g, T_b, \xi - \xi_{sb}) = \sum_{m=0}^3 \sum_{n=0}^3 \sum_{l=0}^3 b_{lmn} \left( \frac{T_g}{2500} \right)^n \left( \frac{T_b}{2500} \right)^m (\xi - \xi_{sb})^l \quad (3.16)$$

where

$$\xi = \ln(C_{abs}) \quad (3.17)$$

$\xi_{sb}$  introduced to account for the self- broadening and defined as,

$$\xi_{sb} = \sum_{m=0}^3 \sum_{n=0}^2 \sum_{l=0}^3 c_{lmn} \left( \frac{T_b}{2500} \right)^n (\xi_{sb})^m (Y_w)^{l+1} \quad (3.18)$$

Similarly, absorption-line blackbody distribution function for CO<sub>2</sub> is given by,

$$F_c = \frac{1}{2} \tanh \left( P_c(T_g, T_b, \xi) \right) + \frac{1}{2} \quad (3.19)$$

where  $P_c$  is found from,

$$P_c(T_g, T_b, \xi) = \sum_{m=0}^3 \sum_{n=0}^3 \sum_{l=0}^3 d_{lmn} \left( \frac{T_g}{2500} \right)^n \left( \frac{T_b}{2500} \right)^m (\xi)^l \quad (3.20)$$

where

$$\xi = \ln(C_{abs}) \quad (3.21)$$

In above equations,  $b_{lmn}$ ,  $c_{lmn}$  and  $d_{lmn}$  are the coefficients generated from the spectral database (k-distributions) and given in Table 3.3, Table 3.4 and Table 3.5, respectively.

Table 3.3  $b_{lmn}$  coefficients used in Eq. (3.16) for H<sub>2</sub>O [28]

$l = 0$

$m/n$	0	1	2	3
0	1.6103	-4.0931	5.1435	-2.0857
1	-0.81812	15.5525	-21.819	9.8775
2	2.6001	-21.204	31.0828	-14.279
3	-1.3171	9.6524	-14.474	6.6747

$l = 1$

$m/n$	0	1	2	3
0	0.440187	-0.63348	0.871627	-0.38798
1	-0.82164	5.0239	-5.9818	2.6355
2	1.5149	-7.8032	9.8642	-4.1931
3	-0.81023	3.727	-4.874	1.9868

$l = 2$

$m/n$	0	1	2	3
0	0.106647	-0.43116	0.689598	-0.29831
1	-0.38573	1.8865	-2.9712	1.2834
2	0.578351	-2.6218	4.2698	-1.7929
3	-0.28014	1.1785	-1.9568	0.787249

$l = 3$

$m/n$	0	1	2	3
0	8.25027E-03	-3.28556E-02	6.81563E-02	-3.04815E-02
1	-3.10578E-02	0.123369	-0.26154	0.117452
2	4.39319E-02	-0.15792	0.350948	-0.15308
3	-2.03699E-02	6.61142E-02	-0.15283	6.34035E-02

Table 3.4  $c_{lmn}$  coefficients used in Eq. (3.18) for H<sub>2</sub>O [28]

$l = 0$

$m/n$	0	1	2
0	4.72	-8.5482	5.2394
1	-0.84969	0.312478	-0.13804
2	-3.47243E-02	4.02461E-02	-5.80104E-02
3	5.79830E-04	3.94125E-03	-5.29017E-03

$l = 1$

$m/n$	0	1	2
0	-8.9615	16.9547	-10.76
1	1.5861	-2.0166	1.46
2	4.34730E-02	-0.67133	0.633231
3	2.87067E-03	-7.06830E-02	6.23710E-02

$l = 2$

$m/n$	0	1	2
0	9.1461	-17.327	11.1864
1	-1.3975	1.9965	-1.6935
2	8.46419E-02	0.599994	-0.70054
3	7.14719E-03	6.62086E-02	-6.87294E-02

$l = 3$

$m/n$	0	1	2
0	-3.5504	6.624	-4.3058
1	0.485392	-0.7071	0.689109
2	-6.77456E-02	-0.18179	0.269308
3	-5.92726E-03	-2.04694E-02	2.56411E-02



Table 3.5  $d_{lmn}$  coefficients used in Eq. (3.20) for CO<sub>2</sub> [28]

$l = 0$

$m/n$	0	1	2	3
0	2.45702	-5.45334	6.53751	-2.52344
1	-4.0232	15.67297	-24.3247	11.33757
2	7.54549	-23.8023	39.51896	-19.1137
3	-3.63104	11.9078	-20.3606	9.97877

$l = 1$

$m/n$	0	1	2	3
0	7.65678E-02	2.36184	-3.95061	2.17482
1	0.2901819	-12.0041	22.44342	-13.0467
2	-0.64282	21.5003	-40.8667	23.66762
3	0.3942158	-11.5818	22.05176	-12.6536

$l = 2$

$m/n$	0	1	2	3
0	-3.30582E-02	0.4367742	-0.725331	0.4138566
1	0.3672993	-3.52466	6.74885	-3.96295
2	-0.69811	6.60703	-12.9667	7.58713
3	0.3831158	-3.65683	7.19415	-4.16496

$l = 3$

$m/n$	0	1	2	3
0	-1.87927E-03	1.92123E-02	-3.25863E-02	1.98493E-02
1	2.85033E-02	-0.223537	0.4402715	-0.26267
2	-5.49594E-02	0.4370937	-0.881494	0.521958
3	3.04198E-02	-0.247793	0.4990777	-0.291566

### 3.5.3 Treatment of Non-Isothermal and Non-Homogeneous Media in SLW

Spectral nature of gas radiative properties has a complex nonlinear dependence on temperature, pressure and mole fractions of the absorbing gases. In general, gases become more absorbing with increasing temperature due to the growth of hot lines in their spectrum. Therefore, consideration of local variation of the absorption cross section / coefficient with temperature, pressure and composition is of great importance.

SLW model allows spatial dependence of the gray gas absorption cross-sections ( $C_{abs,j}$ ) on temperature, pressure and species concentration. This is achieved by expressing the spectral absorption cross-section as the product of two functions,

$$C_{abs,\eta}(\eta, T_g, P_T, Y_s) = \phi(T_g, P_T, Y_s)\Psi(\eta) \quad (3.22)$$

where  $P_T$  is the total pressure and is taken as 1 atm in this study. Hence, hereafter it will be excluded from the equations for the sake of brevity. It should be noted that the spectral dependence is defined only by the function,  $\Psi(\eta)$ . This idealized behavior of the spectrum for two separate temperatures and mole fractions is illustrated in Figure 3.6. As can be seen from the figure, all wave numbers ( $\eta$ ) corresponding to the intersection points for a given value of the absorption cross-section remain unchanged regardless of temperature and mole fraction. Therefore, spectrum only shifts upwards as the temperature and mole fraction increase from State 1 ( $T_{g,1}, Y_{s,1}$ ) to State 2 ( $T_{g,2}, Y_{s,2}$ ). Figure 3.6 also reveals that absorption-line blackbody distribution functions, demonstrated as the shaded area under the blackbody emissive power curve ( $E_{b,\eta}$  curve), are also identical for States 1 and 2. Based on these observations, following equality is proposed,

$$\begin{aligned} & F_s[C_{abs,j}(T_{g,2}, Y_{s,2}), T_b = T_{ref}, T_g = T_{g,2}, Y_s = Y_{s,2}] \\ &= F_s[C_{abs,j}(T_{g,1}, Y_{s,1}), T_b = T_{ref}, T_g = T_{g,1}, Y_s = Y_{s,1}] \end{aligned} \quad (3.23)$$

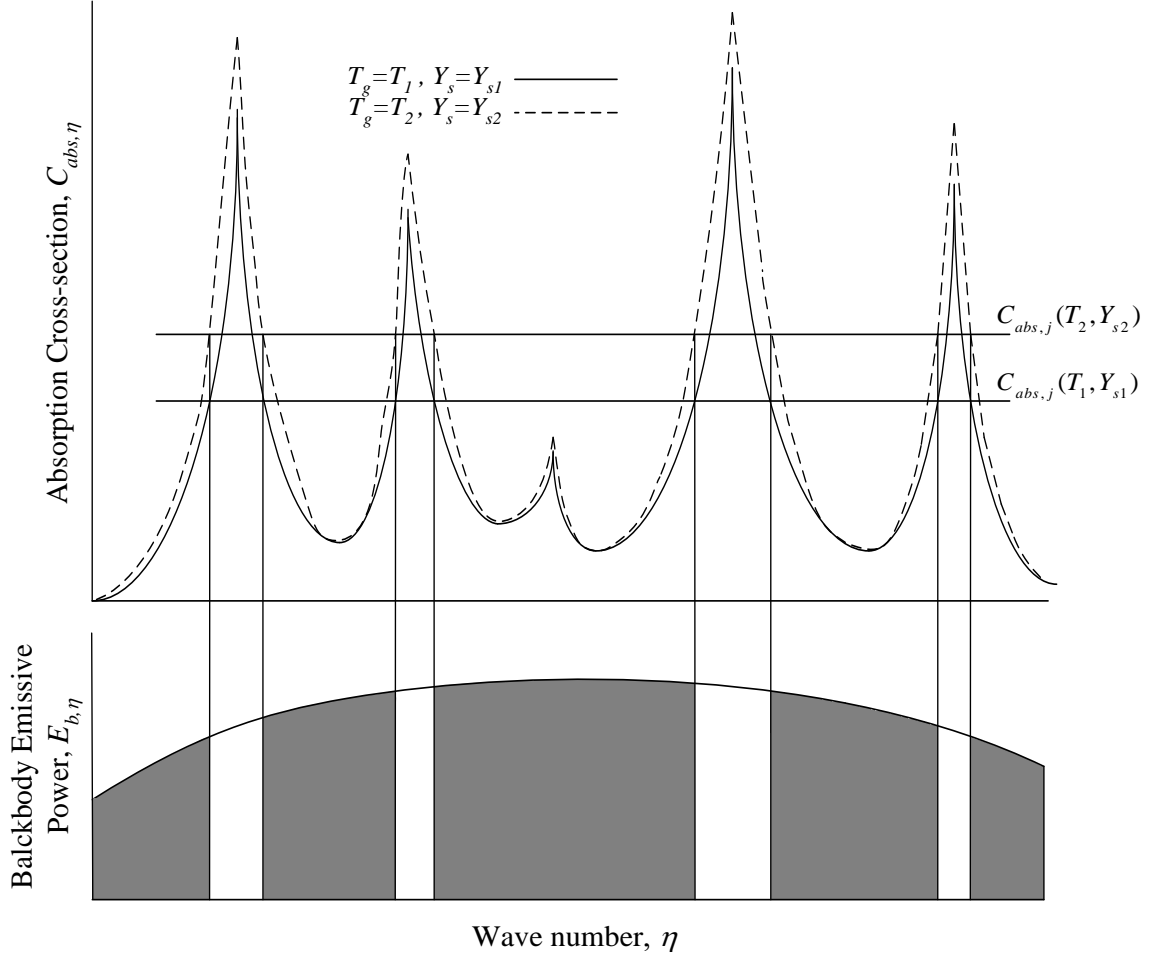


Figure 3.6 Idealized gas temperature dependence of high-resolution spectrum resulting in equivalent blackbody fractions

Equation 3.23 provides an implicit dependence of  $C_{abs,j}(T_{g,i}, Y_{s,i})$  on local gas state (temperature ( $T_{g,i}$ ) and mole fractions of the absorbing species ( $Y_{s,i}$ )). In practice, a reference state is selected as the spatial averages of temperature and mole fraction fields, and Eq. (3.23) is rewritten for equivalent absorption-line blackbody distribution function evaluated at the reference and local states,

$$\begin{aligned}
 & F_s [C_{abs,j}, T_b = T_{ref}, T_g = T_{local}, Y_s = Y_{local}] \\
 & = F_s [C_{abs,j,ref}, T_b = T_{ref}, T_g = T_{ref}, Y_s = Y_{ref}]
 \end{aligned} \tag{3.24}$$

The reference absorption cross-sections ( $C_{abs,j,ref}$ ) are the discrete values determined from Eq. (3.11). Then, the local values of absorption cross-sections ( $C_{abs,j}$ ) are determined from this implicit relation by using an iterative technique. In this study, bisection method was used.

The local absorption coefficients are then found as the product of the local molar density determined from the equation of state (ideal gas) and the local gray gas absorption cross-section evaluated from Eq. (3.12):

$$\kappa_j = N(T_{local}, Y_{s,local}) C_{abs,j}(T_{local}, Y_{s,local}) \quad (3.25)$$

The blackbody weights of the gray gases are calculated from Eq. (3.14),

$$a_j = F_s(\tilde{C}_{abs,j+1}, T_b = T_{local}, T_g = T_{ref}, Y_s = Y_{s,ref}) - F_s(\tilde{C}_{abs,j}, T_b = T_{local}, T_g = T_{ref}, Y_s = Y_{s,ref}) \quad (3.26)$$

where  $T_{local}$  is the local value of the temperature and  $T_{ref}$  and  $Y_{s,ref}$  are the reference temperature and mole fraction, respectively.

### 3.5.4 Treatment of Binary Gas Mixtures in SLW

In order to calculate, total heat transfer rates in a mixture of two gases, H<sub>2</sub>O and CO<sub>2</sub>, RTEs for cylindrical and rectangular coordinate systems (Eqs. (3.8) and (3.9)) are modified by including the gray gas weights and additional gray gas indices to account for the two species,

$$\begin{aligned} k_t \frac{\partial I_{k,l}^{m,\ell}}{\partial t} = & - \left( \frac{\mu_{m,\ell}}{r} \frac{\partial (r I_{k,l}^{m,\ell})}{\partial r} - \frac{1}{r} \frac{(Y_{m,\ell+1/2} I_{k,l}^{m,\ell+1/2} - Y_{m,\ell-1/2} I_{k,l}^{m,\ell-1/2})}{w_{m,\ell}} + \xi_{m,\ell} \frac{\partial I_{k,l}^{m,\ell}}{\partial z} \right) \\ & - (\kappa_{gk,l} + \kappa_p + \sigma_p) I_{k,l}^{m,\ell} + (\kappa_p + \kappa_{gk,l}) a_{k,l} I_b \\ & + \frac{\sigma_p}{4\pi} \sum_{m',\ell'} \Phi(\boldsymbol{\Omega}_{m',\ell'}, \boldsymbol{\Omega}_{m,\ell}) w_{m',\ell'} I_{k,l}^{m',\ell'} \end{aligned} \quad (3.27)$$

$$\begin{aligned}
k_t \frac{\partial I_{k,l}^{m,\ell}}{\partial t} = & -\mu_{m,\ell} \frac{\partial I_{k,l}^{m,\ell}}{\partial x} - \eta_{m,\ell} \frac{\partial I_{k,l}^{m,\ell}}{\partial y} - \xi_{m,\ell} \frac{\partial I_{k,l}^{m,\ell}}{\partial z} - (\kappa_{gk,l} + \kappa_p + \sigma_p) I_{k,l}^{m,\ell} \\
& + (\kappa_p + \kappa_{gk,l}) a_{k,l} I_b \\
& + \frac{\sigma_p}{4\pi} \sum_{m',\ell'} \Phi(\boldsymbol{\Omega}_{m',\ell'}, \boldsymbol{\Omega}_{m,\ell}) w_{m',\ell'} I_{k,l}^{m',\ell'}
\end{aligned} \tag{3.28}$$

The joint gray gas weights ( $a_{k,l}$ ) are defined as the fraction of blackbody energy in the high resolution spectrum where the effective absorption cross-sections of H<sub>2</sub>O and CO<sub>2</sub> are  $C_{abs,k}$  and  $C_{abs,l}$ , respectively (see Figure 3.7). The indices “k” and “l” denote the k<sup>th</sup> and l<sup>th</sup> gray gases for H<sub>2</sub>O and CO<sub>2</sub>, respectively. Including the spectral windows, these joint gray gas weights sum to unity,

$$\sum_k \sum_l a_{k,l} = 1 \tag{3.29}$$

It has been shown that the joint gray gas weights are well approximated by the product of two individual weights [29],

$$a_{k,l} = a_k a_l \tag{3.30}$$

And absorption coefficients of the gas mixture ( $\kappa_{gk,l}$ ) are given as the sum of contributions of the two species,

$$\kappa_{gk,l} = N_k C_{abs,k} + N_l C_{abs,l} \tag{3.31}$$

where  $N_k$  and  $N_l$  are the molar densities of H<sub>2</sub>O and CO<sub>2</sub>, respectively.

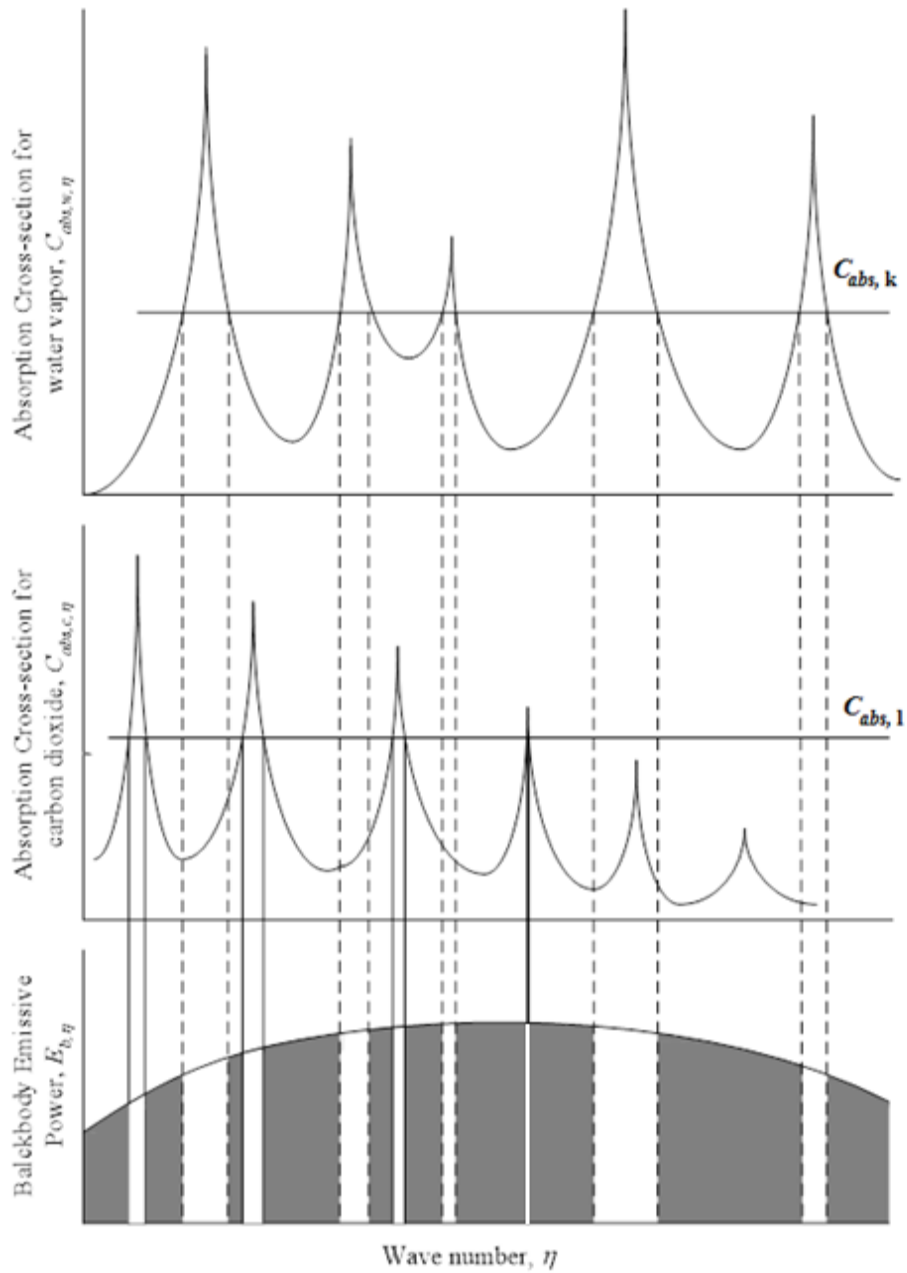


Figure 3.7 Portions of the spectrum where the absorption-line blackbody distribution function for H<sub>2</sub>O-CO<sub>2</sub> mixture is calculated [28]

In the case of non-isothermal and non-homogeneous media, local supplemental absorption coefficients and gray gas weights are calculated separately for each

participating gas (H<sub>2</sub>O and CO<sub>2</sub>) and the mixture absorption coefficient and the corresponding weights are determined through Eqs. (3.31) and (3.30), respectively.

Once the gray gas absorption coefficients and corresponding weights are calculated, they are substituted into Eq. (3.27) / Eq. (3.28) and radiative heat transfer calculations are performed for each gray gas.

### 3.6 Banded Spectral Line-Based Weighted Sum of Gray Gases (banded SLW)

In its classical form, SLW is a global model (see Section 3.5) and each RTE is solved for each gray gas weight ( $a_{k,l}$ ), which represents the fraction of blackbody emissive power of the gas mixture having an absorption coefficient of  $\kappa_{gk,l}$  in the entire spectrum. This is why radiative properties of particles ( $\kappa_p, \sigma_p$ ) in Eq. (3.27) / (3.28) must also represent the particle properties for the entire spectrum. Therefore, SLW in its original form cannot be used with non-gray particles. Nevertheless, SLW weights (Eq. (3.26)) can be related to the cumulative k-distributions through an integration of Planck's function, which allows the calculation of gray gas weights for an arbitrary spectral band [28].

In order to calculate the radiative heat transfer rates in a mixture of two gases, equations for the banded solution RTE (Eq. (3.8)) and for the solution of RTE with SLW for a gas mixture of H<sub>2</sub>O and CO<sub>2</sub> (Eq. (3.27)) are combined to have a banded form of the SLW model.

For an arbitrary  $j^{\text{th}}$  band of the spectrum, form of RTE with banded SLW is then becomes,

$$\begin{aligned}
k_t \frac{\partial I_{j,k,l}^{m,\ell}}{\partial t} = & -\mu_{m,\ell} \frac{\partial I_{j,k,l}^{m,\ell}}{\partial x} - \eta_{m,\ell} \frac{\partial I_{j,k,l}^{m,\ell}}{\partial y} - \xi_{m,\ell} \frac{\partial I_{j,k,l}^{m,\ell}}{\partial z} - (\kappa_{gk,l} + \kappa_{p_j} + \sigma_{p_j}) I_{j,k,l}^{m,\ell} \\
& + (\kappa_{p_j} + \kappa_{gk,l}) \tilde{a}_{j,k} \tilde{a}_{j,l} (F_{0-j+1} - F_{0-j}) I_b \\
& + \frac{\sigma_{p_j}}{4\pi} \sum_{m',\ell'} \Phi_j(\boldsymbol{\Omega}_{m',\ell'}, \boldsymbol{\Omega}_{m,\ell}) w_{m',\ell'} I_{j,k,l}^{m',\ell'}
\end{aligned} \tag{3.32}$$

where the indices  $k$  and  $l$  denote the  $k^{\text{th}}$  and  $l^{\text{th}}$  gray gas for  $\text{H}_2\text{O}$  and  $\text{CO}_2$ , respectively. It should be highlighted at this point that gray gas weights ( $\tilde{a}_{j,k}, \tilde{a}_{j,l}$ ) used in Eq.(3.32) are normalized weights and they are different from those given in Eqs. (3.27) – (3.30). In SLW model, summation of all weights yields unity for each species and this relationship is used to evaluate the weight of the clear gray gas in the entire spectrum,

$$a_{k,\text{NGW}} = 1 - \sum_{k=1}^{\text{NGW}-1} a_k \quad (3.33)$$

$$a_{l,\text{NGC}} = 1 - \sum_{l=1}^{\text{NGC}-1} a_l \quad (3.34)$$

where NGW and NGC represent total number of gray gases and  $a_{k,\text{NGW}}$  and  $a_{l,\text{NGC}}$  are the weights of the clear gases for  $\text{H}_2\text{O}$  and  $\text{CO}_2$ , respectively. In the banded form, however, gray gas weights summed over all bands yields unity as opposed to global SLW model,

$$\sum_{j=1}^{\text{NB}} \sum_{k=1}^{\text{NGW}} a_{j,k} = 1, \quad \sum_{j=1}^{\text{NB}} \sum_{l=1}^{\text{NGC}} a_{j,l} = 1 \quad (3.35)$$

where NB represents the total number of spectral bands. Therefore, clear gas weights for each band cannot be readily evaluated. In order to alleviate this problem, gray gas weights in the  $j^{\text{th}}$  spectral band are normalized by the fraction of blackbody distribution in the  $j^{\text{th}}$  band ( $F_{0-j+1} - F_{0-j}$ ) so that weights of the clear gray gases ( $\text{NGW}^{\text{th}}$  and  $\text{NGC}^{\text{th}}$  gases) can be found from the summation rule in the band of interest (i.e.,  $j^{\text{th}}$  band):

$$\tilde{a}_{j,k} = \frac{a_{j,k}}{F_{0-j+1} - F_{0-j}}, \quad \tilde{a}_{j,l} = \frac{a_{j,l}}{F_{0-j+1} - F_{0-j}} \quad (3.36)$$

$$\tilde{a}_{j,\text{NGW}} = 1 - \sum_{k=1}^{\text{NGW}-1} \tilde{a}_{j,k}, \quad \tilde{a}_{j,\text{NGC}} = 1 - \sum_{l=1}^{\text{NGC}-1} \tilde{a}_{j,l} \quad (3.37)$$

Blackbody weights ( $a_{j,k}, a_{j,l}$ ) within the  $j^{\text{th}}$  band (Eq. (3.36)) are determined from the connection between  $k$ -distributions ( $g_w, g_c$ ) and SLW model as follows:



$$a_{j,k} = \frac{1}{\sigma T^4} \left[ \int_{\eta_j}^{\eta_{j+1}} g_w(\tilde{C}_{abs,k+1}, T, \eta) E_b(T, \eta) d\eta - \int_{\eta_j}^{\eta_{j+1}} g_w(\tilde{C}_{abs,k}, T, \eta) E_b(T, \eta) d\eta \right] \quad (3.38)$$

$$a_{j,l} = \frac{1}{\sigma T^4} \left[ \int_{\eta_j}^{\eta_{j+1}} g_c(\tilde{C}_{abs,l+1}, T, \eta) E_b(T, \eta) d\eta - \int_{\eta_j}^{\eta_{j+1}} g_c(\tilde{C}_{abs,l}, T, \eta) E_b(T, \eta) d\eta \right] \quad (3.39)$$

$$E_b(T, \eta) = \frac{2\pi h c_0 \eta^3}{n^2 \left[ \exp\left(\frac{hc_0 \eta}{nkT}\right) - 1 \right]} = \frac{3.7419 \times 10^{-8} \eta (cm^{-1})^3}{\exp\left(\frac{1.4388 \eta}{T}\right) - 1} \quad (3.40)$$

It should be noted that both trapezoidal integration and Simpson's rule are tested in the evaluation of integrals in Eqs. (3.38) and (3.39) and it is seen that trapezoidal integration leads to significant errors for the systems under consideration. Therefore, Simpson's rule is utilized in the present study.

Data required for each k-distribution for both H<sub>2</sub>O and CO<sub>2</sub> are taken from [28] and hyperbolic mathematical correlations recommended by [27-29] are used to calculate k-distribution functions  $g_w$  and  $g_c$ :

$$g_w(\tilde{C}_{abs,k}, T, \eta) = \frac{1}{2} \tanh(P_w) + \frac{1}{2} \quad (3.41)$$

$$P_w(T, \xi - \xi_{sb}) = \sum_{m=0}^3 \sum_{n=0}^3 b_{lmn} \left(\frac{T}{2500}\right)^n (\xi - \xi_{sb})^m \quad (3.42)$$

$$\xi = \ln(\tilde{C}_{abs,k}) \quad (3.43)$$

$$\tilde{C}_{abs,k} = \exp\left(\ln(C_{min}) + \left(\frac{\ln(C_{max}) - \ln(C_{min})}{NGW - 1}\right)(k - 1)\right) \quad (3.44)$$

$$\xi_{sb} = \sum_{m=0}^3 \sum_{n=0}^3 c_{lmn} \xi^n (y_{H_2O})^{m+1} \quad (3.45)$$

$$g_c(\tilde{C}_{abs,l}, T, \eta) = \frac{1}{2} \tanh(P_c) + \frac{1}{2} \quad (3.46)$$

$$P_c(T, \xi) = \sum_{m=0}^4 \sum_{n=0}^3 d_{lmn} \left( \frac{T}{2500} \right)^n (\xi)^m \quad (3.47)$$

$$\xi = \ln(\tilde{C}_{abs,l}) \quad (3.48)$$

$$\tilde{C}_{abs,l} = \exp \left( \ln(C_{min}) + \left( \frac{\ln(C_{max}) - \ln(C_{min})}{NGC - 1} \right) (k - l) \right) \quad (3.49)$$

It should be noted that Equation 12.1 is needed to be modified at  $2400 \text{ cm}^{-1}$  for the strongest  $\text{CO}_2$  absorption band [28]. At this wavenumber, k-distribution function is given as [28]:

$$g_c(\tilde{C}_{abs,l}, T, P, 2400 \text{ cm}^{-1}) = 0.2535 \tanh(P_{c,a}) + 0.2465 \tanh(P_{c,b}) + \frac{1}{2} \quad (3.50)$$

where functions  $P_{c,a}$  and  $P_{c,b}$  are evaluated by using Eq. (3.47) with the coefficients  $d_{lmn}$  given in [28]. Constants b, c, and d are presented in Appendix B.

Each space between two consecutive supplemental absorption cross sections ( $\tilde{C}_{abs, i}$  and  $\tilde{C}_{abs, i+1}$ ) is considered as a separate gray gas associated with a constant absorption cross section ( $C_{abs,w, i}$ ) and calculated as follows:

$$C_{abs,k} = \exp \left( \frac{\ln(\tilde{C}_{abs,k}) + \ln(\tilde{C}_{abs,k+1})}{2} \right) \quad (3.51)$$

$$C_{abs,l} = \exp \left( \frac{\ln(\tilde{C}_{abs,l}) + \ln(\tilde{C}_{abs,l+1})}{2} \right) \quad (3.52)$$

The absorption coefficient of the gas mixture  $(\kappa_g)_{k,l}$  is then calculated as the sum of contributions of the two species [29] and found from:

$$\kappa_{g,k,l} = N_k C_{abs,k} + N_l C_{abs,l} \quad (3.53)$$

where  $N_k$  and  $N_l$  are the molar densities,  $C_{abs,k}$  and  $C_{abs,l}$  are absorption cross-sections of  $\text{H}_2\text{O}$  and  $\text{CO}_2$ , respectively.

### 3.7 One-Gas Spectral Line-Based Weighted Sum of Gray Gases (SLW-1)

In banded SLW model, SLW is extended to incorporate non-gray particle radiation to the solution of RTE. In this case, however, RTE is needed to be solved several hundreds of times more for a gas mixture with non-gray particles due to high number of gray gases deployed in each spectral band. This increase in the number of RTE becomes a significant CPU burden for multidimensional problems as it leads to several billions of increase in the number of RTE equations ( $N_{\text{RTE}}$ ) to be solved:

$$N_{\text{RTE}} = N_{\text{Time}} \times N_{\text{Grid}} \times N_{\text{direction}} \times N_{\text{spectral band}} \times N_{\text{gray gas,k}} \times N_{\text{gray gas,l}} \quad (3.54)$$

where  $N_{\text{Time}}$  denotes the number of time steps in the MOL solution (see Section 2.3),  $N_{\text{Grid}}$  shows the number of grid points,  $N_{\text{direction}}$  is the number of discrete directions,  $N_{\text{spectral band}}$  is the number of spectral bands and  $N_{\text{gray gas,k}}$ ,  $N_{\text{gray gas,l}}$  are the number of gray gases used for H<sub>2</sub>O and CO<sub>2</sub>, respectively. Fortunately, this CPU burden can be minimized without losing much accuracy for gas radiation by decreasing the number of gray gases in both SLW and banded SLW models with One-Gas Spectral Line-Based Weighted Sum of Gray Gases (SLW-1) approach [98-102].

In SLW-1, gas absorption coefficients of the mixture (Eq. 3.53) and the corresponding blackbody weights of each specie (Eq. (3.38) and (3.39)) are first found for a sufficiently high number of gray gases. Then, total emissivity of the binary gas mixture in the arbitrary  $j^{\text{th}}$  band of the spectrum is calculated for two different path lengths ( $L_1$ ,  $L_2$ ) as shown below,

$$\varepsilon_{j,mix}(L_1) = \sum_{k=0}^{NW} \sum_{l=0}^{NC} \tilde{a}_{j,k} \tilde{a}_{j,l} \left( 1 - e^{(-\kappa_{gk,l} L_1)} \right) \quad (3.55)$$

$$\varepsilon_{j,mix}(L_2) = \sum_{k=0}^{NW} \sum_{l=0}^{NC} \tilde{a}_{j,k} \tilde{a}_{j,l} \left( 1 - e^{(-\kappa_{gk,l} L_2)} \right) \quad (3.56)$$

where the gray gas weights are found by using Eq. (3.38) and Eq. (3.39) and the absorption coefficient of the gas mixture are obtained from Eq. (3.53).

In the next step, gray gas parameters of SLW-1 ( $\kappa_{j,1}$  and  $a_{j,1}$ ) are found from the system of two algebraic equations for the  $j^{\text{th}}$  band, which has unique solution for  $\kappa_{j,1} > 0$ :

$$\varepsilon_{j,mix}(L_1) = a_{j,1} (1 - e^{-\kappa_{j,1}L_1}) \quad (3.57)$$

$$\varepsilon_{j,mix}(L_2) = a_{j,1} (1 - e^{-\kappa_{j,1}L_2}) \quad (3.58)$$

In the present study,  $\varepsilon_{j,mix}(L_1)$  is divided by  $\varepsilon_{j,mix}(L_2)$  to eliminate  $a_{j,1}$  in Eq. (3.57) and Eq. (3.58). Then  $\kappa_{j,1}$  is found by using Newton's method with an error tolerance of 0.00001. After obtaining  $\kappa_{j,1}$ ,  $a_{j,1}$  is calculated by using Eq. (3.57).

For each band (j), clear gas parameters of SLW-1 model are defined as follows,

$$\kappa_{j,0} = 0 \quad (3.59)$$

$$a_{j,0} = 1 - a_{j,1} \quad (3.60)$$

It should be noted that SLW-1 approximation can be used to reduce the number of gray gases in both SLW model (Section 3.5) and banded SLW model (Section 3.6). Equations presented in this section are given for the banded SLW model. In the case of SLW model, the same procedure is applied to obtain SLW-1 parameters ( $\kappa_1$  and  $a_1$ ) for the entire spectrum, i.e., Eqs. (3.55)-(3.60) are solved only once and index "j" disappears from the equations.

## CHAPTER 4

### RADIATIVE PROPERTY MODELS FOR PARTICLES

Particles<sup>3</sup> continuously emit and absorb radiation in the entire spectrum and may also scatter radiation depending on their size. In general, interaction between particles and incident radiation depends on four major factors: (i) shape of the particle, (ii) ratio of its size to the wavelength of the incident radiation, called size parameter ( $x=\pi d_p/\lambda$ ), (iii) optical properties of particle and (iv) the relative distance between the particles ( $c/\lambda$ ).

In radiative heat transfer analysis, particles are usually assumed to have ideal shapes like spheres or cylinders, which has been shown to lead to very accurate results due to smoothing of radiant energy distribution over millions of randomly oriented irregular particles [37, 103]. Therefore, in this chapter, particle-radiation interactions are presented only for spherical particles.

In combusting systems, size of particles varies significantly from nanometres scale (soot particles) to millimetres scale (coal particles in fluidized bed combustors). For ash particles, this range is about 1-100  $\mu\text{m}$  for pulverized coal-fired furnaces and about 1-1000  $\mu\text{m}$  for fluidized bed combustors (with a mean diameter usually less than 20  $\mu\text{m}$ , 50

---

<sup>3</sup> In this study, term “particle” refers to particles present in combusting systems: coal, biomass, char, ash and limestone particles. It should also be noted that that fuel (coal / biomass), char and soot particles contribute to the radiative heat transfer in the flame region. Nevertheless, this flame region corresponds to a relatively small portion of the combustors while majority of total heat transfer occurs after soot/char burnout is completed, that is, in the radiant section, where combustion gases and fly ash particles contribute strongly to the radiative transfer process. Therefore, this study focuses on only fly ash particles and particle radiative properties refer to ash particle properties unless stated otherwise.

$\mu\text{m}$  and  $300 \mu\text{m}$ , for pulverized coal-fired furnaces (PC-Fired), bubbling fluidized bed combustors (BFBC) and circulating fluidized bed combustors (CFBC), respectively). Considering the fact that more than 99 % of thermal radiation lies between  $1\text{-}20 \mu\text{m}$ , expected size parameter range becomes  $0.1\text{-}3000$ , which leads to significantly different behaviours while interacting with thermal radiation. Furthermore, particles present in combusting systems are not uniform in size and there always exists a particle size distribution (PSD). Hence dependency of particle radiation on particle size must be represented accurately for the polydisperse particle clouds.

Regarding to the optical properties of particles, it is mainly determined by the physical structure of the particles and their refractive ( $n$ ) and absorption indices ( $k$ ), which are together called the complex index of refraction ( $m = n - ik$ ). Refractive index ( $n$ ) gives information about the scattering behaviour of the particles while the absorption index ( $k$ ) determines the amount of absorption by the particles and emission from the particles. The complex index of refraction (will be referred as RI for the sake of brevity), in general, is a function of wavelength, temperature and chemical composition. Complex index of refraction is one of the principle causes, from which spectral nature of particle properties is originated. Hence its accurate representation is of considerable importance.

Distance between the particles relative to the wavelength of incident radiation is another important factor defining particle-radiation interactions in the presence of many particles. If scattering by a particle is not influenced by the presence of other neighbouring particles, particles are assumed to scatter radiation independently. In this case, single particle properties can be used to determine the particle cloud properties. In the case of dependent scattering, however, particles scatter radiation with a different probability distribution and particles tend to absorb radiation more compared to their individual absorbances. Dependent and independent scattering regimes as a function of particle volume fraction and size parameter is demonstrated in Figure 4.1. As can be seen from the figure, scattering regime is usually independent for combusting systems hence particle property calculation methods are presented for only independent regime in the following subsections.

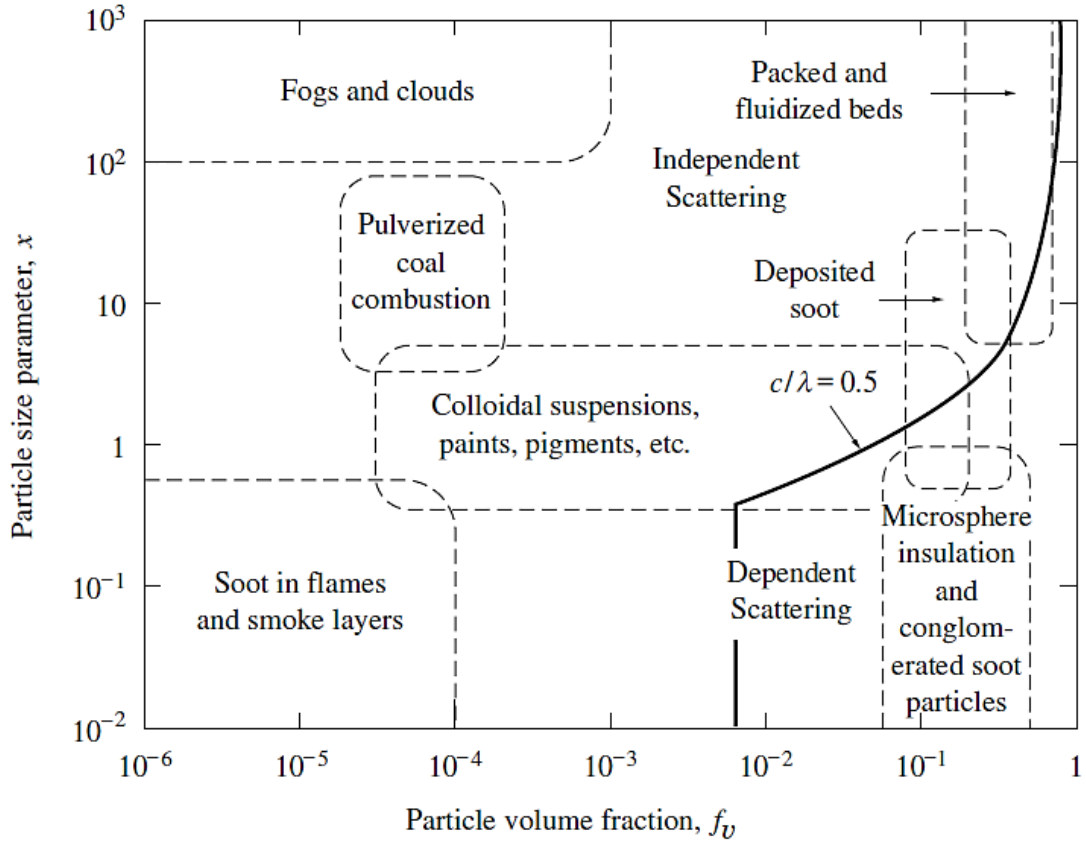


Figure 4.1 Dependent and independent scattering regimes [37]

#### 4.1 Radiative Properties of a Single Spherical Particle

Radiative properties of particles require the solution of the Maxwell equations, which necessitates particle optical properties, particle size, particle shape and wavelength of incident radiation. For homogenous spherical particles, Gustav Mie developed a series solution to Maxwell equations in 1908 for a plane, monochromatic wave [104]. This solution gives the extinction cross section ( $C_e(n, k, x, \lambda)$ ), scattering albedo ( $\omega_0(n, k, x, \lambda)$ ) and the phase function ( $\Phi(n, k, x, \theta, \lambda)$ ) as functions of size parameter ( $x = \pi d_p / \lambda$ ) and RI ( $m(\lambda) = n(\lambda) - ik(\lambda)$ ).

Extinction cross section is the summation of the absorption cross section ( $C_a(n, k, x, \lambda)$ ) and scattering cross section ( $C_s(n, k, x, \lambda)$ ), which define the amount of absorption and scattering of radiation by the particle, respectively,

$$C_e(n, k, x, \lambda) = C_a(n, k, x, \lambda) + C_s(n, k, x, \lambda) \quad (4.1)$$

Although Mie solution of Maxwell equations gives the absorption and scattering cross sections, particle properties are usually expressed in terms of efficiencies rather than cross sections, which are defined as the ratio of cross sections to the projected surface area of particles,

$$Q_e(n, k, x, \lambda) = C_e(n, k, x, \lambda)/\pi R^2 \quad (4.2)$$

$$Q_a(n, k, x, \lambda) = C_a(n, k, x, \lambda)/\pi R^2 \quad (4.3)$$

$$Q_s(n, k, x, \lambda) = C_s(n, k, x, \lambda)/\pi R^2 \quad (4.4)$$

Scattering albedo ( $\omega_0$ ) is the ratio of scattering cross section to extinction cross section and used to evaluate absorption and scattering cross sections separately from the Mie solution. Scattering phase function ( $\Phi$ ) is a probability distribution function describing how the incident radiation scattered away from its original propagation direction. It should be noted at this point that scattering of thermal radiation by a particle occurs through three different mechanisms; reflection, refraction and diffraction (see Figure 4.2). Reflection is simply the reflection of incident radiation from the particle surface while refraction is the change in the direction of electromagnetic wave after travelling through the particle, during which it is partially absorbed. Diffraction is the change in the direction of incident radiation by the presence of particles without any direct contact. It should also be noted that in radiative heat transfer calculations, almost all radiant energy is scattered elastically, that is, wavelength of the incident radiation does not change upon scattering.

Although Mie theory covers the entire particle size range of combustion applications, there are some simple limiting solutions, which provide simple analytical expressions hence they are much more CPU efficient compared to exact Mie solutions. In the following sub-sections, these limiting solutions are presented, which is followed by exact Mie solutions.



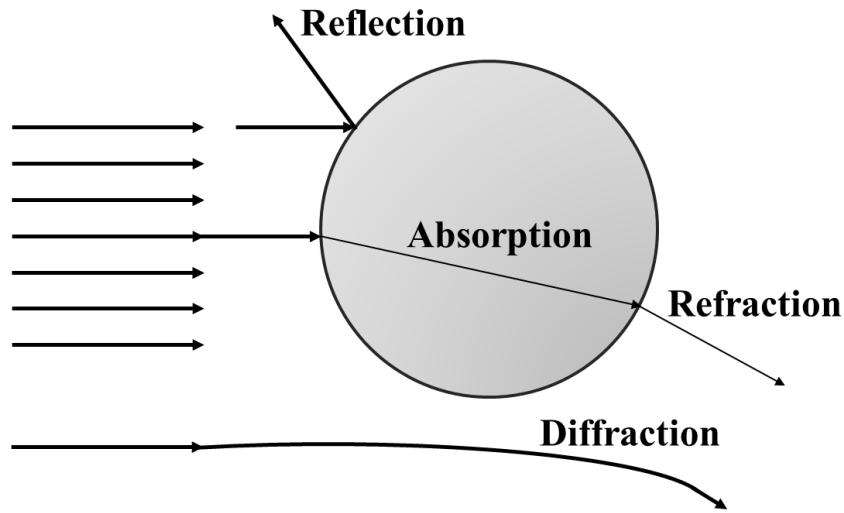


Figure 4.2 Scattering of incident radiation by a particle

#### 4.1.1 Limiting Solutions of Maxwell Equations

Limiting solutions of Maxwell equations are defined by the particle size parameter and complex index of refraction. The first approximation was established even before the Mie theory by Lord Rayleigh for very small particles ( $x \ll 1$ ), which has a moderate refractive index ( $x|n - 1| \ll 1$ ). It is called Rayleigh Scattering. If the refractive index of particle is about one ( $n \approx 1$ ) and its absorption index is low ( $k \ll 1$ ) where ( $x|n - 1| \ll 1$ ) is satisfied, incident radiation is practically unattenuated and unrefracted. This special case is called Rayleigh-Gans Scattering and has a simple analytical solution for particle radiative properties. Another special case occurs for large particles ( $x \gg 1$ ) if refractive index of particle is about one ( $n \approx 1$ ) called Anomalous Diffraction, where mathematical functions describing the absorption and diffraction of waves can be separated. Finally, if particles are very large ( $x \gg 1$ ) and refractive index is not small ( $x|n - 1| \gg 1$ ), then geometric optic approximation (GOA) with diffraction can be used to evaluate particle properties. Considering the fact that particles involved in the current study are large, opaque particles, GOA is the only limiting solution that can be applied. This is why it will be presented in more detail in the following section.

### 4.1.2 Geometric Optics Approximation (GOA)

Number of terms required in the series solution of Mie theory is proportional to the size parameter. Therefore, if a particle is relatively large compared to wavelength of incident radiation ( $x \gg 1$ ), numerical solution of Mie theory converges very slowly [105] and becomes CPU inefficient. Fortunately, large size parameter ( $x \rightarrow \infty$ ) is mathematically equivalent to the limiting solution of Maxwell equations,  $\lambda \rightarrow 0$ , for which simple laws of geometric optics are demonstrated to be valid [37, 105]. The large size of the particle is related to the optical depth within the particle [105] and  $x > 25$  is usually considered to be large enough for opaque particles [105].

For large, diffusely reflecting, opaque particles, extinction efficiency converges to a limiting value and becomes independent of particle composition, shape and size,

$$Q_e = 2.0 \quad (4.5)$$

which is also called the extinction paradox. Half of this extinction efficiency comes from the projected surface area ( $\pi R^2$ ) of the particle while the other half comes from the diffracted radiation (also known as Fraunhofer diffraction). Absorption and scattering efficiencies are simply expressed as follows and depend on particle surface properties,

$$Q_a = 1 - \rho_\lambda - \tau_\lambda \quad (4.6)$$

$$Q_s = 1 + \rho_\lambda + \tau_\lambda \quad (4.7)$$

where  $\rho_\lambda$  is the spectral hemispherical reflectivity and  $\tau_\lambda$  is the spectral particle transmissivity. “1” in Eq. (4.7) comes from the diffraction. For opaque particles, as in the case of coal, char or ash particles,  $\tau_\lambda$  simply becomes zero. Therefore, GOA only requires the spectral hemispherical reflectivity ( $\rho_\lambda$ ) for the evaluation of single particle properties. If  $\rho_\lambda$  is not readily known, it can be calculated from spectral directional–hemispherical reflectivities.

If a monochromatic electromagnetic wave hits a particle with the spectral complex index of refraction  $m(\lambda) = n(\lambda) - ik(\lambda)$  at an angle of  $\theta_1$  with the surface normal, then spectral

perpendicular ( $\rho_{\perp,\lambda}$ ) and parallel ( $\rho_{\parallel,\lambda}$ ) reflectivities can be found by using Fresnel's relations [37, 105],

$$\rho_{\perp,\lambda} = \frac{(\cos\theta_1 - p)^2 + q^2}{(\cos\theta_1 + p)^2 + q^2} \quad (4.8)$$

$$\rho_{\parallel,\lambda} = \frac{(p - \sin\theta_1 \tan\theta_1)^2 + q^2}{(p + \sin\theta_1 \tan\theta_1)^2 + q^2} \rho_{\perp,\lambda} \quad (4.9)$$

where

$$p^2 = 0.5 \left( \left( \sqrt{(n^2 - k^2 - \sin^2\theta_1)^2 + 4n^2k^2} \right) + (n^2 - k^2 - \sin^2\theta_1) \right) \quad (4.10)$$

$$q^2 = 0.5 \left( \left( \sqrt{(n^2 - k^2 - \sin^2\theta_1)^2 + 4n^2k^2} \right) - (n^2 - k^2 - \sin^2\theta_1) \right) \quad (4.11)$$

If the incident radiation is unpolarised, then spectral directional-hemispherical reflectivity ( $\rho'_\lambda$ ) can be expressed as a mean average,

$$\rho'_\lambda = \frac{\rho_{\perp,\lambda} + \rho_{\parallel,\lambda}}{2} \quad (4.12)$$

Finally, spectral hemispherical reflectivity ( $\rho_\lambda$ ) can be calculated numerically from the following expression,

$$\rho_\lambda = \frac{1}{\pi} \int_{2\pi} \rho'_\lambda \cos(\theta_1) d\Omega = 2 \int_0^{\frac{\pi}{2}} \rho'_\lambda \cos(\theta_1) \sin(\theta_1) d\theta_1 \quad (4.13)$$

where  $\rho'_\lambda$  is the directional-hemispherical reflectivity evaluated at  $\theta_1$ .

Since Eq. (4.13) can only be solved numerically, it is usually simplified to obtain simple algebraic equations. In the literature, spectral directional-hemispherical reflectivity is often assumed to be independent of the direction of incident radiation ( $\theta_1$ ) and the absorption index ( $k$ ). This is achieved by assuming  $\theta_1 = 0$  and  $n \gg k$  (so that  $(n - 1)^2$  becomes much larger than  $k^2$ ), which leads to the following simple expression,

$$\rho_\lambda = \left( \frac{n - 1}{n + 1} \right)^2 \quad (4.14)$$

It should be noted that this expression is only valid for the normal direction. Nevertheless, it is considered to be a good approximation as the emissivity (so does the reflectivity for an opaque particle) is almost constant between 0-60° (see Figure 4.3), which is the range where majority of the incident radiation may be expected to fall.

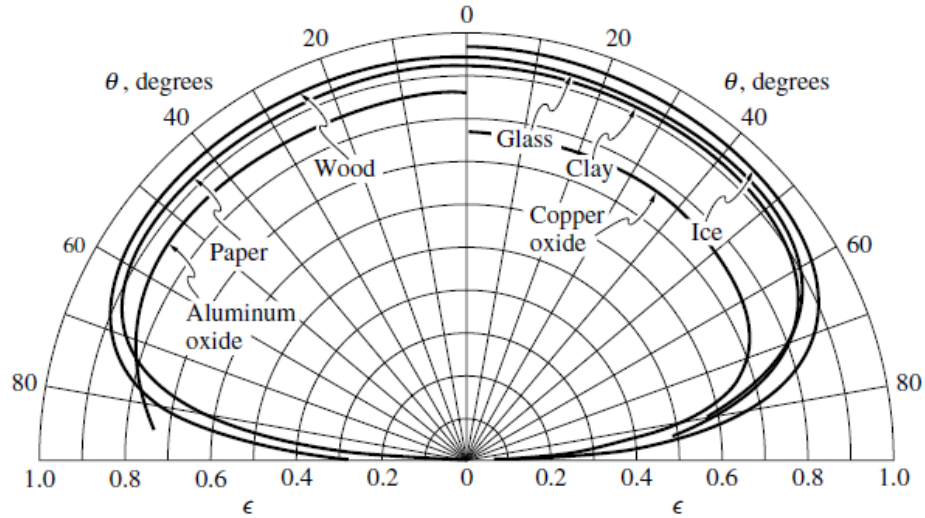


Figure 4.3 Emissivity of different materials as a function of  $\theta_1$  [37]

However, in the case of a scattering medium, especially if the scattering albedo is high, this simplifying assumption may lead to considerable errors. To include this angular dependency, spectral hemispherical reflectivity can be evaluated with the condition  $n \gg k$ , which makes it possible to obtain an analytical solution for Eq. (4.13) [106],

$$\rho_\lambda = \frac{1}{2} + \frac{(3n+1)(n-1)}{6(n+1)^2} + \frac{n^2(n^2-1)^2}{(n^2+1)^3} \ln\left(\frac{n-1}{n+1}\right) - \frac{2n^3(n^2+2n-1)}{(n^2+1)(n^4-1)} + \frac{8n^4(n^4+1)}{(n^2+1)(n^4-1)^2} \ln n \quad (4.15)$$

It should be highlighted that Eq. (4.14) is the standard method used in the literature. In fact, Eq. (4.15) has been utilized in only few studies [106] while numerical solution of Eq. (4.13) has not been used in the combustion community before. Furthermore,

absorptive index ( $k$ ) is strongly wavelength dependent and presence of lattice deficiencies and/or impurities within the particle can increase the value of  $k$  up to several orders of magnitude [36].

Scattering phase function ( $\Phi$ ) for large particles is also very simple compared to complete Mie solutions. In GOA limits, scattering by reflection and diffraction are represented by two different formulations.

For large particles, diffracted radiation is determined by the size of the particle and is not a function of its optical properties. It is defined in terms of a Bessel function,

$$\Phi = 4 \frac{J_1^2(x \sin(\theta))}{\sin^2(\theta)} \quad (4.16)$$

Where  $J_1$  is the Bessel function,  $\theta$  is the angle between the incident and scattered directions. The diffraction phase function is demonstrated in Figure 4.4 for two different size parameters. As can be seen from the figure, majority of the diffracted energy goes into forward direction ( $\theta = 1-5^\circ$ ) and forward scattering increases with increasing size parameter.

On the other hand, scattering due to reflection is defined as a function of optical properties and it is independent of the particle size,

$$\Phi = \left( \frac{1}{2} (\pi - \theta) \right) \frac{\rho'_\lambda}{\rho_\lambda} \quad (4.17)$$

where  $(\pi - \theta)/2$  refers to angle relative to the particle surface. For large, opaque and diffusely reflecting particles,  $\Phi$  becomes independent of surface properties as well and takes the following form,

$$\Phi = \frac{8}{3\pi} (\sin \theta - \theta \cos \theta) \quad (4.18)$$

Scattering phase function due to reflection is demonstrated in Figure 4.5. As can be seen from the figure, reflection of incident radiation is mainly in the backward direction.

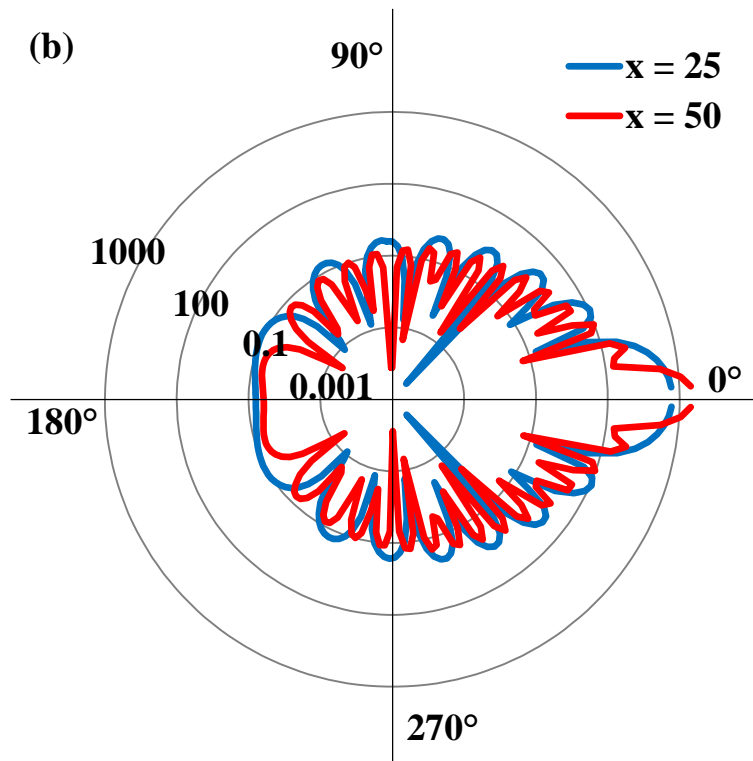
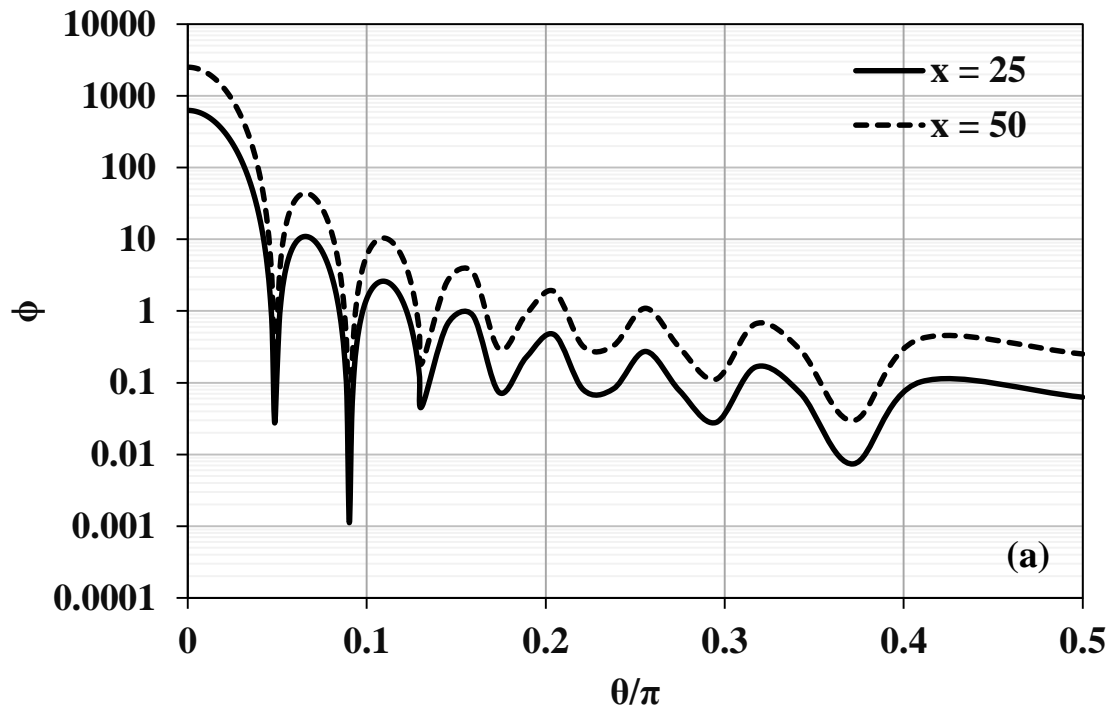


Figure 4.4 (a) Diffraction phase function in GOA limit and (b) its demonstration in polar coordinates

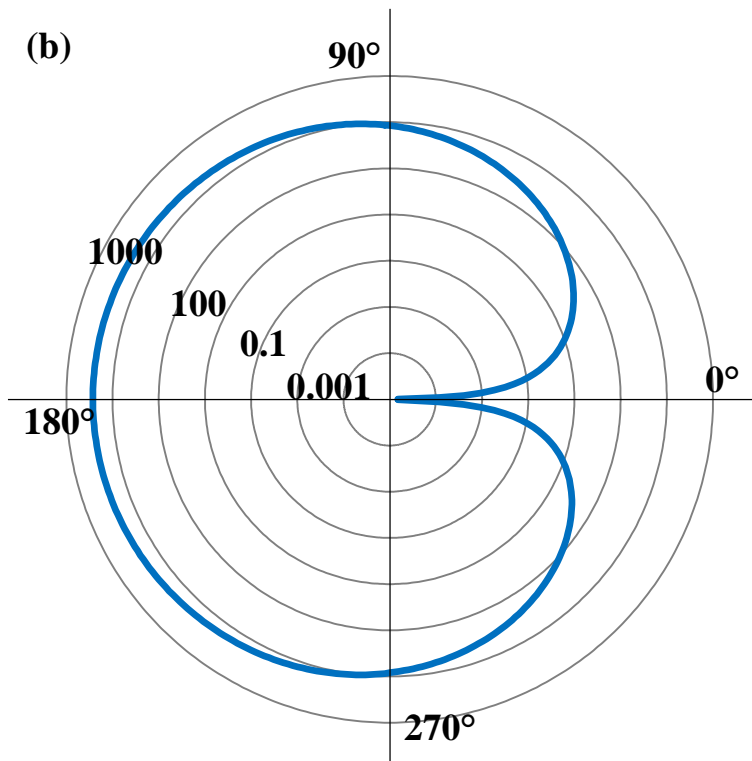
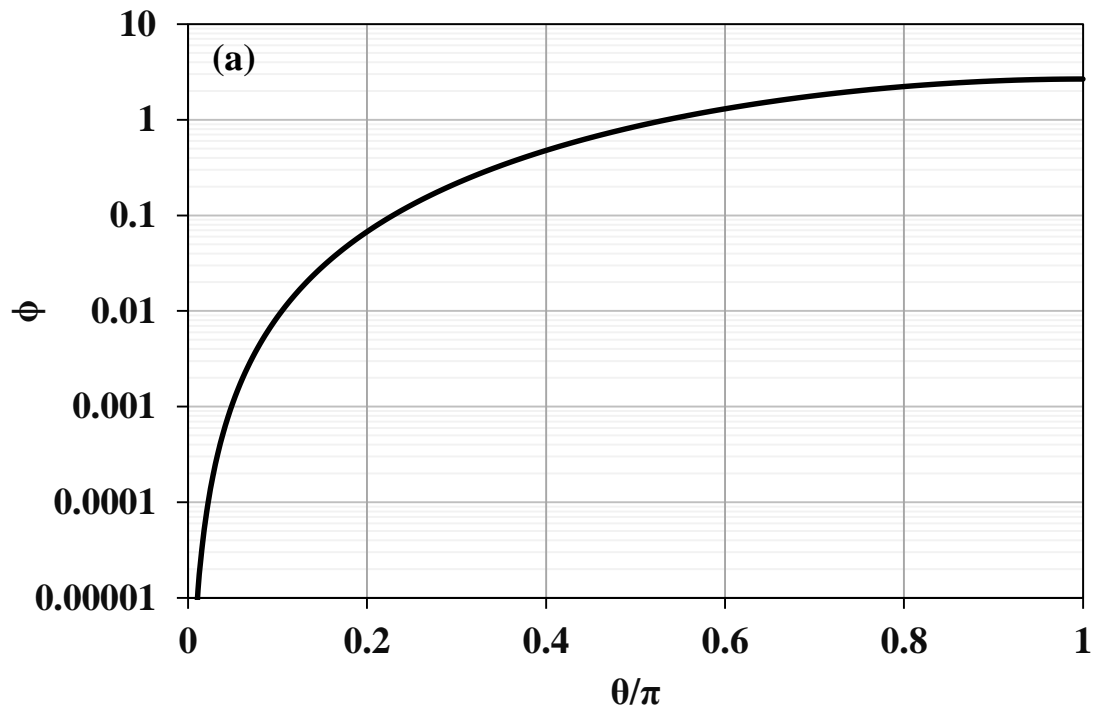


Figure 4.5 (a) Reflection phase function in GOA limit (b) its demonstration in polar coordinates

### 4.1.3 Mie Theory

Mie solution of the particle extinction and scattering cross sections are expressed in terms of complex amplitude functions  $S_1(\theta)$  and  $S_2(\theta)$  as a function of complex index of refraction ( $m$ ) and size parameter ( $x$ ),

$$S_1(\theta) = \sum_{n=1}^{\infty} \frac{(2n+1)}{n(n+1)} [a_n \pi_n(\cos \theta) + b_n \tau_n(\cos \theta)] \quad (4.19)$$

$$S_2(\theta) = \sum_{n=1}^{\infty} \frac{(2n+1)}{n(n+1)} [b_n \pi_n(\cos \theta) + a_n \tau_n(\cos \theta)] \quad (4.20)$$

where  $\pi_n$  and  $\tau_n$  are defined as Legendre polynomials,

$$\pi_n(\cos \theta) = \frac{dP_n(\cos \theta)}{d \cos \theta} \quad (4.21)$$

$$\tau_n(\cos \theta) = \cos \theta \pi_n(\cos \theta) - \sin^2 \theta \frac{d\pi_n(\cos \theta)}{d \cos \theta} \quad (4.22)$$

and  $a_n$  and  $b_n$  are the Mie scattering coefficients,

$$a_n = \frac{\psi_n'(mx)\psi_n(x) - m\psi_n(mx)\psi_n'(x)}{\psi_n'(mx)\xi_n(x) - m\psi_n(mx)\xi_n'(x)} \quad (4.23)$$

$$b_n = \frac{m\psi_n'(mx)\psi_n(x) - \psi_n(mx)\psi_n'(x)}{m\psi_n'(mx)\xi_n(x) - \psi_n(mx)\xi_n'(x)} \quad (4.24)$$

$\psi_n$  and  $\xi_n$  functions are the Ricatti-Bessel functions and expressed as [37],

$$\psi_n(z) = \left(\frac{\pi z}{2}\right)^{\frac{1}{2}} J_{n+\frac{1}{2}}(z) \quad (4.25)$$

$$\xi_n(z) = \left(\frac{\pi z}{2}\right)^{\frac{1}{2}} H_{n+\frac{1}{2}}(z) \quad (4.26)$$

where  $J$  and  $H$  are the Bessel and Hankel functions, respectively.



It should be noted that Legendre polynomial  $P_n$  is expressed by,

$$P_n(i) = \frac{1}{2} \sum_{k=0}^n \binom{n}{k}^2 (i-1)^{n-k} (i+1)^k \quad (4.27)$$

so that  $P_n$  becomes as follows for  $n = 0, 1, 2, 3 \dots$ ,

$$P_0(\cos \theta) = 1 \quad (4.28)$$

$$P_1(\cos \theta) = \cos \theta \quad (4.29)$$

$$P_2(\cos \theta) = \frac{1}{2} (3(\cos \theta)^2 - 1) \quad (4.30)$$

$$P_3(\cos \theta) = \frac{1}{2} (5(\cos \theta)^3 - 3 \cos \theta) \quad (4.31)$$

These amplitude functions  $S_1(\theta)$  and  $S_2(\theta)$  given in Eqs. (4.19) and (4.20) are used to express particle properties as follows [37],

$$C_e = \frac{4\pi R^2}{x^2} \Re(S(0)) \quad (4.32)$$

$$C_s = \frac{\pi R^2}{x^2} \int_0^\pi (i_1 + i_2) \sin(\theta) d\theta \quad (4.33)$$

where

$$i_j = |S_j|^2 \quad (4.34)$$

If amplitude functions  $S_1(\theta)$  and  $S_2(\theta)$  are substituted into Eqs. (4.32) and (4.33), then extinction and scattering cross sections becomes functions of Mie scattering coefficients,  $a_n$  and  $b_n$ ,

$$C_e = \frac{2\pi R^2}{x^2} \sum_{n=1}^{\infty} (2n+1) \Re(a_n + b_n) \quad (4.35)$$

$$C_s = \frac{2\pi R^2}{x^2} \sum_{n=1}^{\infty} (2n+1) (|a_n|^2 + |b_n|^2) \quad (4.36)$$

Ratio of the scattered energy into any given direction  $\theta$  to total incident radiation is defined as,

$$\frac{I_{scattered}(\theta)}{I_{incident}} = \frac{1}{2} \frac{i_1 + i_2}{x^2} \quad (4.37)$$

If scattered energy into any direction (Eq. (4.37)) is divided by total scattered energy, fraction of the energy scattered into that particular direction is found, which is the scattering phase function,

$$\Phi = \frac{\frac{I_{scattered}(\theta)}{I_{incident}}}{\frac{1}{\pi} \int_{4\pi} \frac{I_{scattered}(\theta)}{I_{incident}} d\Omega} = \frac{i_1 + i_2}{\frac{1}{4\pi} \int_{4\pi} (i_1 + i_2) d\Omega} = 2 \frac{i_1 + i_2}{Q_s} \quad (4.38)$$

Nevertheless, calculation of scattering phase function through Eq. (4.38) is extremely laborious as each calculation must be carried out from the very beginning (Eq. (4.19)) for each angle  $\theta$ . This difficulty has been overcome [37] by expressing the phase function in terms of Legendre polynomials,

$$\Phi = 1 + \sum_{n=1}^{\infty} A_n P_n(\cos \theta) \quad (4.39)$$

where  $A_n$  coefficients are calculated only once from  $a_n$  and  $b_n$ . However, even this formulation is still complicated for scattering phase function calculations. Therefore, scattering probability distribution is usually expressed as a mean quantity by the averaging cosine of the scattering angle, called asymmetry factor ( $g$ ),

$$g = \overline{\cos \theta} = \frac{1}{4\pi} \int_{4\pi} \Phi(\theta) \cos \theta d\Omega \quad (4.40)$$

which changes from -1 to +1 representing purely backward scattering and purely forward scattering, respectively.

In the present study, radiative properties of particles are calculated by extending the BHMIE code based on Mie theory [37]. In the present code, logarithmic derivative,  $D_n$ ,

is used to evaluate the Mie scattering coefficient  $a_n$  and  $b_n$  for a range of particle sizes, wavelengths and complex index of refraction values,

$$D_n(z) = \frac{d}{dz} \ln \psi_n(z) \quad (4.41)$$

$$a_n = \frac{[D_n(mx)/m + n/x]\psi_n(x) - \psi_{n-1}(x)}{[D_n(mx)/m + n/x]\xi_n(x) - \xi_{n-1}(x)} \quad (4.42)$$

$$b_n = \frac{[mD_n(mx) + n/x]\psi_n(x) - \psi_{n-1}(x)}{[mD_n(mx) + n/x]\xi_n(x) - \xi_{n-1}(x)} \quad (4.43)$$

where the recurrence relations are defined as follows to eliminate  $\psi_n'$  and  $\xi_n'$  in Mie coefficients,

$$\psi_n'(x) = \psi_{n-1}(x) - \frac{n\psi_n(x)}{x} \quad (4.44)$$

$$\xi_n'(z) = \xi_{n-1}(x) - \frac{n\xi_n(x)}{x} \quad (4.45)$$

It should be noted that both  $\psi_n$  and  $\xi_n (= \xi\psi_n - i\chi_n)$  satisfy the following criteria,

$$\psi_{n+1}(x) = \frac{2n+1}{x}\psi_n(x) - \psi_{n-1}(x) \quad (4.46)$$

and are computed by the upward recurrence relation, starting from  $n=0$ ,

$$\psi_{-1}(x) = \cos x, \quad \psi_0(x) = \sin x, \quad \chi_{-1}(x) = -\sin x, \quad \chi_0(x) = \cos x \quad (4.47)$$

It should also be noted that logarithmic derivative satisfies the following recurrence relation,

$$D_{n-1} = \frac{n}{z} - \frac{1}{D_n + \frac{n}{z}} \quad (4.46)$$

In the numerical solution, infinite series are terminated after *NSTOP* terms, where *NSTOP* is the determined from the size parameter as recommended [37],

$$NSTOP = x + 4x^{1/3} + 2 \quad (4.47)$$

Since asymmetry factor simplifies the scattering phase function calculations significantly, its calculation is also added into the code from the following relationship [37],

$$g = \frac{4\pi a^2}{x^2 C_{\text{scat}}} \sum_{n=1}^{\infty} \left[ \frac{n(n+2)}{n+1} \Re\{a_n a_{n+1}^* + b_n b_{n+1}^*\} + \frac{2n+1}{n(n+1)} \Re\{a_n b^*\} \right] \quad (4.48)$$

where  $\Re$  denotes the real part of a complex number.

## 4.2 Radiative Properties of Polydisperse Particle Clouds

Solution of RTE requires the absorption coefficient, scattering coefficient and scattering phase function of the particles in addition to gas absorption coefficient. In all engineering problems involving particulates, there is always large numbers of particles hence it is necessary to establish methods to evaluate particle cloud properties from individual single particle properties. As described in the beginning of this chapter, in the case of independent scattering, particle properties become additive and cloud particle properties presented in this sub-section are limited to independently scattering particles.

Particle absorption cross section, scattering cross section and scattering phase function (or the asymmetry factor) calculated from Mie theory are valid for the specific size parameter  $x$  hence valid only for a single particle size for a given wavelength. If the particle cloud consists of many particles with the same size (or represented by a single particle size), then particle properties per unit volume for  $N_T$  number of particles become,

$$\kappa_{p,\lambda} = N_T C_a = \pi R^2 N_T Q_{a,\lambda} \quad (4.49)$$

$$\sigma_{p,\lambda} = N_T C_s = \pi R^2 N_T Q_{s,\lambda} \quad (4.50)$$

$$\beta_{p,\lambda} = N_T C_e = \pi R^2 N_T Q_{e,\lambda} \quad (4.51)$$

where  $\kappa_{p,\lambda}$ ,  $\sigma_{p,\lambda}$  and  $\beta_{p,\lambda}$  are the spectral absorption, scattering and extinction coefficients. Since all particles have the same size, probability distribution of scattering for the particle cloud does not change and it is equal to scattering phase function for the single particle size,

$$\Phi_\lambda(\theta) = \Phi_{\lambda,\text{single}}(\theta) \quad (4.52)$$

$$g_\lambda(\theta) = g_{\lambda,\text{single}}(\theta) \quad (4.53)$$

In the presence of a particle size distribution, which is always the case in combusting systems, particle radiative properties are defined with a particle size distribution function,

$$\kappa_{p,\lambda} = \int_0^\infty \frac{\pi d_p^2}{4} Q_{a,\lambda}(d_p) N(d_p) dd_p \quad (4.54)$$

$$\sigma_{p,\lambda} = \int_0^\infty \frac{\pi d_p^2}{4} Q_{s,\lambda}(d_p) N(d_p) dd_p \quad (4.55)$$

$$\overline{\Phi}_\lambda = \int_0^\infty \frac{\pi d_p^2}{4} Q_{s,\lambda}(d_p) \Phi_\lambda(d_p) N(d_p) dd_p / \int_0^\infty \frac{\pi d_p^2}{4} Q_{s,\lambda}(d_p) N(d_p) dd_p \quad (4.56)$$

$$\overline{g}_\lambda = \frac{1}{\sigma_{p,\lambda}} \int_0^\infty \frac{\pi d_p^2}{4} Q_{s,\lambda}(d_p) g_\lambda(d_p) N(d_p) dd_p \quad (4.57)$$

where  $\overline{\Phi}_\lambda$  and  $\overline{g}_\lambda$  denote scattering phase function and asymmetry factor averaged over the particle size distribution, respectively.  $N(d_p)$  is the particle number density and  $N(d_p)dd_p$  shows the number of particles per unit volume with a diameter between  $d_p$  and  $d_p + dd_p$ .

Total number of particles and particle volume fraction are defined as,

$$N_T = \int_0^\infty N(d_p) dd_p \quad (4.58)$$

$$f_V = \frac{4}{3}\pi \int_0^\infty \frac{d_p^3}{8} N(d_p) dd_p \quad (4.59)$$

In general, particle size distribution is represented with continuous functions such as Gamma Distribution or Rosin-Rammler Distribution functions. If PSD is measured experimentally and the data cannot be fitted to these generic distribution functions,

continuous particle number density function can be discretized. For that purpose, first number density function is written in terms of a mass based PSD,

$$N(d_p) = \frac{6m(d_p)}{\pi d_p^3 \rho_p} \quad (4.60)$$

where mass distribution function,  $m(d_p)$ , is defined as a function particle load corresponding to a mean diameter of two consecutive sieve sizes in the  $j^{\text{th}}$  interval with a differential weight fraction of  $w_j$ ,

$$m(d_p) = \frac{Bw_j}{(\Delta d_p)_j} \quad (4.61)$$

where B is the total particle load. If Eq. (4.61) is substituted in to Eqs. (4.54) and (4.55), following expressions are obtained for two consecutive sieves with openings corresponding to particle diameters  $dp_1$  and  $dp_2$ ,

$$(\kappa_{p,\lambda})_j = \int_{dp_1}^{dp_2} \frac{\pi d_p^2}{4} Q_{a,\lambda}(d_p) \frac{6 \frac{dB_j}{(\Delta d_p)_j}}{\pi d_p^3 \rho_p} dd_p = \frac{1.5Bw_j}{\rho_p(\Delta d_p)_j} \int_{dp_1}^{dp_2} \frac{Q_{a,\lambda}(d_p)d(d_p)}{d_p} \quad (4.62)$$

$$(\sigma_{p,\lambda})_j = \int_{dp_1}^{dp_2} \frac{\pi d_p^2}{4} Q_{s,\lambda}(d_p) \frac{6 \frac{dB_j}{(\Delta d_p)_j}}{\pi d_p^3 \rho_p} dd_p = \frac{3/2 Bw_j}{\rho_p(\Delta d_p)_j} \int_{dp_1}^{dp_2} \frac{Q_{s,\lambda}(d_p)d(d_p)}{d_p} \quad (4.63)$$

In GOA, efficiencies are independent of particle size. In that case, integrals given in Eqs. (4.62) and (4.63) can be directly solved for the size interval j,

$$(\kappa_{p,\lambda})_j = Q_{a,\lambda} \frac{3/2 Bw_j}{\rho_p(dp_2 - dp_1)_j} (\ln(dp_2) - \ln(dp_1)) \quad (4.64)$$

$$(\sigma_{p,\lambda})_j = Q_{s,\lambda} \frac{3/2 Bw_j}{\rho_{p,j}(dp_2 - dp_1)} (\ln(dp_2) - \ln(dp_1)) \quad (4.65)$$

Absorption and scattering coefficients of the particle cloud is then calculated by summing over all sieve intervals,

$$\kappa_{p,\lambda} = \sum_{j=1}^J (\kappa_{p,\lambda})_j \quad (4.66)$$

$$\sigma_{p,\lambda} = \sum_{j=1}^J (\sigma_{p,\lambda})_j \quad (4.67)$$

In Mie solutions, since efficiencies depend on particle size, integrals in Eqs. (4.54) and (5.55) are replaced by summations. In this case, Mie solutions for absorption and scattering efficiencies are first obtained for each particle size and then particle cloud properties are evaluated from Eqs. (4.68) and (4.69),

$$\kappa_{p,\lambda} = \frac{3}{2} \sum_{i=1}^{N_t} \frac{Q_{a,\lambda}(d_{p_i}) Bw_i}{\rho_p d_{p_i}} \quad (4.68)$$

$$\sigma_{p,\lambda} = \frac{3}{2} \sum_{i=1}^{N_t} \frac{Q_{s,\lambda}(d_{p_i}) Bw_i}{\rho_p d_{p_i}} \quad (4.69)$$

Similarly, asymmetry factor is evaluated starting from Eq. (4.57) as follows,

$$\overline{g_\lambda} = \frac{\sum_{i=1}^{N_t} \frac{Q_{s,\lambda}(d_{p_i}) g_\lambda(d_{p_i}) Bw_i}{\rho_p d_{p_i}}}{\sum_{i=1}^{N_t} \frac{Q_{s,\lambda}(d_{p_i}) Bw_i}{\rho_p d_{p_i}}} \quad (4.70)$$

It should be noted that scattering efficiency in Eq. (4.70) is used as a weighing factor so that averaged asymmetry factor will be mainly determined by particles which have higher scattering efficiencies. Nevertheless, asymmetry factors averaged over the projected surface area ( $\pi d_{p_i}^2/4$ ) is also used in the literature. In that case,  $\overline{g_\lambda}$  becomes,

$$\overline{g_\lambda} = \frac{\sum_{i=1}^{N_t} \frac{g_\lambda(d_{p_i}) Bw_i}{\rho_p d_{p_i}}}{\sum_{i=1}^{N_t} \frac{Bw_i}{\rho_p d_{p_i}}} \quad (4.71)$$

Which gives closed results to Eq. (4.70).

### 4.3 Scattering Phase Function Simplifications

In the previous sections, it is shown that scattering of radiation can be determined from Mie theory provided that the complex index of refraction and the size parameter of the particles are known. Scattering phase function  $\Phi_\lambda$  can then be represented by an infinite series of Legendre polynomials with the coefficients determined from the Mie theory (see Eq. (4.39)). Nevertheless, both absorption / scattering efficiency and scattering phase function demonstrate strong oscillations with the variations in particle size, wavelength and the refractive index. These oscillations not only cause problems in obtaining the Mie solutions, but also affect the stability of the RTE solution and high orders of approximations are needed to handle these stability problems (see Chapter 2). Although oscillations in absorption and scattering efficiencies may be smoothed out to some extent due to presence of polydisperse particles or averaging these properties over the spectrum, oscillations in the phase functions are always present [37]. This is why approximated phase functions are usually preferred in the community.

In fact, the first fundamental simplification is achieved by introducing the asymmetry factor,  $g$  (see Eq. (4.40)). This nondimensional quantity changes from -1 to +1, which represent purely backward scattering and purely forward scattering, respectively. The simplest approximations are the cases where  $g$  is either 0 or +1. In the former case, equal amounts of radiation are scattered into all directions (i.e.  $\Phi_\lambda = 1$ ) giving isotropic scattering while in the latter medium becomes nonscattering.

In combusting systems, particle sizes are relatively large and these large particles predominantly have strong forward scattering peaks ( $g \sim 0.5 - 0.95$ ). A renowned successful approximation method for such highly forward scattering media is the Henyey-Greenstein phase function [67], which only depends on the asymmetry factor  $g$  and  $\theta$ ,

$$\Phi_\lambda(\theta) = \frac{1 - g_\lambda^2}{(1 + g_\lambda^2 - 2g_\lambda \cos\theta)^{1.5}} \quad (4.72)$$

where  $g_\lambda$  is the spectral asymmetry factor. Figure 4.6 shows the Henyey-Greenstein phase function for several asymmetry factors. As can be seen from the figure, Henyey-



Greenstein phase function has a non-oscillatory smooth behavior while acute forward scattering peak increases with the increasing asymmetry factor.

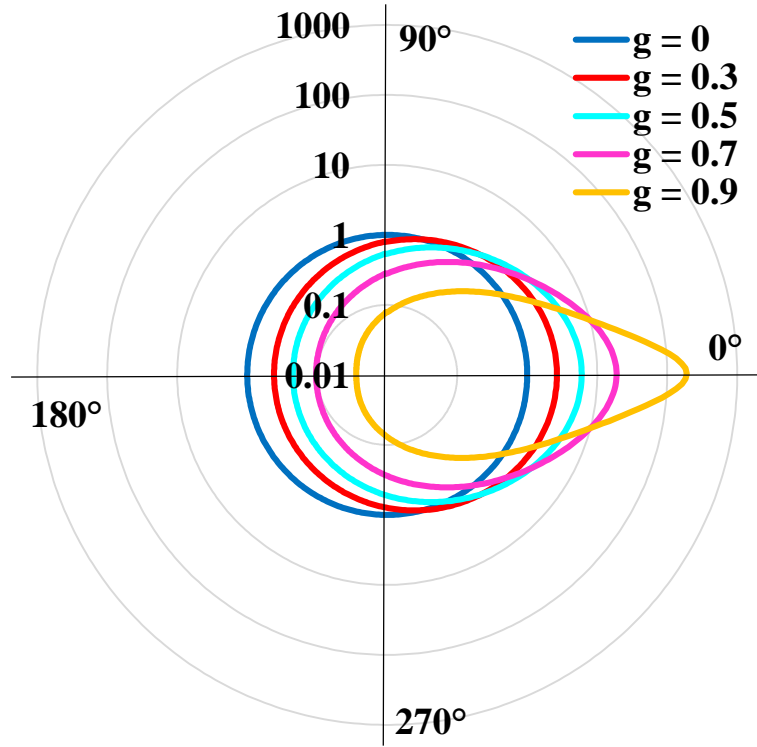


Figure 4.6 Henyey-Greenstein phase function for several  $g$  values in polar coordinates

In the solution of RTE, integral term representing the in-scattered radiation is replaced by a summation term (see Chapter 2) and this discretization must not violate the conservation of the scattered energy:

$$\int_{4\pi} \Phi_{\lambda}(\boldsymbol{\Omega}', \boldsymbol{\Omega}) I_{\lambda}(\mathbf{r}, \boldsymbol{\Omega}') d\boldsymbol{\Omega}' \approx \sum_{m'=1}^M \sum_{\ell'=1}^L \Phi_{\lambda}(\boldsymbol{\Omega}_{m'\ell'}, \boldsymbol{\Omega}_{m,\ell}) w_{m'} I_{\lambda}^{m'\ell'} \quad (4.73)$$

Therefore, any discretization method such as DOM, FEM or FVM must satisfy the conservation criteria given in Eq. (4.74),

$$\frac{1}{4\pi} \int \Phi_\lambda(\mathbf{\Omega}', \mathbf{\Omega}) d\mathbf{\Omega}' = \frac{1}{4\pi} \sum_{m'=1}^M \sum_{\ell'=1}^L \Phi_\lambda(\mathbf{\Omega}_{m',\ell'}, \mathbf{\Omega}_{m,\ell}) w_{m'} = 1.0 \quad (4.74)$$

When the phase function  $\Phi_\lambda(\mathbf{\Omega}_{m',\ell'}, \mathbf{\Omega}_{m,\ell})$  is isotropic, this criterion is exactly satisfied in DOM [67]. However, for anisotropic scattering, scattered energy cannot be conserved and the error gets larger as the anisotropy increases [67]. It was previously shown that [74, 107-110] these discrepancies can be eliminated by introducing a normalization method. However, it was later found that these normalization methods lead to alterations in the overall shape of the scattering phase function and the value of asymmetry factor, which may cause even larger errors in the RTE solution [110]. In order to overcome this problem, another conservation criterion was proposed to preserve the asymmetry factor [110], in addition to Eq. (4.74),

$$g_\lambda = \frac{1}{4\pi} \sum_m \sum_\ell \Phi_\lambda(\mathbf{\Omega}_{m',\ell'}, \mathbf{\Omega}_{m,\ell}) w_{m,\ell} \cos\theta(\mathbf{\Omega}_{m',\ell'}, \mathbf{\Omega}_{m,\ell}) \quad (4.75)$$

A new and simple phase function normalization method, which can satisfy both criteria given in Eqs. (4.74) and (4.75) for Henyey-Greenstein phase function, has recently been suggested [110]. In this method, only the forward ( $\cos\theta(\mathbf{\Omega}_{m',\ell'}, \mathbf{\Omega}_{m,\ell}) = 1$ ) and backward ( $\cos\theta(\mathbf{\Omega}_{m',\ell'}, \mathbf{\Omega}_{m,\ell}) = -1$ ) scattering terms are normalized with the normalization parameters A and B:

$$\Phi_\lambda(\mathbf{\Omega}_{m',\ell'}, \mathbf{\Omega}_{m',\ell'}) = (1 + A_{m',\ell'}) \Phi_\lambda(\mathbf{\Omega}_{m',\ell'}, \mathbf{\Omega}_{m',\ell'}) \quad (4.76)$$

$$\Phi_\lambda(\mathbf{\Omega}_{m',\ell'}, \mathbf{\Omega}_{m'^-, \ell'^-}) = (1 + B_{m'^-, \ell'^-}) \Phi_\lambda(\mathbf{\Omega}_{m',\ell'}, \mathbf{\Omega}_{m'^-, \ell'^-}) \quad (4.77)$$

where

$$A_{m',\ell'} = \frac{1}{2\Phi_\lambda(\mathbf{\Omega}_{m',\ell'}, \mathbf{\Omega}_{m',\ell'}) w_{m',\ell'}} \times \left( 4\pi(1 + g_\lambda) - \sum_{m,\ell}^{M,L} \Phi_\lambda(\mathbf{\Omega}_{m',\ell'}, \mathbf{\Omega}_{m,\ell}) w_{m,\ell} (1 + \cos\theta(\mathbf{\Omega}_{m',\ell'}, \mathbf{\Omega}_{m,\ell})) \right) \quad (4.78)$$

$$B_{m'^-, \ell'^-} = \frac{1}{2\Phi_\lambda(\mathbf{\Omega}_{m',\ell'}, \mathbf{\Omega}_{m'^-, \ell'^-}) w_{m'^-, \ell'^-}}$$

$$\times \left( 4\pi(1 - g_\lambda) + \sum_{m,\ell}^{M,L} \Phi_\lambda(\boldsymbol{\Omega}_{m',\ell'}, \boldsymbol{\Omega}_{m,\ell}) w_{m,\ell} (\cos\Theta(\boldsymbol{\Omega}_{m',\ell'}, \boldsymbol{\Omega}_{m,\ell}) - 1) \right) \quad (4.79)$$

Predictions of DOM with this normalization technique were benchmarked against those of both Monte Carlo and finite volume method and were found to be in good agreement with benchmark solutions [110-114]. Proposed normalization technique is also tested in a recent study for an axisymmetric cylindrical test problem with optically thin and thick media [67]. It is shown that CPU times required for the normalization of the scattering phase function are negligible and accurate results are obtained with DOM for various optical thicknesses and asymmetry factors. In this study, this normalization procedure is also applied for anisotropically scattering particles.

In addition to the above described method to solve the conservation problem of scattered energy and asymmetry factor for strongly forward scattering particles, Henyey–Greenstein phase function can be approximated by simpler phase functions which do not require normalization procedures. One of these methods is the transport approximation [106] where the forward scattering peak is represented by a Dirac-delta function while the rest of the scattering is taken as isotropic. This is achieved by solving RTE as if the phase function is isotropic with the modified scattering coefficient:

$$\sigma_p^{tr} = \sigma_p (1 - g) \quad (4.80)$$

In this study, both Henyey–Greenstein phase function with the presented normalization method and transport approximation are utilized to represent the anisotropic scattering by the particles.

#### 4.4 Complex Index of Refraction Models

Complex index of refraction (RI) is one of the fundamental input parameters for all particle property estimation techniques. Therefore, its accurate representation is very

crucial for accurate modelling of particle radiation. Regarding to ash particles, model equations describing the complex index of refraction can be classified into three main groups: (i) semi-empiric model equations, (ii) empiric model equations and (iii) heuristic equations. In this section, RI models available in the literature from all three categories are presented in detail.

In the last a few decades, there have been several attempts to measure the optical properties of ash particles [36, 115-120], which have been treated as a basis for empiric and semi-empiric model equations. However, major problems in some of these studies are either the experimental uncertainties [115-118] due to the methodology applied as explained in [36, 121] or limited number of ash samples investigated [115-119], from which it is not possible to establish general relationships between the measurements and the factors affecting the RI (wavelength, temperature and chemical composition of the ash). In other words, measurements presented in some of these studies [115-119] are valid only under specific conditions hence cannot be used as a generic database. However, studies of Goodwin [36] present the first comprehensive measurements under controlled laboratory conditions, covering a wide range of wavelengths, temperatures and ash compositions relevant to combusting systems. His measurements cover a spectral range of 0.7-13  $\mu\text{m}$ , from which he developed semi-empirical correlations for estimation of optical properties of ash particles as functions of chemical composition, particle density, wavelength and temperature. Input parameters of his correlations for these bands are given in Table 4.1. As can be seen from the table, Goodwin's correlations highly rely on tabulated data for the absorption index ( $k$ ), which is a disadvantage when the model equations are implemented in a radiation code. More importantly, Goodwin's correlations require the oxidation state of iron atoms (ratio of  $\text{Fe}^{+2}/(\text{Fe}^{+2}+\text{Fe}^{+3})$ ), which is rarely known and a function of operating conditions. Nevertheless, his measurements and correlations have been accepted as a reference in the majority of the relevant literature [39, 40, 41, 43, 44, 45, 49, 50, 65, 71, 122, 123]

Table 4.1 Input Parameters for Goodwin's Model Equations

Wavelength Interval ( $\mu\text{m}$ )	Input Parameters	
	Refractive Index, n	Absorption Index, k
1-4	<ul style="list-style-type: none"> <li>• Mass fractions of <math>\text{SiO}_2</math>, <math>\text{Al}_2\text{O}_3</math>, <math>\text{Fe}_2\text{O}_3</math>, <math>\text{CaO}</math>, <math>\text{MgO}</math> and <math>\text{TiO}_2</math></li> </ul>	<ul style="list-style-type: none"> <li>• <math>\text{Fe}_2\text{O}_3</math> mass fraction</li> <li>• Oxidation state of iron atoms (<math>\text{Fe}^{+2}/(\text{Fe}^{+2}+\text{Fe}^{+3})</math>)</li> <li>• <math>g(\lambda)</math>; tabulated data</li> </ul>
4-8	<ul style="list-style-type: none"> <li>• Particle density</li> </ul>	<ul style="list-style-type: none"> <li>• <math>\text{SiO}_2</math> mass fraction</li> <li>• <math>k_0</math>; tabulated data</li> </ul>
8-13	<ul style="list-style-type: none"> <li>• <math>\text{SiO}_2</math> mass fraction</li> </ul>	<ul style="list-style-type: none"> <li>• <math>\text{SiO}_2</math> mass fraction</li> </ul>

In this study, Goodwin's correlations [36] are also used in the benchmark solutions and details of the model equations can be found in Appendix C.

Another semi-empirical RI model used in this study is the Ebert's work [120], which is a continuation of Goodwin's study. He extended the database on optical properties to higher temperatures and covered a wider range of chemical compositions for the same spectral range [120]. In particular, his model equations can be used for particles with  $\text{SiO}_2$  mass fractions less than 0.95 and  $\text{Fe}_2\text{O}_3$  mass fractions less than 0.30, for temperatures up to 1873 K, with the condition that sum of the weight percentages of  $\text{SiO}_2$ ,  $\text{Al}_2\text{O}_3$ ,  $\text{Fe}_2\text{O}_3$ ,  $\text{CaO}$ ,  $\text{MgO}$  and  $\text{TiO}_2$  must be greater than 80 %, which is usually the case for ash particles [124]. Ebert also included a particle density model to be deployed in refractive index (n) calculations, which was shown to be quite accurate for a variety of ash compositions [124]. Nevertheless, his work has received little attention in the community although its applicability range is much larger than that of Goodwin and it only requires chemical composition of ash particles. Details of the Ebert's model can be found in Appendix C.

There are also empirical model equations presented in the literature. These models utilize simple algebraic functions of wavelength to evaluate (n) and (k) and are based on mainly Goodwin's measurements for a specific ash composition. In other words, these models neglect the dependency of RI on chemical composition and particle density. In this study, six commonly used empirical model equations are included in order to investigate the

sensitivity of particle radiation to chemical composition. These model equations are taken from [43-45, 50, 71] and presented in Appendix C.

Considering the emphasis on the significance of iron oxide content on particle absorption behavior [39, 41, 68, 125-129], an iron oxide content based empirical model is proposed for the first time in this study to compare relative influences of chemical composition and spectral dependency of RI. In this model, refractive index (n) is taken as 1.5 based on the consensus on the value of refractive index in the combustion community while the absorption index (k) is based on Ebert's model. In his work, Ebert suggested a single value absorption index (k) for 0.7-4  $\mu\text{m}$  spectral band based on the iron oxide content of the ash [120],

$$k(\text{Fe}) = (4.02x_{\text{Fe}_2\text{O}_3} + 16.9x_{\text{Fe}_2\text{O}_3}^2)10^{-3} \quad (4.1)$$

where  $x_{\text{Fe}_2\text{O}_3}$  is the iron oxide mass fraction. In this study, his suggestion for the iron oxide absorption band is extended for the entire thermal spectrum and a gray RI model based on iron content is proposed,  $m = 1.5 - k(\text{Fe})i$ . A heuristic model equation is also utilized for the calculation of particle properties, which assumes  $m = 1.5 - 0.02i$  [37]. This gray RI model is the most commonly used approach to represent gray / non-gray particle radiation [130]. In this study, these two gray RI models ( $m = 1.5 - k(\text{Fe})i$ ,  $m = 1.5 - 0.02i$ ) are used for the evaluation of particle / particle cloud properties with two approaches. In the first approach, wavelength ( $\lambda$ ) in size parameter ( $x = \pi d_p / \lambda$ ) is kept as a variable ( $\lambda = f(\lambda) = 1, 2, 3 \dots \mu\text{m}$ ) while in the second approach wavelength in size parameter is kept constant as ( $\lambda = 3 \mu\text{m}$ ) and radiative properties are calculated accordingly in order to identify the source of spectral nature of ash particle properties.

## CHAPTER 5

### DESCRIPTION OF THE TEST CASES

Present work focuses on developing and comparing methods to quantify the effect of physical and chemical properties of combustion gases and particles on radiative heat transfer by means of combining measurements and modelling such that the outcome will provide guidelines when choosing radiative property models for combustion related problems. This investigation is performed through mathematical modelling by using the experimental data obtained from 300 kW<sub>t</sub> Atmospheric Bubbling Fluidized Bed Combustor (ABFBC) and 150 kW<sub>t</sub> Circulating Fluidized Bed Combustor (CFBC) test rig in the Chemical Engineering Department of Middle East Technical University. In this chapter, these two pilot scale fluidized bed combustors and the combustion tests, which provide the experimental data for the radiation models and their validations, are presented in detail.

#### **5.1 300 kW<sub>t</sub> Atmospheric Bubbling Fluidized Bed Combustor Test Rig**

300 kW<sub>t</sub> Atmospheric Bubbling Fluidized Bed Combustion (ABFBC) Test Rig was originally constructed and operated for the investigation of combustion and in-situ desulfurization characteristics of low quality Turkish lignites [4]. It was later modified for co-firing of biomass and coal with limestone addition [8]. The test rig in its present form

is shown in Figure 5.1 and its flow sheet is given in Figure 5.2. As can be seen from the diagram (Figure 5.2), test rig consists of a modular combustor, fuel and limestone feeding systems, ash removal systems, air and flue gas system, cooling water system and instrumentation and control system.

The main body of the ABFBC test rig is a modular combustor formed by five modules of internal cross-section of  $0.45\text{ m} \times 0.45\text{ m}$  and 1 m height. The first and fifth modules from the bottom refer to bed and cooler, respectively, and the ones in between are the freeboard modules. Inner walls of the modules are lined with alumina-based refractory bricks and insulated.

The bed module provides an expanded bed height of about 1 m. It contains 6 water-cooled U-tubes (25 mm OD, stainless steel) providing  $0.35\text{ m}^2$  of cooling surface, 5 ports for thermocouples, 4 ports for gas sampling probes, one port for LPG distributor and two ports for feeding fuel/limestone mixtures. In the freeboard and cooler modules, there are 6 ports for gas sampling probes and 9 ports for thermocouples. There exists a water-cooled tube bundle consisting of 11 tubes (26.7 mm OD, carbon steel) with 14 passes installed across the cross-section of the cooler module providing  $4.3\text{ m}^2$  cooling surface in the cooler module for cooling the flue gases before leaving the combustor.

Bed ash is withdrawn from the bed through water-cooled ash removal pipe. Bed ash drain rate is adjusted from the DCS to obtain the desired bed pressure drop and hence the expanded bed height. Bed ash particles are collected in a continuously weighed ash storage bin. The majority of the elutriable fines produced from solids in the bed and those fed within the solid streams are captured by the cyclone. Cyclone catch particles pass through an air lock and fall onto a diverter. Depending on the position of the diverter, particles are either discharged from the system to a continuously weighted ash storage bin (for experiments without recycle) or flow back to the combustor for re-firing (for experiments with recycle). In order to catch fine fly ash particles leaving the cyclone, jet-pulse type baghouse filter with a 100 % collection efficiency for particles greater than  $1\text{ }\mu\text{m}$  is utilized.





Figure 5.1 METU 300 kW<sub>t</sub> ABFBC Test Rig

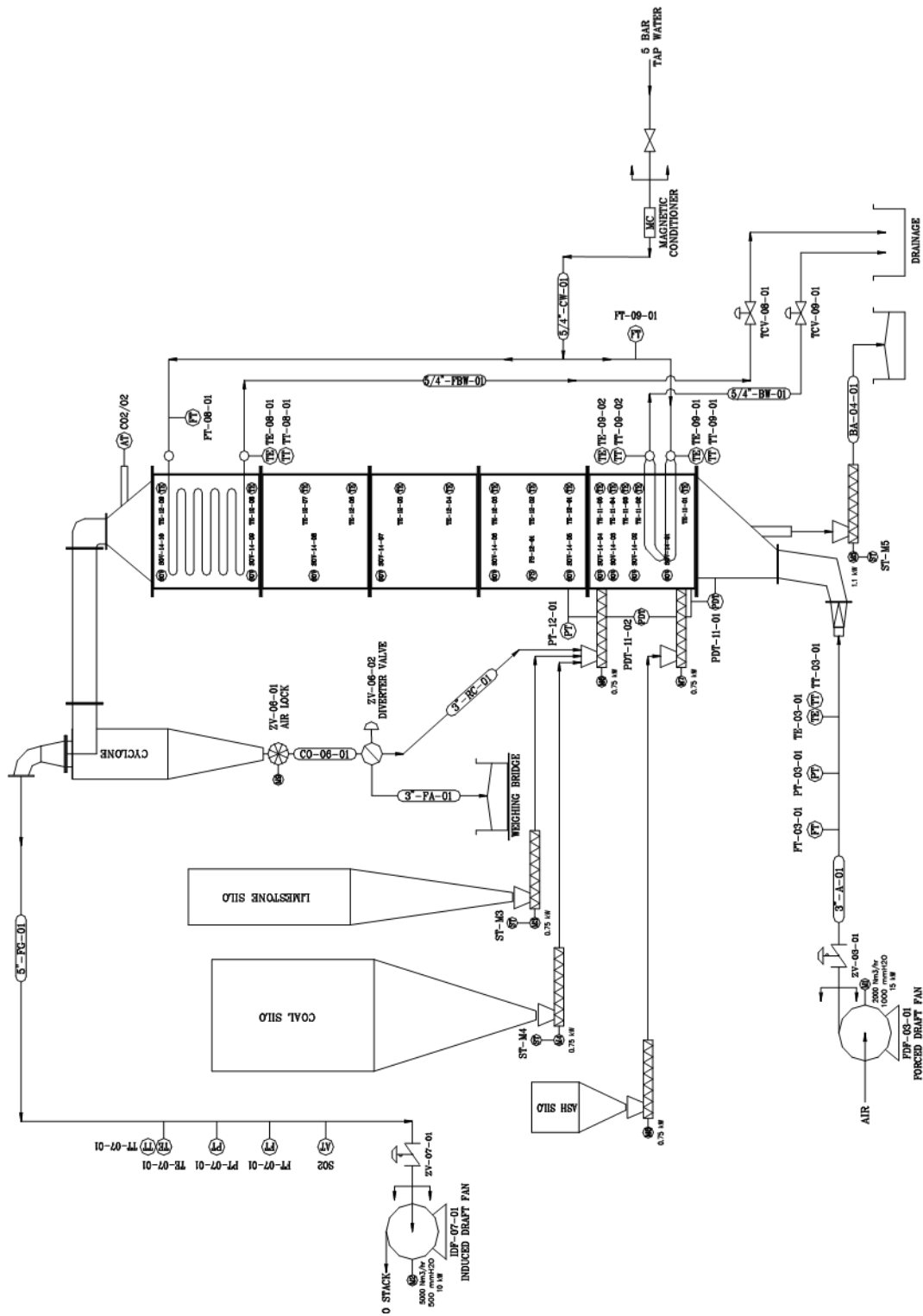


Figure 5.2 Flow sheet of METU 300 kW<sub>t</sub> ABFBC Test Rig

In order to acquire spatially resolved gas composition data from the combustor, the combustion gas is extracted from the symmetry axis of the combustor by using gas sampling probes which are fabricated for in-situ extractive gas sampling. Once through the probe, the sampled combustion gas is passed through a solenoid valve and sent to the gas conditioning and analysis system of the test rig by means of a heated sample line. It should be noted that gas is sampled at a rate which is small enough to cause minimal interference to the combustion system. There exist 7 different on-line continuous gas analysers to measure concentrations of species O<sub>2</sub>, CO, CO<sub>2</sub>, NO, N<sub>2</sub>O and SO<sub>2</sub> along the combustor and also at the cyclone exit on dry basis. There is an additional gas analyser, Bailey SMA 90, which measures temporal variation of O<sub>2</sub> and CO on wet basis at the combustor exit, from which H<sub>2</sub>O content of the flue gas is calculated.

Pressure sensors are used for measuring differential and gauge pressures at various positions on the test rig. Measured differential pressures are the pressure drops over orifice plates, bed and distributor plate pressure drop, and gauge pressures are the pressure at the bed surface and pressure of air feed at the downstream of the vortex flow meter. Spatial and temporal variations of gas temperatures along the height of the combustor are measured by means of thermocouples of K type. The tips of the thermocouples are on the symmetry axis of the combustor.

Radiative heat fluxes incident on the refractory side walls of the freeboard are measured by water cooled Medtherm 48P-20-22K heat flux transducer during the steady state operation of the test rig. The transducer is a Gardon gage with a diameter of 19 mm. Design heat flux range of the transducer is 0-227 kW/m<sup>2</sup>. The certified calibration of the transducer is accurate to  $\pm 0.5\%$  for most ranges. ZnSe window attachment was installed to the transducer to eliminate convective mode of heat transfer, thus making the basic transducer a radiative heat flux transducer, or a radiometer. The sensor absorptance is in the spectral range of 0.5-22  $\mu\text{m}$ , covering most of the thermal radiation spectrum. The view angle of the transducer is 150° with the ZnSe window. Therefore, sensitivity of the basic transducer is reduced to 79 % of the original value and radiative heat flux measurements are corrected accordingly (see Appendix D). Air purging is provided around the periphery of the sapphire window to keep the window clean. Water-cooled

body of the transducer was provided with an integral K type thermocouple for body temperature measurement. During the experiments, radiometer probe was inserted into the gas sampling ports at five different heights along freeboard flush with the inner surface of the refractory side wall. The radiometer output for incident radiative heat flux was read by using Medtherm H-201 digital heat flux meter, which was calibrated by the manufacturer with an accuracy range of  $\pm 1.0\%$ .

The test rig is equipped with a data acquisition and control system namely Bailey INFI 90. Real time process data is monitored, manipulated, collected and analysed with the aid of control software called Bailey LAN-90 Process Control View. The control system scans the signals coming from all of the instruments attached to it in a fraction of a second and reports and logs their averages discretely for 30 seconds of intervals. An uninterruptible power supply is connected to Bailey INFI 90 and PC in order to enable proper shut-down in case of an electricity cut-off by preventing corruption of data logged.

### **5.1.1 Coal Combustion Tests**

Coal combustion tests used in this study were previously carried out in ABFBC test rig with a typical low calorific value Turkish lignite with high ash and sulfur contents, namely Beypazarı Lignite [4]. In this experimental study, lignite was burned in its own ash (due to its high ash content) in order to investigate the effect of recycle on emission performance of the test rig by performing two sets of experiments at several recycle rates; one without (SET I) and the other with limestone addition (SET II). In this study, only two experiments from SET I (Run 1, Run 3) are used to model the radiative heat transfer within the freeboard of the combustor, for which radiative heat flux measurements are available. Table 5.1 and Table 5.2 show the characteristics of the indigenous lignite and Table 5.3 lists the operating conditions for the two combustion tests.

Table 5.1 Fuel characteristics of the Beypazarı Lignite

Ultimate analysis (Dry, % by wt.)		Proximate Analysis (As received, % by wt.)	
<b>C</b>	38.10	<b>Moisture</b>	13.70
<b>H</b>	3.20	<b>Ash</b>	36.40
<b>O</b>	12.40	<b>Volatile Matter</b>	32.70
<b>N</b>	1.40	<b>Fixed Carbon</b>	17.20
<b>S<sub>combustible</sub></b>	2.70	<b>HHV (cal/g)</b>	3154
<b>S<sub>total</sub></b>	4.50	<b>Bulk Density (kg/m<sup>3</sup>)</b>	905
<b>Ash</b>	42.20	<b>Particle Density (kg/m<sup>3</sup>)</b>	1580

Table 5.2 Fuel ash analysis of the lignite used in SET I

Component	Weight (%)
<b>SiO<sub>2</sub></b>	36.6
<b>Al<sub>2</sub>O<sub>3</sub></b>	12.5
<b>Fe<sub>2</sub>O<sub>3</sub></b>	9.4
<b>CaO</b>	0.7
<b>MgO</b>	1.1
<b>TiO<sub>2</sub></b>	3.0
<b>K<sub>2</sub>O</b>	1.3
<b>Na<sub>2</sub>O</b>	6.5
<b>SO<sub>3</sub></b>	27.4

Table 5.3 Operating conditions for the combustion tests in ABFBC

	<b>Test 1</b>	<b>Test 2</b>
<b>Superficial velocity (m/s)</b>	3.0	2.8
<b>Coal flow rate (kg/h)</b>	101	101
<b>Bed drain flow rate (kg/h)</b>	7	11
<b>Cyclone ash flow rate (kg/h)</b>	22.57	239.22
<b>Baghouse filter ash flow rate (kg/h)</b>	1.08	3.43
<b>Carryover flow rate (kg/h)</b>	23.65	242.65
<b>Recycle ratio (-)</b>	0	2.37
<b>Excess air (%)</b>	43.0	36.0
<b>Particle load (kg/m<sup>3</sup>)</b>	0.011	0.131
<b>Bed height (m)</b>	0.9	0.9
<b>Freeboard height (m)</b>	3.35	3.35
<b>Mean beam length (m)</b>	0.38	0.38
<b>Average bed temperature (K)</b>	1148	1119
<b>Equivalent top surface temperature (K)</b>	908	940
<b>Average freeboard temperature (K)</b>	1144	1163
<b>Average side wall temperature (K)</b>	1103	1110
<b>Average H<sub>2</sub>O concentration (%)</b>	10	10
<b>Average CO<sub>2</sub> concentration (%)</b>	10	11

In order to apply the radiation models to the freeboard of the 300 kW<sub>t</sub> METU Test Rig, it is required to provide medium and wall temperatures, gas concentrations, particle size distributions, particle densities, chemical compositions and particle load as input data for the in-house developed radiation codes.

Wall and medium temperature measurements were performed on a discrete grid of points along the freeboard at steady state operation. To facilitate the use of these measurements as input data in the calculation of radiative exchange, the experimental data were

represented by high order polynomials as displayed in Table 5.4. These temperature profiles are also illustrated in Figure 5.3. CO<sub>2</sub> and H<sub>2</sub>O concentrations<sup>4</sup> are found to be uniform in the freeboard measurements [4] for Test 1 and Test 2 as given in Table 5.3.

Table 5.4 Polynomials for temperature profiles

	<b>Test 1</b>	<b>Test 2</b>
<b>Medium temperature profile, K</b> $T_m(z) = \sum_{i=0}^6 a_i z^i$	$a_0 = 1149.66$ $a_1 = -15.50$ $a_2 = -1.351$ $a_3 = 42.65$ $a_4 = -30.56$ $a_5 = 7.84$ $a_6 = -0.71$	$a_0 = 1106.52$ $a_1 = 16.62$ $a_2 = -90.85$ $a_3 = 116.33$ $a_4 = -50.22$ $a_5 = 9.59$ $a_6 = -0.73$
<b>Wall temperature profile, K</b> $T_w(z) = \sum_{i=0}^6 b_i z^i$	$b_0 = 1146.50$ $b_1 = 40.50$ $b_2 = -129.23$ $b_3 = 137.01$ $b_4 = -62.89$ $b_5 = 13.14$ $b_6 = -1.04$	$b_0 = 1110.44$ $b_1 = 61.59$ $b_2 = -226.77$ $b_3 = 246.25$ $b_4 = -106.20$ $b_5 = 20.58$ $b_6 = -1.52$

---

<sup>4</sup> It should be noted that only CO<sub>2</sub> concentrations are measured along the freeboard while H<sub>2</sub>O concentration is calculated from the measured wet and dry O<sub>2</sub> concentrations.

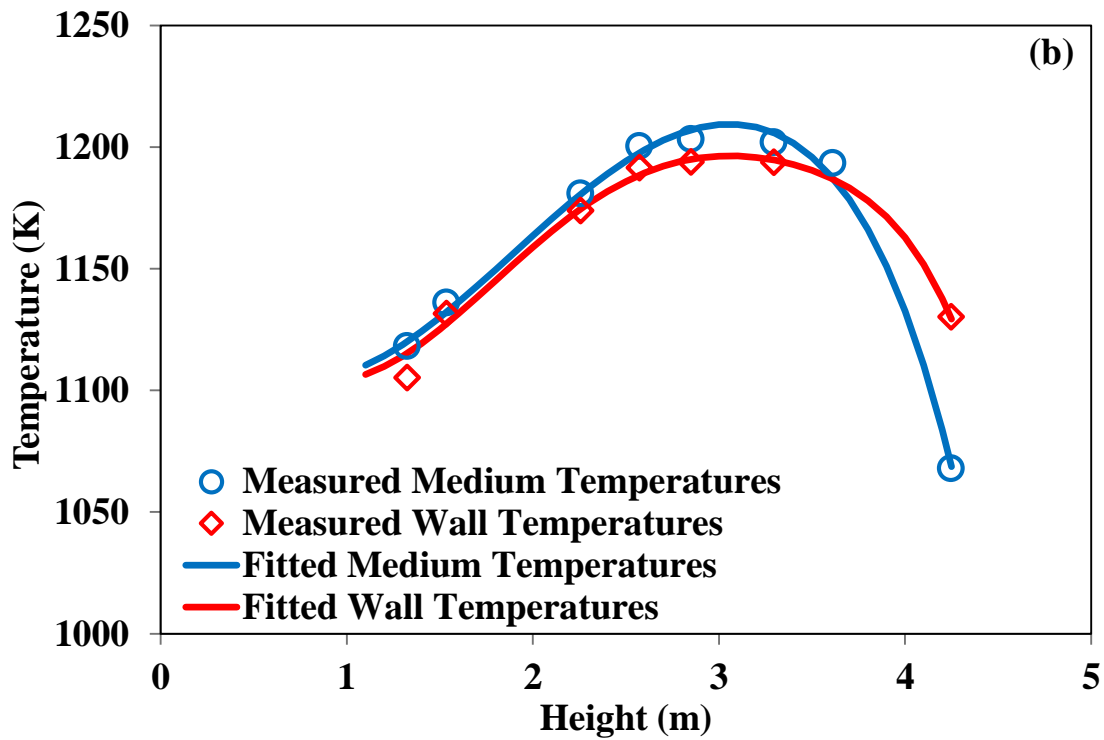
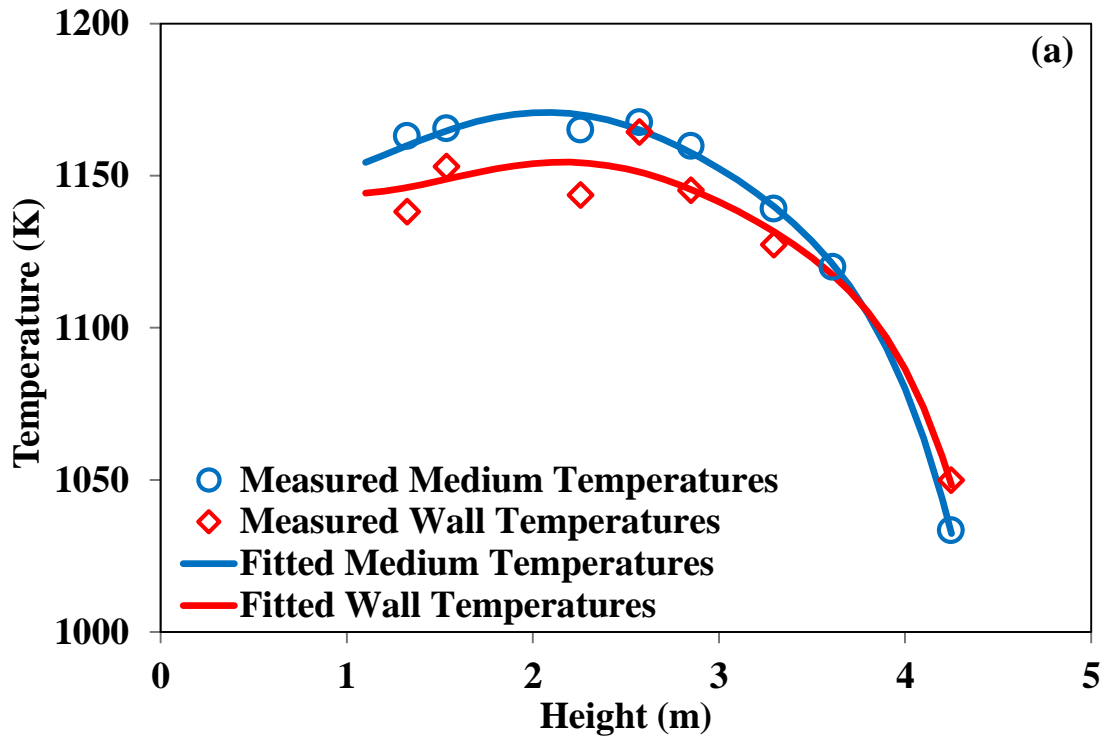


Figure 5.3 Temperature profiles along the freeboard for (a) Test 1 and (b) Test 2



Particles collected from both cyclone and baghouse downstream of the freeboard are subjected to sieve analysis and laser light scattering technique, respectively, for particle size distribution (PSD). These PSD measurements are presented as tables in Appendix E. In radiative property calculations, PSD of the cyclone and baghouse filter ashes are combined to obtain the actual size distributions along the freeboard, which is shown in Figure 5.4. Ash content of the collected fly ash particles determined by chemical analysis was 98% for both Test 1 and Test 2, hence particles are considered to be pure ash in radiative property calculations. Ash analysis of the samples collected from the cyclone and bag filter together with their measured densities are given in Table 5.5.

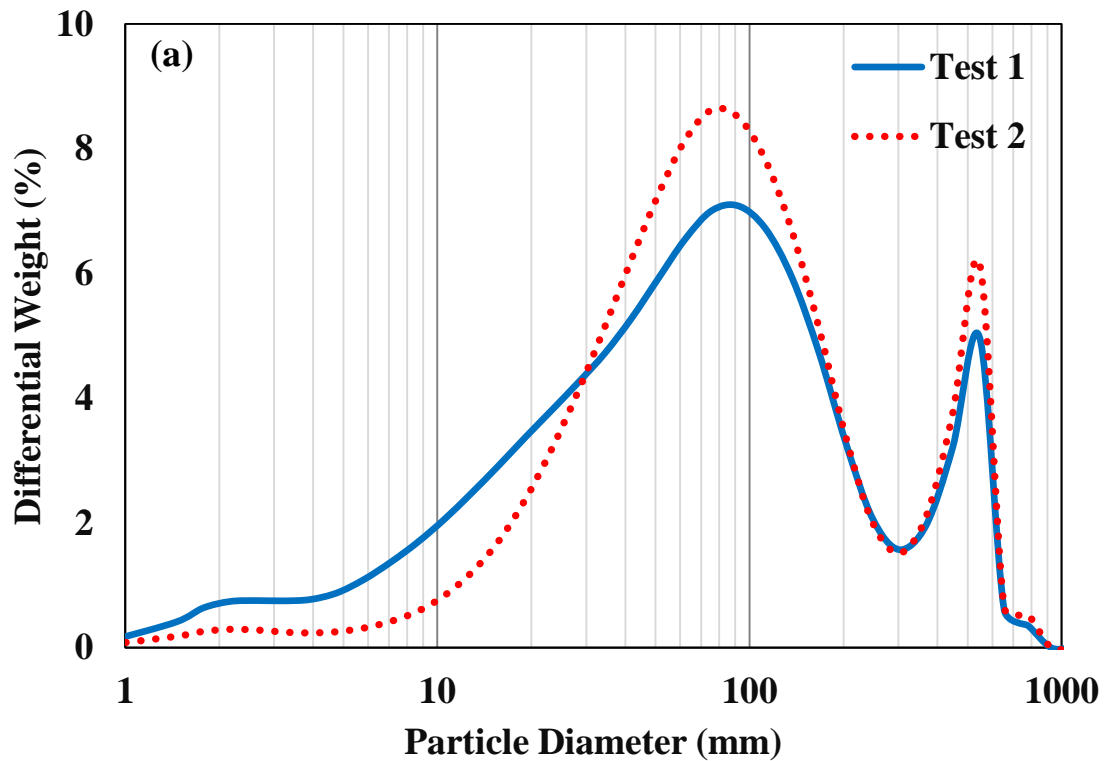


Figure 5.4 (a) Differential and (b) cumulative particle size distributions in the freeboard for Test 1 and Test 2

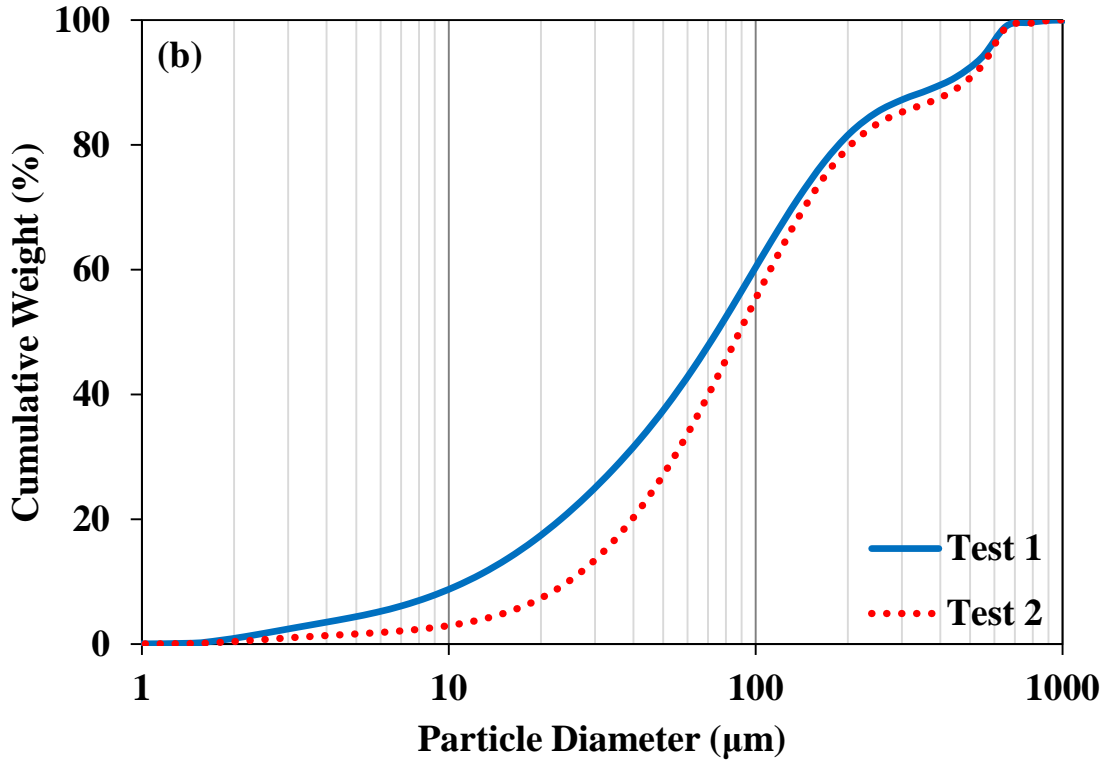


Figure 5.4 (a) Differential and (b) cumulative particle size distributions in the freeboard for Test 1 and Test 2 (cont'd)

Table 5.5 Fly ash compositions and densities

	Test 1		Test 2	
	<i>Cyclone</i>	<i>Bag Filter</i>	<i>Cyclone</i>	<i>Bag Filter</i>
SiO <sub>2</sub> (wt %)	46.52	28.37	47.40	36.41
Al <sub>2</sub> O <sub>3</sub> (wt %)	16.58	13.00	16.92	12.97
Fe <sub>2</sub> O <sub>3</sub> (wt %)	12.98	23.80	13.08	18.82
CaO (wt %)	0.37	1.16	0.41	2.37
MgO (wt %)	0.99	1.20	1.01	0.99
TiO <sub>2</sub> (wt %)	4.92	8.05	3.58	7.29
K <sub>2</sub> O (wt %)	2.28	1.52	1.90	1.32
SO <sub>3</sub> (wt %)	8.44	18.16	8.63	15.85
Na <sub>2</sub> O (wt %)	6.92	4.73	7.07	3.99
Particle density (kg/m <sup>3</sup> )	1029	610	931	690
Skeletal density (kg/m <sup>3</sup> )	2994	3949	2221	3606

Particle load ( $B$ ) is assumed to be uniform throughout the freeboard owing to insignificant pressure drops and it is determined as a mean value from solid stream measurements as follows,

$$B = \frac{F_{cyclone} + F_{bagfilter}}{u_0 A_c} \quad (5.1)$$

where  $u_0$  is the superficial gas velocity,  $A_c$  is the cross section of the combustor,  $F_{cyclone}$  and  $F_{bagfilter}$  are the measured ash flow rates collected by the cyclone and baghouse filter, respectively (see Table 5.3).

### 5.1.2 Coal Combustion Tests with Limestone and Biomass Addition

Combustion tests with limestone and biomass addition were also previously carried out in the ABFBC test rig with a typical low calorific value Turkish lignite with high ash and sulfur contents, namely Çan Lignite [8]. In this experimental study, lignite and biomass blends were burned in ash due to high ash content of the lignite in the presence of limestone in order to investigate the effect of biomass share on gaseous pollutant emissions. This was achieved by co-firing three different biomass sources (olive residue, hazelnut shell and cotton residue) with low calorific value indigenous lignite in ten different combustion tests. In this study, eight of those experiments are used to model the radiative heat transfer within the freeboard of the combustor, for which complete experimental data are available [8]. These combustion tests were performed sequentially for lignite only (Test 1), lignite with limestone addition (Test 2), followed by 15, 31 and 49 wt % shares of olive residue in the fuel mixture for the same Ca/S ratio (Test 3-5), followed by 11, 30 and 42 wt % shares of hazelnut shell in the fuel mixture for the same Ca/S ratio (Test 6-8). The characteristics of Çan lignite, olive residue and hazelnut shell burned in these tests are summarized in Table 5.6. Table 5.7 lists the operating conditions of the combustion tests. Ash constituents of lignites and biomasses are also shown in Table 5.9. With regard to ash composition, lignite ash is mainly composed of acidic oxides whereas olive residue ash is mainly composed of basic oxides. It is worth noting at this

point that sulfur content of the fuel is reduced from Test 3 to Test 5 and from Test 6 to Test 8 by co-firing lignite with biomass, which contains little amount of sulfur so that Ca/S ratio could be kept constant with lower limestone shares (Table 5.7). Furthermore, operating parameters other than biomass share were tried to be maintained constant from one test to another in these six combustion tests (Test 3-8).

In order to apply the radiation models to the freeboard of the 300 kW<sub>t</sub> METU Test Rig, it is required to provide medium and wall temperatures, gas concentrations, particle size distributions, particle densities, chemical compositions and particle load as input data for the in-house developed radiation codes.

Similar to previous experiments, medium temperature measurements were performed on a discrete grid of points along the freeboard at steady state operation. These temperature profiles are illustrated in Figure 5.5. To facilitate the use of these measurements as input data in the calculation of radiative exchange, the experimental data were represented by high order polynomials as displayed in Table 5.8. These polynomial functions are also demonstrated in Figure 5.5 as dash lines. It should be noted that wall temperature measurements are not available and they are assumed to be 15 K lower than medium temperatures based on previous measurements on the same test rig [4]. For all tests, CO<sub>2</sub> and H<sub>2</sub>O concentrations<sup>5</sup> are found to be almost uniform in the freeboard measurements [8] and averaged gas concentration values given in Table 5.7 are used for radiative property calculations.

.

---

<sup>5</sup> It should be noted that only CO<sub>2</sub> concentrations are measured along the freeboard continuously while H<sub>2</sub>O concentration is calculated from the measured wet and dry O<sub>2</sub> concentrations.

Table 5.6 Characteristics of Çan lignite, olive residue and hazelnut shell

	Lignite								Olive residue	Hazelnut Shell
	Test 1	Test 2	Test 3	Test 4	Test 5	Test 6	Test 7	Test 8		
<b>Proximate Analysis (As received, % by wt.)</b>										
<b>Moisture</b>	16.35	16.48	16.98	16.6	16.75	17.19	16.05	17.14	6.07	7.62
<b>Ash</b>	28.78	26.74	24.56	22.68	23.89	25.29	24.36	27.46	4.24	1.46
<b>Volatile matter</b>	29.79	31.05	31.58	32.52	32.04	31.22	32.17	30.36	75.69	73.04
<b>Fixed carbon</b>	25.17	25.74	26.88	28.2	27.33	26.3	27.42	25.04	14.00	17.89
<b>Ultimate Analysis (Dry, % by wt.)</b>										
<b>C</b>	44.6	44.93	45.42	43.81	44.83	46.47	42.22	41.92	50.22	49.77
<b>H</b>	3.95	4.09	4.37	3.86	4	4.26	4.23	4.01	6.38	5.86
<b>N</b>	1.09	1.14	1.11	1.16	1.2	1.15	1.01	0.96	1.72	0.56
<b>O</b>	11.97	13.96	15.85	20.64	17.66	13.95	19.35	15.64	37.03	42.15
<b>S Combustible</b>	3.98	3.86	3.67	3.34	3.61	3.63	4.17	4.33	0.14	0.08
<b>Ash</b>	34.41	32.02	29.58	27.19	28.7	30.54	29.02	33.14	4.51	1.58
<b><math>\rho_{\text{Bulk}}</math>, kg/m<sup>3</sup></b>	905	905	905	905	905	905	905	905	591	320
<b>LHV, MJ/kg</b>	12.3	13.3	13.6	14.6	14.0	13.4	13.9	12.5	18.1	17.5
<b>Fuel ash composition, % by wt.</b>										
<b>SiO<sub>2</sub></b>	57.29	56.56	51.33	55.26	52.70	50.02	51.43	51.91	31.19	2.28
<b>Al<sub>2</sub>O<sub>3</sub></b>	19.67	17.49	21.84	20.43	19.14	23.81	22.80	21.83	5.29	2.59
<b>Fe<sub>2</sub>O<sub>3</sub></b>	12.05	10.99	10.59	10.42	11.26	12.03	12.28	12.15	5.17	7.11
<b>CaO</b>	4.85	9.21	9.06	7.50	7.78	8.19	7.26	7.92	17.52	38.84
<b>MgO</b>	0.82	0.57	0.63	0.59	0.52	0.63	0.52	0.58	2.51	6.60
<b>SO<sub>3</sub></b>	2.00	2.05	3.49	2.63	5.23	2.43	2.23	2.31	2.64	5.50
<b>Na<sub>2</sub>O</b>	1.58	1.45	1.24	1.34	1.62	1.05	1.59	1.60	5.21	7.40
<b>K<sub>2</sub>O</b>	0.21	0.31	0.27	0.19	0.21	0.24	0.26	0.33	27.95	27.86
<b>TiO<sub>2</sub></b>	1.53	1.38	1.55	1.63	1.54	1.59	1.63	1.37	2.52	1.81

Table 5.7 Operating conditions of the combustion tests

	<b>Test 1</b>	<b>Test 2</b>	<b>Test 3</b>	<b>Test 4</b>	<b>Test 5</b>	<b>Test 6</b>	<b>Test 7</b>	<b>Test 8</b>
<b>Coal flow rate, kg/h</b>	76.5	68.7	56.6	40.9	30.2	54.3	41.0	32.4
<b>Biomass flow rate, kg/h</b>	0	0	10.0	18.8	28.8	7.0	17.2	23.3
<b>Biomass share, wt. %</b>	0	0	15	31	49	11	30	42
<b>Biomass share (on thermal basis), %</b>	0	0	19	36	55	14	35	50
<b>Limestone flow rate, kg/h</b>	0	22.4	19.1	13.9	11.2	18.6	14.1	13.9
<b>Ca/S molar ratio (based on total S)</b>	0	3	3	3	3	3	3	3
<b>Limestone flow rate / total solid input</b>	0	0.25	0.22	0.19	0.16	0.23	0.20	0.20
<b>Sulfur content of the fuel, wt. %</b>	4.0	3.9	3.1	2.3	1.9	3.2	3.0	2.6
<b>Bottom ash flow rate, kg/h</b>	6.9	8.3	8	3.6	1.5	5.5	2.5	2.2
<b>Cyclone ash flow rate, kg/h</b>	14.2	19.4	16.6	12.5	11	17.1	14.5	12.1
<b>Baghouse filter ash flow rate, kg/h</b>	0.4	1.2	0.8	1.3	1.7	1	1.4	1.9
<b>Particle load, g/m<sup>3</sup></b>	9	15	13	10	9	13	11	10
<b>Air flow rate, kmol/h</b>	16	14	14	14	14	14.2	14	14
<b>Flue gas flow rate, kmol/h</b>	16.8	14.6	14.5	14.2	14.3	14.4	14.1	14.3
<b>Excess air, %</b>	23	21	18	23	28	20	21	22
<b>Superficial velocity, m/s</b>	2.2	1.9	1.9	1.9	1.9	1.9	1.9	1.9
<b>Average bed temperature, K</b>	1174	1124	1138	1125	1132	1133	1130	1132
<b>Top surface temperature, K</b>	873	837	850	852	875	875	857	857
<b>Average freeboard temperature, K</b>	1139	1090	1112	1105	1122	1104	1105	1108
<b>Average side wall temperature, K</b>	1124	1075	1097	1090	1107	1089	1090	1093
<b>Bed height, m</b>	1.02	1.12	1.18	1.14	1.10	1.22	1.16	1.10
<b>Average H<sub>2</sub>O concentration (%)</b>	12.39	14.43	17.43	17.33	20.31	8.75	18.37	19.08
<b>Average CO<sub>2</sub> concentration (%)</b>	13.27	13.75	13.65	12.99	12.46	11.6	13.32	12.91

Particles collected from both cyclone and baghouse downstream of the freeboard are subjected to sieve analysis and laser light scattering technique, respectively, for PSD (Figure 5.6, Figure 5.7) . These PSD measurements are also presented in tabulated form in Appendix E. In radiative property calculations, PSD of the cyclone and baghouse filter ashes are combined to obtain the actual size distributions in the freeboard. Ash analysis of the samples collected from the cyclone and bag filter together with their measured densities are given in Table 5.9. Particle load is again calculated from solid stream flow rates (Eq. (5.1) and assumed to be uniform throughout the freeboard owing to insignificant pressure drops.

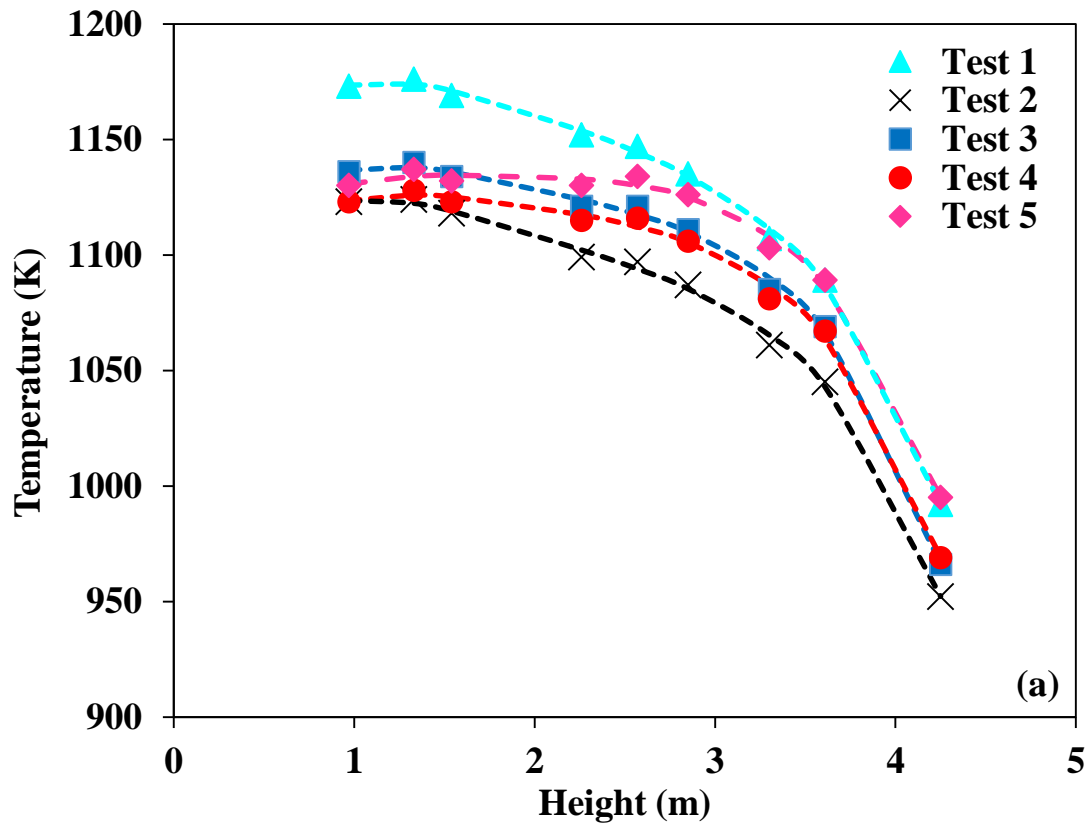


Figure 5.5 Temperature profiles along the freeboard for (a) Test 1-5 and (b) Test 1, 2, 6-

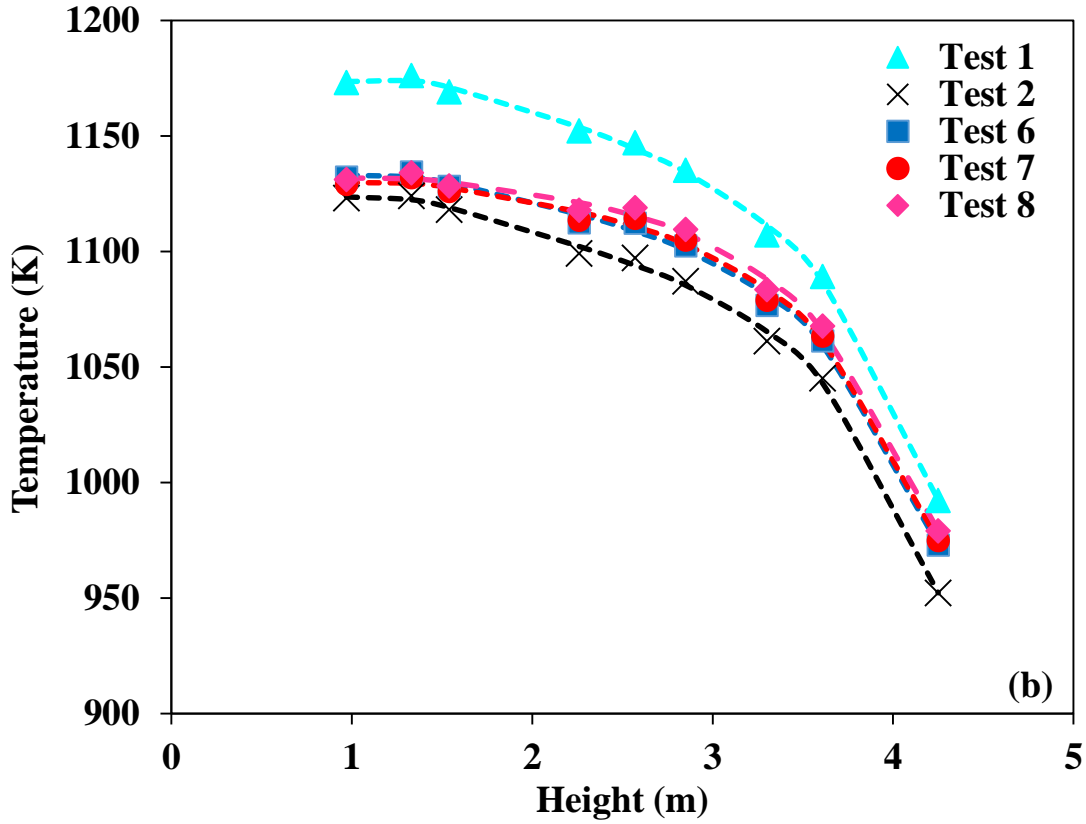


Figure 5.5 Temperature profiles along the freeboard for (a) Test 1-5 and (b) Test 1, 2, 6-8 (cont'd)

Table 5.8 Polynomials for temperature profiles

		Test 1	Test 2	Test 3	Test 4
<b>Medium temperature profile, K</b>	a <sub>0</sub>	1097.91813	1054.75387	1061.84019	1060.25529
	a <sub>1</sub>	170.22417	162.52220	169.06791	138.32243
	a <sub>2</sub>	-127.79054	-128.32891	-129.59071	-103.21697
	a <sub>3</sub>	38.03943	39.53512	40.66308	32.72933
	a <sub>4</sub>	-4.41646	-4.62880	-4.88813	-4.06663
$T_m(z) = \sum_{i=0}^4 a_i z^i$					
		Test 5	Test 6	Test 7	Test 8
<b>Medium temperature profile, K</b>	a <sub>0</sub>	1084.88832	1078.09613	1086.92818	1098.31422
	a <sub>1</sub>	97.15457	129.09152	100.67882	79.56123
	a <sub>2</sub>	-71.88098	-102.04443	-80.10107	-64.49580
	a <sub>3</sub>	24.41634	31.85503	25.75476	21.44397
	a <sub>4</sub>	-3.30535	-3.84948	-3.27981	-2.87639
$T_m(z) = \sum_{i=0}^4 a_i z^i$					



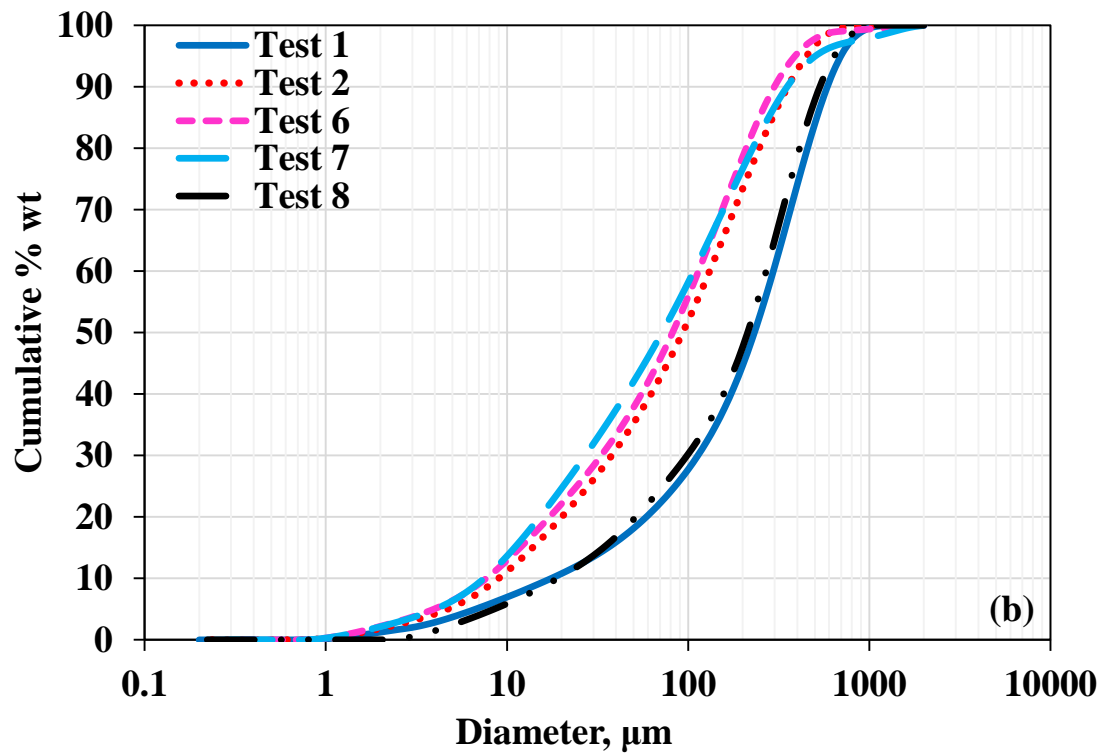
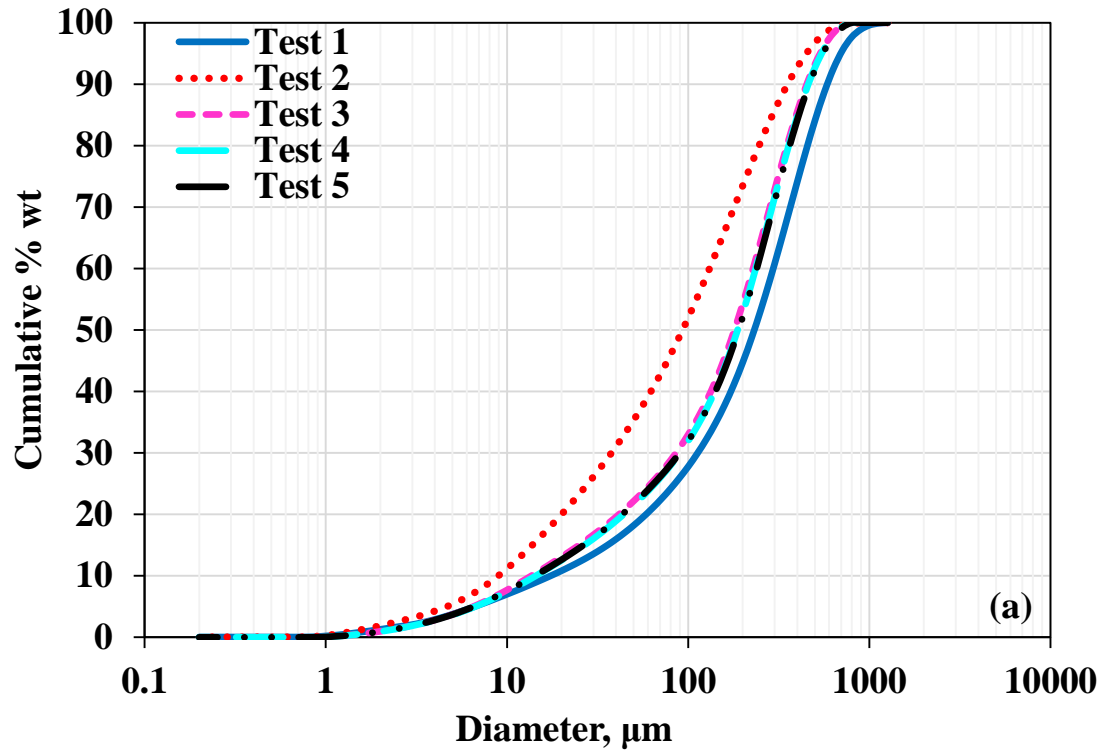


Figure 5.6 Cumulative particle size distributions for the particles collected from the cyclone for (a) olive residue and (b) hazelnut shell co-firing experiments

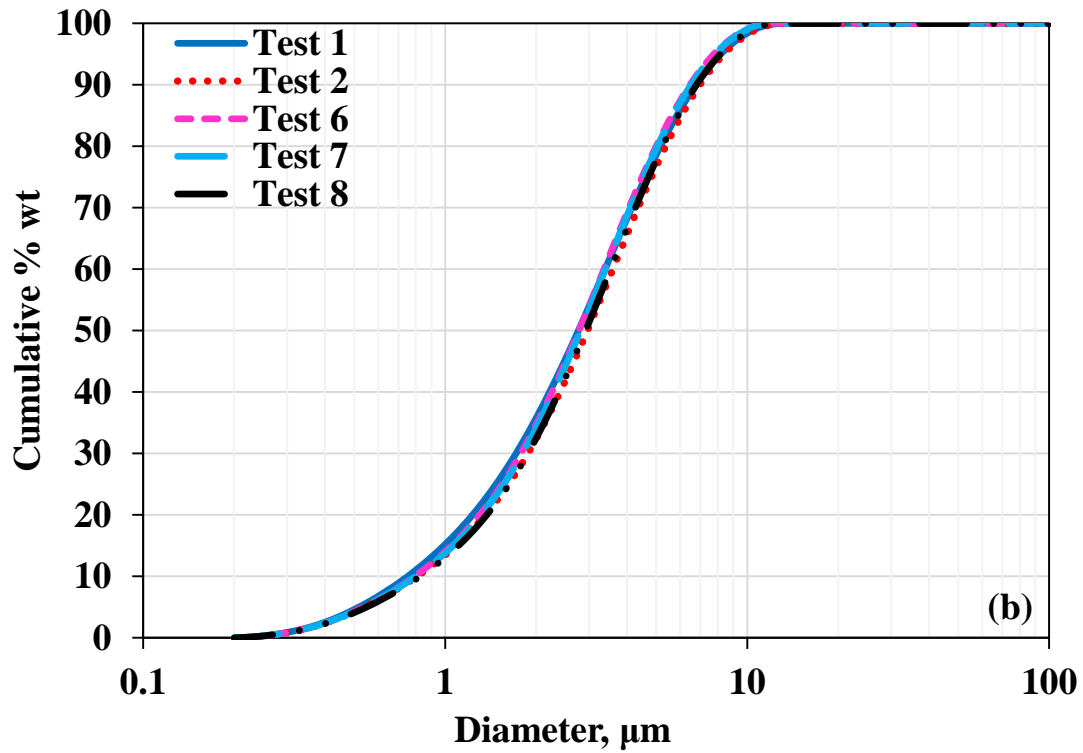
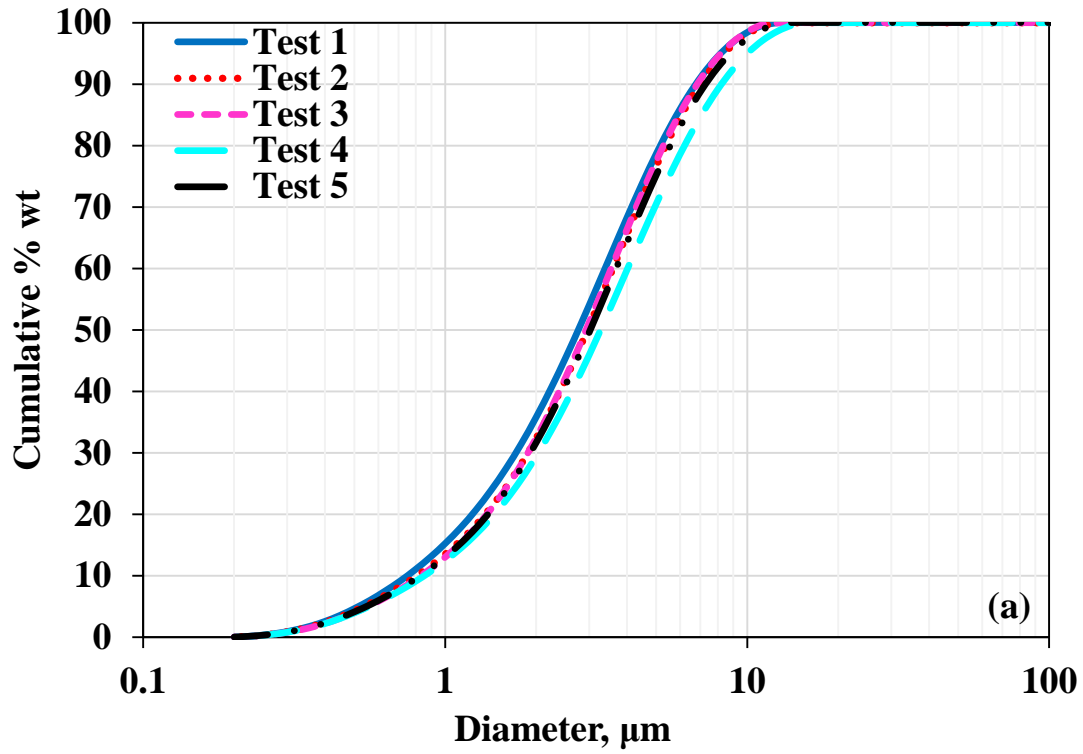


Figure 5.7 Cumulative particle size distributions for the particles collected from the baghouse filter for (a) olive residue and (b) hazelnut shell co-firing experiments

Table 5.9 Fly ash compositions

	Test 1	Test 2	Test 3	Test 4	Test 5	Test 6	Test 7	Test 8
<b>Cyclone particles</b>								
<b>SiO<sub>2</sub> (wt %)</b>	51.61	23.27	29.71	25.92	19.58	24.83	21.91	31.51
<b>Al<sub>2</sub>O<sub>3</sub> (wt %)</b>	20.92	8.04	7.75	8.76	7.51	6.77	9.40	7.96
<b>Fe<sub>2</sub>O<sub>3</sub> (wt %)</b>	10.48	7.40	6.18	5.67	6.67	7.64	8.01	6.98
<b>CaO (wt %)</b>	7.41	39.96	33.01	38.93	45.10	40.60	38.71	31.48
<b>MgO (wt %)</b>	0.69	4.61	4.51	5.05	4.63	2.92	2.12	2.06
<b>SO<sub>3</sub> (wt %)</b>	4.05	13.47	15.56	12.46	12.65	13.66	15.64	15.94
<b>Na<sub>2</sub>O (wt %)</b>	2.34	1.36	1.18	1.35	1.60	1.72	1.82	1.46
<b>K<sub>2</sub>O (wt %)</b>	0.77	0.97	0.81	0.99	1.43	1.00	1.17	1.31
<b>TiO<sub>2</sub> (wt %)</b>	1.73	0.91	1.29	0.88	0.83	0.86	1.22	1.30
<b>Particle density (kg/m<sup>3</sup>)</b>	1214	1247	1438	1392	1356	1198	1278	1319
<b>Bag filter particles</b>								
<b>SiO<sub>2</sub> (wt %)</b>	45.82	32.19	25.74	26.53	22.21	22.34	29.55	27.60
<b>Al<sub>2</sub>O<sub>3</sub> (wt %)</b>	14.68	9.69	6.60	9.22	8.49	10.29	8.78	8.42
<b>Fe<sub>2</sub>O<sub>3</sub> (wt %)</b>	17.36	12.61	12.59	13.18	14.29	15.95	14.80	14.68
<b>CaO (wt %)</b>	9.49	22.95	32.46	28.25	27.80	27.58	25.24	27.46
<b>MgO (wt %)</b>	0.80	1.40	2.01	2.76	3.11	3.24	2.54	1.95
<b>SO<sub>3</sub> (wt %)</b>	7.93	17.80	16.67	15.94	18.79	15.69	14.75	15.27
<b>Na<sub>2</sub>O (wt %)</b>	1.57	1.14	1.72	1.57	2.37	1.98	1.67	1.55
<b>K<sub>2</sub>O (wt %)</b>	0.47	0.51	1.00	0.86	1.19	1.26	1.12	1.02
<b>TiO<sub>2</sub> (wt %)</b>	1.88	1.72	1.20	1.68	1.76	1.66	1.56	2.04
<b>Particle density (kg/m<sup>3</sup>)</b>	796	818	943	913	890	786	838	865

### 5.1.3 Treatment of the Freeboard in Radiative Heat Transfer Calculations

The physical system under consideration is the freeboard region of METU 300 kW<sub>t</sub> Atmospheric Bubbling Fluidized Bed Combustor (ABFBC) for above-mentioned 10 combustion tests. In all radiation models, freeboard section of the combustor is treated as a 3-D rectangular enclosure containing gray / non-gray, absorbing, emitting gas with gray / non-gray absorbing, emitting, non/isotropically/anisotropically scattering particles bounded by diffuse, gray / black walls. The physical system and the treatment of the freeboard section are schematically illustrated in Figure 5.8. The enclosure is assumed to be bounded by three surfaces. Top and bottom surfaces are assumed to be at uniform temperature with constant radiative properties while the temperature of the refractory side-walls are represented by high order polynomials given in Table 5.4 and Table 5.8 with uniform surface radiative properties.

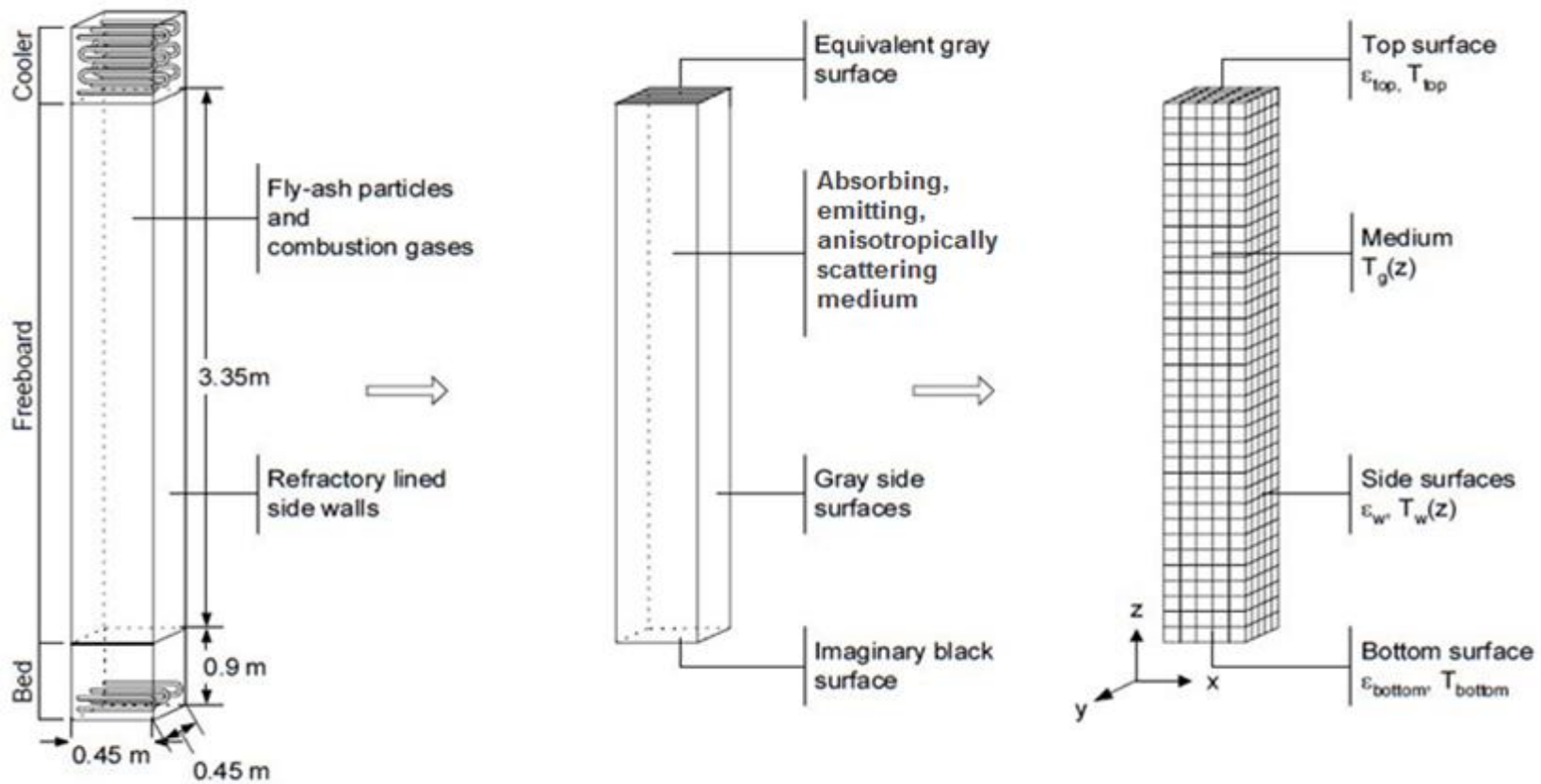
The side walls of the freeboard are taken as gray, diffusely emitting and reflecting surfaces with an emissivity of 0.33 [37, 131]. The top surface ( $z = 4.25$  m) consists of two components, cooling tubes and gas lanes. In order to simplify the problem, top surface is represented by an equivalent emissivity and temperature, which gives the same total emissive power,

$$A_{eqv}\epsilon_{eqv}T_{eqv}^4 = A_{tubes}\epsilon_{tubes}T_{tubes}^4 + A_{gas\ lane}\epsilon_{gas\ lane}T_{gas\ lane}^4 \quad (5.2)$$

$$A_{eqv}\epsilon_{eqv} = A_{tubes}\epsilon_{tubes} + A_{gas\ lane}\epsilon_{gas\ lane} \quad (5.3)$$

where gas lanes are assumed to act like black cavities ( $\epsilon_{gas\ lane} = 1.0$ ) and emissivity of the carbon steel tube ( $\epsilon_{tubes}$ ) is taken from [131] as 0.79. Equivalent emissivity ( $\epsilon_{eqv}$ ) is found from area-weighted average emissivities (Eq. (5.3)). Temperature of the tubes are taken from cooling water temperature measurements as a mean value ( $T_{tubes} = (T_{w,inlet} + T_{w,outlet})/2$ ) and gas temperature is taken from the measurements. The boundary with the bed section at the bottom is represented as a black surface due to Hohlraum effect [13].

Radiative properties of participating combustion gases and particles are found from the property models described in Chapter 3 and Chapter 4, respectively.



The physical system: Freeboard of the ABFBC and its boundaries

Treatment of the freeboard as a 3-D rectangular enclosure

Solution domain and boundary conditions used in MOL solution of DOM

Figure 5.8 Treatment of freeboard as a 3-D enclosure

## 5.2 150 kW<sub>t</sub> Circulating Fluidized Bed Combustor Test Rig

150 kW<sub>t</sub> Circulating Fluidized Bed Combustor (CFBC) Test Rig was designed and constructed in Chemical Engineering Department of Middle East Technical University to investigate combustion characteristics of an indigenous lignite in a circulating fluidized bed combustor [3]. The test rig in its present form is shown in Figure 5.9 and its flow sheet is given in Figure 5.10. The components of the test unit are listed below [3];

- |                                 |                       |
|---------------------------------|-----------------------|
| 1. Combustion air supply        | 7. Cyclone            |
| 2. Coal handling                | 8. Loop seal          |
| 3. Limestone handling           | 9. Bag filter         |
| 4. Solids feeding               | 10. Induced draft fan |
| 5. CFB combustor                | 11. Stack             |
| 6. Bottom ash withdrawal system | 12. Control room      |

The reactor which is made of five modules is equipped with a cyclone, downcomer, and a loop-seal. Inner surface of the reactor is coated with refractory and the outer surface of the second and third modules is surrounded by vertical cooling water tubes. The height of the combustor chamber is 8 m, and the diameter is 0.25 m. Bed drain, circulating ash, and fly ash are collected from the bottom of the riser, the loop seal, and the bag filter, respectively. More detailed descriptions of the test rig can be found elsewhere [3].

There are 6 ports for gas sampling along the combustor connected to on-line continuous gas analysers to measure concentrations of species O<sub>2</sub>, CO, CO<sub>2</sub>, NO, N<sub>2</sub>O and SO<sub>2</sub> along the combustor and also at the cyclone exit on dry basis. There is an additional analyser, Bailey SMA 90, which measures temporal variation of O<sub>2</sub> and CO on wet basis at the combustor exit, from which H<sub>2</sub>O content of the flue gas is calculated.



Figure 5.9 METU 150 kW<sub>t</sub> CFBC Test Rig



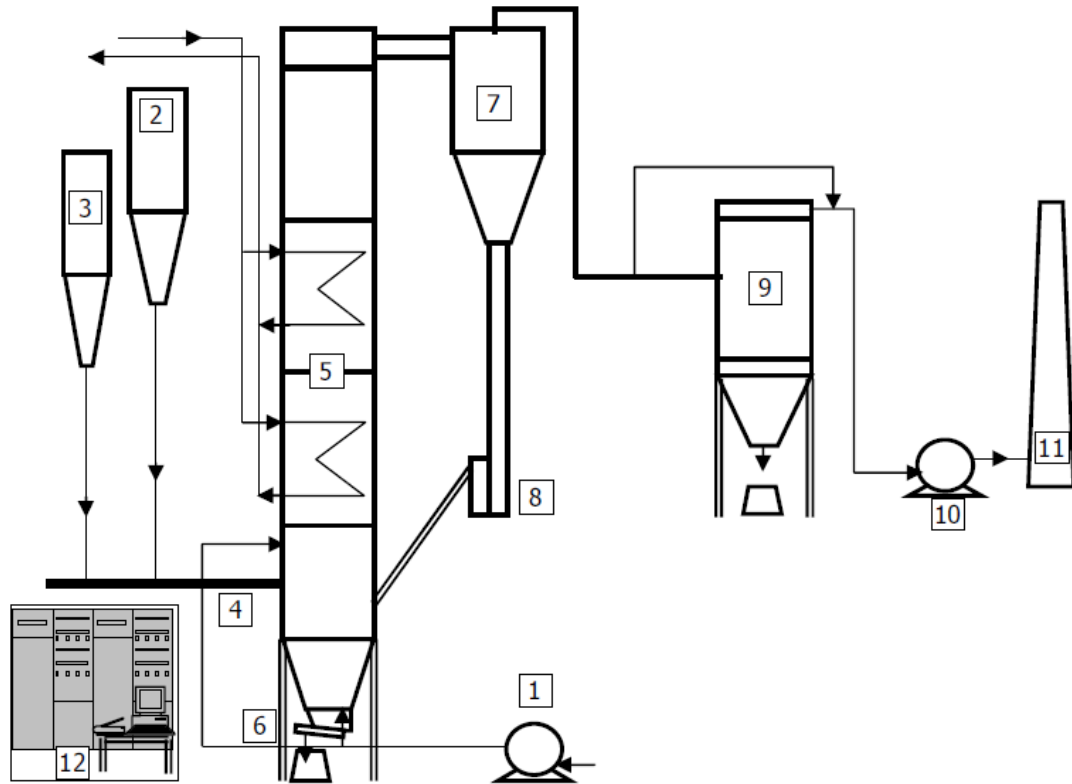


Figure 5.10 Process diagram of the CFBC test rig

Pressure sensors are used for measuring differential (DPT) and gauge pressures (PT) at 13 positions along the combustor. PTs are placed in the windbox and the exit module while DPTs are distributed along the dense and dilute zones. Spatial and temporal variations of gas temperatures along the combustor are measured by 12 K-type thermocouples continuously.

The test rig is equipped with a data acquisition and control system. Real time process data is monitored, manipulated, collected and analysed with the aid of its control software, DeltaV. DCS hardware includes controller, analog input, analog output, digital input and digital output cards. The control system scans the signals coming from all of the instruments attached to it in a fraction of a second and reports and logs their averages discretely. An uninterruptible power supply is connected to the DCS system in order to

enable proper shut-down in case of an electricity cut-off by preventing corruption of data logged.

### 5.2.1 Coal Combustion Test

Coal combustion test used in this study was previously carried out in the CFBC test rig with a typical Turkish lignite, namely Çan Lignite [3]. In this experimental study, lignite was burned in two combustion tests in order to investigate the combustion characteristics of an indigenous lignite in a circulating fluidized bed combustor [3]. In the current study, only the second experiment is used to model the radiative heat transfer. Analysis of the coal used in the experiment is given in Table 5.10. As can be seen from the table, Çan lignite is characterized by its low calorific value with high volatile matter/fixed carbon (VM/FC) ratio and high ash content. Due to its high ash content, the experiment was carried out by burning lignite in its own ash, analysis of which is given in Table 5.11. Operating of the combustion test is given in Table 5.12.

Table 5.10 Characteristics of Çan lignite

Proximate Analysis (As received)		Ultimate Analysis (Dry)	
Component	Weight (%)	Component	Weight (%)
Moisture	16.24	C	41.05
Ash	32.72	H	3.31
VM	29.20	O	12.18
FC	21.44	N	1.10
LHV: 12.9 MJ/kg		S <sub>comb</sub> *	3.30
$\rho_b$ : 932 kg/m <sup>3</sup>		S <sub>total</sub>	4.59
d <sub>50</sub> : 1.29 mm		Ash	39.06
* S <sub>comb</sub> is the combustible sulfur content of coal, that is, sum of pyritic and organic sulfur.			

Table 5.11 Çan lignite ash composition

<b>Compound</b>	<b>Weight %</b>
<b>SiO<sub>2</sub> (wt %)</b>	57.29
<b>Al<sub>2</sub>O<sub>3</sub> (wt %)</b>	19.67
<b>Fe<sub>2</sub>O<sub>3</sub> (wt %)</b>	12.05
<b>CaO (wt %)</b>	4.85
<b>MgO (wt %)</b>	0.82
<b>TiO<sub>2</sub> (wt %)</b>	1.53
<b>K<sub>2</sub>O (wt %)</b>	0.21
<b>SO<sub>3</sub> (wt %)</b>	2.00
<b>Na<sub>2</sub>O (wt %)</b>	1.58

Table 5.12 Operating parameters of the combustion test in CFBC

<b>Parameter</b>	<b>Value</b>
<b>Superficial gas velocity (m/s)</b>	5.1
<b>Terminal velocity (m/s)</b>	1.9
<b>Minimum fluidization voidage (-)</b>	0.43
<b>Solid circulation rate (kg/m<sup>2</sup>s)</b>	19.0
<b>Coal flow rate (kg/h)</b>	48.55
<b>Carryover flow rate (kg/h)</b>	3355.5
<b>Baghouse filter flow rate (kg/h)</b>	7.04
<b>Ash particle density (kg/m<sup>3</sup>)</b>	1200
<b>Recycle ratio* (-)</b>	69.04
<b>Excess air (%)</b>	16.5
<b>Primary air flow rate (Nm<sup>3</sup>/s)</b>	0.0495
<b>Secondary air flow rate (Nm<sup>3</sup>/s)</b>	0.0063
<b>Primary air/secondary air (%)</b>	88.7/11.3
<b>Pressure drop through dense bed (mmH<sub>2</sub>O)</b>	367.2
<b>Pressure drop through dilute zone (mmH<sub>2</sub>O)</b>	27.2

Table 5.12 Operating parameters of the combustion test in CFBC (cont'd)

<b>Parameter</b>	<b>Value</b>
<b>Average bed temperature (K)</b>	1102
<b>Average dilute zone temperature (K)</b>	1136
<b>Average side wall temperature (K)</b>	737
<b>Average H<sub>2</sub>O concentration (%)</b>	8
<b>Average CO<sub>2</sub> concentration (%)</b>	11
*Recycle ratio = (Recycle flow rate)/(Coal flow rate)	

In order to apply the radiation models to the dilute zone of the 150 kW<sub>t</sub> METU CFBC test rig, it is required to provide medium and wall temperatures, gas concentrations, particle size distributions, particle densities, chemical compositions and particle load as input data for the in-house developed radiation codes.

Medium temperature measurements were performed on a discrete grid of points along the combustor at steady state operation. However, wall temperature measurements were not available in the experimental work [3]. This is why temperature and gas composition data are obtained from the outputs of a mathematical modeling study, which was previously developed and validated against the experimental data of the combustion test [132]. This model is based on dense and dilute zone hydrodynamics, volatiles release and combustion, char combustion, temperature and size distribution of char particles as well as heat transfer to cooling water channels and refractory while the chemical species considered are O<sub>2</sub>, CO, CO<sub>2</sub>, H<sub>2</sub>O, SO<sub>2</sub>, NH<sub>3</sub>, and NO. These temperature profiles are illustrated in Figure 5.11. To facilitate the use of these measurements as input data in the calculation of radiative exchange, the experimental data were represented by high order polynomials as displayed in Table 5.13. CO<sub>2</sub> and H<sub>2</sub>O concentrations are important for radiative heat transfer due to the fact that these gases have strong absorption bands in the spectrum at high temperatures. Therefore, only CO<sub>2</sub> and H<sub>2</sub>O are taken into account for radiative transfer in this study. Figure 5.12 shows the calculated concentration profiles of CO<sub>2</sub> and H<sub>2</sub>O along the dilute zone (see [132]), which are represented by linear functions in the radiation models (Table 5.14).

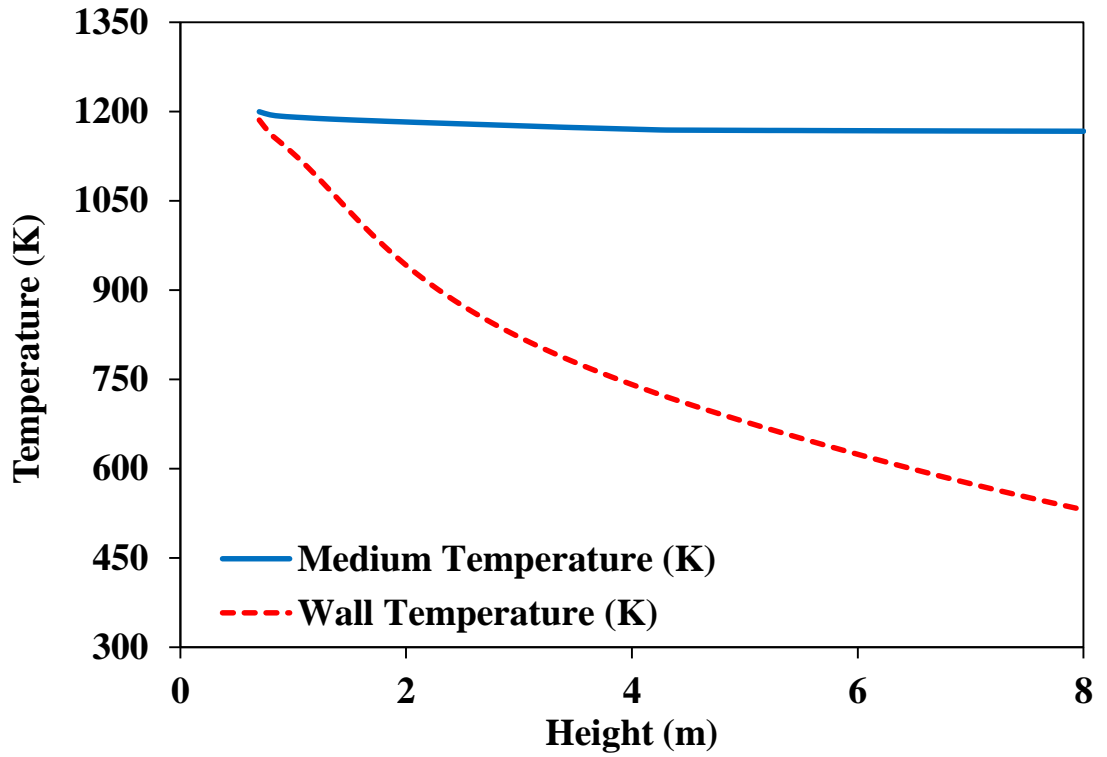


Figure 5.11 Temperature profiles along the dilute zone

Table 5.13 Polynomials for temperature profiles

<b>Medium temperature profile, K</b> $T_m(z) = \sum_{i=0}^6 a_i z^i$	$a_0 = 1164.60$	<b>Wall temperature profile, K</b> $T_w(z) = \sum_{i=0}^6 b_i z^i$	$b_0 = 1461.80$
	$a_1 = -11.14$		$b_1 = -323.92$
	$a_2 = 1.82$		$b_2 = 44.97$
	$a_3 = -0.25$		$b_3 = -2.39$
	$a_4 = 0.014$		$b_4 = 0$
	$a_5 = 0$		$b_5 = 0$
	$a_6 = 0$		$b_6 = 0$

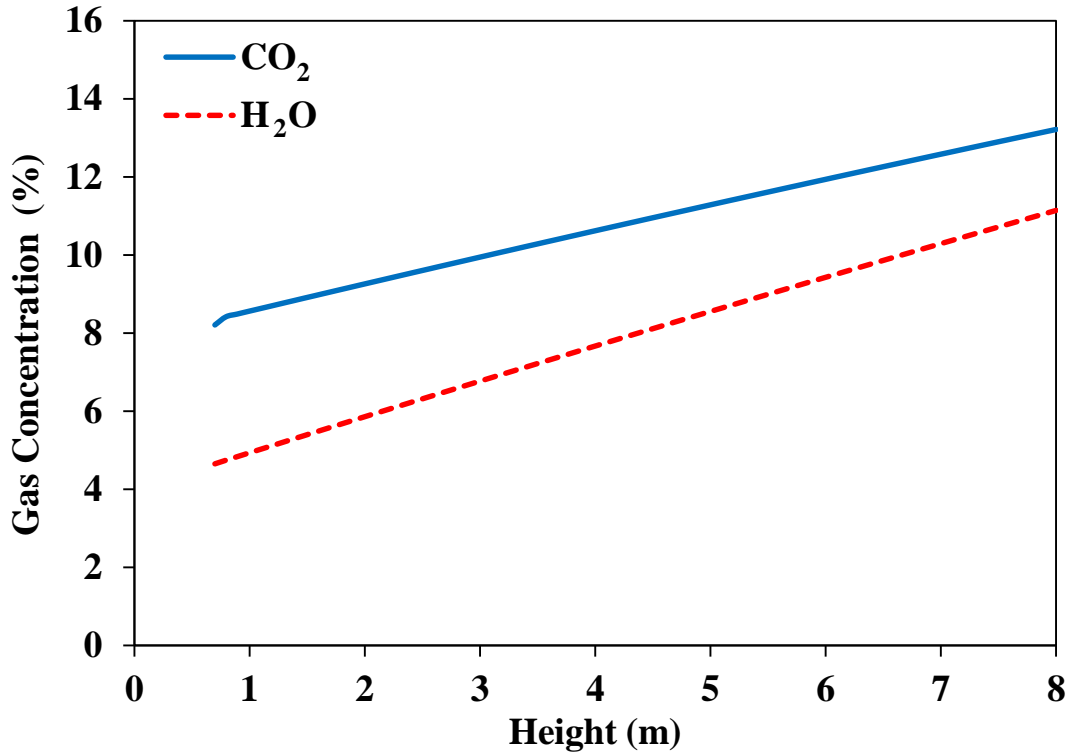


Figure 5.12 Gas concentration profiles along the dilute zone

Table 5.14 CO<sub>2</sub> and H<sub>2</sub>O Concentration profiles

<b>CO<sub>2</sub> Concentration (%)</b>	$a_0 = 7.59$	<b>H<sub>2</sub>O Concentration (%)</b>	$b_0 = 3.68$
$x_{CO_2}(z) = \sum_{i=0}^1 a_i z^i$	$a_1 = 0.70$	$x_{H_2O}(z) = \sum_{i=0}^1 b_i z^i$	$b_1 = 0.94$

Particles collected from the cyclone (taken from the bottom of the loop-seal) and baghouse downstream of the dilute zone are subjected to sieve analysis and laser light scattering technique for particle size distribution (PSD). PSD of the cyclone and bag filter ashes are then combined to obtain actual size distribution in the dilute zone. PSD of particles collected by the cyclone and baghouse filter are demonstrated in Figure 5.13. Furthermore, axial and radial variations in PSD are neglected and it is assumed to be uniform throughout the riser owing to high superficial gas and solid circulation rates [133,

134]. Ash content of fly ash particles determined by chemical analysis was 99.9 % [3] indicating that the fly-ash can be treated as pure ash in the radiative property estimation. Ash analysis of the samples collected from the cyclone and bag filter are given in Table 5.15.

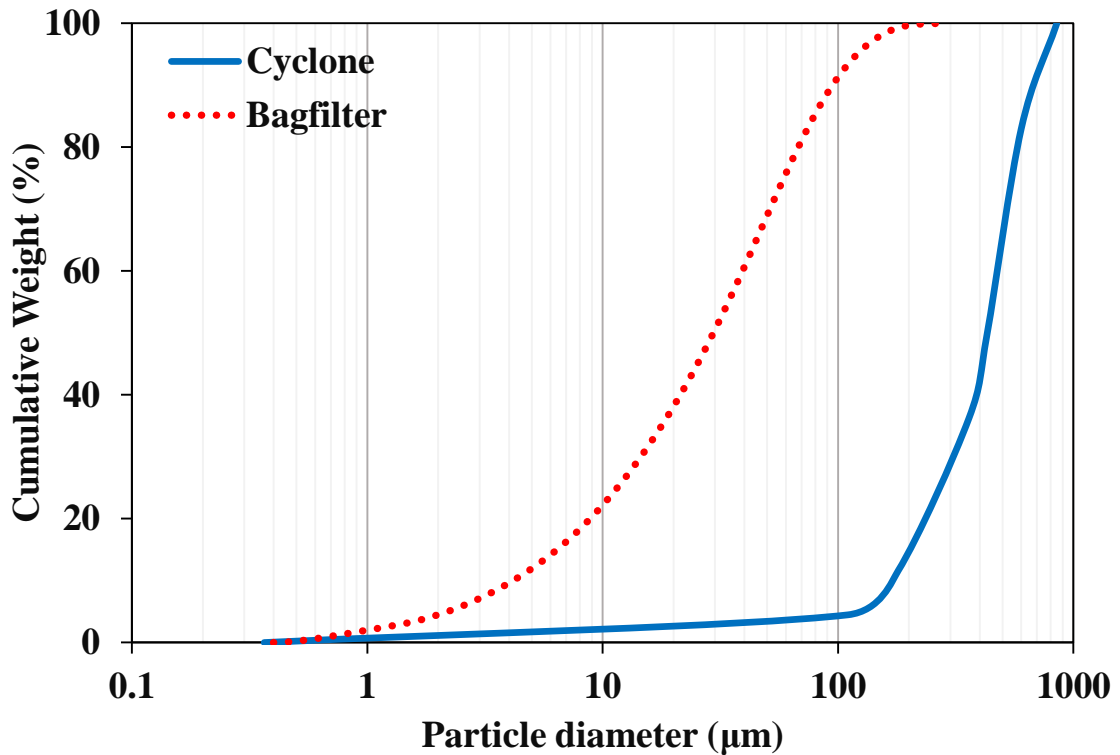


Figure 5.13 Measured particle size distributions for CFBC combustion test

Table 5.15 Fly ash compositions

	<i>Cyclone*</i>	<i>Bag Filter</i>
SiO <sub>2</sub> (wt %)	58.09	56.51
Al <sub>2</sub> O <sub>3</sub> (wt %)	19.48	20.25
Fe <sub>2</sub> O <sub>3</sub> (wt %)	7.10	12.27
CaO (wt %)	1.84	0.41
MgO (wt %)	1.34	0.64
TiO <sub>2</sub> (wt %)	7.29	5.24
K <sub>2</sub> O (wt %)	1.46	2.31
SO <sub>3</sub> (wt %)	1.48	0.42
Na <sub>2</sub> O (wt %)	1.93	1.97
* In the experiment, ash sample was collected from the dense zone. Since the recycle ratio is very high, it is taken as the ash composition of the particles collected from the cyclone.		

## 5.2.2 Treatment of the Dilute Zone in Radiative Heat Transfer Calculations

The physical system under consideration is the splash and dilute zones of METU 150 kW<sub>t</sub> CFBC for the above-mentioned combustion test. In all radiation models, splash and dilute zones of the combustor is treated as a 2D axisymmetric cylindrical enclosure containing gray / non-gray, absorbing, emitting gas with gray / non-gray absorbing, emitting, non/isotropically/anisotropically scattering particles bounded by diffuse, gray / black walls. The physical system and its treatment are schematically illustrated in Figure 5.14. The enclosure is assumed to be bounded by three surfaces. Top and bottom surfaces are assumed to be at uniform temperature with constant radiative properties while the temperature of the refractory surrounding wall is represented by high order polynomials given in Table 5.13 with uniform surface radiative properties. Both the surrounding wall and top surface are taken as gray, diffusely emitting and reflecting surface with an emissivity of 0.33 [37, 131]. The boundary with the dense zone at the bottom is represented as a black surface due to Hohlraum effect [13].

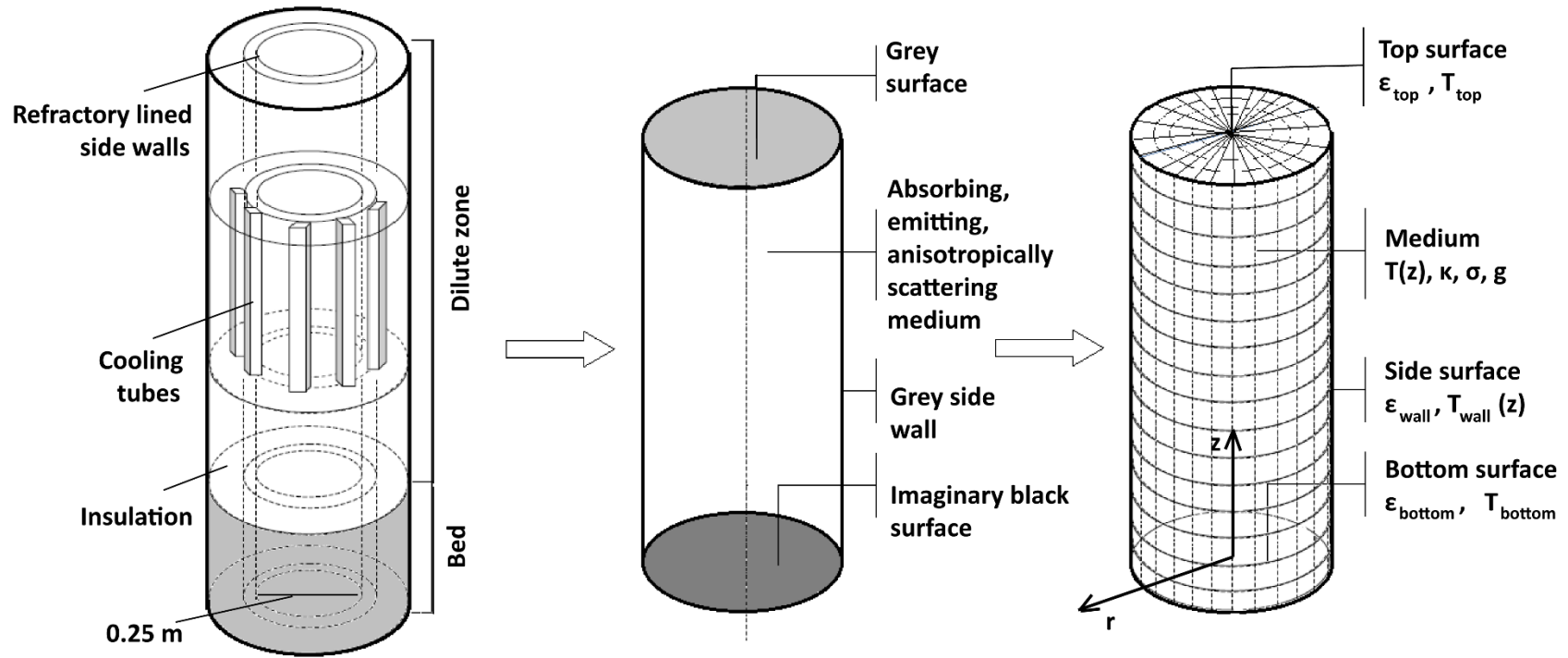


It is widely known that there exist different solid distribution regimes in CFBCs, which creates variations in particle load within the combustor. This is why in the radiation models, particle load is represented by 2D-axisymmetric and 1D axial particle load distribution models in addition to 0D approximation.

The combustor is considered to be composed of three hydrodynamically differing regions which are dense bed, splash zone and dilute zone. Height of the dense zone is assumed to be 0.70 m based on the measured pressure profile along the combustor [3]. Hydrodynamic representation of the dense bed is obtained by modified two-phase model of Johnsson et al. [135], which is developed for Geldart Group B and D particles under high gas velocity, while the variation in solid concentration in the splash and dilute zones are represented with 0D, 1D and 2D-axisymmetric models.

In the simplest approximation, solid concentration (particle load) above the dense bed is considered to be uniform ( $\bar{\rho}$ ) owing to the insignificant pressure drop in the dilute zone as can be seen from Table 5.12 and calculated from the force balance for the gas-solid flow in the riser [136] as  $3.72 \text{ kg/m}^3$ :

$$\bar{\rho} = \frac{(-\Delta P)}{g H_{\text{dilute}}} \quad (5.3)$$



The physical system: CFBC and its boundaries

Treatment of the dilute zone as a 3-D cylindrical enclosure

Solution domain and boundary conditions used in MOL solution of DOM

Figure 5.14 Treatment of the dilute zone as a 3-D enclosure

In the 1D model, axial solid distribution is determined from a semi-empirical correlation [137], which has been shown to give good agreement with measured particle load profiles for a wide range of thermal loads in both splash and dilute zones [138]:

$$\rho_1(z) = (\rho_x - \rho_2(H_x)) \exp(-a(z - H_x)) \quad (5.4)$$

$$\rho_2(z) = \rho_{\text{exit}} \exp(K(H_{\text{exit}} - z)) \quad (5.5)$$

$$\rho(z) = \rho_1(z) + \rho_2(z) \quad (5.6)$$

$$a = 4 \frac{u_t}{u_g} \quad (5.7)$$

$$K = \frac{0.23}{u_g - u_t} \quad (5.8)$$

where  $\rho_1(z)$  and  $\rho_2(z)$  represents the back-mixing of clusters dominating the splash zone and the back-mixing at the walls in the dilute zone, respectively.  $a$  and  $K$  are the decay constants. Particle load at the end of the dense bed ( $\rho_x$ , i. e.,  $\rho(z) = \rho(H_x)$ ) is calculated from the bed hydrodynamic model as  $420.61 \text{ kg/m}^3$  and the particle load in the upper zone ( $\rho_{\text{exit}}$  i. e.,  $\rho(z) = \rho(H_{\text{exit}})$ ) is calculated from solid stream flowrates as  $3.72 \text{ kg/m}^3$  (see Eq. (5.1)). In order to predict the decay constants ( $a$  and  $K$ ),  $d_{50}$  of the circulating ash particles is used to determine the terminal velocity ( $u_t$ ) as recommended in [137, 139]. The gas velocity ( $u_g$ ) is taken as the superficial air velocity ( $u_0$ ) and the increase in  $u_0$  after the secondary air injection at 1.1 m is taken into consideration. In order to investigate the core-annulus structure formed by the separation of solids to the walls in the dilute zone and its effect on the gas velocity, wall layer thickness as a function of height is estimated with the following relationship, which was derived for risers of circular cross sections [136]:

$$\delta(z) = \frac{D}{2} \left( 1 - \sqrt{1.34 - 1.3(\varepsilon_{sAv}(z))^{0.2} + (\varepsilon_{sAv}(z))^{1.4}} \right) \quad (5.9)$$

where  $\varepsilon_{sAv}(z)$  is the solids holdup (volume fraction) averaged over cross-sectional area at height  $z$ :

$$\varepsilon_{sAv}(z) = \frac{\rho(z)}{\rho_p} \quad (5.10)$$

It should be highlighted at this point that wall layer thickness defined in Eq. (5.9) is based on the distance at which time-average solids flux changes its direction.

Decay in particle load due to the back-mixing of clusters,  $\rho_1(z)$ , and back-mixing at the walls,  $\rho_2(z)$ , as well as the axial particle load profile  $\rho(z)$  are illustrated in Figure 5.15(a). As can be seen from the figure, particle load shows a strong exponential decay in the splash zone while decrease in particle load is less pronounced in the dilute zone. Furthermore, particle load profile is dominated by the dispersed solid phase in the dilute zone ( $\rho_2(z)$ ), in which core-annulus flow structure is expected. Thickness of this annular region as a function of height is demonstrated in Figure 5.15(b). As can be seen from the figure, wall layer thickness is insignificant compared to column diameter (25 cm). Therefore, the effect of core-annulus structure on gas velocity ( $u_g$ ) is neglected in the 1D model (see Eq. (5.8)).

In the 2D model, radial variation in the particle load is estimated from the local voidage at any radial position based on the correlation given in [140], developed for a wide range of operating conditions and systems:

$$\rho(r, z) = (1 - \varepsilon(r, z))\rho_p \quad (5.11)$$

$$\varepsilon(r, z) = \varepsilon_{mf} + (\varepsilon_{Av}(z) - \varepsilon_{mf})(\varepsilon_{Av}(z))^{-1.5+2.1\left(\frac{r}{R}\right)^{3.1}+5.0\left(\frac{r}{R}\right)^{8.8}} \quad (5.12)$$

$$\varepsilon_{Av}(z) = 1 - \varepsilon_{sAv}(z) \quad (5.13)$$

where  $\varepsilon_{mf}$  is the voidage of the bed at minimum fluidization velocity, which is calculated based on the operating parameters given in Table 5.12.  $\varepsilon_{Av}(z)$  is the cross-sectional averaged voidage along the bed height and estimated from the particle loads given by Eqs. (5.4-8).

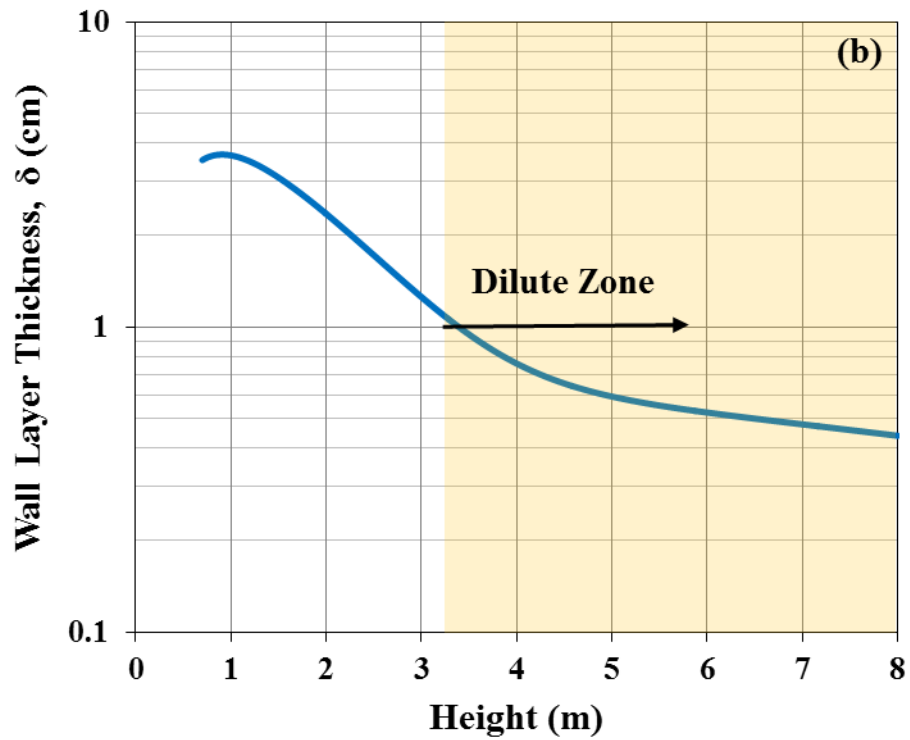
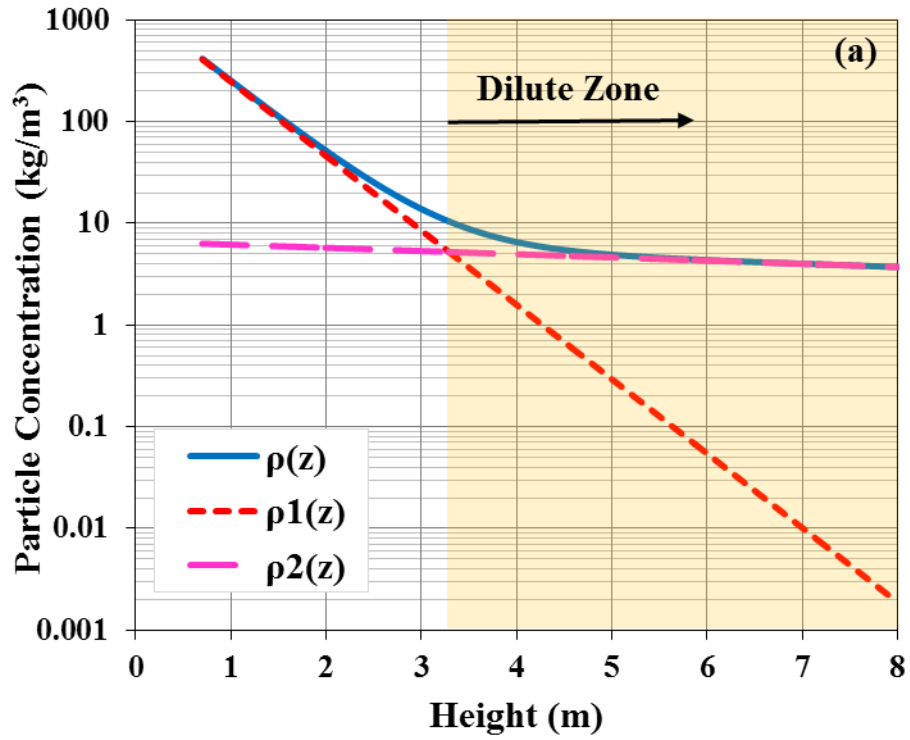


Figure 5.15 Particle load (a) and wall layer thickness (b) profiles along the riser in 1D model

Axial and radial variations in the particle load, generated with the 2D model are shown in Figure 5.16. It is seen that both splash and dilute sections of the riser have approximately parabolic particle load distribution profiles in radial direction and particle load does not change significantly beyond the splash zone (Figure 5.16(a)). Furthermore, development of the core-annulus flow structure and the presence of thin annular region in the dilute zone are evident (Figure 5.16(b)).

Radiative properties of participating combustion gases and particles are found from the property models described in Chapter 3 and Chapter 4, respectively.

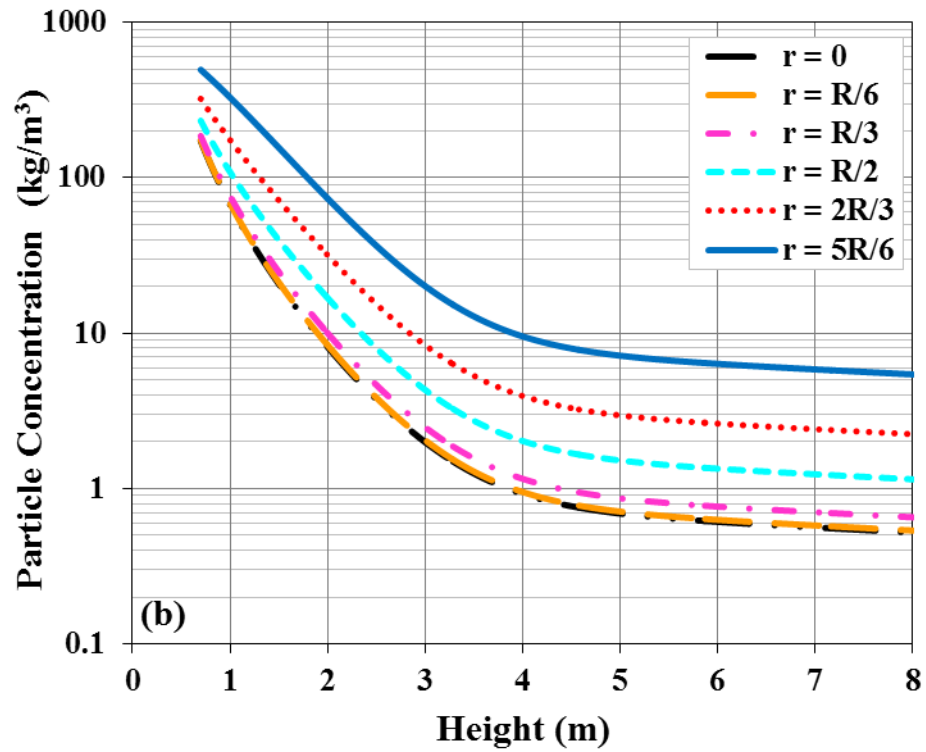
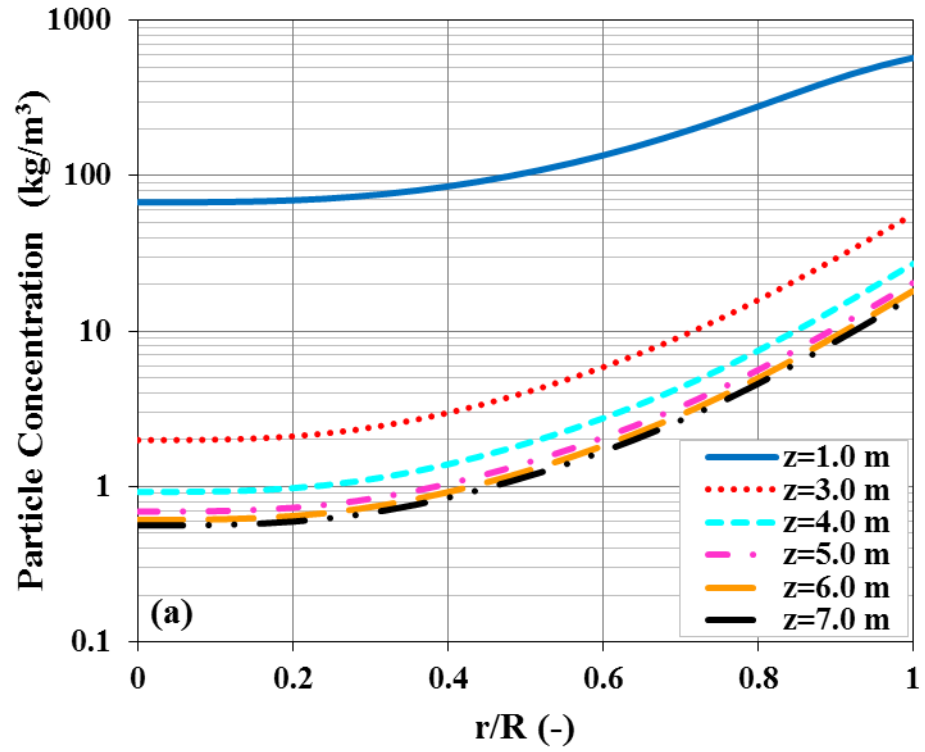


Figure 5.16 Variations in particle load in (a) radial and (b) axial directions in 2D model





## CHAPTER 6

### RESULTS AND DISCUSSIONS

Turkish lignite reserves are characterized by its high moisture, ash and sulphur contents and low calorific value and the fluidized bed combustion technology is a technically, economically and environmentally feasible alternative for the utilization of these low quality fuels. Furthermore, thermal radiation accounts for the majority of the heat transferred in fluidized bed combustors where it is constituted of the contributions from both participating gases and solid particles; hence gas and particle radiative properties play an important role. Absence of studies on the influence of spectral particle properties in FBCs on one hand, and the need for the utilization of local coal reserves in industry and utility boilers on the other, necessitate investigation of the effect of spectral gas and particle radiation on radiative heat transfer under FBC conditions.

Present work addresses the existing gap in the literature regarding to the influence of spectral gas and particle properties on radiative heat transfer through mathematical modelling by using the experimental data previously obtained from 300 kW<sub>t</sub> Atmospheric Bubbling Fluidized Bed Combustor (ABFBC) and 150 kW<sub>t</sub> Circulating Fluidized Bed Combustor (CFBC) test rigs in Middle East Technical University. In particular, present work focuses on developing and comparing methods to quantify the effect of physical and chemical properties of particles on radiative heat transfer by means of combining measurements and modelling such that the outcome will provide guidelines when

choosing radiation models for the combustion related investigations in fluidized bed combustors.

In this chapter, predictive accuracy of various gas and particle property models and related sub-models described in Chapter 3 and Chapter 4 for gray/non-gray, absorbing, emitting, non/isotropic/anisotropic scattering media is evaluated by applying these models to combustion tests described in Chapter 5. Methods are assessed in terms of accuracy and computational efficiency by comparing their predictions with exact solutions, measurements and/or benchmark solutions obtained from the most accurate methods. Results and their discussions are organized and presented according to the objectives of the study listed in Section 1.1.

## **6.1 Directional Nature of Particle Radiation**

One of the most important challenges in modelling radiative heat transfer is including the spectral variation of gas and particle properties as spectral resolution of gas and particle properties included in the solution of radiative transfer equation (RTE) is directly reflected on the computational cost of the global model as it directly determines the number of intensity equations to be solved. Furthermore, in addition to this spectral dependency, if particles are large enough to scatter thermal radiation (as in combustion systems), angular discretization of 3D spatial domain must also be increased to track in-scattered and out-scattered radiation accurately. Therefore, in the case of a non-gray absorbing, emitting and scattering medium, a wise selection of gas property and scattering phase function models becomes of significant importance for CPU economy.

It is worthy of note here that scattering of radiation by particles was previously represented by isotropic phase function in the studies carried out on 300 kWt ABFBC [14]. This assumption was justified by a former study, in which incident radiative fluxes predicted by the zone method and by MOL solution of DOM were found to be in good agreement with each other and with the measurements [13]. This agreement may be attributed to low particle load ( $0.01 \text{ kg/m}^3$ ) in the ABFBC under consideration. Use of

isotropic scattering assumption in pulverized coal (PC) fired furnaces with the same order of magnitude particle load [41, 49] has also been found to lead to fairly accurate results, as reported in recent literature [51-57]. However, in some of these studies, isotropic scattering was found to underestimate wall heat fluxes, mostly due to fly ash [50], compared to measurements [65, 66]. Considering circulating fluidized bed combustors (CFBC) have three orders of magnitude larger particle loads, particle radiation is expected to dominate total radiation even more compared to PC furnaces. Hence, more detailed studies of this assumption are considered to be significantly important for combustion community.

To address this need, first directional nature of particle radiation is investigated under CFBC conditions in the presence of gray and non-gray participating medium. For that purpose, effect of scattering phase function simplifications on both incident radiative heat fluxes and source terms are analyzed. First, a two-dimensional axisymmetric radiation code based on MOL of DOM is extended for incorporation of anisotropic scattering and predictive accuracy of the in-house developed code is tested on a benchmark problem. Then, predictive accuracy and computational efficiency of the code with different property models are evaluated by applying it to dilute zone of the lignite-fired 150 kWt METU CFBC containing a gray/non-gray, absorbing, emitting gas with gray absorbing, emitting non/isotropically/anisotropically scattering particles.

Radiative properties of the participating combustion gases are calculated from Leckner's correlations (Section 3.2) and SLW model with 10 gray gases (Section 3.5). Radiative properties of the polydisperse particle cloud are found from GOA (4.1.2) and Mie theory (Section 4.1.3). In GOA, reflectivity of the particles is calculated based on both normal reflectivity (Eq. (4.14)) and reflectivity averaged over  $\theta$  (Eq. (4.15)), which will be referred to as GOA1 and GOA2, respectively. Scattering phase function is represented by isotropic scattering / nonscattering assumption, transport approximation and Henyey-Greenstein phase function with normalization (Section 4.3). Particles are assumed to be gray and complex index of refraction is taken from the traditional RI model,  $m = 1.5 - 0.02i$ . Independent scattering is assumed to take place in the dilute zone of the test rig as the particle volume fraction in the most part of the dilute zone is in the order of  $10^{-3}$ .

Particle load is assumed to be uniform throughout the dilute zone. The size parameter is determined by using a representative wavelength ( $3 \mu\text{m}$ ) as suggested in [141]. All input data necessary for the radiative property models are taken from Sections 5.2.1 and 5.2.2. In MOL solution DOM, two-point upwind differencing scheme DSS012 is employed for the difference relations of spatial derivatives. All simulations are carried out on a workstation with Intel® Core™ 7i CPU 2600 3.40 GHz processor having 16.00 GB of RAM. CPU times were recorded for an error tolerance of 0.001 % throughout the analyses.

### 6.1.1 Benchmarking the Predictive Accuracy of In-House Developed Code

First, predictive accuracy of the in-house developed radiation code based on MOL solution of DOM is investigated on a benchmark problem, which has been examined in the literature to validate various solution methods [142, 143]. The physical system under consideration is a cylindrical enclosure containing a cold medium ( $T = 0$  K) surrounded by hot side walls with a constant emissive power ( $E_{bw} = 1$ ). All walls are assumed to be black. Medium has an extinction coefficient of  $1 \text{ m}^{-1}$  with a scattering albedo of unity. Cylinder has a height of 2 m with a radius of 1 m. In the present study, the same computational grid and scattering phase functions (forward and isotropic scattering) are used to compare the results with the previous work. Figure 6.1 illustrates the net wall heat flux predictions of the present code and the benchmark solution. Here it is confirmed that forward-scattering phase function gives larger heat fluxes than isotropic scattering and the difference increases away from the cold end walls. As can be seen in Figure 6.1, predictions are in reasonable agreement with the benchmark solutions [142, 143].

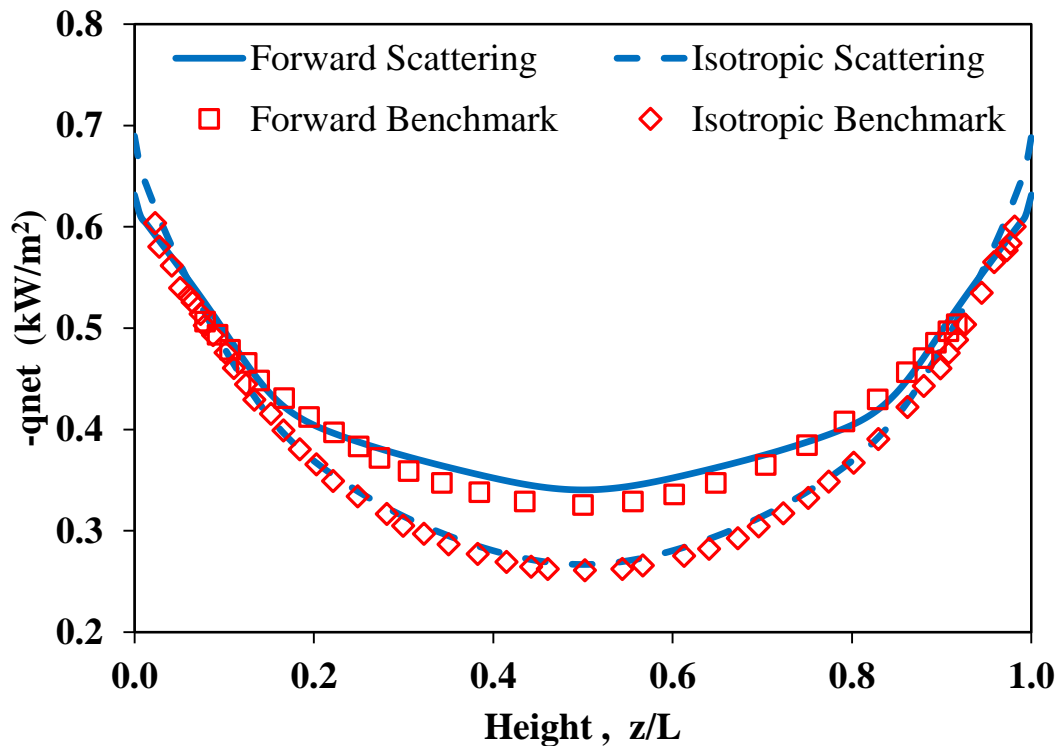


Figure 6.1 Effect of anisotropic scattering on the net radial radiative heat distribution

### 6.1.2 Selection of Gas Radiative Property Estimation Model

Effect of gray gas (GG) assumption on predictive accuracy and CPU efficiency of the developed code in the optically thick medium of the test rig under consideration is investigated by comparing its predictions against those of SLW. In both cases, particle radiation is estimated by Mie theory with Henyey-Greenstein phase function with normalization (HG). In order to evaluate the deviation in the predictions due to GG assumption reasonably well, fine angular ( $S_{12}$ ) and spatial discretizations (13x275) are utilized. Absolute percentage errors in incident fluxes along the side wall and source term predictions along the centerline of the dilute zone with corresponding CPU times are tabulated in Table 6.1. As can be seen from the table, GG provides good accuracy (about 1 % error) with two orders of magnitude less CPU time. Hence, from the viewpoints of accuracy and computational economy, GG model is found to be sufficient for the optically thick medium under consideration and utilized as the gas property model in the rest of the present section.

Table 6.1 Effect of gray gas model on predictive accuracy and CPU efficiency

Model	Average Absolute % Error		CPU Time(s)
	Incident Heat Flux	Source Term	
<b>Gas (GG) + Particle (Mie with HG)</b>	0.71	1.12	108
<b>Gas (SLW) + Particle (Mie with HG)</b>	Reference Solution		20897

In order to evaluate contribution of particle radiation to total radiation, the same radiation codes are run with and without gas radiation. Figure 6.2 illustrates comparison between total and particle radiation predictions. As can be seen from the figure, particle radiation dominates total radiation in both incident heat flux and source term predictions. Although heat fluxes are not sensitive to absence of gas radiation (1 % average relative difference), source terms are affected by the contribution of gas radiation (8 % average relative difference). Therefore, it is considered necessary to take into consideration both gas and particle radiation in the radiation code.

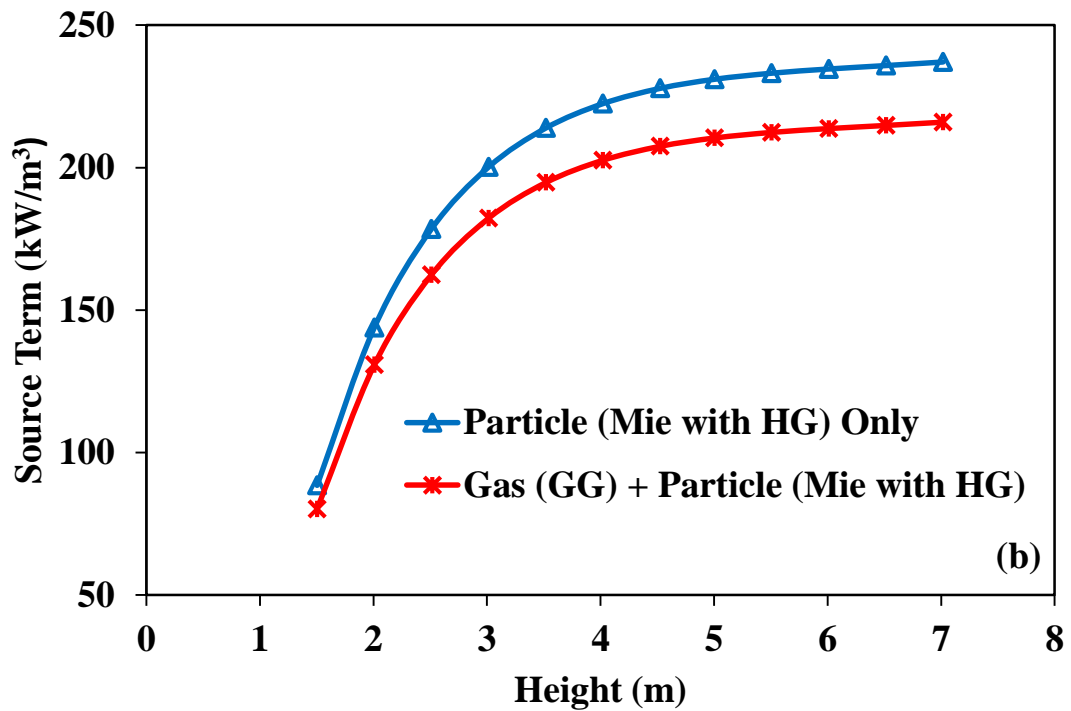
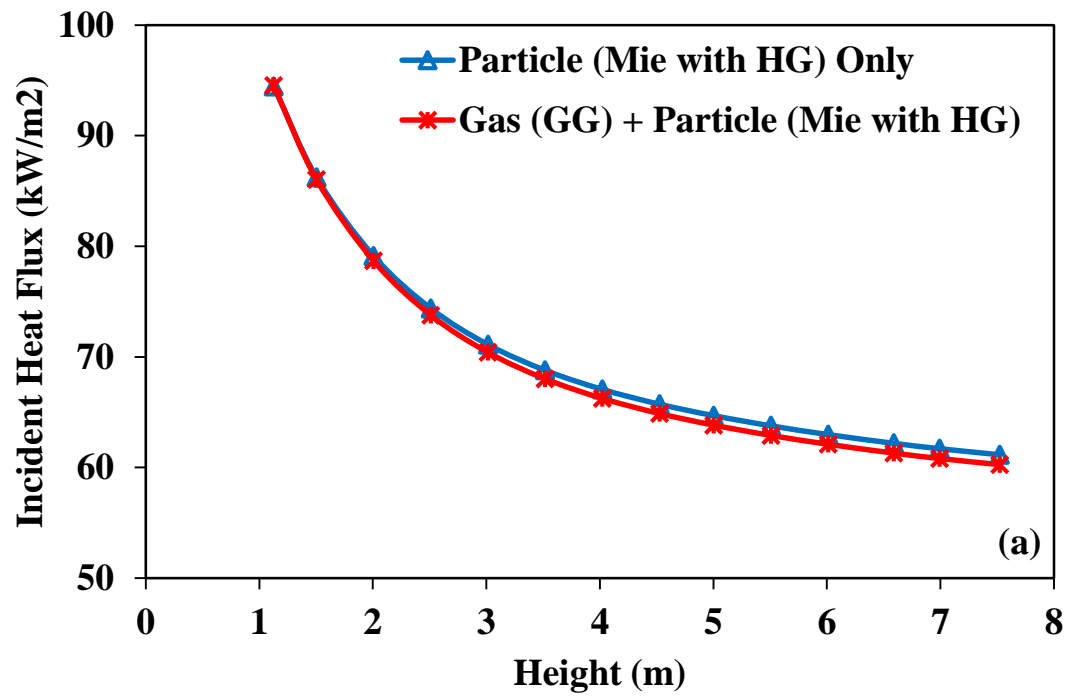


Figure 6.2 Effect of particle radiation on (a) incident wall heat flux and (b) source term predictions

### 6.1.3 Selection of Particle Radiative Property Estimation Model

Considering that over 96 % of the fly ash particles have a size parameter  $x > 25$  (Figure 5.13), radiative properties of fly ash particles can be represented by GOA. Effect of this approximation on predicted heat flux and source term distributions is investigated by comparing predictions of GOA1 and GOA2 with those of Mie theory. In all cases, scattering phase function is estimated by using HG phase function and fine angular ( $S_{12}$ ) and spatial discretizations ( $13 \times 275$ ) are utilized. Asymmetry factor used in GOA1 and GOA2 are calculated by using Sauter mean diameter of the PSD ( $291 \mu\text{m}$ ).

Figure 6.3 shows comparisons between predicted incident heat fluxes and source terms. As can be seen from the figure, heat fluxes are in good agreement with the reference Mie solution. However, GOA1 is found to under-predict the source terms. Table 6.2 reveals that GOA2 is an accurate approximation of Mie theory in both heat fluxes and source terms. Therefore, from the viewpoints of accuracy and computational economy, GOA2 is selected as the particle property model for the rest of the current section.



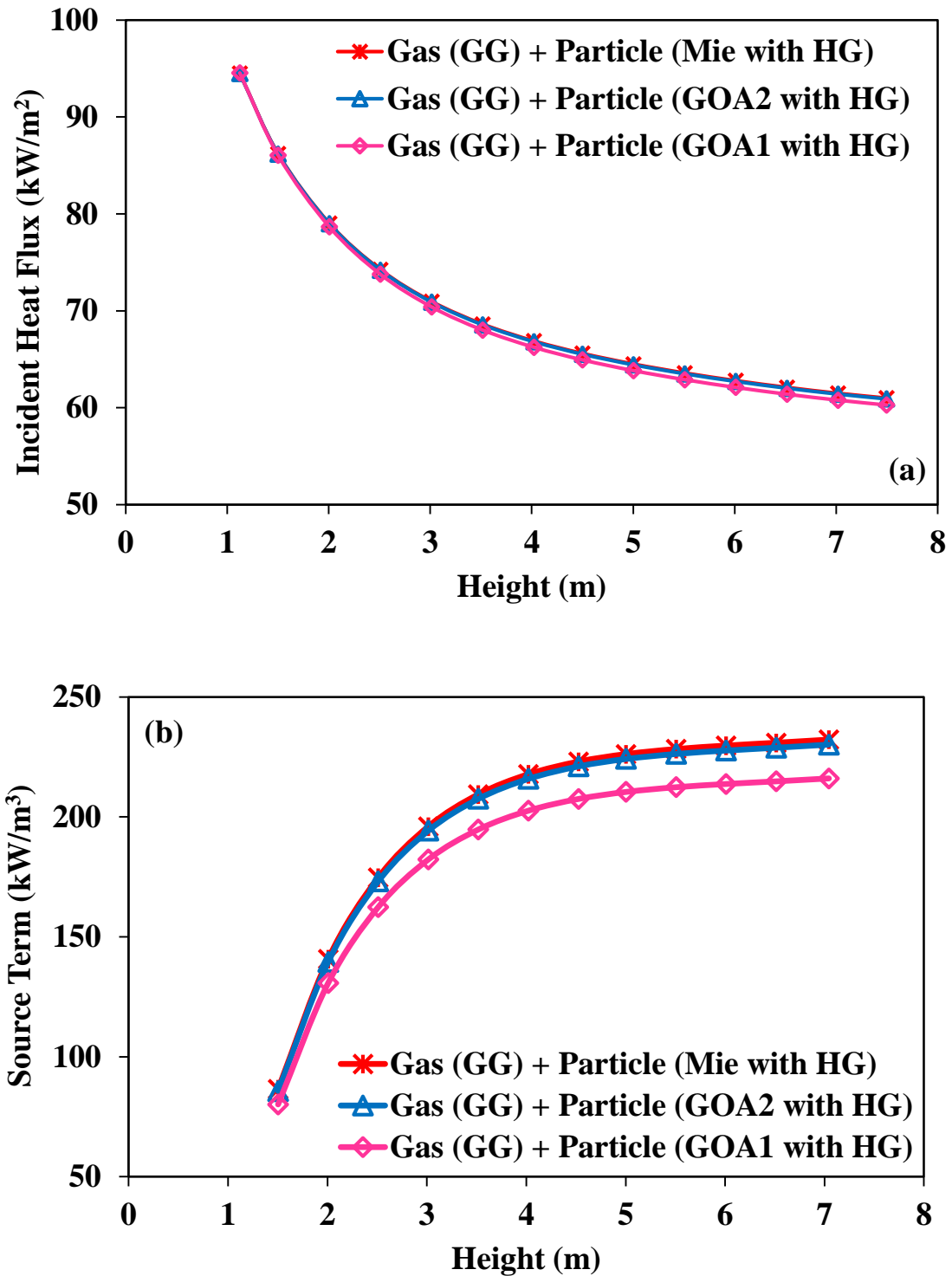


Figure 6.3 Effect of particle radiation model on (a) incident wall heat flux and (b) source term predictions

Table 6.2 Effect of particle radiation model on predictive accuracy and CPU efficiency

Particle Model	Average Absolute % Error		CPU Time(s)
	Incident Heat Flux	Source Term	
Gas (GG) + Particle (GOA1 with HG)	0.87	6.99	108
Gas (GG) + Particle (GOA2 with HG)	0.10	0.85	108
Gas (GG) + Particle (Mie with HG)	Reference Solution		132

#### 6.1.4 Spatial and Angular Discretization Refinement

Numerical accuracy and computational economy of the MOL solution of DOM with respect to angular and spatial discretization are investigated by comparing its steady-state predictions with those obtained by the reference cases carried out with the finest spatial/angular discretization for both forward (HG phase function) and isotropic scattering phase functions. GG and GOA2 are used for the evaluation of participating medium properties.

For the angular discretization, different orders ( $N = 4, 6, 8, 10, 12, 14$ ) of approximation of DOM are studied to evaluate the effect of order of approximation on the predictive accuracy of  $S_N$  method by comparing its results against the highest number of rays per quadrature,  $N_{14}$ .  $13 \times 275$  spatial grid resolution is selected for the numerical solution. Incident wall heat fluxes and source terms for both phase functions are illustrated in Figure 6.4 and Figure 6.5. It is found that incident wall heat fluxes are not affected by angular discretization for both phase functions (Figure 6.4) while forward scattering phase function is found to be more sensitive to angular discretization in source term predictions than isotropic scattering (Figure 6.5). Relative errors for the source terms and corresponding CPU times are tabulated in Table 6.3. As can be seen from the table,  $S_{12}$  provides satisfactory solutions in terms of accuracy and computational efficiency and therefore is utilized as the angular quadrature scheme in the rest of the present study.

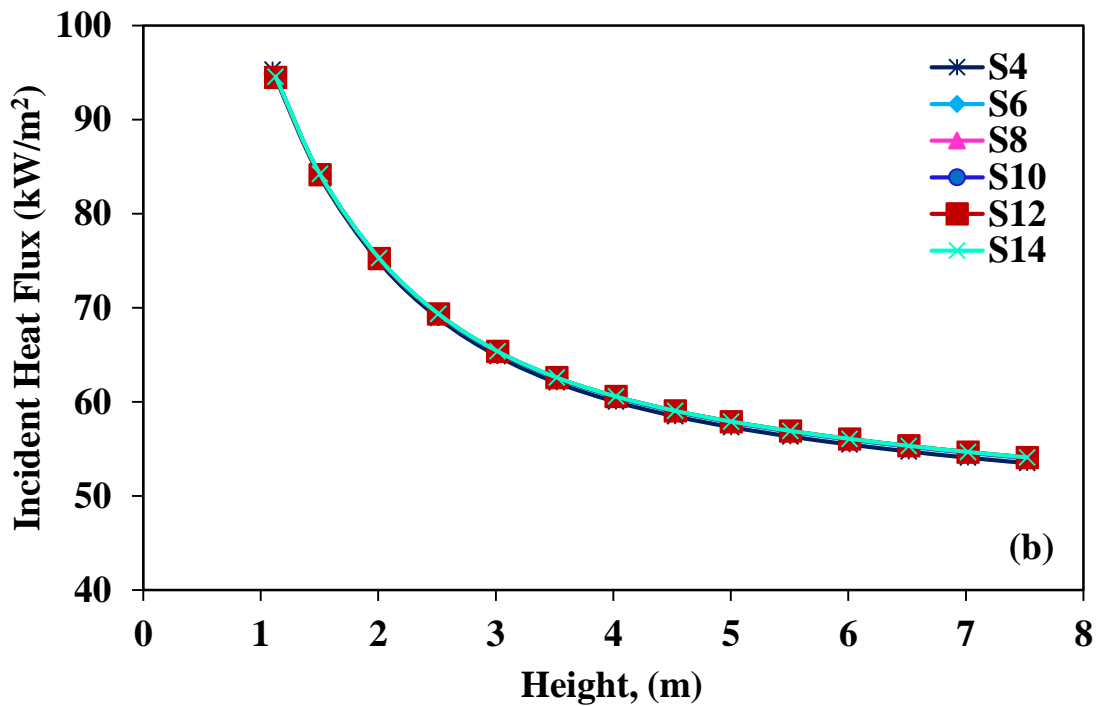
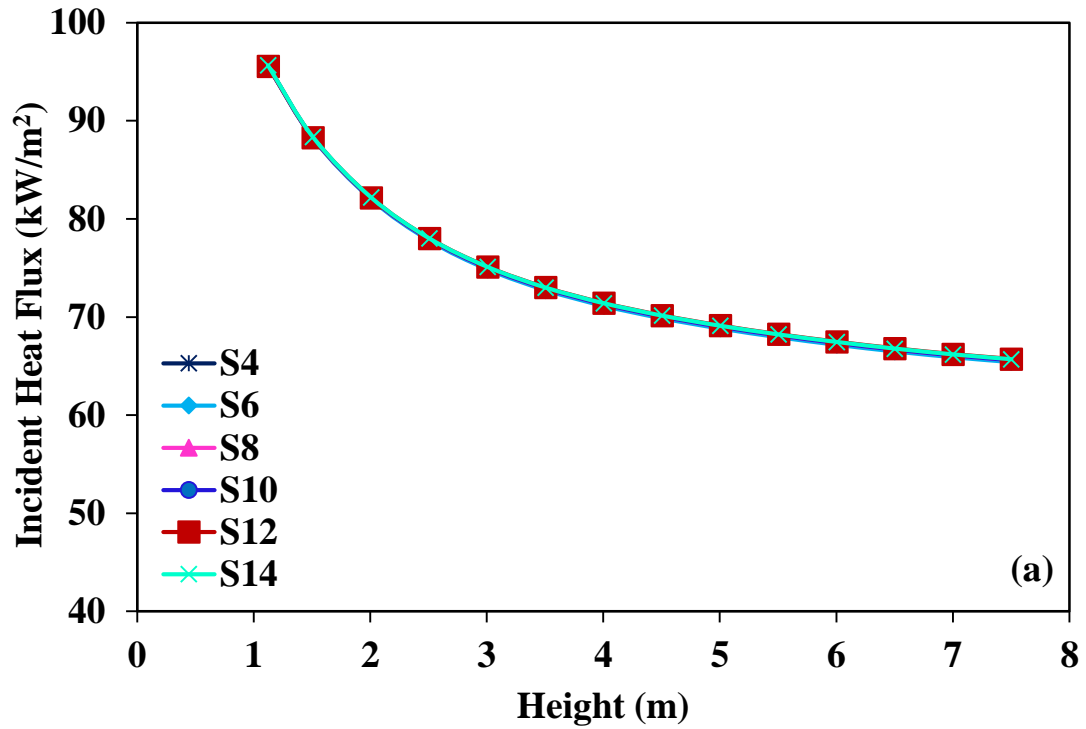


Figure 6.4 Angular discretization for the incident wall heat flux predictions with (a) forward scattering and (b) isotropic scattering

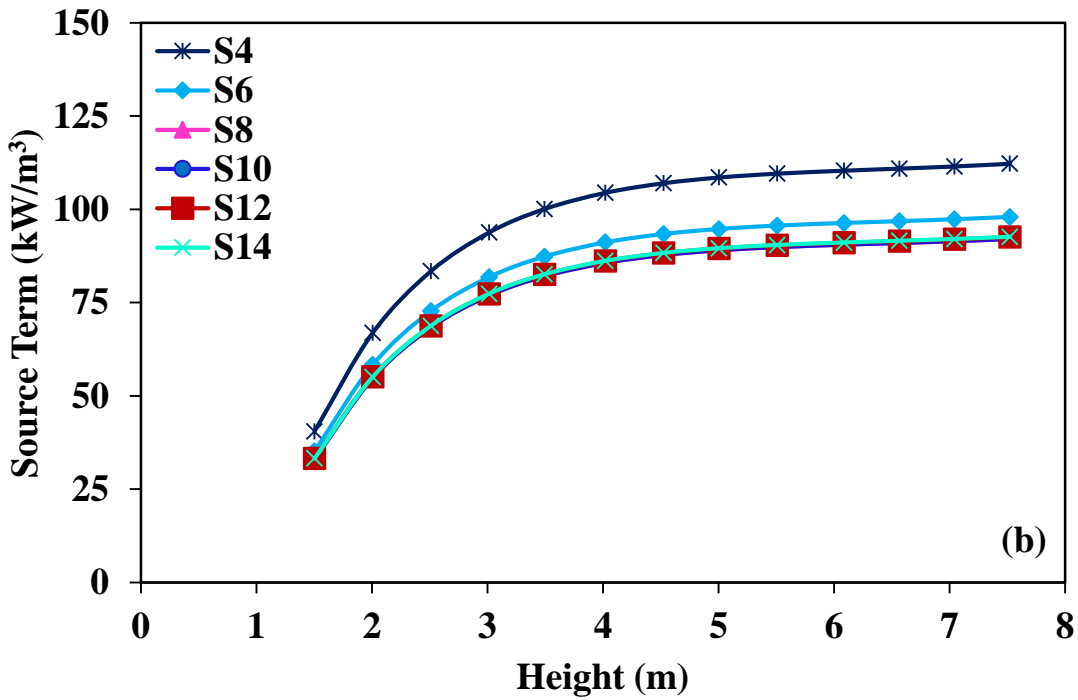
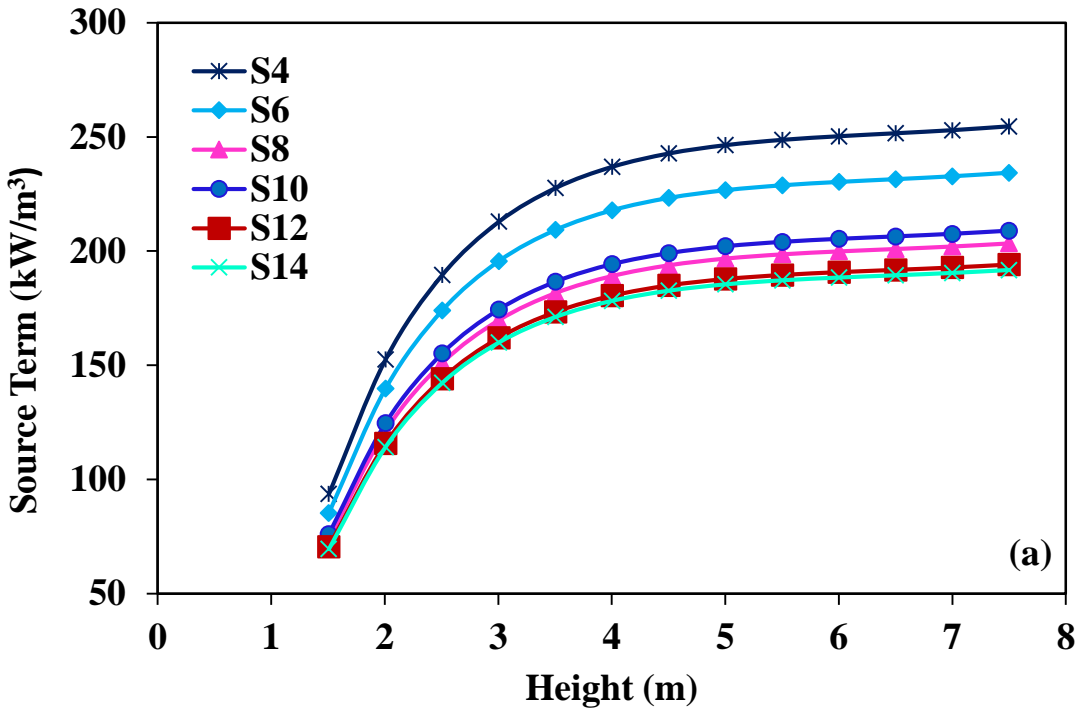


Figure 6.5 Angular discretization for the source term predictions with (a) forward scattering and (b) isotropic scattering

Table 6.3 Effect of angular scheme refinement on predictive accuracy and CPU efficiency for the source term predictions

$S_N$	<b>HG Forward Scattering</b>		<b>Isotropic Scattering</b>	
	Average % Error	CPU Time (s)	Average % Error	CPU Time (s)
$S_4$	33.85	6	21.11	5
$S_6$	22.89	17	5.69	9
$S_8$	9.36	41	-0.32	21
$S_{10}$	6.38	94	-2.11	47
$S_{12}$	1.43	157	0.03	89
$S_{14}$	Reference Solution	320	Reference Solution	311

Average % Error: Average percent relative error for predicted incident heat fluxes and source terms at  $S_N$  with respect to the predictions of the reference case with  $S_{14}$

With regard to spatial discretization,  $5 \times 120$ ,  $7 \times 200$ ,  $11 \times 251$ ,  $13 \times 275$ ,  $15 \times 295$ ,  $17 \times 305$  and  $19 \times 325$  grid resolutions are tested for the spatial discretization in radial and axial directions respectively. Comparisons are illustrated in Figure 6.6 for only forward scattering. As can be seen from the figure, incident heat fluxes and source terms predicted with  $15 \times 295$  and  $17 \times 305$  control volumes are found to be in good agreement with the reference solution. Moreover, predictions obtained with coarser grids lead to under-prediction of the incident heat fluxes while they lead to over-prediction of the source term. Absolute percentage errors in incident heat fluxes and source term predictions with corresponding CPU times are given in Table 6.4. As can be seen from the table, use of  $17 \times 305$  control volumes with  $S_{12}$  approximation was found to be sufficient from the viewpoints of accuracy and computational economy for the problem under consideration.

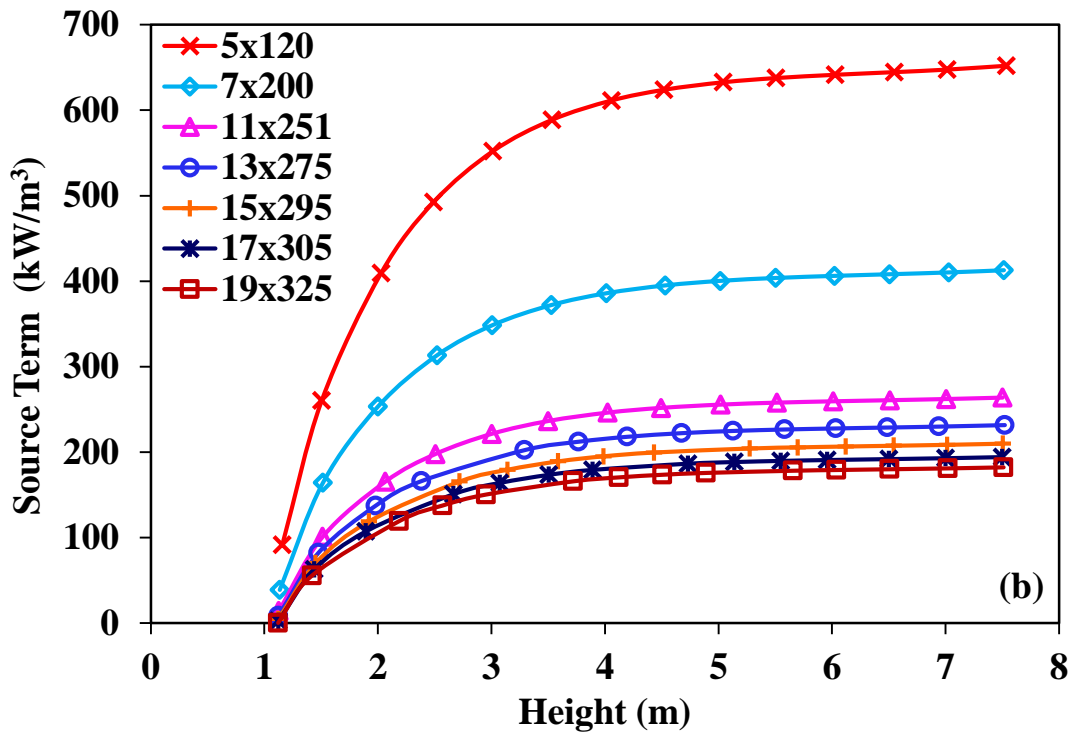
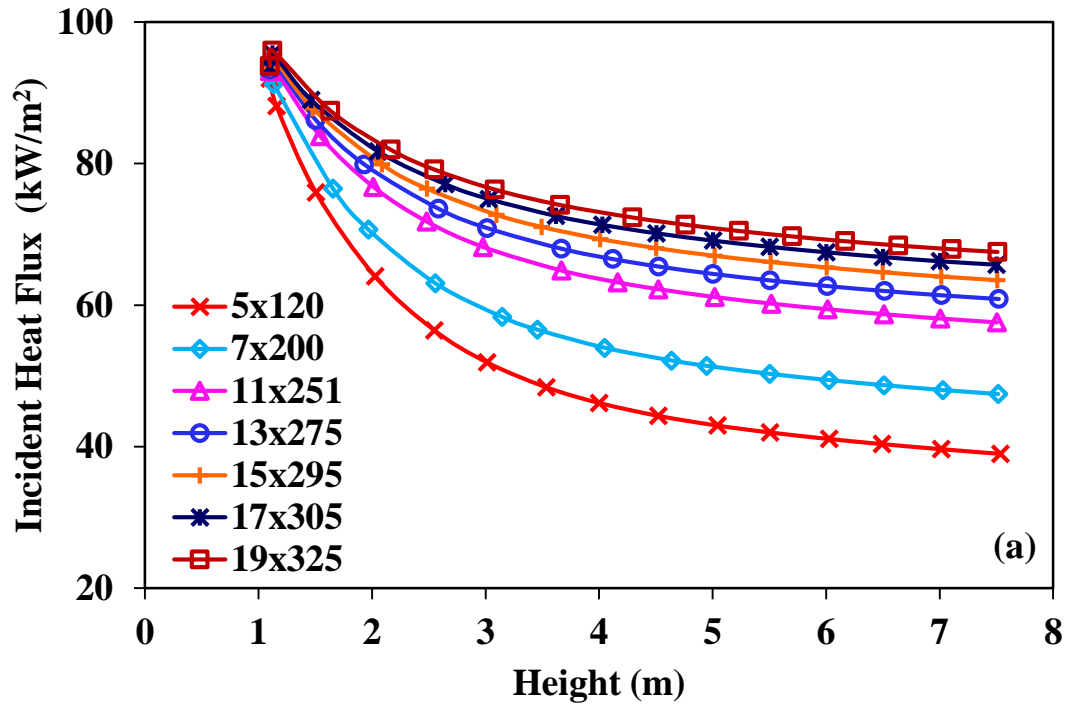


Figure 6.6 Effect of spatial discretization for (a) incident wall heat flux and (b) source term predictions

Table 6.4 Effect of grid refinement on predictive accuracy and CPU efficiency

Number of Control volumes	Average Absolute % Error		CPU Time(s)
	Incident Heat Flux	Source Term	
5 x 120	34.70	257.7	9
7 x 200	24.92	127.0	24
11 x 251	13.16	45.4	65
13 x 275	9.28	27.6	97
15 x 295	5.55	15.5	137
17 x 305	2.71	6.7	157
19 x 325	Reference Solution		211
Absolute % Error: Average percent relative error for predicted incident heat fluxes and source terms at grid points with respect to the predictions of the reference case with 19x325 and $S_{12}$			

### 6.1.5 Effect of Particle Scattering on Radiative Heat Transfer

Presence of highly forward scattering fly ash particles in high-temperature combustion systems requires extensive computational effort when solution of RTE is coupled with the solution of conservation equations. This is why it is considered necessary to investigate the predictive accuracy and computational efficiency of nonscattering assumption, isotropic scattering assumption and transport approximation by benchmarking their predictions against those of forward scattering represented by Henyey-Greenstein phase function.

Effect of scattering on incident heat fluxes along the side wall and radiative energy source terms are shown in Figure 6.7. As can be seen from the figure, heat flux distributions obtained with nonscattering assumption and transport approximation are found to be in good agreement with the reference solution whereas nonscattering assumption leads to over-prediction of the source terms. Furthermore, isotropic scattering assumption underestimates both heat fluxes and source terms.

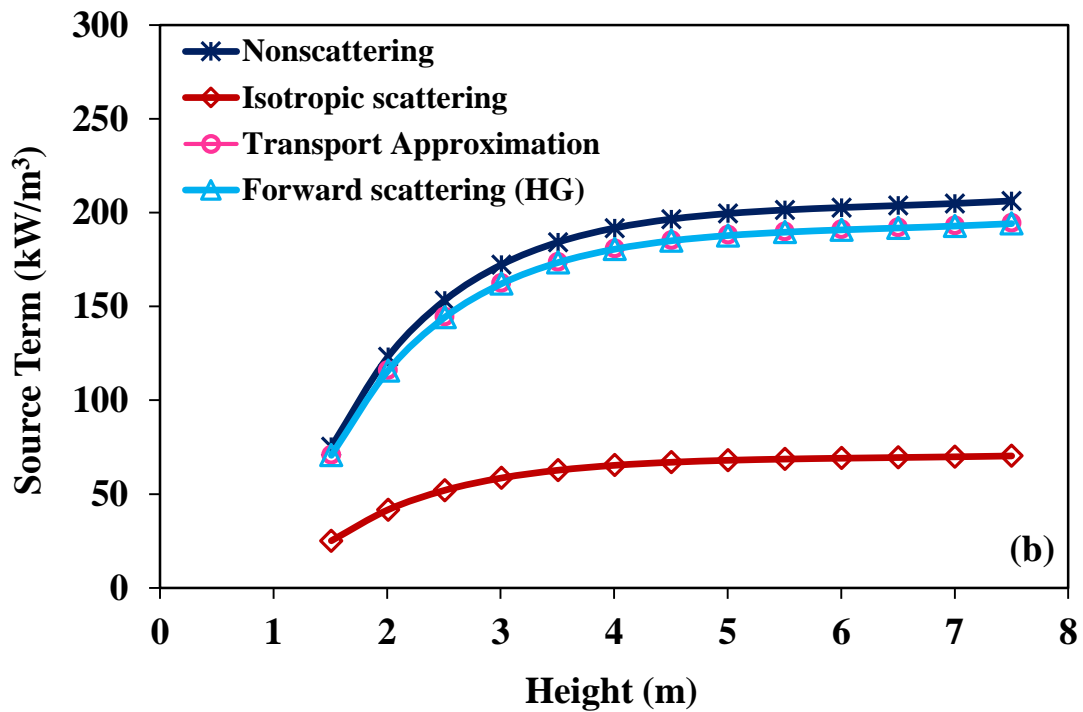
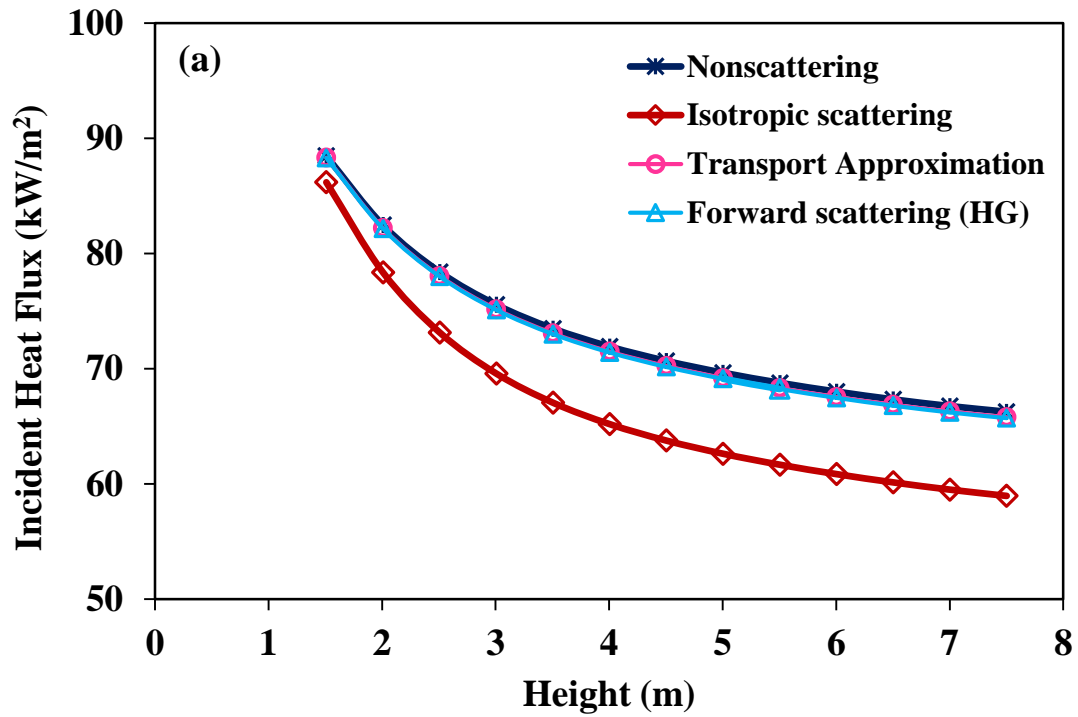


Figure 6.7 Effect of scattering phase function simplifications on radiative (a) heat fluxes and (b) source terms



Percentage relative errors in heat flux and source term predictions with corresponding CPU times are given in Table 6.5. As can be seen from the table, isotropic scattering assumption is incorrect for the system under consideration, particularly for the source terms. On the other hand, nonscattering assumption was found to produce acceptable accuracy with minimum CPU time for both incident fluxes and source terms. These findings are in agreement with those reported in the literature for some simple test problems [43, 143-145]. Transport approximation is found as accurate as the reference solution, however, with no improvement in CPU economy. Nevertheless, comparison between transport approximation and HG phase function with regard to algorithm development and its implementation shows that transport approximation requires significantly less set-up time to program.

Table 6.5 Effect of scattering phase function simplifications on incident heat fluxes and sources terms

	%Average Relative Error		CPU Time
	Incident Heat Flux	Source Term	
<b>Nonscattering</b>	1	6	40
<b>Isotropic scattering</b>	-8	-66	139
<b>Transport Approximation</b>	0.08	0.24	164
<b>Forward scattering (HG)</b>	Reference Solution		157

In order to find out whether it is possible to decrease CPU time of transport approximation without losing much accuracy, effect of angular discretization on transport approximation is also tested. Heat flux and source term predictions are illustrated in Figure 6.8 and relative percentage errors obtained with different  $S_N$  quadratures are given in Table 6.6. These comparisons reveal that although transport approximation deploys isotropic phase function (Eq. (4.80)), it still needs high  $S_N$  quadrature for the desired accuracy.

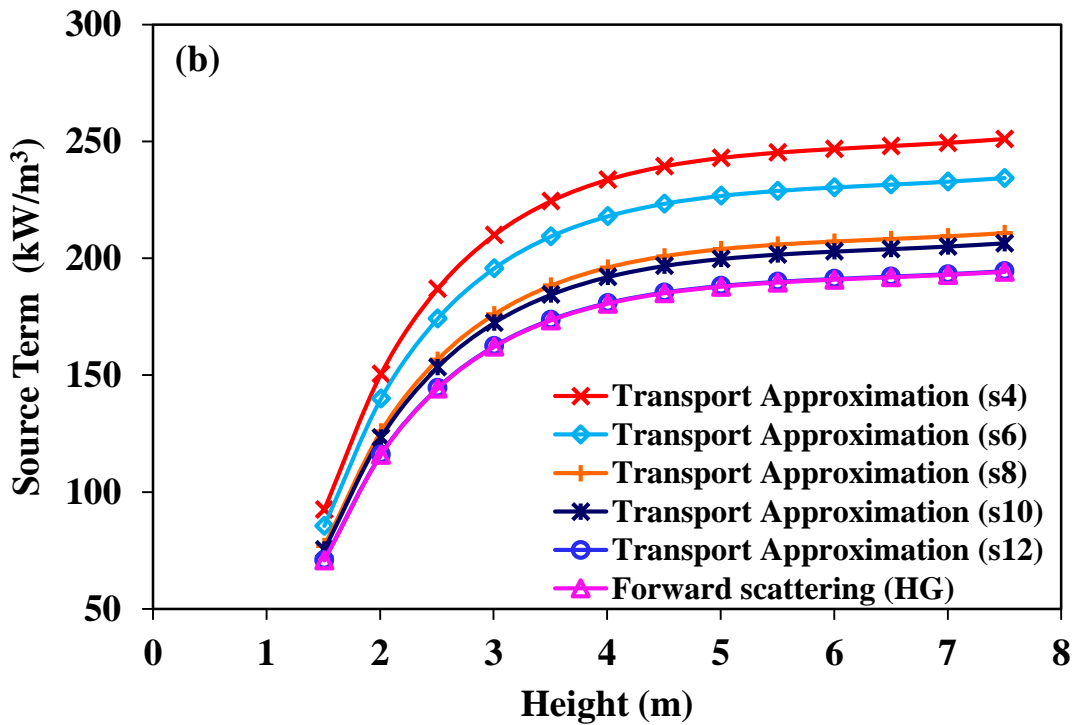
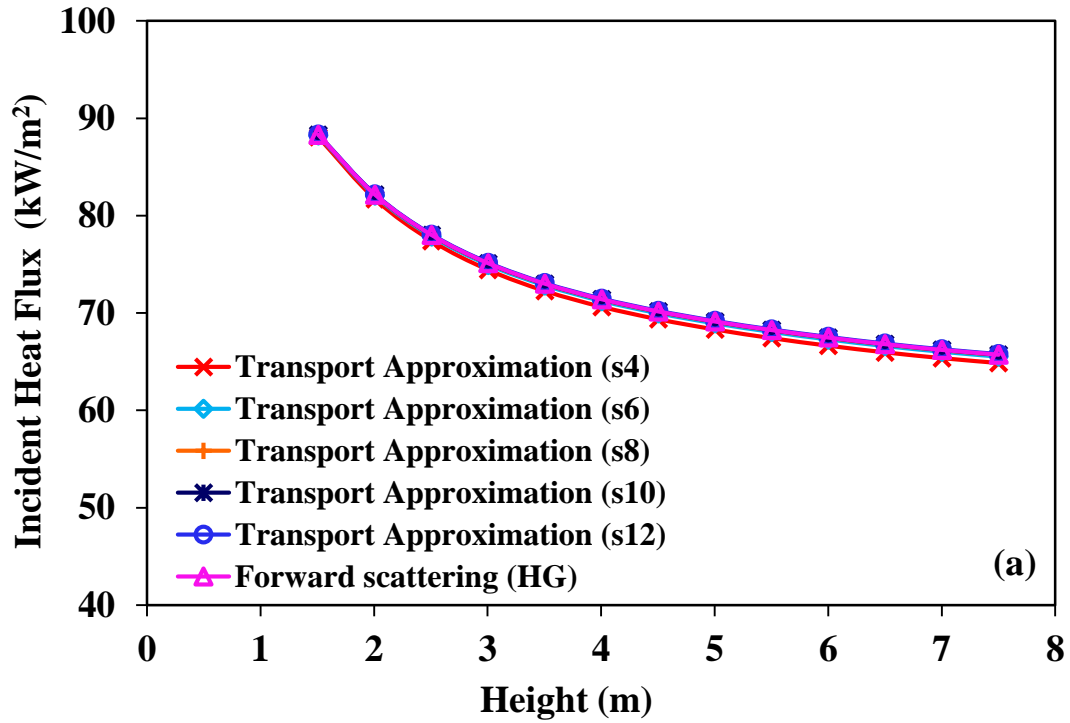


Figure 6.8 Sensitivity of transport approximation to angular discretization in (a) incident heat fluxes and (b) source terms calculations

Table 6.6 Effect of angular discretization refinement on predictive accuracy and CPU efficiency of transport approximation

Phase Function Approximation	Heat Flux	Source Term	CPU Time (s)
	%Av. Relative Error	%Av. Relative Error	
Transport Approximation (S4)	-1.01	30.05	6
Transport Approximation (S6)	-0.25	21.18	16
Transport Approximation (S8)	-0.05	8.82	42
Transport Approximation (S10)	-0.02	6.57	99
Transport Approximation (S12)	0.08	0.24	164
Forward scattering (HG- S12)	Reference Solution		157

As highlighted at the beginning of this section, spectral dependency of gas property models and complex directional nature of particle-radiation interactions due to scattering are two major factors increasing the CPU requirement of the radiation model. Investigations presented in this section reveal that contribution of an accurate non-gray gas radiation model such as SLW, which requires considerably large CPU time, is marginal compared to that of simple gray gas model for the optically thick medium under consideration and gray gas approximation is sufficient. Furthermore, it is demonstrated that geometric optics approximation based on reflectivity with angular dependency (GOA2) is an accurate approximation to Mie theory in both heat flux and source term predictions and negligence of this angular dependency leads to considerable errors in source term predictions. Regarding to directional nature of particle radiation, it is shown that isotropic scattering assumption leads to under-prediction of both incident heat fluxes and source terms, for which discrepancy is much larger. Furthermore, nonscattering assumption is found to have an insignificant effect on incident heat fluxes and leads to slight over-prediction of the source terms. Neglecting highly forward scattering by assuming nonscattering behavior reduces CPU requirement significantly. Therefore, it is more realistic to neglect scattering than to assume it to be isotropic. Finally, transport approximation is demonstrated to be as accurate as Henyey-Greenstein phase function with normalization, however, with no improvement in CPU time.

## 6.2 Effect of Particle Size on Radiative Heat Transfer Calculations

Radiative properties of particles can be evaluated from Mie theory, which covers the entire particle size range of combustion applications. Nevertheless, there are some simple limiting solutions which provide simple analytical expressions, as described in Chapter 4. In the previous section, it is shown that GOA can provide acceptable accuracy with minimum CPU time under CFBC conditions. In this section, accuracy and CPU efficiency of GOA is assessed for different optical thicknesses involved in the fluidized bed coal combustion tests presented in Sections 5.1.1 and 5.2.1, which will be referred as Test 1 (ABFBC without recycle), Test 2 (ABFBC with recycle) and Test 3 (CFBC), respectively.

In the assessment study, effect of GOA on both incident radiative heat fluxes and source terms are analyzed for these 3 combustion tests. In the radiation models, radiative properties of the participating combustion gases are estimated by using Leckner's correlations (Section 3.2). Although gray gas assumption is not the most accurate way to represent the spectral variations of radiative gas properties, there are two reasons behind this simplifying assumption. One is the marginal contribution of an accurate non-gray gas radiation model, which requires considerably large CPU time, compared to that of Leckner's correlations under FBC conditions as presented in the previous section and the dominant role of particles in radiative heat transfer compared to those of gases under both air-fired and oxy-fired conditions as highlighted in the recent literature [56, 57, 146-149]. The other reason is the fact that this section focuses on errors introduced with GOA in radiative heat transfer calculations and these comparisons are still relevant, despite the possible errors introduced with the gray gas assumption.

In particle property calculations, particles are assumed to be gray. Both Mie theory and geometric optics approximations (GOA) are used considering that over 77, 88 and 96 % (in weight) of the fly ash particles have a size parameter greater than 25 in Test 1, Test 2 and Test 3 respectively (see Figure 5.4 and Figure 5.13). In gray Mie calculations, wavelength independent refractive index of  $m = 1.5 - 0.02i$  and a representative wavelength of  $3 \mu\text{m}$  are used as suggested in [141]. In GOA, particle reflectivity is calculated from (i) normal reflectivity (Eq. (4.14)), (ii) reflectivity averaged over  $\theta$  (Eq. (4.15)) and (iii) the

numerical integration of directional-hemispherical reflectivities (Eq (4.13)), which will be referred to as GOA1, GOA2 and GOA3, respectively. Scattering phase function is represented by Henyey-Greenstein phase function with normalization. In GOA, size parameter is determined by using a representative wavelength (3  $\mu\text{m}$ ) as suggested in [141] and it is used together with the Sauter mean diameters to evaluate the asymmetry factors (Sauter mean diameters are 22, 39 and 291  $\mu\text{m}$  for Test 1-3, respectively). Independent scattering is assumed to take place in the dilute zone of the test rig as the particle volume fractions are in the order of  $10^{-5}$ ,  $10^{-4}$  and  $10^{-3}$  for Test 1-3, respectively. Particle load is assumed to uniform throughout the freeboard and the dilute zone sections of the combustors. All input data necessary for the radiative property models are taken from Sections 5.1.1, 5.1.3, 5.2.1 and 5.2.2.

In MOL solution DOM, a combination of  $S_{10}$  and  $13 \times 13 \times 96$  and  $S_{12}$  and  $17 \times 305$  grid nodes are utilized for ABFBC (in Test 1 and 2) and CFBC (in Test 3) test rigs based on a previous grid refinement study [150] and the results presented in Section 6.1.4. For the difference relations of spatial derivatives, two-point upwind differencing scheme DSS012 is employed. All simulations are carried out on a computer with Intel® Core™ 5i CPU 4200 1.60 GHz processor having 4.00 GB of RAM. CPU times are recorded for an error tolerance of 0.001 % throughout the analyses.

### **6.2.1 Comparison between Geometric Optics Approximations for Particle Properties**

Predictive accuracy of widely used GOA1 and recently proposed GOA2 approximations are first compared to solution of Fresnel's equations without any simplifying assumptions (GOA3) with respect to particle absorptivity and reflectivity for a wide range of optical properties. Range of RI is selected based on the optical property measurements of ash particles presented in [36]. In GOA3, numerical integration of Eq (4.13) is performed with  $0.1^\circ$  intervals via Simpson's method. Predictions obtained with all three GOA are summarized in Table 6.7. As can be seen from the table, GOA1 and GOA2 are only a

function of refractive index ( $n$ ) and there is a noticeable difference between these two models if  $n \geq 1.5$ , which is usually the case for ash particles. Furthermore, there is good agreement between GOA2 and GOA3 for the majority of the absorption indices and GOA2 can be utilized to estimate particle absorptivity and reflectivity unless the absorption index ( $k$ ) is very high. These comparisons reveal that GOA2 can be utilized without losing any accuracy for the evaluation of gray ash particle properties. Therefore, it will be utilized as the GOA model for further investigations.

Table 6.7 Comparison of geometric optics approximations for various complex index of refraction values

RI		GOA1		GOA2		GOA3	
n	k	$\alpha$	$\rho$	$\alpha$	$\rho$	$\alpha$	$\rho$
<b>1.50</b>	<b>0.000001</b>	0.960	1.040	0.908	1.092	0.908	1.092
<b>1.50</b>	<b>0.00001</b>	0.960	1.040	0.908	1.092	0.908	1.092
<b>1.50</b>	<b>0.0001</b>	0.960	1.040	0.908	1.092	0.908	1.092
<b>1.50</b>	<b>0.001</b>	0.960	1.040	0.908	1.092	0.908	1.092
<b>1.50</b>	<b>0.01</b>	0.960	1.040	0.908	1.092	0.908	1.092
<b>1.50</b>	<b>0.05</b>	0.960	1.040	0.908	1.092	0.908	1.092
<b>1.50</b>	<b>0.1</b>	0.960	1.040	0.908	1.092	0.906	1.094
<b>1.50</b>	<b>0.5</b>	0.960	1.040	0.908	1.092	0.863	1.137
<b>1.50</b>	<b>1</b>	0.960	1.040	0.908	1.092	0.767	1.233
<b>1.00</b>	<b>0.02</b>	1.000	1.000	1.000	1.000	0.991	1.009
<b>1.25</b>	<b>0.02</b>	0.988	1.012	0.947	1.053	0.947	1.053
<b>1.50</b>	<b>0.02</b>	0.960	1.040	0.908	1.092	0.908	1.092
<b>1.75</b>	<b>0.02</b>	0.926	1.074	0.873	1.127	0.873	1.127
<b>2.00</b>	<b>0.02</b>	0.889	1.111	0.839	1.161	0.839	1.161

### 6.2.2 Accuracy of GOA in Radiative Heat Transfer Predictions

Effect of GOA on predicted heat flux and source term distributions is investigated by comparing its predictions with those of gray Mie theory. Radiative properties of the particle laden flue gas for Test 1, Test 2 and Test 3 are given in Table 6.8. As can be seen

from the table, optical thickness of the medium ( $\tau$ ) increases from Test 1 to Test 3 with increasing particle load (B). This is due to the fact that magnitudes of particle radiative properties increase from Test 1 to Test 3. It is also seen that gas and particle properties are in the same order of magnitude for Test 1 while there is a significant difference for Test 2 and Test 3. These comparisons show that particle radiation is much more dominant under CFBC conditions compared to ABFBC conditions.

Table 6.8 Gray gas and gray particle properties for Test 1-3

	Test 1 ( $\tau=0.85$ )		Test 2 ( $\tau=4.77$ )		Test 3 ( $\tau=10.66$ )	
<b>B (kg/m<sup>3</sup>)</b>	0.011		0.131		3.72	
<b><math>\kappa_g</math> (m<sup>-1</sup>)</b>	0.44		0.44		0.55	
	GOA	Mie Theory	GOA	Mie Theory	GOA	Mie Theory
<b><math>\kappa_p</math> (m<sup>-1</sup>)</b>	0.70	0.43	4.98	3.78	20.87	20.62
<b><math>\sigma_p</math> (m<sup>-1</sup>)</b>	0.84	1.36	5.99	8.34	25.10	27.30
<b>g</b>	0.91	0.76	0.94	0.82	0.95	0.94

Effect of GOA on predicted heat flux and source term distributions is investigated by comparing its predictions with those of gray Mie theory. Predicted and measured wall heat fluxes and source terms are demonstrated in Figure 6.9 and Figure 6.10. As can be seen from Figure 6.9, heat fluxes are in good agreement with both measurements and reference Mie solutions for all cases. However, GOA is found to over-predict the source terms compared to gray Mie solutions in Test 1 and Test 2.

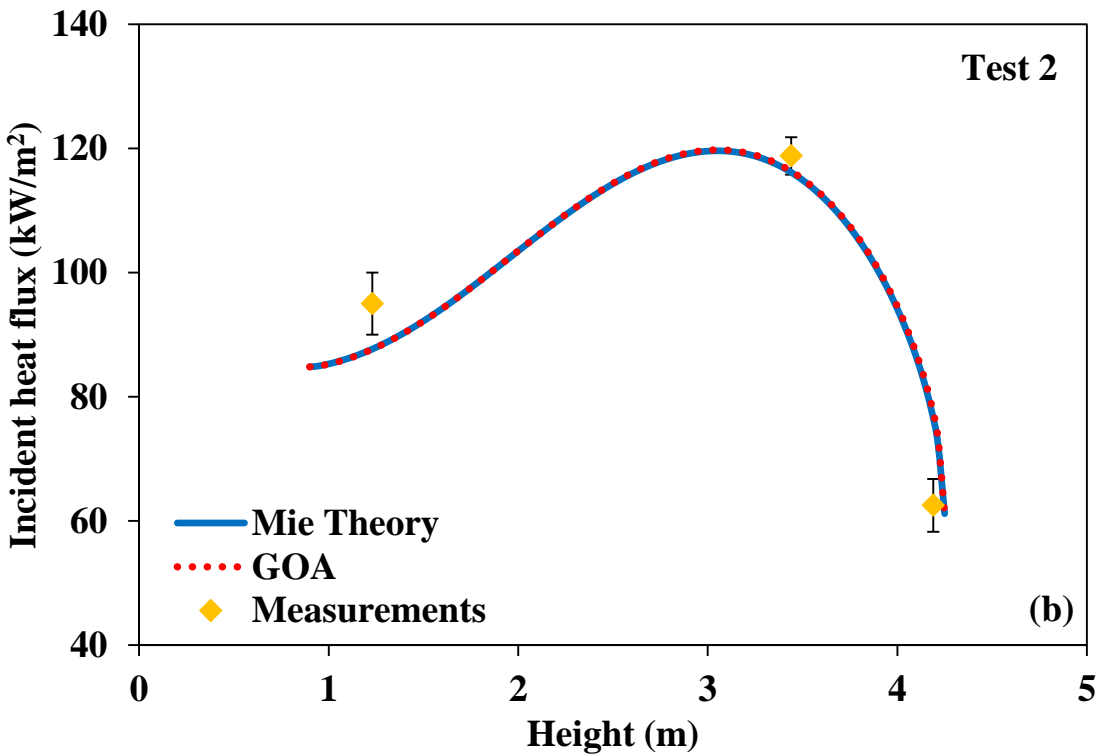
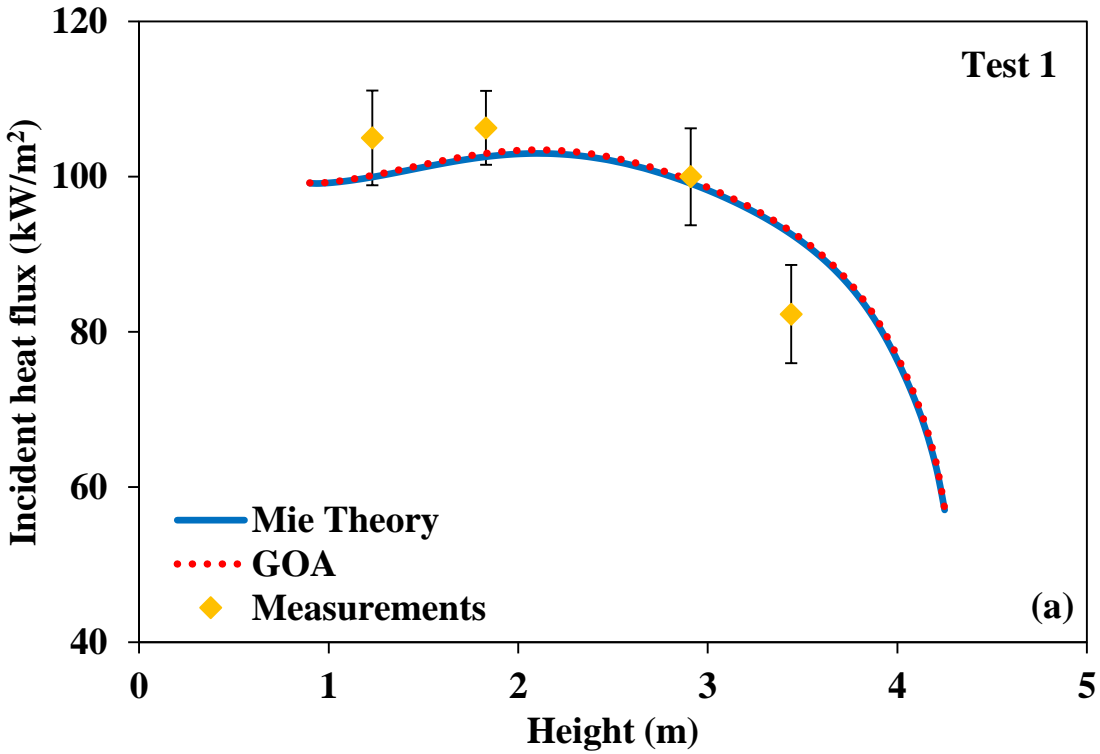


Figure 6.9 Effect of GOA on incident heat fluxes for (a) Test 1, (b) Test 2 and (c) Test 3



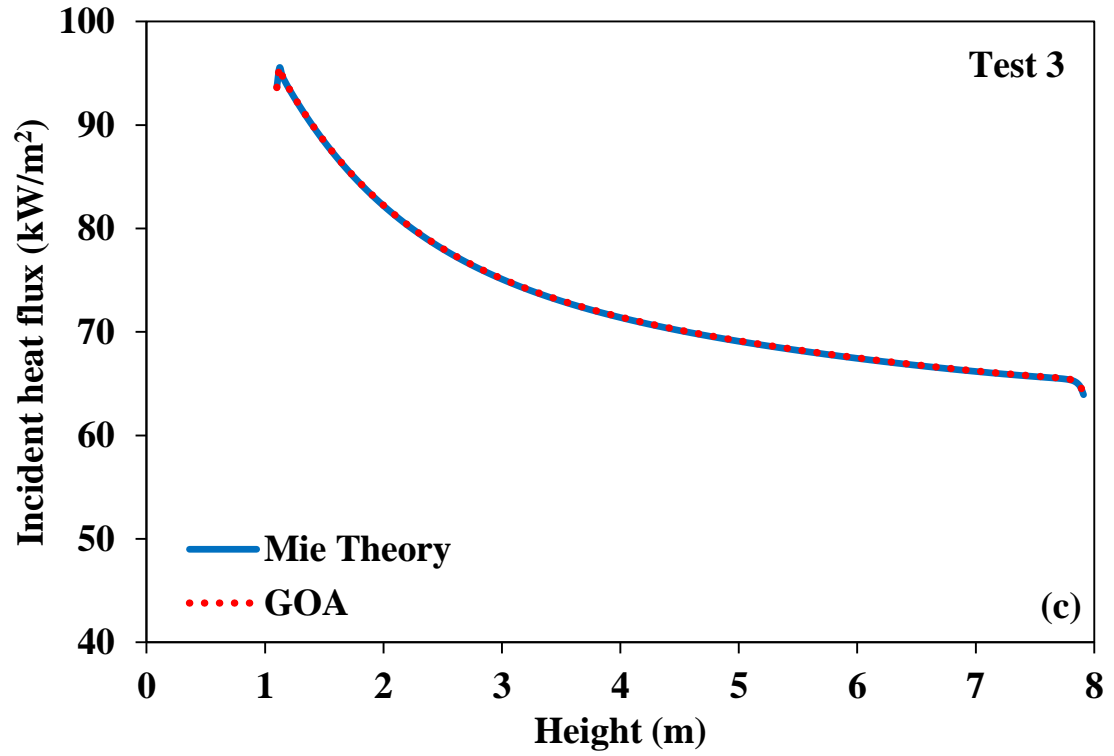


Figure 6.9 Effect of GOA on incident heat fluxes for (a) Test 1, (b) Test 2 and (c) Test 3  
(cont'd)

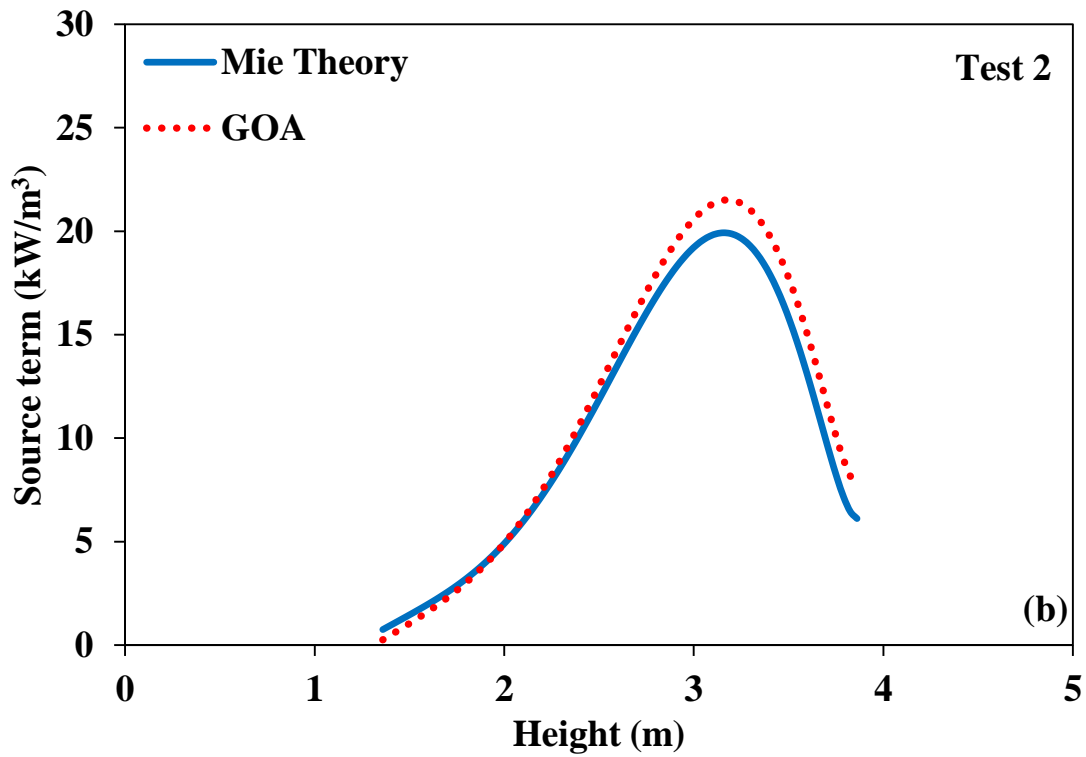
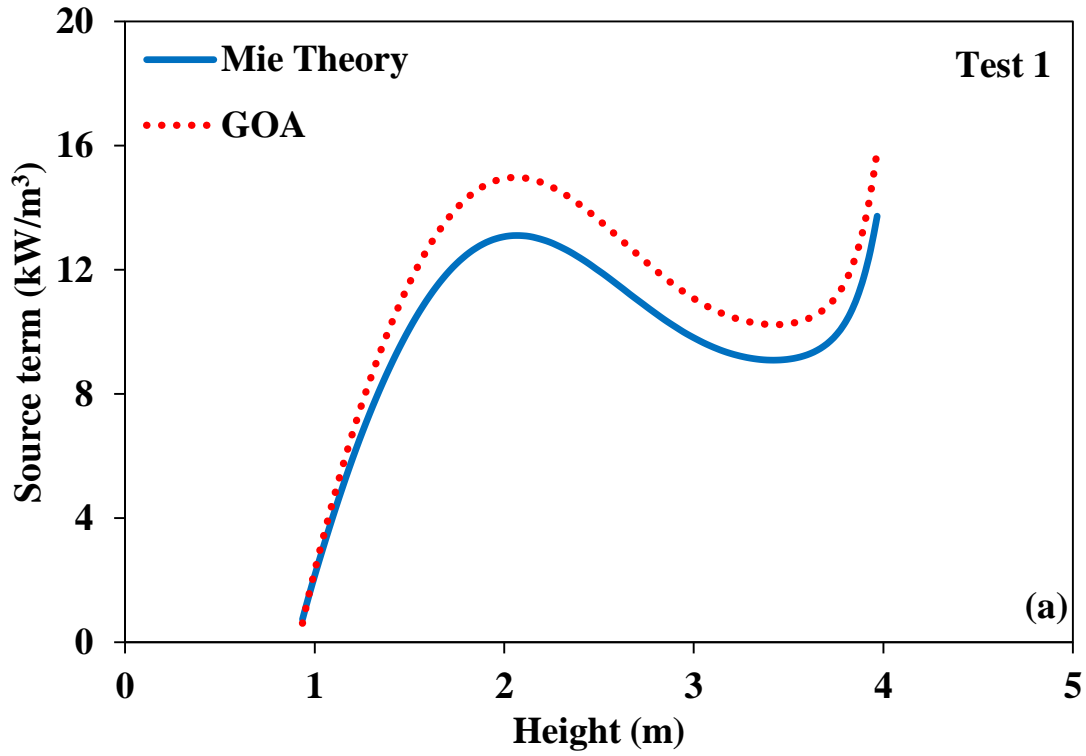


Figure 6.10 Effect of GOA on source terms for (a) Test 1, (b) Test 2 and (c) Test 3

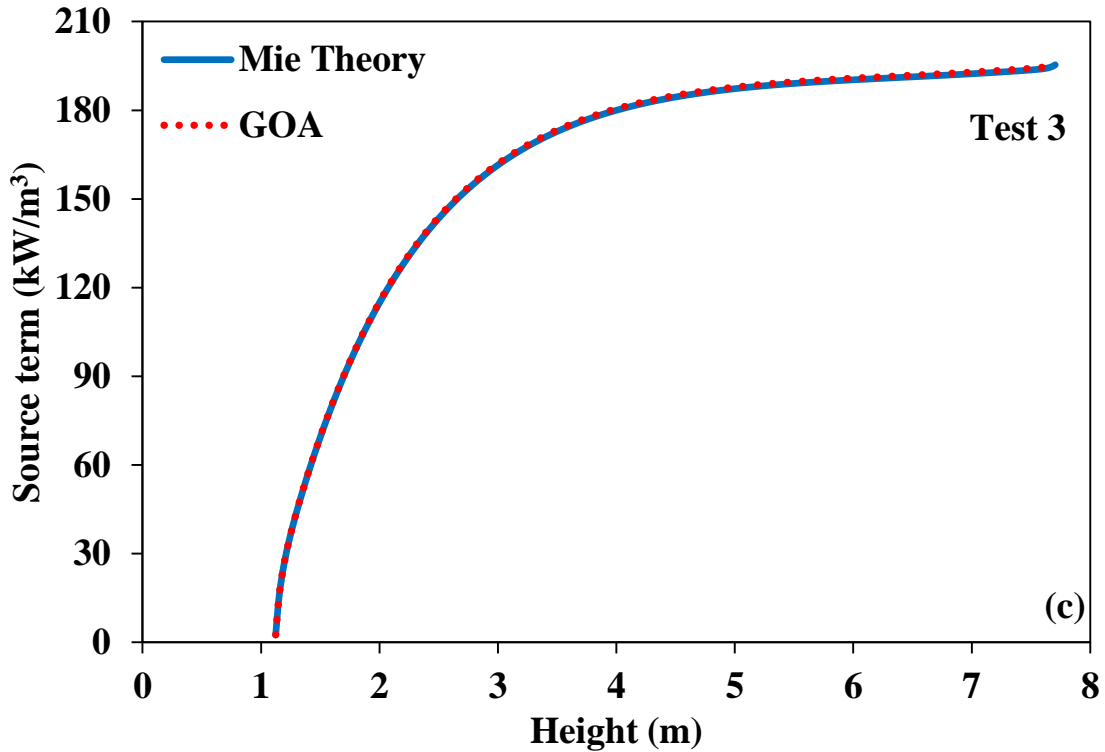


Figure 6.10 Effect of GOA on source terms for (a) Test 1, (b) Test 2 and (c) Test 3  
(cont'd)

The percentage relative errors in incident heat fluxes and source term predictions with corresponding CPU times are given in Table 6.9. As can be seen from the table, error in source term predictions due to GOA is the largest for Test 1 and it decreases from Test 1 to Test 3. It should be reminded that for GOA to be applicable, size parameters of the particles are expected to be at least larger than 25. As a matter of fact, surface mean diameter (Sauter mean diameter) of the combustion tests are 22, 39 and 291  $\mu\text{m}$  for Test 1-3, respectively. Furthermore, over 77, 88 and 96 % (in weight) of the fly ash particles have a size parameter greater than 25 in Test 1, Test 2 and Test 3, respectively, based on their cumulative weight distributions (see Figure 5.4 and Figure 5.13). Nevertheless, GOA still fails in source term predictions for both Test 1 and Test 2.

Table 6.9 Effect of GOA on incident heat fluxes and sources terms

Combustion Test	Particle Model	Average % Error in Heat Fluxes	Average % Error in Source Term	CPU Time (s)
<b>Test 1</b> ( $\tau = 0.85$ )	GOA2	0.4	15.4	701
	Mie Theory	Reference	Reference	620
<b>Test 2</b> ( $\tau = 4.77$ )	GOA2	0.1	9.7	308
	Mie Theory	Reference	Reference	340
<b>Test 3</b> ( $\tau = 10.66$ )	GOA2	0.1	0.7	225
	Mie theory	Reference	Reference	268

Cumulative cross sectional area as a function of size parameter  $x$  is presented in Figure 6.11 for Test 1-3, where GOA applicability zone is shaded in orange color. As can be seen from the figure, fine particles in Test 1 ( $x < 25$ ) constitute 78 % of the total cross sectional area of the entire particle cloud despite their low weight fraction (23 %) (Figure 5.4). For Test 2, it is found that fine particles constitute about 51 % of the total cross sectional area of the entire particle cloud, which corresponds to a weight percentage of 22% in cumulative weight distribution (Figure 5.4). For Test 3, 95 % of the cumulative cross sectional area is created by the large particles present in Test 3, which falls into shaded GOA zone. These comparisons reveal that Mie and GOA predictions become closer to one another as the total cross sectional area constituted by fine particles decreases. Therefore, if PSD involves both fine and coarse particles, it is recommended to base the applicability of GOA on cumulative cross sectional area distribution rather than the common practices seen in the literature such as surface mean diameter or cumulative weight percent distribution of particles.

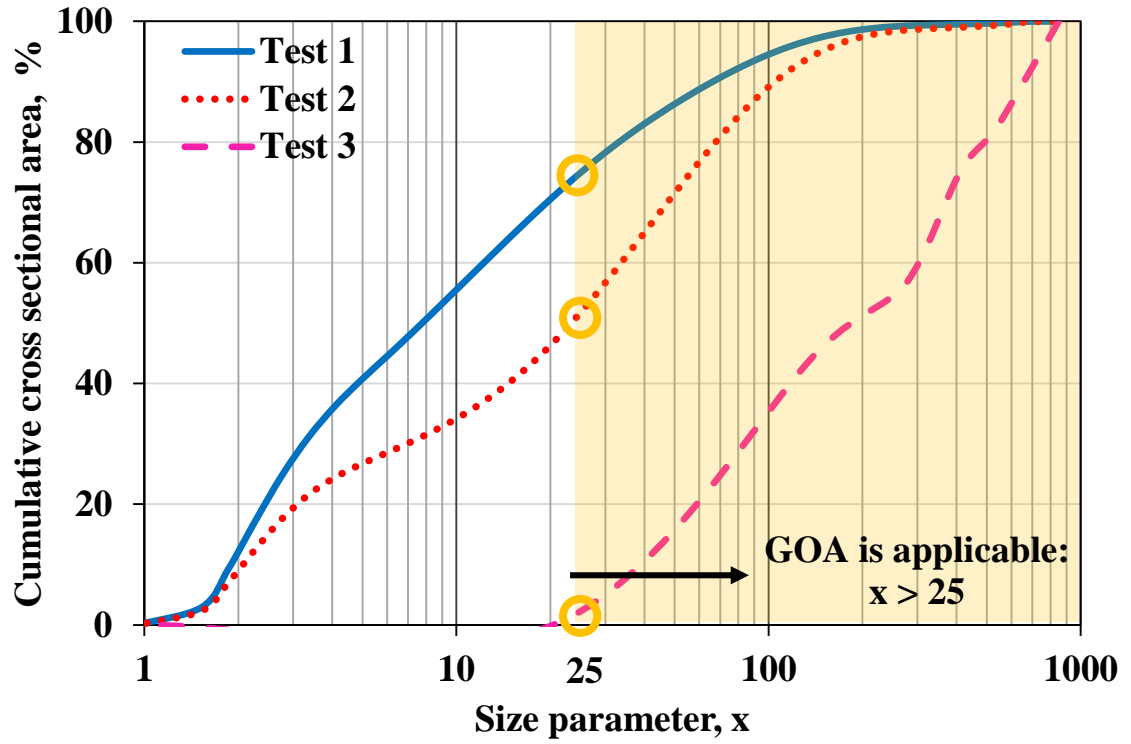


Figure 6.11 Demonstration of the applicability of GOA limit based on cumulative cross sectional area distribution

### 6.3 Effect of Particle Size Distribution on Radiative Heat Transfer Calculations

In the previous section, it is demonstrated that GOA cannot predict particle properties accurately in the presence fine particles, which makes the other alternative for particle property calculations a necessity, that is Mie theory. However, solution of Mie theory is a function of particle size hence necessitates to evaluate particle properties for each particle size (or size interval in the particle size distribution) at each wavelength, which brings an additional computational burden to Mie calculations.

Sauter mean diameter ( $d_{32}$ ) is an averaged quantity and is defined as the equivalent diameter having the same volume/surface ratio as the polydisperse particle cloud. As described in Section 4.2, representing the radiative properties of particle cloud (absorption coefficient, scattering coefficient and scattering phase function) with a uniform particle size significantly simplifies property calculations. This is why  $d_{32}$  has been commonly used in the combustion community to represent the actual PSD in modelling radiative heat transfer.

In this section, effect of using Sauter mean diameter instead of the actual PSD on radiative heat transfer is investigated under FBC conditions. For that purpose, radiative heat flux and source term predictions are evaluated for the fluidized bed coal combustion tests presented in Sections 5.1.1 and 5.2.1, which will be referred as Test 1 (ABFBC without recycle), Test 2 (ABFBC with recycle) and Test 3 (CFBC), respectively. In the radiation models, both participating combustion gases and particles are assumed to be gray. Radiative properties of the gases and particles are calculated by using Leckner's correlations (Section 3.2) and Mie theory (Section 4.1.3), respectively. In Mie calculations, wavelength independent refractive index of  $m = 1.5-0.02i$  and a representative wavelength of  $3 \mu\text{m}$  are used as suggested in [141]. In all cases, scattering phase functions are represented by Henyey-Greenstein phase function with normalization (Section 4.3). All input data necessary for the radiative property models are taken from Sections 5.1.1, 5.1.3, 5.2.1 and 5.2.2. In MOL solution of DOM, a combination of  $S_{10}$  and  $13 \times 13 \times 96$  and  $S_{12}$  and  $17 \times 305$  grid nodes are utilized for ABFBC (in Test 1 and 2) and CFBC (in Test 3) test rigs based on a previous grid refinement study [150] and the

results presented in Section 6.1.4. For the difference relations of spatial derivatives, two-point upwind differencing scheme DSS012 is employed.

Radiative properties of the particle clouds calculated by using Sauter mean diameter ( $d_{32}$ ) and actual PSD are given in Table 6.10. As can be seen from the table, representing the PSD with a single particle diameter leads to significant errors in cloud properties, especially for the absorption index,  $\kappa_p$ . Furthermore, it is seen that absorption coefficients are consistently over-estimated while the scattering coefficient is under-estimated for all combustion tests.

Table 6.10 Effect of PSD on radiative properties of particles

	Test 1 ( $\tau = 0.85$ )			Test 2 ( $\tau = 4.77$ )			Test 3 ( $\tau = 10.66$ )		
<b><math>d_{32}</math> (<math>\mu\text{m}</math>)</b>	22			39			291		
<b><math>B</math> (<math>\text{kg}/\text{m}^3</math>)</b>	0.011			0.131			3.72		
<b><math>\kappa_g</math> (<math>\text{m}^{-1}</math>)</b>	0.44			0.44			0.55		
	$d_{32}$	PSD	Error (%)	$d_{32}$	PSD	Error (%)	$d_{32}$	PSD	Error (%)
<b><math>\kappa_p</math> (<math>\text{m}^{-1}</math>)</b>	0.69	0.43	62	5.28	3.78	40	21.51	20.62	4
<b><math>\sigma_p</math> (<math>\text{m}^{-1}</math>)</b>	1.10	1.36	-19	6.51	8.34	-22	25.75	27.30	-6
<b><math>g</math></b>	0.91	0.76	20	0.94	0.82	14	0.95	0.94	2

It should be reminded that calculation of absorption / scattering coefficient of particles necessitates not only the projected surface area of particles but also the extinction and scattering efficiencies predicted by the Mie theory. Figure 6.12 illustrates the dependency of those efficiencies on particle diameter for the particle sizes of interest in Tests 1-3. Efficiencies corresponding to Sauter mean diameters are also demonstrated with vertical lines (at 22, 39 and 291  $\mu\text{m}$  for Test 1-3, respectively). As can be seen from the figure, these efficiencies have a nonlinear dependency on particle size and demonstrate strong oscillatory behaviors for fine particles ( $d_p < 30 \mu\text{m}$ ). It is also seen that extinction efficiency of fine particles (1-30  $\mu\text{m}$ ) is much larger than the limiting value of 2.0 (the

extinction paradox, see Section 4.1.2) indicating that extinction cross section is much larger than the geometric cross sectional area of particles. This is why it is not possible to capture this nonlinear behavior with a surface-mean diameter like  $d_{32}$  approximation. Regarding to scattering efficiencies, Figure 6.12 reveals that scattering efficiency of fine particles are much larger than its limiting value ( $Q_s \sim 1.1$ ), which results in under-estimation of the scattering coefficients (Table 6.10). On the other hand, absorption efficiency of fine particles is small compared to its limiting value ( $Q_a \sim 0.9$ ), which leads to over-estimation of the absorption coefficients (Table 6.10). Figure 6.13 shows the effect of particle size on the asymmetry factor,  $g$ . As can be seen from the figure, asymmetry factor increases with increasing particle size and reaches an asymptotic value of 0.95. In the presence of a PSD, small asymmetry factor of fine particles and large asymmetry factor of large particles are combined based on weighted sum of individual asymmetry factors (see Eq. 4.70), which leads to a smaller value (Table 6.10). If  $d_{32}$  approximation is utilized, however, asymmetry factor is overestimated (Figure 6.13).

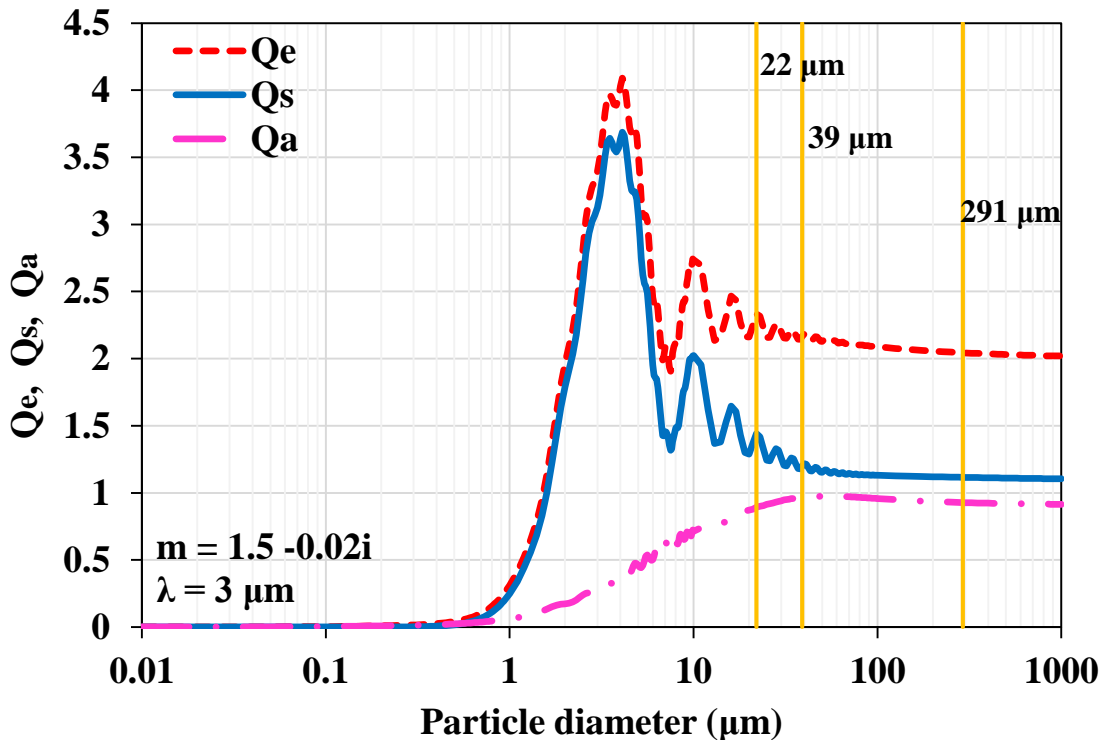


Figure 6.12 Effect of particle size on the extinction, scattering and absorption efficiencies



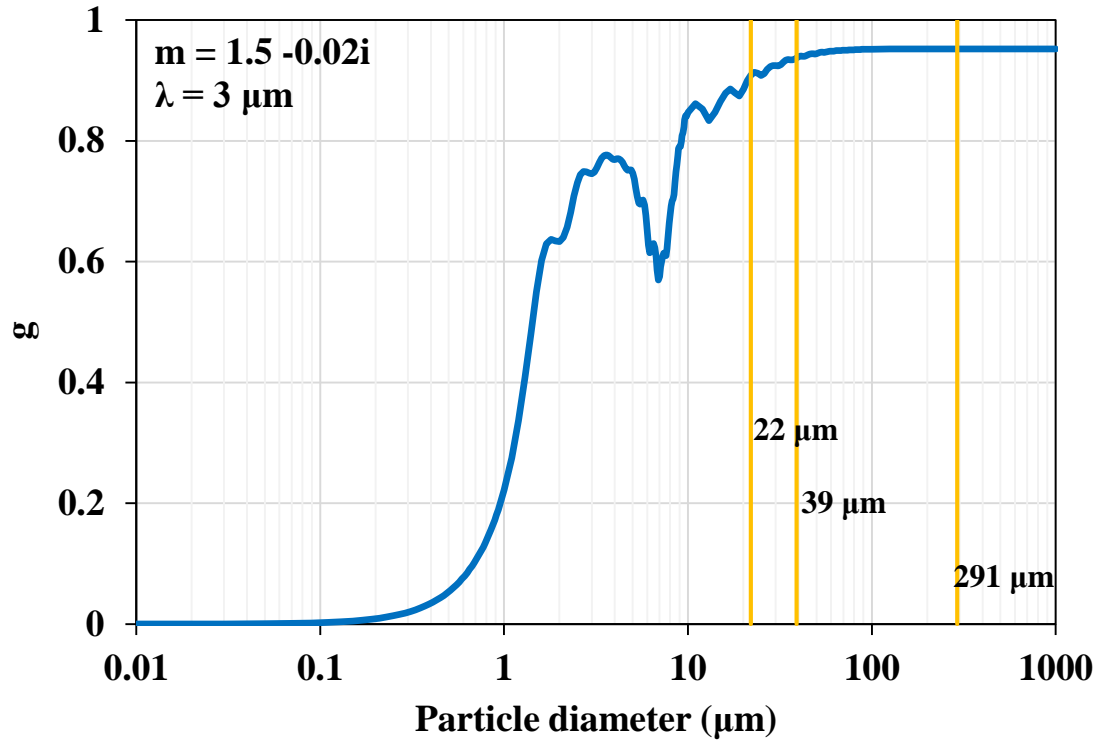


Figure 6.13 Effect of particle size on the asymmetry factor

Comparisons of source terms predicted by using Sauter mean diameter and actual PSD in particle property calculations are demonstrated in Figure 6.14. As can be seen from the figure, source term predictions are noticeably higher for Test 1 while the difference becomes insignificant for Test 2 and Test 3. Average relative percentage errors in heat flux and source term predictions are given in Table 6.11. As can be seen from the table, approximation of the size distribution by a single mean diameter is able to give a good representation of the heat fluxes for all combustion tests under consideration while errors in source term predictions reaches almost 12 % in Test 1, where the amount of fine particles constitute 78 % of the total projected surface area (Figure 6.11). Nevertheless, errors in source term predictions are much smaller than the errors in absorption coefficients (Table 6.10), especially for Test 1. This is considered to be due to the relative significance of gas radiation to particle radiation in this combustion test, where gas and particle absorption coefficients are comparable in magnitude (Table 6.10).

These results show that predictive accuracy of using surface mean diameter for the calculation of the radiative properties depends mainly on the percentage of total cross sectional area constituted by fine particles. Therefore, it is not sufficient to consider only the total geometric cross sectional area of particles (as in the case of Sauter mean diameter) in the calculation of absorption coefficient, scattering coefficient and asymmetry factor. Furthermore, using a surface mean diameter ( $d_{32}$ ) to represent PSD in modelling radiative heat transfer may lead to considerable errors in source term predictions depending on the cumulative cross sectional area constituted by fine particles.

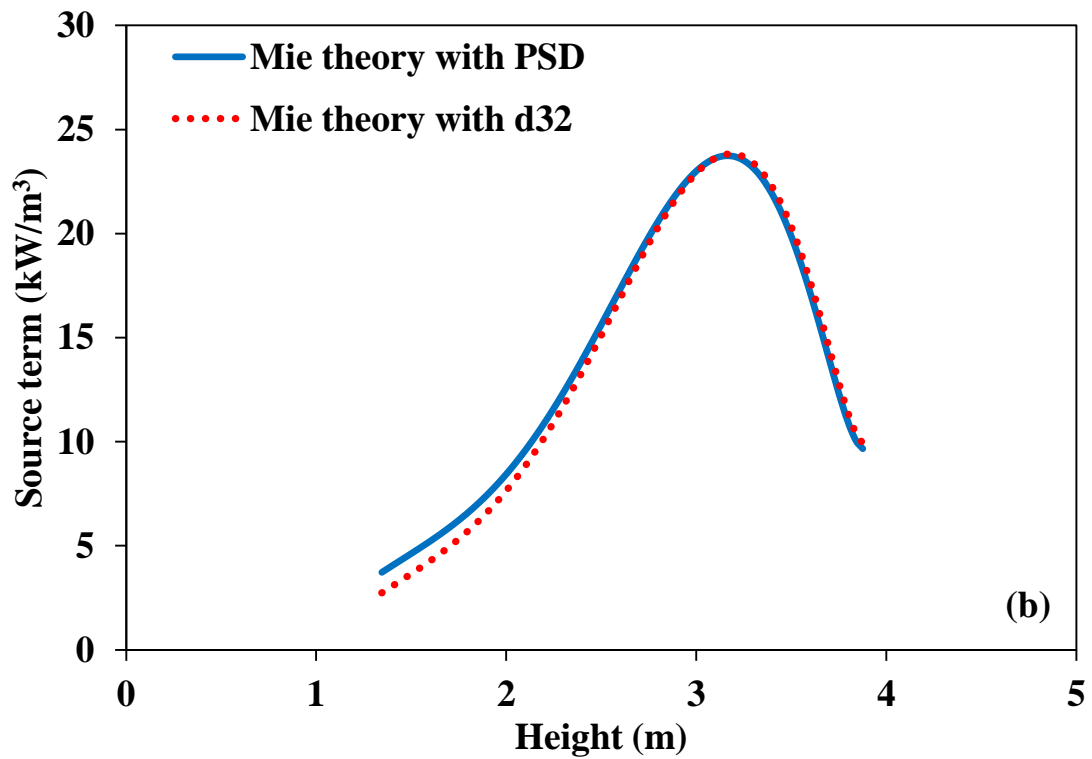
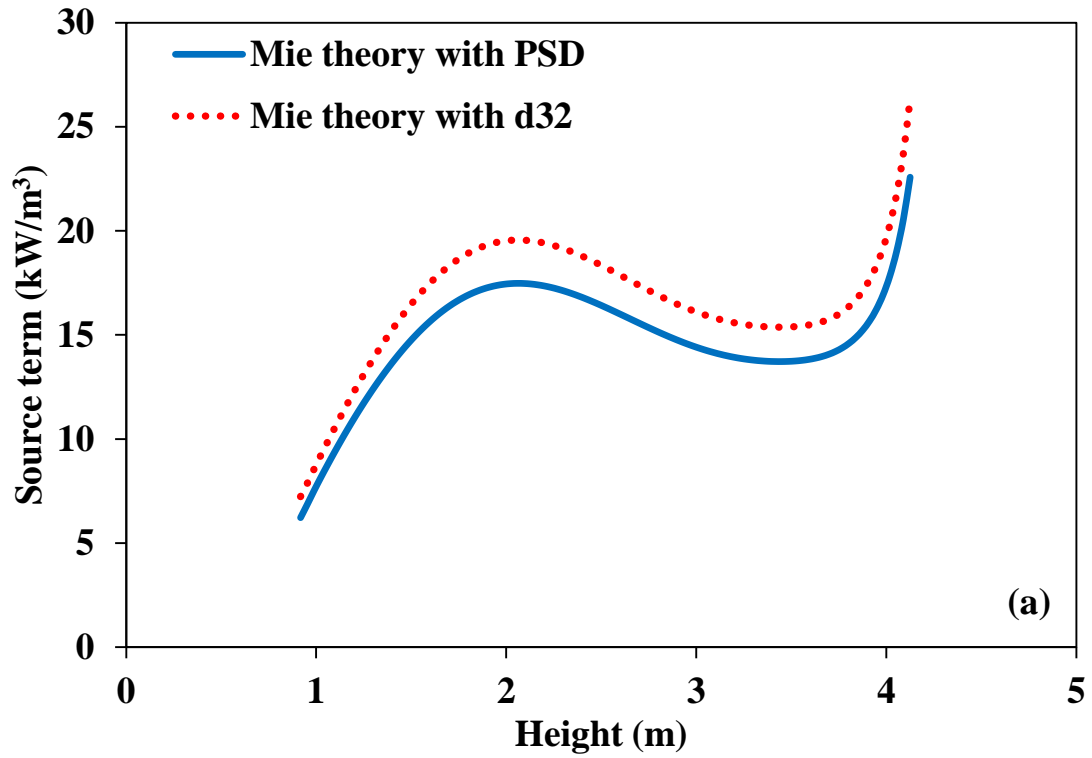


Figure 6.14 Effect of PSD on source term predictions for (a) Test 1 (b) Test 2 and (c) Test 3

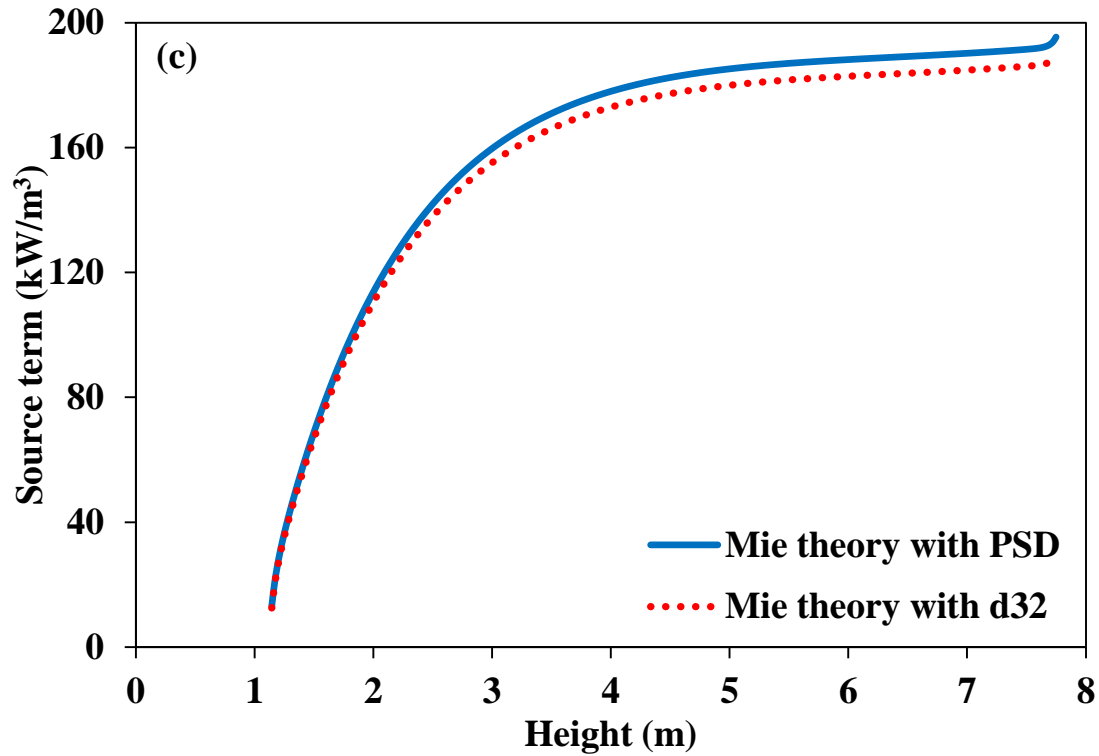


Figure 6.14 Effect of PSD on source term predictions for (a) Test 1 (b) Test 2 and (c) Test 3

Table 6.11 Effect of PSD on incident heat flux and source term predictions

Combustion Test	Particle Model	Average % Error in Heat Flux	Average % Error in Source Term
Test 1 (78 %)*	Gray Mie with d <sub>32</sub>	0.7	11.8
	Gray Mie with PSD	Reference Solution	
Test 2 (51 %)*	Gray Mie with d <sub>32</sub>	0.3	-3.5
	Gray Mie with PSD	Reference Solution	
Test 3 (5 %)*	Gray Mie with d <sub>32</sub>	-0.2	-2.8
	Gray Mie with PSD	Reference Solution	

\* Percentage of total cross sectional area constituted by fine particles

## 6.4 Effect of Particle Load Distribution on Radiative Heat Transfer

In the previous sections, particle load was assumed to be uniform along the freeboard/dilute zone of the combustors. In this section, effect of particle load distribution on radiative heat transfer in circulating fluidized bed combustors (CFBCs) is investigated. The aim is to identify how important it is to include axial and radial variations of particle load along the splash and dilute zones in radiative heat transfer calculations and to determine the predictive accuracy of simple 0D and 1D approximations for particle load distribution in the riser by benchmarking their predictions against a semi-empiric 2D axisymmetric model developed for a wide range of operating conditions and systems (see Section 5.2.2 for the details of particle load distribution models). Input data required for the radiation model are provided from the coal combustion test presented in Section 5.2.1. RTE is solved for 2-D axisymmetric cylindrical enclosure which contains gray, absorbing, emitting gas mixture with gray, absorbing, emitting, anisotropically scattering particles bounded by diffuse, gray/black walls (see Section 5.2.2 for details). Radiative properties of the gases and particles are calculated by using Leckner's correlations (Section 3.2) and GOA3 (Section 4.1.2), respectively, based on the assessment studies given in Sections 6.1.2 and 6.1.3. In GOA3, wavelength independent refractive index of  $m = 1.5 - 0.02i$  and a representative wavelength of  $3 \mu\text{m}$  are used as suggested in [141]. Scattering phase functions are represented by Henyey-Greenstein phase function with normalization (Section 4.3). In MOL solution of DOM, two-point upwind differencing scheme DSS012 is deployed for the difference relations of spatial derivatives. All simulations are carried out on a computer with Intel® Core™ 7i CPU 2600 3.40 GHz processor having 16.00 GB of RAM. CPU times are recorded for an error tolerance of 0.001 % throughout the analyses.

### 6.4.1 Spatial Discretization Refinement

In Section 6.1.4, angular and spatial grid refinement of the CFBC combustion test was presented when particle load is assumed to be 0D. As shown Figure 5.15 and Figure 5.16 (in Section 5.2.2), however, local particle loads at any radial and axial position along the splash and dilute zones are much higher than the case in 0D particle load approximation ( $3.72 \text{ kg/m}^3$ ). Considering the proportionality between particle load and optical thickness of the medium, spatial grid refinement study is needed for the 1D and 2D axisymmetric particle load models.

For that purpose, numerical accuracy and computational economy of the RTE solutions with respect to spatial discretization are investigated by comparing their steady-state predictions with those obtained by the reference case carried out with the finest discretization. 17x305, 19x325, 21x350, 23x385 and 25x425 grid resolutions (number of computational cells in radial and axial directions, respectively) are tested for the spatial discretization. A high angular quadrature scheme,  $S_{12}$ , is selected in order to alleviate to stability problems at fine grid resolutions [84].

Incident wall heat fluxes and source terms along the centerline calculated with 0D, 1D and 2D axisymmetric particle load distribution models are illustrated in Figure 6.15 and Figure 6.16. As can be seen from the figures, incident wall heat fluxes (Figure 6.15) are not as much affected as the source terms (Figure 6.16) by spatial discretization. Moreover, predictions obtained from coarser grids lead to under-prediction of the incident heat fluxes along the side wall while they lead to over-prediction of the source term.

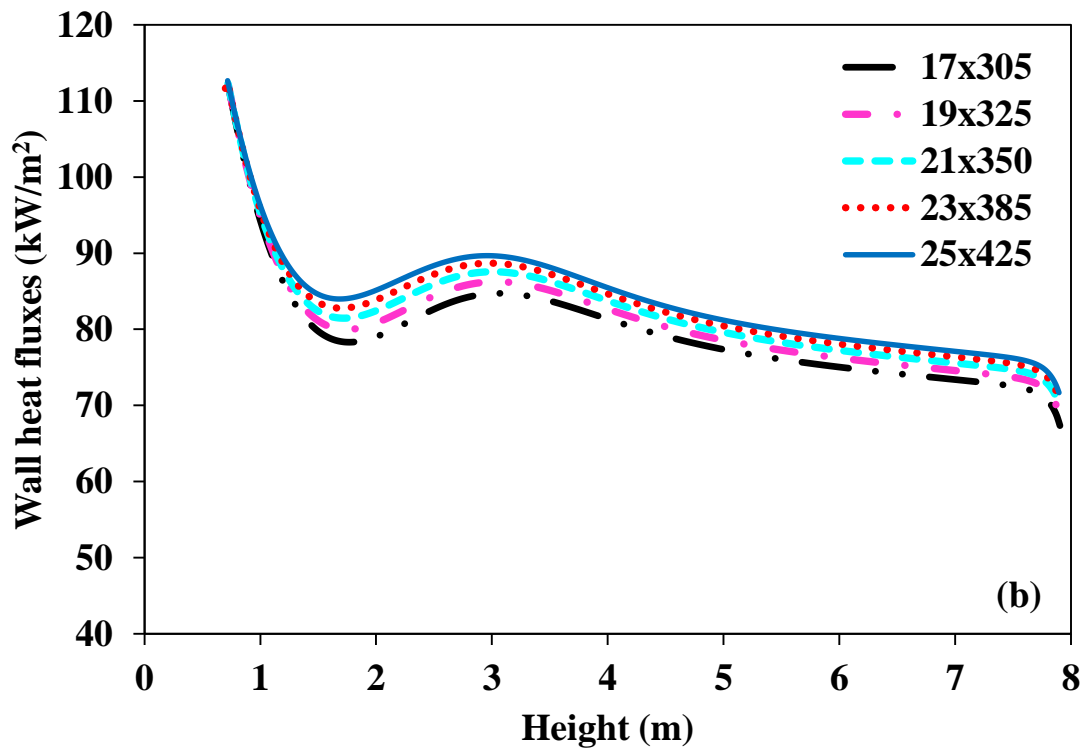
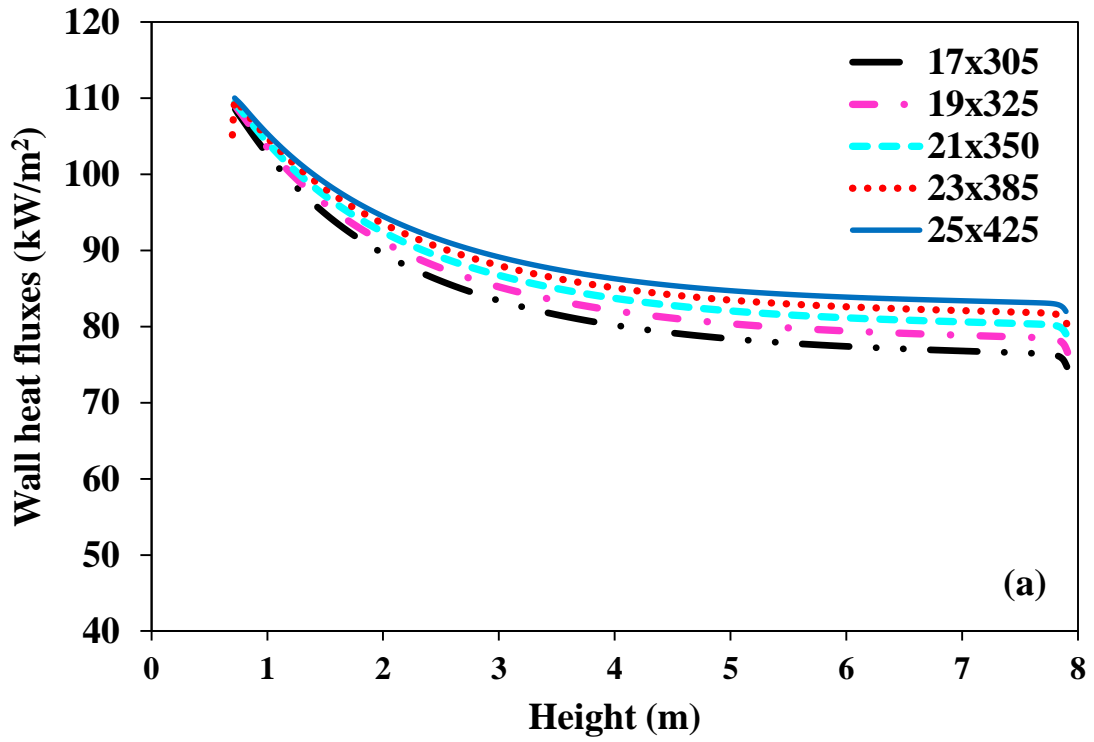


Figure 6.15 Effect of spatial discretization on incident wall heat fluxes for (a) 0D, (b) 1D and (c) 2D particle load distribution models

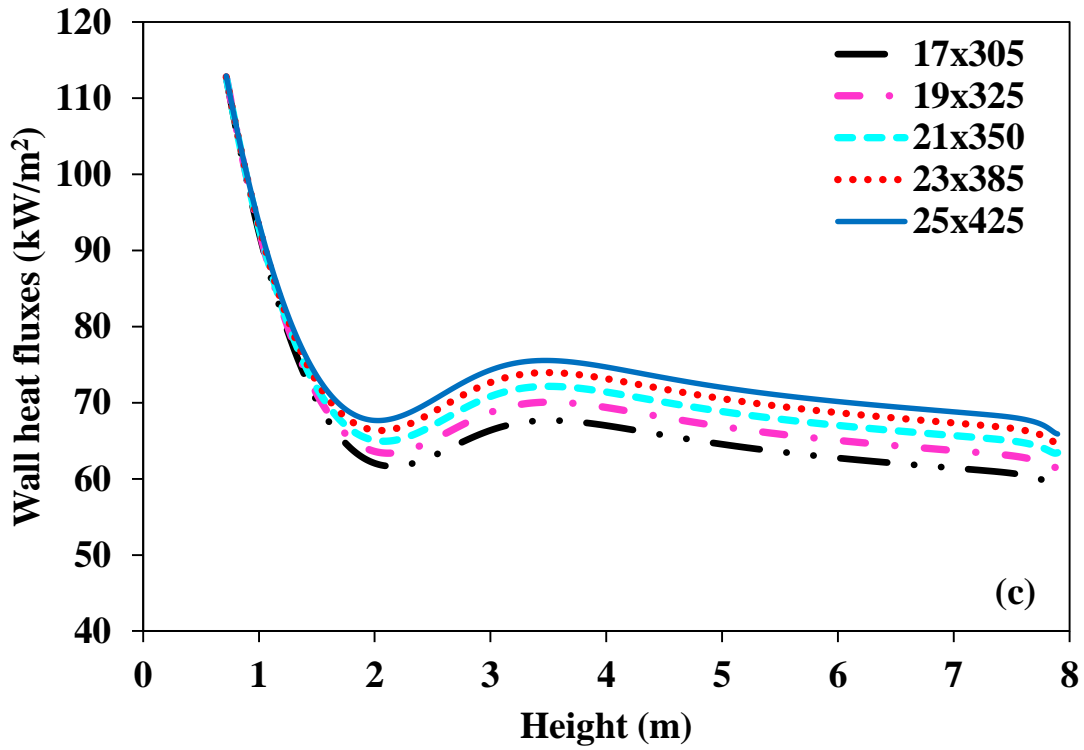


Figure 6.15 Effect of spatial discretization on incident wall heat fluxes for (a) 0D, (b) 1D and (c) 2D particle load distribution models (cont'd)



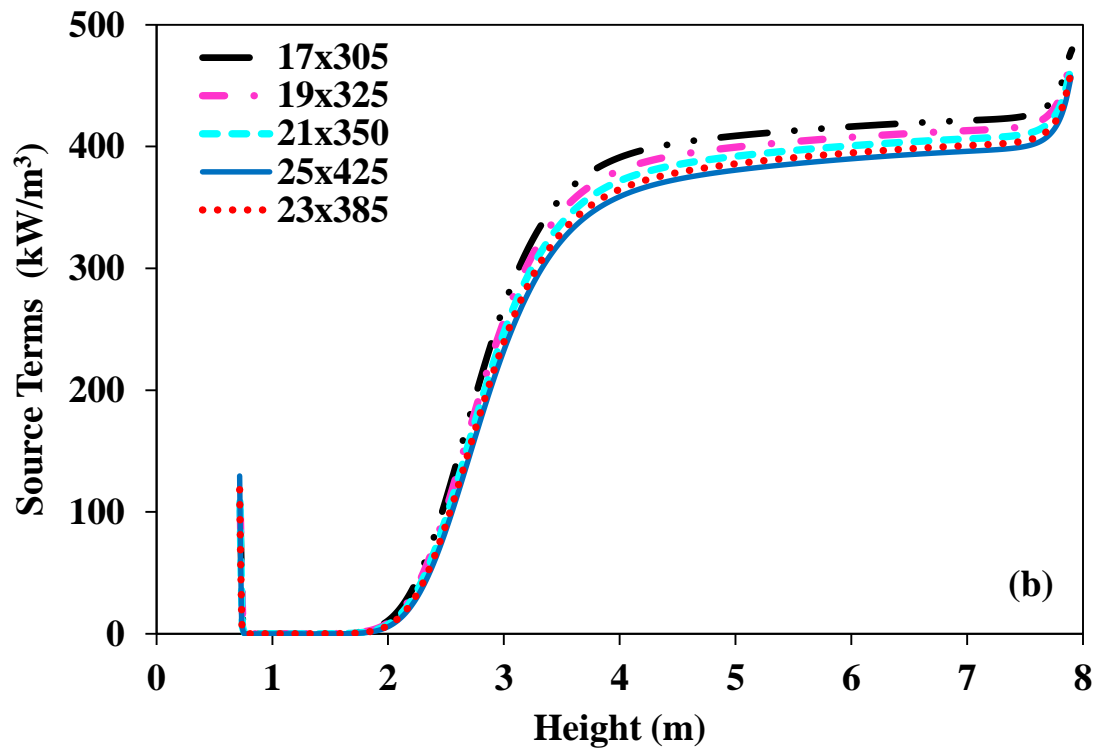
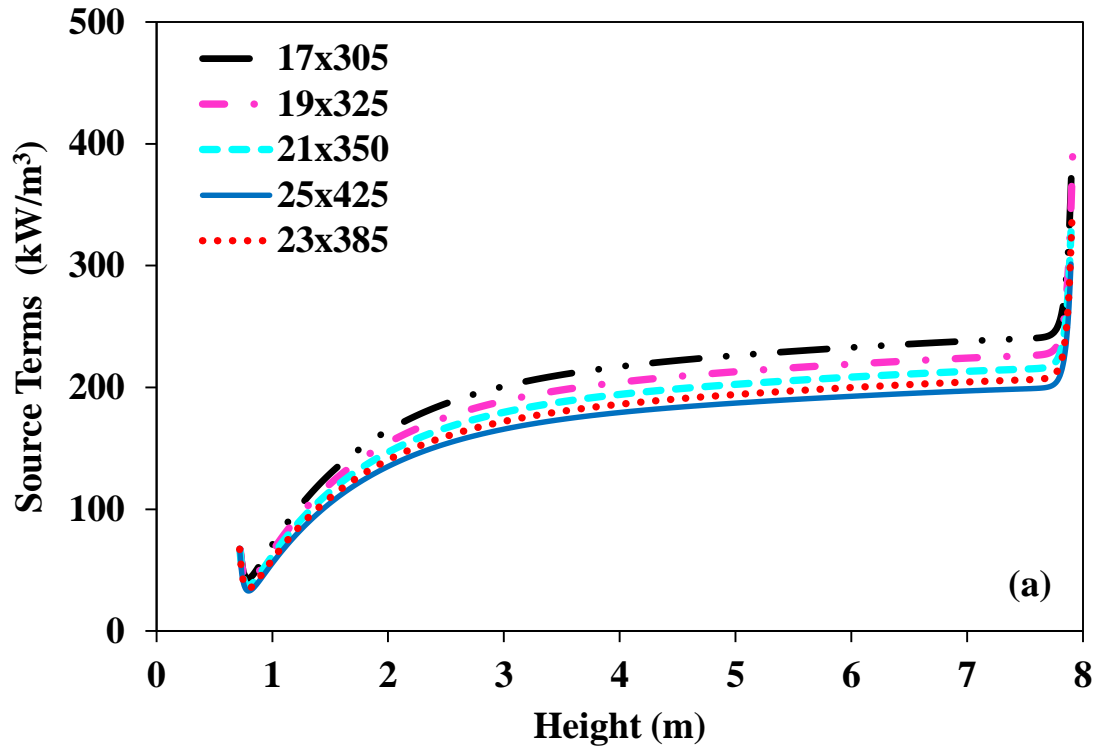


Figure 6.16 Effect of spatial discretization on source terms for (a) 0D, (b) 1D and (c) 2D particle load distribution models

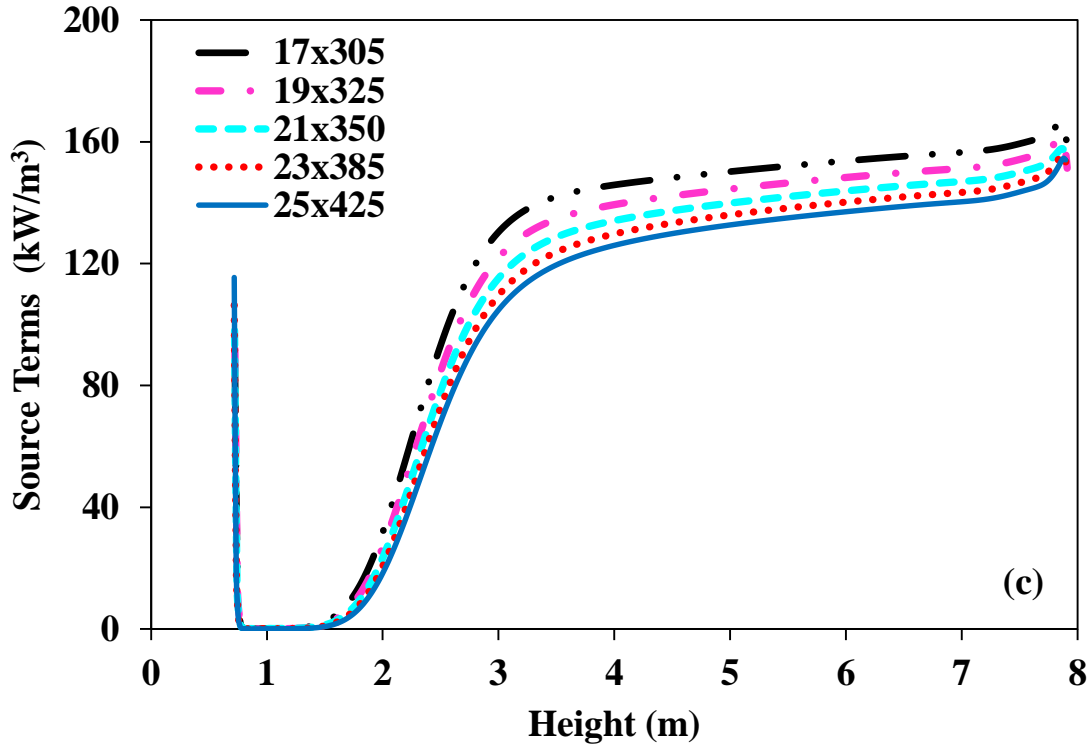


Figure 6.16 Effect of spatial discretization on source terms for (a) 0D, (b) 1D and (c) 2D particle load distribution models (cont'd)

Percentage relative errors for the incident wall heat fluxes and source terms with corresponding CPU times are given in Table 6.12 for all three particle load distribution models. As can be seen from the table, errors decrease with number of grids at the expense of CPU times, which increase almost four-fold for the reference grid in all cases. Furthermore, it is found that CPU times increase about 10 folds from 0D to 2D particle load distribution model due to the increase in number of iterations required for convergence in MOL solution of DOM with non-uniform particle load. It is seen that obtaining a grid independent solution is possible with MOL solution of DOM while deploying a uniform grid structure when strongly non-uniform particle distribution (see Figure 5.16) is integrated into the RTE code. From the viewpoints of accuracy and computational economy, use of 23x385 control volumes with  $S_{12}$  approximation is found to be sufficient for the problem under consideration and therefore utilized in the rest of the present section.

Table 6.12 Effect of grid refinement on predictive accuracy and CPU efficiency

Number of Control volumes	<b>0D Model</b>		
	Average % Error		<b>CPU Time(s)</b>
	<b>Incident Heat Flux</b>	<b>Source Term</b>	
<b>17x305</b>	6.4	-21.1	164
<b>19x325</b>	4.4	-14.1	221
<b>21x350</b>	2.7	-8.2	290
<b>23x385</b>	1.3	-3.8	574
<b>25x425</b>	Reference		663
Number of Control volumes	<b>1D Model</b>		
	Average % Error		<b>CPU Time(s)</b>
	<b>Incident Heat Flux</b>	<b>Source Term</b>	
<b>17x305</b>	5.0	-7.4	650
<b>19x325</b>	3.4	-5.0	875
<b>21x350</b>	2.1	-2.9	1195
<b>23x385</b>	1.0	-1.3	2027
<b>25x425</b>	Reference		2575
Number of Control volumes	<b>2D Model</b>		
	Average % Error		<b>CPU Time(s)</b>
	<b>Incident Heat Flux</b>	<b>Source Term</b>	
<b>17x305</b>	9.0	-13.1	2216
<b>19x325</b>	6.3	-8.8	3761
<b>21x350</b>	3.9	-5.3	3963
<b>23x385</b>	1.8	-2.4	6087
<b>25x425</b>	Reference		7167
Number of Iterations in MOL of DOM	<b>0D Model</b>	<b>1D Model</b>	<b>2D Model</b>
	2	5	16
* Errors are with respect to the predictions of the reference case with 25x425 grid resolution.			

## 6.4.2 Effect of Particle Load Distribution on Radiative Heat Transfer

Particle radiation is of key importance in radiative heat exchange between particle laden flue gas and heat transfer surfaces due to its dominant share in total radiation while a major factor affecting the particle radiation is the particle load. This is why it is considered necessary to investigate the predictive accuracy and computational efficiency of 0D and 1D approximations of particle load distribution by benchmarking their predictions against those of 2D approximation represented by a semi-empiric correlation developed for a wide range of operating conditions and systems.

In this section, effect of particle load variations within the CFBC riser on incident wall heat fluxes and source terms is demonstrated. As can be seen from Figure 6.17, neither of the approximations (0D, 1D) can give satisfactory results. Both models over-predict the heat fluxes in both splash and dilute zones, where the discrepancy in 0D approximation is larger.

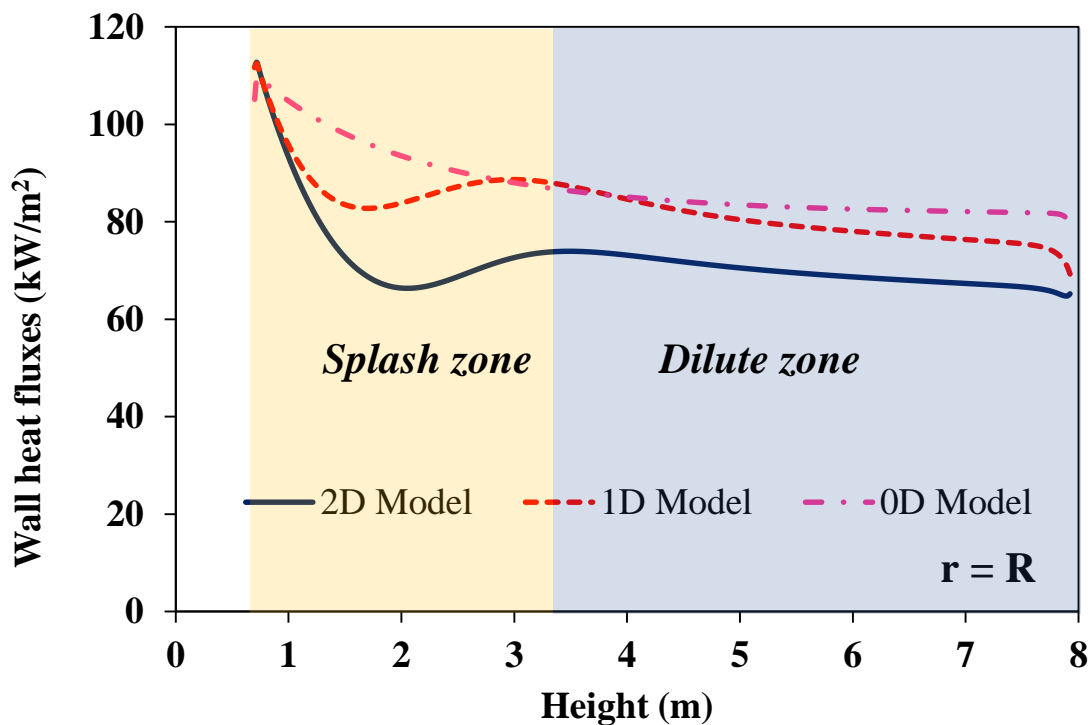


Figure 6.17 Effect of particle load distribution on incident wall heat fluxes

The percentage relative errors in the incident heat fluxes are given in Table 6.13. It is seen that increase in the amount of particles around the walls with the 2D model (Figure 5.16) leads to a thicker radiation shield between the hot particle laden flue gas and the walls hence decreases the radiative wall heat fluxes in both splash and dilute zones. Axial particle load distribution used in 1D model (Figure 5.15) yields a similar heat flux distribution trend compared to that of benchmark solution yet still over-predicts the heat fluxes due to cross-sectional averaging of the particle load, which under predicts the particle loads near the wall ( $r \rightarrow R$ ). On the other hand, 0D model cannot even capture the trend due to its low particle load, which gives superficially reduced radiation blockage between the particle laden flue gas and cold walls.

Table 6.13 Effect of particle load on incident heat fluxes

Zone	% Relative Error*	
	0D Model	1D Model
Splash	-27.3	-18.2
Dilute	-19.6	-14.3
* Errors are with respect to the predictions of the reference case, 2D Model		

Figure 6.18 shows the source term distribution against radial distance at six axial locations for the three particle load models. Predictions obtained by the 2D model reveal that at the beginning of the splash zone where the particle load is high (1 m), emitted particle radiation is immediately absorbed by the surrounding particles at very high particle loads, which leads to zero source terms near the centerline ( $r \rightarrow 0$ ). On the other hand, higher particle loads present near the wall ( $r \rightarrow R$ ) together with the cold wall effect (that is; wall emits much less radiation due to its lower temperature, see Figure 5.11) result in positive source term predictions. This trend in source term predictions, a constant source term near the centerline ( $r \rightarrow 0$ ) followed by a quadratic increase towards to the wall ( $r \rightarrow R$ ), is continued up to the end of the dilute zone. With 1D particle load model, zero source term predictions near the centerline ( $r \rightarrow 0$ ) are accurately represented in the splash zone while

0D model predictions are incorrect. In 1D model, source terms distribution profile of the 2D model (a constant source term near the centerline ( $r \rightarrow 0$ ) followed by a quadratic increase towards to the wall ( $r \rightarrow R$ )) is not observed along the dilute zone due to the negligence of radial variation in particle load. Interestingly, 0D model yields quite similar source term profiles compared to those of 2D model in the dilute zone. The reason behind this similarity is considered to be due to the decrease in particle load in dilute zone relative to the splash zone (see Figure 5.16), which leads to decrease in both particle emission and absorption. In other words, both emission and absorption terms, difference of which constitutes the source term, are reduced by the same factor with the decreasing particle load.

In Figure 6.19, source term distributions against axial distance at six radial locations are shown for the three cases. It is seen that axial source term distributions demonstrate three distinct regions. In the first half of the splash zone, radiative source terms are found to be zero regardless of the radial position due to very high particle loads. The only exception for this extinction phenomenon is the region which is very close to the cold walls. This finding is also in agreement with the sharp decrease in the wall heat flux up to 2 m; that is, hot center region ( $r \rightarrow 0$ ) cannot exchange radiation with the wall as the emitted particle radiation is immediately absorbed by the surrounding particles at this high particle load (Figure 6.17). In the second half of the splash zone (2-3.3 m), where a very sharp decrease in particle load is observed (Figure 5.16), a transition region occurs. Here, the source terms are found to follow the reciprocal of the particle load profile and increase as the particle load decreases. In the dilute zone (3.3-8 m), source term distribution near the centerline ( $r \rightarrow 0$ ) remains constant where the slight decrease in particle load (Figure 5.16(b)) is compensated by the increasing difference between the medium and wall temperatures (Figure 5.11). On the other hand, sharper decay in particle load near the wall ( $r = 5R/6$ , Fig. 5(b)) results in a local maximum and a decreasing source term trend.

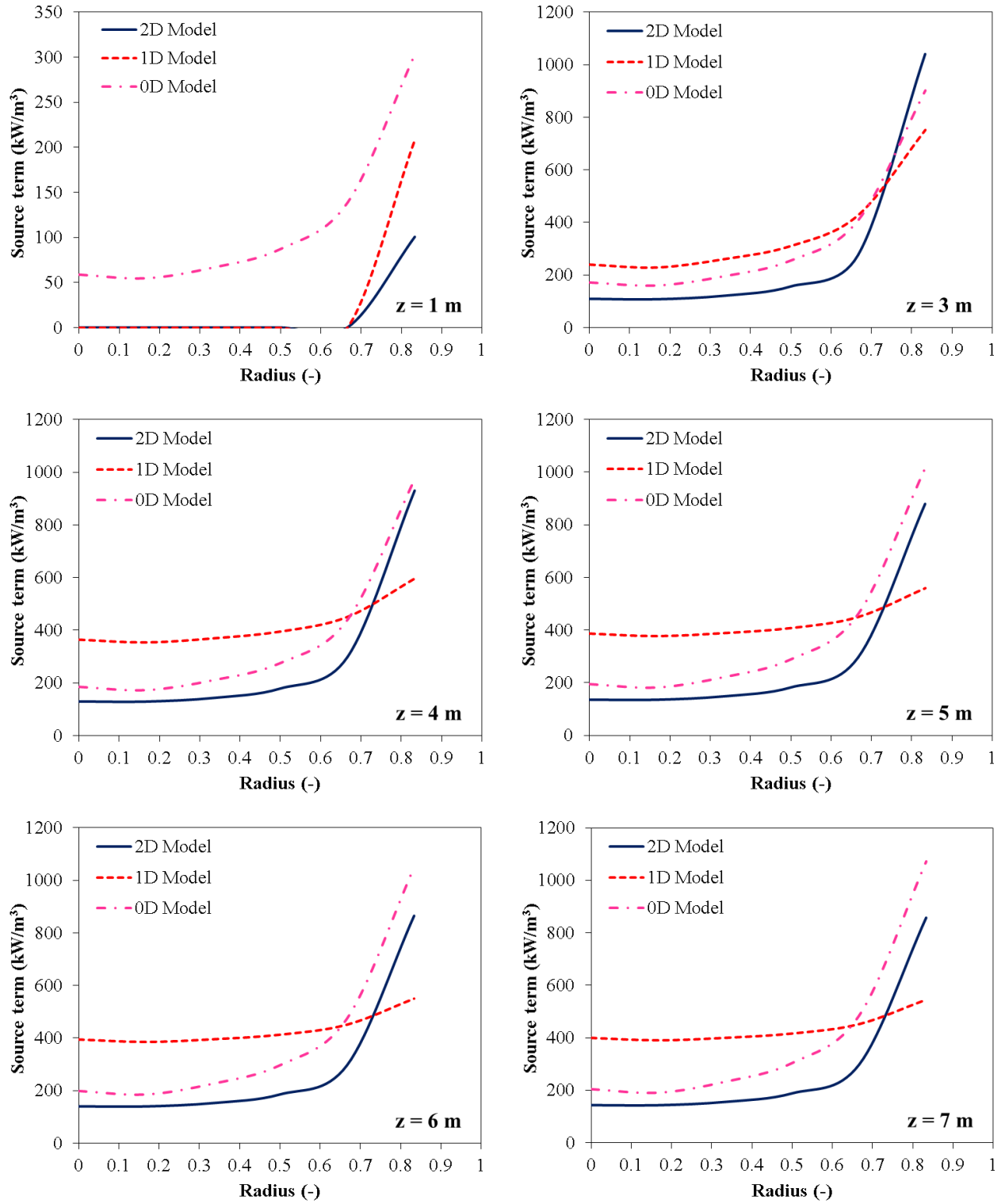


Figure 6.18 Effect of particle load on radial source term distributions

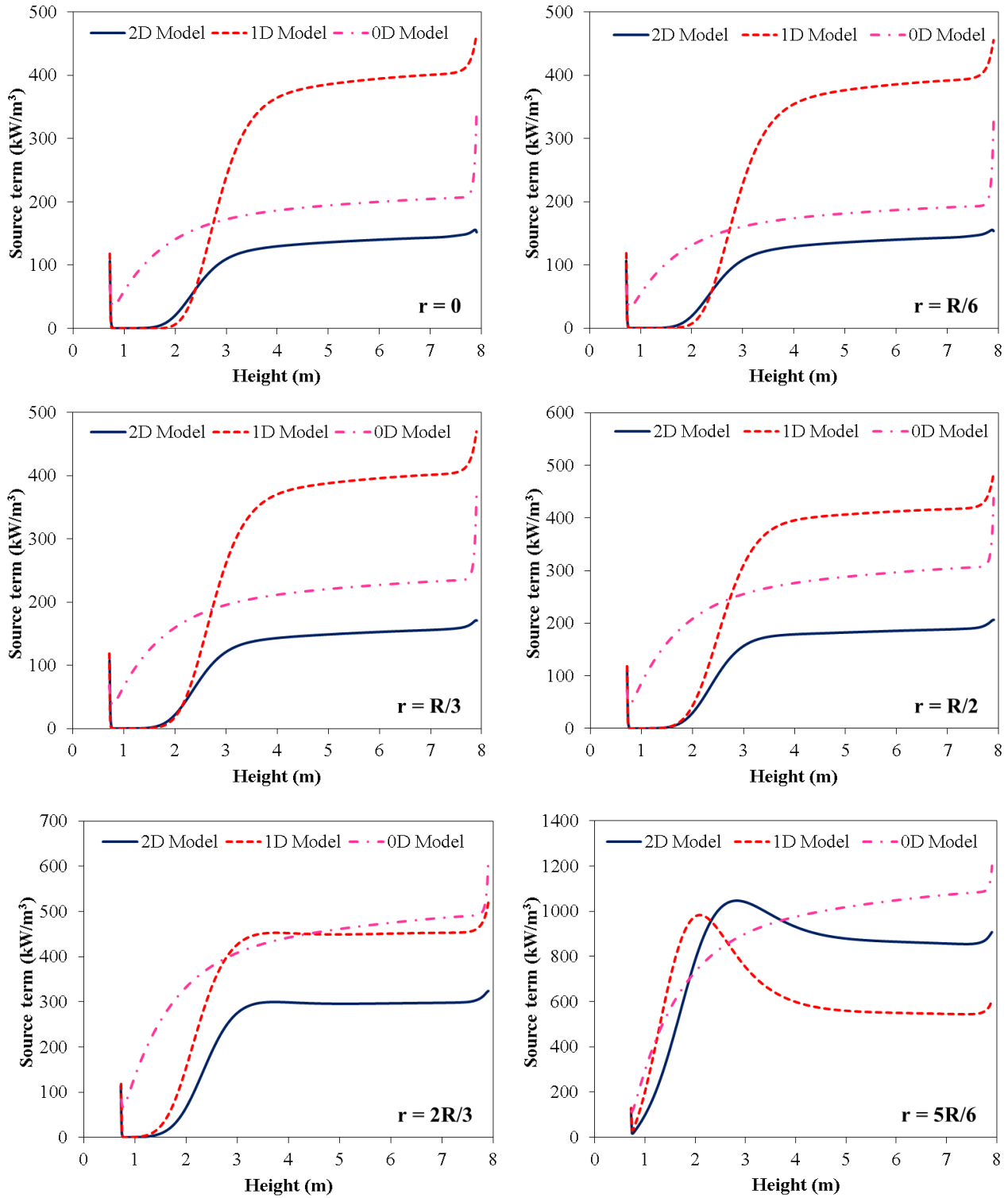


Figure 6.19 Effect of particle load on axial source term distributions



Comparisons between the model predictions reveal that neither of the approximations can give satisfactory results. In the first half of the splash zone, 0D model gives significant errors and cannot capture the physical phenomenon as it assumes a very low particle load, which leads to superficially reduced radiation blockage. Although 1D model can accurately represent the source term distribution near the centerline of the splash zone, discrepancy becomes significant near the wall ( $r \rightarrow R$ ) where 1D model underestimates the particle load. Moreover, both 0D and 1D models over-predict the axial source term distributions in the second half of the splash zone and the dilute zone, where the error in 1D model predictions is much greater. The reason behind this tremendous error is considered to be due to the over-estimated particle load near the centerline ( $r \rightarrow 0$ ) caused by the inherent cross-sectional averaging of the particle load distribution deployed in the model. On the contrary, 0D model can achieve higher accuracy as 0D model underestimates both emissions and incident radiation by decreasing the particle load. Furthermore, cold wall effect is found to be more dominant in 0D model due to its superficially low particle load, which creates an increasing source term profile independent of the radial position, while particle-particle radiative exchange is dominant in 1D and 2D models. This dominant effect is seen best at  $r = 5R/6$ , where the source term decreases with decreasing particle load along the riser.

The percentage relative errors<sup>6</sup> in the source terms at several radial distances and heights are given in Table 6.14. As can be seen from the table, 1D model gives better accuracy in the regions where particle load is high. On the other hand, 0D model is more successful in the dilute zone where the particle load is low. Furthermore, errors in source term predictions do not vary significantly in axial direction while there is a notable change in the radial direction along the dilute zone. Nevertheless, errors in source term predictions introduced by simplifying the particle load distribution via deploying 0D and 1D models are significantly large. Therefore, rigorous evaluation of particle load distribution in both

---

<sup>6</sup> It should be noted that absolute relative percentage errors between  $r = 0$  and  $2R/3$  at 1 m is calculated with respect to the average source term in the splash zone given by 2D model. The reason to consider this average value for the comparison is to avoid the large influence of the near zero source terms in error predictions in that region.

axial and radial directions is essential for accurate prediction of radiative heat fluxes and source terms under CFBC conditions, despite its high CPU requirements.

Table 6.14 Absolute percentage relative errors in the source terms at various axial and radial positions

<b>1D Model</b>						
	z = 1 m	z = 3 m	z = 4 m	z = 5 m	z = 6 m	z = 7 m
r = 0	0	119	181	184	182	180
r = R/6	0	112	174	177	176	174
r = R/3	0	115	159	161	159	157
r = R/2	0	98	121	123	123	122
r = 2R/3	0	55	51	52	52	52
r = 5R/6	107	28	36	36	36	36
<i>Radially Av. % Error</i>	18	88	120	122	121	120
<b>0D Model</b>						
	z = 1 m	z = 3 m	z = 4 m	z = 5 m	z = 6 m	z = 7 m
r = 0	37	57	44	43	43	43
r = R/6	34	49	34	34	33	33
r = R/3	42	61	48	48	49	49
r = R/2	55	63	55	58	60	61
r = 2R/3	87	48	48	56	60	63
r = 5R/6	201	13	5	16	21	25
<i>Radially Av. % Error</i>	76	49	39	42	44	46

## 6.5 Effect of Limestone Addition on Radiative Heat Transfer

FBCs are widely used for combusting low quality fuels like lignite, which is not only the world's most abundant fossil fuel but also one of the two major indigenous sources of energy in Turkey with an estimated quantity of 15.6 billion tons of reserves [2]. A major proportion of this quantity is characterized by its high sulfur content, which makes in-situ desulfurization hence the presence of limestone particles in the combustor an inevitable part of the application.

Despite its role in the FBC applications, effect of limestone addition on radiative heat transfer has received little attention even though much effort has been placed in understanding the radiative heat transfer in FBCs. In fact, there is only one study available in the literature reported by Filla and Scalabrin [151], who studied the emissivity of the particles in the freeboard of a 1 MW<sub>t</sub> FBC with coal and limestone feeding and found that optical properties of the particle cloud does not change with limestone addition. Although this technology is regarded as a mature technology for in-situ desulfurization, there is still a lack of research addressing the influence of limestone addition together with biomass co-firing on radiation heat exchange taking place between the particle laden combustion gases and the heat transfer surfaces.

To address this need, influence of limestone addition on radiative heat transfer during co-firing of high-sulfur content lignite with/without olive residue is investigated. Investigation is performed through mathematical modeling by using the experimental data on four combustion tests previously performed in 300 kW<sub>t</sub> ABFBC test rig. Selected combustion tests are the followings: lignite only, lignite with limestone addition and lignite with 30 and 50 wt % shares of olive residue in the fuel mixture with limestone addition for the same Ca/S ratio (see Section 5.1.2). These combustion tests will be referred as Test 1-4, respectively. In the radiation models, freeboard is treated as a 3D rectangular enclosure containing gray, absorbing, emitting gas with gray absorbing, emitting, anisotropically scattering particles surrounded by black/gray diffuse walls (Section 5.1.3). Radiative properties of the particle laden combustion gases are evaluated by using Leckner's correlations (Section 3.2) and Mie theory (Section 4.1.3), respectively.

In Mie calculations, Goodwin's correlations (Section 4.4) are employed to estimate spectral RI of particles collected from the cyclone and bag filter as a function of wavelength and chemical composition (Table 5.9). Non-gray particle properties are then used to evaluate gray Planck mean particle properties (see Appendix F). The main reason behind using Goodwin's correlations is the fact that there is no experimental study available in the literature on the optical constants of mixtures constituted by limestone and ash particles. Nevertheless, chemical analysis of the particles collected from the cyclone and the bag filter (Table 5.9) reveal that most influential components on both refractive and absorption indices are common and compositions of the collected samples are similar to those of Goodwin. Furthermore, it has been previously shown that limestone and biomass ashes have similar optical properties to that of coal ashes [45, 152]. Hence, optical constants data provided by Goodwin is considered to be applicable in this study. In MOL solution of DOM, a combination of  $S_{10}$  and  $13 \times 13 \times 96$  grid structure is utilized which was found to provide accurate and CPU efficient solutions in a previous grid refinement study [150]. For the difference relations of spatial derivatives, two-point upwind differencing scheme DSS012 is employed.

### **6.5.1 Effect of Limestone Addition on Radiative Properties of the Particle Cloud**

Spectral refractive ( $n$ ) and absorption ( $k$ ) indices calculated from Goodwin's correlations (Appendix C) are illustrated in Figure 6.20 and Figure 6.21. As can be seen from Figure 6.20, refractive index is almost constant about 1.7 between 0- 10  $\mu\text{m}$  for all cases, which covers 95 % of the thermal radiation and only slight differences are found between the samples collected from the cyclone and baghouse filter (see Table 5.9). These findings are in agreement with refractive indices reported in the literature for separate coal ash and limestone particles [39, 151, 152]. Therefore, it can be stated that presence of limestone / biomass ash particles does not affect the refractive index of the particle cloud significantly.

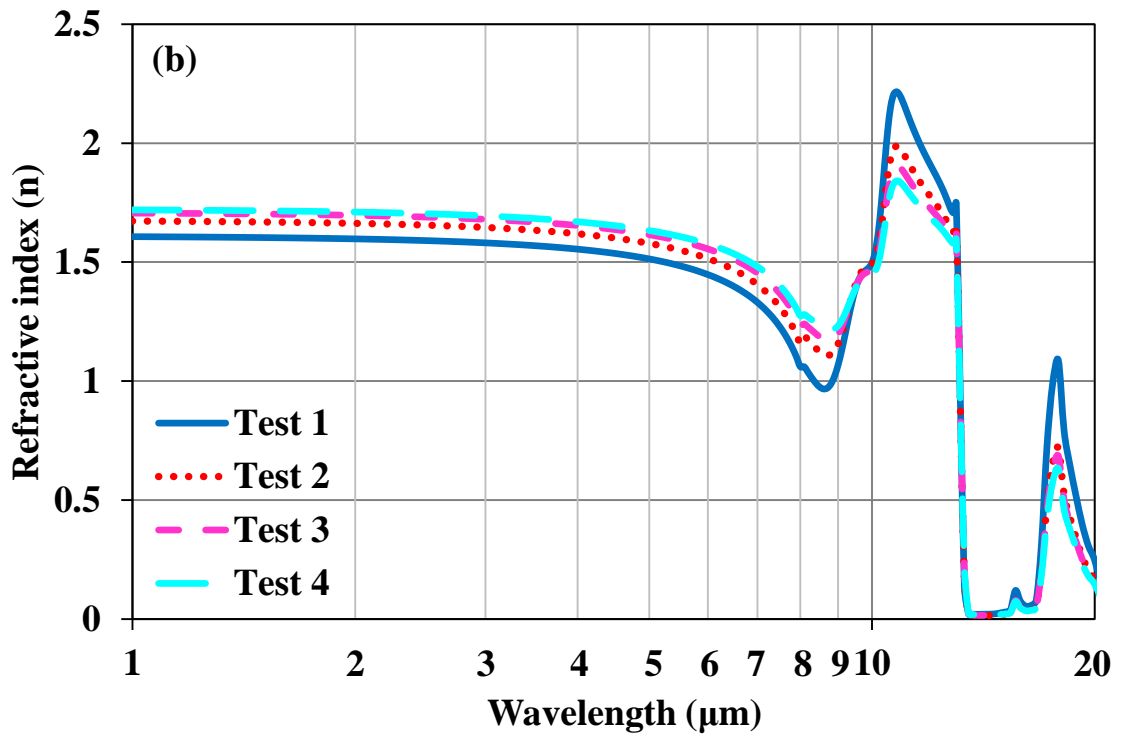
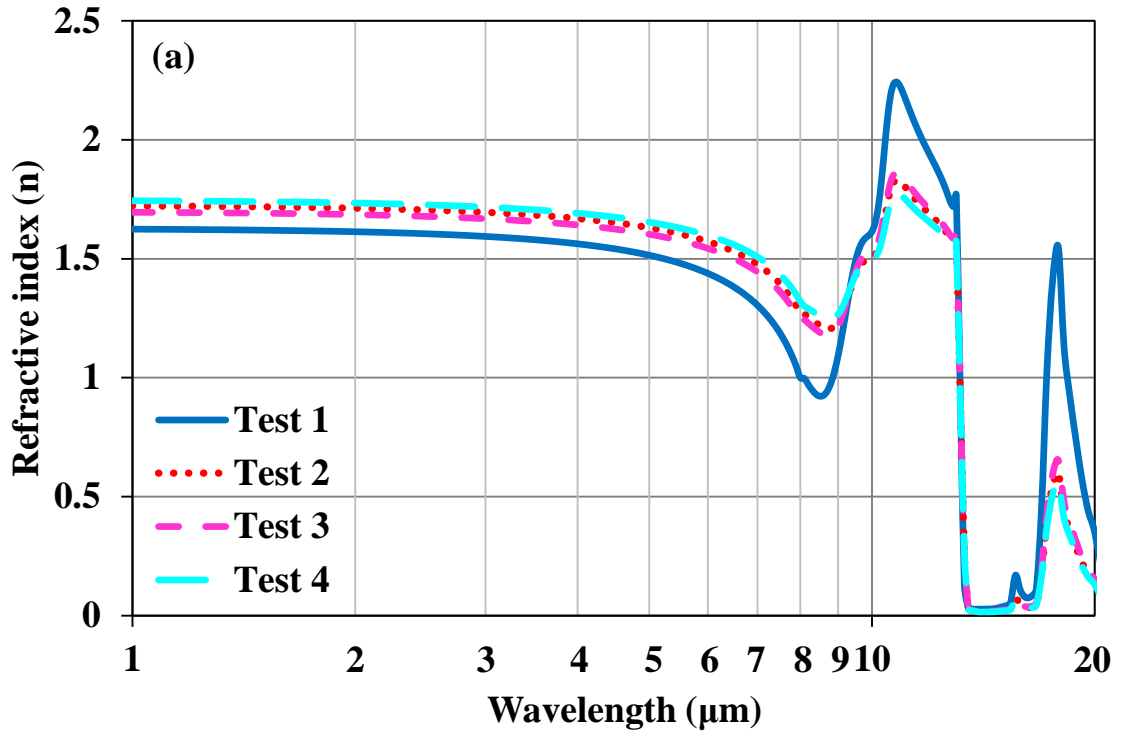


Figure 6.20 Spectral refractive indices for (a) cyclone and (b) baghouse filter particles

On the other hand, comparisons between the absorption indices of the solid samples collected from the cyclone reveal that limestone addition has a noticeable influence on the absorption behavior of the particles (Figure 6.21(a)) by changing the chemical composition of the particle mixture. It is seen that (Table 5.9) limestone addition decreases both iron oxide and silicon oxide contents of the particles, which leads to a decrease in the absorption index in the iron oxide (0.7-4  $\mu\text{m}$ ) and silicon oxide (4-13  $\mu\text{m}$ ) absorption bands. At the long wavelength region (13-20  $\mu\text{m}$ ),  $\text{Al}_2\text{O}_3$  and  $\text{MgO}$  Reststrahlen absorption bands are evident for all cases, where decrease in  $\text{Al}_2\text{O}_3$  content with limestone addition results in a decrease in the absorption index. These differences between the absorption indices for Test 1-4 become much smaller for the particles collected from the baghouse filter (Figure 6.21(b)) due to little variations in the ash compositions (Table 5.9).

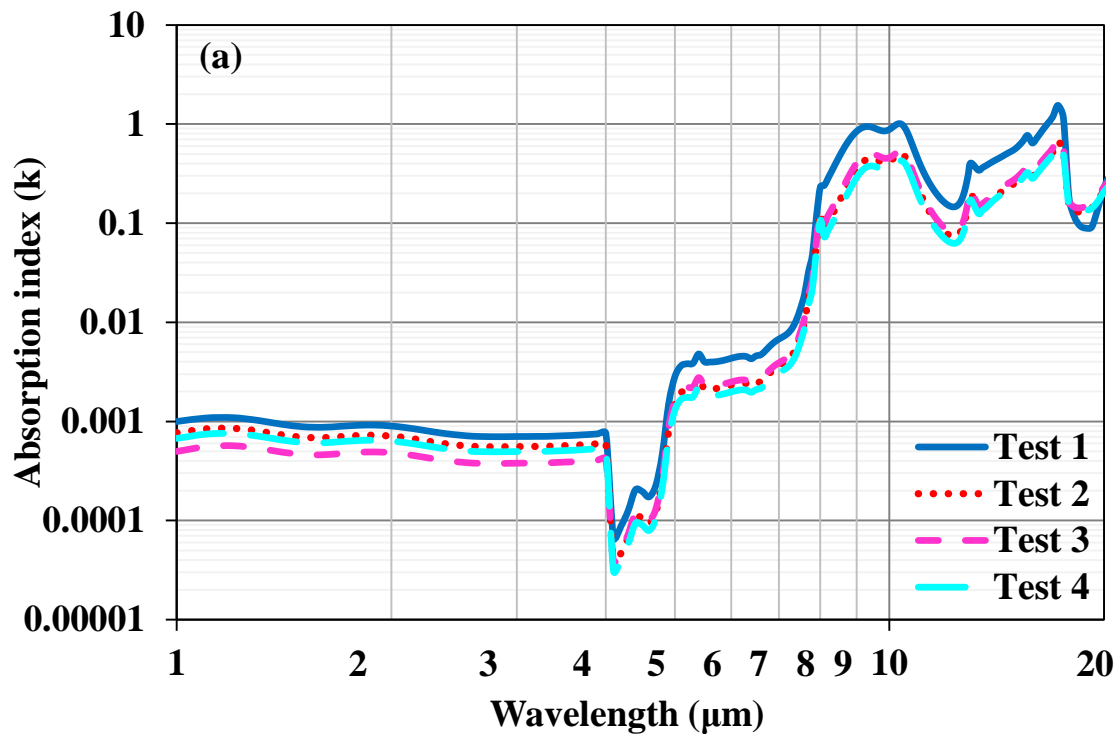


Figure 6.21 Spectral absorption indices for (a) cyclone and (b) baghouse filter particles

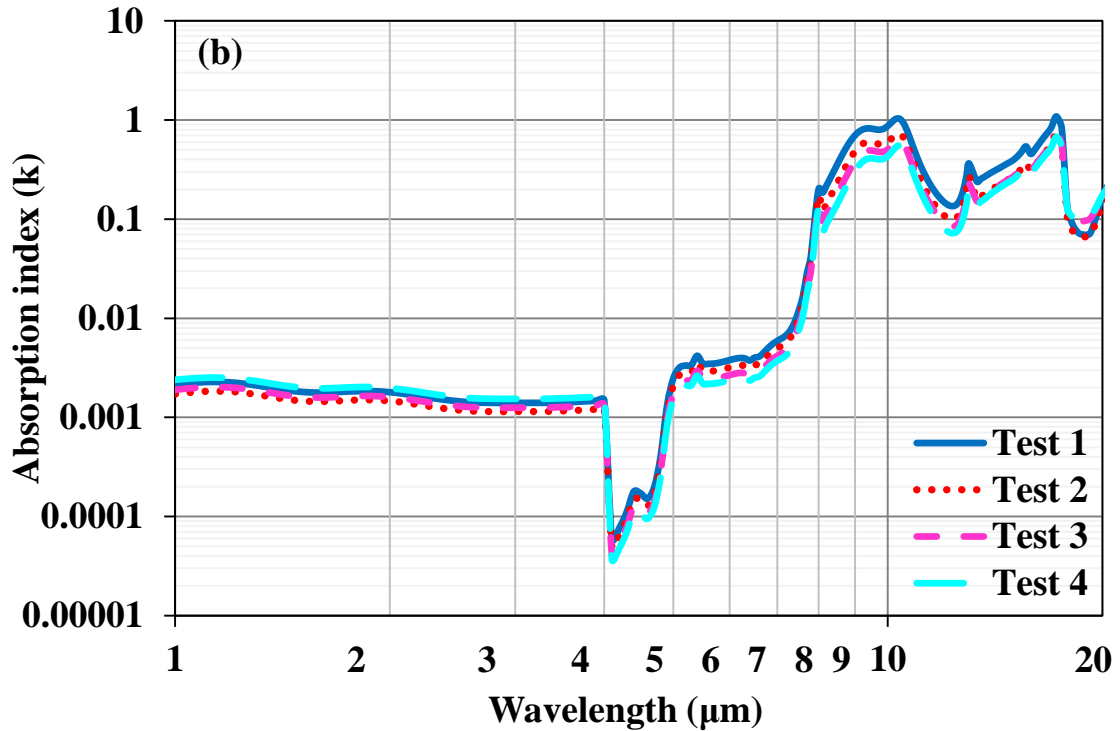


Figure 6.21 Spectral absorption indices for (a) cyclone and (b) baghouse filter particles (cont'd)

Radiative properties of the particle laden combustion gases and related parameters are summarized in Table 6.15. The most evident effects of limestone addition are the increase in the particle load (67 % increase from Test 1 to Test 2) and projected surface area of particles (183 % increase from Test 1 to Test 2). PSD comparison shows that all  $d_{32}$ ,  $d_{50}$  and  $d_{90}$  are decreased with the addition of limestone due to the decreasing size of the particles collected from the cyclone (Figure 5.6 (a)). Figure 6.22 demonstrates the cumulative cross sectional area distribution of particles for Test 1-4 with the corresponding number densities of each particle size in the PSD. As can be seen from the figure, number of fine particles increases significantly from Test 1 to Test 2 (Figure 6.22 (b)), which causes an increase in the cross sectional area constituted by these fine particles (Figure 6.22 (a)). It is also seen that projected surface area is decreased with the decrease in limestone share while it is increased with increasing biomass share, although it has a less strong impact on PSD (Table 5.7). The main reason behind these outcomes is

considered to be due to the decrease in particle sizes with limestone addition (Figure 5.6) and increase in the bag filter ash flow rate with the biomass addition (Table 5.7).

Effect of limestone addition due to the changes in particle size distribution and particle number densities is seen clearly in the calculated particle properties presented in Table 6.15. Absorption, scattering and extinction coefficients (hence the optical thickness) are found to follow the same trend with the total projected surface areas, which is a function of PSD, load and ratio of cyclone ash flow rate / bag filter ash flow rate. This finding is also supported with the increase in scattering albedo with limestone addition and with the decrease in asymmetry factor with biomass addition.

Therefore, it is concluded that addition of limestone to the fuel affects the radiative properties of the particles in the freeboard through the change of particle load and size distribution rather than optical properties of particles, considering the fact that both refraction ( $n$ ) and absorption ( $k$ ) indices do not vary significantly from one another up to 10  $\mu\text{m}$ , which covers the 95 % of the thermal radiation under FBC conditions.



Table 6.15 Radiative properties of particle laden combustion gases

	<b>Test 1</b>	<b>Test 2</b>	<b>Test 3</b>	<b>Test 4</b>
<b>Particle load, B (g/m<sup>3</sup>)</b>	9	15	10	9
<b>Particle density ( kg/m<sup>3</sup>)</b>	1202	1222	1347	1294
<b>Sauter mean diameter, d<sub>32</sub> (μm)</b>	22	13	13	10
<b>d<sub>50</sub> (μm)</b>	194	47	13	162
<b>d<sub>90</sub> (μm)</b>	464	283	446	446
<b>Projected surface area of particles (m<sup>2</sup>)</b>	0.6	1.7	1.1	1.4
<b>Absorption coefficient of the gas, κ<sub>g</sub> (m<sup>-1</sup>)</b>	0.49	0.53	0.55	0.57
<b>Absorption efficiency of the particle cloud*, Q<sub>a</sub></b>	0.36	0.31	0.25	0.27
<b>Scattering efficiency of the particle cloud*, Q<sub>s</sub></b>	1.12	1.19	1.12	0.99
<b>Absorption coefficient of the particles , κ<sub>p</sub> (m<sup>-1</sup>)</b>	0.22	0.53	0.27	0.39
<b>Scattering coefficient of the particles, σ<sub>p</sub> (m<sup>-1</sup>)</b>	0.68	2.03	1.23	1.41
<b>Extinction coefficient of the medium, β (m<sup>-1</sup>)</b>	1.39	3.09	2.05	2.37
<b>Scattering albedo of the medium, ω</b>	0.49	0.66	0.60	0.59
<b>Asymmetry factor, g</b>	0.48	0.47	0.42	0.39
<b>Optical thickness, τ</b>	0.53	1.17	0.78	0.90
* Efficiency values reported here are calculated as a weight averaged quantity based on cross sectional area of particles for the PSD given in Figure 5.6 and Figure 5.7. In κ <sub>p</sub> and σ <sub>p</sub> calculations, however, efficiencies are calculated for each particle size and κ <sub>p</sub> and σ <sub>p</sub> are found for the entire PSD accordingly.				

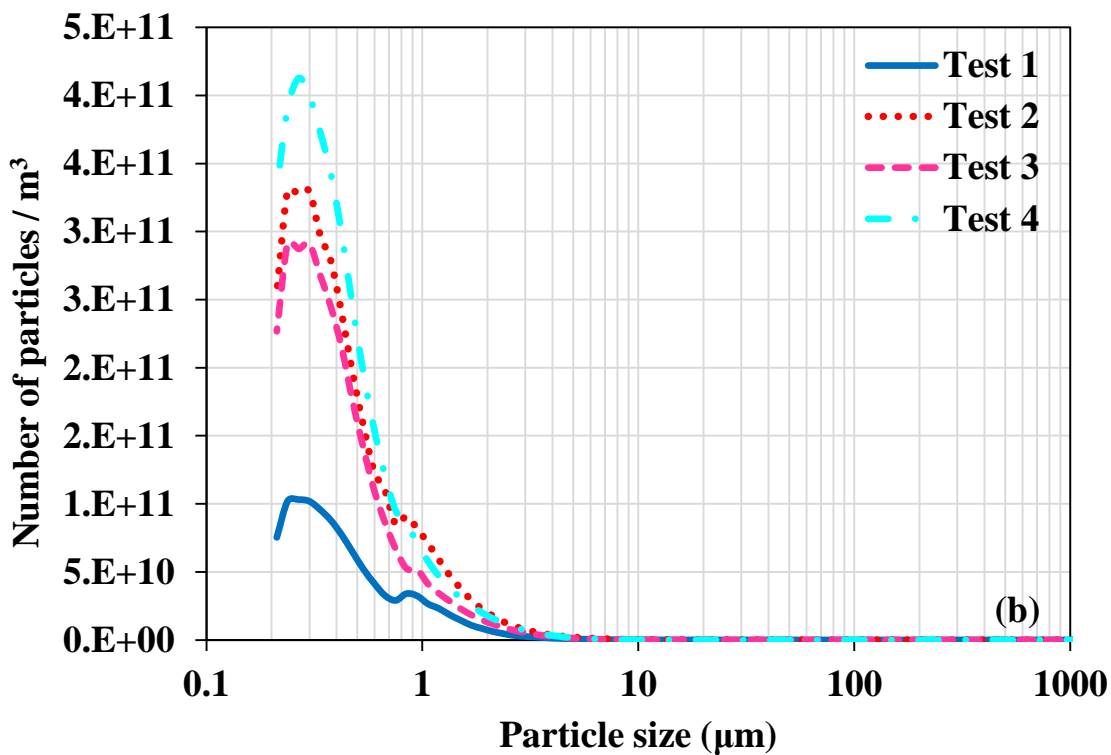
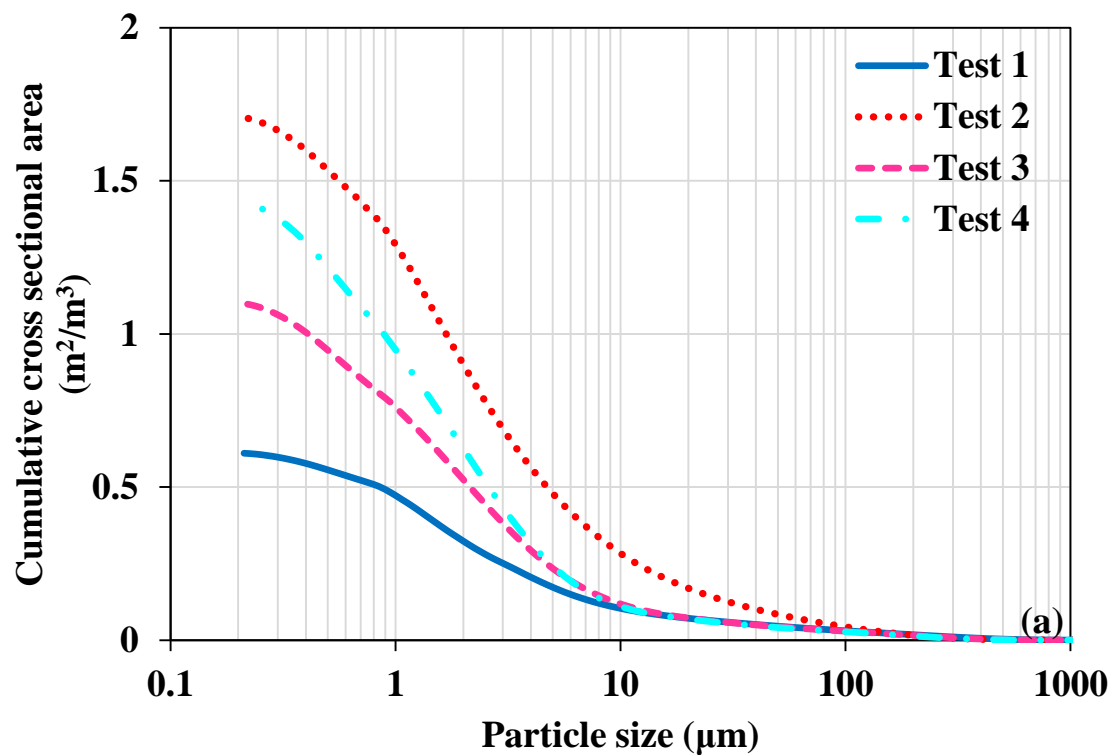


Figure 6.22 (a) Cumulative cross sectional area distribution and (b) particle number densities for Test 1-4

### **6.5.2 Effect of Limestone Addition on Radiative Heat Transfer**

Effect of limestone addition on incident heat fluxes along the side walls are shown in Figure 6.23. As can be seen from the figure, addition of limestone decreases the wall heat fluxes along the freeboard by increasing the optical thickness of the medium and decreasing the temperature of the particle laden flue gas due to endothermic calcination reaction (see Table 5.7). It is found that addition of limestone for sulfur capture causes 15.7 % reduction in average heat fluxes. This difference is found to be decreasing if the limestone share in solid input flow rate decreases while biomass share increases (Table 5.7); to 11.8 % and 5.7 % for Test 3 and Test 4, respectively (Figure 6.23). These results indicate that it is possible to increase wall heat fluxes in a FBC by co-firing with biomass containing virtually no sulfur.

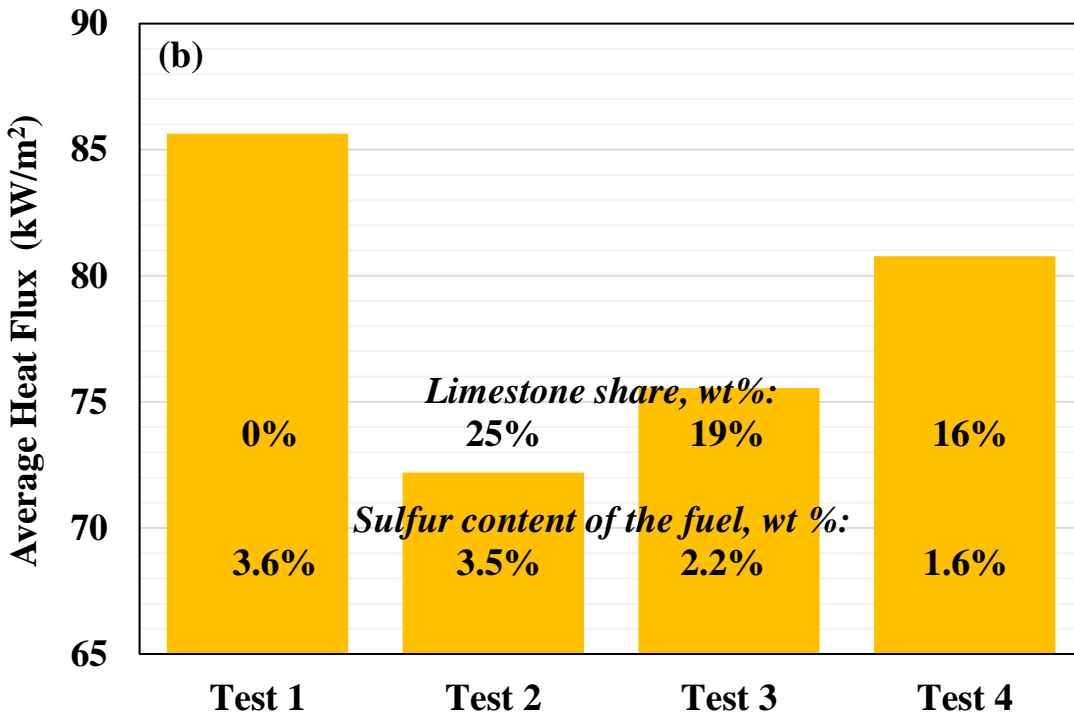
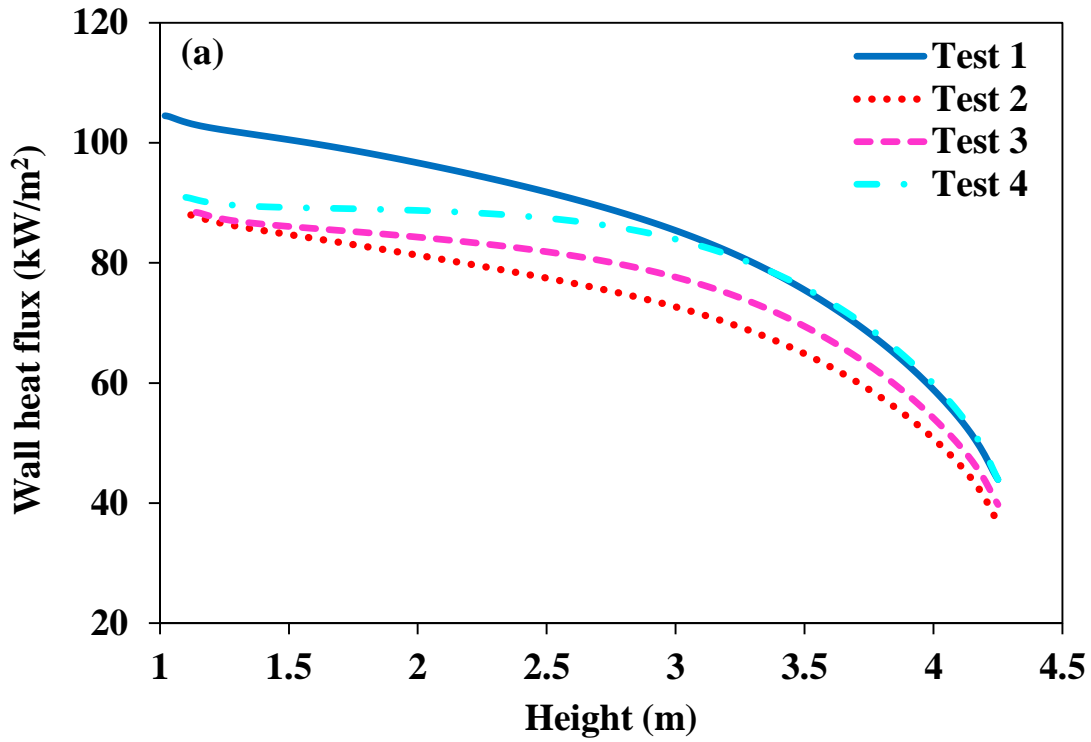


Figure 6.23 Effect of limestone share on (a) radiative incident wall heat fluxes and (b) heat fluxes averaged over the entire freeboard

Source terms along the centerline calculated for Test 1-4 are illustrated in Figure 6.24. It is found that source terms are not as much affected as the incident wall heat fluxes by limestone addition and differences in source term predictions are noticeable only around the boundaries of the freeboard. Slight differences at the bottom of the freeboard are considered due to the differences in bottom surface temperatures (Table 5.7), which is about 45 K lower in the combustion tests with limestone addition due to the calcination of limestone particles. On the other hand, increase in the source term around the top boundary for Test 2 and Test 4 is found to be due to increase in particle absorption coefficients with increasing projected surface area. Nevertheless, it should be highlighted that small variations in source term predictions might be due to high temperatures of refractory-lined freeboard walls and high surface to volume ratio ( $Surface\ area/Volume=9.4$ ) of the test rig where radiative heat transfer is expected to be dominated by walls rather than particle laden gas emissions. Therefore, variations in source term might be different from the findings at a lower surface to volume ratio / higher optical thickness.

To sum up, it is found that addition of limestone affects the radiative properties of the particles in the freeboard through the change of particle size distribution and load rather than optical properties. The increase in the amount of fine particles with limestone addition leads to a thicker radiation shield between the hot particle laden flue gas and the walls hence decreases the radiative wall heat fluxes along the freeboard. Source term predictions are not much affected as heat fluxes by limestone / biomass addition in the investigated combustion tests, probably due to the high surface to volume ratio of the test rig under consideration. Furthermore, incident wall heat fluxes can be increased by decreasing the sulfur content of the fuel blend by co-firing with biomass as less limestone is utilized in almost direct proportion to the coal replacement.

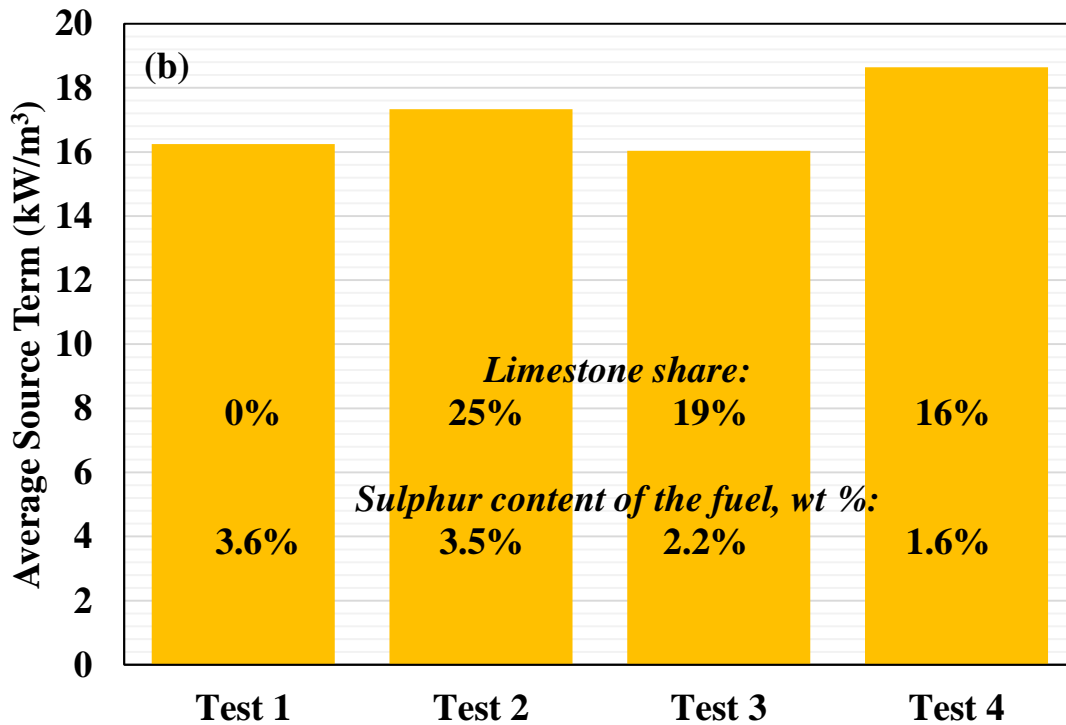
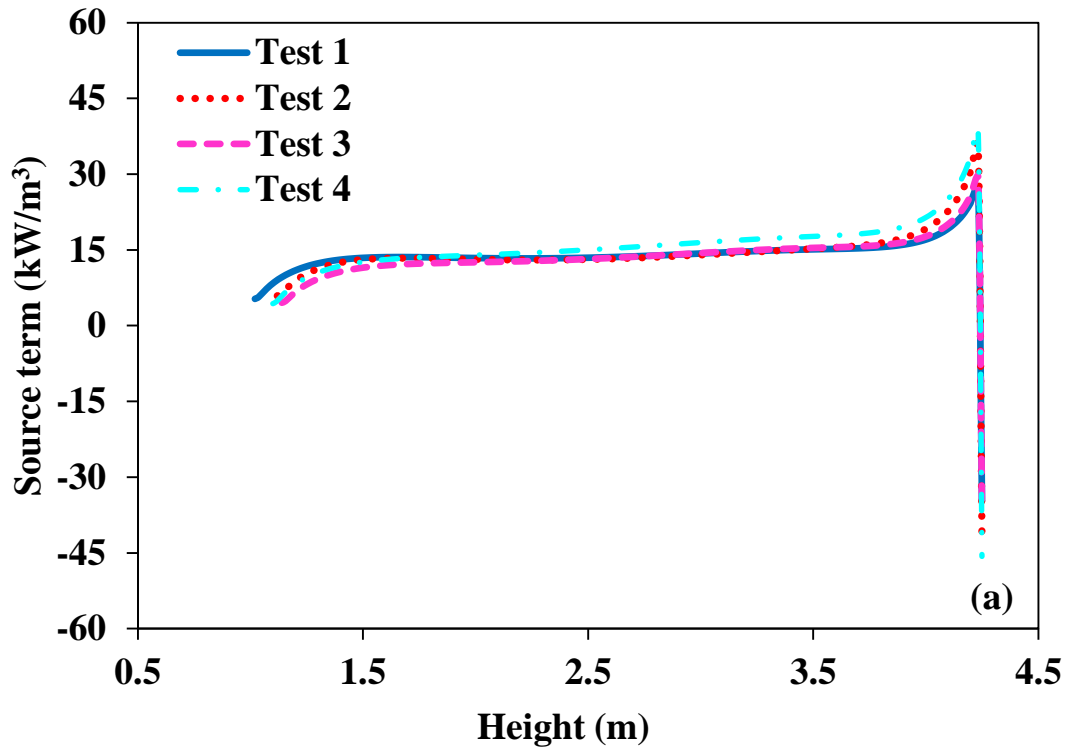


Figure 6.24 Effect of limestone share on (a) source terms averaged in cross sectional planes and (b) source terms averaged over the entire freeboard

## 6.6 Effect of Changing Biomass Source on Radiative Heat Transfer

Gradual introduction of increasingly restrictive legislations on emissions from combustion sources has been increasing the interest in biomass combustion. However, biomass combustion brings with it some operational problems when burned alone. The most common problems encountered in industry and utility boilers are severe fouling, slagging and corrosion. Co-firing biomass with coal is a promising alternative which leads to reduce ash related problems in biomass combustion and at the same time provides an economical and environmentally friendly use of coals by reducing pollutant emissions [8, 153, 154]. Nevertheless, there remain technical issues associated with biomass supply, handling and storage in co-firing applications due to its low energy density, seasonal characteristics and scattered geographical distribution [155, 156].

Biomass itself is usually cheap but the cost of transportation directly affects the economic feasibility of biomass co-combustion due to its low bulk density together with the high moisture content, which necessitates huge amounts of biomass to be transported for even a small share of total heat input [154]. Optimum biomass transport distances and means of transportation are shown to depend on the capacity of the power plant [155] and maximum distance over which biomass can feasibly be collected, which is found to be between 25 and 100 km for highway transportation [155, 157-160]. In particular, it has been shown that railway conveyance is needed if the capacity of the plant is larger than 5 MW<sub>e</sub> [155] to ensure economic and environmental feasibility, which may not always be accessible in the vicinity of the plant. One of the possible solutions to mitigate biomass shortages encountered at high plant capacities is having access to different biomass sources within the geological boundaries designated by logistic constraints.

Changing the biomass source, on the other hand, should not or at worst slightly affect the performance of the boiler. Heat transfer has always been an important parameter in the design, operation and optimization of industrial combustors with and without biomass co-firing [10, 161]. Recent studies in pulverized coal fired furnaces reveal that measured total / radiative heat fluxes are lower in the case of biomass co-firing compared to that of coal combustion under both air and oxy fired conditions and heat transfer to the walls decrease

with increasing biomass content of the fuel for the same thermal input [54, 55, 162-166]. This decrease is correlated to high moisture content of the biomass, however, significant differences in heat fluxes are still observed when the biomass moisture content is one third of the coal moisture content [165], indicating that high moisture content of the biomass particles cannot be the only reason for the decreased heat fluxes. In an experimental study, it is shown that number of fine particles increases logarithmically with increasing biomass share for constant thermal input while the mass concentration of particles remains the same for all cases from 0% coal to 100% coal [167]. This finding is confirmed by another study performed in a pilot scale fluidized bed combustor [168]. Considering the dominant role of particles in radiative heat transfer in combusting systems [56, 57, 146-149], understanding the change in number of fine particles as well as particle properties such as density and chemical composition with alternating biomass sources is of key importance.

Even though much effort has been placed in understanding the radiative heat transfer in FBCs, effect of biomass addition on radiative properties of particles has received little attention despite the important role of particles in radiative heat transfer. To address this need, effect of changing biomass source on radiative heat transfer during co-firing of high-sulfur content lignite is investigated. Investigation is performed through mathematical modeling by using the experimental data on six combustion tests previously performed in 300 kWt ABFBC test rig. Data on combustion tests were collected for lignite-limestone-biomass blends with different thermal shares of olive residue (OR) and hazelnut shells (HS) in the fuel mixture for the same Ca/S ratio (Section 5.1.2). These combustion tests will be referred based on the biomass source and its thermal share in the fuel mixture: OR 19 %, OR 36 %, OR 55 %, HS 14 %, HS 35 % and HS 50 %, respectively. In the radiation models, freeboard is treated as a 3D rectangular enclosure containing gray, absorbing, emitting gas with gray absorbing, emitting, anisotropically scattering particles surrounded by black/gray diffuse walls (Section 5.1.3). Radiative properties of the particle laden combustion gases are evaluated by using Leckner's correlations (Section 3.2) and Mie theory (Section 4.1.3), respectively. In Mie calculations, Goodwin's correlations (Section 4.4) are employed to estimate spectral RI of particles collected from the cyclone and bag filter as a function of wavelength and chemical composition (Table 5.9). RI calculated by Goodwin's correlations are used together with the PSDs (Figure 5.6, Figure 5.7) to predict



spectral absorption coefficient, scattering coefficient and asymmetry factors from the Mie theory. Gray particle properties are then calculated based on Planck's distribution from the spectral Mie solutions (see Appendix F). Particle properties are calculated up to 20  $\mu\text{m}$  as it is considered to be sufficient enough for the majority of thermal radiation in coal fired systems. In MOL solution of DOM, a combination of  $S_{10}$  and  $13 \times 13 \times 96$  grid structure is utilized which was found to provide accurate and CPU efficient solutions in a previous grid refinement study [150]. For the difference relations of spatial derivatives, two-point upwind differencing scheme DSS012 is employed.

### **6.6.1 Effect of Changing Biomass Source on Radiative Properties of the Particle Cloud**

Spectral refractive ( $n$ ) and absorption ( $k$ ) indices calculated from Goodwin's correlations (Appendix C) are illustrated in Figure 6.25 and Figure 6.26. As can be seen from Figure 6.25, refractive index is almost constant about 1.7 between 0- 10  $\mu\text{m}$  for all cases, which covers 95 % of the thermal radiation. Furthermore, it is seen that real part of the refractive index of coal ash / biomass ash- limestone mixture does not differ from one another despite the differences in biomass fuel ash at different shares of biomass in the fuel blend (See Table 5.6).

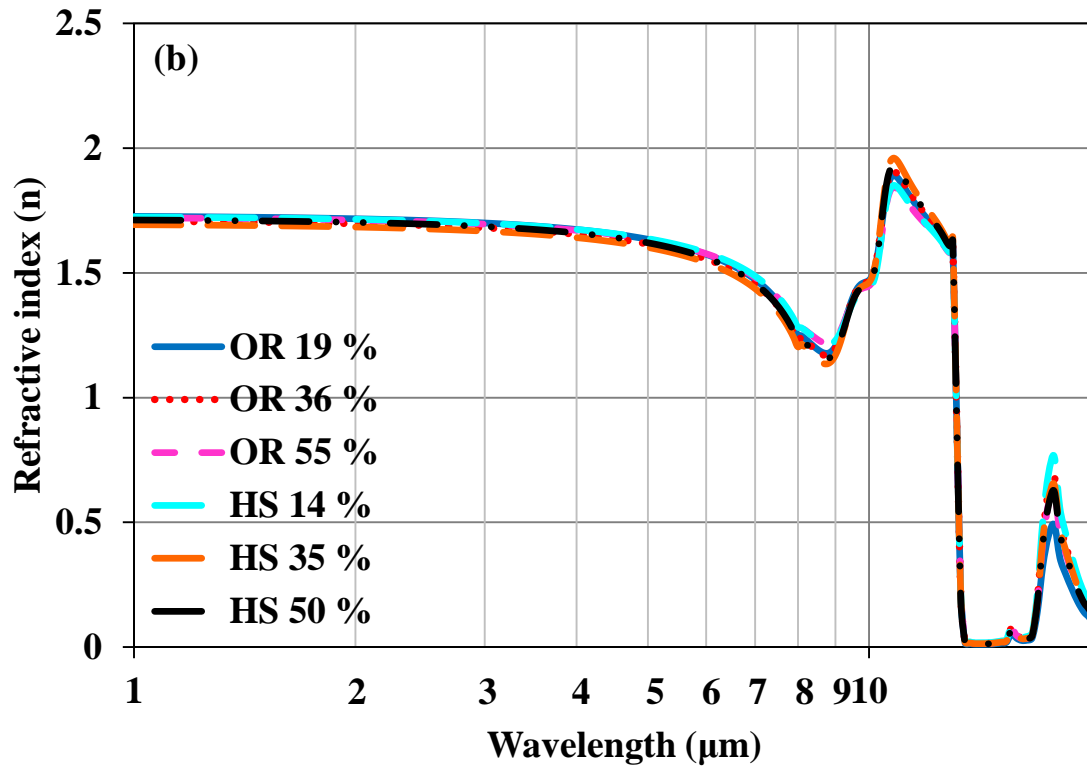
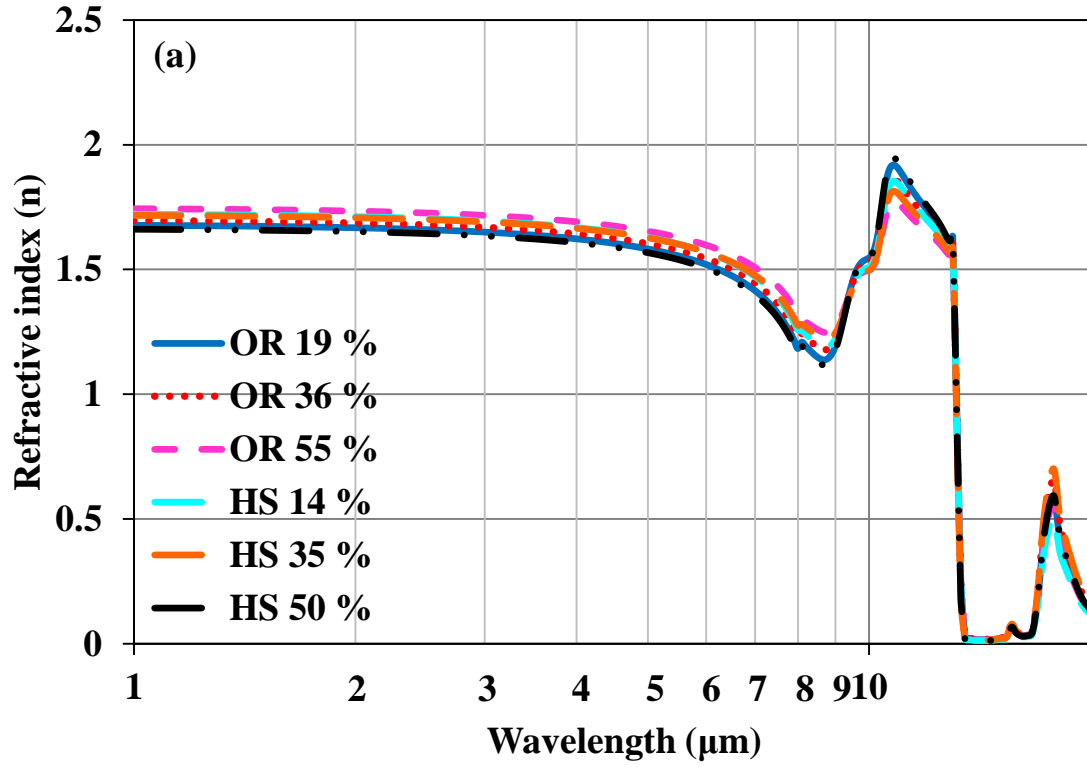


Figure 6.25 Spectral refractive indices for (a) cyclone and (b) baghouse filter particles

Figure 6.26 demonstrates that small differences in  $\text{Fe}_2\text{O}_3$  and  $\text{SiO}_2$  contents of particles lead to small variations in absorption indices up to  $13\ \mu\text{m}$ . For the low biomass share (Figure 6.26(a)), there are some differences in the magnitude of absorption index in the iron oxide absorption band ( $0.7\text{-}4\ \mu\text{m}$ ). Effect of  $\text{Fe}_2\text{O}_3$  content in this band can be seen more clearly for the 35 % biomass share (Figure 6.26(b)). Interestingly, absorption indices for HS co-firing is found to be higher than those of OR co-firing in the silicon oxide region ( $8\text{-}13\ \mu\text{m}$ ) at high biomass loads (Figure 6.26 (c)) despite the high silica content of the OR ash (Table 5.6). It is also seen that optical constants do not vary from one another at the long wavelength region. Regarding to optical properties of baghouse filter particles, differences in absorption indices are found to be insignificant in the entire spectrum for moderate and high biomass shares. (Figure 6.26 (e, f)).

When ash contents of the fuels are compared, it is seen that both olive residue and hazelnut shell have very low ash contents (4.2 and 1.5 wt %, respectively) compared to that of Çan lignite (24.7 wt %). Therefore, particles present in the freeboard are expected to be mainly constituted by the coal ash and limestone particles. This is why variations in chemical compositions of the solid streams (cyclone and baghouse filter) are found to be small (Table 5.9) compared to those of coal/biomass ash analysis (Table 5.6). Hence, chemical compositions as well as the optical properties of particles are dominated by ash and limestone particles and variations in refractive ( $n$ ) and absorption ( $k$ ) indices are found to be insignificant up to  $20\ \mu\text{m}$  between OR and HS co-firing cases for all biomass shares in the fuel blends.

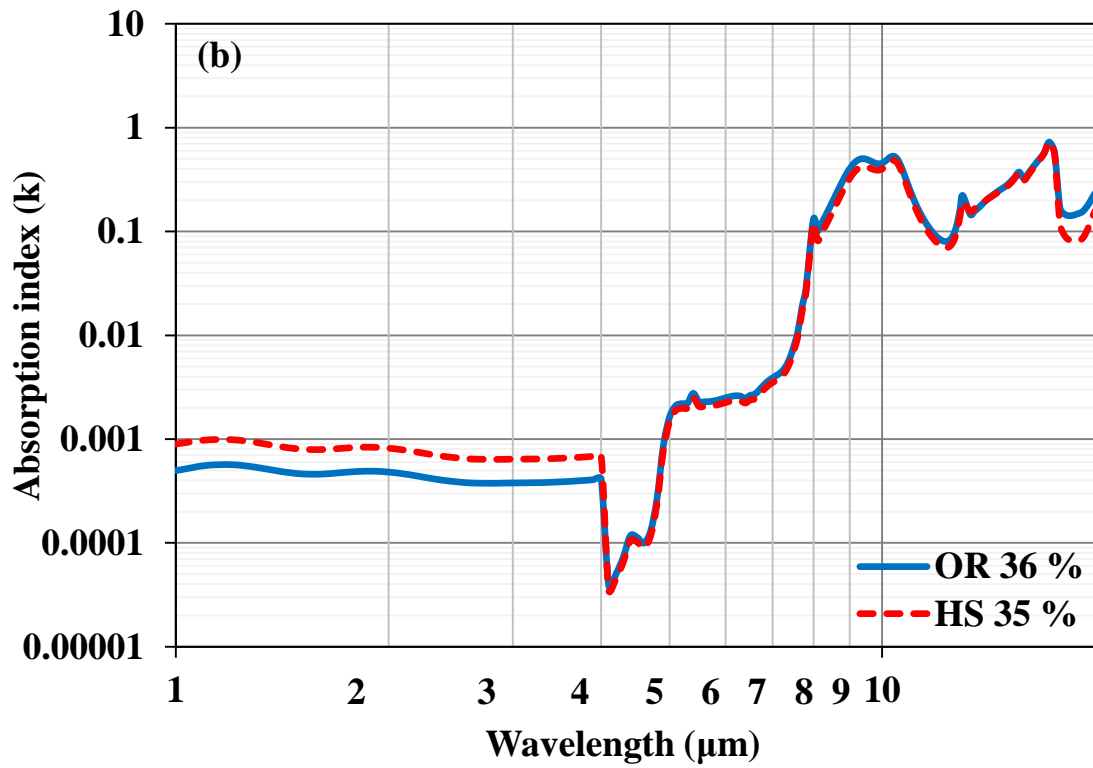
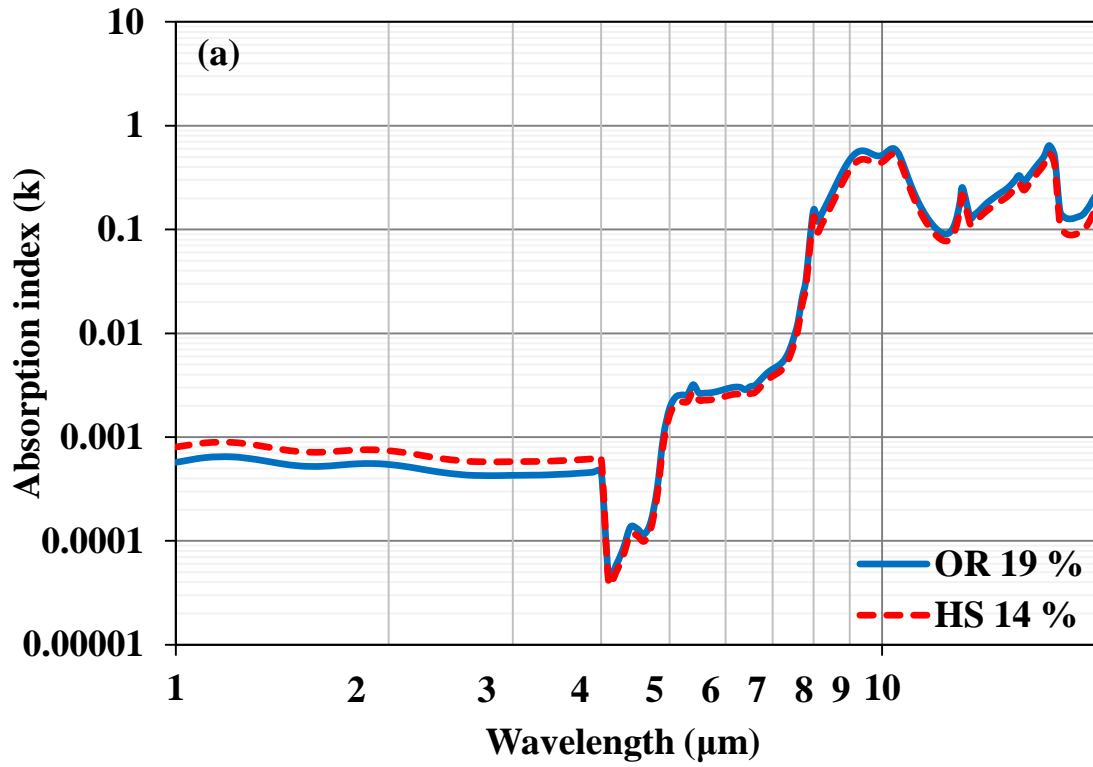


Figure 6.26 Spectral absorption indices for (a-c) cyclone and (d-f) baghouse filter particles

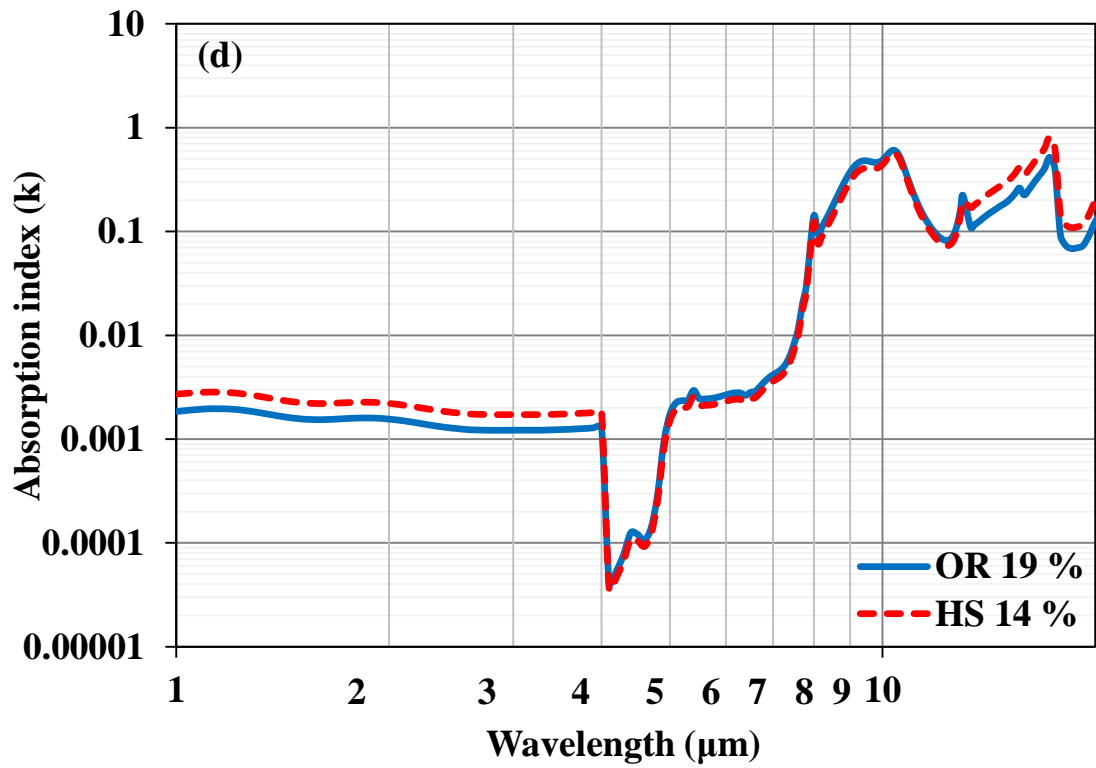
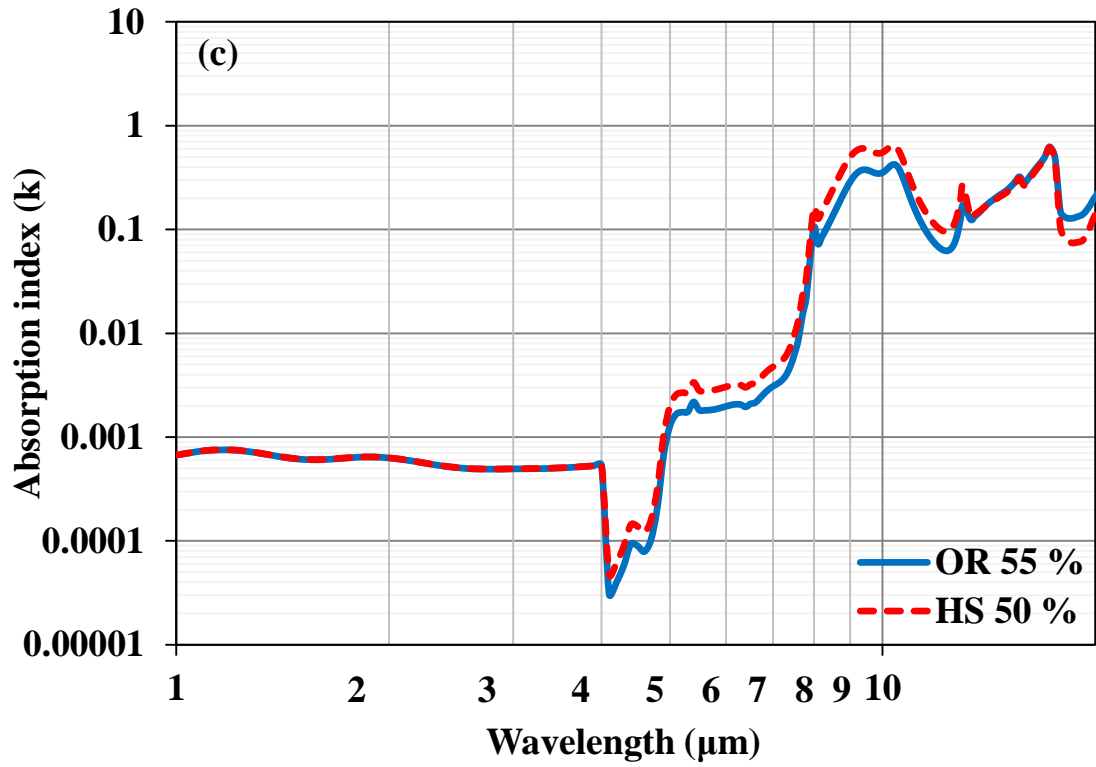


Figure 6.26 Spectral absorption indices for (a-c) cyclone and (d-f) baghouse filter particles (cont'd)

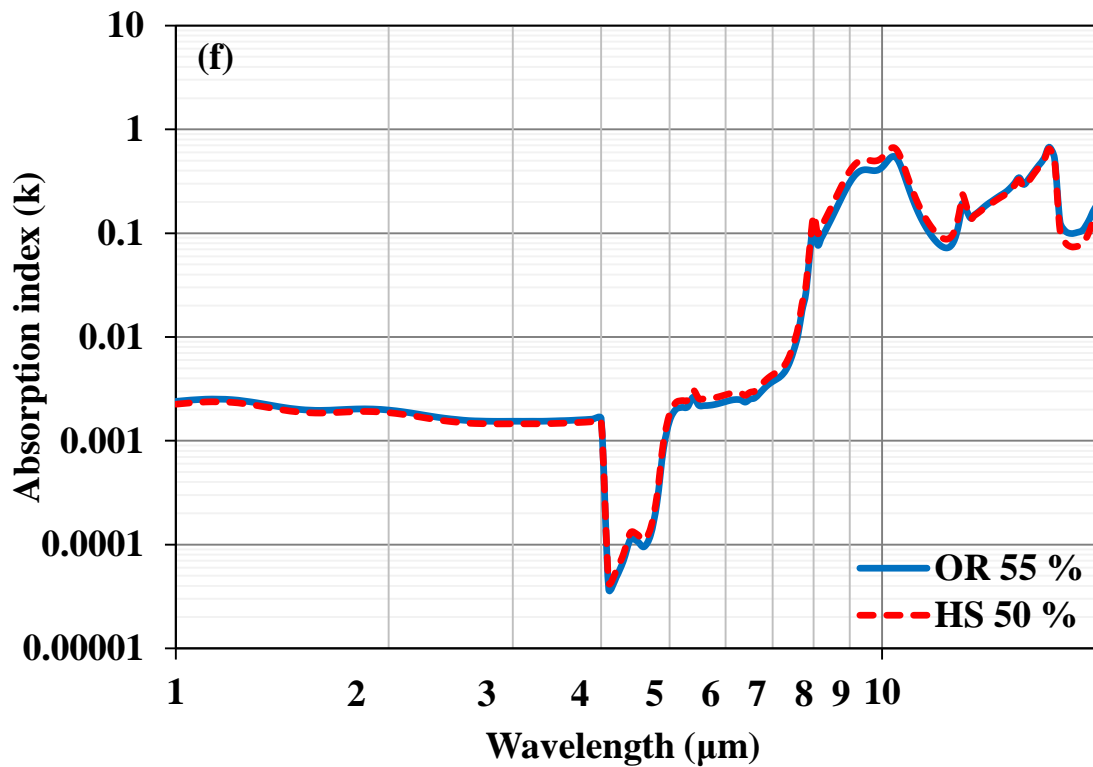
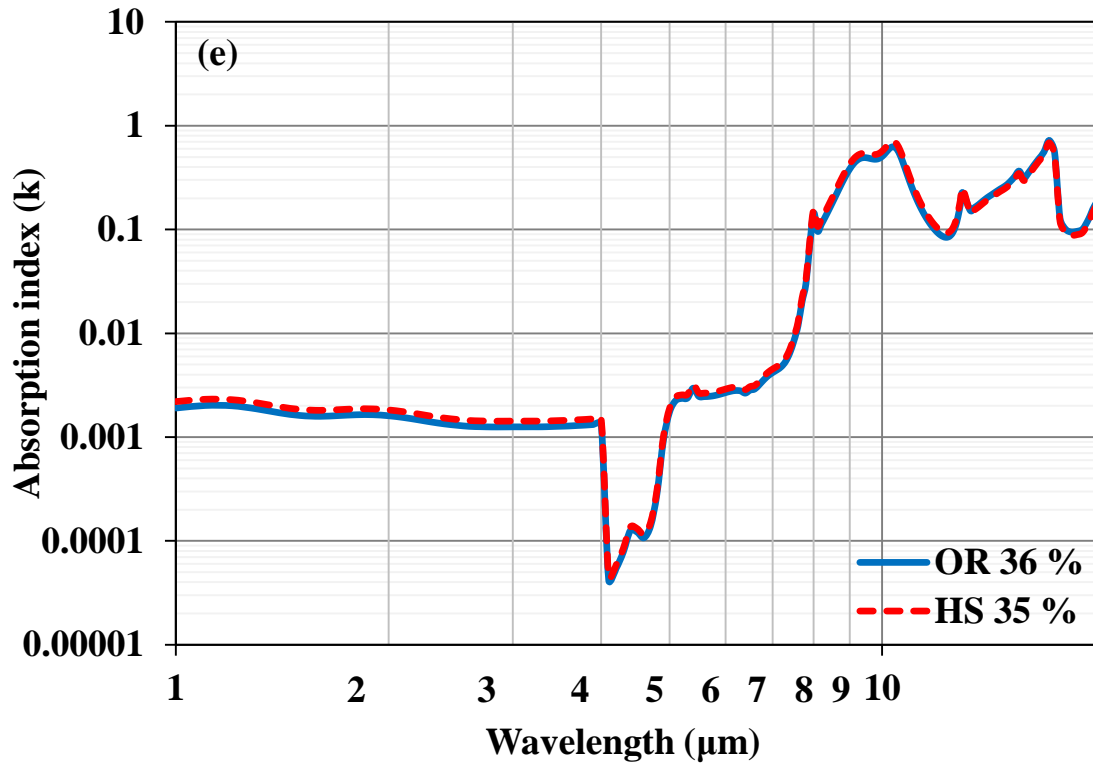


Figure 6.26 Spectral absorption indices for (a-c) cyclone and (d-f) baghouse filter particles (cont'd)

Changing the biomass source, on the other hand, is found to be influential on radiative properties, which are summarized in Table 6.16. It is found that changing the biomass feed from OR to HS directly affects the size distribution of particles in the freeboard, which is essentially one of the most important physical parameters determining the interaction between the particles and electromagnetic waves. PSD comparison reveals that all  $d_{32}$ ,  $d_{50}$  and  $d_{90}$  are decreasing with increasing biomass share and the differences in particle sizes become quite significant when OR is replaced by HS. Figure 6.27 demonstrates the changes in particle number densities and cumulative cross sectional area distribution, which is calculated from the particle density, size distribution and load (Table 5.7). As can be seen from the Figure 6.27(a), presence of fine particles ( $< 30 \mu\text{m}$ ) dominates the cross sectional area distribution due to their high number densities (Figure 6.27 (b)) and the amount of fine particles (hence the total cross sectional area) increases with increasing biomass share for both OR and HS co-firing tests. Furthermore, number of fine particles is found to be much higher during HS co-firing tests compared to those of OR co-firing for all biomass shares, which leads to 82, 57 and 34 % increase in the total projected surface areas of particles when OR is replaced by HS (Table 6.16). Extinction coefficients (hence the optical thickness) are found to follow the same trend with the total projected surface area, which is also supported with the decrease in asymmetry factor with increasing number of fine particles present in the freeboard.

Therefore, it is concluded that changing the biomass source affects the radiative properties of the particles in the freeboard through the change of particle load and size distribution rather than optical properties of particles. This is considered to be due to the fact that both refraction ( $n$ ) and absorption ( $k$ ) indices do not vary significantly from one another up to  $10 \mu\text{m}$ , which covers the 95 % of the thermal radiation under FBC conditions.

Table 6.16 Radiative properties of particle laden combustion gases

	<b>OR 19 %</b>	<b>OR 36 %</b>	<b>OR 55 %</b>	<b>HS 14 %</b>	<b>HS 35 %</b>	<b>HS 50%</b>
<b>Particle load, B (g/m<sup>3</sup>)</b>	13	10	9	13	11	10
<b>Particle density ( kg/m<sup>3</sup>)</b>	1415	1347	1294	1175	1239	1257
<b>d<sub>32</sub> (μm)</b>	18	13	10	12	10	8
<b>d<sub>50</sub> (μm)</b>	179	173	162	78	59	51
<b>d<sub>90</sub> (μm)</b>	445	447	446	290	321	312
<b>Total projected surface area of particles (m<sup>2</sup>/m<sup>3</sup>)</b>	0.9	1.1	1.4	1.7	1.7	1.9
<b>Gas absorption coefficient, κ<sub>g</sub> (m<sup>-1</sup>)</b>	0.55	0.55	0.57	0.44	0.56	0.56
<b>Particle absorption coefficient, κ<sub>p</sub> (m<sup>-1</sup>)</b>	0.29	0.32	0.41	0.53	0.56	0.58
<b>Particle scattering coefficient, σ<sub>s</sub> (m<sup>-1</sup>)</b>	1.12	1.22	1.47	2.03	1.98	2.04
<b>Extinction coefficient, β(m<sup>-1</sup>)</b>	1.97	2.08	2.46	2.99	3.09	3.18
<b>Scattering albedo, ω</b>	0.57	0.58	0.60	0.68	0.64	0.64
<b>Asymmetry factor, g</b>	0.47	0.42	0.39	0.47	0.44	0.41
<b>Mean beam length, L<sub>m</sub> (m)</b>	0.38	0.38	0.38	0.38	0.38	0.38
<b>Optical thickness, τ</b>	0.75	0.79	0.93	1.14	1.18	1.21



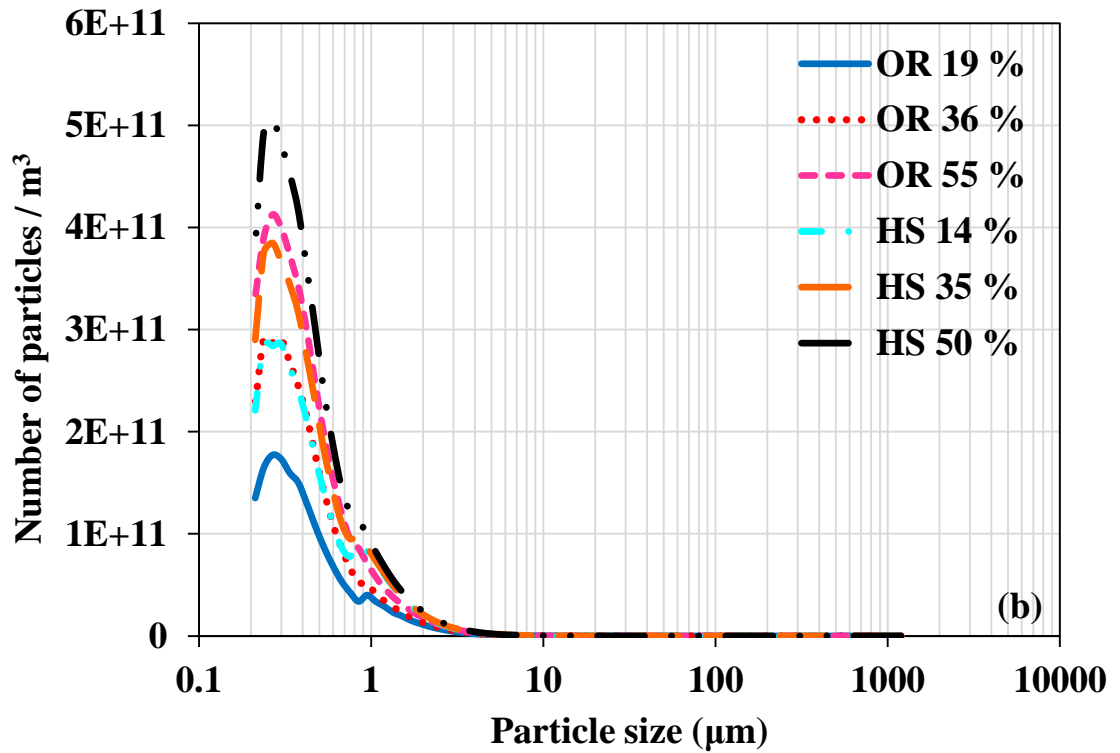
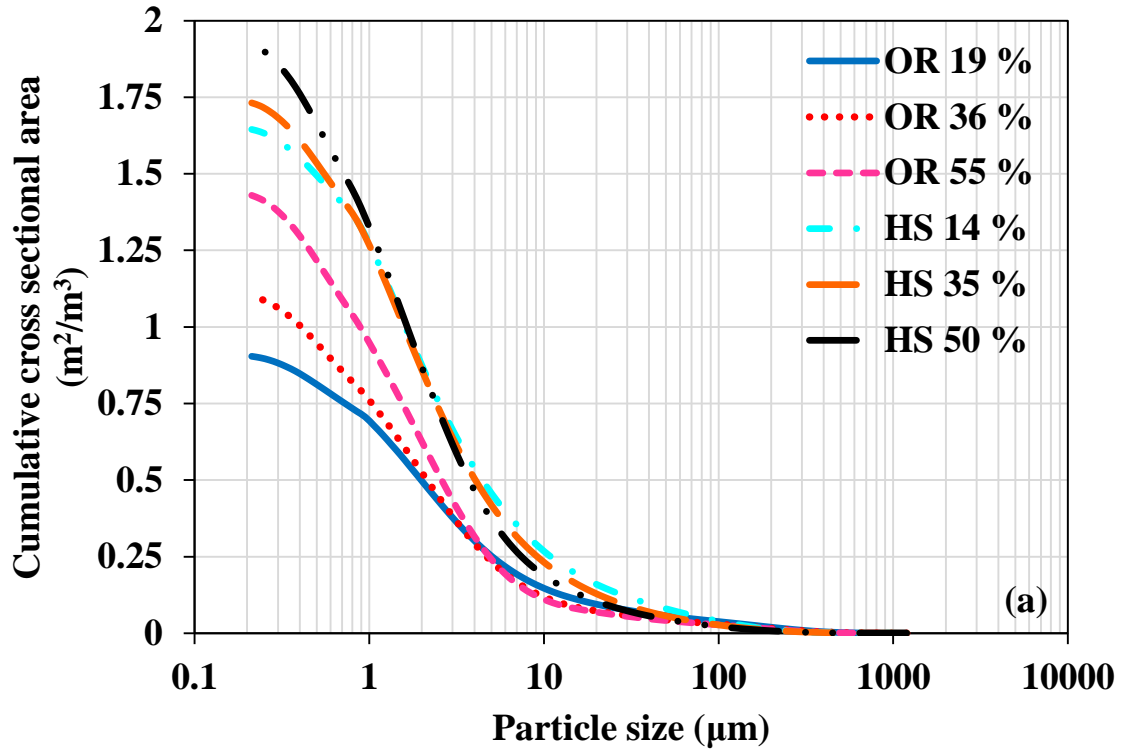


Figure 6.27 (a) Cumulative cross sectional area and (b) particle number density distributions

## 6.6.2 Effect of Changing Biomass Source on Radiative Heat Transfer

Effect of changing the biomass source from olive residue to hazelnut shell on incident heat fluxes along the side walls are shown in Figure 6.28. As can be seen from the figure, changing the biomass source while keeping the thermal input and Ca/S ratio the same has no influence on radiative wall heat fluxes for 15 (0.1 % increase in average) and 35 % (0.7 % increase in average) biomass shares. On the other hand, slight differences (4 % decrease in average) are observed for 50 % thermal share (Figure 6.28 (c)) where OR gives higher heat fluxes. The same trend is observed in the predicted source terms for the three biomass shares, which is demonstrated in Figure 6.29. It is seen that source terms slightly increase when OR is replaced by HS for 15 % (4.6 % increase in average) and 35 % (9.6 % increase in average) biomass shares but they are almost equal to one another at 50 % share (0.8 % increase in average). The reason behind this trend observed for high biomass shares in both heat fluxes and source terms is considered to be due to the differences between measured temperatures. Comparisons reveal that temperatures increase in the freeboard region with increasing OR share in the fuel feed (Figure 5.3(a)) while the particle laden flue gas temperatures almost stay constant along the freeboard irrespective of the HS share (Figure 5.3(b)).

Nevertheless, it should be highlighted that small variations in wall heat flux predictions might be due to the high temperatures of refractory-lined freeboard walls, high surface to volume ratio ( $Surface\ area/Volume=9.4$ ) of the test rig and low optical thickness of the medium where radiative heat transfer is expected to be dominated by walls rather than particle laden gas emissions. Considering the fact that temperature profiles of all tests (except 55 % OR share) were almost identical, variations in heat fluxes might be different from the findings if the freeboard was bounded by conventional panel tube walls instead of hot refractory walls. In order to test this hypothesis, effect of wall temperature on heat fluxes is also investigated with a parametric study where the top and side wall temperatures are assumed to be 537 K with an emissivity of 0.80 for all cases based on the experimental work performed in the 16 MW<sub>t</sub> FBC located at Chalmers University of Technology [169], which reports similar temperature profiles and optical thickness for the

particle laden combustion gases. To be more precise, temperature profile measured along the freeboard of the 16 MW<sub>t</sub> FBC is only 1.3 % different than those of measured in METU ABFBC test rig. Furthermore, effective emissivities of the gas mixture and the particle laden gaseous mixture were reported as 0.28 and 0.42 respectively [169], which gives an optical thickness [170] very close to the ones investigated in this study. Based on those similarities, a wall temperature of 537 K is considered to be acceptable for the sake of the parametric investigation which eliminates the hot refractory wall effect. As a result, in the parametric studies, heat flux and source term predictions are calculated by keeping the operating conditions of the combustion tests the same (Table 5.7) except the wall temperatures and emissivities.

Predicted incident wall heat fluxes and source terms for these parametric studies are compared in Figure 6.30 and Figure 6.31. As seen in Figure 6.30, radiative heat fluxes increase with increasing biomass share from 14% to 50% for HS due to the increase in number of fine particles in the freeboard. However, radiative heat fluxes are not much affected from increasing biomass share from 19% to 35% for OR (Figure 6.30 (a, b) while there is a noticeable increase for 50% OR share due to higher particle laden flue gas temperature. The same trend is observed in the predicted source terms for the three biomass shares, which are demonstrated in Figure 6.31. These differences in heat fluxes and source term predictions are found to be due to the increase in particle emissions with increasing number of fine particles when HS is utilized instead of OR during the co-firing of lignite.

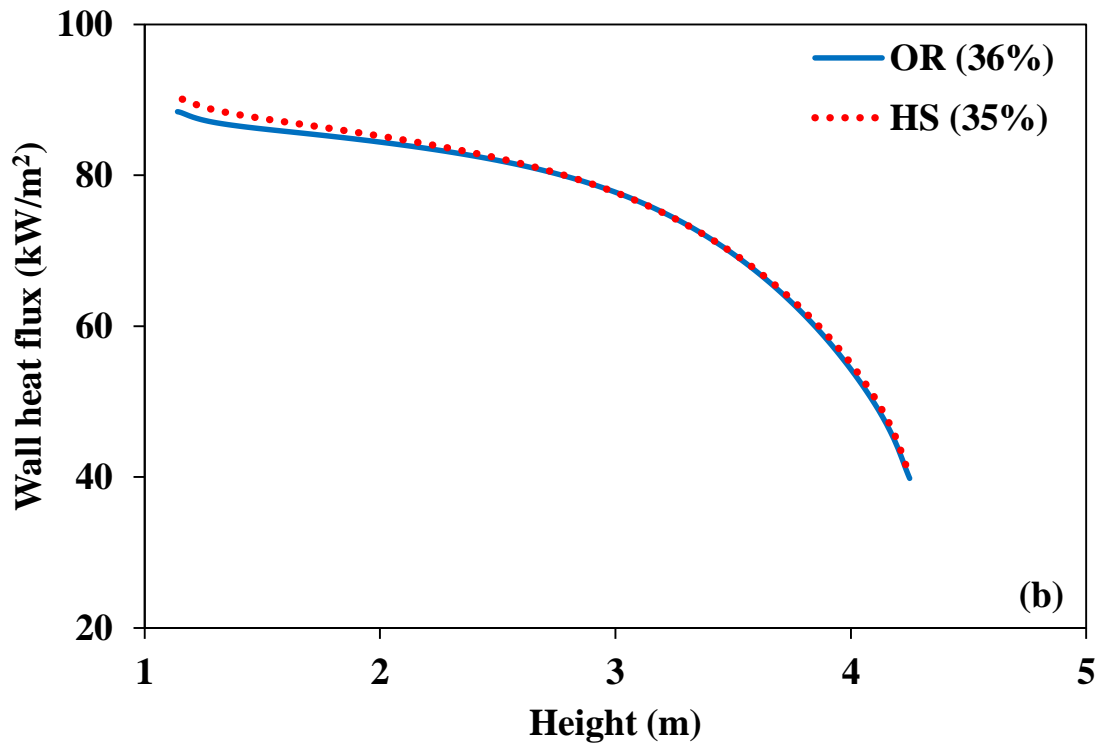
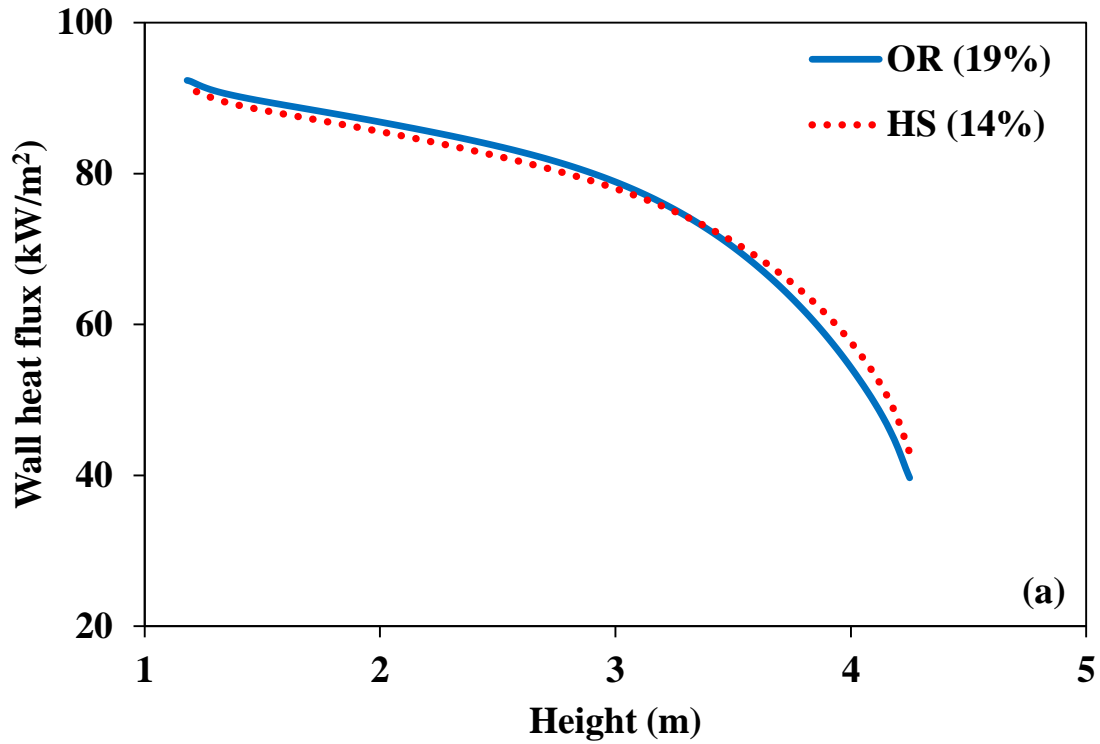


Figure 6.28 Effect of changing the biomass source on radiative incident wall heat fluxes for about (a) 15, (b) 35 and (c) 50 % biomass shares on thermal basis

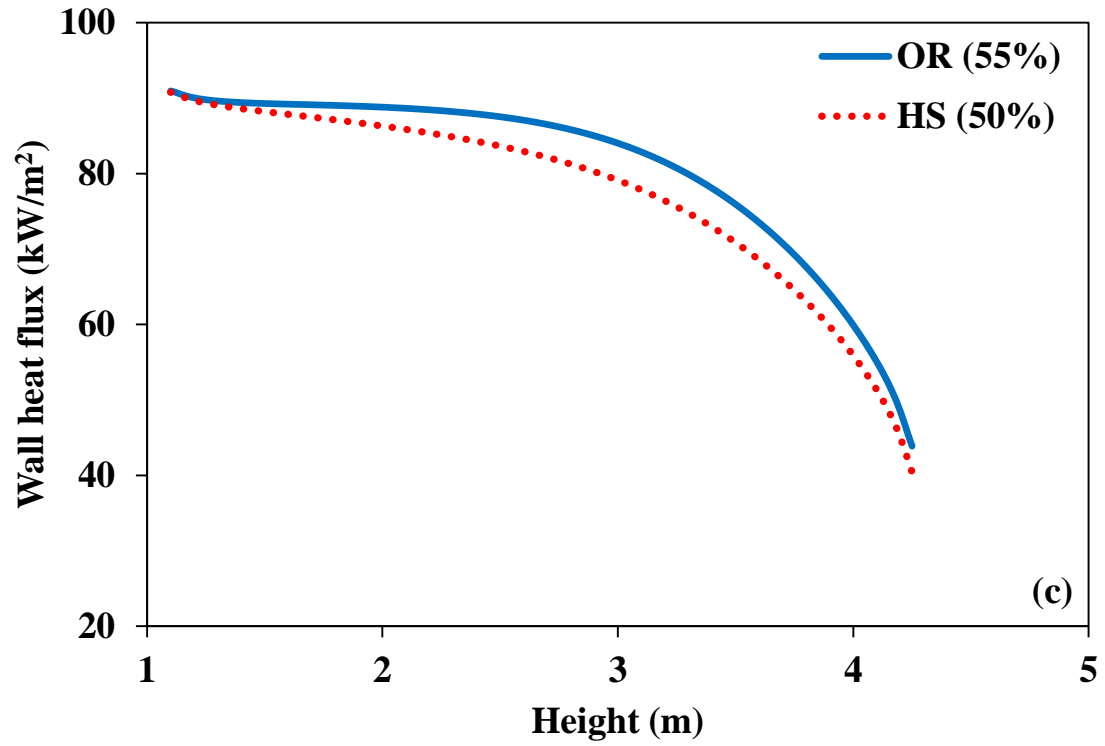


Figure 6.28 Effect of changing the biomass source on radiative incident wall heat fluxes for about (a) 15, (b) 35 and (c) 50 % biomass shares on thermal basis (cont'd)

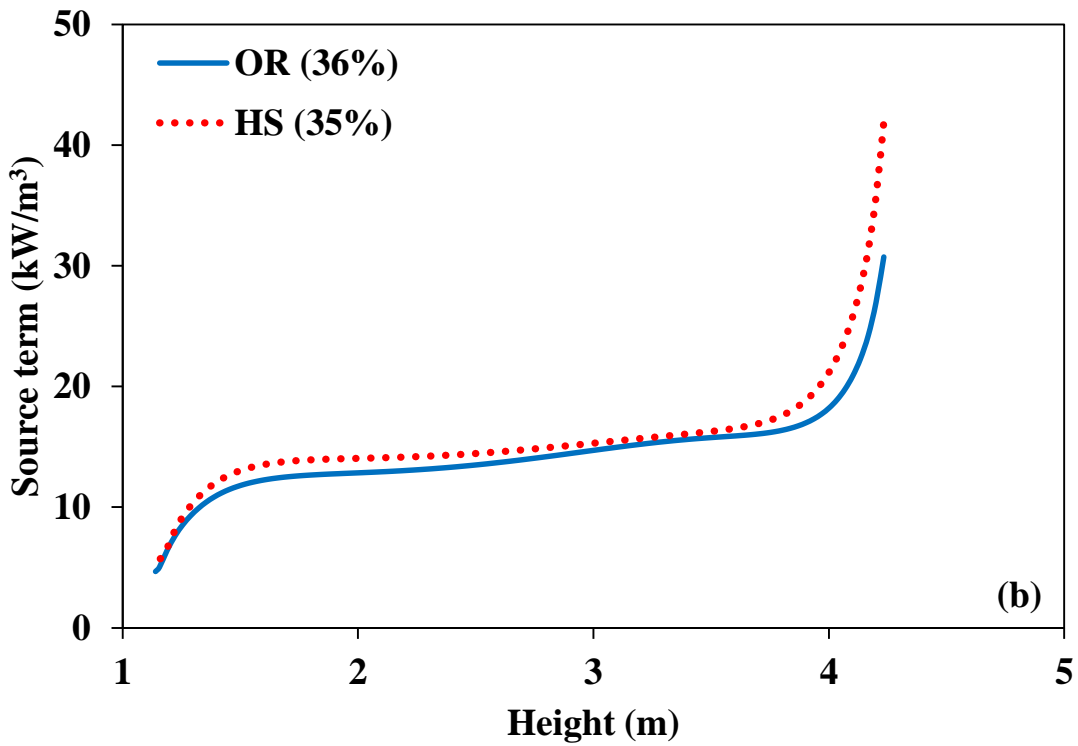
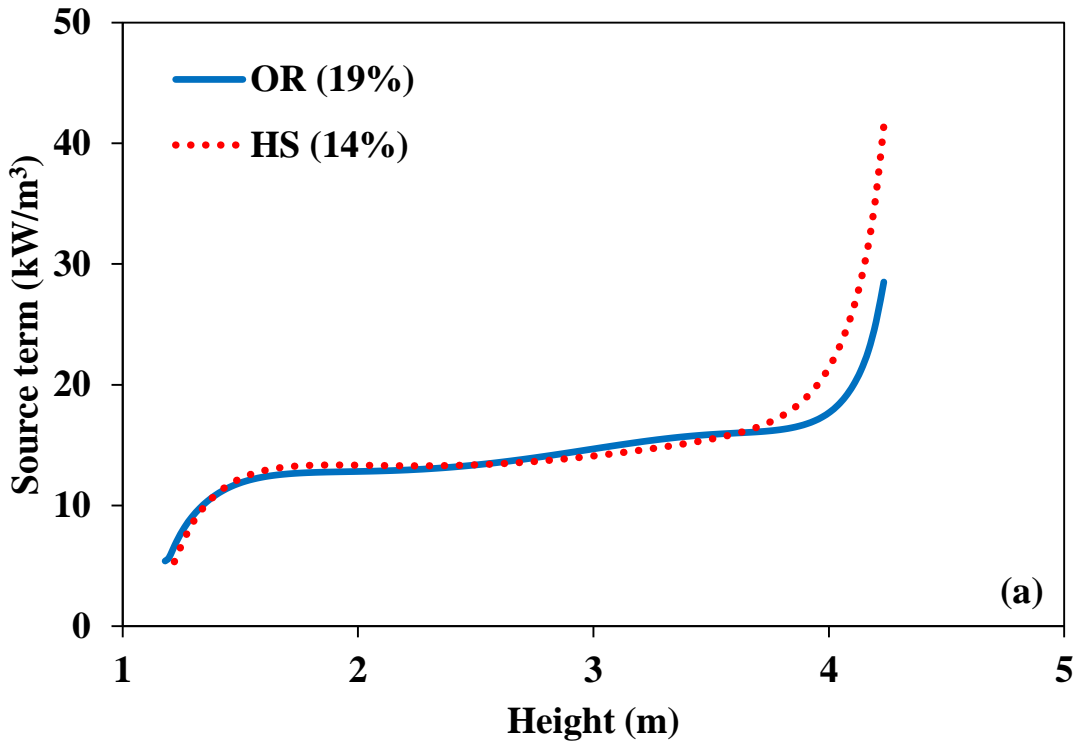


Figure 6.29 Effect of changing the biomass source on source terms for about (a) 15, (b) 35 and (c) 50 % biomass shares on thermal basis

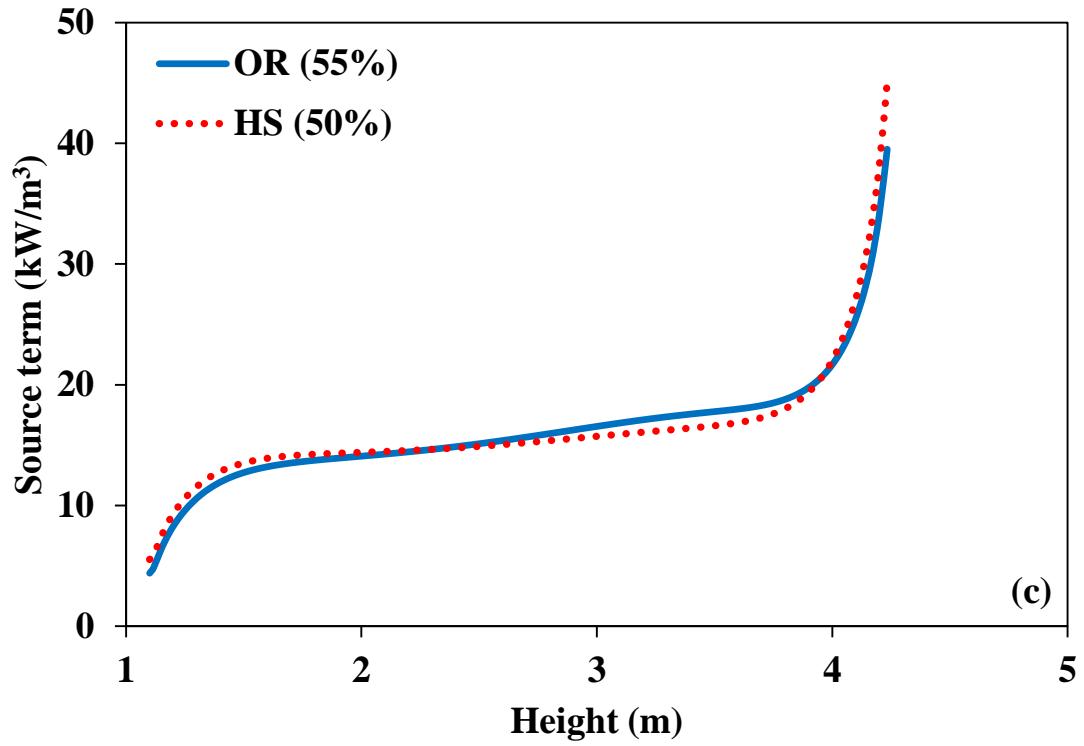


Figure 6.29 Effect of changing the biomass source on source terms for about (a) 15, (b) 35 and (c) 50 % biomass shares on thermal basis (cont'd)

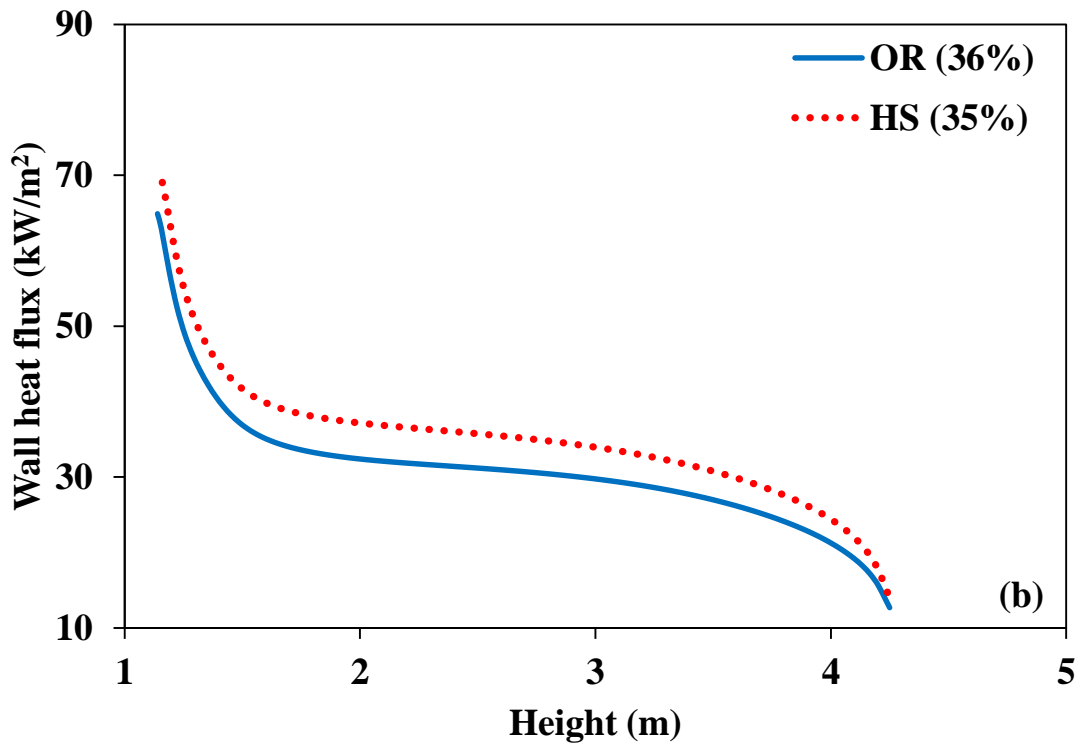
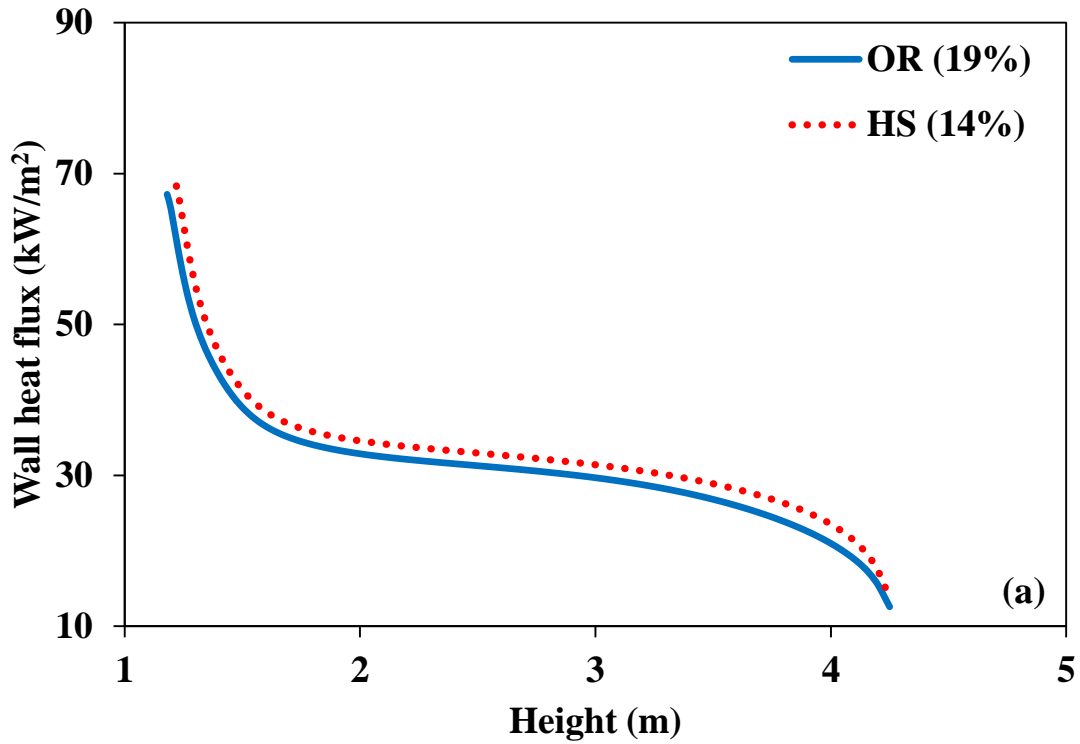


Figure 6.30 Effect of changing the biomass source on heat fluxes with cold wall assumption for (a) 15, (b) 35 and (c) 50 % biomass shares



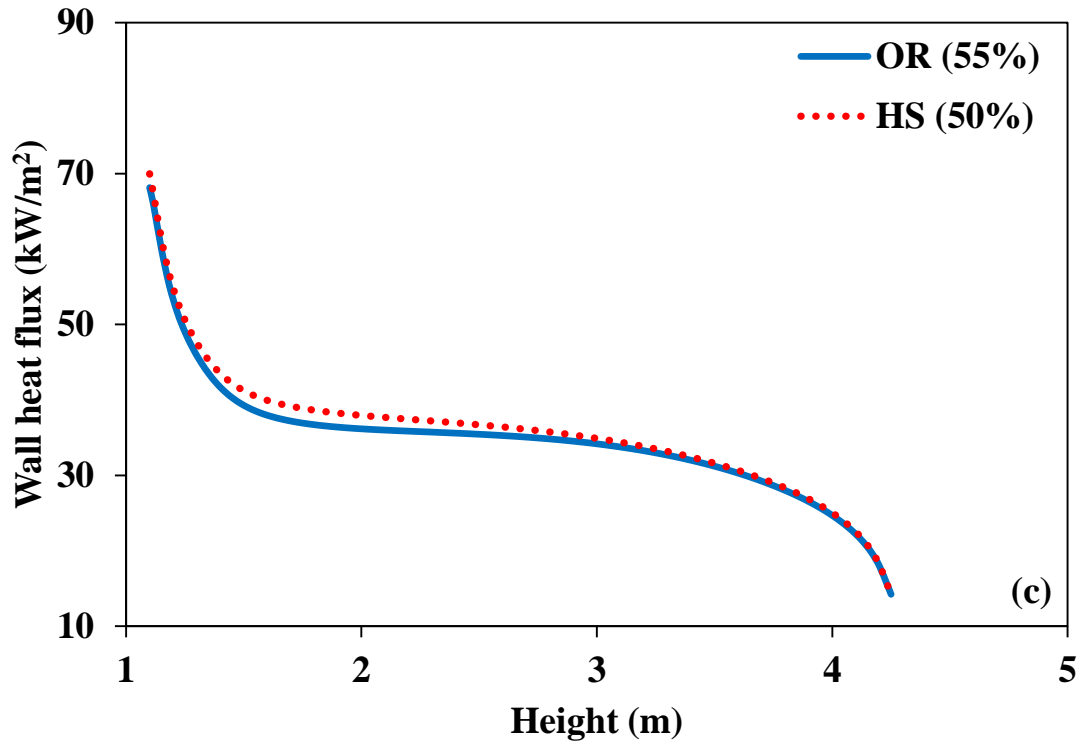


Figure 6.30 Effect of changing the biomass source on heat fluxes with cold wall assumption for (a) 15, (b) 35 and (c) 50 % biomass shares (cont'd)

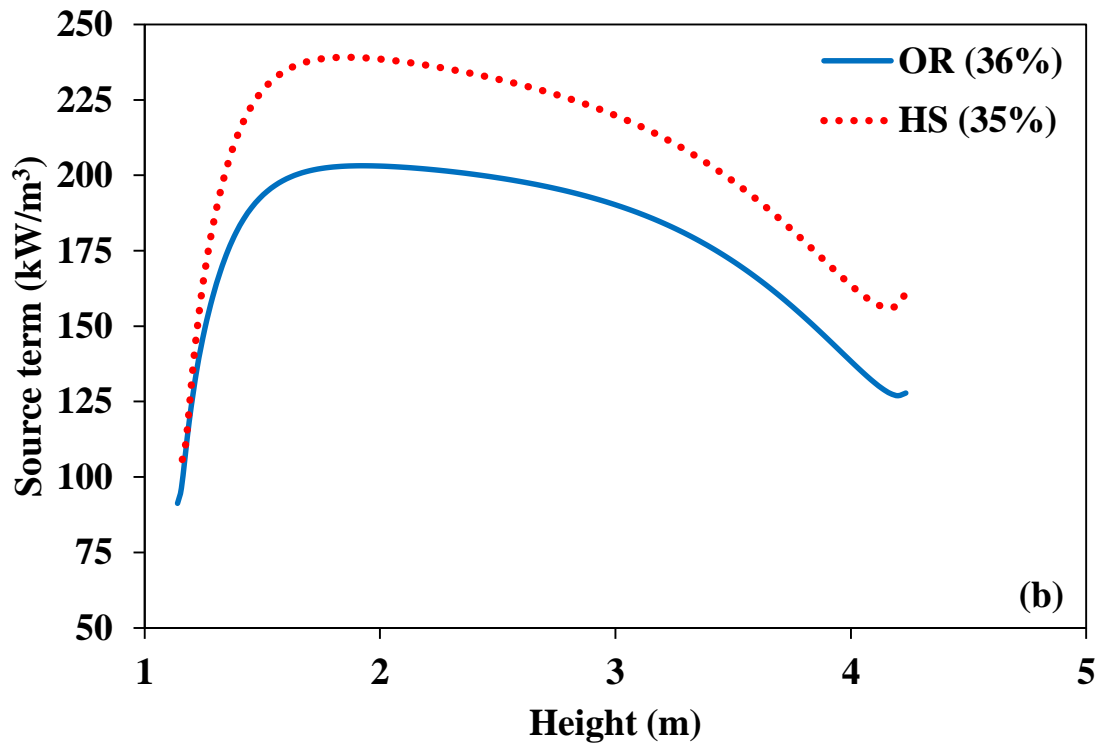
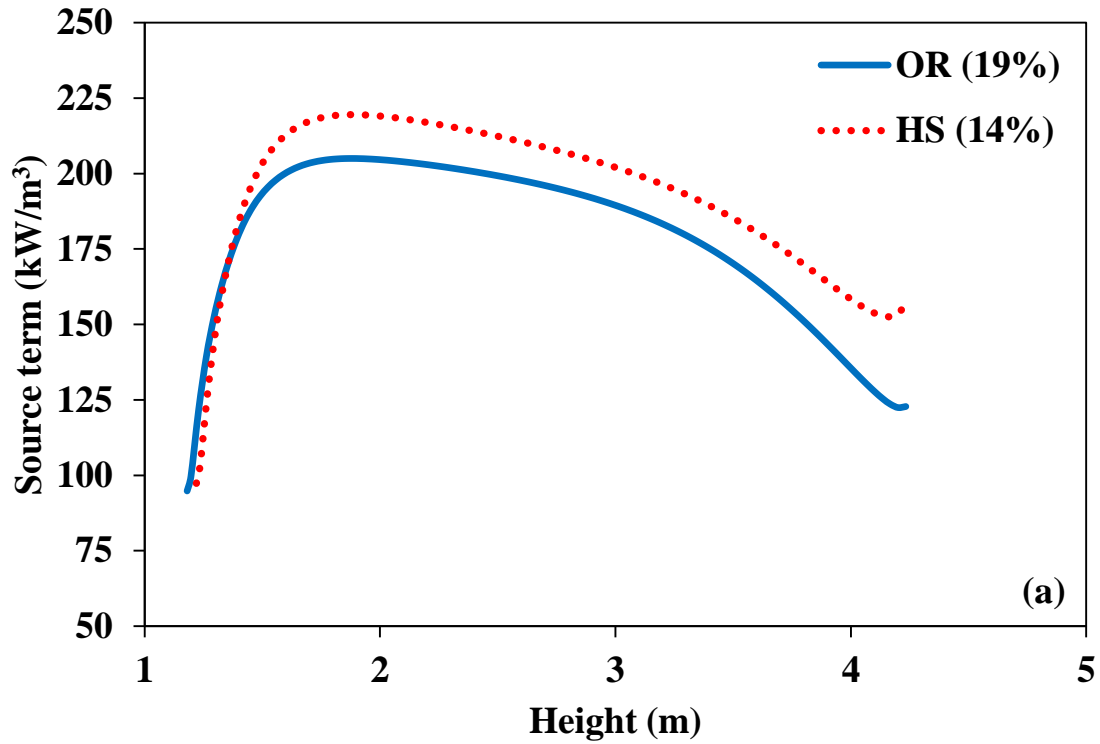


Figure 6.31 Effect of changing the biomass source on source terms with cold wall assumption for (a) 15, (b) 35 and (c) 50 % biomass shares

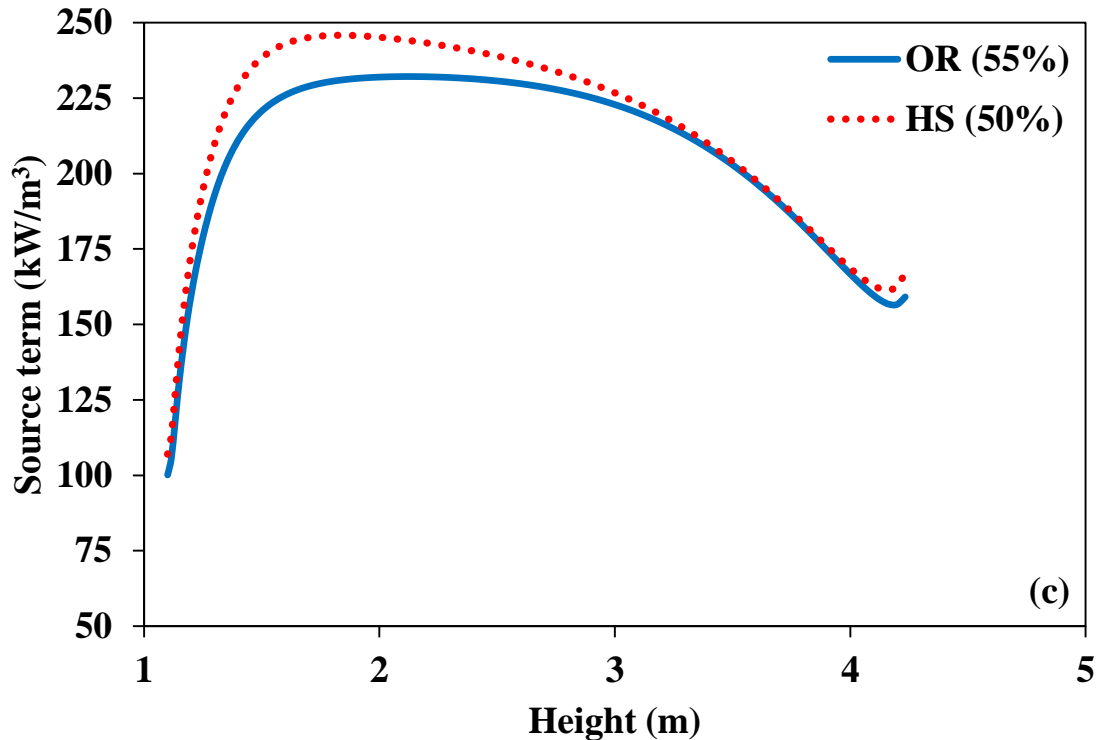


Figure 6.31 Effect of changing the biomass source on source terms with cold wall assumption for (a) 15, (b) 35 and (c) 50 % biomass shares (cont'd)

Percentage relative differences for the incident wall heat fluxes and source terms are also summarized in Table 6.17 for both hot refractory-lined experimental cases and parametric cold conventional panel tube wall cases. As can be seen from the table, both incident wall heat fluxes and source terms are affected from changing the biomass source. As presented in the previous section, changing the biomass source from olive residue to hazelnut shell affects the radiative properties of the particles in the freeboard through the change of particle size distribution rather than optical properties. Therefore, possible variations in PSD should be elaborated if multiple biomass sources are to be utilized in an FBC to minimize the influence of fuel source on radiative heat exchange.

Table 6.17 Differences in heat flux and source term predictions when OR is replaced by HS

	<b>Hot refractory walls (experimental)</b>			<b>Conventional panel tube walls (parametric)</b>		
	15%	35%	50%	15%	35%	50%
<b>Biomass thermal share, %</b>	15%	35%	50%	15%	35%	50%
<b>Av. Difference in heat flux, %</b>	0.08	0.65	- 4.38	6.10	13.34	2.9
<b>Av. Difference in source terms, %</b>	4.58	9.63	0.83	8.71	17.11	3.78

## 6.7 Investigation of the Spectral Nature of Particle Radiation

Spectral properties of particles are claimed to demonstrate a less complex behavior contrary to that of gas radiation. This is why spectral dependency of particle properties is often neglected in the majority of relevant literature and it is common to use a gray approach by deploying representative complex index of refraction values for different particles such as coal, char and ash [37]. Owing to the important role of particles in radiative heat transfer, however, spectral properties of particles have been considered in some of the previous studies [38-50], which highlighted the importance of deploying spectral particle properties in RTE solution (see Chapter 1 for details).

In this section, the existing gap in the literature regarding the influence of spectral particle properties on radiative heat transfer in combusting systems is addressed by using experimental data required for radiation model and its validation from the same combustion tests. The objective is to bring further clarity to how important it is to involve spectral particle properties on radiative heat transfer predictions and to assess the accuracy of gray particle property approximations in different combustion applications. An additional objective is to evaluate the effect of phase function simplifications on the predictive accuracy and computational efficiency when spectral particle properties are considered.

To address these questions, spectral nature of particle radiation is investigated as follows:

- (i) First, predictive accuracy of wide-banded solution of RTE (see Section 3.3) is tested for different optical thicknesses involving non-gray particles to have a CPU efficient solution method,
- (ii) Then, origins of the spectral nature of particle radiation is thoroughly explored,
- (iii) Influence of spectral particle properties on phase function simplifications is evaluated.

Details and outcomes of these investigations are presented in the following sub-sections.

### 6.7.1 Banded Solution of RTE for Spectral Particle Radiation

In spectrally resolved solution of radiative heat transfer, spectral forms of RTE (Eqs. (2.37), (2.38)) must be solved at each wavelength of the spectrum followed by an integration over all wavelengths ( $\sim 10^6$  wavelengths exists in the absorption spectrum) to obtain total radiative heat transfer rates. Such an approach, however, would be computationally very expensive for engineering problems. This is why gray particle approximation is widely used in the community. As an alternative, thermal spectrum can be divided into several spectral bands in which particle properties can be assumed to be uniform. In this case, RTE is only needed to be solved for several times. After radiative intensity distribution is found at each spectral band, radiative heat fluxes and source terms can then be evaluated at each band separately, from which total heat fluxes and source terms can be found by a simple summation rule.

It should be noted that radiative properties of a particle cloud (absorption coefficient, scattering coefficient, asymmetry factor of the particle cloud) are expected to be much less complex than those of participating gases due to smoothening of nonlinear single particle properties (i.e., absorption efficiency, scattering efficiency, individual particle asymmetry factor; see Figure 6.12, Figure 6.13) over the particle size distribution. Therefore, it might be possible to represent particle cloud properties with several simple step functions, which is also the condition that must be satisfied in order to solve spectral RTE (Eqs. (2.37), (2.38)) in a spectrally banded form (Eqs. (3.8), (3.9)). In order to investigate whether that is the case, spectral particle properties, radiative heat flux and source term predictions are evaluated for the fluidized bed coal combustion tests presented in Sections 5.1.1 and 5.2.1, which will be referred as Test 1 (ABFBC without recycle), Test 2 (ABFBC with recycle) and Test 3 (CFBC), respectively.

In the radiation models, participating combustion gases are assumed to be gray and calculated by using Leckner's correlations (Section 3.2). Spectral radiative properties of the polydisperse ash particles are calculated by using Mie theory (Section 4.1.3) for each particle size (34 discrete size classes) and wavelength (147 spectral points). Goodwin's correlations (Section 4.4) are employed to estimate spectral RI of particles collected from

the cyclone and bag filter as a function of density, wavelength and chemical composition (Table 5.5, Table 5.15). Particle properties are calculated up to 20  $\mu\text{m}$  as it is considered to be sufficient enough for the majority of thermal radiation in coal fired systems. In all cases, scattering phase functions are represented by Henyey-Greenstein phase function with normalization (Section 4.3). All input data necessary for the radiative property models are taken from Sections 5.1.1, 5.1.3, 5.2.1 and 5.2.2. In MOL solution DOM, a combination of  $S_{10}$  and  $13 \times 13 \times 96$  and  $S_{12}$  and  $17 \times 305$  grid nodes are utilized for ABFBC (in Test 1 and 2) and CFBC (in Test 3) test rigs based on a previous grid refinement study [150] and the results presented in Section 6.1.4. For the difference relations of spatial derivatives, two-point upwind differencing scheme DSS012 is employed.

#### **6.7.1.1 Banded Particle Properties**

Spectral particle properties are first evaluated from the Mie theory. In the calculations, spectral interval of 1-13  $\mu\text{m}$  is divided into 130 bands with uniform bandwidth (0.1  $\mu\text{m}$ ). RI values necessary for the Mie calculations are taken directly from the outputs of Goodwin's correlations (Appendix C). Between 13-20  $\mu\text{m}$ , spectrum is divided into 17 bands with non-uniform widths. As described in Section 4.4, Goodwin's experiments cover the spectral range of 1-13  $\mu\text{m}$ , in which semi-empiric RI model equations are defined. Nevertheless, it is suggested that  $\text{Al}_2\text{O}_3$  and MgO Reststrahlen bands dominate the optical constants at that long wavelength region and a simple mixture rule can be used to determine the complex RI of an ash particle [126]. Following the suggestion, required spectral complex refractive index data of pure  $\text{Al}_2\text{O}_3$  and MgO for 13-20  $\mu\text{m}$  range are taken from [171], which includes only 17 spectral points. Details of the RI measurements are also available in Appendix C.

In order to see whether the spectral resolution in particle property calculations is sufficient or not, cumulative ( $f$ ) and differential ( $\Delta f$ ) blackbody emissive power distributions under FBC conditions are generated from the Planck's law for the above-mentioned 147 spectral

bands (Figure 6.32). As can be seen from the figure, 95 % and 99 % of the thermal radiation lies between 1-10  $\mu\text{m}$  and 1-20  $\mu\text{m}$ , respectively. It is also seen that maximum fraction of blackbody emissive power ( $\Delta f$ ) within these 147 bands is around 0.026. Therefore, spectral resolution of the particle properties is considered to be sufficient for the problems under consideration.

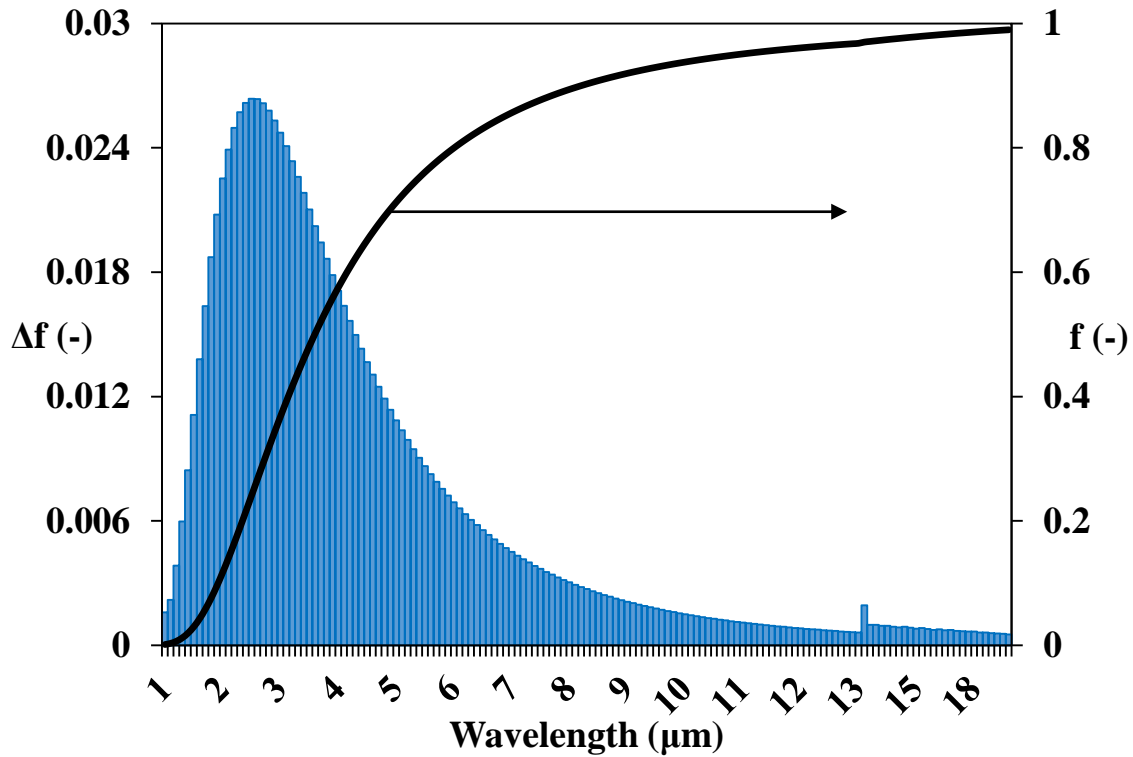


Figure 6.32 Cumulative ( $f$ ) and differential ( $\Delta f$ ) blackbody emissive power distributions under FBC conditions

Particle cloud absorption coefficients, scattering coefficients and asymmetry factors as a function of wavelength are demonstrated in Figure 6.33, Figure 6.34 and Figure 6.35 for Test 1, Test 2 and Test 3, respectively. As can be seen from the figures, spectral absorption (Figure 6.33(a), Figure 6.34(a), Figure 6.35(a)) and scattering coefficients (Figure 6.33(b), Figure 6.34(b), Figure 6.35(b)) vary several orders of magnitude in the thermal spectrum. On the other hand, spectral asymmetry factors (Figure 6.33(c), Figure 6.34(c),



Figure 6.35(c)) decrease with increasing wavelength. More importantly, spectral variation in particle properties are found to be much less pronounced compared to highly nonlinear behaviour of flue gas properties (see Figure 3.1, Figure 3.2) for all combustion tests. Based on this comparison, banding approach is considered to be worthy of further investigation.

In order to test the suitability of banded RTE solution for particle radiation, spectral radiative properties are divided into 4, 8, 16 wide bands for Test 1-2 and 7, 14, 28 bands for Test 3. Banding approach is based on two factors: (i) distribution of black body emissive power in each band, (ii) spectral dependency of the property (i.e., shape of the function). 4, 8, 16 banded properties for Test 1, 2 and 7, 14, 28 banded properties for Test 3 are demonstrated in Figure 6.33, Figure 6.34 and Figure 6.35, respectively. Distribution of radiant energy among the spectral bands is also illustrated in Figure 6.36 for Test 1. 4 banded and 8 banded representations of particle absorption coefficients are also presented separately in Figure 6.37 for the sake of clarity. As can be seen from the figure, radiant energy is not distributed among the bands in equal amounts. The reason behind this uneven distribution is the local variations in the property distribution; that is, if there is a local minimum / maximum in the spectral properties, this region is treated separately even though it includes less radiant energy.

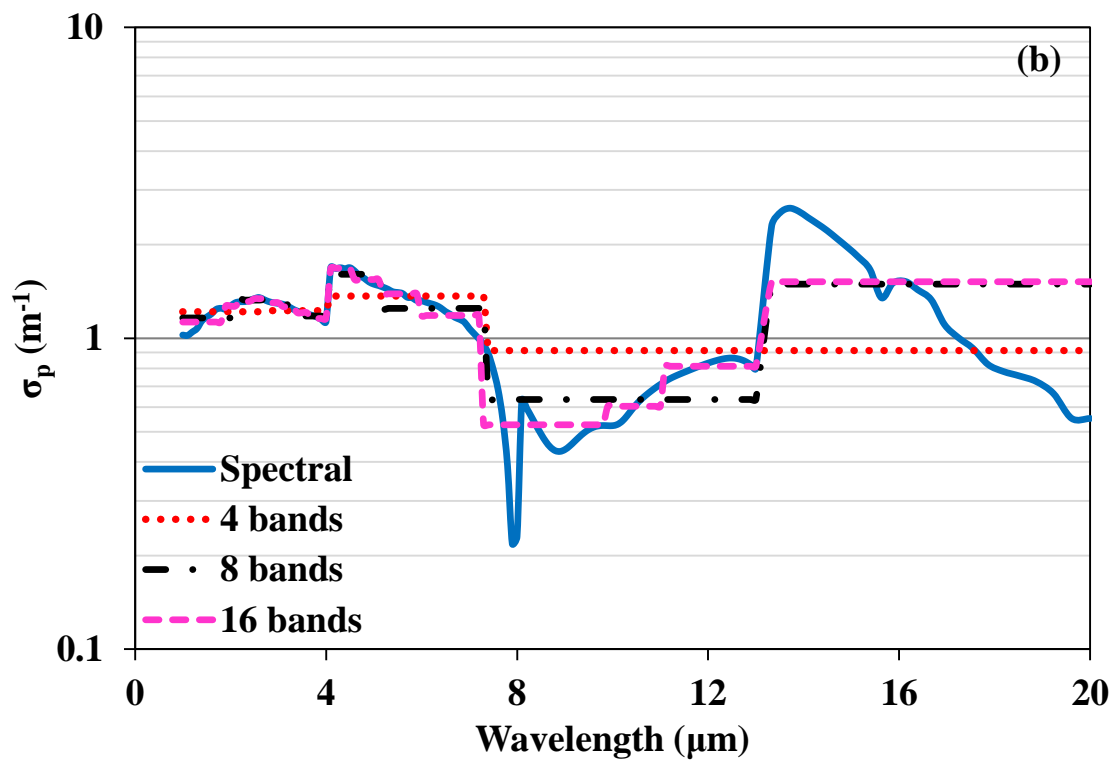
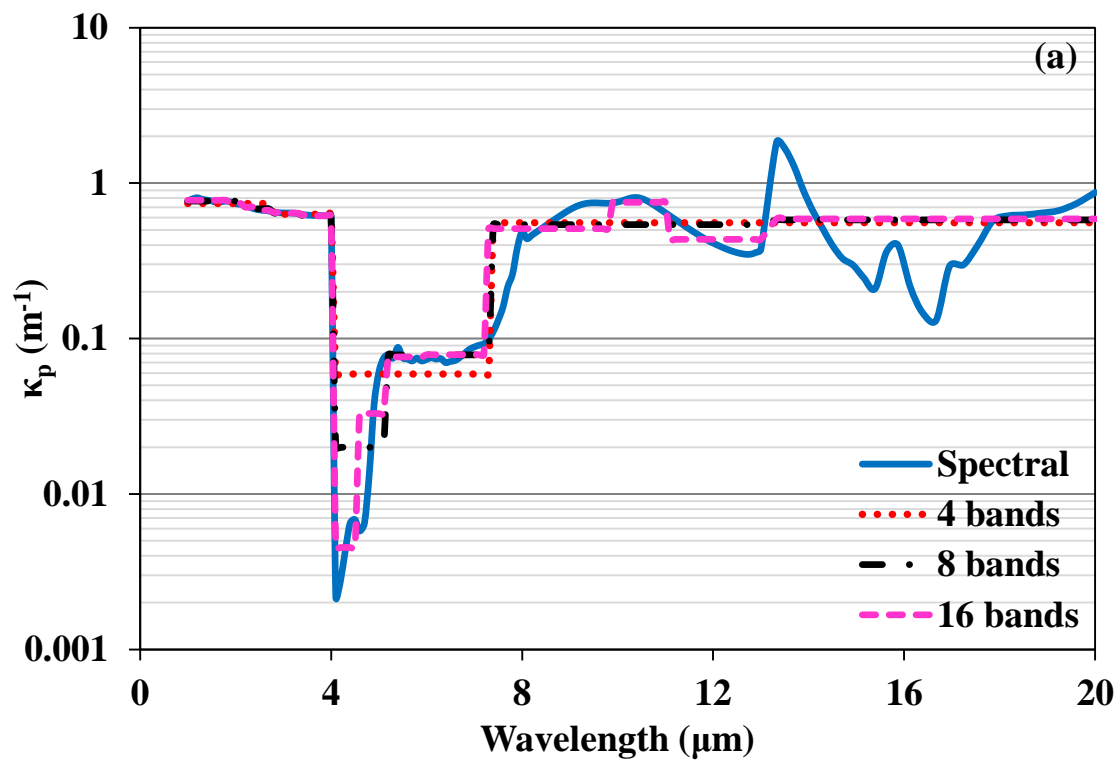


Figure 6.33 Spectral particle (a) absorption coefficient, (b) scattering coefficient and (c) asymmetry factor with their banded representations for Test 1

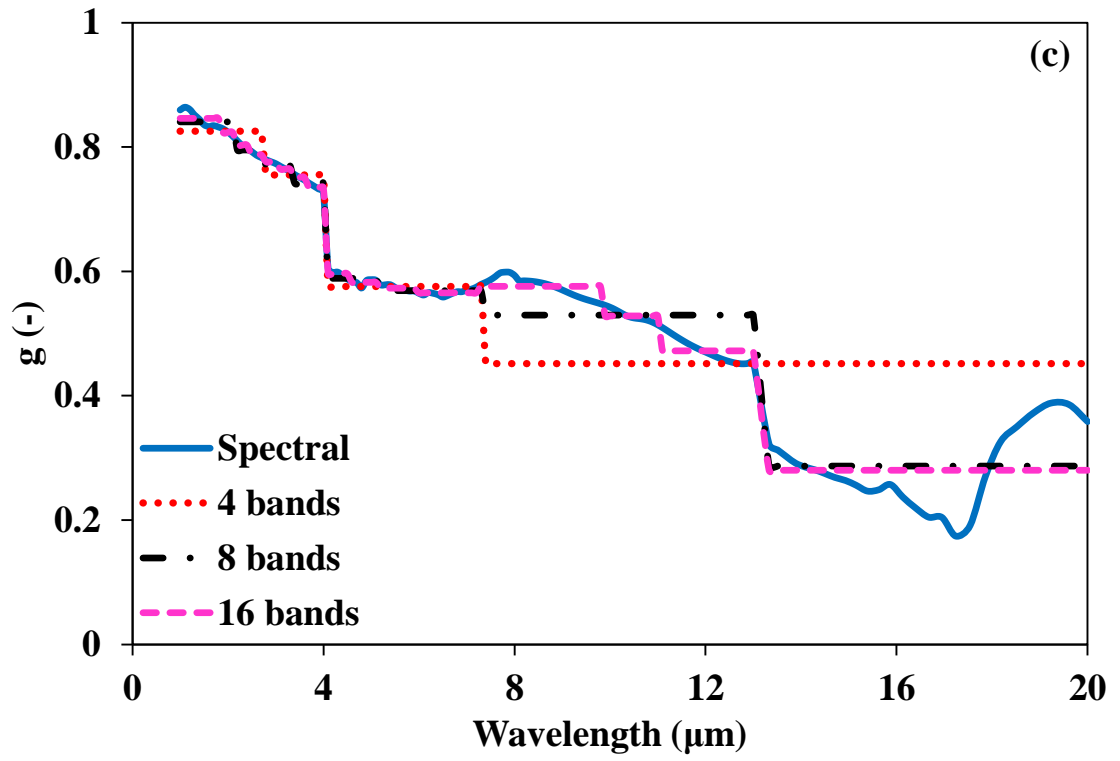


Figure 6.33 Spectral particle (a) absorption coefficient, (b) scattering coefficient and (c) asymmetry factor with their banded representations for Test 1 (cont'd)

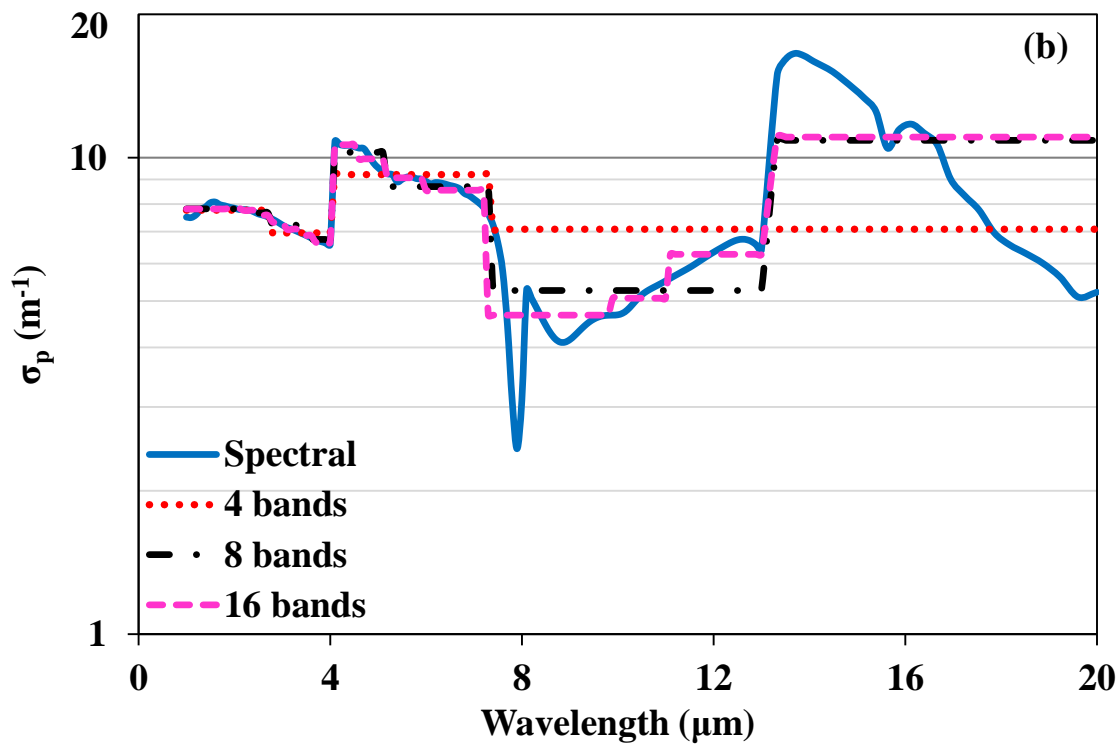
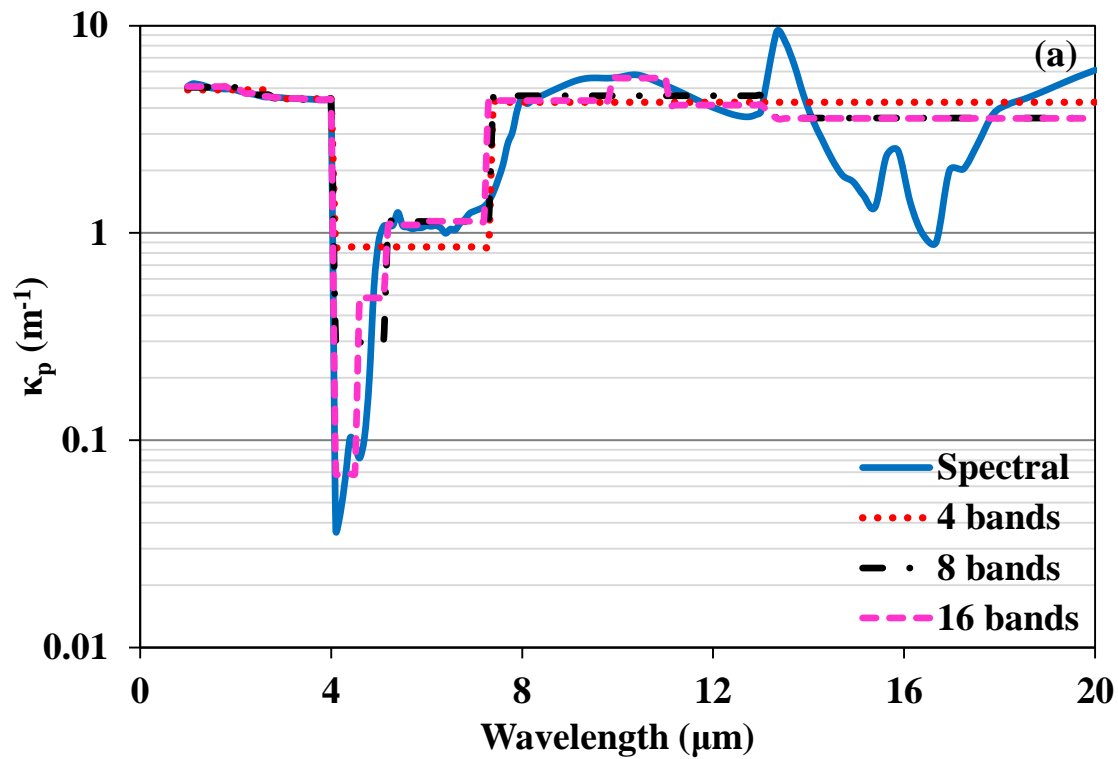


Figure 6.34 Spectral particle (a) absorption coefficient, (b) scattering coefficient and (c) asymmetry factor with their banded representations for Test 2

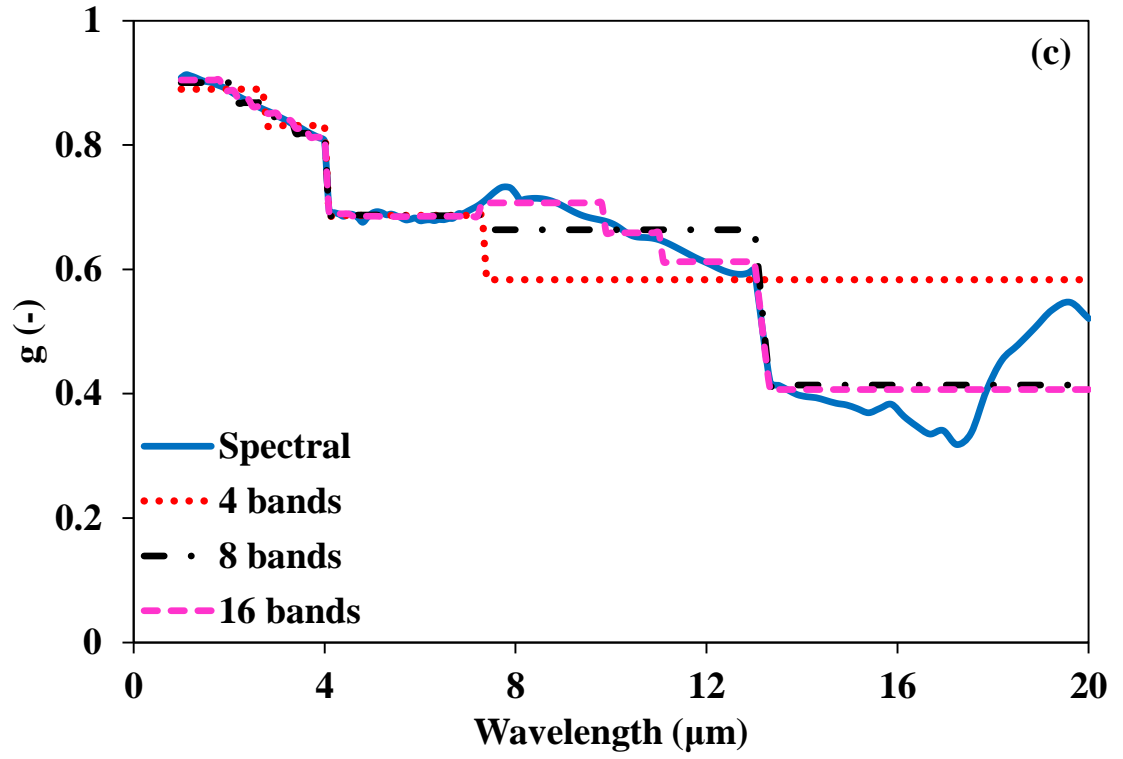


Figure 6.34 Spectral particle (a) absorption coefficient, (b) scattering coefficient and (c) asymmetry factor with their banded representations for Test 2 (cont'd)

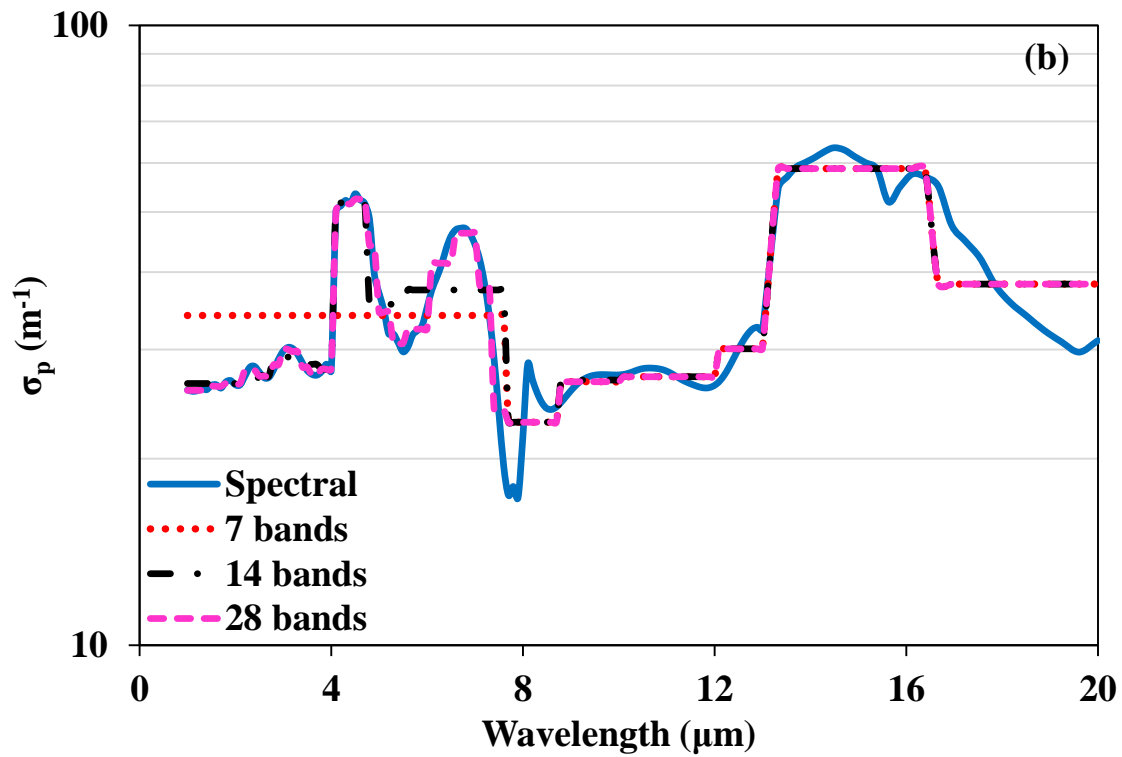
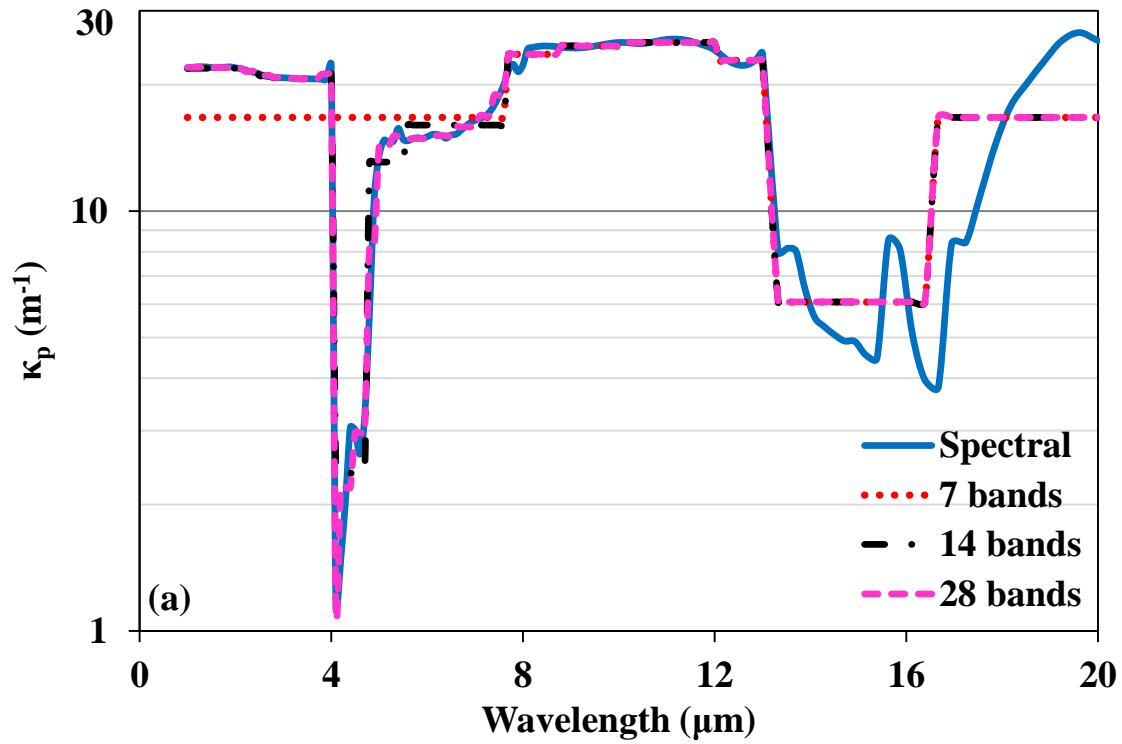


Figure 6.35 Spectral particle (a) absorption coefficient, (b) scattering coefficient and (c) asymmetry factor with their banded representations for Test 3

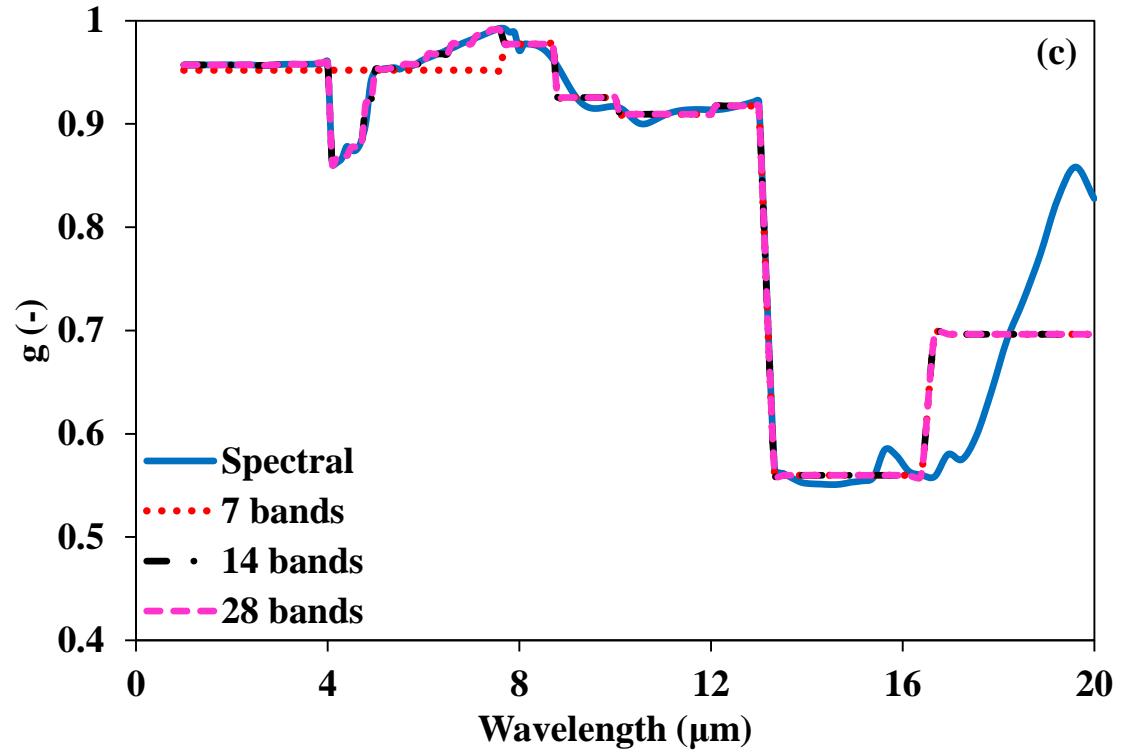


Figure 6.35 Spectral particle (a) absorption coefficient, (b) scattering coefficient and (c) asymmetry factor with their banded representations for Test 3 (cont'd)

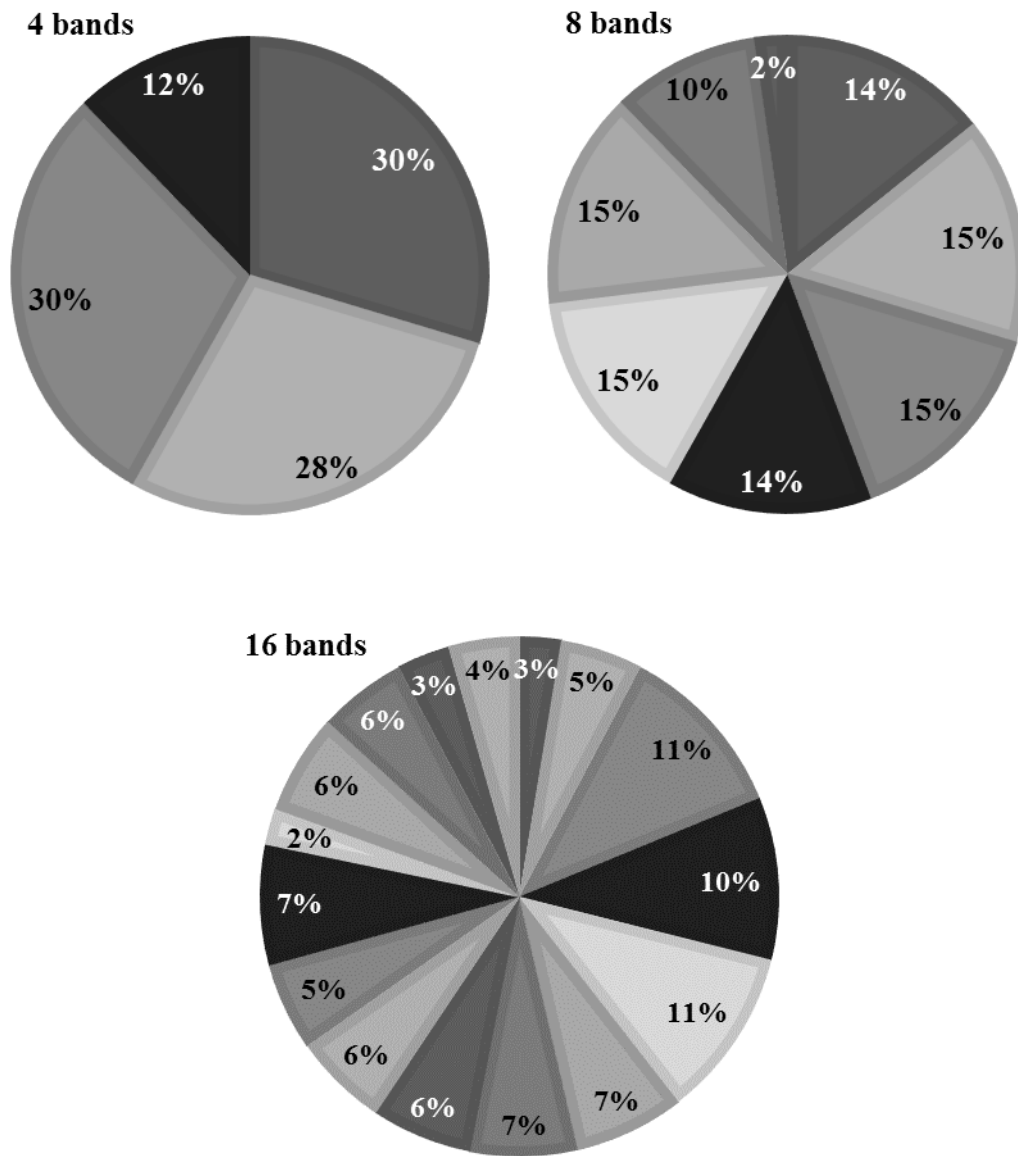


Figure 6.36 Distribution of radiant energy in spectral bands for Test 1



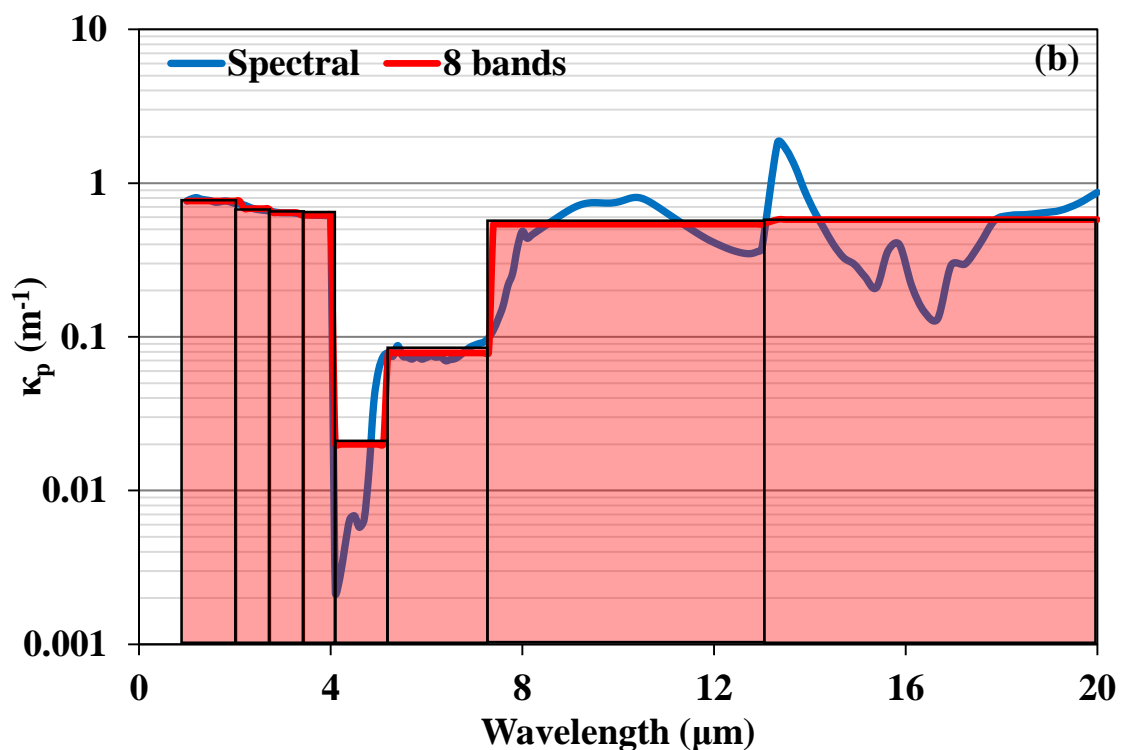
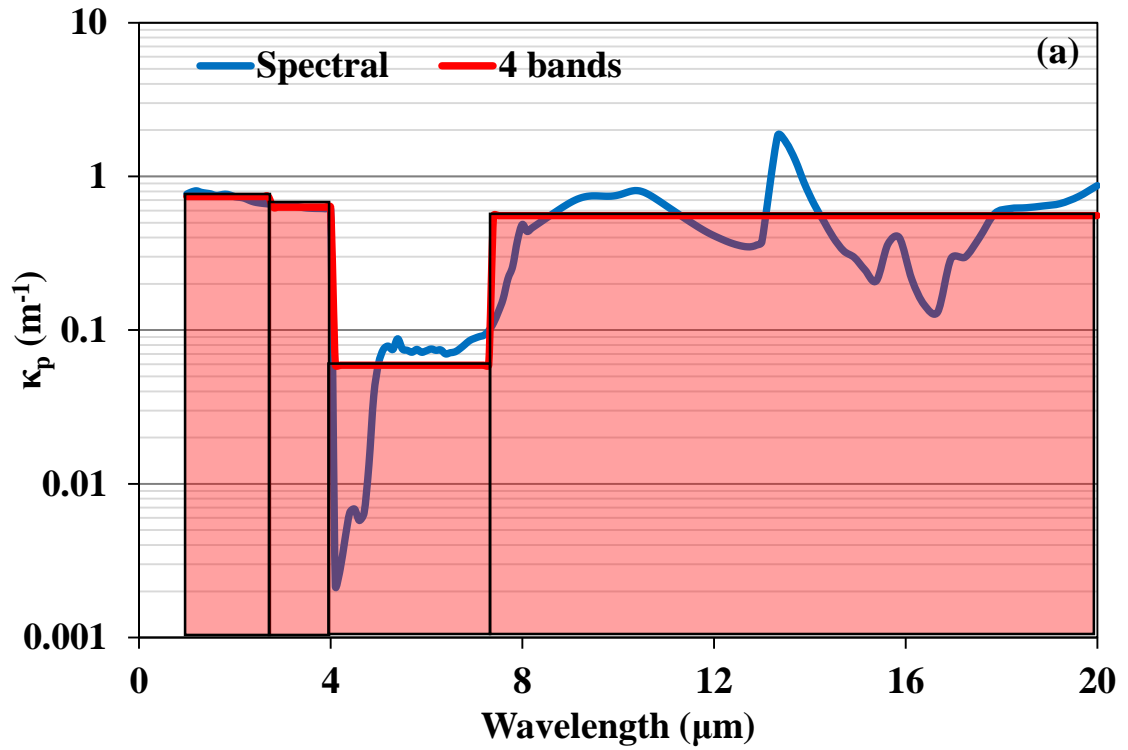


Figure 6.37 (a) 4 banded and (b) 8 banded representations of spectral particle absorption coefficients for Test 1

### 6.7.1.2 Banded Solution of RTE for Spectral Particle Radiation and its Validation

Numerical accuracy and computational economy of the RTE solutions with respect to spectral discretization are investigated by comparing their steady-state predictions with those obtained by the reference case carried out with the finest spectral discretization. Incident wall heat fluxes and source terms along the centerline calculated for Test 1, Test 2 and Test 3 are illustrated in Figure 6.38 and Figure 6.39. As can be seen from the figures, incident wall heat fluxes (Figure 6.38) are not as much affected as the source terms (Figure 6.39) by spectral discretization.

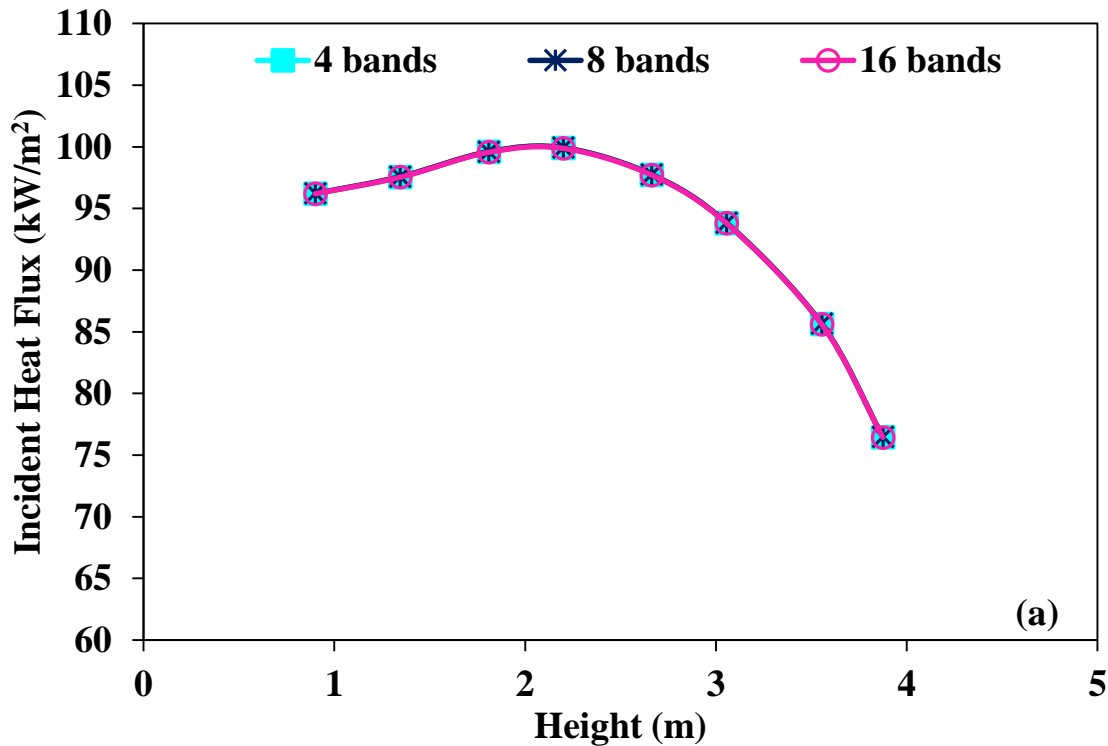


Figure 6.38 Effect of spectral discretization in heat flux predictions for (a) Test 1, (b) Test 2 and (c) Test 3

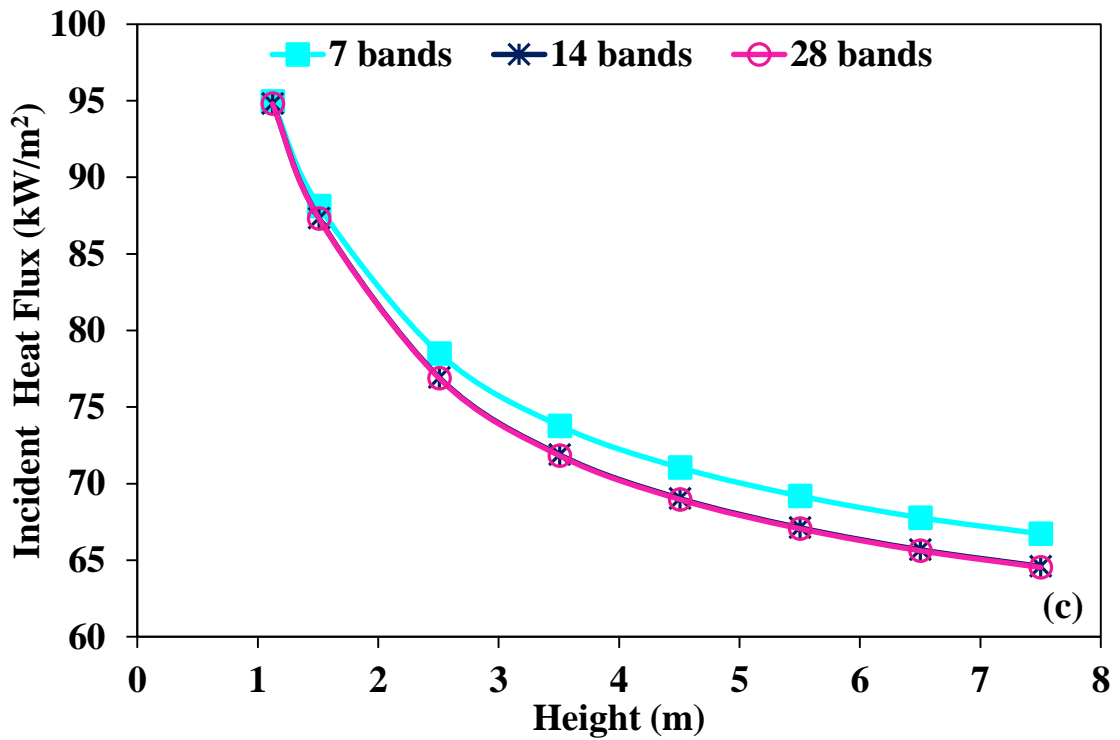
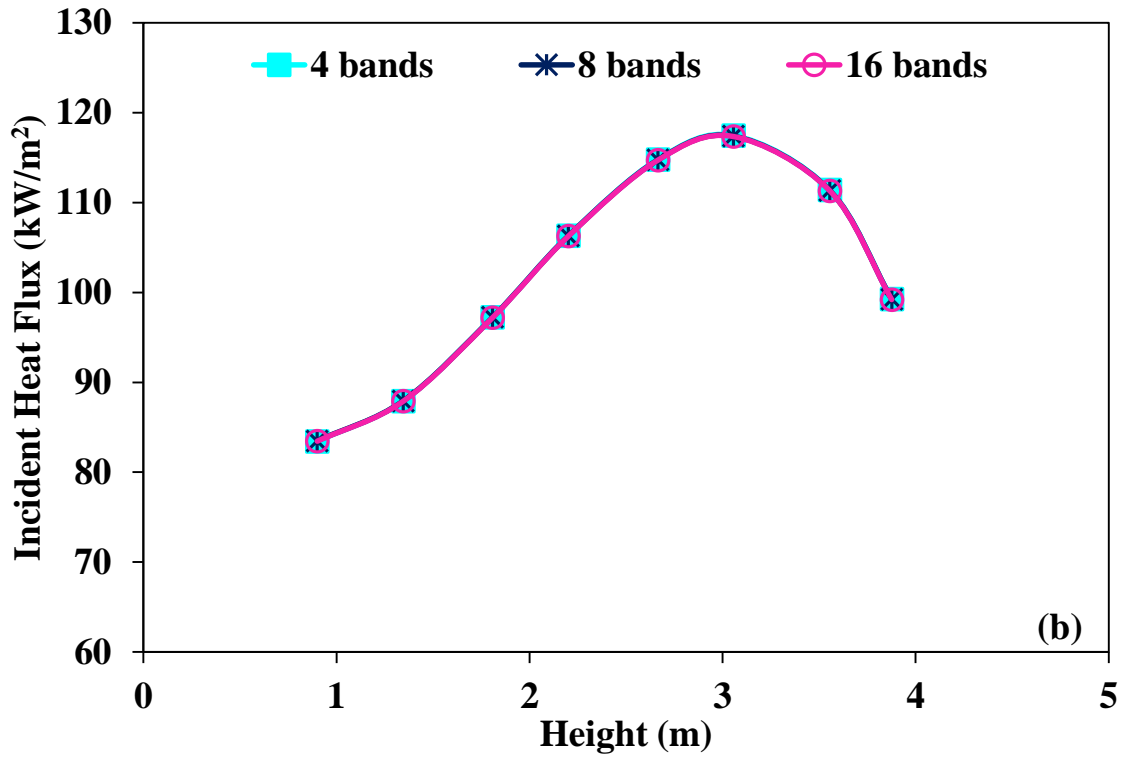


Figure 6.38 Effect of spectral discretization in heat flux predictions for (a) Test 1, (b) Test 2 and (c) Test 3 (cont'd)

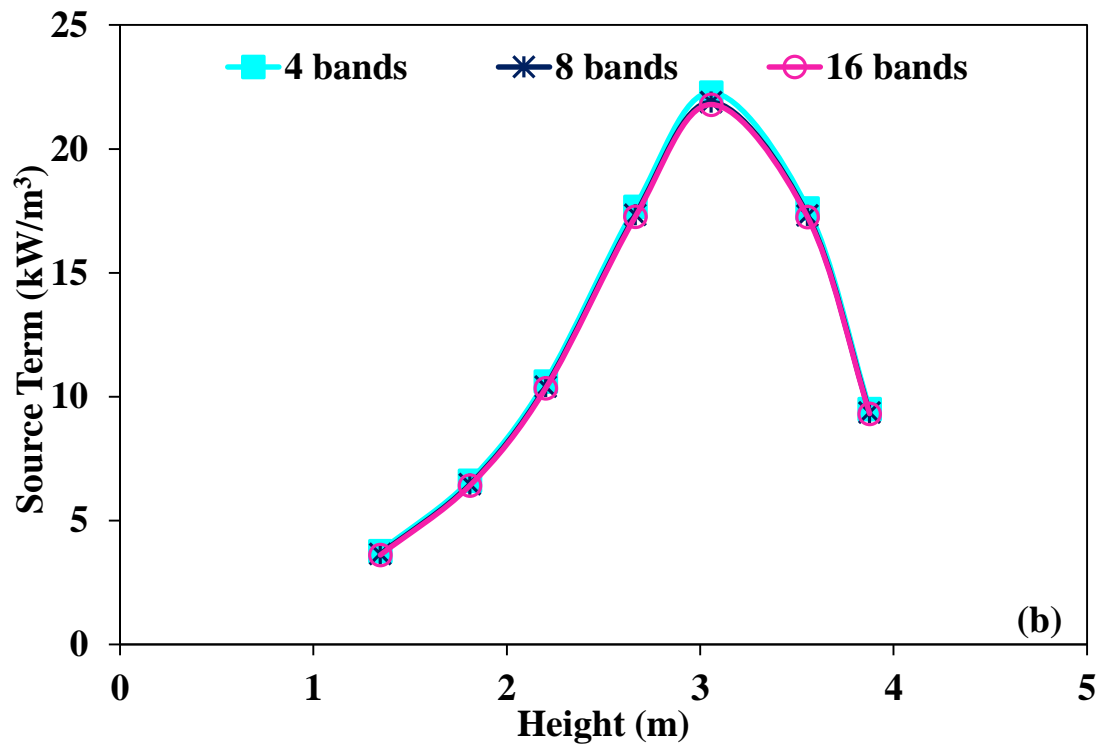
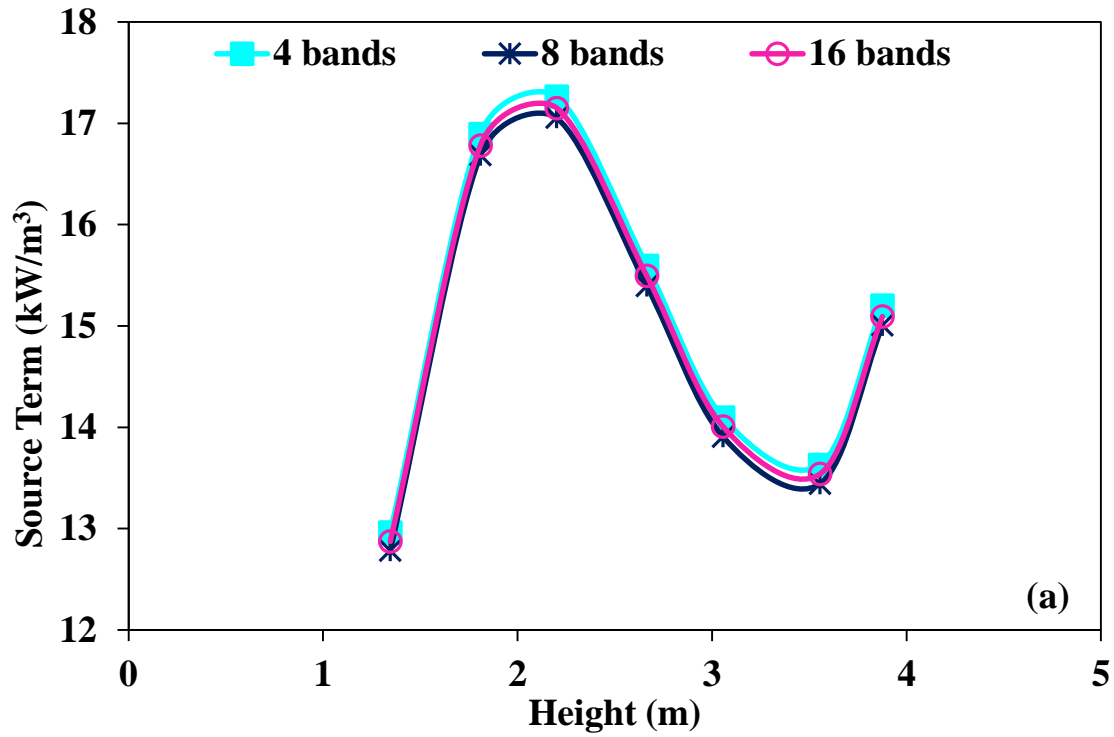


Figure 6.39 Effect of spectral discretization in source term predictions for (a) Test 1, (b) Test 2 and (c) Test 3

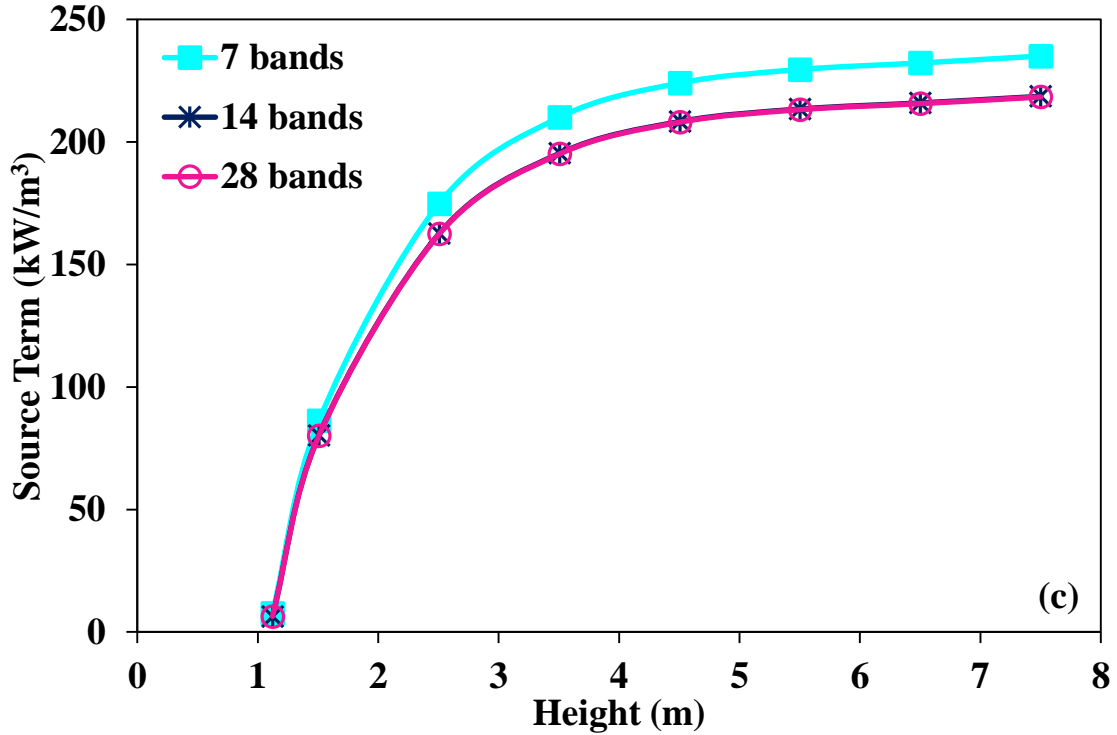


Figure 6.39 Effect of spectral discretization in source term predictions for (a) Test 1, (b) Test 2 and (c) Test 3 (cont'd)

Relative errors for the incident wall heat fluxes and source terms with corresponding CPU times are tabulated in Table 6.18. As can be seen from the table, spectral particle properties represented with 4 bands (Test 1), 8 bands (Test 2) and 14 bands (Test 3) are found to be sufficient from the viewpoints of accuracy and computational economy for the problem under consideration. Increase in number of bands from Test 1 (4 bands) to Test 3 (14 bands) reveals that sensitivity of predictions to spectral discretization increases with increasing optical thickness from 0.85 to 10.66. Reason behind sufficient accuracy obtained with relatively low number of bands, on the other hand, is considered to be due to the smoothing of oscillatory spectral properties with the wide PSDs under consideration in the present study.

Table 6.18 Effect of spectral discretization on predictive accuracy and CPU efficiency for the incident wall heat flux and source term predictions

Combustion Test	Spectral Resolution	Average % Error in Heat Flux	Average % Error in Source Term	CPU Time (s)
<b>Test 1</b> ( $\tau=0.85$ )	4 bands	0.1	0.7	4443
	8 bands	0.1	-0.7	10323
	16 bands	Reference Solution		20607
<b>Test 2</b> ( $\tau=4.77$ )	4 bands	0.1	2.5	2097
	8 bands	0.1	0.5	8766
	16 bands	Reference Solution		13555
<b>Test 3</b> ( $\tau=10.66$ )	7 bands	2.7	7.6	3126
	14 bands	0.1	0.1	8111
	28 bands	Reference Solution		17027

Figure 6.40 illustrates comparison between incident radiative heat fluxes predicted by the banded RTE solution with non-gray Mie particles and measurements in Test 1 and Test 2. In the model, spectral particle properties are represented by 16 spectral bands, which is the reference solution for the results presented in Table 6.18. As can be seen from the figure, predictions obtained with 16 banded RTE solution are in good agreement with the measurements. Discrepancy between the predictions and the measurement at the uppermost port is considered to be due to the fact that radiometer is located (4.19 m) nearly adjacent to the cooling tubes (4.25 m), where the tip of the radiometer is only 6 cm away from the cold tubes (~310 K). This is why measured wall heat fluxes were measured to be very low at this location. This difference, on the other hand, is found to be much smaller for Test 2, where increased radiative emissions from higher particle load compensate lower emissions from the cold cooling tubes.

Comparisons presented in this section reveal that sensitivity of wall heat flux and source term predictions to spectral discretization of particle properties increases with increasing optical thickness from Test 1 to Test 3. Nevertheless, small numbers of spectral bands are sufficient to represent spectral particle properties accurately in both optically thin and thick media. Therefore, spectrally banded particle properties and banded solution of RTE will be utilized in the rest of the present study for non-gray particle radiation.

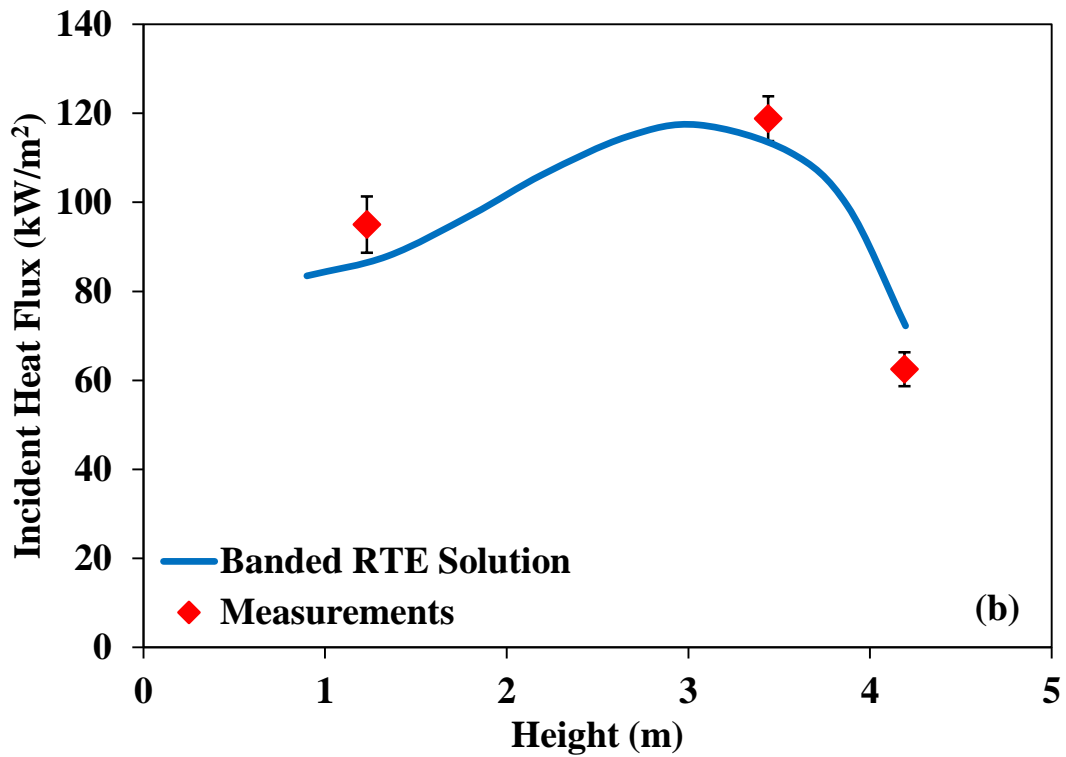
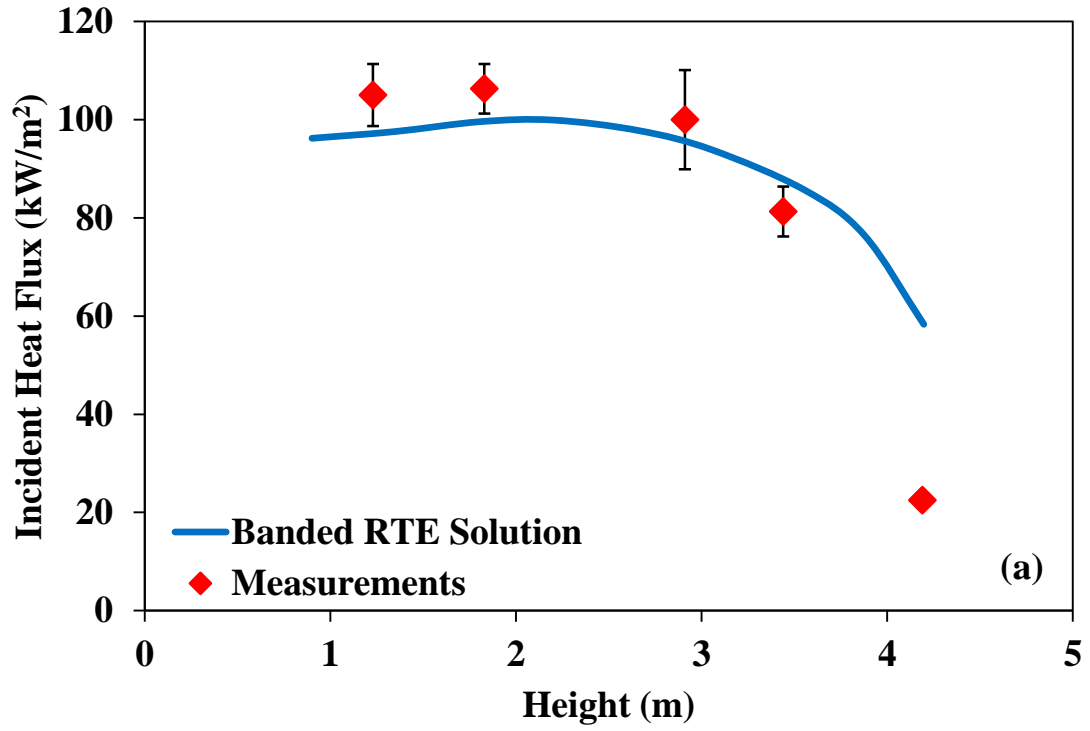


Figure 6.40 Validation of banded RTE solution for (a) Test 1 and (b) Test 2

## 6.7.2 Origins of the Spectral Nature of Particle Radiation

Spectral nature of particle radiation is originated from two sources; complex index of refraction (RI) and wavelength of the incident radiation. As described in Section 4.4, RI is a material property, which is function of chemical composition, density and temperature. Nevertheless, these dependencies are often neglected in the relevant literature [37] and it is common to use the traditional gray approach or empirical RI models (see Section 4.4), which neglect the chemical composition dependency of RI despite the experimental evidence [36, 120, 124-129]. Considering the variations in ash composition even for the same coal mine, validity of these simple empirical RI model equations, generated based on a specific ash composition (or spectral particle property models which do not include the effect of chemical composition), becomes questionable. In view of the facts that chemical composition independent spectral / gray RI models are widely used in the evaluation of particle properties of fly ash particles [40, 41, 43, 44, 45, 49, 50, 65, 71, 122, 123] and that experimental data in the literature points out the spectral and chemical composition dependency of RI for ash particles [36, 120, 124-129], there is a need for investigating the influence of spectral nature of complex index of refraction and its composition dependency on non-gray particle radiation in combusting systems.

Therefore, objectives of this section are (i) to bring further clarity to how important it is to account for the spectral nature of RI for calculation of non-gray particle properties and its influence on radiative heat transfer predictions (ii) to evaluate the effects of chemical composition dependency of RI on non-gray particle properties and radiative heat exchange, (iii) to assess the accuracy of gray RI approximations and (iv) to discuss the errors introduced by using gray and spectrally-averaged particle properties for different combustion applications (PC-Fired furnaces, BFBC, CFBC). To address these questions, 9 different RI models (see Section 4.4) are compared for five different ash compositions with respect to (i) spectral complex index of refractions, (ii) single particle absorption, scattering efficiencies and asymmetry factors for a wide range of particle sizes and wavelengths, (iii) spectral particle cloud properties representing PC-Fired furnaces, BFBC and CFBC, (iv) radiative heat flux and source term predictions.



In order to investigate the effect of ash composition on radiative heat transfer, ash compositions required for the calculation of RI are taken from the measurements presented in Section 5.1.1 and Section 5.2.1 for Beypazari and Çan lignite, respectively. Other ash compositions are taken from [119, 126]. Ash analysis of all samples are given in Table 6.19.

Table 6.19 Fly ash compositions

	Ash I (Texas)	Ash II (Canada)	Ash III (Çan)	Ash IV (Beypazari)	Ash V (Pittsburg)
SiO <sub>2</sub> (wt. %)	70.46	51.21	58.08	47.25	39.30
Al <sub>2</sub> O <sub>3</sub> (wt. %)	17.07	20.55	19.48	16.87	20.20
Fe <sub>2</sub> O <sub>3</sub> (wt. %)	2.72	5.37	7.55	14.45	30.50
CaO (wt. %)	4.31	10.04	1.84	0.44	3.00
MgO (wt. %)	0.00	1.82	1.34	1.01	0.80
TiO <sub>2</sub> (wt. %)	1.05	0.94	1.93	3.63	1.17
K <sub>2</sub> O (wt. %)	1.55	1.57	1.48	1.89	1.42
SO <sub>3</sub> (wt. %)	0.74	7.34	6.84	7.44	2.04
Na <sub>2</sub> O (wt. %)	2.10	1.16	1.46	7.02	1.57

For single particle absorption, scattering efficiencies and asymmetry factors, particle size is changed from 1 µm to 1000 µm while the wavelength of incident radiation is varied from 1 µm to 12 µm. For spectral particle cloud properties, three different particle size distributions (PSD) are taken from experimental measurements in pilot scale PC-Fired furnace [43], BFBC (Section 5.1.1, Test 2) and CFBC (Section 5.2.1), which are demonstrated in Figure 6.41. Particle loads for BFBC (0.131 kg/m<sup>3</sup>) and CFBC (3.72 kg/m<sup>3</sup>) are taken from measurements (Section 5.1.1, Section 5.2.1) while a typical projected surface area (0.25 m<sup>2</sup>/m<sup>3</sup> corresponds to a particle load of 6 g/m<sup>3</sup>) is used for PC-Fired furnace particle cloud properties based on the study of [43].

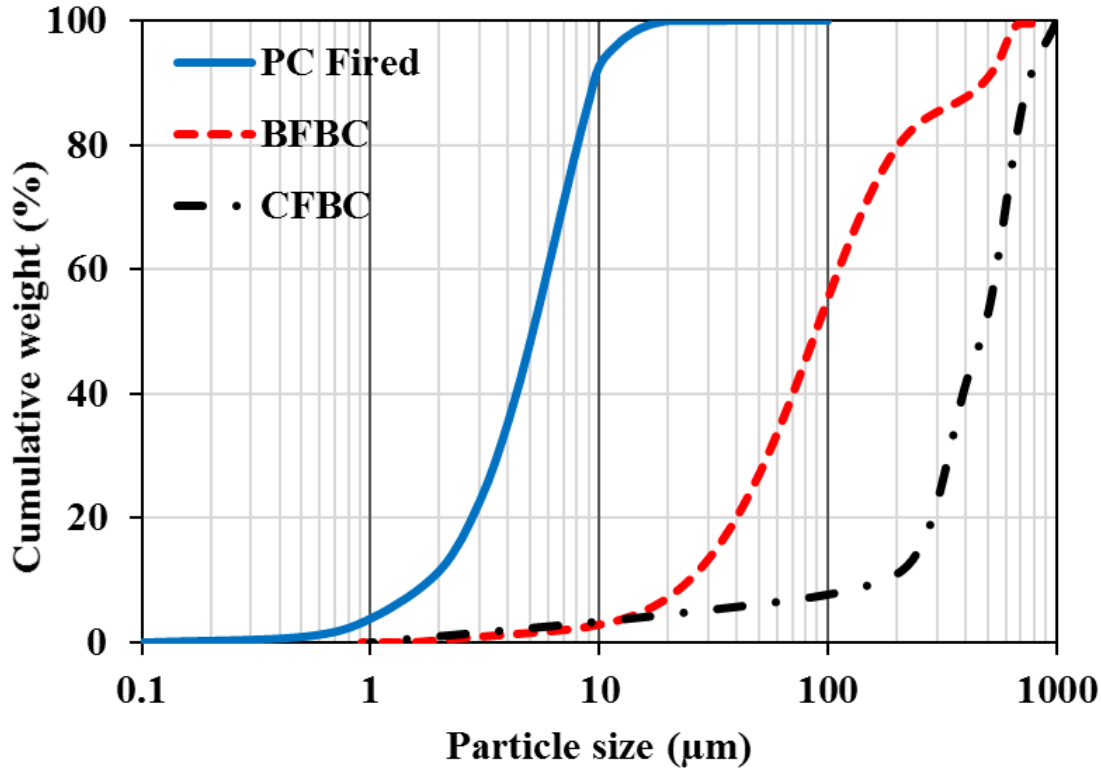


Figure 6.41 Particle size distributions used in the evaluation of non-gray particle properties

For evaluation of the effect of chemical composition on heat flux and source term predictions, input data required for the radiation model and its validation are provided from the coal combustion test given in Section 5.1.1 (combustion test with recycle: Test 2). In the radiation models, freeboard is treated as a 3D rectangular enclosure containing non-gray, absorbing, emitting gas with gray/non-gray absorbing, emitting, anisotropically scattering particles surrounded by black/gray diffuse walls (Section 5.1.3). Radiative properties of the particle laden combustion gases are evaluated by using GWB approximation (Section 3.3) and Mie theory (Section 4.1.3), respectively. Non-gray particle absorption coefficients, scattering coefficients and asymmetry factors are represented by 8 wide bands based on the comparisons presented in Section 6.7.1. In all cases, scattering phase functions are represented by Henyey-Greenstein phase function with normalization (Section 4.3). In MOL solution DOM, a combination of  $S_6$  and 11 x

11 x 81 grid nodes (x, y and z directions, respectively) is utilized for the freeboard based on a previous grid refinement study [150]. For the difference relations of spatial derivatives, three-point upwind differencing scheme DSS014 is employed.

### 6.7.2.1 Selection of Spectral Complex Index of Refraction Models

There are several alternatives for empiric spectral RI model equations in the literature. In this section, most widely used empiric model equations, proposed by Liu, Marakis, Bahador and Johansson (2 RI models; one of which is for ash particles containing carbon residue and the other is for ash particles containing  $\text{Fe}_2\text{O}_3$ ), are compared with Goodwin's correlations for five different ash compositions (presented in Table 6.19) in order to select one chemical composition independent model for further analysis. Refractive (n) and absorption (k) indices are calculated up to 12  $\mu\text{m}$  as it is the common upper limit for those model equations (see Appendix C).

Calculated refractive (n) and absorption (k) indices from these five empiric spectral models and Goodwin's correlations are illustrated in Figure 6.42 and Figure 6.43. As can be seen in Figure 6.42, real part of complex refractive index is about 1.5 up to 12  $\mu\text{m}$  for all cases, which covers about 95% of the thermal radiation. It is also seen that effect of chemical composition has negligible effects on the refractive index for Ash-I to Ash-IV. The only noticeable difference is for Ash-V, which has a very high iron content, hence density. On the other hand, differences in spectral absorption indices (k) are found to be significant between 1-4  $\mu\text{m}$  for all ashes, which corresponds to iron oxide absorption band [36]. In this zone, simpler models overestimate the absorption index (k) for particles containing low iron oxide (Figure 6.43(a)) and underestimate the absorption index (k) for particles containing high iron oxide content (Figure 6.43(d, e)). Furthermore, it is seen that Johansson's proposal for ash particles containing iron yields better predictions than his suggestion based on measurements of [119] in all cases. This is due to the fact that measurements presented in [119] is for ash particles with carbon hence yields high absorption indices for all cases (Figure 6.43 (a-e)). In  $\text{SiO}_2$  absorption band (4-12  $\mu\text{m}$ ), predictions obtained with empiric model equations are found to be more accurate

compared to iron oxide band. The only exception is the Johansson's model representing ash particles with carbon residue.

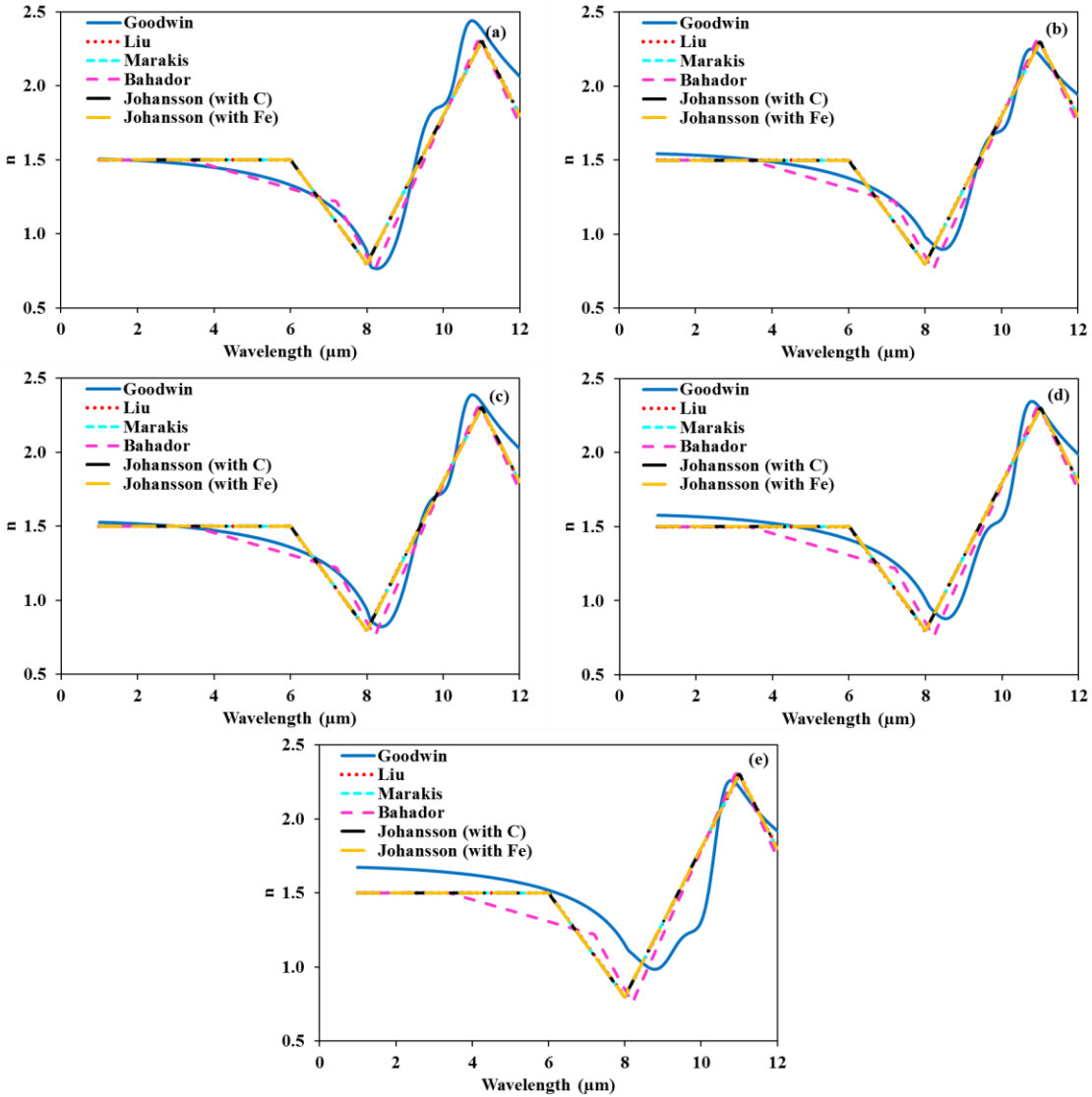


Figure 6.42 Spectral refractive indices calculated by using different RI models for (a) Ash-I to (e) Ash-V

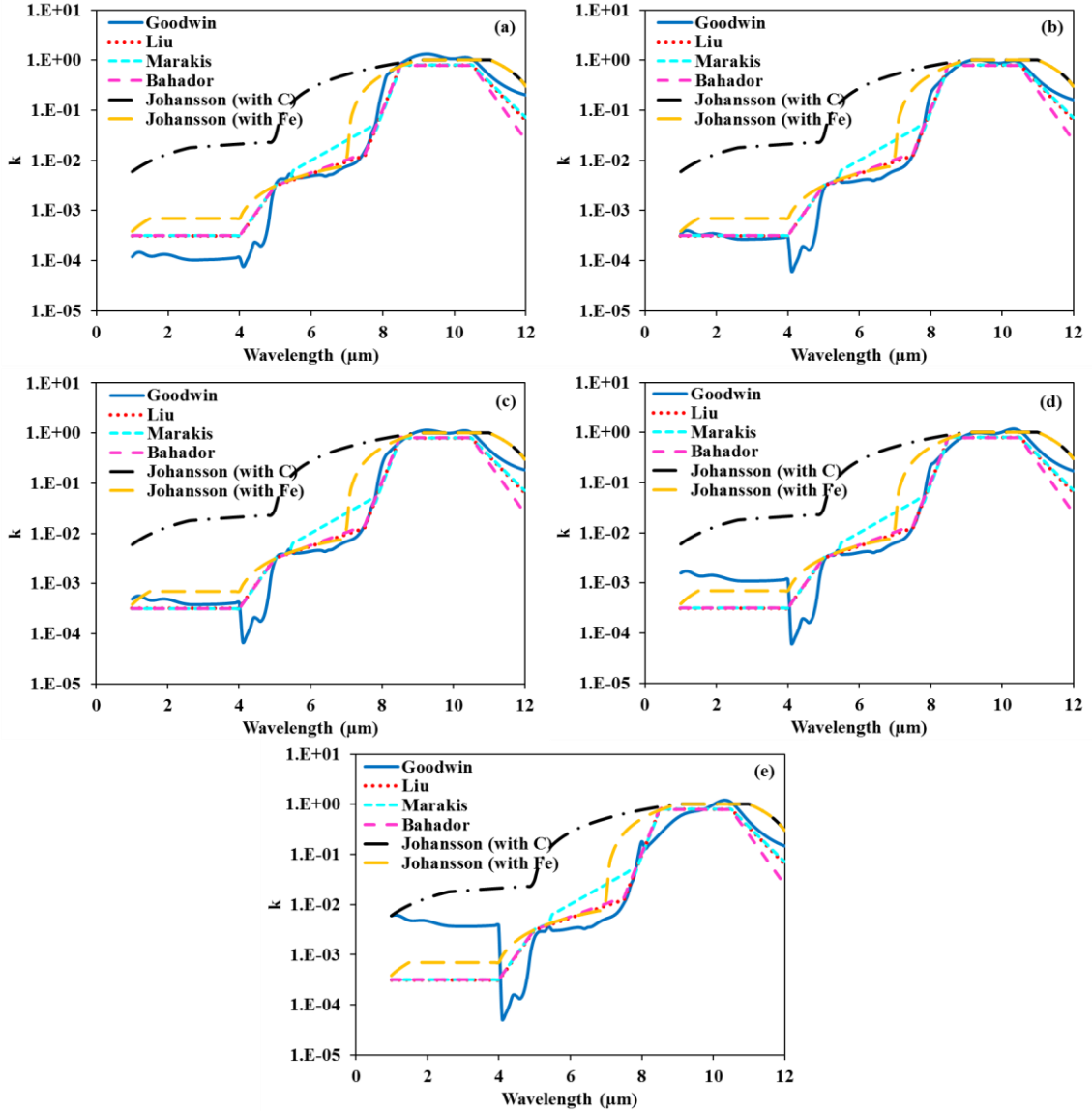


Figure 6.43 Spectral absorption indices calculated by using different RI models for (a) Ash-I to (e) Ash-V

Relative percentage errors in spectral refractive ( $n$ ) and absorption ( $k$ ) indices are given in Table 6.20. As can be seen from the table, refractive indices ( $n$ ) are in good agreement with Goodwin's correlations for all RI models and predictive accuracies of all models are in the same order of magnitude. For the absorption indices ( $k$ ), however, there is a noticeable difference in the predictive accuracies, especially at low iron oxide content (Ash-I, Ash-II). It is also seen that Liu's model gives the highest accuracy among the

models neglecting the chemical composition dependency of ash particles. Therefore, only Liu's model will be further investigated for the effects of RI on particle radiative properties and heat flux / source term distributions.

Table 6.20 Average relative percentage errors in spectral refractive (n) and absorption (k) indices

RI Model	$Error^* \% = 100x \left  \sum_{i=1}^N \frac{\varphi_{Ref_i} - \varphi_{j_i}}{\varphi_{Ref_i}} / N \right $									
	Ash-I (3 % Fe <sub>2</sub> O <sub>3</sub> )		Ash-II (5 % Fe <sub>2</sub> O <sub>3</sub> )		Ash-III (8 % Fe <sub>2</sub> O <sub>3</sub> )		Ash-IV (15 % Fe <sub>2</sub> O <sub>3</sub> )		Ash-V (31 % Fe <sub>2</sub> O <sub>3</sub> )	
	n	k	n	k	n	k	n	k	n	k
Liu	7	96	5	58	6	59	7	77	12	104
Marakis	7	124	5	93	6	90	7	112	12	146
Bahador	4	100	4	63	4	63	7	81	13	110
Johansson (with C)	8	4939	6	3384	6	2796	5	2419	9	2693
Johansson (with Fe)	8	186	6	114	6	88	5	90	9	128
Goodwin	Reference		Reference		Reference		Reference		Reference	
* i represents the spectral points ( $\lambda=1, 1.1, \dots, 12 \mu\text{m}$ ), N is the total number of spectral points (111), $\varphi$ represents the spectral property										

### 6.7.2.2 Effect of Complex Index of Refraction on Spectral Particle Properties

Effect of chemical composition and spectral dependency of RI on spectral absorption efficiencies, scattering efficiencies and asymmetry factors are investigated by comparing Mie solutions obtained with two chemical-composition-dependent (Ebert (spectral),  $m=1.5-k(\text{Fe})i$  (gray)) and two chemical-composition-independent (Liu (spectral),  $m=1.5-0.02i$  (gray)) RI models with those of Goodwin. It should be noted that spectral dependency of Mie solutions (that is  $Q_a(\lambda, m(\lambda))$ ,  $Q_s(\lambda, m(\lambda))$ ,  $g(\lambda, m(\lambda))$ ) comes from two input parameters; wavelength of incident radiation ( $\lambda$ ) and spectral dependency of RI ( $m(\lambda)$ ). Therefore, spectral Mie solutions can still be achieved even if the RI model is gray (spectrally independent).

Mie solutions for single particles ( $Q_a(\lambda, m(\lambda))$ ,  $Q_s(\lambda, m(\lambda))$ ,  $g(\lambda, m(\lambda))$ ) are generated for 217 different particle sizes (between 1 and 1000  $\mu\text{m}$ ), 111 spectral points (between 1 and 12  $\mu\text{m}$ ) and 5 different ash compositions (Ash-I to Ash-V), which gives more than 600,000 Mie solutions covering the particle sizes, compositions and wavelengths relevant to combusting systems. Spectral absorption efficiencies  $Q_a(\lambda, m(\lambda))$ , scattering efficiencies  $Q_s(\lambda, m(\lambda))$  and asymmetry factors  $g(\lambda, m(\lambda))$  at three different wavelengths (3, 6 and 10  $\mu\text{m}$ , representing iron oxide, mixed region and silicon oxide absorption bands, respectively) are demonstrated in Figure 6.44, Figure 6.45 and Figure 6.46, respectively, for Ash-I, III, and V (representing low, medium and high iron oxide contents in ash, respectively). Results for Ash-II and IV are not given here for the sake of brevity. A more detailed demonstration of Mie solutions for increasing wavelength and particle sizes for Ash I-V can be found in Appendix G.

Absorption efficiencies calculated by using different RI models are demonstrated in Figure 6.44. When the  $Q_a$  obtained by using Goodwin's correlations are compared, it is seen that absorption efficiency increases with increasing wavelength and particle size and reaches to asymptotic values for large particles, for all RI models. In the 1-4  $\mu\text{m}$  region (Figure 6.44(a, d, g)), where the absorption is due to the iron oxide content, chemical-composition-dependent RI models (Ebert's model and gray RI model based on iron content ( $1.5-k(\text{Fe})i$ )) yield very close absorption efficiencies to those of Goodwin. Liu's

approach, however, is found to be accurate only for Ash II (see Appendix G) which has an iron oxide content around 5 %. For other ash compositions, Liu's model is found to either over-predict (Ash-I) or under predict (for Ash III-V) the absorption efficiencies. This is considered to be due to the fact that Liu's model is based on an ash composition with 6 %  $\text{Fe}_2\text{O}_3$  content [43]. In other words, Liu's model yields accurate results if the ash composition of the investigated coal is the same as that of Liu's model. For all ashes (Ash-I to V), gray RI approximation (1.5-0.02i), which neglects the chemical composition dependency, is found to be over-estimating the absorption efficiencies for the majority of the particle sizes due to its high absorption index ( $k=0.02$ ).

In the wavelength region of 4-8  $\mu\text{m}$ , in which the absorption is due to combination of  $\text{Fe}_2\text{O}_3$  and  $\text{SiO}_2$  mechanisms [36], absorption efficiencies are noticeably higher compared to those of  $\text{Fe}_2\text{O}_3$  region due to the addition of stronger  $\text{SiO}_2$  absorption band. Hence accuracy of RI models is found to be mainly correlated to the  $\text{SiO}_2$  content. In this mixed region (Figure 6.44(b, e, h)), Ebert's model gives the closest absorption efficiencies to Goodwin's predictions where the predictive accuracy of Liu's approximation (55 %  $\text{SiO}_2$  [43]) is found to be decreasing with decreasing  $\text{SiO}_2$  content of the ash (From Ash I to III, II, IV, V, see also Appendix G). On the other hand, gray RI model based on iron content (1.5- $k(\text{Fe})i$ ) is found to underestimate  $Q_a$  unless the iron oxide content is very high (Ash-V) due to the negligence of silica absorption band (see Eq. (4.1)). Moreover, gray RI approximation (1.5-0.02i) still over-predicts the absorption efficiencies due to its high absorption index.

Between 8-12  $\mu\text{m}$  (Figure 6.44(c, f, i)), which is dominated by the broad Reststrahlen band of  $\text{SiO}_2$ , absorption efficiencies are found to be significantly high for small particles due to several orders of magnitude increase in the absorption index ( $k$ ) in this region (see also Appendix G). Both Ebert's and Liu's models are found to be sufficiently accurate for particles larger than 10  $\mu\text{m}$ . For very small particles, however, Liu's model under-predicts the absorption efficiencies where discrepancy increases with decreasing  $\text{SiO}_2$  content. It is also seen that both gray and iron oxide based RI models underestimate absorption efficiencies for the majority of particle sizes of interest.



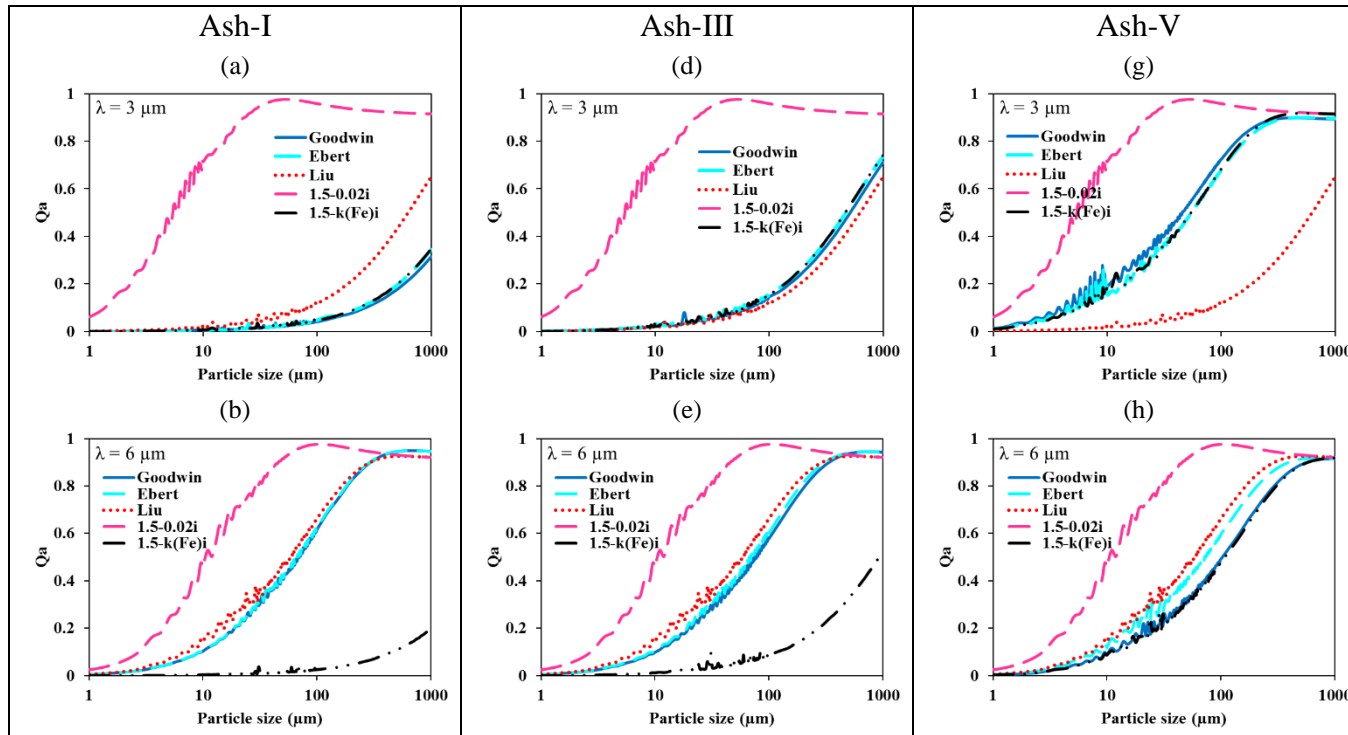


Figure 6.44 Comparison of absorption efficiencies ( $Q_a$ ) for (a-c) Ash-I, (d-f) Ash-III and (g-i) Ash-V

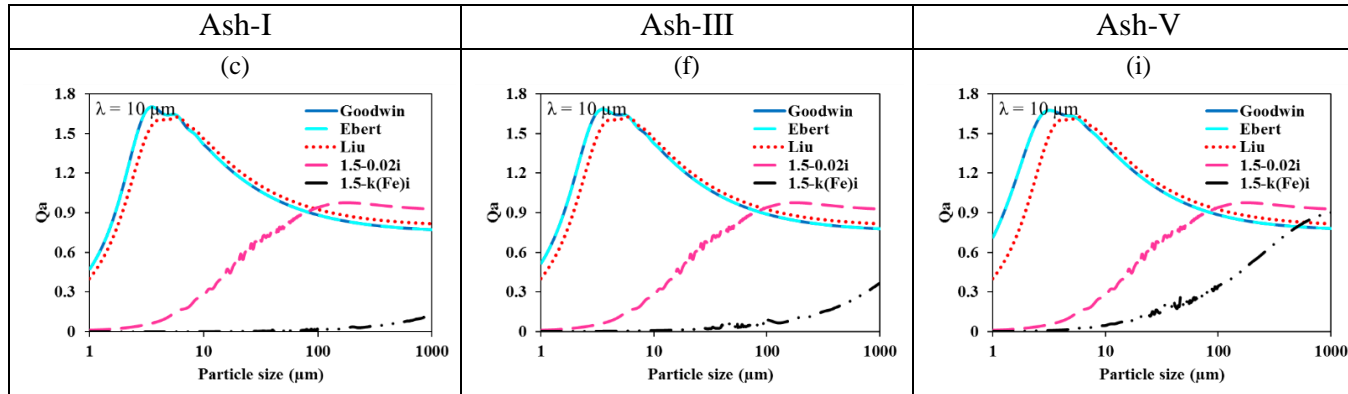


Figure 6.44 Comparison of absorption efficiencies ( $Q_a$ ) for (a-c) Ash-I, (d-f) Ash-III and (g-i) Ash-V (cont'd)

Scattering efficiencies calculated by using different RI models are shown in Figure 6.45. It is seen that predictive accuracy of all RI models are noticeably better in scattering efficiency calculations compared to those of absorption efficiency calculations. In particular, Ebert's model is found to give very accurate results for all particle sizes and wavelengths (Figure 6.45). On the other hand, predictive accuracy of Liu's approximation is found to be dependent on chemical composition only in the short wavelength region ( $<4 \mu\text{m}$ ) if the particle diameter is large (Figure 6.45(a, d, g)). This is considered to be due to the extinction efficiency limit for large particles, that is, under-estimation of absorption efficiency (see Figure 6.44) leads to over-estimation of the scattering efficiency as their summation always gives " $Q_e = 2.0$ ". Gray RI approximation (1.5-0.02i) is found to under-estimate the scattering efficiencies for  $\lambda < 8 \mu\text{m}$  (Figure 6.45(b, e, h)). Beyond  $8 \mu\text{m}$ , it is found to over-estimate the scattering efficiencies. It is also seen that discrepancy between gray RI approximation and Goodwin's correlations increases with decreasing iron oxide content (Figure 6.45(c, f, i)). On the other hand, gray RI model based on iron content (1.5-k(Fe)i) leads to very accurate results in the 1-4  $\mu\text{m}$  region but its accuracy is found to decrease with increasing wavelength.

Asymmetry factors calculated by using different RI models are demonstrated in Figure 6.46. As can be seen from the figure, predictive accuracy of Ebert's model is very good. Similar to scattering efficiencies, negligence of iron oxide content dependency is found to lead errors in Liu's approximation for large particles if  $\lambda < 4 \mu\text{m}$  (Figure 6.46 (a, d, g)). Gray RI approximation (1.5-0.02i) over-estimates the asymmetry factor for particles larger than  $10 \mu\text{m}$  while Gray RI model based on iron content (1.5-k(Fe)i) leads to very accurate results in the 1-4  $\mu\text{m}$  region but its accuracy decreases with increasing wavelength, especially for large particles. Nevertheless, effect of chemical composition on predictive accuracy of asymmetry factor predictions are not significant compared to those of  $Q_a$  or  $Q_s$  and all RI models yield sufficiently accurate predictions for the majority of particle sizes and wavelengths (see also; Appendix G).

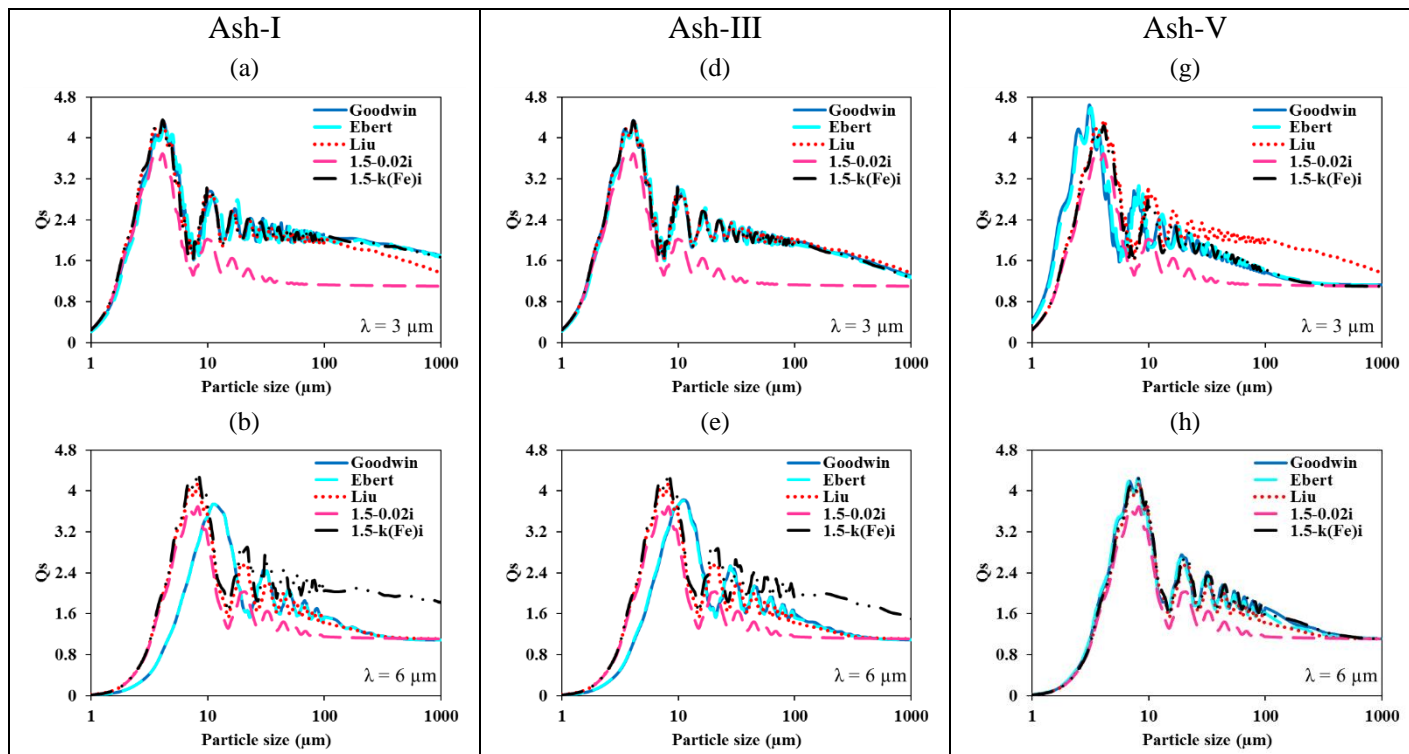


Figure 6.45 Comparison of scattering efficiencies ( $Q_s$ ) for (a-c) Ash-I, (d-f) Ash-III and (g-i) Ash-V

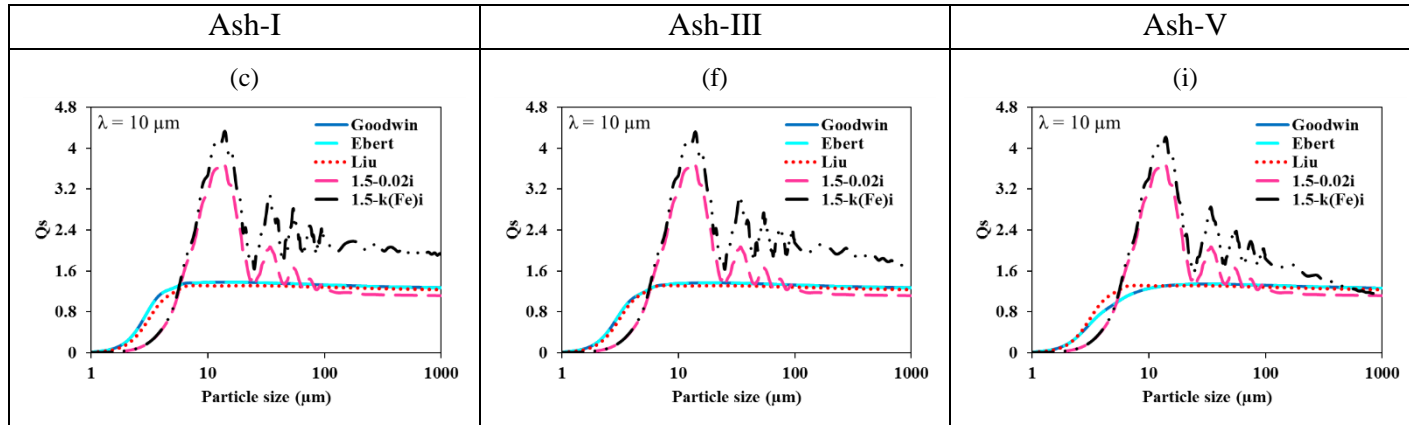


Figure 6.45 Comparison of scattering efficiencies ( $Q_s$ ) for (a-c) Ash-I, (d-f) Ash-III and (g-i) Ash-V (cont'd)

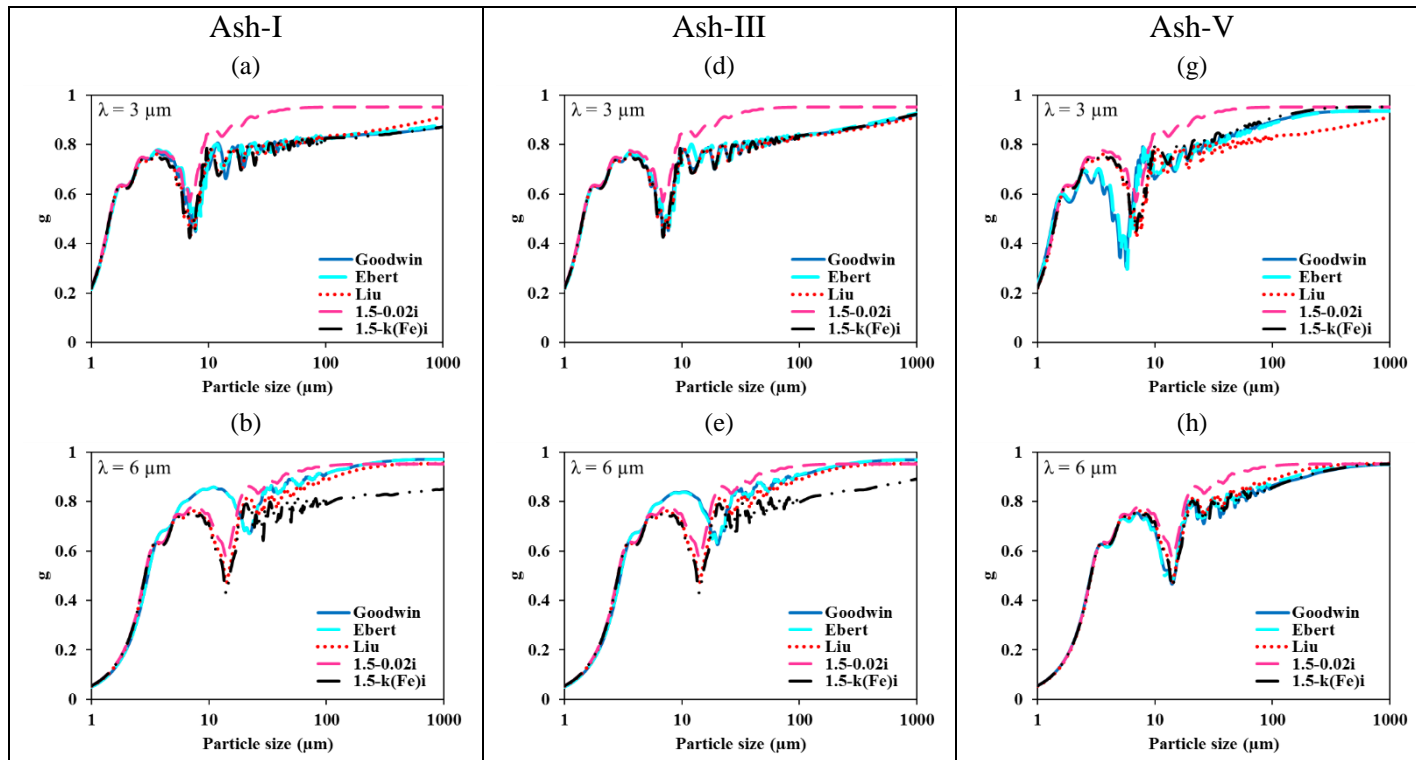


Figure 6.46 Comparison of asymmetry factors ( $g$ ) for (a-c) Ash-I, (d-f) Ash-III and (g-i) Ash-V

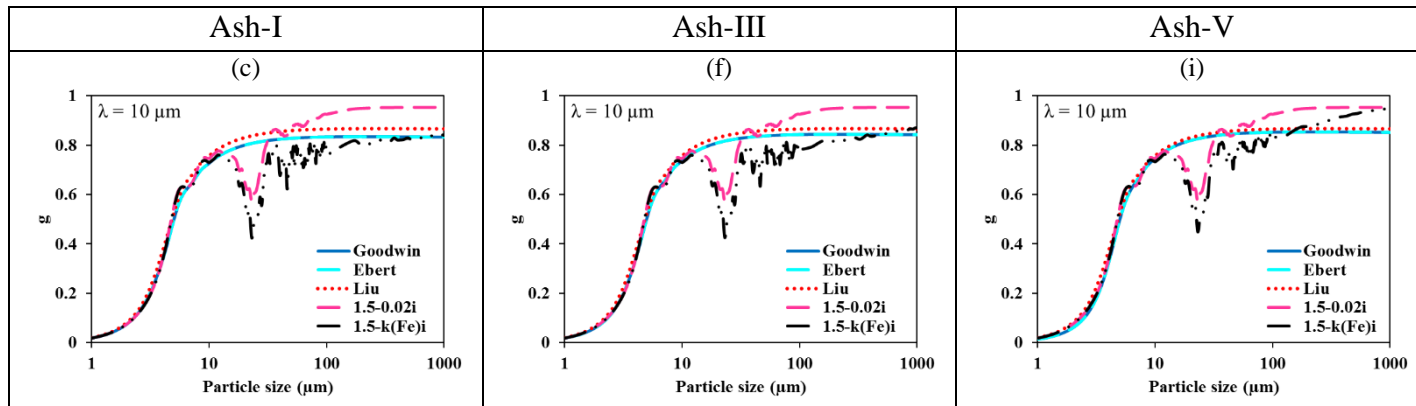


Figure 6.46 Comparison of asymmetry factors ( $g$ ) for (a-c) Ash-I, (d-f) Ash-III and (g-i) Ash-V (cont'd)

Spectrally averaged relative percentage errors in absorption efficiencies ( $Q_a$ ), scattering efficiencies ( $Q_s$ ) and asymmetry factor ( $g$ ) are given in Table 6.21 for five different ash compositions (Ash-I to V) and for three different particle diameters (10, 50 and 250  $\mu\text{m}$ ). As can be seen from the table, negligence of chemical composition dependency in Liu's model does not lead to significant errors in either scattering efficiencies or asymmetry factors. Negligence of spectral variation in RI, on the other hand, causes significant errors in scattering efficiencies especially if the particle size is small. More importantly, Table 6.21 reveals that absorption efficiency is a strong function of chemical composition and RI models neglecting this dependency cause significant errors whether they are spectral (Liu) or gray (1.5-0.02i). It is also seen that this discrepancy in absorption efficiencies becomes larger with decreasing particle size, which is of considerable importance as fine particles usually constitute the larger fraction of the total cross-sectional area in a polydisperse particle cloud.



Table 6.21 Average relative percentage errors in absorption efficiencies (Qa), scattering efficiencies (Qs) and asymmetry factor (g) for 10, 50 and 250 μm particles

RI models and particle diameter	$Error^* \% = 100x \sum_{i=1}^N \frac{\varphi_{Ref_{i,k}} - \varphi_{j_{i,k}}}{\varphi_{Ref_{i,k}}} / N$														
d <sub>p</sub> = 10 μm	Ash-I (3 % Fe <sub>2</sub> O <sub>3</sub> )			Ash-II (5 % Fe <sub>2</sub> O <sub>3</sub> )			Ash-III (8 % Fe <sub>2</sub> O <sub>3</sub> )			Ash-IV (15 % Fe <sub>2</sub> O <sub>3</sub> )			Ash-V (31 % Fe <sub>2</sub> O <sub>3</sub> )		
	Qa	Qs	g	Qa	Qs	g	Qa	Qs	g	Qa	Qs	g	Qa	Qs	g
Ebert	-10	-7	0	5	18	0	8	13	0	9	13	-1	7	9	-1
Liu	85	1	-3	45	-5	-2	31	-2	-3	19	-4	-1	22	5	2
1.5-k(Fe) <sub>i</sub> , λ=f(λ)	-63	310	-5	-55	156	-5	-47	208	-5	-6	132	-4	127	121	1
1.5-0.02i, λ=f(λ)	3488	252	3	1881	118	3	1532	164	3	1091	98	4	990	93	8
Goodwin	Reference solution														
d <sub>p</sub> = 50 μm	Ash-I (3 % Fe <sub>2</sub> O <sub>3</sub> )			Ash-II (5 % Fe <sub>2</sub> O <sub>3</sub> )			Ash-III (8 % Fe <sub>2</sub> O <sub>3</sub> )			Ash-IV (15 % Fe <sub>2</sub> O <sub>3</sub> )			Ash-V (31 % Fe <sub>2</sub> O <sub>3</sub> )		
	Qa	Qs	g	Qa	Qs	g	Qa	Qs	g	Qa	Qs	g	Qa	Qs	g
Ebert	-6	-2	0	8	1	0	7	4	0	8	1	0	6	2	-1
Liu	70	-1	2	40	-3	1	23	-2	1	17	0	1	20	9	0
1.5-k(Fe) <sub>i</sub> , λ=f(λ)	-65	36	-8	-55	35	-8	-50	34	-8	-8	31	-7	100	27	-5
1.5-0.02i, λ=f(λ)	1133	-16	8	705	-16	7	527	-16	7	434	-14	7	411	-9	6
Goodwin	Reference solution														

Table 6.21 Average relative percentage errors in absorption efficiencies (Qa), scattering efficiencies (Qs) and asymmetry factor (g) for 10, 50 and 250 μm particles (cont'd)

RI models and particle diameter	$Error^* \% = 100x \sum_{i=1}^N \frac{\varphi_{Ref_{i,k}} - \varphi_{j_{i,k}}}{\varphi_{Ref_{i,k}}} / N$														
d <sub>p</sub> = 250 μm	Ash-I (3 % Fe <sub>2</sub> O <sub>3</sub> )			Ash-II (5 % Fe <sub>2</sub> O <sub>3</sub> )			Ash-III (8 % Fe <sub>2</sub> O <sub>3</sub> )			Ash-IV (15 % Fe <sub>2</sub> O <sub>3</sub> )			Ash-V (31 % Fe <sub>2</sub> O <sub>3</sub> )		
	<b>Qa</b>	<b>Qs</b>	<b>g</b>	<b>Qa</b>	<b>Qs</b>	<b>g</b>	<b>Qa</b>	<b>Qs</b>	<b>g</b>	<b>Qa</b>	<b>Qs</b>	<b>g</b>	<b>Qa</b>	<b>Qs</b>	<b>g</b>
Ebert	-7	0	0	4	0	0	7	0	0	6	0	0	6	0	0
Liu	61	-6	3	28	-3	1	19	-1	1	11	5	0	16	11	-1
1.5-k(Fe) <sub>i</sub> , λ=f(λ)	-62	43	-6	-51	40	-6	-42	37	-5	-5	27	-3	62	8	1
1.5-0.02i, λ=f(λ)	257	-20	9	147	-18	7	119	-17	7	90	-13	6	98	-9	5
Goodwin	Reference solution														
* i represents the spectral points (λ=1, 1.1,...,12 μm), N is the total number of spectral points (111), φ represents the spectral property															

Considering the nonlinear dependency of absorption and scattering efficiencies on particle size and the fact that there always exists particle size distribution in combustion applications, these large differences in absorption and scattering efficiencies due to chemical composition dependency (as can be seen in Figure 6.44-Figure 6.46 and Table 6.21) may be decreased by the presence of wide particle size distributions (PSD). In order to test this hypothesis, radiative properties of three different particle clouds are calculated by using five RI models discussed above for five different ash compositions (Ash-I to V). PSDs and particle loads, necessary for the evaluation of particle absorption and scattering coefficients, are selected from the experimental measurements available in the literature (see Figure 6.41).

Radiative properties of Ash-IV particle clouds for three combusting systems are demonstrated in Figure 6.47. As can be seen from the Figure 6.47 (a-c), using gray RI model (1.5-0.02i,  $\lambda=3 \mu\text{m}$ ) leads to significant over-estimation in the absorption coefficients of the particle clouds even in the presence of a PSD. Furthermore, changing only the wavelength in Mie solutions (i.e.,  $\lambda$  in size parameter,  $x = \pi d_p/\lambda$ ) while keeping the RI constant (1.5-0.02i,  $\lambda=f(\lambda)$ ) only leads to a monotonic decrease in the particle properties compared to that of gray particles (1.5-0.02i,  $\lambda=3 \mu\text{m}$ ). Hence, changing only the wavelength of incident radiation cannot capture the spectral behavior of the particles even with a PSD and chemical composition dependency of RI is very influential on particle absorption coefficients. Similar to single particle absorption efficiencies, predictive accuracy of Liu's approximation is found to be sensitive to chemical composition, especially in the iron oxide band (1-4  $\mu\text{m}$ ). Furthermore, spectral particle absorption coefficients calculated by using Ebert's model are in good agreement with the reference solution for all PSDs. On the other hand, Gray RI models taking chemical composition dependency into consideration (1.5-k(Fe)i,  $\lambda=f(\lambda)$ ; 1.5-k(Fe)i,  $\lambda=3 \mu\text{m}$ ) are found to be accurate only in iron oxide band and they underestimate the absorption coefficients beyond 4  $\mu\text{m}$ .

Scattering absorption coefficients calculated with three different PSDs and loads are shown in Figure 6.47 (d-f). Predictive accuracy of gray RI models which neglect chemical composition dependency (1.5-0.02i,  $\lambda=f(\lambda)$ ; 1.5-0.02i,  $\lambda=3 \mu\text{m}$ ) is found to be decreasing

with decreasing particle size (from CFBC to PC-Fired). Both Ebert's and Liu's models give very accurate results for PC-Fired furnaces while the discrepancy between Liu's model and reference solution increases with increasing particle size (from PC-Fired to CFBC). It is also seen that RI models based on iron content ( $1.5-k(\text{Fe})_i$ ,  $\lambda=f(\lambda)$ ;  $1.5-k(\text{Fe})_i$ ,  $\lambda=3 \mu\text{m}$ ) yields better predictions compared to those of gray RI models neglecting chemical composition dependency.

Asymmetry factors averaged over the particle size distribution (weighing factor is based on the geometric cross-sectional area of particles) are demonstrated in Figure 6.47 (g-i). As can be seen from the figures, presence of PSD does not affect the predictive accuracy of all RI models, which have already been shown to be accurate for single size particles (see Figure 6.46).

Average relative percentage errors in absorption coefficient ( $\kappa_p$ ), scattering coefficient ( $\sigma_p$ ) and asymmetry factor ( $g$ ) of Ash-IV for three particle clouds are given in Table 6.22. As can be seen from the table, errors in absorption coefficients, introduced by neglecting the chemical composition dependency of RI, are quite large and presence of PSDs does not smooth over the differences in single-particle absorption efficiencies (seen in Figure 6.44, Figure 6.45, Figure 6.46 and Table 6.21). Although it is reduced, errors in using gray RI models ( $1.5-0.02i$ ,  $\lambda=f(\lambda)$ ;  $1.5-0.02i$ ,  $\lambda=3 \mu\text{m}$ ) are still significant. Utilization of a chemical-composition-dependent gray RI model ( $1.5-k(\text{Fe})_i$ ,  $\lambda=f(\lambda)$ ;  $1.5-k(\text{Fe})_i$ ,  $\lambda=3 \mu\text{m}$ ) is found to decrease the error in chemical-composition-independent gray RI assumption ( $1.5-0.02i$ ,  $\lambda=f(\lambda)$ ;  $1.5-0.02i$ ,  $\lambda=3 \mu\text{m}$ ). Nevertheless, the error is still considerably large. Furthermore, it is also seen that changing only the wavelength of incident radiation while neglecting the spectral dependency of RI does not improve the predictive accuracy.

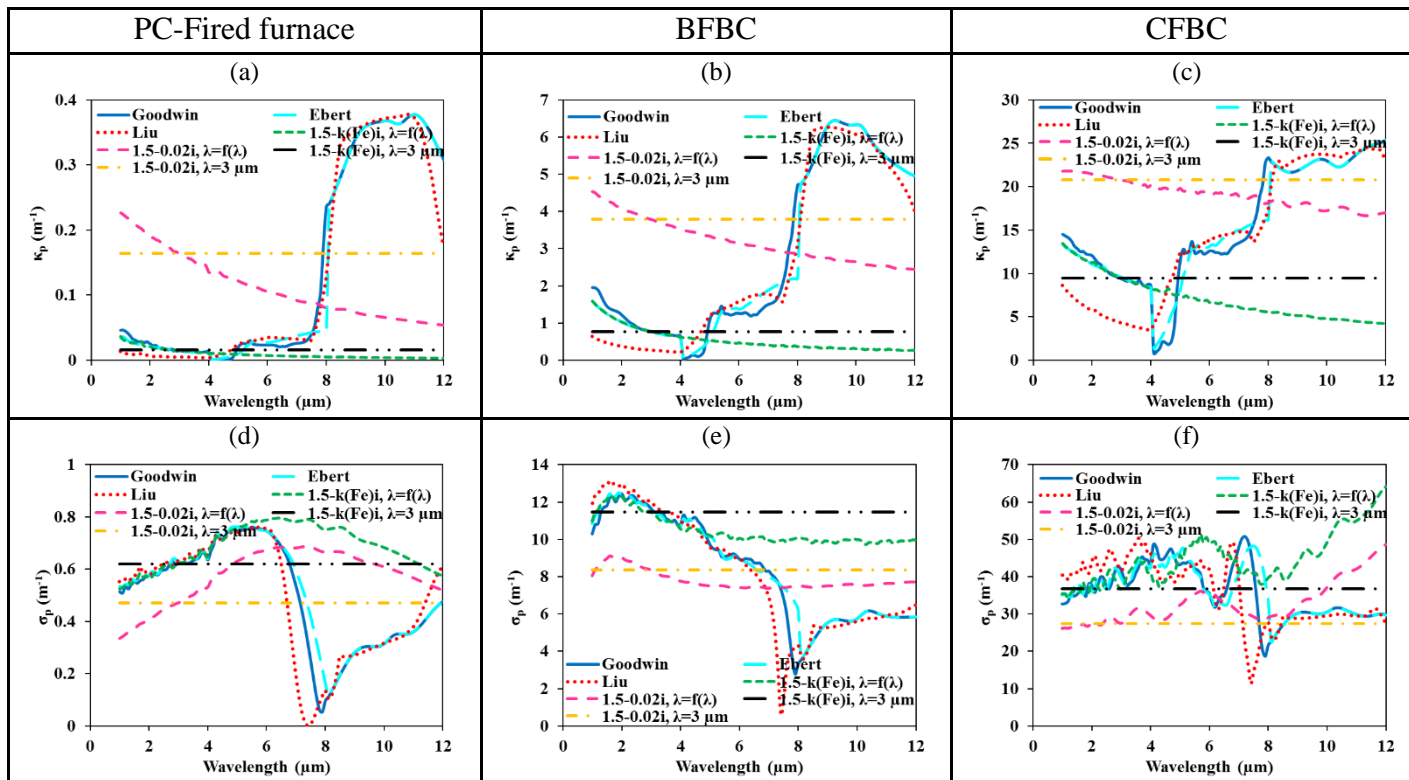


Figure 6.47 Comparison of representative (a-c) particle absorption coefficients, (d-f) scattering coefficients and (g-i) asymmetry factors for PC-Fired furnace, BFBC and CFBC for Ash-IV

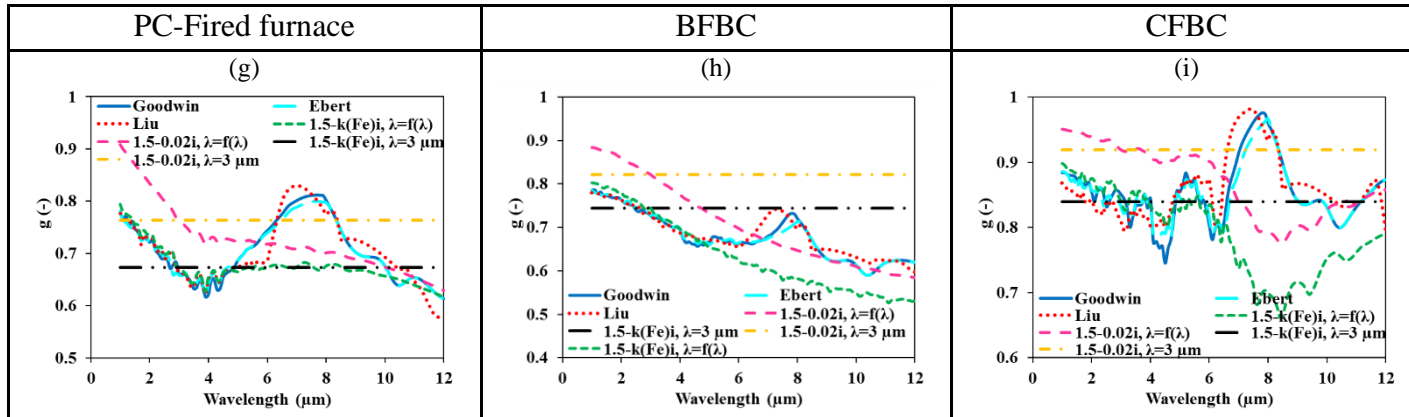


Figure 6.47 Comparison of representative (a-c) particle absorption coefficients, (d-f) scattering coefficients and (g-i) asymmetry factors for PC-Fired furnace, BFBC and CFBC for Ash-IV (cont'd)

Table 6.22 Average relative percentage errors in absorption coefficient ( $\kappa_p$ ), scattering coefficient ( $\sigma_p$ ) and asymmetry factor ( $g$ ) of Ash-IV for three particle clouds

Comparison of averaged spectral properties	$Error^* \% = 100x \sum_{i=1}^N \frac{\varphi_{j_i} - \varphi_{Ref_i}}{\varphi_{Ref_i}} / N$								
	<i>PC-Fired</i>			<i>BFBC</i>			<i>CFBC</i>		
RI Model	$\kappa_p$	$\sigma_p$	$g$	$\kappa_p$	$\sigma_p$	$g$	$\kappa_p$	$\sigma_p$	$g$
Ebert	0	2	0	-1	0	0	-1	-1	0
Liu	-17	-2	0	-18	-2	1	-14	1	1
1.5-k(Fe)i, $\lambda=f(\lambda)$	-64	60	-3	-60	34	-5	48	30	-5
1.5-0.02i, $\lambda=f(\lambda)$	301	36	3	110	1	4	34	-4	2
1.5-k(Fe)i, $\lambda=3 \mu\text{m}$	-55	44	-3	-53	50	11	-35	5	0
1.5-0.02i, $\lambda=3 \mu\text{m}$	370	9	10	129	9	22	42	-22	9
Goodwin	Reference solution								
* i represents the spectral points ( $\lambda=1, 1.1, \dots, 12 \mu\text{m}$ ), N is the total number of spectral points (111), $\varphi$ represents the spectral property.									

In order to further demonstrate the influence of chemical composition on radiative properties in the presence of a PSD, average relative percentage errors in absorption coefficient ( $\kappa_p$ ), scattering coefficient ( $\sigma_p$ ) and asymmetry factor ( $g$ ) are given in Table 6.23 for five different ash compositions (Ash I-V) at BFBC conditions. It is seen that absorption coefficient of particles can be accurately calculated by using Ebert's model for a wide variety of ash compositions. On the other hand, Liu's approximation, which is a spectral RI model neglecting chemical composition dependency, is found to be accurate if the ash composition is similar to that of Liu [43] (~ 6 % Fe<sub>2</sub>O<sub>3</sub>, ~ 55 % SiO<sub>2</sub>). In other cases, Liu's model either under-predicts or over-predicts the absorption coefficients depending on the iron content of the ash. Furthermore, RI models based on iron content (1.5-k(Fe)i,  $\lambda=f(\lambda)$ ; 1.5-k(Fe)i,  $\lambda=3 \mu\text{m}$ ) are found to be more accurate than gray RI models neglecting chemical composition dependency (1.5-0.02i,  $\lambda=f(\lambda)$ ; 1.5-0.02i,  $\lambda=3 \mu\text{m}$ ) for absorption coefficients and difference between these approaches increases with decreasing iron oxide content. Predictive accuracy in scattering coefficients and

asymmetry factors are found to be much better than those of absorption coefficients for all RI models. However, RI models based on iron content over-predict the scattering coefficients noticeably, which can also be seen in Figure 6.47.

Comparisons presented in Table 6.22 and Table 6.23 reveal that complex index of refraction (RI) plays a major role in determining radiative properties of particle clouds for combusting systems. Furthermore, it is seen that spectral nature of particle properties is originated from the spectral nature of RI rather than the spectral nature of the incident radiation ( $\lambda$ ). These results also show that RI is a strong function of chemical composition and negligence of either spectral nature or chemical composition dependency of the RI leads to significant errors in spectral particle properties.



Table 6.23 Average relative percentage errors in absorption coefficient ( $\kappa_p$ ), scattering coefficient ( $\sigma_p$ ) and asymmetry factor ( $g$ ) of Ash-I to V for BFBC particle cloud

Comparison of averaged spectral properties	$Error^* \% = 100x \sum_{i=1}^N \frac{\varphi_{j_i} - \varphi_{Ref_i}}{\varphi_{Ref_i}} / N$														
	Ash-I (3 % Fe <sub>2</sub> O <sub>3</sub> )			Ash-II (5 % Fe <sub>2</sub> O <sub>3</sub> )			Ash-III (8 % Fe <sub>2</sub> O <sub>3</sub> )			Ash-IV (15 % Fe <sub>2</sub> O <sub>3</sub> )			Ash-V (31 % Fe <sub>2</sub> O <sub>3</sub> )		
RI Model	$\kappa_p$	$\sigma_p$	$g$	$\kappa_p$	$\sigma_p$	$g$	$\kappa_p$	$\sigma_p$	$g$	$\kappa_p$	$\sigma_p$	$g$	$\kappa_p$	$\sigma_p$	$g$
Ebert	1	0	0	-1	0	0	0	0	0	-1	0	0	-2	0	0
Liu	46	-5	1	5	-3	1	-6	-4	1	-18	-2	1	-19	3	1
1.5-k(Fe) <sub>i</sub> , $\lambda=f(\lambda)$	-67	34	-7	-68	37	-7	-65	34	-7	-60	34	-5	-43	15	-3
1.5-0.02i, $\lambda=f(\lambda)$	966	-3	4	391	0	4	277	-2	4	110	1	4	50	7	4
1.5-k(Fe) <sub>i</sub> , $\lambda=3 \mu\text{m}$	-70	52	1	-68	56	9	-64	51	9	-53	50	11	-26	46	14
1.5-0.02i, $\lambda=3 \mu\text{m}$	970	5	22	406	8	22	293	6	22	129	9	22	72	15	23
Goodwin	Reference solution														
* i represents the spectral points ( $\lambda=1, 1.1, \dots, 12 \mu\text{m}$ ), N is the total number of spectral points (111), $\varphi$ represents the spectral property															

### 6.7.2.3 Effect of Refractive Index on Heat Flux and Source Term Predictions

In the previous section, effect of chemical composition on non-gray particle properties is demonstrated for ash particles. Nevertheless, this difference may be reduced when heat flux and source term distributions are calculated by using these particle cloud properties considering the fact that errors in single particle efficiencies (Table 6.21) are reduced for polydisperse particle clouds (Table 6.22, Table 6.23).

Table 6.24 demonstrates comparison between incident heat fluxes and source terms predicted by MOL solution of DOM coupled with non-gray gas and non-gray particle properties, predicted by using different RI models in Mie solutions (see Section 2.3 for the solution method). Visual comparison of heat flux predictions with measurements and source terms with the reference solution are also illustrated in Figure 6.48 for Ash-IV. As can be seen from the table, incident heat fluxes obtained with all RI models are in good agreement with the reference solution and measurements for all ash compositions under the experimental conditions presented in Section 5.1.1. Predictive accuracy of RI models in source term predictions, on the other hand, shows a similar trend to those in particle absorption coefficients given in Table 6.23. It is seen that Ebert's model yields very accurate source term predictions while the predictive accuracy of Liu's model is a strong function of the iron content of the ash. Although errors in source term predictions are less than those of absorption coefficients, they are still high, especially for low and high iron oxide contents. These comparisons indicate that a complex index of refraction model that does not include the effect of chemical composition (such as Liu's approximation) may yield significant errors in source term predictions. Gray RI approximations (either spectral,  $1.5-0.02i$ ,  $\lambda=f(\lambda)$ , or gray,  $1.5-0.02i$ ,  $\lambda=3 \mu\text{m}$ ) are found to give the highest errors in all cases, especially if the iron oxide content is low. On the other hand, using an iron oxide content based absorption index (as in  $1.5-k(\text{Fe})_i$ ,  $\lambda=3 \mu\text{m}$ ) noticeably increases the accuracies of gray particle predictions and this approach can be utilized if gray particle assumption is needed to reduce the CPU requirement of the radiation model.

Table 6.24 Average relative percentage errors in incident wall heat fluxes ( $q_w$ ) and source terms along the centerline ( $\nabla q$ ) of Ash-I to V for BFBC combustion test

Comparison of averaged spectral properties	$Error \% = 100x \sum_{i=1}^N \frac{\varphi_{j_i} - \varphi_{Ref_i}}{\varphi_{Ref_i}} / N$									
	Ash-I (3 % Fe <sub>2</sub> O <sub>3</sub> )		Ash-II (5 % Fe <sub>2</sub> O <sub>3</sub> )		Ash-III (8 % Fe <sub>2</sub> O <sub>3</sub> )		Ash-IV (15 % Fe <sub>2</sub> O <sub>3</sub> )		Ash-V (31 % Fe <sub>2</sub> O <sub>3</sub> )	
RI Model	$q_w$	$\nabla q$	$q_w$	$\nabla q$	$q_w$	$\nabla q$	$q_w$	$\nabla q$	$q_w$	$\nabla q$
Ebert	0	2	0	0	0	-1	0	-2	0	-2
Liu	0	17	0	2	0	-6	-1	-21	-1	-30
1.5-k(Fe) <sub>i</sub> , $\lambda=f(\lambda)$	-1	-31	-1	-21	-1	-13	0	-10	0	-3
1.5-0.02i, $\lambda=f(\lambda)$	2	84	2	57	2	42	1	20	1	8
1.5-k(Fe) <sub>i</sub> , $\lambda=3 \mu m$	-1	-26	-1	-19	0	-11	0	-8	0	0
1.5-0.02i, $\lambda=3 \mu m$	2	90	2	56	2	35	1	18	1	8
Goodwin	Reference									
* i represents the spatial grid node, N is the total number of grid nodes, $\varphi$ represents either incident wall heat flux ( $q_w$ ) or the source term ( $\nabla q$ )										

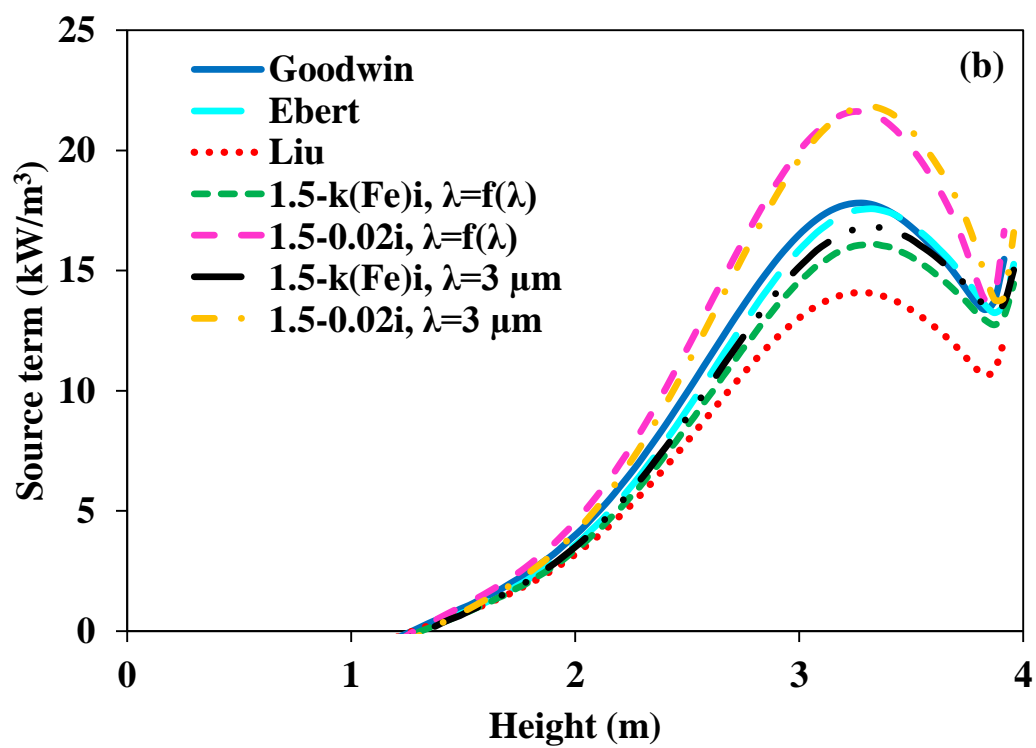
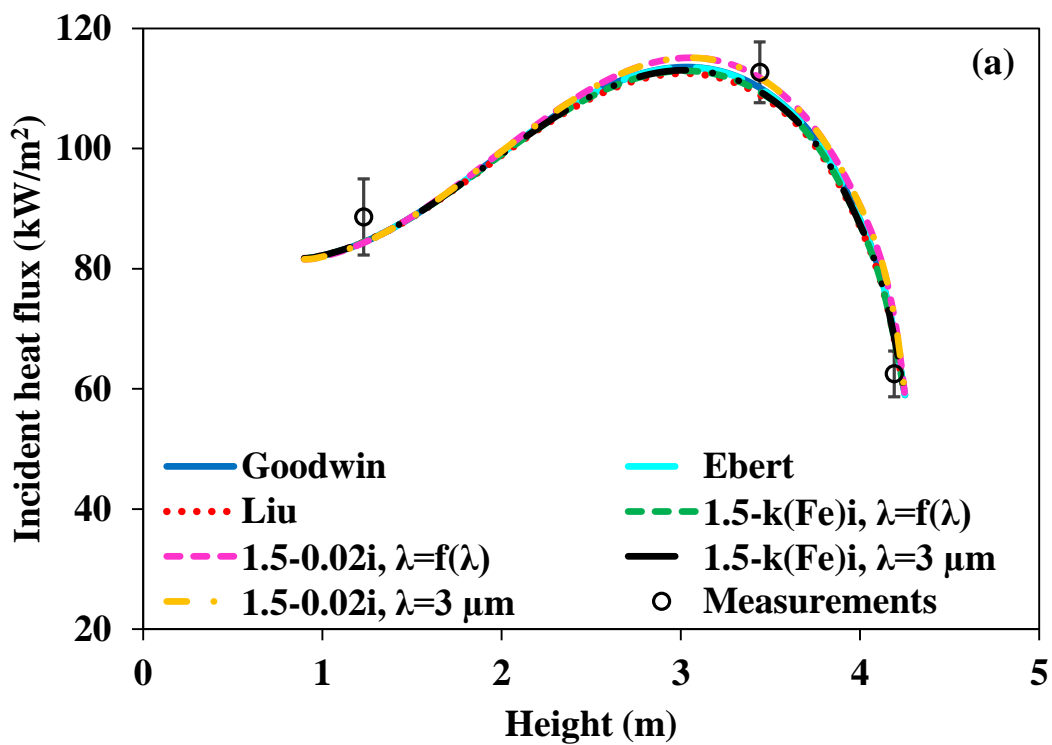


Figure 6.48 Comparison of (a) heat flux and (b) source term predictions for Ash-IV

#### 6.7.2.4 Sensitivity of Heat Flux and Source Term Predictions on Temperature Dependency of the Absorption Index ( $k$ )

Calculations and comparisons presented up to this section are based on different RI models, in which complex indices of refraction are evaluated at room temperature (295 K). It has been previously shown that temperature dependency of absorption index ( $k$ ) is small in the iron oxide absorption band while the temperature dependency is significant in the vibrational absorption band (4-8  $\mu\text{m}$ ) [36]. Considering the significance of absorption index in particle absorption coefficient and the fact that a RI model based on solely iron oxide content still leads to significant errors in source term predictions (see Table 6.24), sensitivity of heat flux and source term predictions on temperature dependency of the absorption index ( $k$ ) is needed to be investigated. Investigation is performed by modelling the radiative heat transfer in BFBC test rig combustion test (see Section 5.1.1). Spectral complex indices of refraction are calculated at both 295 K and 1163 K (mean temperature of the freeboard in the experiment) by using the correlations given in [120] (also given in Appendix C).

Figure 6.49 illustrates comparisons between absorption indices, particle absorption coefficients, heat flux and source term distributions calculated by using Ebert's model at 295 K and 1163 K for spectral particle properties. As can be seen from Figure 6.49 (a, b), increase in temperature results in increase in both absorption index (48 % in average) and spectral absorption coefficient (34 % in average). Nevertheless, this increase in absorption coefficient between 4-8  $\mu\text{m}$  has little influence on heat flux and source term distributions, 0 % and 2 % increase in average, respectively (Figure 6.49 (c, d)). As can be seen in Figure 6.49 (b), differences in absorption coefficients become significant especially after 6  $\mu\text{m}$ , which corresponds to the significant increase in the absorption index ( $k$ ) at this location. However, region between 6-8  $\mu\text{m}$  covers less than 10 % of the thermal radiation at 1167 K hence only a slight increase is observed in source term distribution (Figure 6.49 (d)). Therefore, it can be concluded that sensitivity of heat flux and source term predictions on temperature dependency of the absorption index ( $k$ ) is negligible at high operating temperatures.

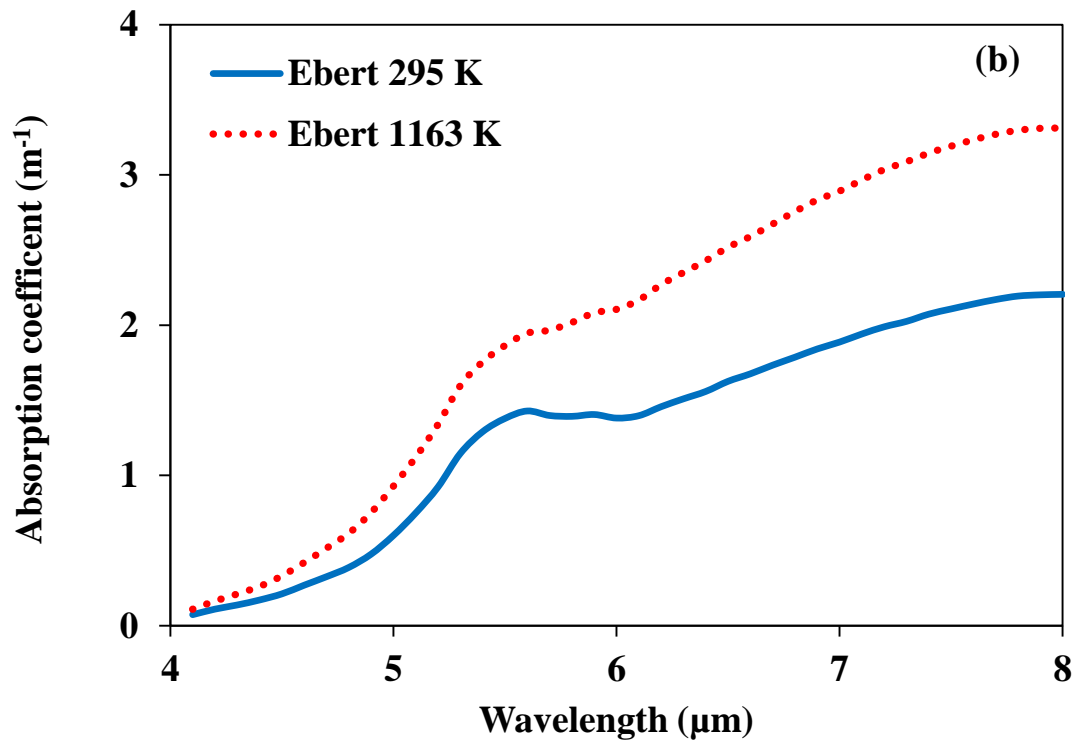
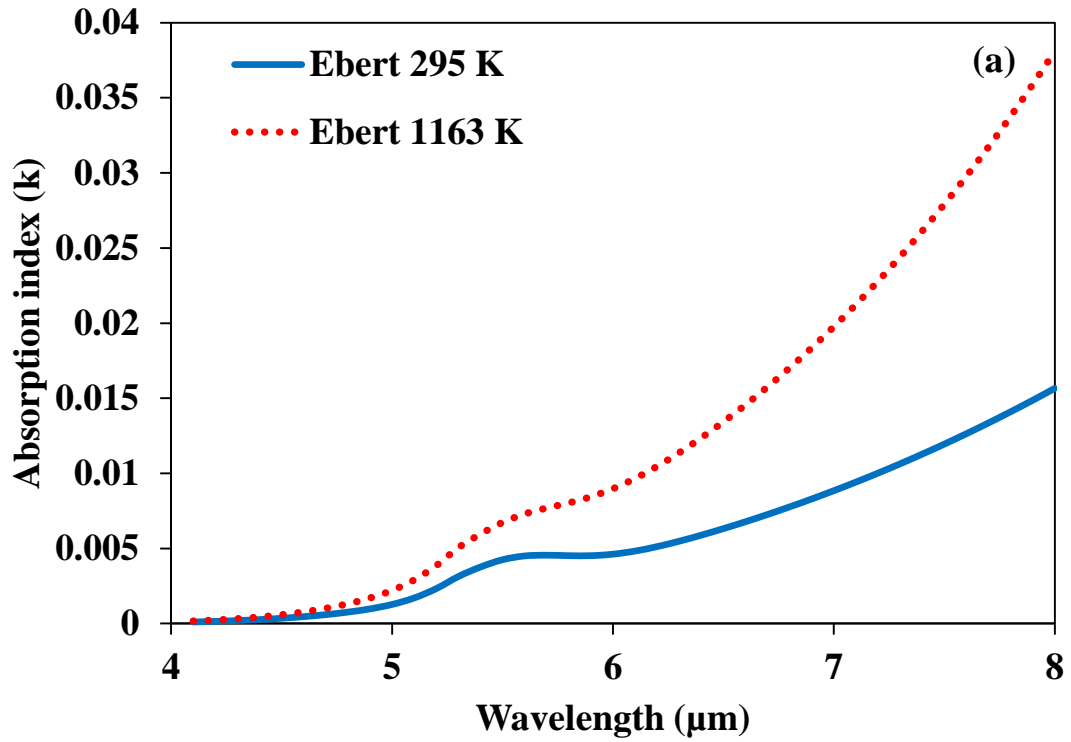


Figure 6.49 Comparison of (a) absorption indices, (b) particle absorption coefficients, (c) heat flux and (d) source term distributions for Ash-IV at 295 K and 1163 K

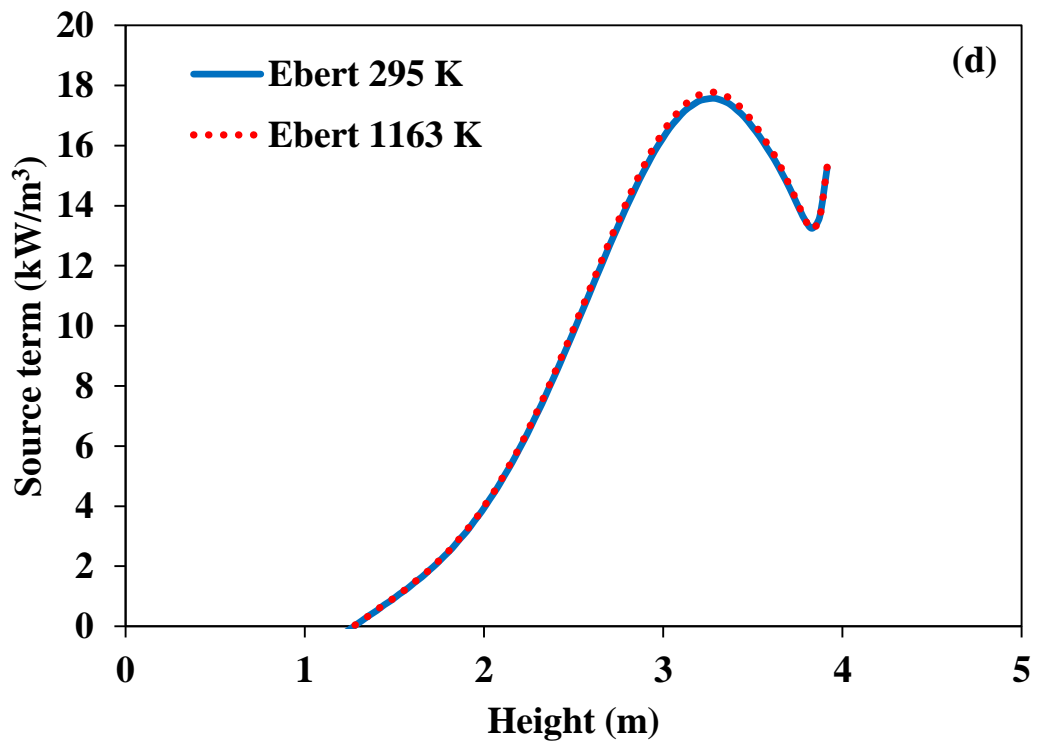
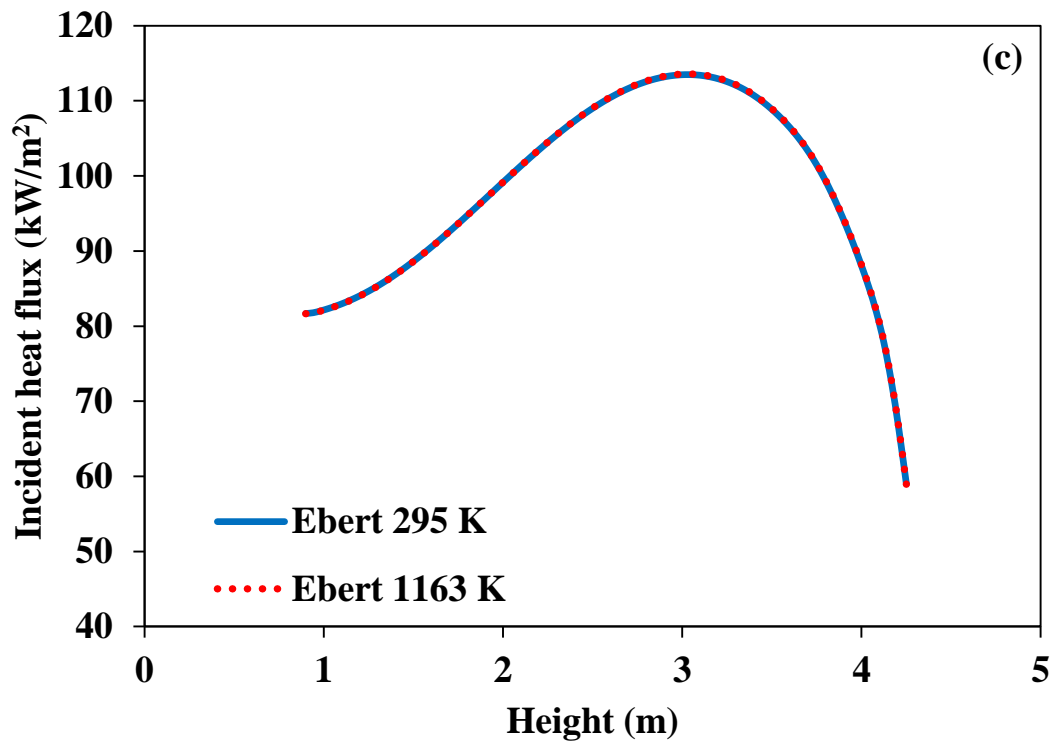


Figure 6.49 Comparison of (a) absorption indices, (b) particle absorption coefficients, (c) heat flux and (d) source term distributions for Ash-IV at 295 K and 1163 K (cont'd)

### 6.7.2.5 Influence of Wall Temperature on Heat Flux and Source Term Predictions

Heat flux comparisons presented in Sections 6.7.2.3 and 6.7.2.4 indicate that neither chemical composition nor spectral dependency of particle properties affects the incident heat flux predictions and all approaches agree well with the measured radiative heat fluxes (see Figure 6.48(a), Figure 6.49 (c)). Nevertheless, it should be highlighted that these small variations in wall heat flux predictions might be due to the high temperatures of refractory-lined freeboard walls (1110 K in average), high surface to volume ratio (Surface area/Volume  $\approx 10$ ) of the test rig and low optical thickness of the medium, where radiative heat transfer is expected to be dominated by hot refractory walls rather than particle laden gas emissions. Dominance of hot boundaries is also seen in the low magnitudes of the radiative source terms, especially just above the bed (Figure 6.48(b), Figure 6.49(d)).

Therefore, variations in heat fluxes might be different from the findings if the freeboard was bounded by conventional panel tube walls, as in utility or industrial furnaces, instead of hot refractory walls of the pilot scale test rig. In order to test this hypothesis, effect of wall temperature on heat fluxes is also investigated with a parametric study where the top and side wall temperatures are assumed to be 537 K with an emissivity of 0.80. Heat fluxes and source terms are calculated by keeping all operating conditions of the combustion tests the same except the top and side wall temperatures and emissivities.

Table 6.25 demonstrates comparison between incident heat fluxes and source terms predicted by MOL solution of DOM coupled with non-gray gas and non-gray particle properties, predicted by using different RI models in Mie solutions (see Section 2.3 for the solution method). Visual comparison of heat flux and source term predictions with the reference solution is also illustrated in Figure 6.50 for Ash-IV. As can be seen from the table, errors in heat flux predictions increase significantly if the surrounding walls are at a lower temperature (537 K) and are in the same order of magnitude with the errors in source term predictions. Furthermore, it is seen that errors in source term predictions are increased compared to refractory lined cases for all RI models and ash compositions (Table 6.24). This is considered to be due to the fact that when wall temperature is



reduced, share of hot refractory walls in incident radiation is decreased (note that  $\nabla \cdot \mathbf{q} = \text{Emission} - \text{Absorption}$ ), which makes the source term ( $\nabla \cdot \mathbf{q}$ ) more sensitive to the errors in spectral absorption coefficients as the emissions from the medium becomes the dominant factor in source term values. This can also be observed in the magnitudes of the source terms (Figure 6.50), which are significantly higher than those of refractory-lined walls (Figure 6.48) and difference between different RI models are more uniform along the combustor for both heat flux and source term predictions.

Table 6.25 Average relative percentage errors in incident wall heat fluxes ( $q_w$ ) and source terms along the centerline ( $\nabla q$ ) of Ash-I to V for the parametric study with panel tube walls (537 K)

Comparison of averaged spectral properties	$Error^* \% = 100x \sum_{i=1}^N \frac{\varphi_{j_i} - \varphi_{Ref_i}}{\varphi_{Ref_i}} / N$									
	Ash-I (3 % Fe <sub>2</sub> O <sub>3</sub> )		Ash-II (5 % Fe <sub>2</sub> O <sub>3</sub> )		Ash-III (8 % Fe <sub>2</sub> O <sub>3</sub> )		Ash-IV (15 % Fe <sub>2</sub> O <sub>3</sub> )		Ash-V (31 % Fe <sub>2</sub> O <sub>3</sub> )	
RI Model	$q_w$	$\nabla q$	$q_w$	$\nabla q$	$q_w$	$\nabla q$	$q_w$	$\nabla q$	$q_w$	$\nabla q$
Ebert	0	0	3	1	-1	-1	-2	-2	-3	-3
Liu	11	18	2	3	-3	-5	-18	-24	-32	-38
1.5-k(Fe) <sub>i</sub> , $\lambda=f(\lambda)$	-30	-36	-25	-29	-23	-25	-16	-15	-8	-5
1.5-0.02i, $\lambda=f(\lambda)$	99	117	83	91	73	76	46	40	21	15
1.5-k(Fe) <sub>i</sub> , $\lambda=3 \mu\text{m}$	-29	-35	-24	-27	-20	-21	-13	-12	-5	-1
1.5-0.02i, $\lambda=3 \mu\text{m}$	95	114	80	88	70	74	43	39	20	14
Goodwin	Reference									
* i represents the spatial grid node, N is the total number of grid nodes, $\varphi$ represents either incident wall heat flux ( $q_w$ ) or the source term ( $\nabla q$ )										

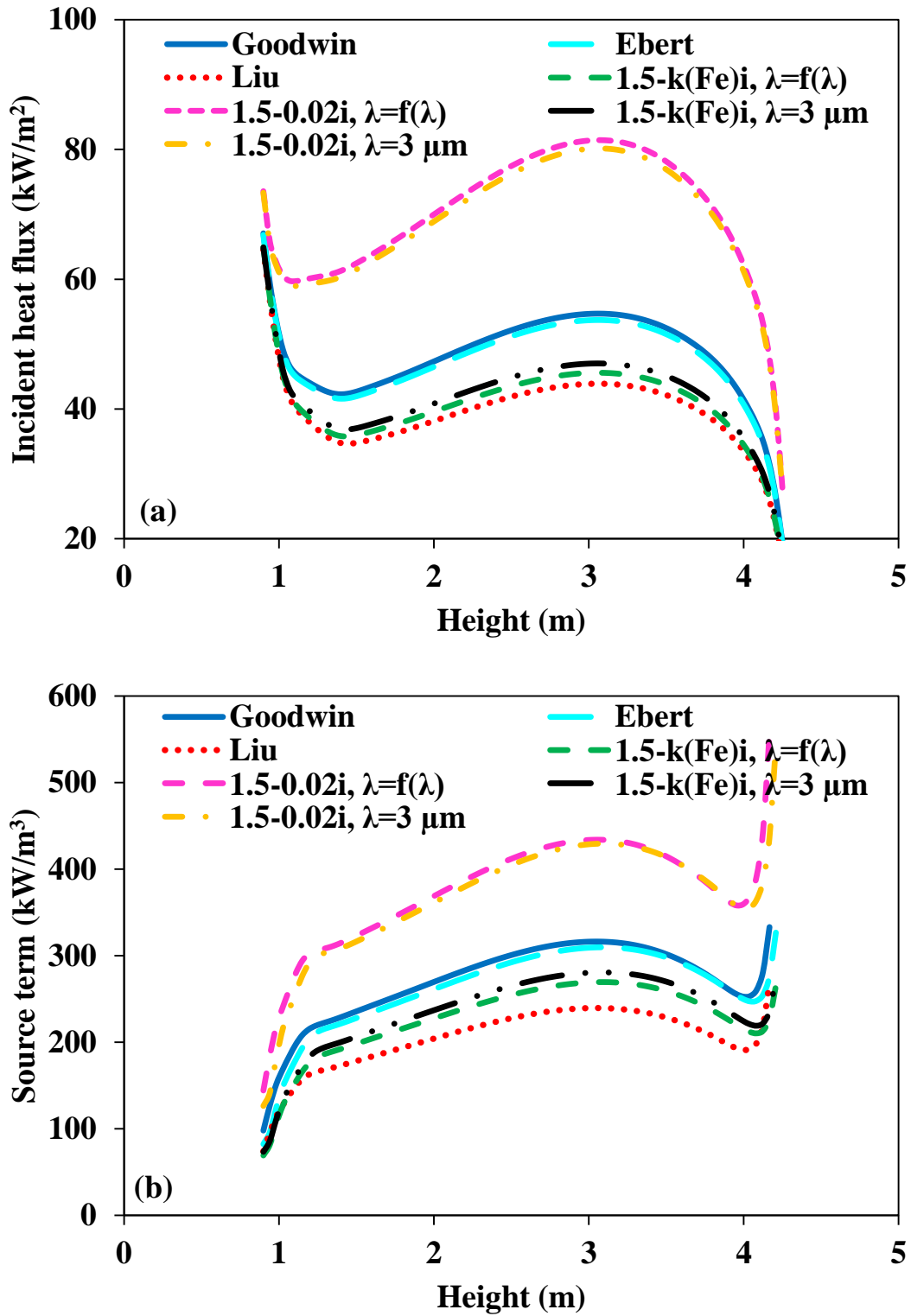


Figure 6.50 Comparison of heat flux (a) and source term predictions (b) for Ash-IV in the parametric study with panel tube walls (537 K)

Another important outcome is revealed when errors in particle absorption coefficients (Table 6.23) and errors in heat flux / source term predictions are compared (Table 6.25). Although errors in heat flux / source term predictions obtained with RI models neglecting chemical composition and/or spectral dependency are smaller than those in particle cloud properties, they are still significant for all models except Ebert's.

It should be noted that above-mentioned discussions on heat flux and source term predictions are based on the operating conditions of BFBC test rig. However, in both hot refractory wall and cold panel tube wall cases, it is seen that errors in spectral absorption coefficients (Table 6.23) are reflected on heat flux and source term predictions and are still significant (Table 6.24, Table 6.25). This is why above discussions can also be extended for PC-Fired furnaces and CFBCs considering the errors in particle cloud properties presented in Table 6.22. These comparisons highlight the significance of spectral particle properties and influence of chemical composition dependency on particle radiation in combusting systems.

### **6.7.2.6 Comparison between Spectrally-Averaged and Spectral Properties: Effect on Heat Flux and Source Term Predictions**

As demonstrated in the previous sections, spectral particle radiation is of significant importance for accurate calculation of radiative heat transfer in combusting systems burning coal. Nevertheless, spectral resolution of particle properties included in RTE solution is directly reflected on the computational cost of the global model as it directly determines the number of intensity equations (RTE) to be solved. This is why it is considered necessary to investigate the predictive accuracy of Planck mean properties by benchmarking their predictions against those of non-gray particle properties to see whether it is possible to represent spectral particle properties with a reasonable accuracy by deploying spectrally averaged particle properties. For this purpose, two spectrally averaged particle models are tested. In the first approximation, first a Planck mean RI is found by using the spectral RI data generated by Goodwin's correlations and then this averaged RI is used to evaluate "pseudo-gray" particle properties from Mie theory at 3  $\mu\text{m}$  (called "Planck Mean RI,  $\lambda=3 \mu\text{m}$ "). In the second approach, first spectral particle properties (see Eqs. (4.54-57)) are calculated by using the spectral RI ( $m(\lambda)$ ) generated by using Goodwin's correlations followed by calculation of Planck mean absorption coefficient, scattering coefficient and asymmetry factor (called "Planck Mean Property"). Table 6.26 demonstrates the comparison between incident heat fluxes and source terms predicted by using Planck mean particle property models for the actual experimental conditions with hot refractory-lined walls and for the parametric study with conventional panel tube walls at 537 K. Visual comparison of heat flux and source term predictions with the reference solution is also illustrated in Figure 6.51 for Ash-II. As can be seen from the table, both Planck mean approximations fail to yield accurate heat flux and source term predictions unless the iron oxide content is very high (30 %), which is rarely the case.

Table 6.26 Average relative percentage errors in incident wall heat fluxes ( $q_w$ ) and source terms along the centerline ( $\nabla q$ ) of Ash-I to V for Planck mean property models

Comparison of averaged spectral properties	$Error^* \% = 100x \sum_{i=1}^N \frac{\varphi_{j_i} - \varphi_{Ref_i}}{\varphi_{Ref_i}} / N$									
	Ash-I (3 % Fe <sub>2</sub> O <sub>3</sub> )		Ash-II (5 % Fe <sub>2</sub> O <sub>3</sub> )		Ash-III (8 % Fe <sub>2</sub> O <sub>3</sub> )		Ash-IV (15 % Fe <sub>2</sub> O <sub>3</sub> )		Ash-V (31 % Fe <sub>2</sub> O <sub>3</sub> )	
RI Model	$q_w$	$\nabla q$	$q_w$	$\nabla q$	$q_w$	$\nabla q$	$q_w$	$\nabla q$	$q_w$	$\nabla q$
<b>Hot refractory-lined walls</b>										
Planck Mean RI, $\lambda=3 \mu\text{m}$	2	89	2	52	2	26	1	13	1	4
Planck Mean Property	1	41	1	26	0	21	0	7	0	1
<b>Parametric study with conventional panel tube walls at 537 K</b>										
Planck Mean RI, $\lambda=3 \mu\text{m}$	108	112	90	87	81	72	52	37	25	12
Planck Mean Property	23	43	16	28	13	23	5	9	0	1
Goodwin	Reference									
* i represents the spatial grid node, N is the total number of grid nodes, $\varphi$ represents either incident wall heat flux ( $q_w$ ) or the source term ( $\nabla q$ )										

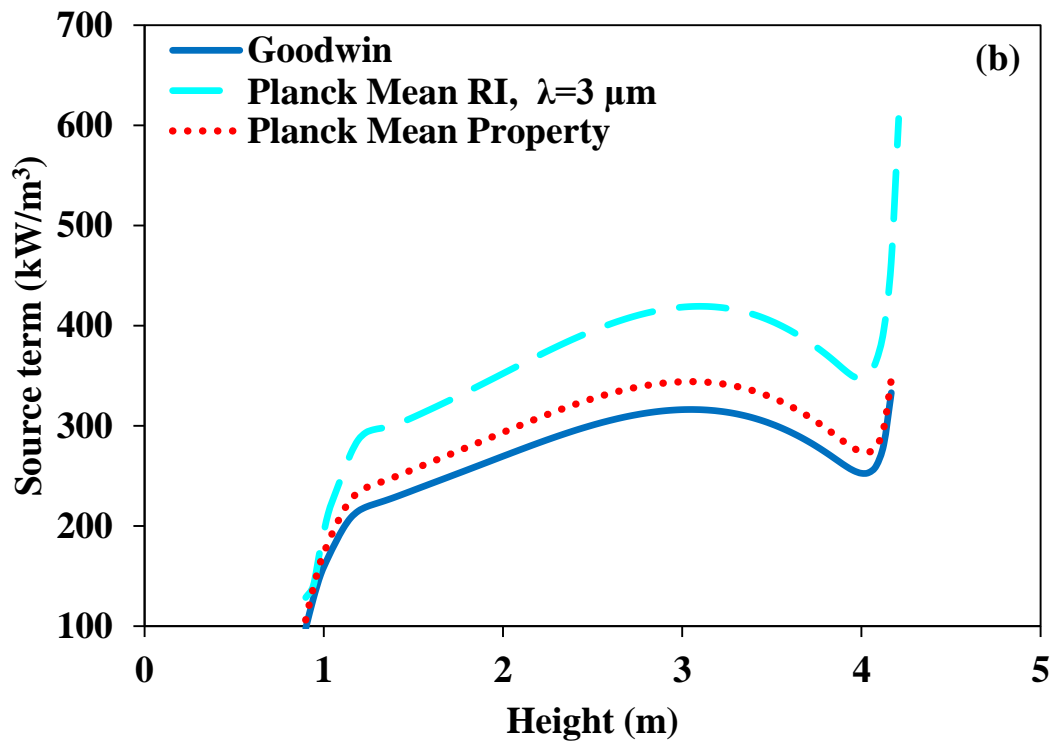
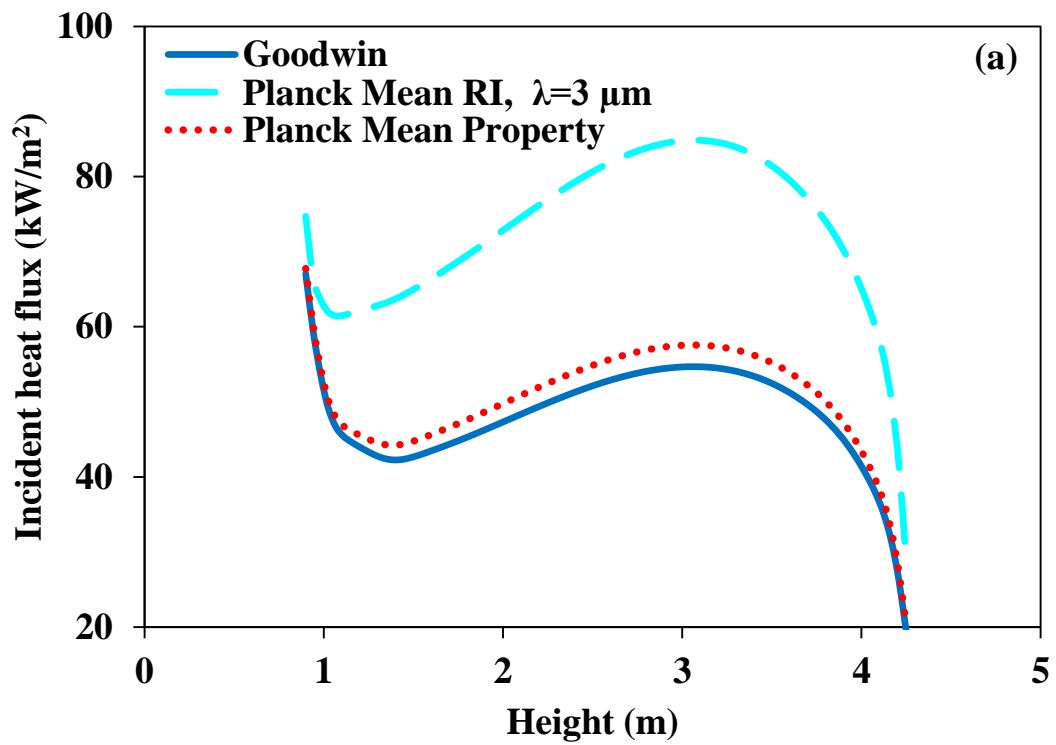


Figure 6.51 Comparison of heat flux (a) and source term predictions (b) of Planck mean approximations for Ash-II in the parametric study with panel tube walls (537 K)

### 6.7.2.7 Concluding Remarks on the Spectral Nature of Particle Radiation

In this section, spectral nature of particle radiation and its influence on radiative heat transfer in combusting systems are investigated starting from the very first input parameter RI to the quantities of interest such as wall heat fluxes and radiative source terms. These detailed investigations reveal that spectral particle radiation is of significant importance for accurate calculation of radiative heat transfer in combusting systems. Furthermore, it is shown that spectral nature of particle properties is mainly originated from the spectral nature of the complex index of refraction. Hence keeping only the wavelength as a spectral variable is not sufficient to represent non-gray behavior of particles. It gives almost identical results compared to that of gray particles. Therefore, both complex index of refraction and wavelength must be kept as spectrally dependent variables to consider a particle to be “non-gray”. Another important outcome of the investigation presented in this section is the presentation of Ebert’s model to the attention of the community. Ebert’s model is shown to be in very good agreement with Goodwin’s correlations for a wide variety of particle sizes and compositions relevant to combusting systems. Hence, Ebert’s approach is recommended for calculation of spectral RI indices of ash particles as it requires less input parameters and covers a wider range of chemical compositions. It is also seen that chemical composition has a significant effect on particle absorption properties as well as heat flux/source term predictions and that complex index of refraction models used in radiative property estimations must take into consideration this composition dependency.

Traditional gray particle assumption ( $m=1.5-0.02i$ ,  $\lambda=3\mu\text{m}$ ) is found to lead to significant errors in heat flux and source term predictions, where the error increases with decreasing iron oxide content. As an alternative, a gray iron content based RI model ( $m=1.5-k(\text{Fe})i$ ,  $\lambda=3\mu\text{m}$ ) is proposed, which increases the accuracy of gray particle predictions, especially if particles have a high iron oxide content. Finally, it is demonstrated that Planck mean averaged RI and radiative properties fail to yield accurate heat flux and source term predictions. Therefore, non-gray particle properties are required to be taken into consideration for accurate radiative heat transfer predictions.



### 6.7.3 Spectral Dependency of Phase Function Simplifications

In the previous section, it is shown that radiative heat fluxes and source terms are strongly influenced by the spectral nature of particle radiation. Furthermore, at the beginning of the current Chapter (Section 6.1.5), it is demonstrated that incorrect representation of the directional nature of particle radiation by deploying phase function simplifications can lead to errors up to 65 % in source term predictions. However, influence of the phase function simplification presented in Section 6.1.5 was assessed within the scope of gray particle assumption, which is demonstrated to be incorrect in the previous section. This is why it is considered necessary to investigate predictive accuracy and computational efficiency of nonscattering and isotropic scattering assumptions by benchmarking their predictions against those of Henyey-Greenstein phase function with normalization in the presence of non-gray particles.

For that purpose, spectral particle properties, radiative heat flux and source term predictions are evaluated for the fluidized bed coal combustion tests presented in Sections 5.1.1 and 5.2.1, which will be referred as Test 1 (ABFBC without recycle), Test 2 (ABFBC with recycle) and Test 3 (CFBC), respectively. In the radiation models, participating combustion gases are assumed to be gray and calculated by using Leckner's correlations (Section 3.2). Spectral radiative properties of the polydisperse ash particles are calculated by using Mie theory (Section 4.1.3) for each particle size (34 discrete size classes) and wavelength (147 spectral points). Goodwin's correlations (Section 4.4) are employed to estimate spectral RI of particles collected from the cyclone and bag filter as a function of density, wavelength and chemical composition (Table 5.5, Table 5.15). Particle properties are calculated up to 20  $\mu\text{m}$  as it is considered to be sufficient enough for the majority of thermal radiation in coal fired systems. All input data necessary for the radiative property models are taken from Sections 5.1.1, 5.1.3, 5.2.1 and 5.2.2. In MOL solution DOM, a combination of  $S_{10}$  and  $13 \times 13 \times 96$  and  $S_{12}$  and  $17 \times 305$  grid nodes are utilized for ABFBC (in Test 1 and 2) and CFBC (in Test 3) test rigs based on a previous grid refinement study [150] and the results presented in Section 6.1.4. For the difference

relations of spatial derivatives, two-point upwind differencing scheme DSS012 is employed.

Effect of scattering on incident heat fluxes along the side walls and radiative energy source term predictions with spectral particle properties are shown in Figure 6.52 and Figure 6.53. In heat flux predictions, nonscattering and isotropic scattering phase function simplifications are found to be in good agreement with the reference forward scattering solution for Test 1 and Test 2 (Figure 6.52 (a, b)). This is considered to be due to the hot wall effect presented in Section 6.7.2.5. On the other hand, in Test 3, isotropic scattering underestimates the wall heat fluxes noticeably while nonscattering assumption is found to produce acceptable accuracy (Figure 6.52 (c)) due to the high values of asymmetry factor for large particles (as in the case of Test 3, see Figure 6.13). As can be seen in Figure 6.53, both simplifications give reasonable accuracy in source term predictions in optically thin media of Test 1 while isotropic phase function is closer to the reference solution, which is expected considering the low asymmetry factor (Figure 6.35). As the optical thickness of the medium increases, discrepancy in the source term predictions due to phase function simplifications are found to increase. Both nonscattering and isotropic scattering assumptions give same order of magnitude errors for Test 2 whereas isotropic assumption causes significant errors in Test 3.

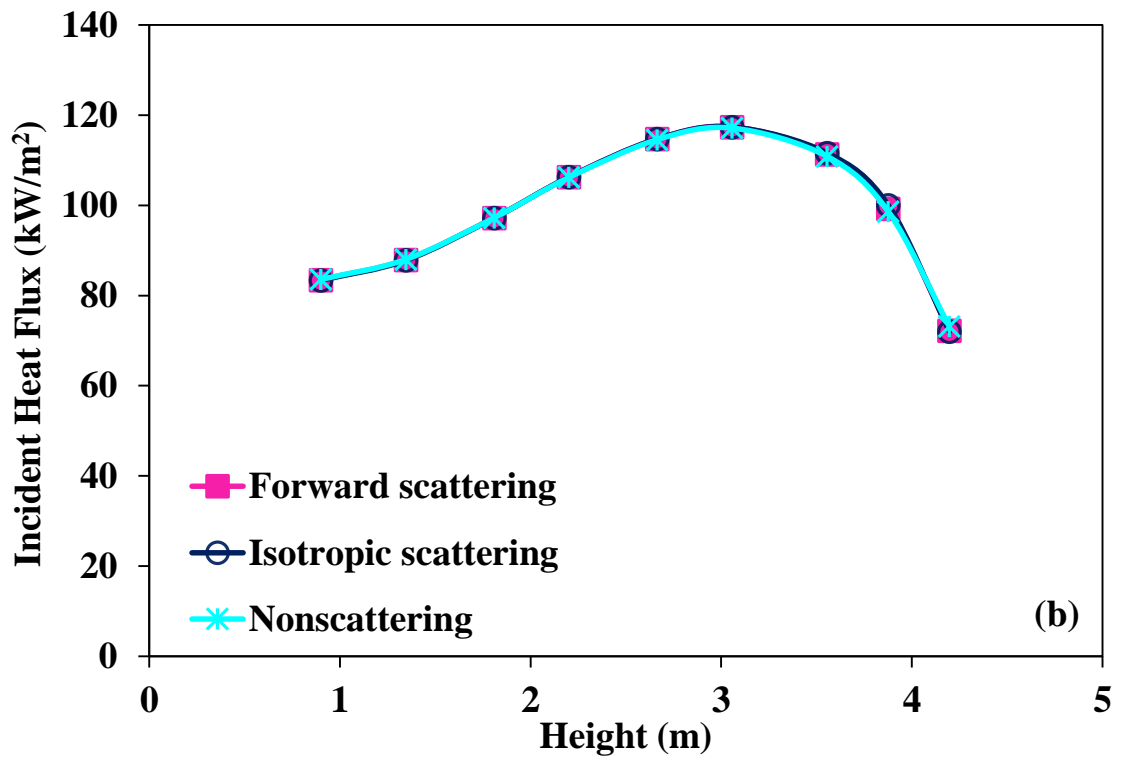
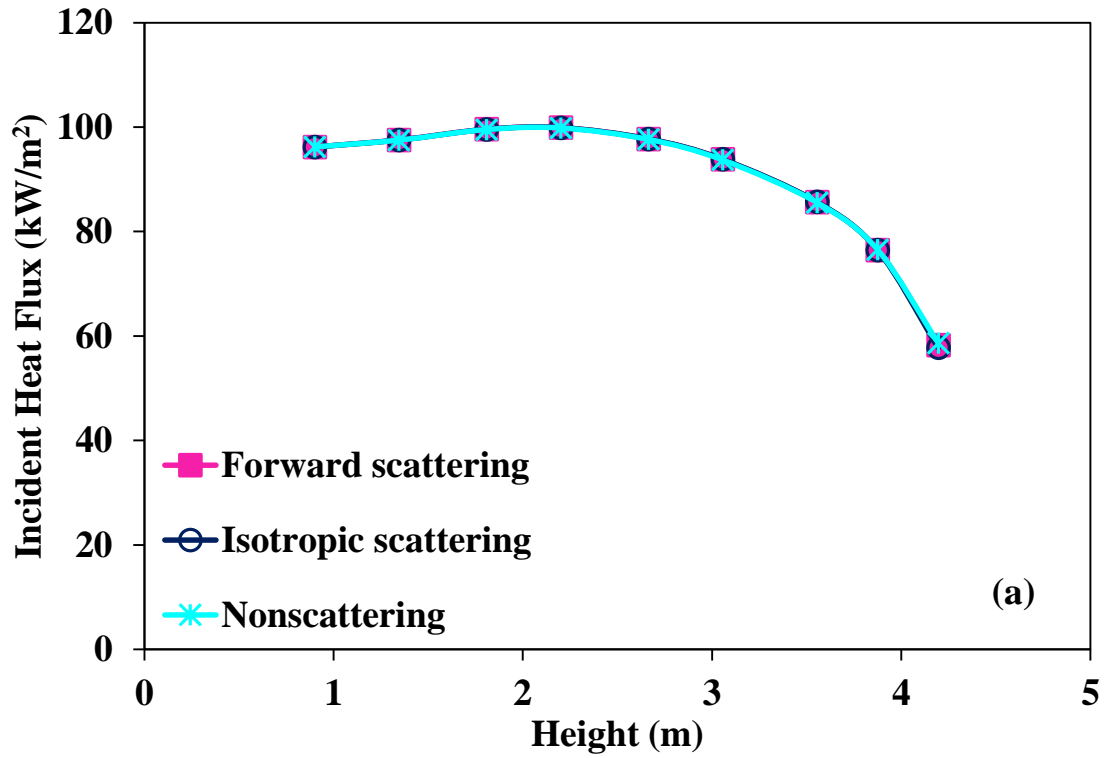


Figure 6.52 Effect of phase function simplifications on incident heat fluxes for (a) Test 1, (b) Test 2 and (c) Test 3 in the presence of non-gray particles

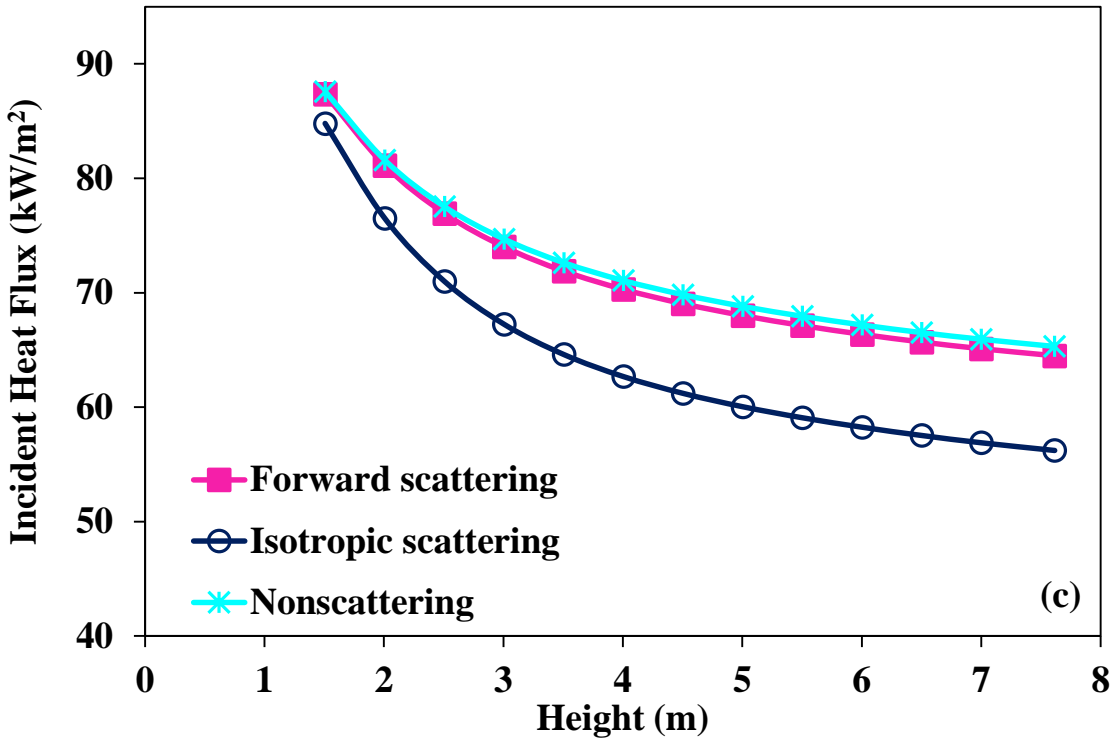


Figure 6.52 Effect of phase function simplifications on incident heat fluxes for (a) Test 1, (b) Test 2 and (c) Test 3 in the presence of non-gray particles (cont'd)

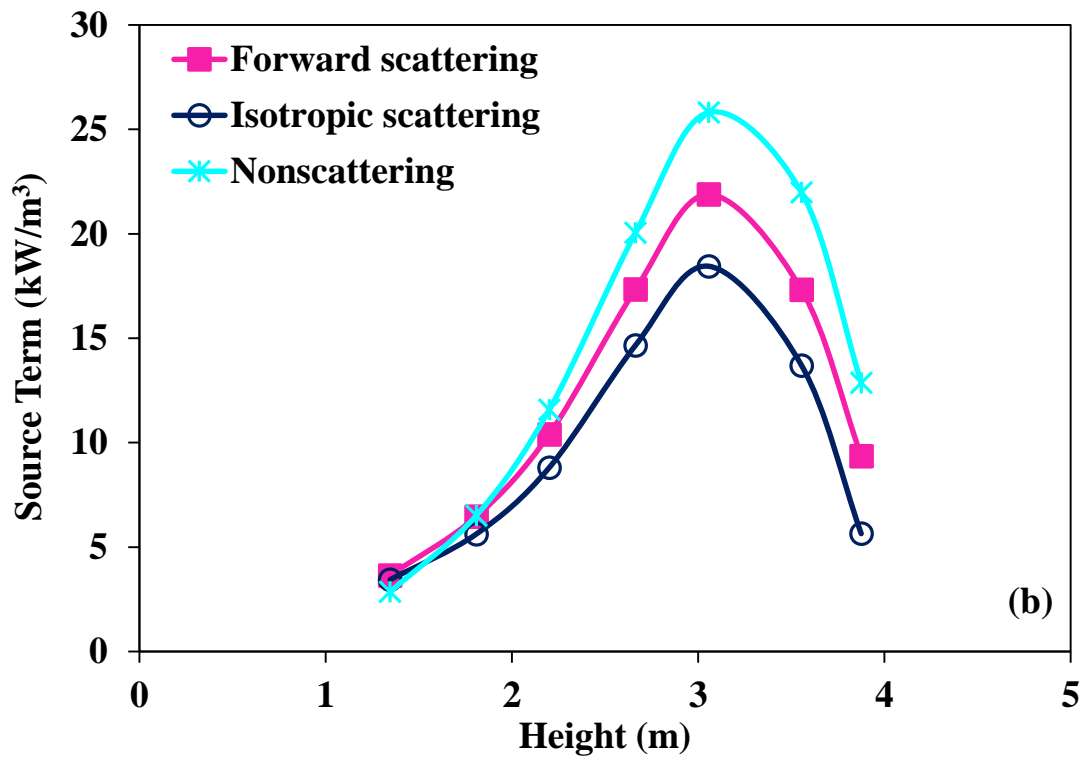
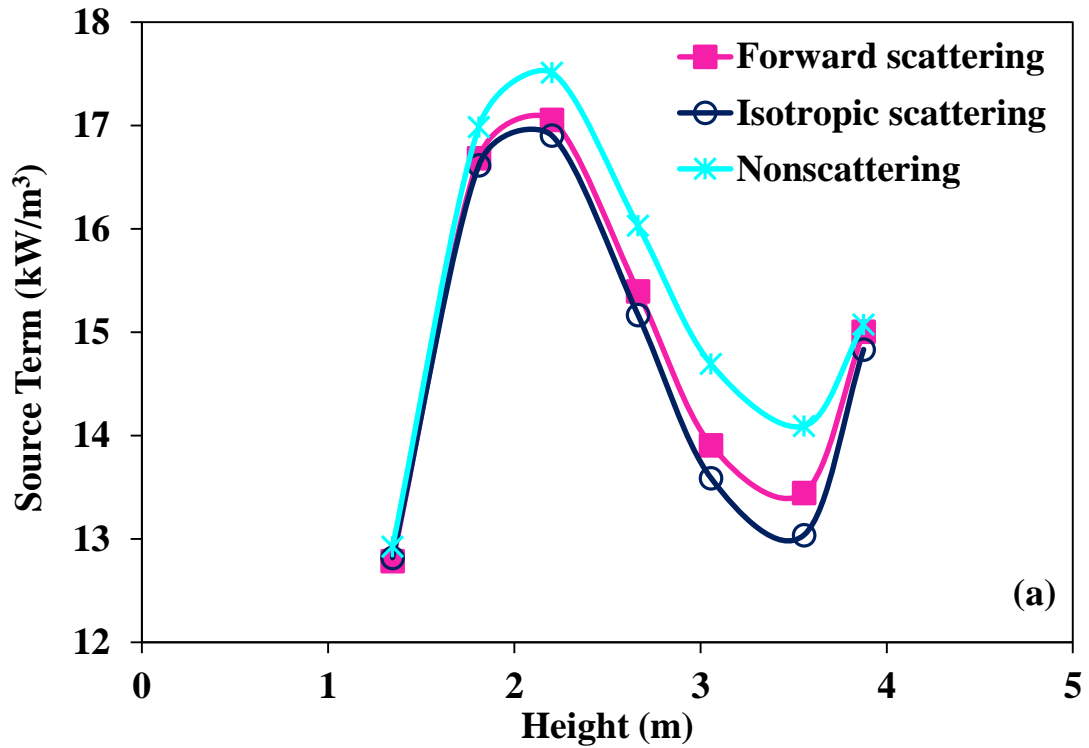


Figure 6.53 Effect of phase function simplifications on sources terms for (a) Test 1, (b) Test 2 and (c) Test 3 in the presence of non-gray particles

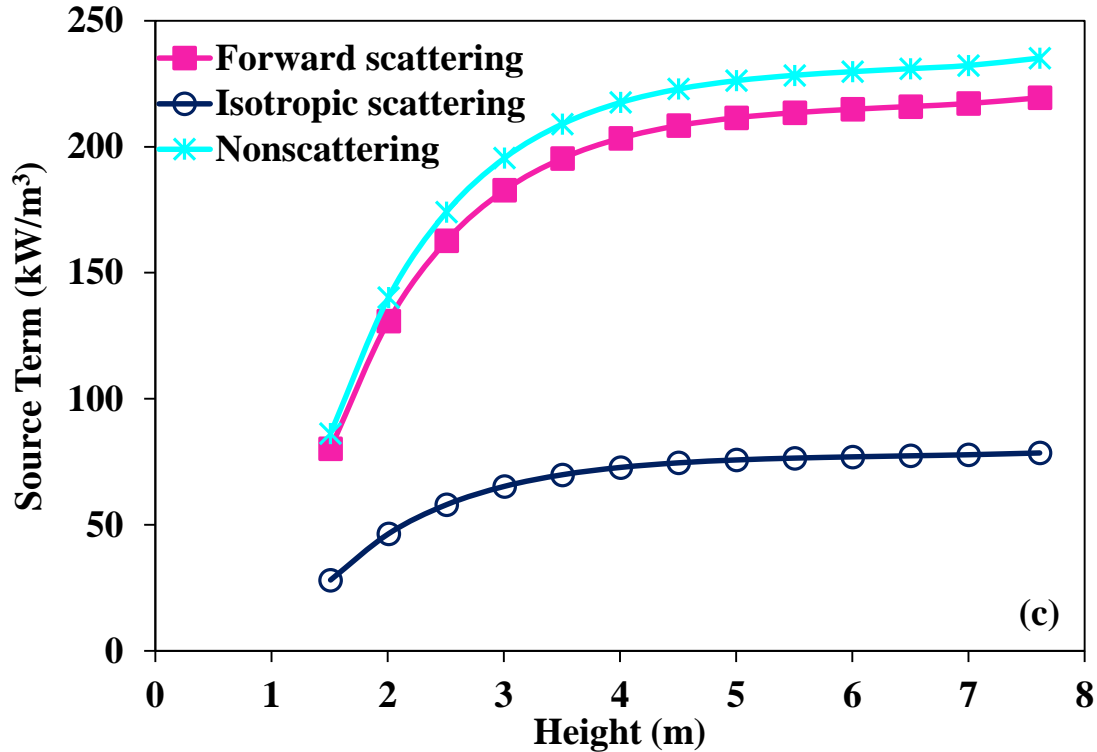


Figure 6.53 Effect of phase function simplifications on sources terms for (a) Test 1, (b) Test 2 and (c) Test 3 in the presence of non-gray particles (cont'd)

The percentage errors in incident heat fluxes along the side wall and source term predictions with corresponding CPU times are given in Table 6.27. It should be reminded that that one of the main reasons for phase function simplifications is to reduce computational effort in RTE solution. As can be seen from Table 6.27, however, no improvement in CPU economy is observed in any of the studied combustion tests in the presence of non-gray particles. Nevertheless, it should also be noted that comparison between isotropic / nonscattering and forward scattering phase functions with regard to algorithm development and its implementation shows that isotropic / nonscattering assumption requires significantly less set-up time to program and hence can be implemented for optically thin media as in the case of Test 1.

Table 6.27 Effect of phase function simplifications on incident heat fluxes and sources terms in the presence of non-gray particles

Combustion Test	Phase function	Average % Error in Heat Flux	Average % Error in Source Term	CPU Time (s)
<b>Test 1</b> ( $\tau = 0.85$ )	Nonscattering	0.0	3	9347
	Isotropic	0.0	-2	6774
	Forward	Reference Solution		4443
<b>Test 2</b> ( $\tau = 4.77$ )	Nonscattering	-0.2	14	10057
	Isotropic	0.0	-15	6570
	Forward	Reference Solution		8766
<b>Test 3</b> ( $\tau = 10.66$ )	Nonscattering	1	7	7047
	Isotropic	-10.1	-64	8766
	Forward	Reference Solution		8111

In order to find out whether it is possible to extend above mentioned conclusions to gray particles, effect of phase function simplifications is also tested with gray Mie particles ( $m=1.5-0.02i$ ,  $\lambda=3 \mu\text{m}$ ). The reason behind this investigation is the fact that there are several investigations presented in the literature regarding to phase function simplifications in the presence of gray particles and it might be possible to extend the outcomes of these investigations to non-gray particles.

Comparison of heat flux and source term predictions obtained with phase function simplifications in the presence of gray particles are presented in Table 6.28 for Test 1-3. When Table 6.27 and Table 6.28 are compared, it is seen that spectral dependency of phase function simplifications is negligible as those simplifications yield to the same order of magnitude errors for both spectral and gray particle properties. Therefore, it can be concluded that spectral variation of particle properties can be neglected while assessing the accuracy of simpler phase functions (isotropic, nonscattering) under FBC conditions as gray solution of RTE necessitates much less CPU time.

Table 6.28 Effect of phase function simplifications on incident heat fluxes and sources terms with gray Mie particles

Combustion Test	Phase function	Average % Error in Heat Flux	Average % Error in Source Term	CPU Time (s)
<b>Test 1</b> ( $\tau = 0.85$ )	Nonscattering	0.0	3	1014
	Isotropic	-0.1	-3	880
	Forward	Reference Solution		620
<b>Test 2</b> ( $\tau = 4.77$ )	Nonscattering	0.0	14	398
	Isotropic	-0.1	-18	469
	Forward	Reference Solution		340
<b>Test 3</b> ( $\tau = 10.66$ )	Nonscattering	0.9	9	308
	Isotropic	-8.5	-66	220
	Forward	Reference Solution		268



## **6.8 Investigation of the Gas Property Models Compatible with Spectral Particle Radiation**

Results presented in Section 6.1 reveal that effect of an accurate spectral gas property model (SLW) on radiative heat flux and source term predictions can become marginal compared to that of even gray gas approximation (Leckner) in the presence of high particle loads (under CFBC conditions), where particle radiation dominates the total radiation. In Section 6.1-6.7, parameters affecting the particle radiation (size, size and load distribution, fuel source, limestone addition, spectral nature) are investigated and discussed in detail. One of the most important outcomes of these investigations is the strong dependency of radiative heat transfer on the spectral nature of particle radiative properties, which has been neglected in the majority of previous relevant literature.

A wide variety of gas spectral radiative property models with different degrees of complexity and accuracy are available in the literature and these gas property models are being used for decades in modelling combustion systems. Nevertheless, there are relatively few studies where spectral particle properties are considered together with spectral gas properties. These studies usually focus on soot particles and spectral absorption of the soot is usually included either in a narrow band gas model [32, 55, 149] or accounted as if a gaseous specie in a global gas radiation model like SLW [99, 172, 173]. For fuel / ash particles, number of studies which involves both spectral gas and particle properties are even less and limited to the narrow band models [50, 122, 174], which requires a tremendous amount of CPU time. Considering the significance of spectral particle radiation demonstrated in Section 6.7, an accurate and CPU efficient gas radiation model, in which spectral fuel / ash particle properties can be implemented, is needed, especially for combustion chambers with low particle loads such as PC-fired furnaces and BFBCs. To address this need, three gas property models, namely GWB approximation, GNB approximation and banded SLW, are proposed and investigated within the scope of this section. Details of these models are presented in Section 3.3, Section 3.4 and Section 3.6, respectively.

Investigation is performed through mathematical modeling by using the experimental data on two coal combustion tests previously performed in 300 kWt ABFBC test rig (see Section 5.1.1). In the radiation models, freeboard is treated as a 3D rectangular enclosure containing gray/non-gray, absorbing, emitting gas with non-gray, absorbing, emitting, anisotropically scattering particles surrounded by black/gray diffuse walls (Section 5.1.3).

Radiative properties of the particle laden combustion gases are evaluated by using GWB, GNB, SLW and banded SLW models for gases (Section 3.3-3.6) and Mie theory for particles (Section 4.1.3), respectively. Non-gray particle absorption coefficients, scattering coefficients and asymmetry factors are represented by 8 wide bands based on the comparisons presented in Section 6.7.1. In all cases, scattering phase functions are represented by transport approximation (Section 4.3). For the difference relations of spatial derivatives, three-point upwind differencing scheme DSS014 is employed. All simulations are carried out on a computer with Intel® Core™ 7i CPU 2600 3.40 GHz processor having 16.00 GB of RAM. CPU times are recorded for an error tolerance of 0.001 % throughout the analyses.

### **6.8.1 Benchmarking the predictive accuracy of the radiation code**

The predictive accuracy of the radiation code based on the MOL solution of DOM with the proposed gas property models is investigated on two 3D benchmark problems for which Monte Carlo solutions are available in the literature [175]. The physical system under consideration is a 3-D cubical enclosure containing uniform, gray, isotropically scattering media confined within diffuse, gray walls. The first test problem is characterized by a purely scattering medium and non-symmetric boundary conditions whereas the second problem contains an isothermal, absorbing, emitting, scattering medium with symmetric boundary conditions. Specified parameters of these two problems are presented in Table 6.29.  $\kappa^*$ , and  $\sigma^*$  are the non-dimensional radiative properties defined as  $\kappa^* = \kappa_p L_0$ ,  $\sigma^* = \sigma_p L_0$ , where  $L_0$  is the dimension of the cubical enclosure.

Table 6.29 Input data for the benchmark problems

	Test Problem 1	Test Problem 2
<b>Medium</b>		
<b>Absorption coefficient, <math>\kappa^*</math></b>	0.0	5.0
<b>Scattering coefficient, <math>\sigma^*</math></b>	1.0	5.0
<b>Temperature</b>	0.0	$T_0$
<b>Boundaries</b>		
<b>Temperature, <math>z = 0</math></b>	$T_0$	0.0
<b>Temperature, others</b>	0.0	0.0
<b>Emissivity</b>	1.0	1.0
Dimension of Cubical Enclosure, $L_0 = 1.0$ m		
Reference Temperature, $T_0 = 648$ K		

In the present study, the same computational grid (equivalent to  $25 \times 25 \times 25$ ,  $S_8$ ) and scattering phase function (isotropic) are used to compare the results obtained by the in-house developed radiation codes with different gas property models by benchmarking their predictions with the previous Monte Carlo solutions. It should be noted that forms of RTE used with banded gas models (Eq. (3.8)) and SLW models (Eqs. (3.27), (3.32)) are different and necessitates two different algorithms / codes. This is why both of their predictions were benchmarked against those of MC.

Figure 6.54 illustrates the dimensionless heat flux  $Q_z^*$  ( $=Q_z/\sigma T_0^4$ ) predictions for Test Problem 1 and dimensionless heat flux  $Q_z^*$  ( $=Q_z/\sigma T_0^4$ ) and incident radiation predictions  $G^*$  ( $=Q_z/(4\sigma T_0^4)$ ) for Test Problem 2. As can be seen from the figure, predictions obtained with the current codes<sup>7</sup> are in good agreement with the benchmark solutions. Therefore, it is concluded that integration of proposed gas property models into the in-house developed radiation code is successful.

<sup>7</sup> Radiation codes with different number of bands, 1, 8, 12 and 423 (GWB / GNB) yields identical predictions for the test problems under consideration. Hence their predictions are referred as Banded Code in .

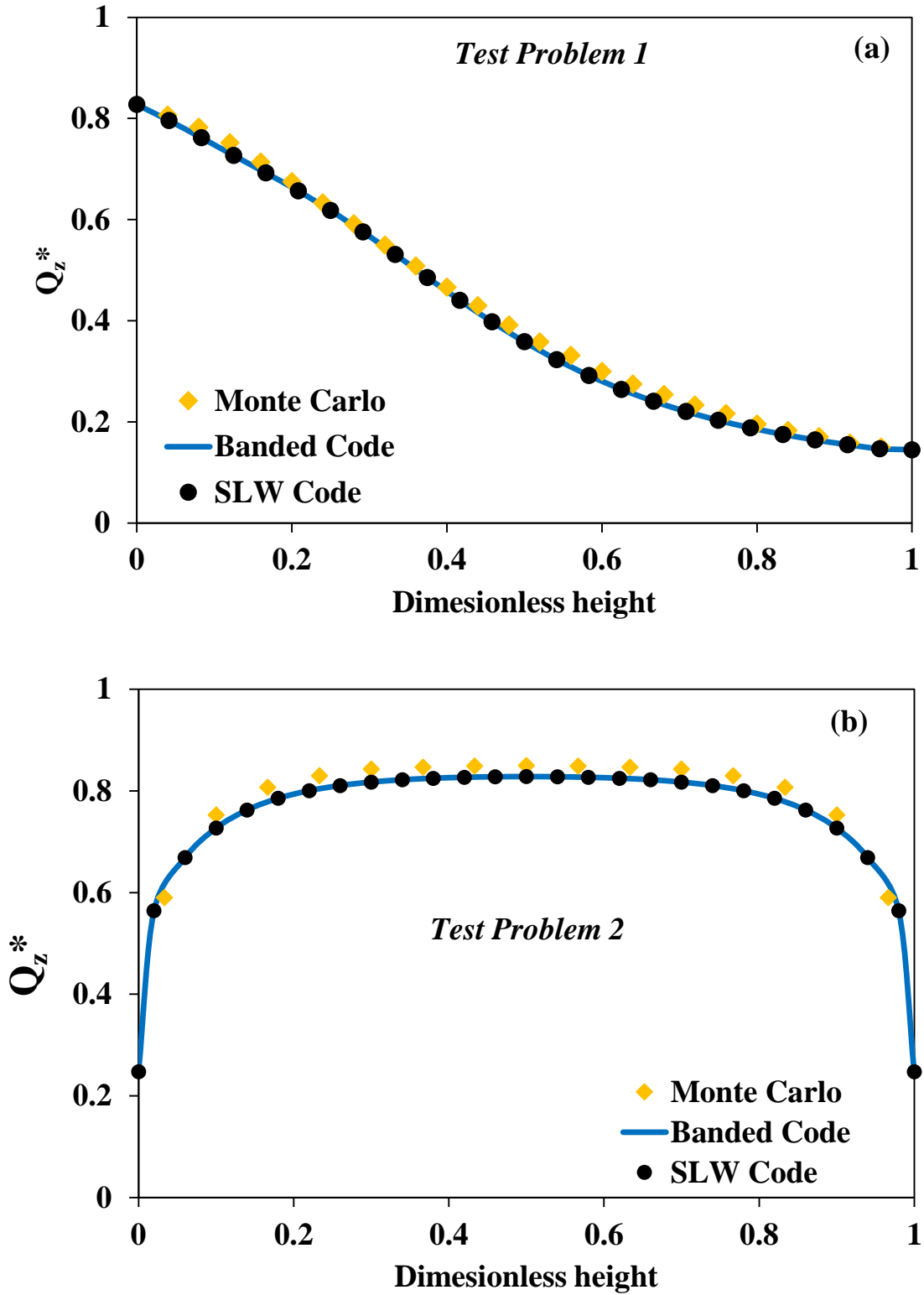


Figure 6.54 Comparison between in-house developed radiation codes and MC solution for (a) Test Problem 1 and (b, c) Test Problem 2

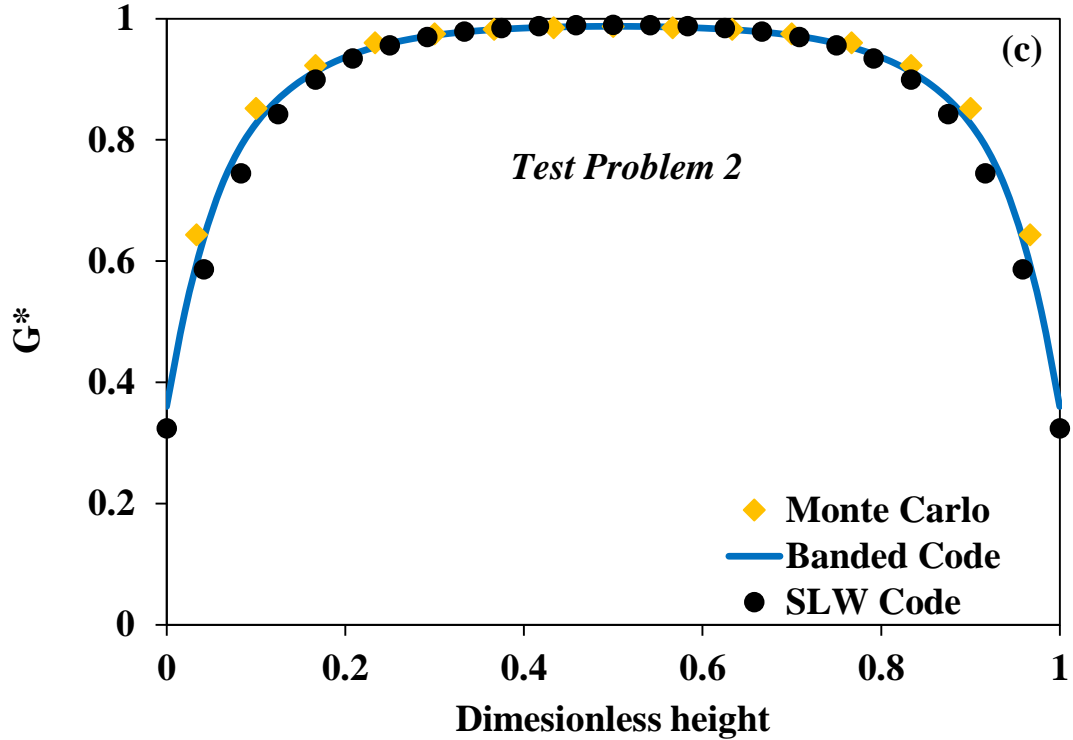


Figure 6.54 Comparison between in-house developed radiation codes and MC solution for (a) Test Problem 1 and (b, c) Test Problem 2 (cont'd)

### 6.8.2 Spatial and Angular Discretization for ABFBC Test Rig

Predictive accuracy and computational economy of the MOL solution of DOM with respect to spatial discretization, order of approximation and number of gray gases are investigated by comparing their steady-state predictions with those obtained by the reference cases carried out with the finest spatial/angular discretization or highest number of gray gases. Refinement studies are performed only on Test 2 due to the fact that finer angular and spatial discretization are required for higher particle loading in RTE solution as demonstrated in Sections 6.1.4 and 6.4.1 as particle load is one order of magnitude higher in Test 2.

For the spatial discretization, 5x5x35, 7x7x53, 9x9x67, 11x11x81 and 13x13x96 grid resolutions are tested in x, y and z directions respectively (see Figure 5.8 for the coordinate

system).  $S_N$  method with the order of 6 is selected for the angular discretization. Incident wall heat fluxes and source terms are illustrated in Figure 6.55. As can be seen from the figure, incident wall heat fluxes are not affected by the spatial discretization whereas the source term predictions are sensitive to spatial discretization.

The absolute percentage errors in the incident flux along the side wall and source term predictions with corresponding CPU ratios are given in Table 6.30. As can be seen from the table,  $11 \times 11 \times 81$  control volumes provide satisfactory solutions in terms of accuracy and computational efficiency.

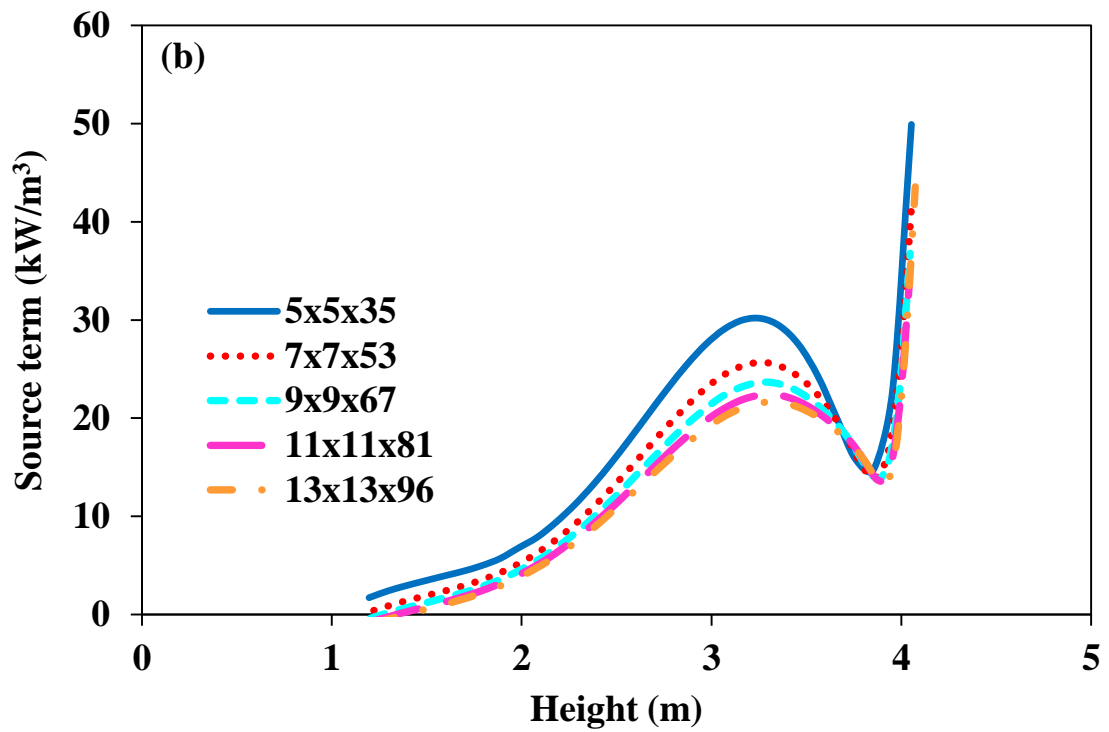
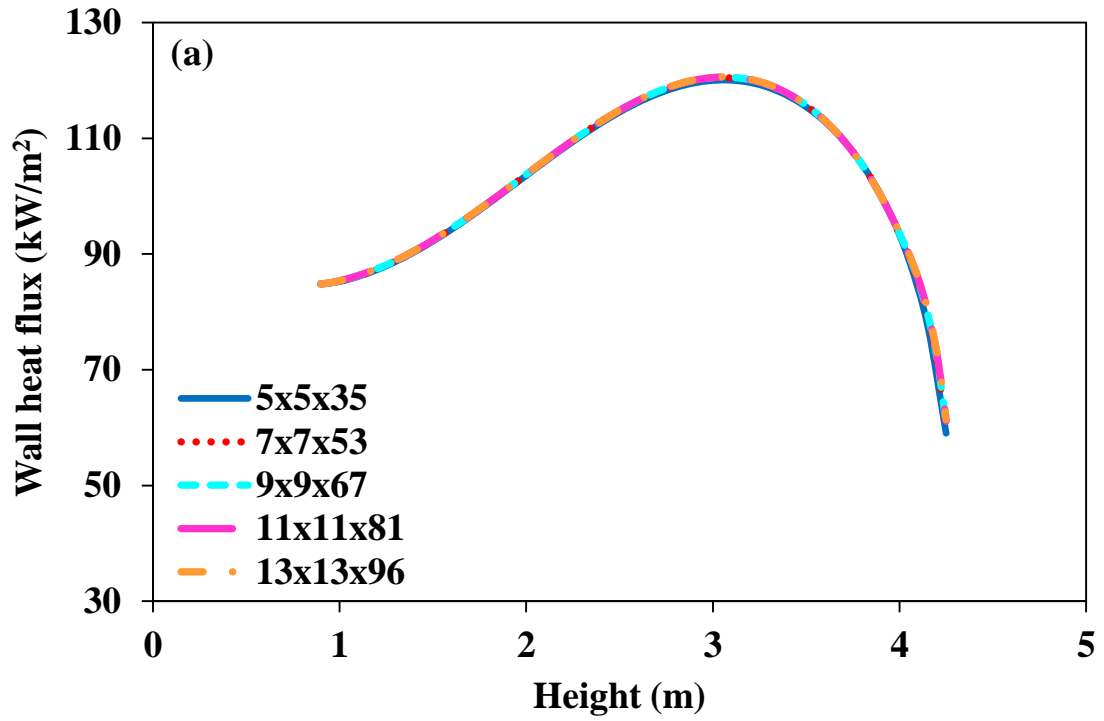


Figure 6.55 Effect of spatial discretization on (a) incident wall heat fluxes and (b) source terms

Table 6.30 Effect of spatial grid refinement on predictive accuracy and CPU efficiency

	% Relative Error*		CPU Ratio**
	Heat Flux	Source Term	
5x5x35	1.0	-40.6	0.0
7x7x53	0.4	-18.8	0.1
9x9x67	0.2	-7.3	0.2
11x11x81	0.1	0.0	0.5
13x13x96	Reference solution		1.0
* Errors are with respect to the predictions of the reference case with 13x13x96 grid resolution.			
** CPU ratio = (CPU time of a grid resolution)/(CPU time of 13x13x96)			

For the angular discretization, different orders ( $N = 4, 6, 8$ ) of approximation of DOM are investigated to evaluate the effect of order of approximation on the predictive accuracy of  $S_N$  method by comparing its results against the highest number of rays per quadrature,  $N_8=80$  rays. 11x11x81 spatial grid resolution is selected for the numerical solution. Heat flux and source term distributions with different  $S_N$  approximations are illustrated in Figure 6.56, for which the corresponding relative errors and CPU times are tabulated in Table 6.31. As can be seen from the table, heat fluxes are not sensitive to angular discretization and further increase in the number of rays is not necessary as  $S_6$  and  $S_8$  solutions give almost identical source term distributions. Hence, from the viewpoints of accuracy and computational economy, the use of 11x11x81 control volumes with  $S_6$  approximation was found to be sufficient for the problem under consideration.



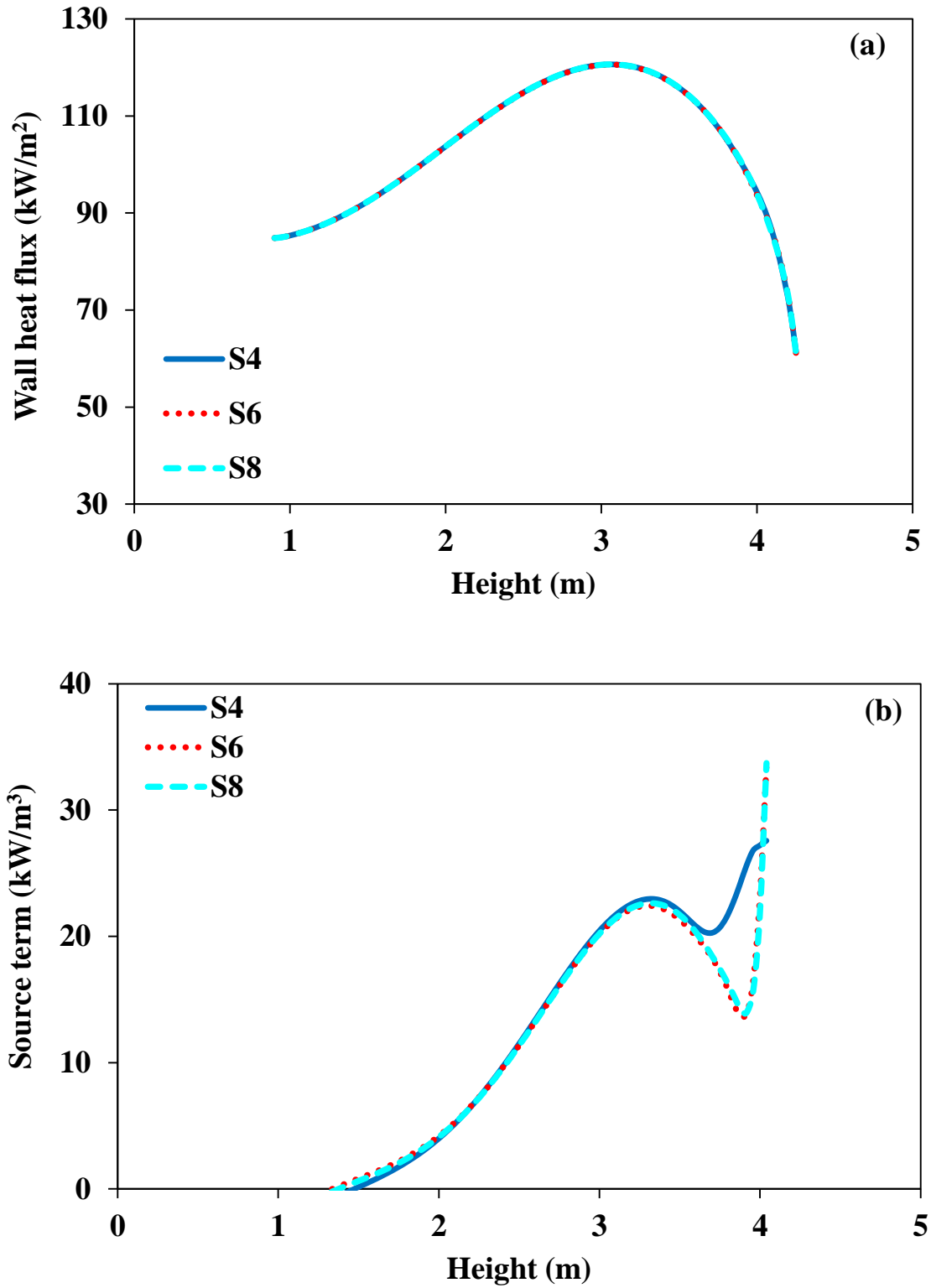


Figure 6.56 Effect of angular discretization on (a) wall heat fluxes and (b) source terms

Table 6.31 Effect of angular grid refinement on predictive accuracy and CPU efficiency

	% Relative Error*		CPU Ratio**
	Heat Flux	Source Term	
<b>S<sub>4</sub></b>	0.0	-5.9	0.2
<b>S<sub>6</sub></b>	0.0	0.0	0.6
<b>S<sub>8</sub></b>	Reference solution		1.0
* Errors are with respect to the predictions of the reference case with S <sub>8</sub> .			
** CPU ratio = (CPU time of a S <sub>N</sub> ) / (CPU time of S <sub>8</sub> )			

Effect of number of gray gases (3x3, 5x5, 7x7 and 10x10 for H<sub>2</sub>O and CO<sub>2</sub> respectively) on the predictive accuracy of SLW model is also investigated in order to maximize the CPU efficiency of the benchmark solution for both Test 1 and Test 2. Relative errors and corresponding CPU times are compared in Table 6.32. It is seen that 5x5 gray gases provide satisfactory solutions in terms of accuracy and computational efficiency even for Test 1, where the particle load is one order of magnitude smaller than that of Test 2. Therefore, 5x5 gray gases are utilized in the rest of the present study for both SLW and banded SLW models.

Table 6.32 Effect of number of gray gases on predictive accuracy and CPU efficiency

Number of Gray Gases	Test 1			Test 2		
	% Relative Error*		CPU Ratio	% Relative Error*		CPU Ratio
	Heat Flux	Source Term		Heat Flux	Source Term	
<b>3x3</b>	0.3	40.8	0.0	0.1	7.4	0.0
<b>5x5</b>	0.1	4.7	0.2	0.0	1.6	0.2
<b>7x7</b>	0.1	3.3	0.4	0.0	1.2	0.4
<b>10x10</b>	Reference solution		1.0	Reference solution		1.0
* Errors are with respect to the predictions of the reference case with 10x10 gray gases.						
** CPU ratio = (CPU time of n x n gray gas mixture) / (CPU time of 10 x 10 gray gas mixture)						

### 6.8.3 Testing the Predictive Accuracy of Proposed Gas Property Models

In this section, proposed gas property models (GWB, GNB, banded SLW) are compared by benchmarking their predictions against those of SLW by considering only gas radiation to create a baseline for simpler gas property models before including the effect of spectral particle radiation. Input data necessary for the radiation models (boundary conditions, temperature and concentration profiles, dimensions of the test rig) are taken from Test 1 (Section 5.1.1). Wide band gas model (GWB) is solved for 1, 8 and 12 wide bands while 423 bands are utilized in the narrow band model (GNB), which will be referred as Gray Gas (1 banded GWB), GWB (8 and 12 banded GWB) and GNB, respectively. In banded SLW model, spectrum up to 20  $\mu\text{m}$  is divided into 8 wide bands (8 spectral bands<sup>8</sup> x 25 gray gases = 200 RTE solutions).

In both banded (GWB and GNB) and SLW models (SLW and banded SLW), calculation of gas absorption coefficients are based on high-resolution HITRAN database [28, 176], as spectrally resolved database for banded SLW (constants required to evaluate  $g_w$  and  $g_c$  in Eqs. (3.41) and (3.46)) from HITEMP is not available in the literature yet. Fortunately, spectral gas absorption coefficients calculated from HITRAN [28, 176] and HITEMP [30, 177] databases are found to be quite similar under FBC conditions (see Table 5.3). Comparison between gas absorption coefficients calculated from HITRAN and HITEMP databases and their banded representations are shown in Figure 6.57. As can be seen from Figure 6.57 (a), there are only slight variations in the spectral gas absorption coefficients between two databases.

Incident wall heat fluxes and source terms predicted by different gas models are demonstrated in Figure 6.58. As can be seen from the Figure 6.58 (a), heat flux predictions obtained from all models are in good agreement with the reference solution. On the other hand, all banded gas approximations lead to over-prediction of the source terms where the predictive accuracy of GWB and GNB approximations are found to be close to one another (Figure 6.58 (b)). It is also seen that banded SLW model (Section 3.6) gives a

---

<sup>8</sup> Spectral bands used in banded SLW models covers the same spectral ranges as in the banded spectral particle properties given in section 6.7.1.1.

very good agreement with the classic SLW model (Section 3.5) in both heat flux and source term predictions and banding the spectrum as described in Section 3.6 does not lead to any significant errors in banded SLW approximation.

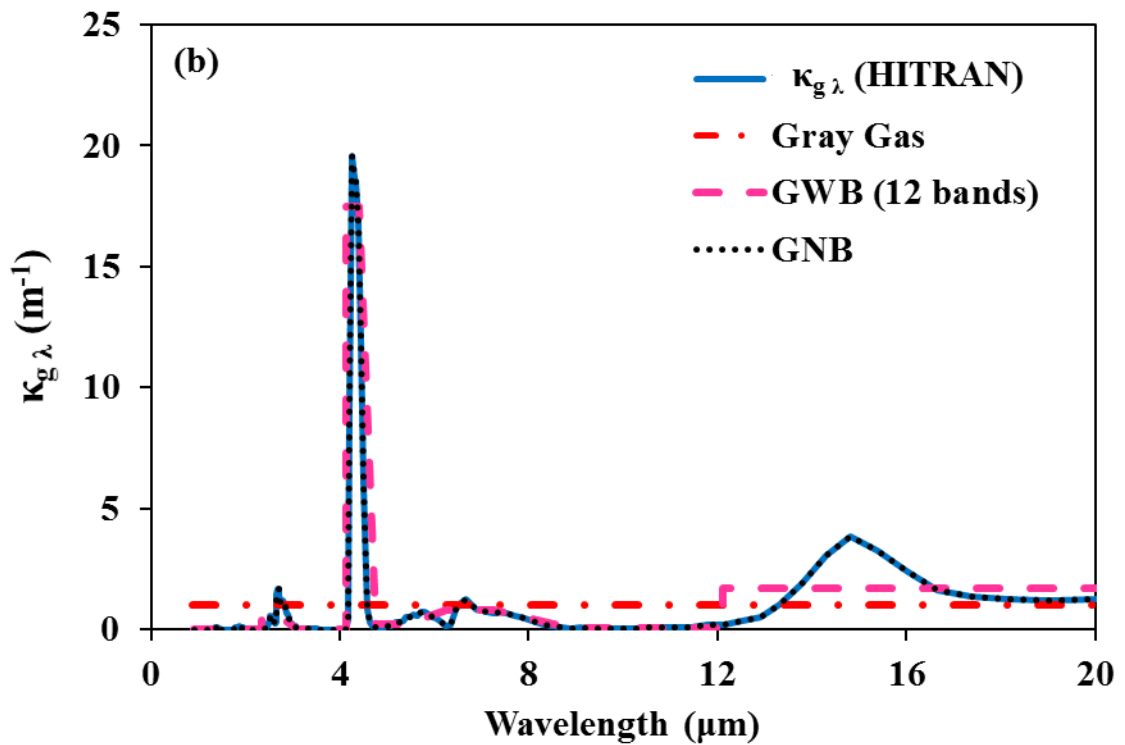
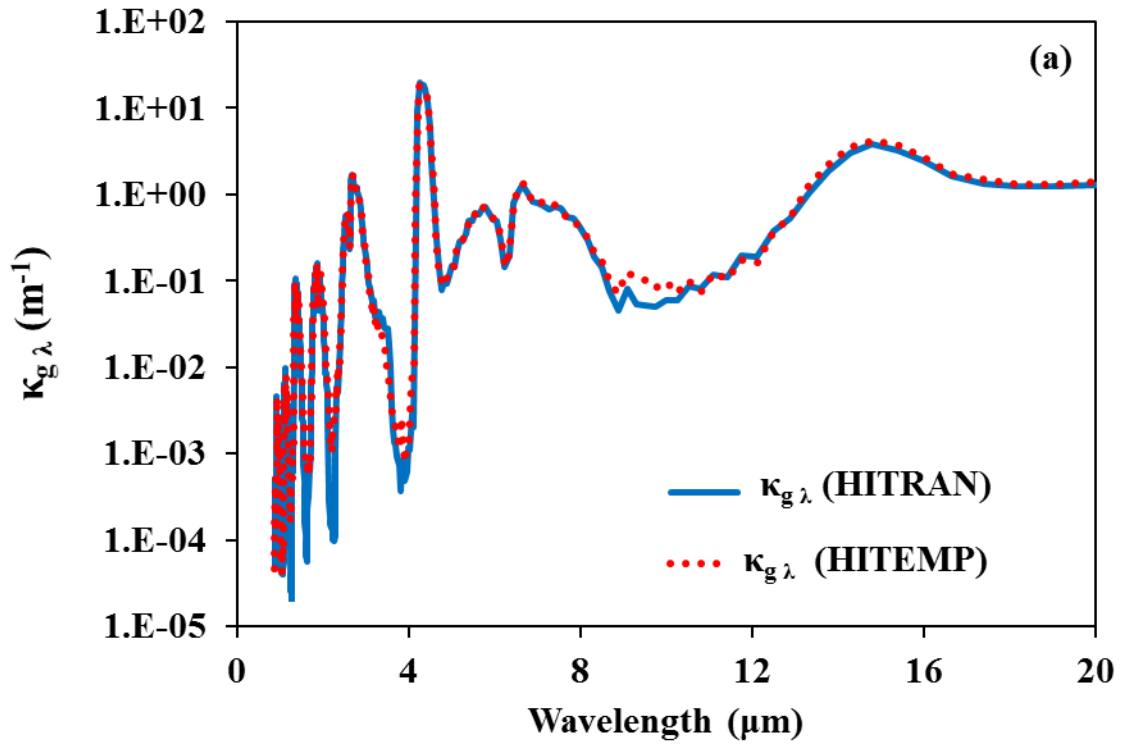


Figure 6.57 (a) Comparison of spectral gas absorption coefficients ( $\kappa_{g,\lambda}$ ) calculated from HITRAN and HITEMP databases and (b) their banded representations

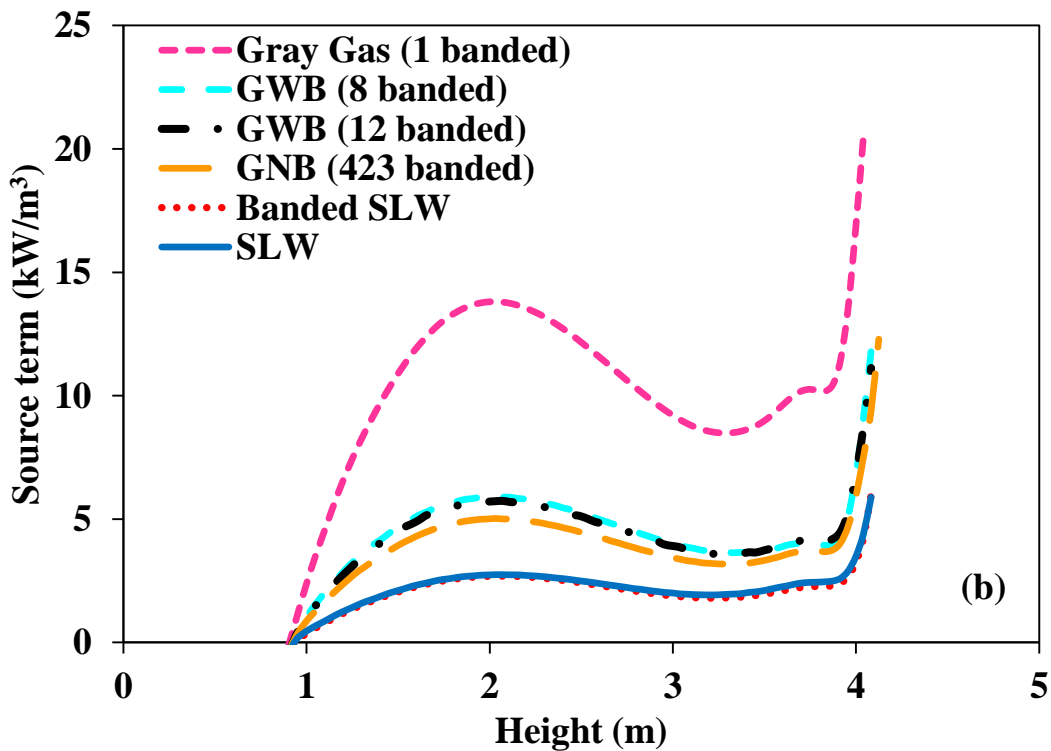
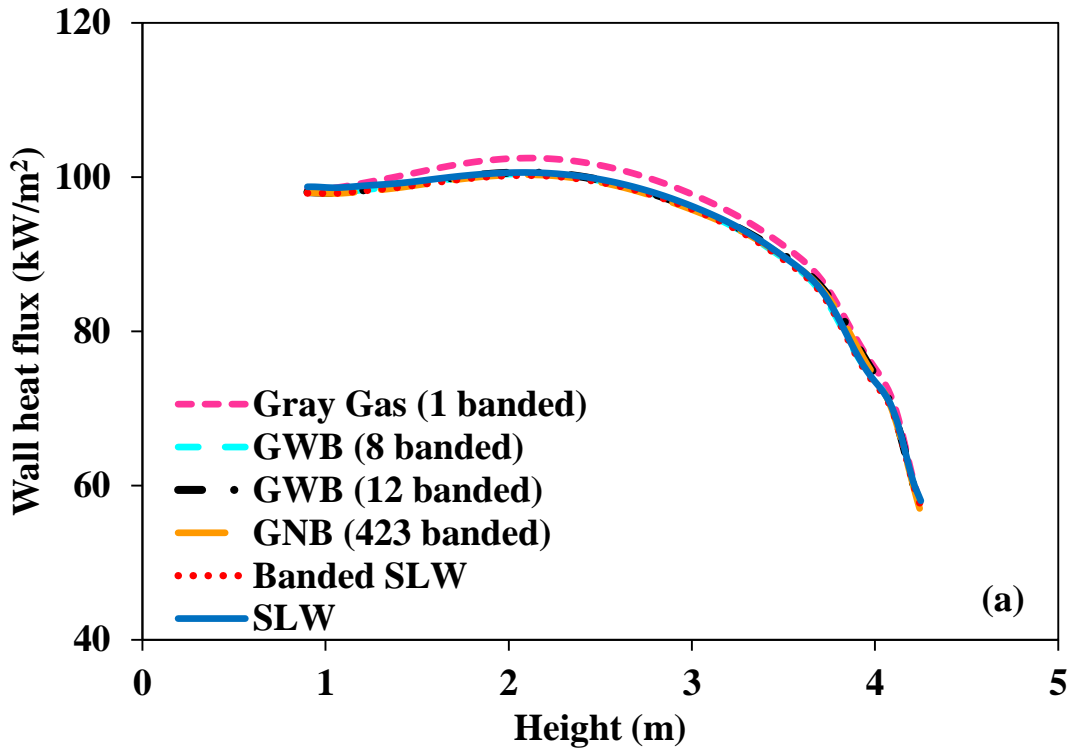


Figure 6.58 Comparison between (a) heat flux and (b) source term predictions of different gas models

The percentage relative errors in heat flux and source term predictions with corresponding CPU times are given in Table 6.33. As can be seen from the table, error in using gray gas approximation by averaging the gas absorption coefficient over the entire spectrum (red line in Figure 6.57 (b)) leads to significant error in source term predictions. It is also seen that increasing the number of bands in GWB approximation from 8 to 12 only slightly increases the accuracy while doubling the CPU time. Increasing the number of spectral bands from 12 to 423 by using GNB approximation, on the other hand, noticeably increases the accuracy at the expense of 40 times more CPU time. Nevertheless, GNB approximation is still far from the accuracy of the SLW model when only gas radiation is considered. These results underline that it is not possible to represent the complex gas behavior with the crude gray gas assumption deployed at each band even if the band width is very narrow ( $25 \text{ cm}^{-1}$ ) as in the case of GNB approximation. It is also seen that banded SLW model is as successful as the global SLW model in modeling spectral gas radiative properties. Therefore, it can be utilized in the presence of non-gray particles without loss of accuracy in gas radiation.

Table 6.33 Predictive accuracy and CPU efficiency of gas models

	<b>Gray Gas (1 banded)</b>	<b>GWB (8 banded)</b>	<b>GWB (12 banded)</b>	<b>GNB (423 banded)</b>	<b>Banded SLW</b>	<b>SLW</b>
% Av. error in heat fluxes	2	0	0	0	0	Reference
% Av. error in source terms	362	100	95	68	-2	Reference
CPU time (s)	28	748	2258	95204	11755	1184
CPU ratio	0	1	2	80	10	1



#### 6.8.4 Accuracy of GWB Approximation in the Presence of Non-gray Particles

In this section, accuracy and CPU efficiency of GWB approximations with non-gray particles are assessed for the two test cases described in Section 5.1.1 by benchmarking their predictions against those of banded SLW model. Spectral gas absorption coefficients in GWB approximation are represented by 1, 8 and 12 wide bands. In both GWB and banded SLW models, non-gray particle absorption coefficient, scattering coefficient and asymmetry factor (see Figure 6.33, Figure 6.34) are represented with 8 wide bands based on the results presented in Section 6.7.1.1 and Section 6.7.1.2.

Figure 6.59 demonstrates the heat flux distributions obtained with different gas property models for both Test 1 and Test 2. As can be seen from the figure, predictions with GWB approximations are in good agreement with the measurements as well as the reference solution for both low (Test 1;  $A_p = 0.77 \text{ m}^2/\text{m}^3$ ) and moderate particle loads (Test 2;  $A_p = 5.46 \text{ m}^2/\text{m}^3$ ).

Source term distributions obtained with different gas property models for both Test 1 and Test 2 are demonstrated in Figure 6.60. Similar to gas radiation (see Figure 6.58 (b)), all GWB approximations leads to over-prediction of the source terms. Nevertheless, it is seen that difference between the gas approximations and the benchmark solution decreases with increasing number of bands and particle load.

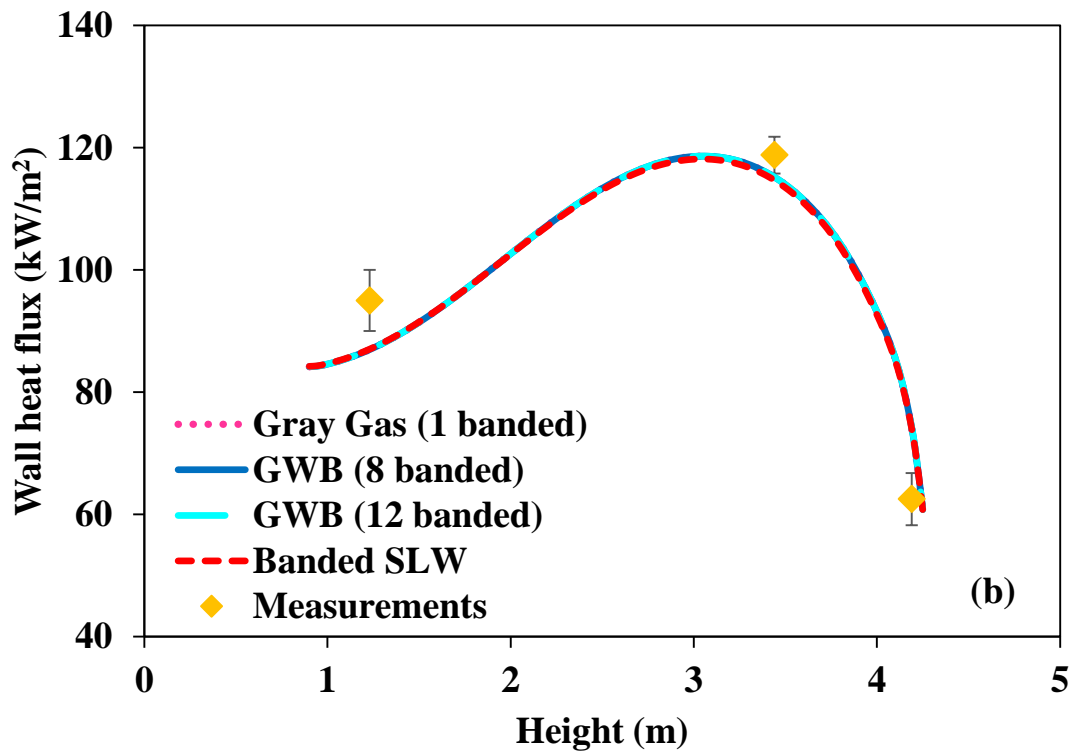
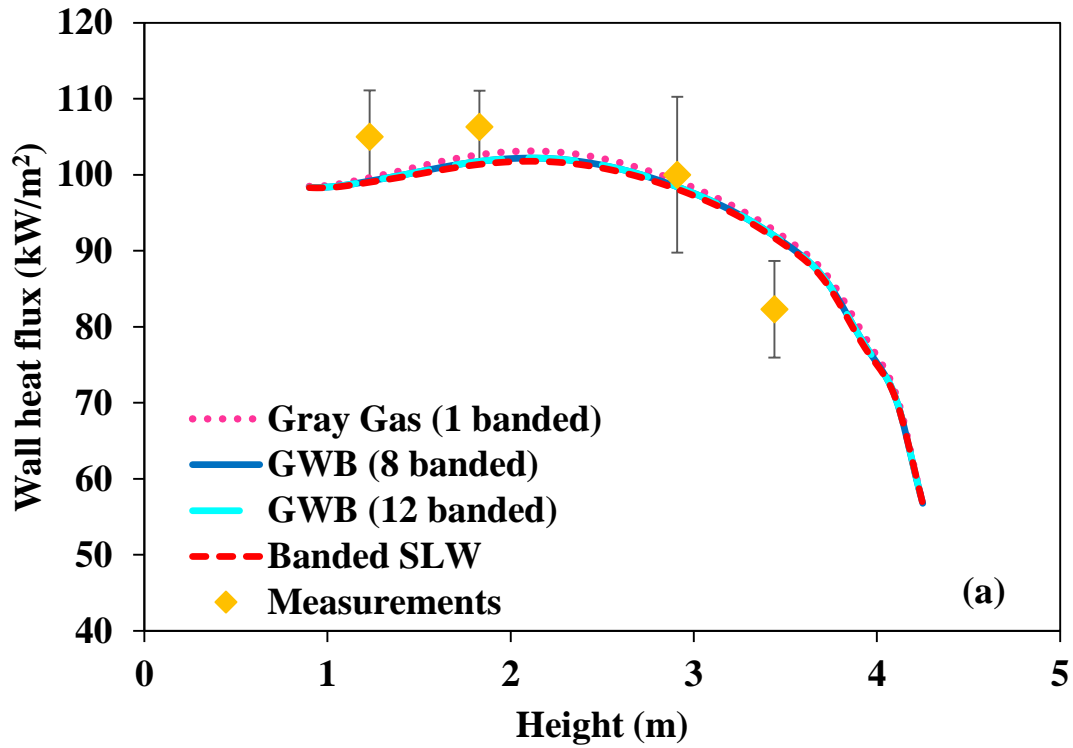


Figure 6.59 Measured and predicted incident radiative heat fluxes for (a) Test 1 and (b) Test 2

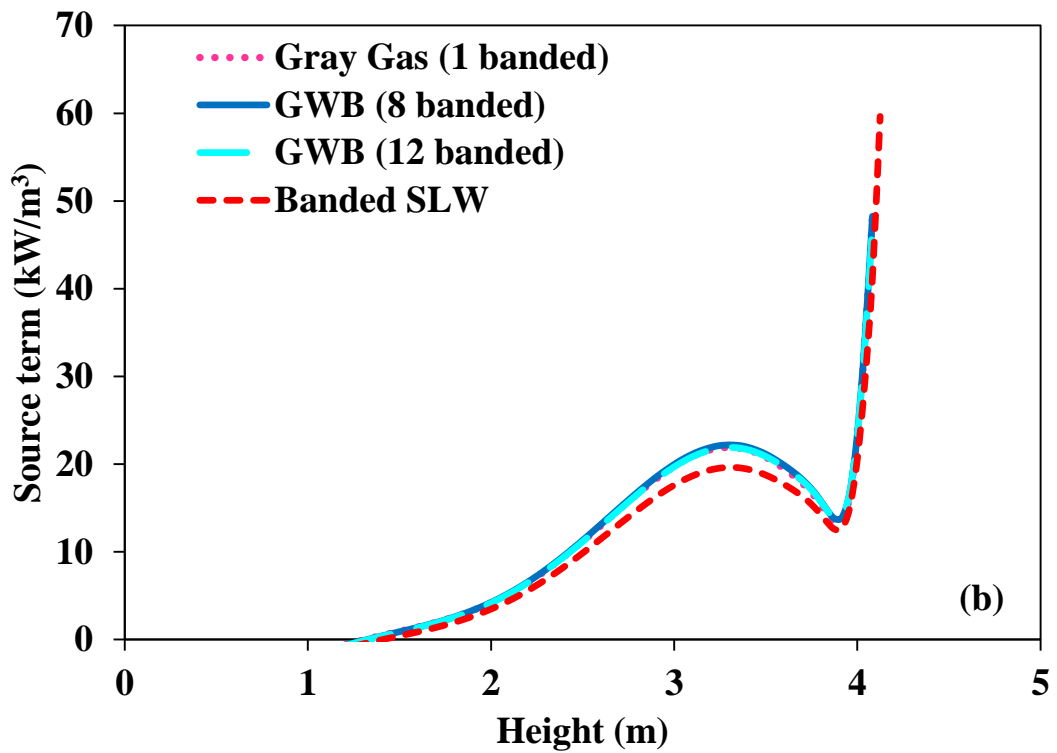
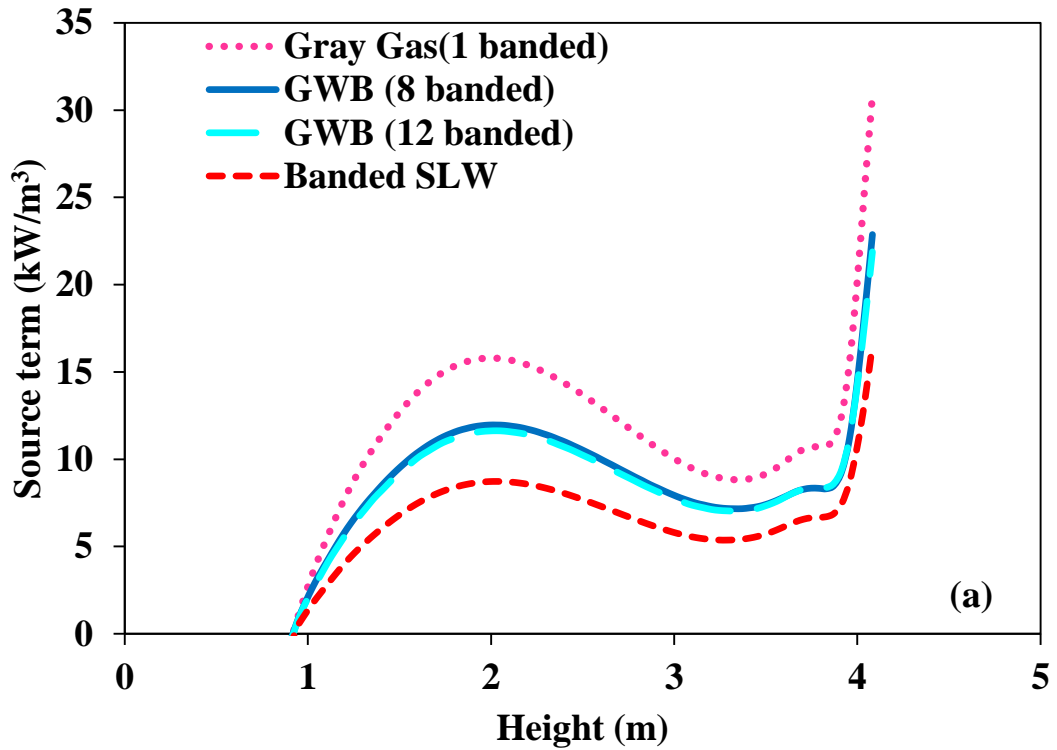


Figure 6.60 Effect of GWB approximation on source term predictions for (a) Test 1 and (b) Test 2

The percentage errors in incident heat fluxes and source term predictions with corresponding CPU times are given in Table 6.34. The first important result concerning the GWB approximations is the significant decrease in the errors for source term predictions with increasing particle load. For Test 1, where the particle load is low ( $B = 0.01 \text{ kg /m}^3$ ), accuracy of 1 Banded GWB model improves noticeably compared to that of gas radiation (see Table 6.33). It is also seen that increasing the number of wide bands in GWB model increases the predictive accuracy although GWB approximation is still far from being accurate. At higher particle concentration of Test 2 ( $B = 0.13 \text{ kg /m}^3$ ), however, error in source term predictions is about 10 % for the GWB approximation with a considerably less CPU time.

Considering the Planck mean absorption coefficient of the gas mixture ( $1.0 \text{ m}^{-1}$ ) and ash particles for Test 1 ( $0.4 \text{ m}^{-1}$ ) and Test 2 ( $3.8 \text{ m}^{-1}$ ), these results suggest that GWB approximation can be used to reduce the CPU requirement of the spectral RTE solution when the order of magnitude of the particle absorption coefficient is higher than that of gas absorption coefficient. Nevertheless, if the absorption coefficients of the gas mixture and particles are in the same order of magnitude, more accurate gas radiative property models such as banded SLW are needed.

Results presented in this section show that SLW model can be converted to the banded SLW model to incorporate non-gray particle radiation in the solution of spectral RTE without sacrificing from the accuracy. Therefore, banded SLW model can be considered as an accurate and CPU efficient model to be used in the presence of non-gray particles. In other words, banded SLW model can alleviate the need for narrow band models requiring excessive CPU time to evaluate spectral particle radiation. Furthermore, GWB approximation is only recommended if the order of magnitude of the particle absorption coefficient is higher than that of gas absorption coefficient.

Table 6.34 Effect of gas property approximations on incident heat fluxes and sources terms in the presence of non-gray particles

<b>Test 1 (<math>A_p = 0.77 \text{ m}^2/\text{m}^3</math>)</b>				
	<b>Gray Gas (1 banded)</b>	<b>GWB (8 banded)</b>	<b>GWB (12 banded)</b>	<b>Banded SLW</b>
% Av. error in heat fluxes	1	0	0	Reference
% Av. error in source terms	73	34	31	Reference
CPU time (s)	488	516	1629	11398
CPU ratio	0.0	0.0	0.1	1
<b>Test 2 (<math>A_p = 5.46 \text{ m}^2/\text{m}^3</math>)</b>				
	<b>Gray Gas (1 banded)</b>	<b>GWB (8 banded)</b>	<b>GWB (12 banded)</b>	<b>Banded SLW</b>
% Av. error in heat fluxes	0.2	0.2	0.2	Reference
% Av. error in source terms	12	12	11	Reference
CPU time (s)	371	325	1174	6440
CPU ratio	0.1	0.1	0.2	1

## **6.9 Influence of Spectral Particle Radiation on Predictive Accuracy of Gas Property Approximations**

In the previous sections, it was shown that spectral particle radiation is of significant importance for accurate calculation of radiative heat transfer in combustors even at low particle concentrations (as in the case of pulverized coal fired furnaces) and that negligence of the spectral behavior of either combustion gases or particles can lead to significant errors in both heat flux and source term predictions depending on the relative magnitudes of gas and particle properties.

Studies involving both participating combustion gases and absorbing-emitting-scattering particles, on the other hand, state that improvement achieved in predictive accuracy by deploying accurate gas property models can become marginal compared to that of gray gas approximation in the presence of particles [56, 146] as particle radiation dominates total radiation [32, 147-149]. In this case, spectral gas properties can be represented by simple gas models, where RTE is solved only several times with a high CPU efficiency. However, these previous assessment studies ignore the spectral dependency of the particle cloud properties and hence validity of simpler gas property models are only discussed within the frame of gray particle assumption.

Considering the fact that spectral emission / absorption bands of the participating combustion gases (see Figure 6.57) and ash particles (see Figure 6.33-Figure 6.35) are significantly different in nature, there is a need for the investigation of the influence of spectral particle properties on the predictive accuracy of gas property models.

Therefore, objective of this section is to investigate predictive accuracy of simpler gas property models, namely gray gas and gray wide band approximations, by benchmarking their predictions against those of SLW in the presence of gray and non-gray particles. Investigation is performed through mathematical modeling by using the experimental data on two coal combustion tests previously performed in 300 kWt ABFBC test rig (see Section 5.1.1). In addition to these two combustion tests, two additional parametric studies are also included, in which freeboard walls are assumed to be bounded by conventional panel tube walls, as in utility or industrial furnaces instead of hot refractory walls of the

pilot scale test rig. In these parametric studies, top and side wall temperatures are assumed to be at 537 K with an emissivity of 0.80 while all other operating conditions of the combustion tests are kept the same (see Table 5.3).

In the radiation models, freeboard is treated as a 3D rectangular enclosure containing gray/non-gray, absorbing, emitting gas with gray/non-gray absorbing, emitting, anisotropically scattering particles surrounded by black/gray diffuse walls (Section 5.1.3). Radiative properties of the particle laden combustion gases are evaluated by using GWB, SLW and banded SLW models for gases (Section 3.3-3.6) and Mie theory for particles (Section 4.1.3), respectively.

Regarding to gas property models, wide band gas model (GWB) is solved for 1 and 12 wide bands, which will be referred as Gray Gas (i.e., 1 banded GWB) and GWB (i.e., 12 banded GWB), respectively. In banded SLW model, spectrum up to 20  $\mu\text{m}$  is divided into 8 wide bands (8 spectral bands<sup>9</sup> x 25 gray gases = 200 RTE solutions). In both banded (GWB) and SLW models (SLW and banded SLW), calculation of gas absorption coefficients are based on high-resolution HITRAN database [28, 176], as spectrally resolved database for banded SLW (constants required to evaluate of  $g_w$  and  $g_c$  in Eq. (7)) from HITEMP is not available in the literature yet. Fortunately, spectral gas absorption coefficients calculated from HITRAN [28, 176] and HITEMP [30, 177] databases are found to be quite similar under FBC conditions (Figure 6.57). In all reference solutions, SLW is used in the presence of gray particles while banded SLW is used in the presence of non-gray particles.

In order to investigate the influence of spectral particle properties on the predictive accuracy of gas property models for a wide range of applications, three different particle compositions are tested (will be referred as Ash I, V, VI). Ash I and Ash V represent ash particles with low (3 %) and high (30 %) iron oxide content while Ash VI represents low iron oxide (5-7 %) content ash particles with carbon residue (7-10 %). Correlations based on Ebert's model (see Section 4.4) are employed to estimate the spectral refractive indices of fly ash particles as a function of wavelength and fly ash compositions for Ash I and

---

<sup>9</sup> Spectral bands used in banded SLW models covers the same spectral ranges as in the banded spectral particle properties given in section 6.7.1.1.

Ash V<sup>10</sup> (Section 4.4). For Ash VI, spectral refractive indices are taken from [122] based on the measurements of [118, 119]. Spectral refractive (n) and absorption (k) indices for Ash I, V, VI are demonstrated in Figure 6.61.

Spectral radiative properties of the polydisperse particles are calculated by using Mie theory for each particle size (34 particle diameters) and wavelength (147 spectral points) with corresponding spectral complex index of refraction values presented in Figure 6.61. Calculated spectral particle properties for Test 1 and Test 2 are shown in Figure 6.62. After obtaining the spectral particle properties, their banded representations are then found according to Eq. (3.7), which can directly be used in the banded form of RTE given in Eq. (3.8). For gray particles, wavelength independent refractive index of  $m = 1.5 - 0.02i$  and a representative wavelength of 3  $\mu\text{m}$  are used [141]. It should be noted that all properties are calculated up to 20  $\mu\text{m}$  as it is considered to be sufficient enough for the majority of thermal radiation in coal fired systems. In all cases, scattering phase functions are represented by transport approximation (Section 4.3).

In MOL solution of DOM, a combination of  $S_6$  and 11 x 11 x 81 grid nodes (x, y and z directions, respectively) is utilized which was found to provide accurate and CPU efficient solutions (see Section 6.8.2). For the difference relations of spatial derivatives, three-point upwind differencing scheme DSS014 is employed. All simulations are carried out on a computer with Intel® Core™ 7i CPU 2600 3.40 GHz processor having 16.00 GB of RAM. CPU times are recorded for an error tolerance of 0.001 % throughout the analyses.

---

<sup>10</sup> Spectral refractive and absorption indices of Ash I and Ash V are taken from the calculations presented in Section 6.7.2.



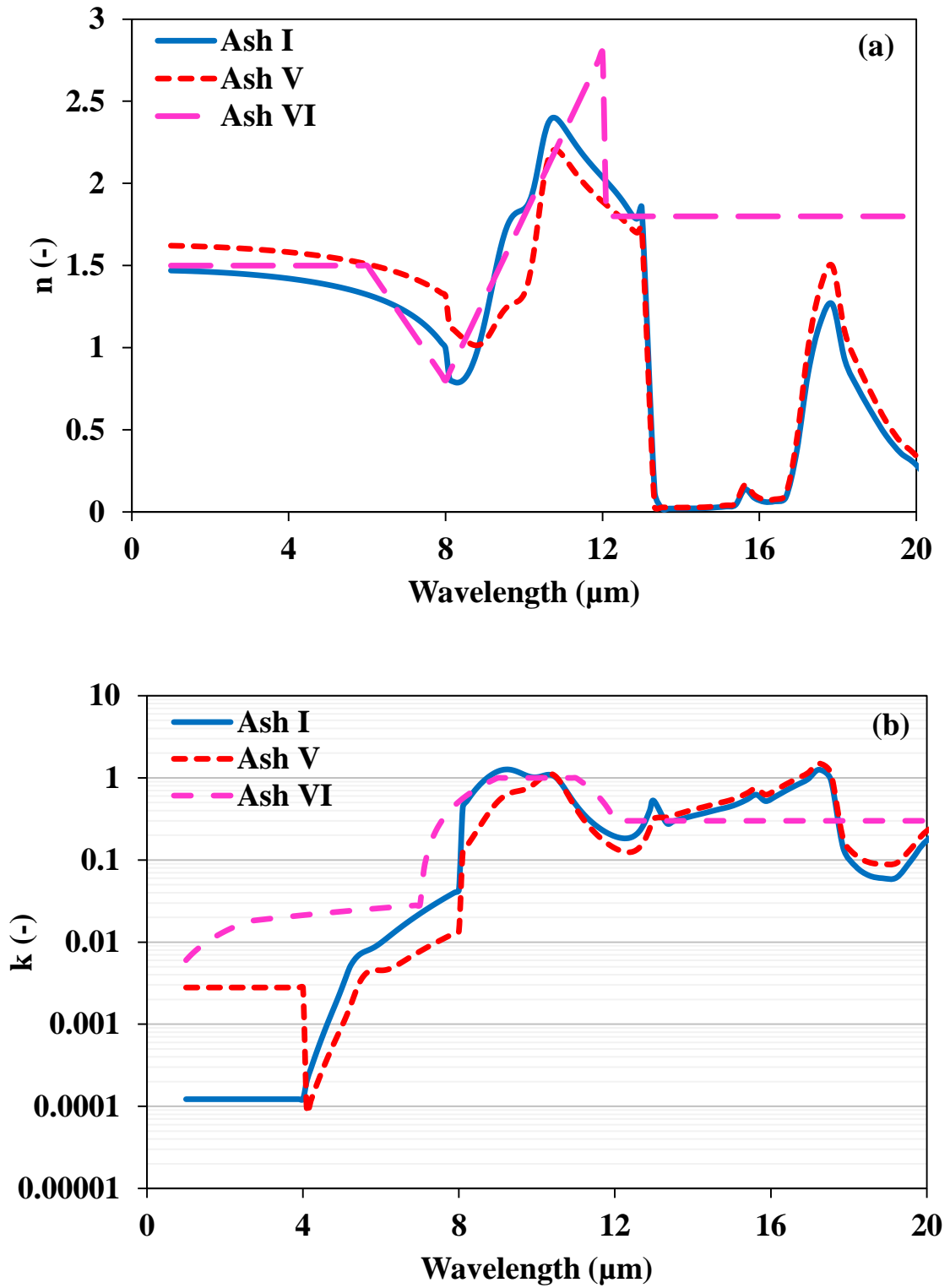


Figure 6.61 Spectral (a) refractive index and (b) absorption index data for Ash I-III

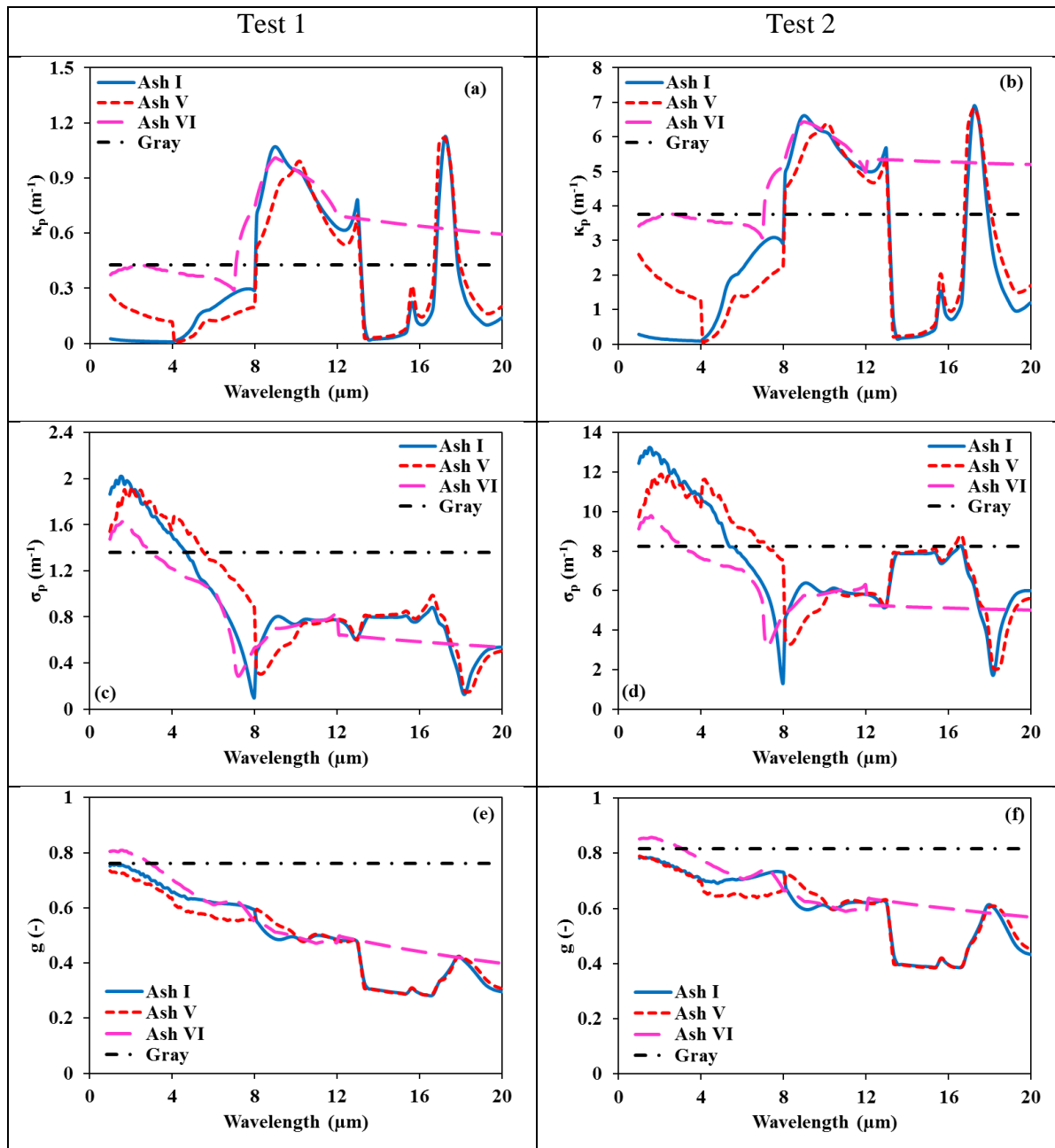


Figure 6.62 (a, b) Particle absorption coefficients, (c, d) scattering coefficients and (e, f) asymmetry factors for (a, c, e) Test 1 and (b, d, f) Test 2

### 6.9.1 Comparison of Gas and Particle Absorption Bands

Spectral emission / absorption bands of the participating combustion gases and ash particles are significantly different in nature. H<sub>2</sub>O and CO<sub>2</sub> gas mixture has several “peak zones” in thermal radiation spectrum (Figure 6.57) while ash particles demonstrate a less complex yet continuous behavior (Figure 6.33-Figure 6.35). Nevertheless, spectral nature of particle radiation is still influential on radiative heat transfer and particle absorption coefficient has been shown to be a strong function of chemical composition (see Section 6.7.2), especially in the iron oxide absorption band (0.7-4 μm). Therefore, it is considered necessary to compare relative magnitudes of spectral gas and particle properties in order to see the influence of spectral nature of particle radiation on gas radiation share in the thermal spectrum. For that purpose, ratio of the spectral gas absorption coefficient to total absorption coefficient ( $\kappa_g / (\kappa_g + \kappa_p)$ ) is calculated for Ash I, Ash V, Ash VI for both Test 1 and Test 2.

Figure 6.63 demonstrates the ratio of the spectral gas absorption coefficient to total absorption coefficient obtained with gray and non-gray particles (Ash I, V, VI). It is seen that if ash particles present in the combustor has a low absorption coefficient as in the case of Ash I (3 % iron oxide in ash), share of gas radiation is significantly underestimated for the majority of the spectrum relevant to thermal radiation (Figure 6.63(a)). Furthermore, error in estimating the spectral gas radiation share is found to be increasing when the particle load is increased one order of magnitude from Test 1 to Test 2, corresponding to an increase in particle surface area from 0.77 m<sup>2</sup>/m<sup>3</sup> to 5.46 m<sup>2</sup>/m<sup>3</sup> (Figure 6.63(d)). The reason behind this discrepancy is the over-estimation of particle absorption coefficient when particles are assumed to be gray, especially in the iron oxide absorption band (shadowed region). When particle absorption coefficient is large due to its high iron content as in the case of Ash V (31 %), it is found that error in gas radiation share is reduced to some extent if particles are assumed to be gray. Nevertheless, there are still noticeable differences for both Test 1 and Test 2 (Figure 6.63(b, e)). In the case of ash particles with carbon residue (Ash VI), comparisons reveal that gray particle assumption does not lead to any significant errors in predicting the gas radiation share

(Figure 6.63(c, f)). These results show that gray particle assumption can lead to over-prediction of particle absorption coefficient, which results in under-estimation of gas radiation share in the thermal radiation spectrum even when the particle load is very high as in the case of Test 2.

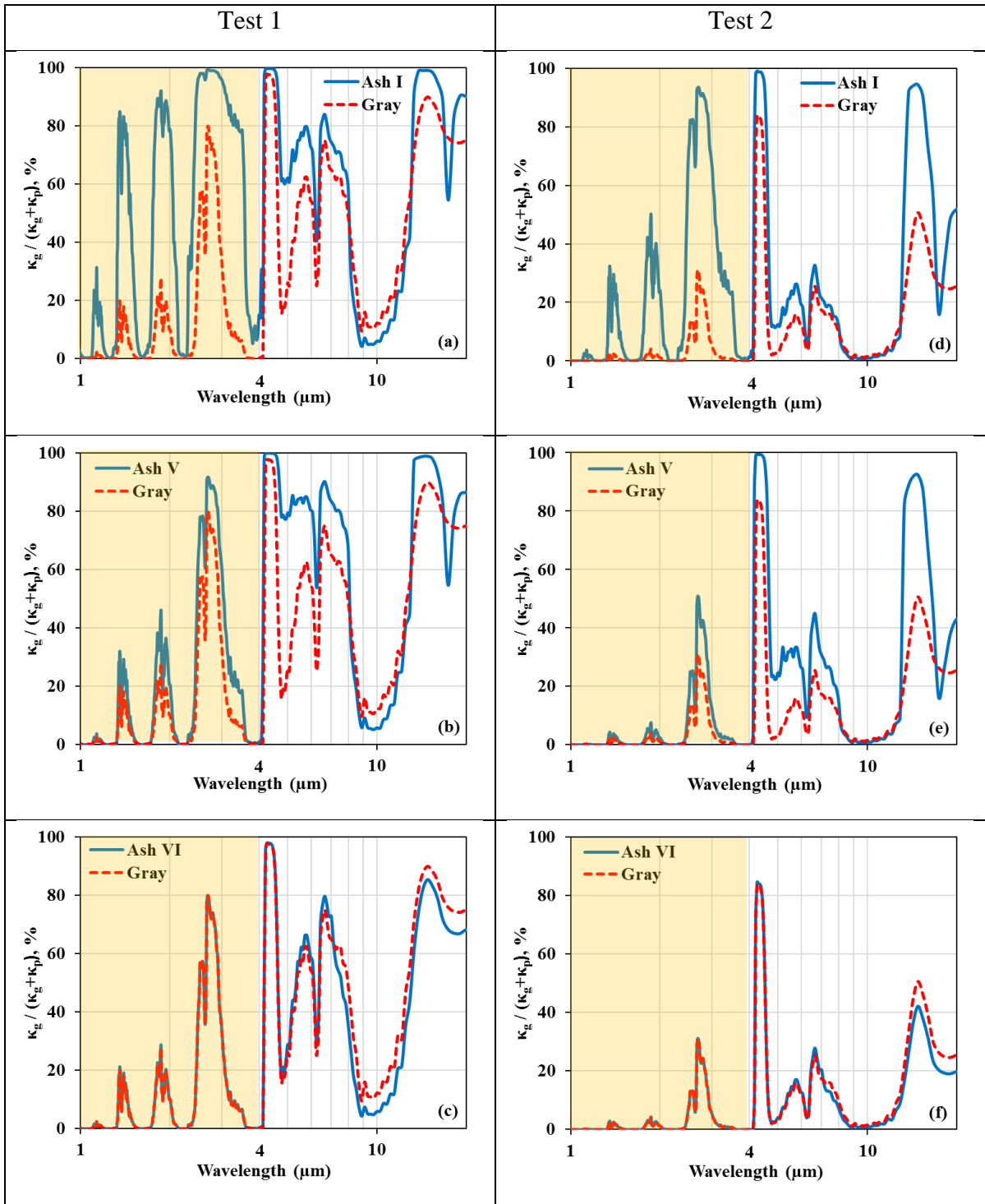


Figure 6.63 Ratio of gas absorption coefficient to total absorption coefficient predicted with gray and non-gray particles for Test 1 (a-c) and Test 2 (d-f)

## 6.9.2 Sensitivity of Gas Property Approximations to Spectral Particle Radiation

In the previous section, it is demonstrated that incorrect treatment of spectral particle radiation may lead to under-estimation of gas radiation share for particle laden flue gases even at high particle loads. This finding is of significant importance as it also indicates that strong gas absorption bands may be disguised by over-estimated particle radiation and particles may be found to dominate total radiation due to gray particle assumption, although it may not be the case. Therefore, more accurate gas property models may still be necessary depending on the spectral nature of particle properties even for the cases with very high particle loads. In order to address this problem, accuracy and CPU efficiency of GWB approximation with gray / non-gray particles are assessed for the four test cases including both gas and particle radiation (described at the beginning of Section 6.9; two experimental and two parametric cases) by benchmarking their predictions against those of SLW. In both GWB and banded SLW, non-gray particle absorption coefficient, scattering coefficient and asymmetry factors (see Figure 6.62) are represented with 8 wide bands.

Table 6.35 demonstrates comparison between incident heat fluxes and source terms predicted by MOL solution of DOM coupled with non-gray gas and non-gray particle properties, for Ash I, V, VI and gray particles. Visual comparison of heat flux and source term predictions with the reference solution is also illustrated in Figure 6.64 and Figure 6.65 for Test 2 for the parametric study with panel tube walls. As can be seen from the table, heat flux predictions with GWB approximations are in good agreement with the reference solution for both low and moderate particle loads whether particles are taken as gray or not if the freeboard is bounded by hot refractory-lined walls as in the test rig. This is considered to be due to the “hot wall effect” (see Section 6.7.2.5), where radiative heat transfer is expected to be dominated by hot refractory walls rather than particle laden gas emissions. If the surrounding walls are bounded by conventional panel tube walls, however, as in utility or industrial furnaces, it is seen that errors in heat flux predictions are found to be quite significant for Ash I and Ash V (Figure 6.64). On the other hand, if particles are assumed to be gray in the assessment of GWB approximation, GWB model

is found to be accurate at high particle load (Test 2). In other words, gray particle assumption suppresses the errors introduced by GWB model for both Test 1 and Test 2.

This disguising effect of gray particle assumption becomes more clear in source term predictions along the combustor. For Test 1, it is seen that error in GWB is reduced by three-folds and its predictive accuracy is found to be much better than its true performance for Ash I and Ash V (Table Table 6.35). This discrepancy becomes even more critical when particle load is increased from Test 1 to Test 2. In that case, GWB is found to be “very accurate” if the comparison is done with gray particles (also see Figure 6.65 (d)) although error introduced by deploying GWB approximation is still significant in the presence of non-gray ash particles (also see Figure 6.65 (a, b)).

Comparisons presented in Table 6.35 also reveal that disguising effect of gray particle assumption is very limited for ash particles containing carbon residue as in Ash VI. In that case, errors in heat flux (Figure 6.64 (c)) and source term predictions ( Figure 6.65 (c)) due to GWB approximation are found to be similar to those with gray particle assumption ( Figure 6.65 (d), Figure 6.65 (d)).

Considering the fact that ash particles usually contain small amounts of iron oxide [124], it can be concluded that accurate gas property models are needed to represent the spectral behaviour of combustion gases even at high particle loads. The only exception may be the case where char burnout is expected to be incomplete.

Table 6.35 Effect of gray particle assumption on the predictive accuracy of GWB model

<b>Hot Refractory-lined walls</b>										
<i>Average relative % errors in using GWB gas model with different particles</i>	Test 1 (11 g/m <sup>3</sup> , 0.77 m <sup>2</sup> /m <sup>3</sup> )					Test 2 (131 g/m <sup>3</sup> , 5.46 m <sup>2</sup> /m <sup>3</sup> )				
	GWB				SLW	GWB				SLW
	Ash I	Ash V	Ash VI	Gray	Reference solution	Ash I	Ash V	Ash VI	Gray	Reference solution
% Av. Error in heat fluxes	0.1	0.2	0.1	0.3		0.1	0.2	0.0	0.0	
% Av. Error in source term	49	43	20	15		15	14	4	1	
<b>Parametric study with panel tube walls</b>										
<i>Average relative % errors in using GWB gas model with different particles</i>	Test 1 (11 g/m <sup>3</sup> , 0.77 m <sup>2</sup> /m <sup>3</sup> )					Test 2 (131 g/m <sup>3</sup> , 5.46 m <sup>2</sup> /m <sup>3</sup> )				
	GWB				SLW	GWB				SLW
	Ash I	Ash V	Ash VI	Gray	Reference solution	Ash I	Ash V	Ash VI	Gray	Reference solution
% Av. Error in heat fluxes	22	21	12	14		8	8	1	1	
% Av. Error in source term	67	55	27	23		18	14	2	0	



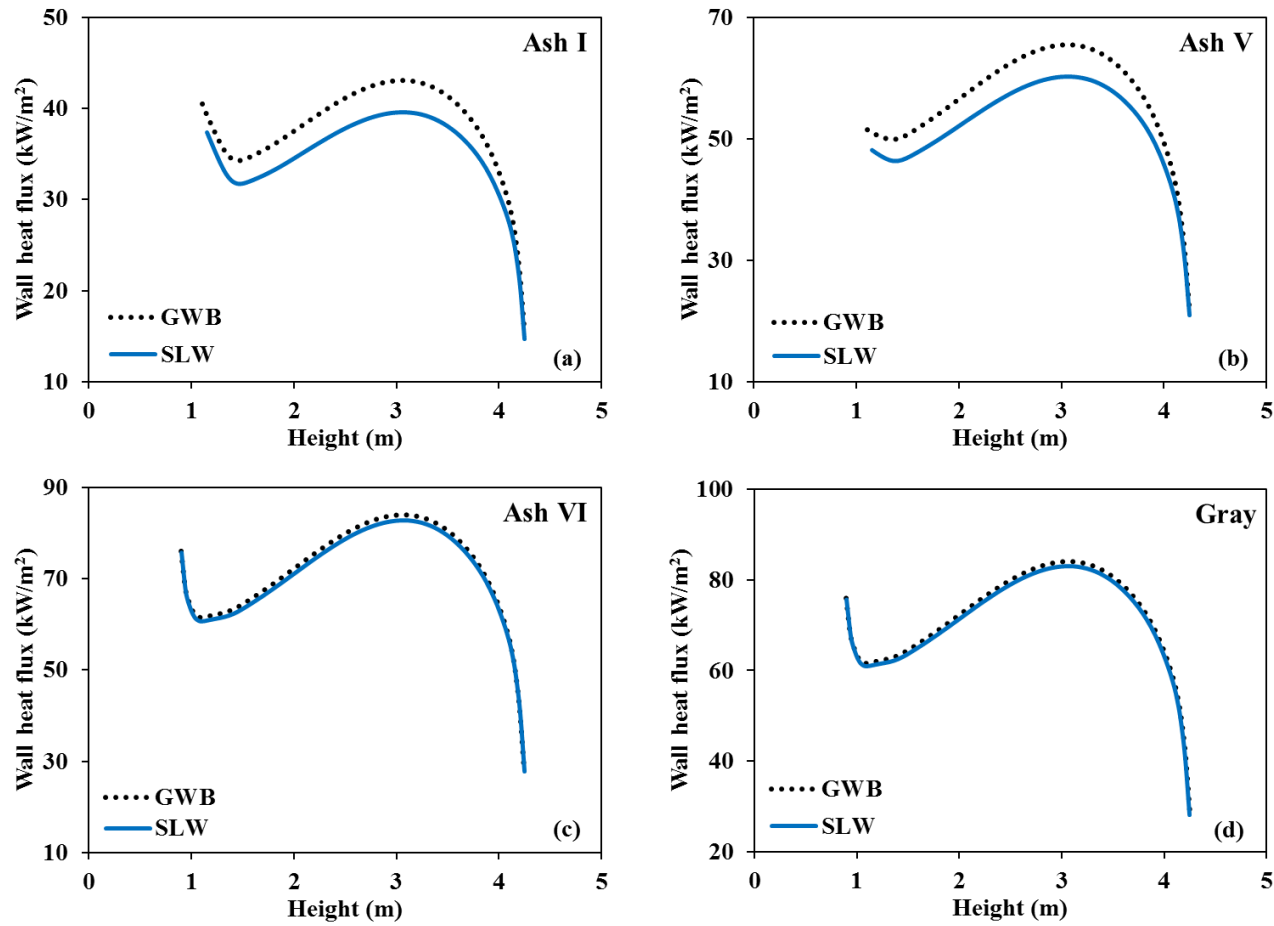


Figure 6.64 Comparison of heat flux predictions with non-gray (a-c) and gray particles (d) for Test 2 in the parametric study with panel tube walls (537 K)

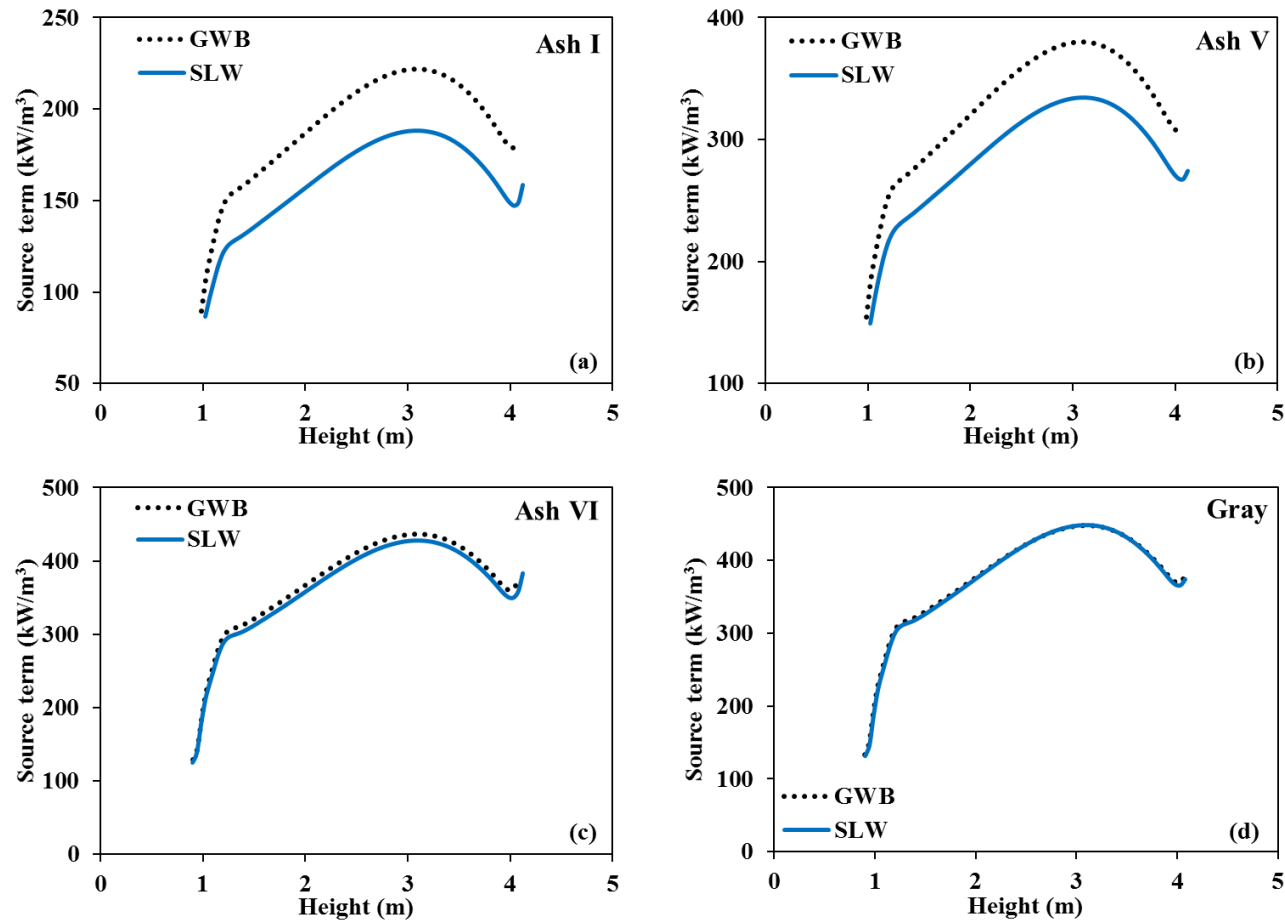


Figure 6.65 Comparison of source term predictions with non-gray (a-c) and gray particles (d) for Test 2 in the parametric study with panel tube walls (537 K)

## 6.10 Assessment of SLW-1 Model in the Presence of Gray / Non-Gray Particles

It was shown in Section 6.7 that spectral particle radiation is of significant importance for accurate calculation of radiative heat transfer in combusting systems even at low particle concentrations, which necessitates CPU efficient spectral gas property models compatible with spectral particle property models. To address this need, well-known SLW model was turned into a banded form in Section 6.8 to incorporate non-gray absorbing, emitting and scattering particles in the spectral solution of RTE in a 3-D enclosure, called “banded SLW”. It was demonstrated that predictive accuracy of banded SLW is very high and it yields heat flux and source term predictions almost identical to SLW model for gas radiation. In this case, however, RTE is still needed to be solved several hundreds of times for a gas mixture with non-gray particles due to high number of gray gases deployed in each spectral band (Number of RTE = 5 gray gas x 5 gray gas x 8 wide bands = 200 RTE for each grid node at each iteration).

It should be reminded that accuracy of SLW model increases with increasing number of gray gases used to represent spectral gas properties. As a rule of thumb, number of gray gases needed for a high accuracy in modeling gas radiation is recommended to be 10 for each specie [28]. In other words, if 100 gray gases are utilized for a gas mixture of CO<sub>2</sub> and H<sub>2</sub>O, SLW model can be accepted as accurate as LBL predictions [28]. These high number of gases, on the other hand, are directly reflected to the number of RTE solution. Fortunately, it has been recently shown that computational efficiency of SLW can be further extended without losing much accuracy for gas radiation with / without soot radiation in simple problems by decreasing the number of gray gases in 1-D model [98-101] and 2-D model [102], usually referred as SLW-1 (see Section 3.7).

In the views of the facts that (i) number of gray gases in SLW can be decreased while maintaining the predictive accuracy in 1-D problems with SLW-1 approach [98-101], (ii) application of SLW-1 model is only available for ideal test problems without absorbing, emitting and scattering particles and (iii) spectral treatment of both gas and particle properties are necessary for accurate calculation of radiative heat transfer in combusting systems, there is a need for investigation of the influence of decreasing number of gray

gases in SLW for multidimensional (3-D) enclosures involving gray / non-gray, absorbing, emitting and scattering particles. Therefore, objectives of this section are (i) to extend SLW-1 approximation to multidimensional enclosures involving gray / non-gray, absorbing, emitting and scattering particles and (ii) to investigate predictive accuracy of Gray Gas and SLW-1 models by benchmarking their predictions against those of SLW in the presence of gray and non-gray particles.

Investigation is performed through mathematical modeling by using the experimental data on two coal combustion tests previously performed in 300 kWt ABFBC test rig (see Section 5.1.1). In the radiation models, freeboard is treated as a 3D rectangular enclosure containing gray/non-gray, absorbing, emitting gas with gray/non-gray absorbing, emitting, anisotropically scattering particles surrounded by black/gray diffuse walls (Section 5.1.3). Radiative properties of the particle laden combustion gases are evaluated by using GWB approximation, SLW-1, SLW and banded SLW models for gases (Section 3.3-3.7) and Mie theory for particles (Section 4.1.3), respectively.

Regarding to gas property models, wide band gas model (GWB) is solved for 1 band, which will be referred as Gray Gas (i.e., 1 banded GWB). In banded SLW model, spectrum up to 20  $\mu\text{m}$  is divided into 8 wide bands (8 spectral bands<sup>11</sup> x 25 gray gases = 200 RTE solutions). In both banded (GWB) and SLW models (SLW and banded SLW), calculation of gas absorption coefficients are based on high-resolution HITRAN database [28], as spectrally resolved database for banded SLW (constants required to evaluate of  $g_w$  and  $g_c$  in Eq. (7)) from HITEMP is not available in the literature yet. Fortunately, spectral gas absorption coefficients calculated from HITRAN [28, 176] and HITEMP [30, 177] databases are found to be quite similar under FBC conditions (Figure 6.57). In all reference solutions, SLW is used in the presence of gray particles while banded SLW is used in the presence of non-gray particles. For SLW model, 10 gray gases for H<sub>2</sub>O and 10 gray gases for CO<sub>2</sub> are utilized. The SLW-1 spectral parameters are found by matching the gas mixture total emissivities calculated for 0.50 and 1.25 times of the freeboard height

---

<sup>11</sup> Spectral bands used in banded SLW models covers the same spectral ranges as in the banded spectral particle properties given in section 6.7.1.1.

with the same number of gray gases as in the SLW approach (10 x 10 gray gases are reduced to one absorbing and one transparent gray gas).

For non-gray particles, spectral complex index of refraction values are calculated by using Ebert's correlations (Section 4.4) by using the ash compositions given in Table 5.5. For gray particles, a composition dependent complex index of refraction model ( $m = 1.5 - k(\text{Fe})i$ ;  $\lambda = 3 \mu\text{m}$ ), which was shown to be much more accurate than the traditional approach ( $m = 1.5 - 0.02i$ ;  $\lambda = 3 \mu\text{m}$ ) is used (see Section 6.7.2 for details). Both gray and non-gray particle properties are demonstrated in Figure 6.66. It should be noted that all properties are calculated up to 20  $\mu\text{m}$  as it is considered to be sufficient enough for the majority of thermal radiation in coal fired systems. In all cases, scattering phase functions are represented by transport approximation (Section 4.3).

In MOL solution of DOM, a uniform grid structure of 9x9x67 and  $S_6$  angular quadrature scheme are employed based on the grid refinement study given in Section 6.8.2. For the difference relations of spatial derivatives, three-point upwind differencing scheme DSS014 is employed. All simulations are carried out on a workstation with Intel (R) Xeon (R) CPU E5-2643 3.40GHz processor having 264.00 GB of RAM. CPU times were recorded for an error tolerance of 0.01 throughout the analyses.

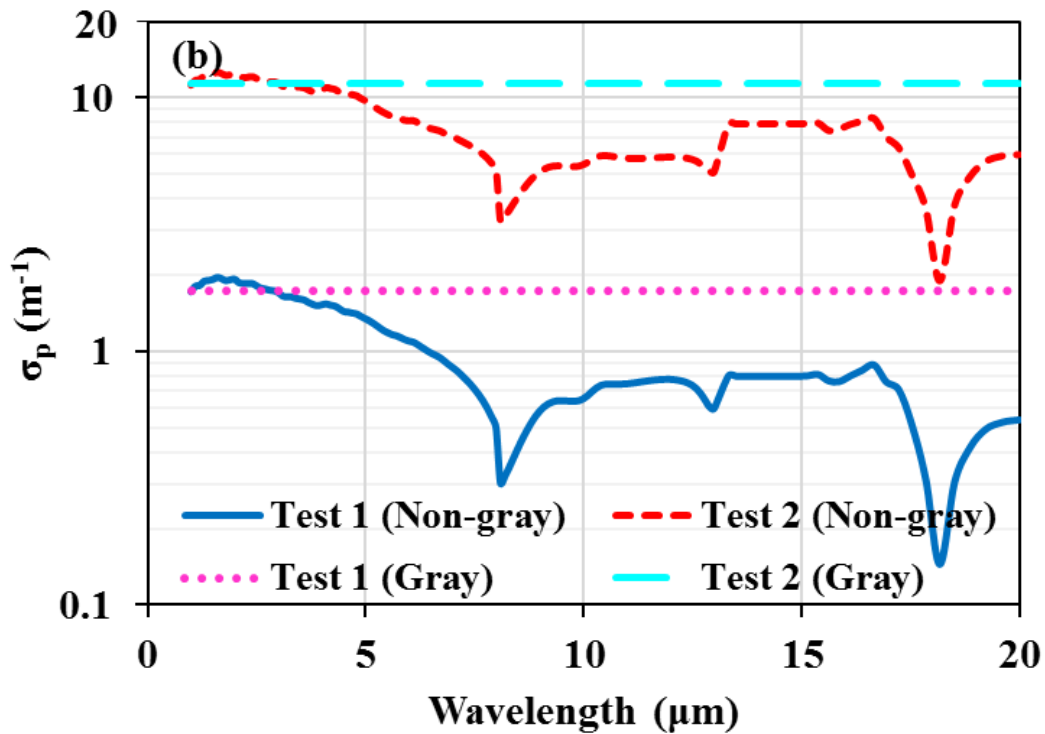
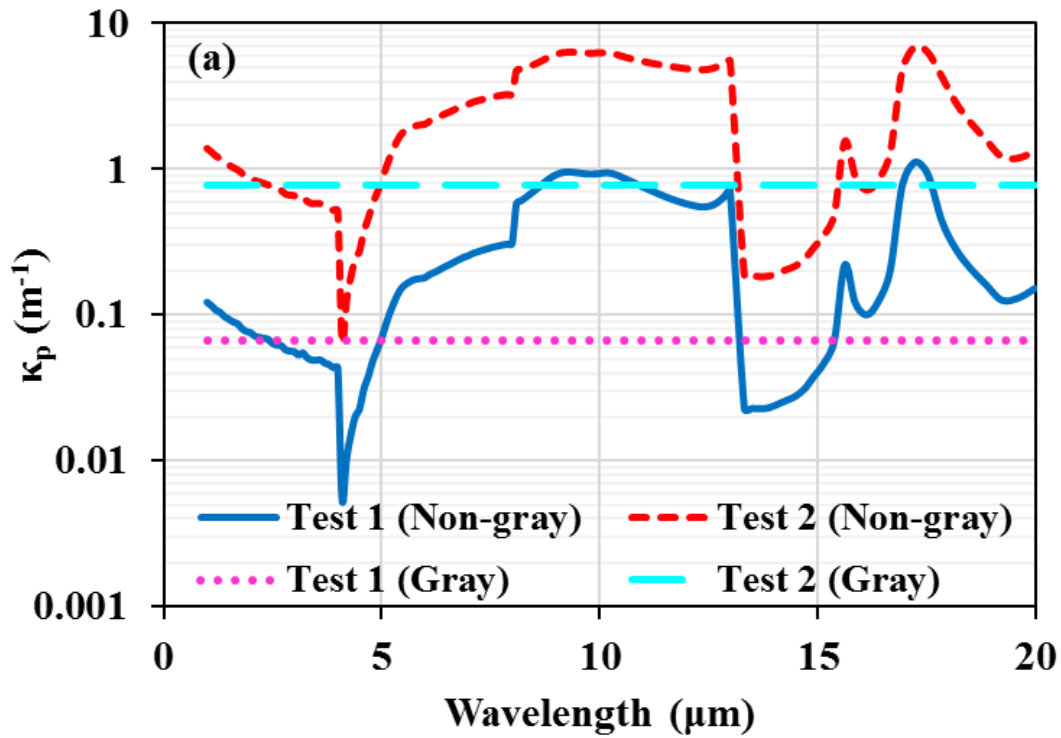


Figure 6.66 Non-gray (a) absorption coefficients, (b) scattering coefficients and (c) asymmetry factors for the polydisperse fly ash particles with their gray representations

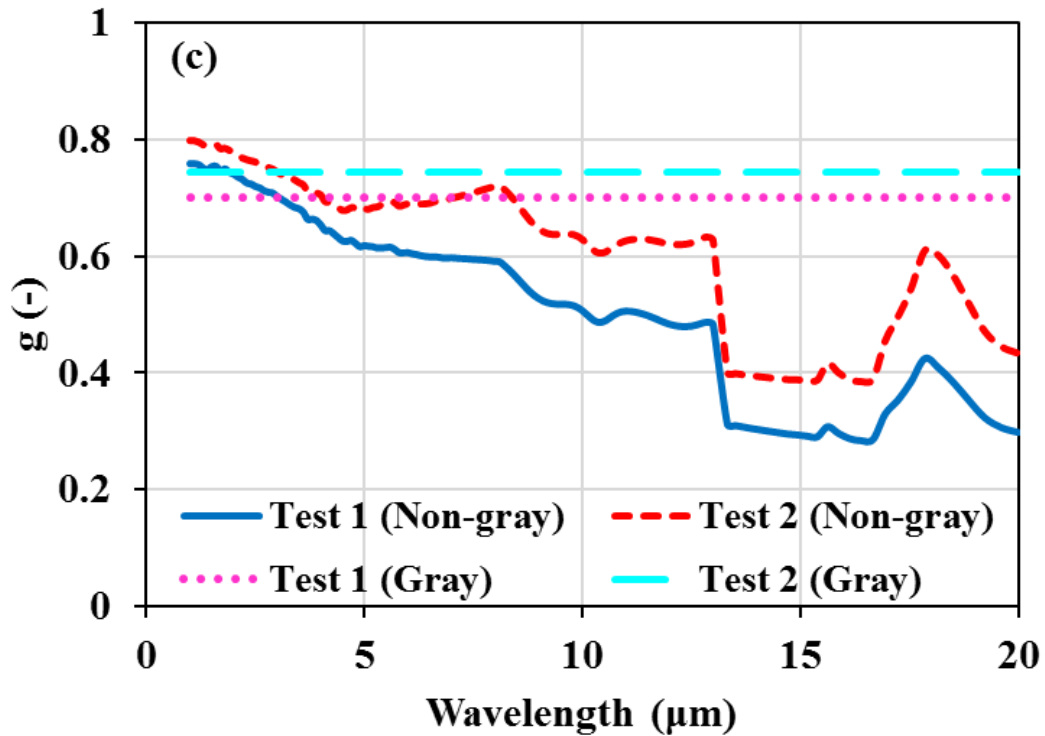


Figure 6.66 Non-gray (a) absorption coefficients, (b) scattering coefficients and (c) asymmetry factors for the polydisperse fly ash particles with their gray representations (cont'd)

### 6.10.1 Benchmarking the predictive accuracy of MOL solution of DOM with SLW-1

The predictive accuracy of the in-house developed radiation code based on the MOL solution of DOM with SLW-1 is first investigated on a benchmark problem. The physical system under consideration is a plane-parallel slab of thickness  $L = 1.0 \text{ m}$  containing an isothermal binary mixture of  $\text{H}_2\text{O}$  and  $\text{CO}_2$  at 1000 K with constant mole fractions of  $y_{\text{H}_2\text{O}}=0.2$  and  $y_{\text{CO}_2}=0.1$ . The walls are taken as black at 0 K. This problem was previously examined to validate SLW-1 [99]. In the present study, uniform grid structure of 100,  $S_4$  angular quadrature scheme and two-point upwind differencing scheme DSS012 is employed. The SLW-1 spectral parameters,  $\kappa_1$  and  $a_1$ , are evaluated by matching the gas

mixture total emissivities calculated for  $L_1 = 0.5L$  and  $L_2 = 1.25L$  by using  $25 \times 25$  gray gases as in the classical SLW approach presented in [99].

Comparisons between the total net heat flux and the total divergence of net heat flux predicted by the present study (MOL solution of DOM with SLW and MOL solution of DOM with SLW-1) and those of the previous work [99] are illustrated in Figure 6.67. As can be seen from the figure, predictions of MOL solution of DOM with SLW and MOL solution of DOM with SLW-1 are found to be in good agreement with the reference solutions [99]. The maximum and average absolute errors are illustrated in Table 6.36. As can be seen from the table, absolute percentage errors obtained by MOL solution of DOM with SLW and MOL solution of DOM with SLW-1 are of the same order of magnitude for both the total net heat flux and the total divergence of net heat flux predictions. In other words, predictions are found to be in good agreement with the benchmark solutions.



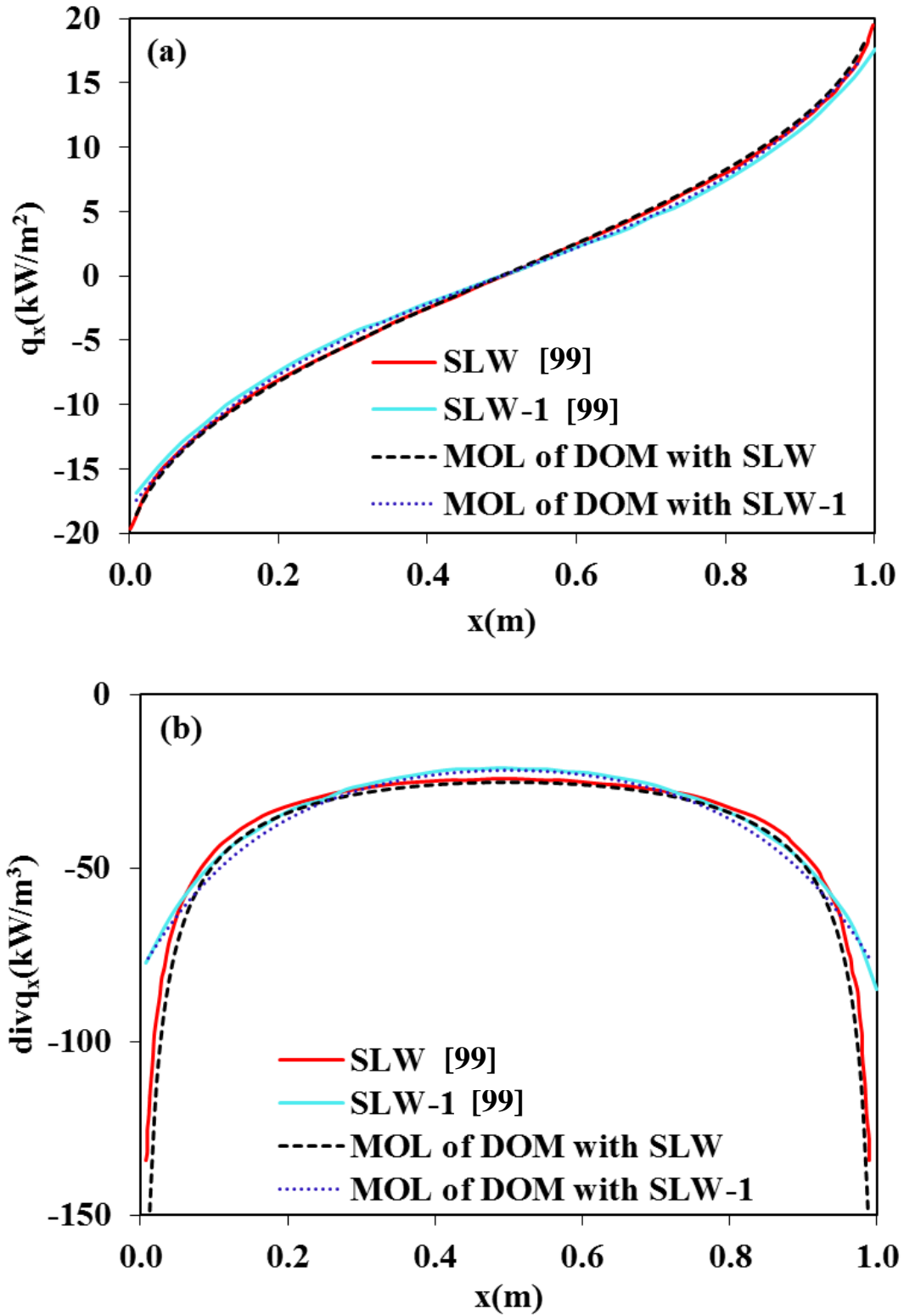


Figure 6.67 Comparison between (a) total net heat flux and (b) total divergence of the net heat flux predictions of the present study and reference solutions

Table 6.36 Maximum and average absolute percentage relative errors in total net heat flux ( $q_x$ ) and total divergence of the net heat flux ( $\text{div}q_x$ ) predictions

	SLW		SLW-1	
	$q_x$	$\text{div}q_x$	$q_x$	$\text{div}q_x$
<b>Max. Abs.% Rel. Error*</b>	2.97	5.84	4.80	6.60
<b>Av. Abs.% Rel. Error*</b>	1.67	3.91	3.04	4.24
*Absolute percentage error= $( \text{predicted}-\text{previous work}[99] /\text{previous work}[99])\times 100$				

### 6.10.2 Testing the Predictive Accuracy of SLW-1 in ABFBC Test Rig

Validating the in-house developed radiation code with SLW-1, predictive accuracy of SLW-1 approach is tested for the two coal combustion tests (Section 5.1.1) previously performed in ABFBC test rig. For that purpose, SLW-1 is tested by considering (i) only gas radiation, (ii) gas and gray particle radiation and (iii) gas and non-gray particle radiation. Details of these investigations are given in the following sub-sections.

#### 6.10.2.1 Testing the Predictive Accuracy of SLW-1 without Particles

In this section, predictive accuracy of gray gas and SLW-1 are compared by benchmarking their predictions against those of SLW by considering only gas radiation. Input data necessary for the radiation model (boundary conditions, temperature and concentration profiles, dimensions of the test rig) are taken from the two combustion tests presented in Section 5.1.1.

Figure 6.68 shows comparison between incident heat fluxes along the centerline of the wall predicted by MOL solution of DOM coupled with gray gas, SLW-1 and SLW for both tests. As can be seen from the figure, predictions of SLW-1 are in good agreement

with those of SLW for both tests while gray gas assumption leads to insignificant discrepancy.

Despite the fact that there is good agreement between the wall fluxes predicted by all models under consideration, it was considered necessary to investigate the source term predictions to be used in the solution of energy conservation equation in CFD codes. Figure 6.69 illustrates the comparison between the source term distributions along the centerline of the freeboard predicted by MOL solution of DOM with gray gas, SLW-1 and SLW for both tests. As can be seen from the figure, the predictions obtained from SLW-1 model are in good agreement with those of SLW for both tests. However, gray gas model leads to over-prediction of the source term distributions for both tests.

The absolute percentage error in the incident fluxes and source term predictions with corresponding CPU times for Test 1 and Test 2 are tabulated in Table 6.37. As can be seen from the table, absolute percentage errors in heat flux predictions are insignificant for both gray gas and SLW-1 approximations for all tests. However, absolute percentage errors in source terms obtained by gray gas models are an order of magnitude higher than those of SLW-1 with the same order of magnitude CPU times for both tests.

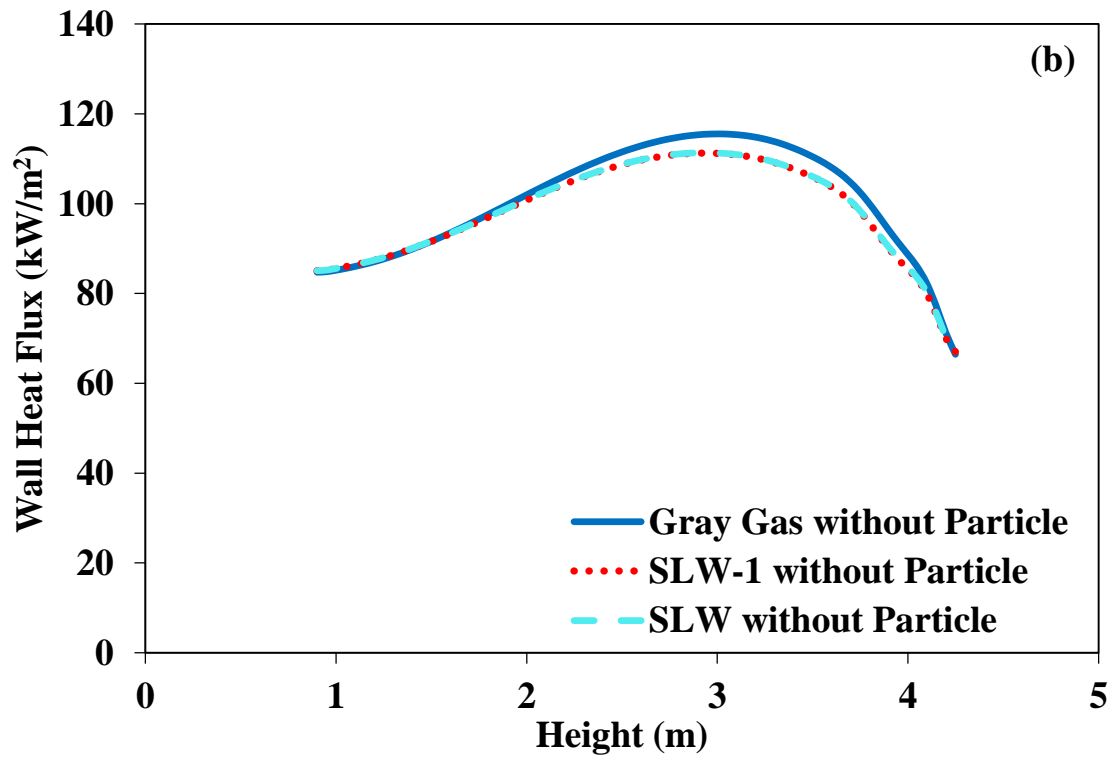
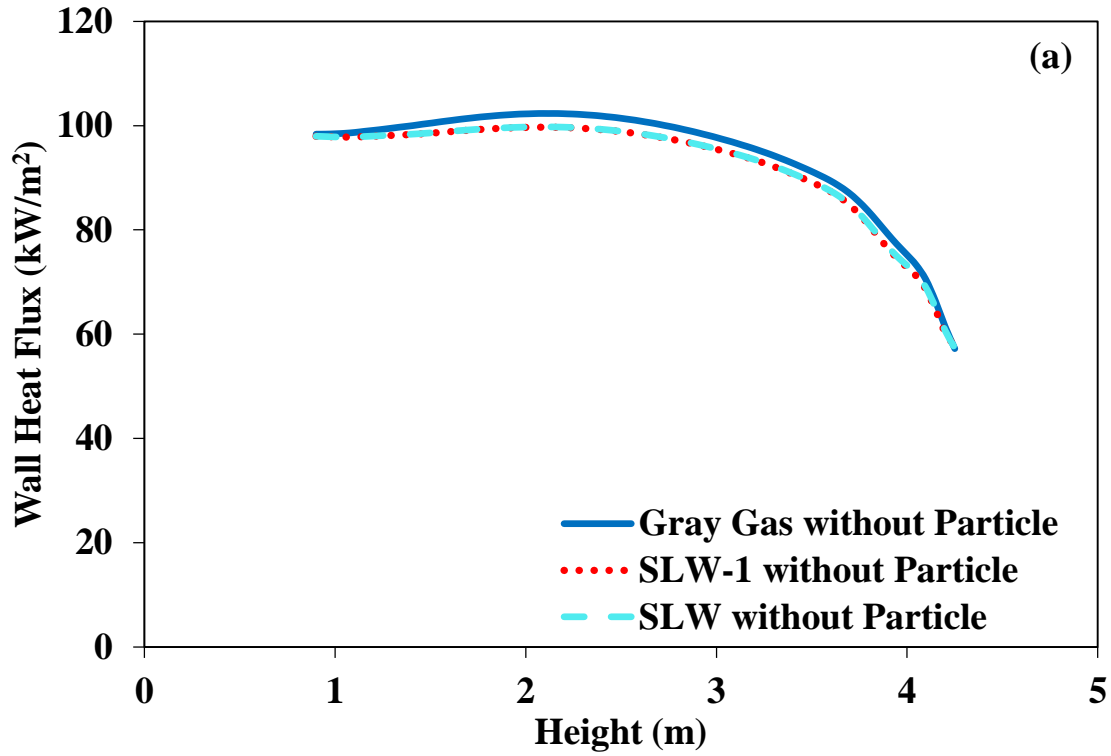


Figure 6.68 Effect of gray gas and SLW-1 models on incident radiative heat fluxes for (a) Test 1 and (b) Test 2

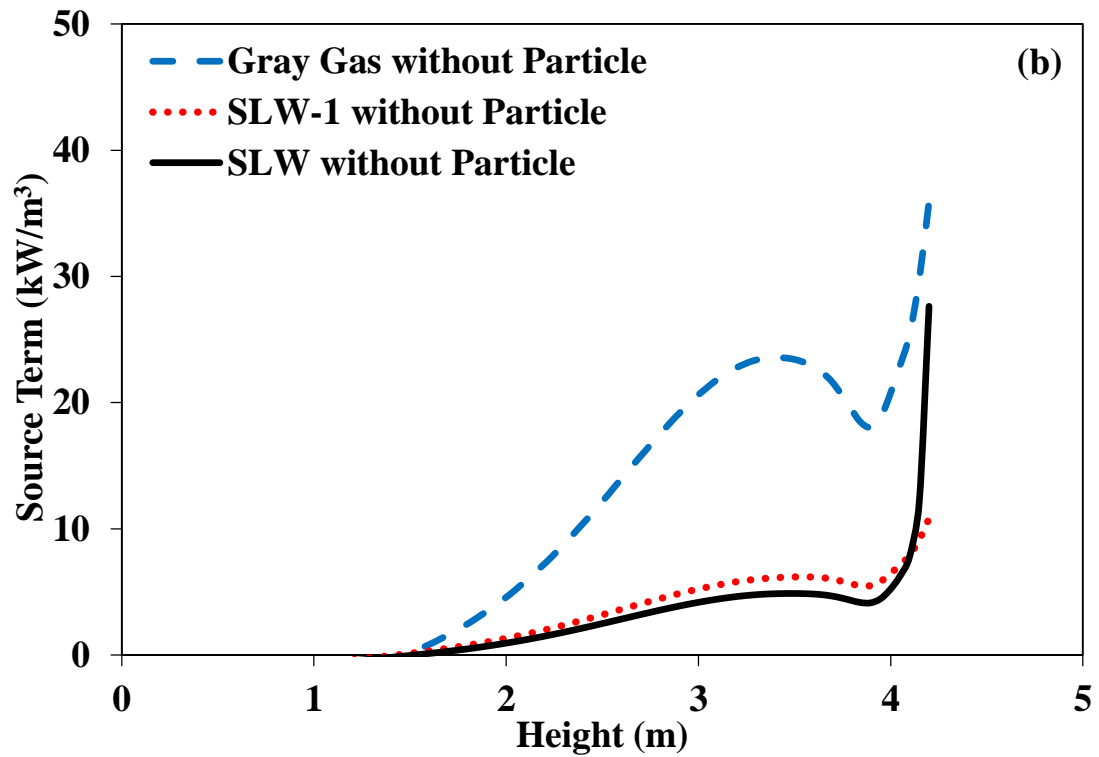
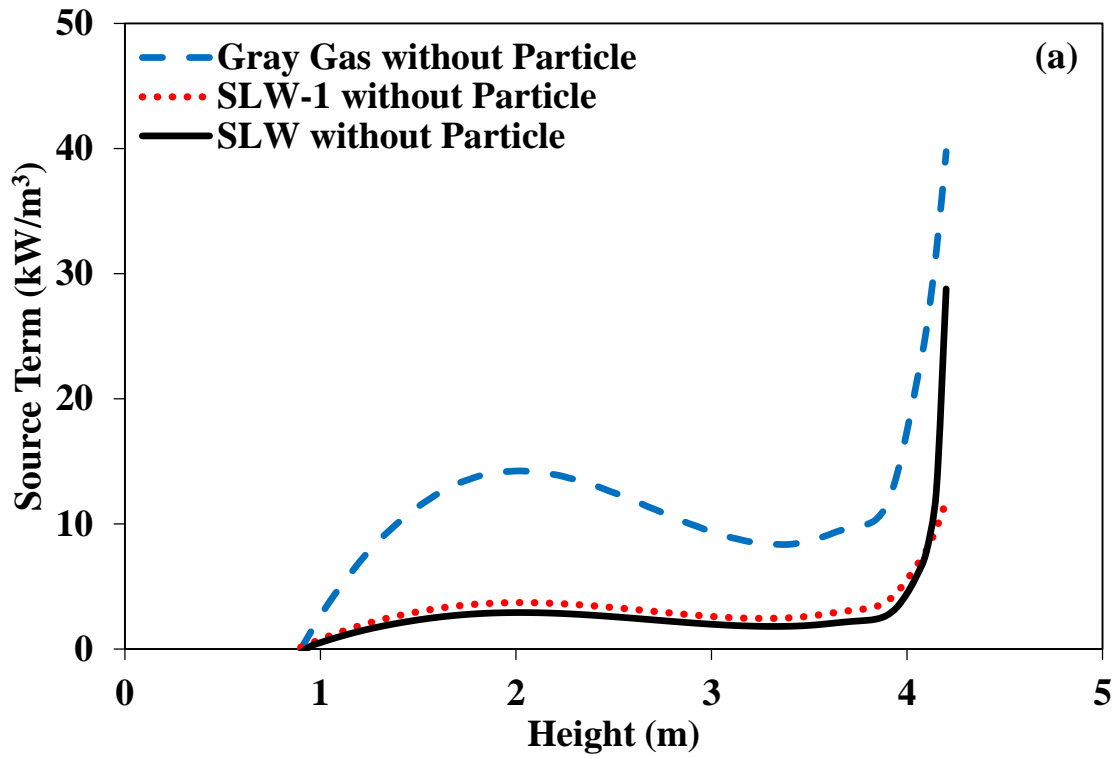


Figure 6.69 Effect of gray gas and SLW-1 models on source terms for (a) Test 1 and (b) Test 2

Table 6.37 Predictive accuracy and CPU efficiency of gas models

	Test 1			Test 2		
	Gray Gas	SLW-1	SLW	Gray Gas	SLW-1	SLW
<b>Abs.% Av. Error in heat fluxes**</b>	2.1	0.1	Reference	2.2	0.1	Reference
<b>Abs.% Av. Error in source term**</b>	294	24	Reference	318	23	Reference
<b>CPU Time (s)</b>	12	54	2995	12	52	3314
<b>CPU Ratio (-)</b>	0.00	0.02	1.00	0.00	0.02	1.00
**Errors are with respect to the predictions of the reference case, SLW model						

### 6.10.2.2 Testing the Predictive Accuracy of SLW-1 in the Presence of Gray Particles

In this section, accuracy and CPU efficiency of gray gas and SLW-1 models with gray particles are assessed for the two combustion tests described in Section 5.1.1 by benchmarking their predictions against those of SLW. Figure 6.70 demonstrates the heat flux distributions along the centerline of the wall obtained with different gas property models with gray particles for both Test 1 and Test 2. As can be seen from the figure, predictions with gray gas and SLW-1 are in good agreement with the measurements as well as the reference solution for both tests. Nevertheless, it should be noted that this agreement with the measurements as well as the reference solution is considered to be due to the dominant role of hot refractory-lined walls of the test rig surrounding the particle laden flue gas, as previously discussed in detail (See Section 6.7.2.5). Source term distributions along the centerline of the freeboard obtained with different gas property models with gray particles for both Test 1 and Test 2 are demonstrated in Figure 6.71. It is seen that predictions of SLW-1 are in good agreement with those of SLW whereas gray gas approximation results in over-prediction of the source terms for both tests.

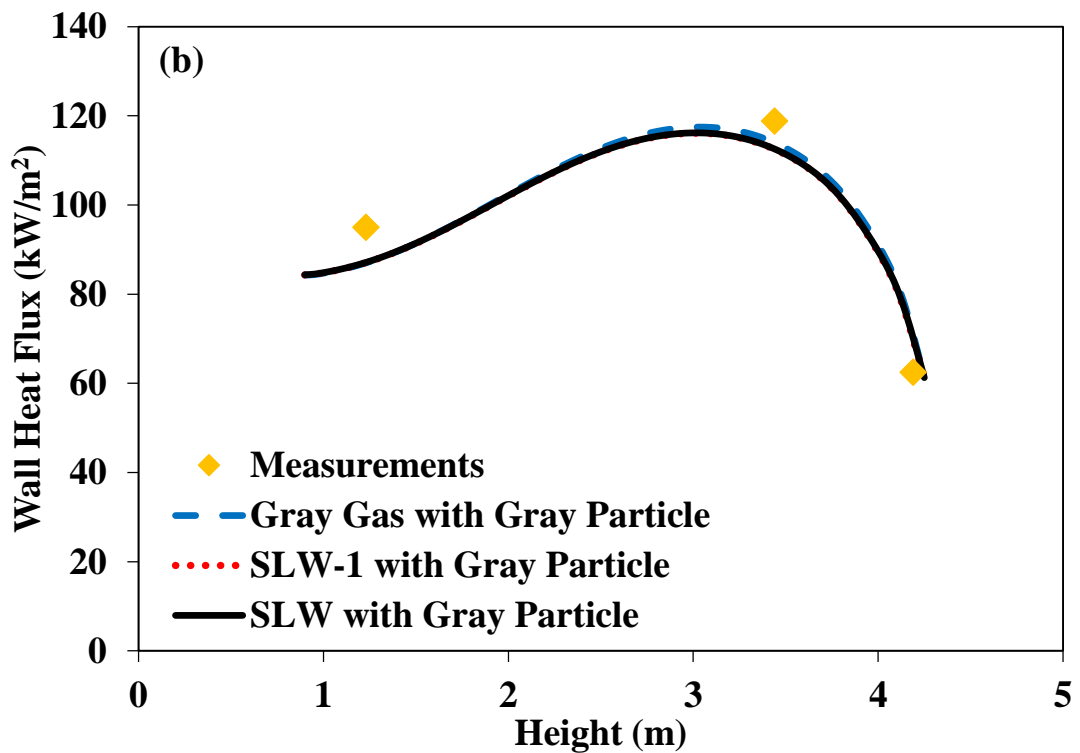
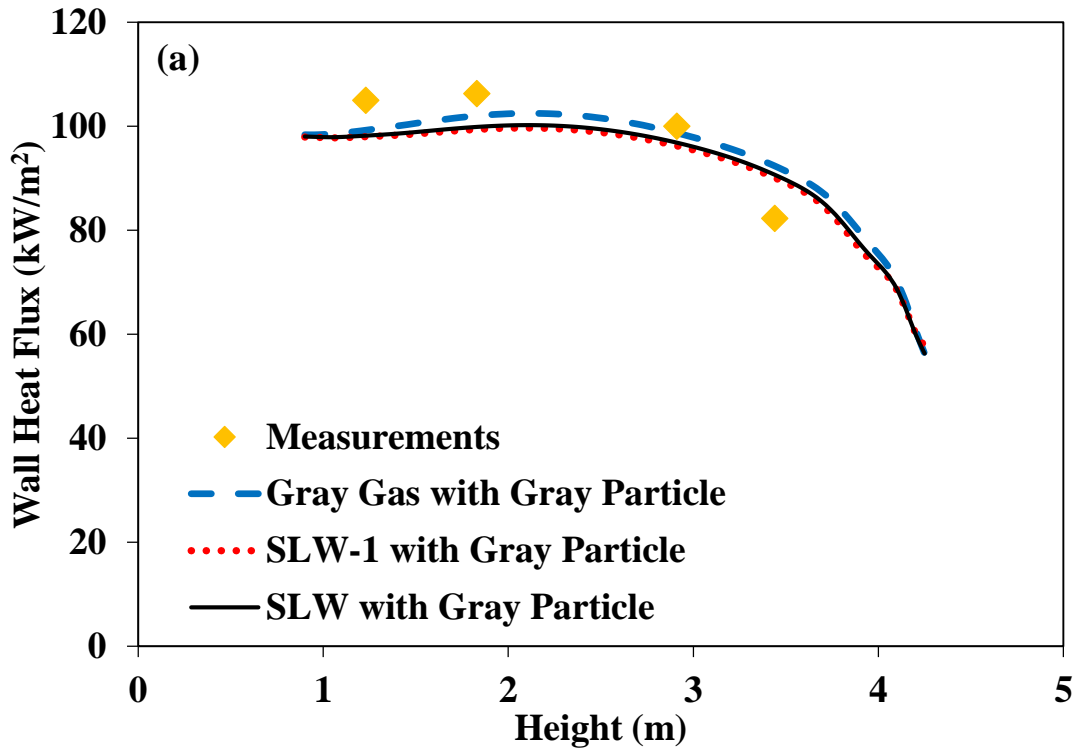


Figure 6.70 Comparisons between measurements and model predictions in the presence of gray particles for (a) Test 1 and (b) Test 2

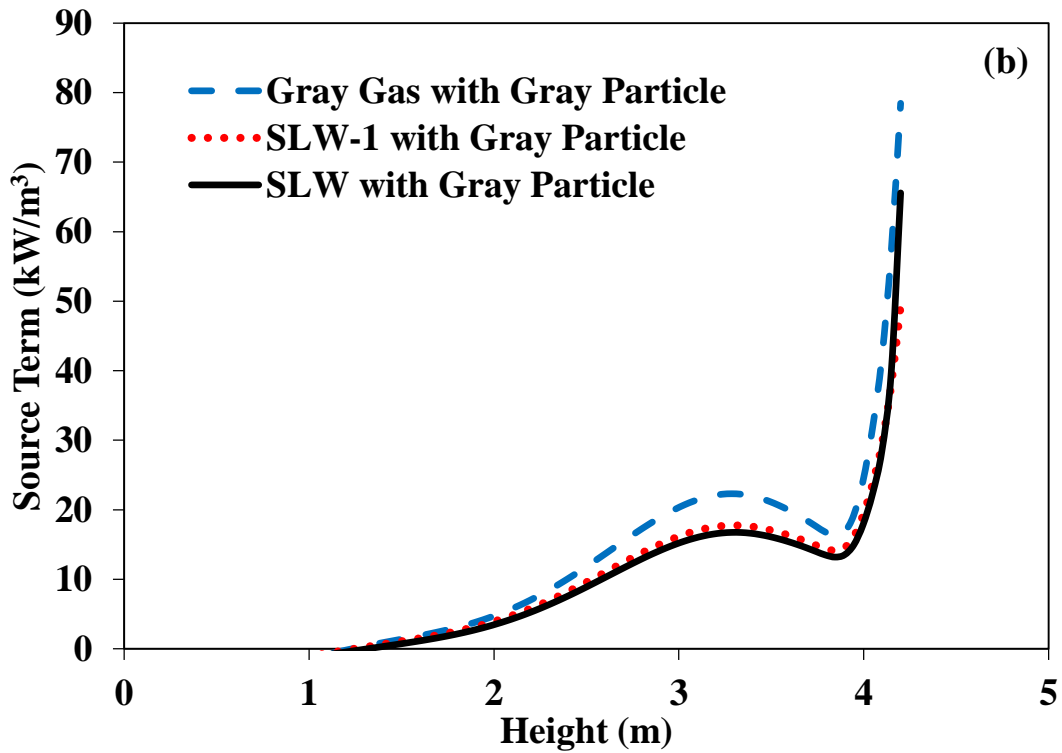
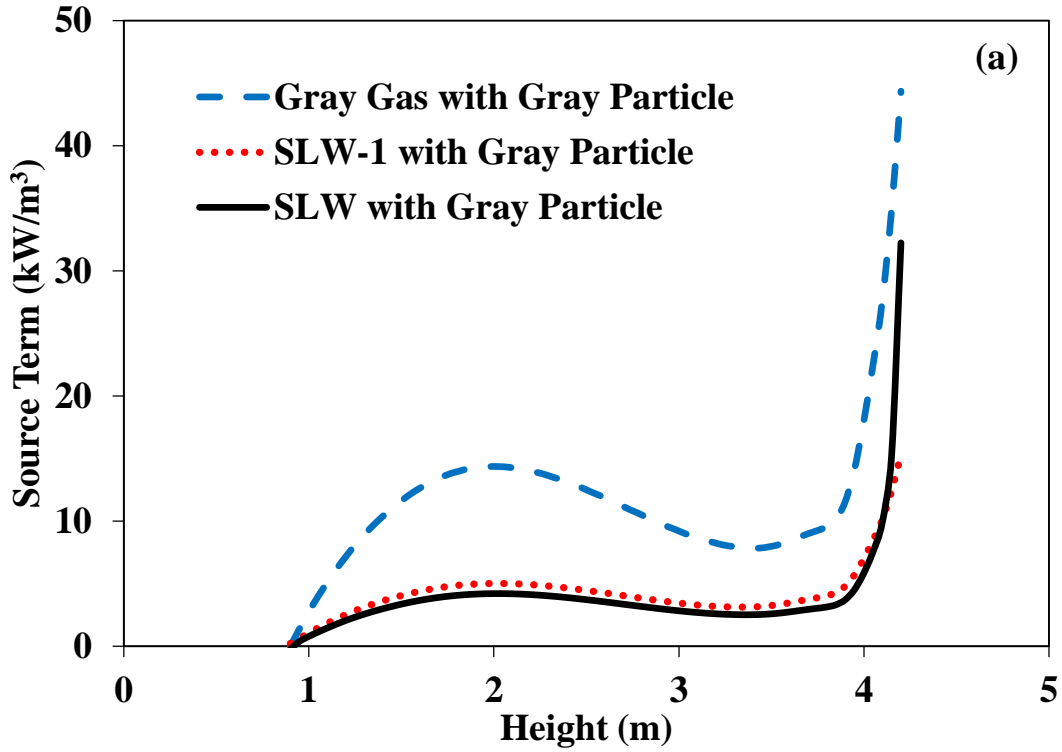


Figure 6.71 Comparison between source term predictions of gray gas, SLW-1, and SLW models in the presence of gray particles for (a) Test 1 and (b) Test 2



The percentage errors in incident heat fluxes and source term predictions with corresponding CPU times are given in Table 6.38. As can be seen from the table, heat flux predictions are in good agreement with each other. In source term predictions, however, accuracy of SLW-1 is found to be an order of magnitude higher than that of gray gas approximation with a similar CPU efficiency. Furthermore, it is seen that errors in source term predictions decrease significantly with increasing particle load from Test 1 to Test 2 for both gray gas and SLW-1 models. This decrease with increasing particle load is also evident when Table 6.37 and Table 6.38 are compared. It is found that with addition of particles, error in source term predictions decrease from 24 % to 18 % in Test 1 and from 23 % to 7 % in Test 2.

Table 6.38 Predictive accuracy and CPU efficiency of gas models in the presence of gray particles

	Test 1			Test 2		
	Gray Gas	SLW-1	SLW	Gray Gas	SLW-1	SLW
<b>Abs.% Av. Error in heat fluxes**</b>	1.9	0.5	Reference	0.7	0.1	Reference
<b>Abs.% Av. Error in source term**</b>	193	18	Reference	30	7	Reference
<b>CPU Time (s)</b>	8	41	3109	7	28	1687
<b>CPU Ratio (-)</b>	0.0002	0.0013	0.0953	0.0003	0.0013	0.0773
**Errors are with respect to the predictions of the reference case, SLW model						

### 6.10.2.3 Testing the Predictive Accuracy of Banded SLW-1 in the Presence of Non-Gray Particles

In this section, accuracy and CPU efficiency of gray gas and banded SLW-1 models are assessed in the presence of non-gray particles for the two tests described in Section 5.1.1 by benchmarking their predictions against those of banded SLW model. Banded SLW model includes 8 spectral bands (as in Section 6.8 where banded SLW model is introduced) and SLW-1 spectral parameters ( $\kappa_{j,1}$  and  $a_{j,1}$ ) are evaluated in each band of the banded SLW. In gray gas, SLW-1 and banded SLW models, non-gray particle absorption coefficient, scattering coefficient and asymmetry factor (Figure 6.66) are represented with eight wide bands based on the assessment study given in Section 6.7.1.

Figure 6.72 shows comparison between incident heat fluxes along the side wall predicted by MOL solution of DOM coupled with gray gas, banded SLW-1 and banded SLW models. As can be seen from the figure, predictions obtained from banded SLW-1 model are in good agreement with both measurements and the reference solution for both tests. Source term distributions along the centerline of the freeboard obtained with different gas property models in the presence of non-gray particles are given in Figure 6.73 for both Test 1 and Test 2. The predictions obtained from SLW-1 model are found to be in agreement with those of banded SLW whereas gray gas approximation leads to over-prediction of the source terms for both tests.

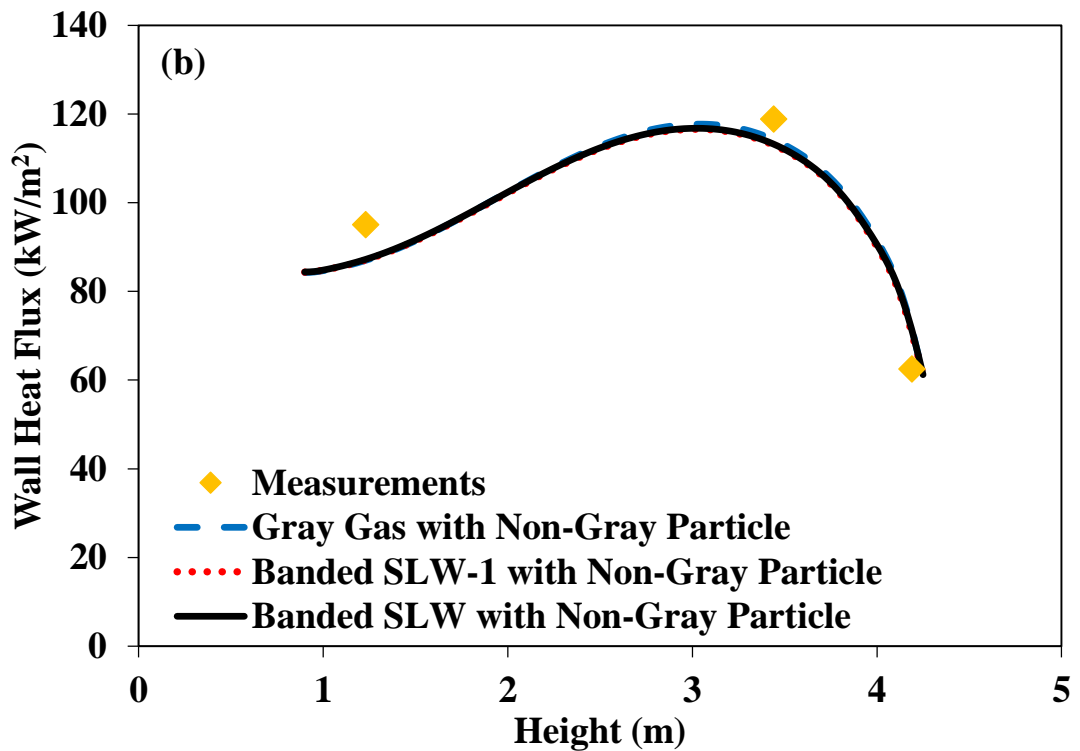
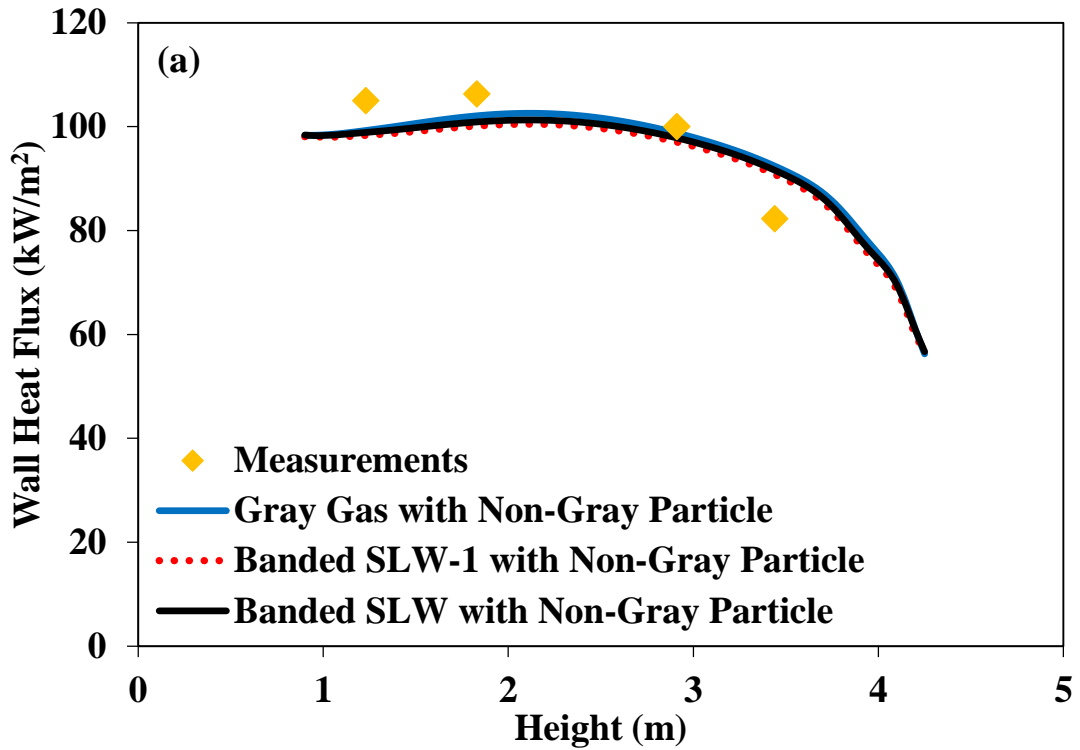


Figure 6.72 Comparisons between measurements and model predictions in the presence of non-gray particles for (a) Test 1 and (b) Test 2

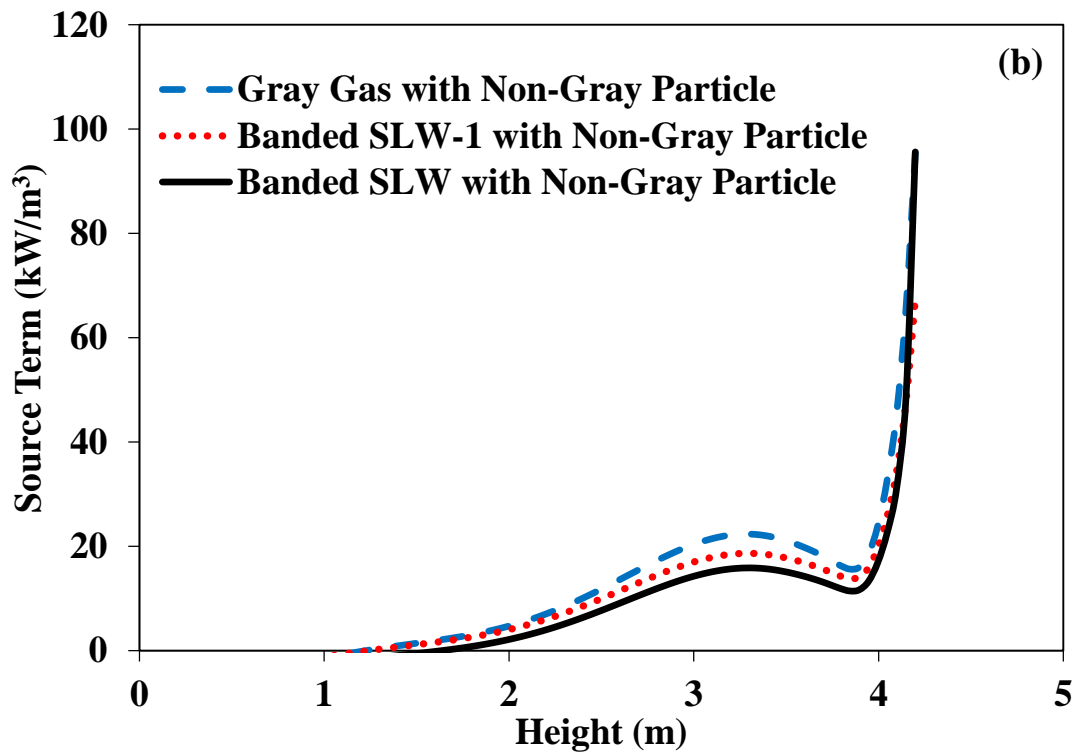
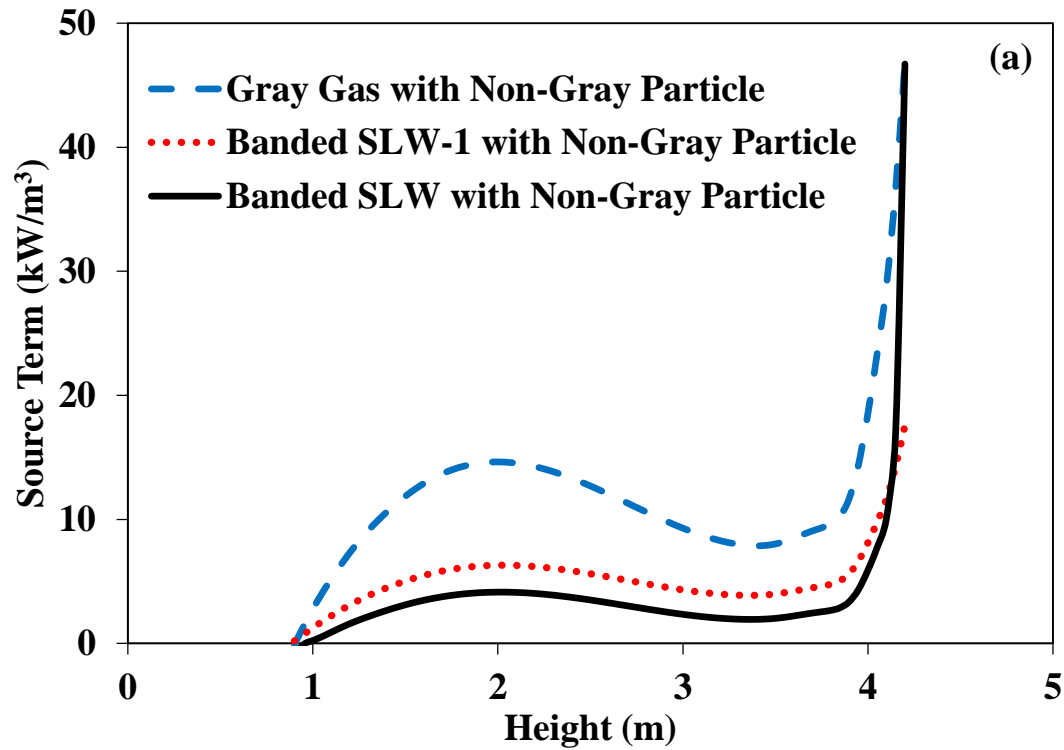


Figure 6.73 Comparison between source term predictions of gray gas, banded SLW-1, and banded SLW models in the presence of non-gray particles for (a) Test 1 and (b) Test 2

The percentage errors in incident heat fluxes and source term predictions with corresponding CPU times are illustrated in Table 6.39. As can be seen from the table, absolute percentage errors in heat fluxes predicted by different gas models are insignificant and of the same order of magnitude. In source term predictions, accuracy of banded SLW-1 is found to be an order of magnitude higher than that of gray gas approximation for Test 1 with a similar CPU efficiency. For Test 2, which has an order of magnitude higher particle load, predictive accuracy of banded SLW-1 is still better than that of gray gas approximation. Nevertheless, errors introduced by banded SLW-1 are found to be noticeably higher in the presence of non-gray particles (Table 6.39) compared to the cases with gray particles (see Table 6.38).

Table 6.39 Predictive accuracy and CPU efficiency of gas model in the presence of non-gray particles

	Test 1			Test 2		
	Gray Gas	Banded SLW-1	Banded SLW	Gray Gas	Banded SLW-1	Banded SLW
<b>Abs.% Av. Error in heat fluxes**</b>	1.0	0.8	Reference	0.5	0.3	Reference
<b>Abs.% Av. Error in source term**</b>	207	50	Reference	42	22	Reference
<b>CPU Time (s)</b>	246	291	32639	197	155	21829
<b>CPU Ratio (-)</b>	0.0075	0.0089	1.0000	0.0090	0.0071	1.0000
**Errors are with respect to the predictions of reference case, banded SLW model						

It should be noted that influence of banding SLW model to incorporate non-gray particle radiation on the predictive accuracy was presented in Section 6.8 (Figure 6.58), where it is shown that banded SLW causes about 2% error in source term predictions compared to SLW (Table 6.33). Therefore, it is considered that increased error in source term

predictions in banded SLW-1 approximation (from 18% to 50% in Test 1 and from 7% to 22% in Test 2) is not related to the banding approach itself.

In order to investigate the reasons behind the decrease in predictive accuracy of SLW-1 approximation in banded form, first predictive accuracy of the model is tested for each spectral band and results are displayed in Table 6.40. As can be seen from the table, errors in source term predictions are not uniform throughout the bands and they are highest for bands 3,4 and 8, in which peaks of the gas absorption coefficient are present (see Figure 6.57).

In banded SLW-1, number of gray gases is reduced by using two different path lengths and the recommended path lengths [98, 99] are used in band 1-8 in banded SLW-1 model (see Section 3.7). However, Table 6.40 reveals that different path lengths may be required as the optical thickness of the gas mixture changes from band to band. In order to test this hypothesis, calculations are repeated for band 4, which gives the largest errors for both Test 1 and Test 2, by using two different path lengths based on the geometric mean free path of the enclosure (“ $0.1xL_m = 3.8 \text{ cm}$ ” and “ $10xL_m = 380 \text{ cm}$ ”) instead of the recommended values (“ $0.50xL = 167.5 \text{ cm}$ ” and “ $1.25L = 418.8 \text{ cm}$ ”). Comparisons of the source terms predicted by banded SLW-1 with two sets of path lengths are illustrated in Figure 6.74 for Test 1. As can be seen from the figure, it is possible to decrease the errors in SLW-1 approximation by selecting a proper path length couple (i.e., path lengths for  $L_1$  and  $L_2$ , which are used to find gas mixture absorption coefficients; see also Section 3.7). Furthermore, gas optical thickness can be used as a guide while selecting these path lengths. Nevertheless, this would require an optimization procedure, which will be the subject of further investigations.

Table 6.40 Predictive accuracy of banded SLW-1 for each spectral band in the presence of non-gray particles

<b>Test 1</b>								
Wide spectral band widths ( $\mu\text{m}$ )	<b>Band 1</b>	<b>Band 2</b>	<b>Band 3</b>	<b>Band 4</b>	<b>Band 5</b>	<b>Band 6</b>	<b>Band 7</b>	<b>Band 8</b>
		1-2.4	2.4-3.1	3.1-4.1	4.1-4.8	4.8-6.3	6.3-8.9	8.9-12.1
<b>Abs.% Av. Error in heat fluxes**</b>	0.5	0.6	0.7	0.8	0.8	0.9	1.2	2.7
<b>Abs.% Av. Error in source term**</b>	30	53	2409	777	54	45	103	338
<b>Test 2</b>								
Wide spectral band widths ( $\mu\text{m}$ )	<b>Band 1</b>	<b>Band 2</b>	<b>Band 3</b>	<b>Band 4</b>	<b>Band 5</b>	<b>Band 6</b>	<b>Band 7</b>	<b>Band 8</b>
		1-2.4	2.4-3.1	3.1-4.1	4.1-4.8	4.8-6.3	6.3-8.9	8.9-12.1
<b>Abs.% Av. Error in heat fluxes**</b>	0.2	0.3	0.4	0.8	0.2	0.1	0.1	0.4
<b>Abs.% Av. Error in source term**</b>	14	24	145	492	25	28	42	156
**Errors are with respect to the predictions of reference case, banded SLW model								

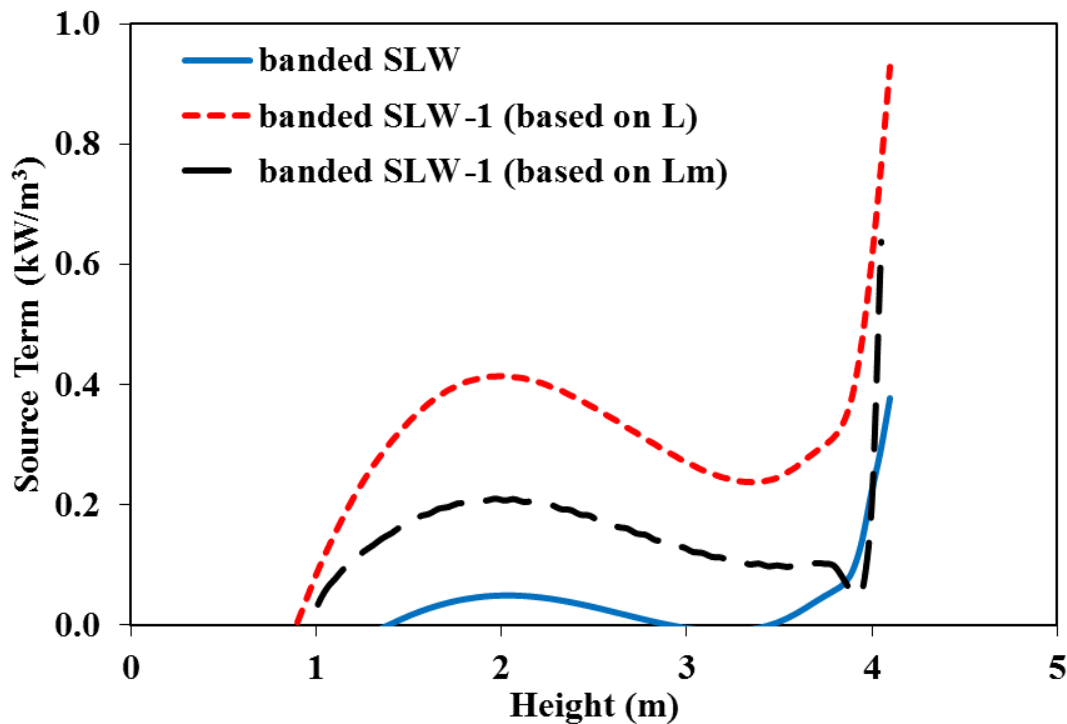


Figure 6.74 Comparison between source term predictions of banded SLW-1 approximations in the presence of non-gray particles for band 4

These results suggest that SLW-1 approach can be applied to multidimensional enclosures to decrease number of gray gases from hundreds to two gray gases. It provides reasonably good accuracy with a high CPU efficiency for particle laden flue gases in combusting systems. Furthermore, presence of gray particles within participating gas mixtures further increases the accuracy of SLW-1 model in heat flux and source term predictions for both low and moderate particle loads. In the presence of non-gray particles, however, errors in source term predictions are found to increase for banded SLW-1 approximation compared to those of gray particles. This is considered to be due to utilization of the same path lengths ( $L_1$ ,  $L_2$ ) for each spectral band of the banded SLW-1. Considering the fact that optical thickness of the medium varies significantly for these bands, a band-wise selection of path length is required if higher accuracy is needed.



## CHAPTER 7

### CONCLUSIONS

Radiation is the predominant mode of heat transfer in fluidized bed combustors (FBCs) due to the presence of high particle loads in the flue gas. Therefore, modelling of radiative heat transfer in such systems is of considerable importance and necessitates not only accurate but also computationally efficient methods for (i) solution of the radiative transfer equation (RTE) in conjunction with the time-dependent conservation equations for mass, momentum, energy, and chemical species and (ii) radiative property estimation of particle-laden combustion gases. Furthermore, sub-models used in estimating gas and particle radiative properties determine the computational cost of the global model as number of radiative intensity equations included in the solution of RTE is directly related to these property models. Therefore, ultimate objective of this study is to develop CPU efficient and accurate gas and particle radiative property models such that the outcome will provide guidelines when choosing radiation models for combustion related investigations. For that purpose, parameters determining spectral gas and particle properties and their influence on radiative heat transfer are quantified and compared in one comprehensive study for the conditions relevant to combustors, particularly FBCs. Major conclusions of these investigation are listed as follows:

- Phase function simplifications lead to significant error in heat flux and source term predictions. Therefore, anisotropic scattering behaviour of particle clouds must be taken into consideration while determining the radiative heat transfer in scattering media. This can be achieved by deploying either Henyey-

Greenstein Phase Function Approximation or Transport Approximation for the phase function. Furthermore, phase function simplifications do not improve CPU efficiency regardless of the optical thickness of the medium when RTE is solved spectrally.

- Geometric optics approximation (GOA) can be used instead of Mie Theory to increase the CPU economy of the particle models. However, there are some conditions that must be satisfied: (i) Angular dependency of the reflectivity must be included in the calculations (ii) Dependency of reflectivity on absorption index ( $k$ ) becomes significant if  $k$  is large (iii) Applicability of GOA should be based on cumulative cross sectional area distribution rather than surface mean diameter or cumulative weight percent distribution of particles if particle size distribution (PSD) involves both fine and coarse particles.
- Using a surface mean diameter ( $d_{32}$ ) to represent PSD in modelling radiative heat transfer may lead to considerable errors depending on the cumulative cross sectional area constituted by fine particles.
- Changing the fuel type affects the radiative properties of the particles in the freeboard through the change of particle size distribution rather than optical properties under FBC conditions. Nevertheless, change in PSD is found to lead to significant variations in both wall heat fluxes and source terms along the combustor.
- In-situ desulfurization with limestone addition is an important advantage of FBCs. Nevertheless, limestone addition increases the amount of fine particles within the combustor, which leads to a thicker radiation shield between the hot particle-laden flue gas and the walls hence decreases the radiative wall heat fluxes along the freeboard.
- Particle load is a very important input parameter for particle radiative properties. Simplifying particle load distribution via deploying 0D and 1D approximations leads to significantly large errors under CFBC conditions. Therefore, rigorous evaluation of particle load distribution is essential for accurate prediction of radiative heat transfer in CFBCs despite its high CPU requirements.

- Spectral particle radiation is of significant importance for accurate calculation of radiative heat transfer in combusting systems even at low particle loads as in the case of PC-fired furnaces.
- Spectrally banded solution of RTE can be achieved by deploying wide spectral bands in thermal radiation spectrum. This approach is shown to provide high accuracy and CPU efficiency in radiative heat transfer predictions.
- Spectral nature of particle properties mainly originates from the spectral nature of the complex index of refraction. Hence keeping only the wavelength as a spectral variable is not sufficient to represent non-gray behavior of particles. It gives almost identical results compared to that of gray particles. Therefore, both complex index of refraction and wavelength must be kept as spectrally dependent variables to consider a particle to be “non-gray”.
- Spectral complex index of refraction (RI) of ash particles is a strong function of chemical composition. Based on the comparisons presented in this study, Ebert’s approach is recommended for calculation of spectral RI of ash particles as it requires less input parameters and covers a wider range of chemical compositions.
- Both traditional gray particle assumption ( $m = 1.5 - 0.02i$ ,  $\lambda = 3 \mu\text{m}$ ) and Planck mean averaging of spectral properties lead to significant errors in heat flux and source term predictions. Therefore, these approaches should be avoided in radiative property calculations.
- Gray particle assumption leads to under-estimation of gas radiation share within the combustors. This is why particle radiation can be found to dominate total radiation if particles are assumed to be gray, although it may not always be the case. Strong gas and particle absorption bands appear at different locations in thermal radiation spectrum (1-20  $\mu\text{m}$ ). Thus, accurate gas property models are needed to represent the spectral behavior of combustion gases even at high particle loads. The only exception may be the case where char burnout is expected to be incomplete.
- Global SLW model has been converted to the banded SLW model to incorporate non-gray particle radiation in the solution of spectral RTE. It can

be considered as an accurate and CPU efficient model to be used in the presence of non-gray particles. In other words, banded SLW model can alleviate the need for narrow band models requiring excessive CPU time to evaluate spectral particle radiation.

- CPU efficiency of SLW model and its banded form (banded SLW) can be increased by reducing the number of gray gases via deploying SLW-1 approach. This approach has been shown to lead to fairly accurate results in the presence of gray particles, where the predicative accuracy of SLW-1 approach increases with increasing particle load. Nevertheless, banded SLW-1 approach leads to significant errors in source term predictions in the presence of non-gray particles. Therefore, banded SLW model should be preferred in the presence of non-gray particles despite its higher CPU requirements.

## **7.1 Suggestions for Future Work**

Present study focuses on the influence of gas and particle radiative property models on radiative heat exchange in combusting systems. Based on the above mentioned outcomes of the study, following recommendations are suggested for the future extension of the current work:

- Investigations presented in this study only focuses on radiative heat transfer with assumption that all temperature and concentration profiles are known prior to calculations. This was achieved by relying on experimental measurements. In the next step, radiative property models selected in this study can be implemented into CFD codes in order to investigate the influence of radiative property methods on temperature, concentration and total energy distribution profiles within the combustor during the simultaneous solution of the conservation equations for energy and chemical species in conjunction with radiative transfer equation.
- GWB approximation is found to be accurate if particle load is moderate and absorption coefficient of the particle cloud is high. This is why banded SLW becomes the other alternative for low particle loads and/or for particle clouds

with low absorption coefficients. Computational burden of banded SLW can be decreased by deploying SLW-1 approach at the expense accuracy. This can be alleviated by an optimization algorithm, which can select the SLW-1 path lengths for each band separately so that gas mixture absorption coefficient can be found more accurately. As an alternative, particle property calculation can be merged into SLW model as a third specie. In that case, particle absorption and scattering efficiencies can be treated as gas absorption cross sections so that they can be ordered into several “gray gases”.

- All radiation models are solved with uniform grid structure in spatial coordinates. Non-uniform grid structures can be tested to further improve the CPU efficiency, especially for the cases where temperature and/or particle load distribution is non-uniform.
- All combustion tests investigated in this study involve low quality Turkish lignites, which was experimentally shown to burn rapidly with almost no carbon residue. Current investigations can be extended for high quality fuels, in which coal and/or char radiation as well as the effect of char burnout on particle properties and/or temperatures are needed to be taken into consideration.



## CHAPTER 8

### REFERENCES

- [1] World Energy Outlook 2016, International Energy Agency, Paris, France (2017).
- [2] 2015 Kömür (Linyit) Sektör Raporu, Türkiye Kömür İşletmeleri Kurumu, T.C. Enerji ve Tabii Kaynaklar Bakanlığı (2016).
- [3] A. Batu, “Investigation of Combustion Characteristics of Indigenous Lignite In a 150 kWt Circulating Fluidized Bed Combustor”, *Ph.D Thesis*, Middle East Technical University, Ankara, Turkey (2008).
- [4] H. Harmandar, “Effect of Recycling on the Performance of Bubbling Fluidized Bed Combustors”, *M.S. Thesis*, Middle East Technical University, Ankara, Turkey (2003).
- [5] E. Ferrer, M. Aho, J. Silvennoinen, R.V. Nurminen, “Fluidized bed combustion of refuse-derived fuel in presence of protective coal ash”, *Fuel Process. Technol.* 87 (2005) 33–44.
- [6] M. Aho, E. Ferrer, “Importance of coal ash composition in protecting the boiler against chlorine deposition during combustion of chlorine-rich biomass”, *Fuel*, 84 (2005) 201–212.
- [7] P. Yrjas, B.J. Skrifvars, H. M. Hupa, J. Roppo, M. Nylund, P. Vainikka, “Chlorine in deposits during co-firing biomass, peat and coal in a full scale CFBC boiler”, In: *Proceedings of 18th International Conference on Fluidized Bed Combustion, ASME*, Paper No. FBC05-097 (2005).

- [8] Z. Göğebakan, “Co-Firing Biomass with Coal in Bubbling Fluidized Bed Combustors”, *Ph.D Thesis*, Middle East Technical University, Ankara, Turkey (2007).
- [9] P. Basu, “Combustion and Gasification in Fluidized Beds”, CRC Press (2006).
- [10] Y. Hua, G. Flamant, J. Lu, D. Gauthier, “3D modelling of radiative heat transfer in circulating fluidized bed combustors: influence of the particulate composition”, *International Journal of Heat and Mass Transfer* 48 (2005)1145–1154.
- [11] H. M. Abdelmotalib, M.A.M. Youssef, A.A Hassan, S.B. Youn, I. Im, “Heat transfer process in gas–solid fluidized bed combustors: A review”, *International Journal of Heat and Mass Transfer* 89 (2015)567–575.
- [12] S.S. Khavidak, D. Pallarès, F. Normann, F. Johnsson, V.Y. Outinen, “Heat transfer in a 4–MWth circulating fluidized bed furnace operated under oxy-fired and air-fired conditions: Modeling and measurements”, *International Journal of Greenhouse Gas Control* 37 (2015) 264–273.
- [13] M. Kozan, N. Selçuk, “Investigation of radiative heat transfer in freeboard of a 0.3 MWt FBC test rig”, *Comb. Sci. Tech.*, 153 (2000) 113.
- [14] N. Selçuk, A. Batu, I. Ayranci, “Performance of method of lines solution of discrete ordinates method in the freeboard of a bubbling fluidized bed combustor” *J. Quant. Spectrosc. Radiat. Transfer*, 73 (2002) 503.
- [15] N. Selçuk, G. Kirbas, “The method of lines solution of discrete ordinates method for radiative heat transfer in enclosures” *Num. Heat Transfer Part B*, 37 (2000) 379.
- [16] G. Demirkaya, F. Arinç, N. Selçuk and I. Ayranci, “Comparison between Performances of Monte Carlo Method and Method of Lines Solution of Discrete Ordinates Method”, Proceedings of Fourth International Symposium on Radiative Transfer (RAD-04)”, Turkey, June 20-25, (2004) 97-105.
- [17] I. Ayranci, N. Selçuk, “MOL solution of DOM for transient radiative transfer in 3-D scattering media”, *J. Quant. Spectrosc. Radiat. Transfer*, 84, 4(2004) 409-422.
- [18] N. Selçuk, I. Ayranci, “The Method of Lines Solution of Discrete Ordinates Method for Radiative Heat Transfer in Enclosures Containing Scattering Media”, *Num. Heat Transfer Part B*, 43 (2003) 179-201.



- [19] I. Ayrancı and N. Selçuk, “Effect of Spatial Differencing Schemes on the Performance of MOL Solution of DOM in anisotropically scattering medium”, Proceedings of 12<sup>th</sup> International Heat Transfer Conference (in CD-ROM), Grenoble, France, August 18-23, Ed. Jean Taine (2002) 639-644.
- [20] S. Harmandar and N. Selçuk, “The method of lines solution of discrete ordinates method for radiative heat transfer in cylindrical enclosures”, *J. Quant. Spectrosc. Radiat. Transfer*, 84, 4 (2004) 395-407.
- [21] M. F. Modest, “The Treatment of Nongray Properties in Radiative Heat Transfer: From Past to Present”, *Journal of Heat Transfer* 135 (2013) 061801-1-12.
- [22] R. M. Goody and Y. L. Yung, *Atmospheric Radiation*, Clarendon Press, Oxford, UK, 1989.
- [23] A. A. Lacis and V. Oinas, “A Description of the Correlated-k Distribution Method for Modeling Nongray Gaseous Absorption, Thermal Emission, and Multiple Scattering in Vertically Inhomogeneous Atmospheres”, *J. Geophys. Res.* 96 (1991) 9027–9063.
- [24] V. Goutière , A. Charette and L. Kiss, “Comparative Performance of Nongray Gas Modeling Techniques”, *Numerical Heat Transfer, Part B: Fundamentals*, 41:3-4 (2010) 361-381.
- [25] P. J. Coelho, P. Perez and M. El Hafı, “Benchmark Numerical Solutions for Radiative Heat Transfer in Two-Dimensional Axisymmetric Enclosures with Nongray Sooting Media”, *Numerical Heat Transfer, Part B: Fundamentals*, 43:5 (2003) 425-444.
- [26] H. C. Hottel and A. F. Sarofim, *Radiative Transfer*, McGraw-Hill, New York, 1967.
- [27] M. K. Denison and B. W. Webb, “An Absorption-Line Blackbody Distribution Function for Efficient Calculation of Gas Radiative Transfer”, *J. Quant. Spectrosc. Radiat. Transfer*, 50 (1993) 499–510.
- [28] M. K. Denison, “A Spectral Line-based Weighted-sum-of-gray-gases Model for Arbitrary RTE Solvers”, *Ph.D. thesis*, Brigham Young University, Provo, UT, 1994.

- [29] M. K. Denison and B. W. Webb, “The Spectral Line-Based Weighted-Sum-of-Gray-Gases Model for H<sub>2</sub>O-CO<sub>2</sub> Mixtures”, *ASME J. Heat Transfer*, 117 (1995) 788–792.
- [30] J. Pearson, B.W. Webb, V.P. Solovjov, J. Ma, “Updated Correlation of the Absorption Line Blackbody Distribution Function for H<sub>2</sub>O Based On The HITEMP2010 Database”, *J. Quant. Spectr. Rad. Transfer*, 128 (2013) 10-17.
- [31] F. N. Çayan and N. Selçuk, “A Comparative Study of Modeling of Radiative Heat Transfer using MOL Solution of DOM with Gray Gas, Wide-Band Correlated-k, and Spectral Line-Based Weighted Sum of Gray Gases Models”, *Numerical Heat Transfer, Part B: Fundamentals*, 52:3 (2007) 281-296.
- [32] R. Demarco, J.L. Consalvi, A. Fuentes, S. Melis, “Assessment of Radiative Property Models in Non-Gray Sooting Media”, *International Journal of Thermal Sciences*, 50 (2011) 1672-1684.
- [33] P.D. Nguen, A. Danda, M. Embouazza, M. Gazdallah, P. Evrards, V. Feldheim, “Application of the Spectral Line-Based Weighted-Sum-Of-Gray-Gases Model (SLWSGG) to the Calculation of Radiative Heat Transfer in Steel Reheating Furnaces Firing on Low Heating Value Gases”, *Journal of Physics: Conference Series*, 369 012008 (2012) 1-10.
- [34] G. Ozen and N. Selçuk, “SLW Model for Computational Fluid Dynamics Modeling of Combustion Systems: Implementation and Validation”, *Numerical Heat Transfer, Part B: Fundamentals*, 70:1 (2016) 47-55.
- [35] B. Garten, F. Hunger, D. Messig, B. Stelzner, D. Trimis, C. Hasse, “Detailed Radiation Modeling of a Particle-Oxidation Flame”, *Int. J. Therm. Sci.*, 87 (2015) 68-84.
- [36] D.G. Goodwin, “Infrared Optical Constants of Coal Slags”, *PhD Thesis*, Stanford University, Stanford, USA, 1986.
- [37] M. F. Modest, *Radiative Heat Transfer*. Third edition. Academic Press, New York, 2013.
- [38] M. P. Mengüç, R. Viskanta, “Effect of Fly-Ash Particles on Spectral and Total Radiation Blockage”, *Combust. Sci. and Tech.*, 60 (1988) 97-115.

- [39] D.G. Goodwin, M. Mitchner, “Flyash radiative properties and effects on radiative heat transfer in coal-fired systems” *Int. J. Heat Mass Transfer*, 32 (1989) 627–638.
- [40] M. P. Mengüç, S. Subramaniam “Radiative Transfer through an Inhomogeneous Fly-Ash Cloud: Effects of Temperature and Wavelength Dependent Optical Properties”, *Numer. Heat. Tr. A-Appl*, 21:3 (1992) 261-273.
- [41] S.P. Bhattacharya, “A theoretical investigation of the influence of optical constants and particle size on the radiative properties and heat transfer involving ash clouds and deposits”, *Chem. Eng. Process.*, 39 (2000) 471–483.
- [42] C. Caliot, V. Eymet, M. El Hafi, Y. Le Maout, G. Flamant, “Parametric study of radiative heat transfer in participating gas–solid flows”, *Int. J. Therm. Sci.*, 47 (2008) 1413–1421.
- [43] F. Liu, J. Swithenbank, “The effects of particle size distribution and refractive index on fly-ash radiative properties using a simplified approach”, *Int. J. Heat Mass Transfer*, 36 (1993) 1905–1912.
- [44] J.G. Marakis, C. Papapavlou, E. Kakaras, “A Parametric Study of Radiative Heat Transfer in Pulverised Coal Furnaces” *Int. J. Heat Mass Transfer*, 43(16) (2000) 2961–2971.
- [45] M. Bahador, B. Sunden, “Investigation on the effects of fly ash particles on the thermal radiation in biomass fired boilers”, *Int. J. Heat Mass Transfer*, 51 (2008) 2411–2417.
- [46] B. W. Butler, M. K. Denison, B. W. Webb, “Radiation Heat Transfer in a Laboratory-Scale, Pulverized Coal-Fired Reactor”, *Exp. Therm. Fluid. Sci.*, 9 (1994) 69-79.
- [47] D. Mischler, A. Steinfeld, “Nonisothermal Nongray Absorbing-Emitting-Scattering Suspension of  $\text{Fe}_3\text{O}_4$  Particles Under Concentrated Solar Irradiation”, *J. Heat Transf.*, 117 (1995) 346-254.
- [48] L.M. Ruan, H.P. Tan, Y.Y. Yan, “A Monte Carlo (Mc) Method Applied to the Medium with Nongray Absorbing-Emitting-Anisotropic Scattering Particles and Gray Approximation” *Numer. Heat. Tr. A-Appl*, 42 (2002) 253– 268.

- [49] H. Hofgren, B. Sunden, "Evaluation of Planck mean coefficients for particle radiative properties in combustion environments", *Heat Mass Transfer*, 51 (2015) 507–519.
- [50] R. Johansson, B. Leckner, K. Andersson, F. Johnsson, "Influence of particle and gas radiation in oxy-fuel combustion", *Int. J. Heat Mass Transfer*, 65 (2013) 143–152.
- [51] J. Pallarés, A. Gil, C. Cortés, C. Herce, "Numerical study of co-firing coal and *Cynara cardunculus* in a 350 MWe utility boiler", *Fuel Processing Technology*, 90 (2009) 1207–1213.
- [52] T. Kangwanpongpan, R. C. Silva, H. J. Krautz, "Prediction of oxy-coal combustion through an optimized weighted sum of gray gases model", *Energy*, 41 (2012) 244-251.
- [53] N. Crnomarkovic, M. Sijercic, S. Belosevic, B. Stankovic, D. Tucakovic, T. Zivanovic, "Influence of forward scattering on prediction of temperature and radiation fields inside the pulverized coal furnace", *Energy*, 45 (2012) 160-168.
- [54] A. Bhuiyan, J. Naser, "Computational modelling of co-firing of biomass with coal under oxy-fuel condition in a small scale furnace", *Fuel* 143 (2015) 455–466.
- [55] A. Bhuiyan, J. Naser, "CFD modelling of co-firing of biomass with coal under oxy-fuel combustion in a large scale power plant", *Fuel*, 159 (2015) 150–168.
- [56] C. Yin, "On gas and particle radiation in pulverized fuel combustion furnaces", *Applied Energy*, 157 (2015) 554–561.
- [57] C. Yin, "Effects of moisture release and radiation properties in pulverized fuel combustion: A CFD modelling study", *Fuel*, 165 (2016) 252–259.
- [58] Y. Fei, S. Black, J. Szuhánszki, L. Ma, D.B. Ingham, P.J. Stanger, M. Pourkashanian, "Evaluation of the potential of retrofitting a coal power plant to oxy-firing using CFD and process co-simulation", *Fuel Processing Technology*, 131 (2015) 45–58.
- [59] N. Hashimoto, H. Watanabe, "Numerical analysis on effect of furnace scale on heat transfer mechanism of coal particles in pulverized coal combustion field", *Fuel Process. Technol.*, 145 (2016) 20–30.

- [60] W. W. Yuen, L.W. Wong, “A Parametric Study of Radiative Transfer with Anisotropic Scattering in a One-Dimensional System”, *Journal of Quantitative Spectroscopy & Radiative Transfer*, 22 (1979) 231-238.
- [61] M. P. Mengüç, R. Viskanta, “A Sensitivity Analysis for Radiative Heat transfer in a Pulverized Coal-Fired Furnace”, *Combustion Science and Technology*, 51 (1987) 51-74, 1987.
- [62] J. S. Truelove, “Three-Dimensional Radiation in Absorbing-Emitting Scattering Media Using the Discrete-Ordinates Approximation”, *J. Quant. Spectrosc. Radiat. Transfer*, 39 (1988) 27-31.
- [63] F. Liu, J. Swithenbank, “Modelling Radiative Heat Transfer in Pulverised Coal-Fired Furnaces”, *EUROTHERM Seminars Heat Transfer in Radiating and Combusting Systems*, 17 (1991) 358-373.
- [64] N. Selçuk, “Exact Solutions for Radiative Heat Transfer in Box-Shaped Furnaces”, *J. Heat Transfer*, 107 (1985) 648-655.
- [65] D. Bäckström, D. Gall, M. Pushp, R. Johansson, K. Andersson, J.B.C. Pettersson, “Particle composition and size distribution in coal flames – The influence on radiative heat transfer”, *Exp. Therm. Fluid Sci.*, 64 (2015) 70–80.
- [66] D. Bäckström, R. Johansson, Klas Andersson, H. Wiinikka, C. Fredriksson, “On the use of alternative fuels in rotary kiln burners — An experimental and modelling study of the effect on the radiative heat transfer conditions”, *Fuel Process. Technol.*, 138 (2015) 210–220.
- [67] P. Granate, P. J. Coelho, M. Roger, “Radiative Heat Transfer in Strongly Forward Scattering Media using the Discrete Ordinates Method”, *Journal of Quantitative Spectroscopy & Radiative Transfer*, 172 (2016) 110–120.
- [68] T. F. Wall, A. Lowe, L. J. Wibberley, T. Mai-Viet, R. P. Gupta, “Fly Ash Characteristics and Radiative Heat Transfer in Pulverized-Coal-Fired Furnaces”, *Combustion Science and Technology*, 26 (1981) 107-121.
- [69] R. P. Gupta, T. F. Wall, J. S. Truelove, “Radiative Scatter by Fly Ash in Pulverized-Coal-Fired Furnaces: Application of The Monte Carlo Method to Anisotropic Scatter”, *J. Heat Mass Transfer*, 26 (1983) 1649-1660.

- [70] M. P. Mengüç, S. Manickavasagam, D. A. D'Sa, "Determination of radiative properties of pulverized coal particles from experiments", *Fuel*, 73 (1994) 613-625.
- [71] R. Johansson, T. Gronarz, R. Kneer, "Influence of index of refraction and particle size distribution on radiative heat transfer in a pulverized coal combustion furnace" *J. Heat Transfer*, 139 (2017) 042702-1-8.
- [72] J. S. Truelove, "An Evaluation of the Discrete Ordinates Approximation for Radiative Transfer in an Absorbing, Emitting, and Scattering Planar Medium", HTFS Report No.R8478, 1976.
- [73] W.A Fiveland, "Discrete Ordinate Methods for Radiative Heat Transfer in Isotropically and Anisotropically Scattering Media", *Journal of Heat Transfer*, 109 (1987) 809-812.
- [74] T. Kimand, H. Lee, "Effect of Anisotropic Scattering on Radiative Heat Transfer in Two-Dimensional Rectangular Enclosures", *International Journal of Heat and Mass Transfer*, 31 (1988) 1711-1721.
- [75] J. S. Truelove, "Three-dimensional Radiation in Absorbing-Emitting-Scattering Media using the Discrete-Ordinates Approximation", *Journal of Quantitative Spectroscopy & Radiative Transfer*, 39 (1988) 27-31.
- [76] A.S. Jamaluddin, and P.J. Smith, "Predicting Radiative Heat Transfer in Rectangular Enclosures using the Discrete Ordinates Method", *Combustion Science and Technology*, 59 (1988) 321-340.
- [77] W.A. Fiveland, "Three-Dimensional Radiative Heat-Transfer Solutions by Discrete-Ordinates Method", *Journal of Thermophysics and Heat Transfer*, 2 (1988) 309-316.
- [78] N. Selçuk, N. Kayakol, "Evaluation of Angular Quadrature and Spatial Differencing Schemes for Discrete Ordinates Method in Rectangular Furnaces", *Proceedings of 31st National Heat Transfer Conference*, ASME HDT, 325 (1996) 151-158.
- [79] N. Selçuk, N. Kayakol, "Evaluation of Discrete Transfer and Discrete Ordinates Methods for Radiative Heat Transfer in Rectangular Furnaces", Invited Lecture, *Proceedings of International Symposium on Glass Problems*, ICG, 1 (1996) 255-276.

- [80] N. Selçuk, N. Kayakol, "Evaluation of Discrete Ordinates Method for Radiative Transfer in Rectangular Furnaces", *International Journal of Heat and Mass Transfer*, 40 (1997) 213-222.
- [81] S.H. Kim, K.Y. Huh, "Assessment of the Finite-Volume Method and the Discrete Ordinate Method for Radiative Heat Transfer in a Three-Dimensional Rectangular Enclosure", *Numerical Heat Transfer, Part B: Fundamentals: An International Journal of Computation and Methodology*, 35 (1999) 85-112.
- [82] B.G. Carlson, K.D. Lathrop, *Transport Theory-The Method of Discrete Ordinates in Computing Methods in Reactor Physics* (Edited by H. Greenspan, C. N. Kelber and D. Okrent), pp.165-266, Gordon & Breach, New York, 1968.
- [83] J. Hyde and J.S. Truelove, "The Discrete Ordinates Approximation for Multidimensional Radiant Heat Transfer in Furnaces", HFTS Report No. R8502, 1977.
- [84] S. Karamehmetoğlu, "The Method of Lines Solution of Discrete Ordinates Method for Radiative Heat Transfer in Cylindrical Enclosures", *M.Sc. Thesis*, METU, Ankara, (2002).
- [85] W. A. Fiveland, "The Selection of Discrete Ordinate Quadrature Sets for Anisotropic Scattering, Fundamentals of Radiation Heat Transfer", *ASME HTD* 160 (1991) 89-96.
- [86] N.E. Wakil, J.F. Sacadura, "Some Improvements of Discrete Ordinates Method for the Solution of the Radiative Transport Equation in Multi-Dimensional Anisotropically Scattering Media", *Developments in Radiative Heat Transfer, ASME HTD* 203 (1992) 119-127.
- [87] N. Kayakol, "Discrete Transfer and Discrete Ordinates Methods for Radiative Heat Transfer in Furnaces", *Ph.D. Thesis*, METU, Ankara, (1998).
- [88] Jessee, J. P., and Fiveland, W. A., "Bounded, High Resolution Differencing Schemes Applied to the Discrete Ordinates Method", *ASME HTD*, 325 (1996), 133-141.

- [89] Liu, F., Becker, H. A., and Pollard, A., "Spatial Differencing Schemes the Discrete Ordinates Method", *Numerical Heat Transfer, Part B: Fundamentals: An International Journal of Computation and Methodology*, 30 (1996) 23-43.
- [90] W. E. Schiesser, "The Numerical Method of Lines in Integration of Partial Differential Equations", Academic Press Inc. 1991.
- [91] P. Saucez, W. E. Schiesser, A. V. Wouwer, "Upwinding in the Method of Lines", *Mathematics and Computers in Simulation*, 56 (2001) 171-185.
- [92] R. Weiner, B.A. Schmitt, H. Podhaisky, "Rowmap-A Row Code with Krylov techniques for Large Stiff Odes", *Applied Numerical Mathematics*, 25 (1997) 303-319.
- [93] J.T. Pearson, "The Development of Updated and Improved SLW Model Parameters and Its Application to Comprehensive Combustion Predictions", *Ph.D. Thesis*, Brigham Young University, Provo, Utah (2013).
- [94] B. Leckner, "Spectral and Total Emissivity of Water Vapor and Carbon Dioxide", *Combust. Flame*, 19 (1972) 33-48.
- [95] C.B. Ludwig, W. Malkmus, J.E. Reardon, J.A.L. Thomson, "Handbook of infrared radiation from combustion gases", NASA SP-3080, 1973.
- [96] A. Soufiani, A., J. Taine, "High Temperature Gas Radiative Property Parameters of Statistical Narrow-band Model for H<sub>2</sub>O, CO<sub>2</sub>, CO, and Correlated-k Model for H<sub>2</sub>O and CO<sub>2</sub>", *International Journal of Heat and Mass Transfer*, 40 (1997) 987-991.
- [97] P.Riviere, A. Soufiani, "Updated Band Model Parameters for H<sub>2</sub>O, CO<sub>2</sub>, CH<sub>4</sub>, and CO Radiation at High Temperature", *International Journal of Heat and Mass Transfer*, 55 (2012) 3349-3358.
- [98] V. P. Solovjov, D. Lemonnier, B. W. Webb, "The SLW-1 Model for Efficient Prediction of Radiative Transfer in High Temperature Gases," *J. Quant. Spectr. Rad. Transfer*, 112 (2011) 1205-1212.
- [99] V. P. Solovjov, D. Lemonnier, B. W. Webb, "SLW-1 Modeling of Radiative Heat Transfer in Nonisothermal Nonhomogeneous Gas Mixtures with Soot", *Journal of Heat Transfer* 133 (2011) 102701-1-9.



- [100] P. Evrard, V. Feldheim, P. Lybaert, “An alternative method to optimise the SLW Grey Gases”, *Journal of Physics: Conference Series* 395 (2012) 012007 1-7.
- [101] J. Meulemans, “An assessment of some non-gray global radiation models in enclosures”, *Journal of Physics: Conference Series* 676 (2016) 012017 1-13.
- [102] H. Amiri, K. Lari, “Comparison of global radiative models in two-dimensional enclosures at radiative equilibrium”, *International Journal of Thermal Sciences* 104 (2016) 423-436.
- [103] T.Gronarz, M. Schnell, C. Siewert, L. Schneiders, W. Schröder, R. Kneer, “Comparison of scattering behaviour for spherical and non-spherical particles in pulverized coal combustion”, *International Journal of Thermal Sciences*, 111 (2017) 116-128.
- [104] G.A. Mie, ‘Beiträge zur optic trüber medien, speziell kolloidaler metallösungen’, *Annalen der Physik*, 25 (1908) 377.
- [105] M.Q. Brewster, “Thermal Radiative Transfer and Properties”, Wiley, 1992.
- [106] L.A. Dombrovsky, “The use of transport approximation and diffusion-based models in radiative transfer calculations”, *Computational Thermal Sciences*, 4 (2012) 297–315.
- [107] W.J. Wiscombe, G.W. Grams, “The Backscattered Fraction in Two-Stream Approximations”, *Journal of the Atmospheric Sciences*, 33 (1976) 2440-2451.
- [108] M.I. Mishchenko, J.M. Dlugach, E.G. Yanovitskij, N.T. Zakharova, “Bidirectional reflectance of flat, optically thick particulate layers: an efficient radiative transfer solution and applications to snow and soil surfaces”, *Journal of Quantitative Spectroscopy & Radiative Transfer*, 63 (1999) 409-432.
- [109] P. Boulet, A. Collin, J.A. Consalvi, “On the finite volume method and the discrete ordinates method regarding radiative heat transfer in acute forward scattering media”, *Journal of Quantitative Spectroscopy & Radiative Transfer*, 104 (2007) 460-473, 2007.
- [110] B. Hunter, Z. Guo, “A New and Simple Technique to Normalize the HG Phase Function for Conserving Scattered Energy and Asymmetry Factor”, *Numerical Heat*

*Transfer, Part B: Fundamentals: An International Journal of Computation and Methodology*, 65 (2014) 195-217.

[111] B. Hunter, Z. Guo, “Conservation of asymmetry factor in phase function discretization for radiative transfer analysis in anisotropic scattering media”, *International Journal of Heat and Mass Transfer*, 55 (2012) 1544-1552.

[112] B. Hunter, Z. Guo, “Reduction of angle splitting and computational time for the finite volume method in radiative transfer analysis via phase function normalization”, *International Journal of Heat and Mass Transfer*, 55 (2012) 2449-2460.

[113] B. Hunter, Z. Guo, “Phase Function Normalization in 3-D Discrete-Ordinates Solution of Radiative Transfer-Part I”, *Numerical Heat Transfer, Part B: Fundamentals: An International Journal of Computation and Methodology*, 62 (2012) 203-222.

[114] B. Hunter, Z. Guo, “Phase Function Normalization in 3-D Discrete-Ordinates Solution of Radiative Transfer-Part II”, *Numerical Heat Transfer, Part B: Fundamentals: An International Journal of Computation and Methodology*, 62 (2012) 223-242.

[115] C. Willis, “The complex refractive index of particles in a flame”, *J. Phys. D: Appl. Phys.*, 3 (1970) 1944-1956

[116] F. E. Volz, “Infrared Optical Constants of Ammonium Sulfate, Sahara Dust, Volcanic Pumice, and Flyash”, *Applied Optics* 12 (1973) 564-568.

[117] P.J. Wyatt, “Some chemical, physical and optical properties of fly ash particles”, *Applied Optics* 19 (1980) 975-983.

[118] R.P. Gupta, T.F. Wall, “The optical properties of fly ash in coal fired furnaces”, *Combust. Flame* 61 (1985) 145–151.

[119] A. Lohi, J.R. Wynnycyk, E. Rhodes, “Spectral measurement of the complex refractive index of fly ashes of canadian lignite and sub-bituminous coals”, *Can. J. Chem. Eng.* 70 (1992) 751–758.

[120] J. L. Ebert, “Infrared Optical Properties of Coal Slag at High Temperatures” PhD Thesis (1994), Stanford University, Stanford, USA.

- [121] C.F. Bohren, D.R. Huffman, “Absorption and Scattering of Light by Small Particles”, John Wiley & Sons, Inc (1983) DOI: 10.1002/9783527618156.
- [122] R. Johansson, “Efficient Treatment of Non-Grey Radiative Properties of Particles and Gases in Modelling of Radiative Heat Transfer in Combustion Environments”, *International Journal of Heat and Mass Transfer*, 108 (2017) 519–528.
- [123] J.Guo, F.Hu, W. Luo, P. Li, Z. Liu, “A full spectrum k-distribution based non-gray radiative property model for fly ash particles”, *Int. J. Heat Mass Transfer*, 118 (2018) 103–115.
- [124] S. Ghosal, “Optical characterization of coal fly ashes and infrared extinction measurements on ash suspensions” PhD Thesis (1994), Stanford University, Stanford, USA.
- [125] R. P. Gupta, T. F. Wall, J. S. Truelove, “Radiative Scatter by Fly Ash in Pulverized-Coal-Fired Furnaces: Application of The Monte Carlo Method to Anisotropic Scatter”, *J. Heat Mass Transfer*, 26 (1983) 1649-1660.
- [126] K. H. Im, R. K. Ahluwalia, “Radiation properties of coal combustion products”, *J. Heat Mass Transfer*, 36 (1993) 293-302.
- [127] S. P. Bhattacharya, “Spectral Emittance of Particulate Ash-Like Deposits: Theoretical Predictions Compared to Experimental Measurement”, *Journal of Heat Transfer*, 126 (2004) 286-289.
- [128] F. Greffrath, J. Gorewoda, M. Schiemann, V. Scherer, “Influence of chemical composition and physical structure on normal radiant emittance characteristics of ash deposits”, *Fuel*, 134 (2014) 307–314.
- [129] Q. Lin, Y. Xuan, Y. Han, “Prediction of the radiative properties of surfaces covered with particulate deposits”, *Journal of Quantitative Spectroscopy & Radiative Transfer* 196(2017)112–122.
- [130] B. Wu, S. P. Roy, X. Zhao, M. F. Modest, “Effect of multiphase radiation on coal combustion in a pulverized coal jet flame”, *Journal of Quantitative Spectroscopy and Radiative Transfer*, 197 (2017) 154-165.

- [131] F.P. Incropera, D.P. DeWitt, T.L. Bergman, A.S. Lavine, “Fundamentals of Heat and Mass Transfer”, 6<sup>th</sup> Edition, John Wiley & Sons, Inc., 2007.
- [132] N. Selçuk, M. Ozkan, ‘Simulation of circulating fluidized bed combustors firing indigenous lignite’, *Int. J Therm Sci.* 50 (2011) 1109-1115.
- [133] B. Hirschberg and J. Werther, “Factors Affecting Solids Segregation in Circulating Fluidized-Bed Riser” *AIChE Journal* 44 (1998) 25-34.
- [134] X. Yao, T. Wang, J. Zhao, H. Yang, H. Zhang, “Modeling of solids segregation in circulating fluidized bed boilers” *Front. Energy Power Eng. China* 4(4) (2010) 577–581.
- [135] F. Johnsson, S. Andersson, B. Leckner, “Expansion of a freely bubbling fluidized bed” *Powder Technology* 68 (1991) 117-123.
- [136] J.R. Grace, C.J. Lim, “Properties of circulating fluidized beds (CFB) relevant to combustion and gasification systems”, in *Fluidized Bed Technologies for Near-Zero Emission Combustion and Gasification* ed. by F. Scala (2013) 147-176.
- [137] F. Johnsson, B. Leckner, “Vertical distribution of solids in a CFB-furnace” *13th International Conference on Fluidized Bed Combustion*, ASME, New York (1995) 671–680.
- [138] D. Pallarès, F. Johnsson, “Macroscopic modelling of fluid dynamics in largescale circulating fluidized beds” *Progress in Energy and Combustion Science*, 32 (5-6) (2006) 539–569.
- [139] D. Pallarès, F. Johnsson, “Modeling of fluidized bed combustion processes” in *Fluidized Bed Technologies for Near-Zero Emission Combustion and Gasification* ed. by F. Scala (2013) 147-176.
- [140] A. S. Issangya, J. R. Grace, D. Bai, J. Zhu, “Radial Voidage Variation in CFB Risers” *The Canadian Journal of Chemical Engineering* 79 (2001) 279-286.
- [141] R. Viskanta, A. Ungan, M. P. Mengüç, “Predictions of radiative properties of pulverized coal and fly-ash polydispersions”, *ASME Paper*, No.81-HT-24 (1981).
- [142] S. Jendoubi, H. S. Lee, T.K. Kim, ‘Discrete-Ordinates Solutions for Radiatively Participating Media in a Cylindrical Enclosure’, *J. Thermophys Heat Tr.*, 7(2) (1993) 213– 219.
- [143] M.Y. Kim, S.W. Baek, “Analysis of Radiative Transfer in Cylindrical Enclosures Using the Finite Volume Method”, *J. Thermophys Heat Tr.*, 11(2) (1997) 246-252.

- [144] T.Gronarz, O. Hatzfeld, M. Habermehl, R. Kneer, ‘On the Importance of Particle Radiation Interaction in the Numerical Simulation of Pulverized Coal Combustion’, *10<sup>th</sup> European Conference on Industrial Furnaces and Boilers : INFUB* (2015), Porto, Portugal.
- [145] T. K. Kim, H. Lee, ‘Effect of Anisotropic Scattering on Radiative Heat Transfer in Two-Dimensional Rectangular Enclosures’, *Int. J. Heat Mass Transfer*, 31 (1988)1711–1721.
- [146] N. Crnomarkovic, M. Sijercic, S. Belosevic, D. Tucakovic, T. Zivanovic, “Numerical investigation of processes in the lignite-fired furnace when simple gray gas and weighted sum of gray gases models are used”, *Int. J. Heat Mass Transfer*, 56 (2013) 197–205.
- [147] K. Andersson, R. Johansson, S. Hjærtstam, F. Johnsson, B. Leckner , “Radiation intensity of lignite-fired oxy-fuel flames”, *Exp. Therm. Fluid Sci.* 33 (2008) 67–76.
- [148] S. Hjærtstam, R. Johansson, K. Andersson F. Johnsson, “Computational Fluid Dynamics Modeling of Oxy-Fuel Flames: The Role of Soot and Gas Radiation”, *Energy Fuels*, 26 (2012) 2786–2797.
- [149] J. Zhang, T. Ito, S. Ito, D. Riechelmann, T. Fujimori, “Numerical investigation of oxy-coal combustion in a large-scale furnace: Non-gray effect of gas and role of particle radiation”, *Fuel* 139 (2015) 87–93.
- [150] Ö. Şen, “Modeling of Radiative Heat Transfer in Strongly Forward Scattering Media of Bubbling Fluidized Bed Combustor with and without Recycle”, *M.S. Thesis*, Middle East Technical University, Ankara, Turkey (2017).
- [151] M. Filla, A. Scalabrin, “Scattering of thermal radiation in the freeboard of a 1 MWt fluidized bed combustor with coal and limestone feeding”, *Twenty-Sixth Symposium (International) on Combustion, The Combustion Institute*, 3295 (1996).
- [152] M. Q. Brewster, T. Kunitomo “The optical constants of coal, char, and limestone”, *J. Heat Transfer*, 106 (1984) 678.
- [153] M. Theis, B.J. Skrifvars, M. Hupa, H. Tran, “Fouling tendency of ash resulting from burning mixtures of biofuels. Part 1: Deposition rates”, *Fuel*, 85 (2006) 1125–1130.
- [154] A.A. Khan, W. de Jong, P.J. Jansens, H. Spliethoff, “Biomass combustion in fluidized bed boilers: Potential problems and remedies”, *Fuel Processing Technology*, 90 (2009) 21-50.

- [155] J.A. Ruiz, M.C. Juarez, M.P. Morales, P. Munoz, M.A. Mendivil, “Biomass logistics: Financial & environmental costs. Case study: 2 MW electrical power plants”, *Biomass and Energy* 56 (2013) 260-267.
- [156] M.K. Delivand, A.R.B. Cammerino, P. Garafalo, “Optimal locations of bioenergy facilities, biomass spatial availability, logistics costs and GHG (greenhouse gas) emissions: a case study on electricity productions in South Italy”, *J. Clean Energy Production* 99 (2015) 129-139.
- [157] Lautala, P.T., Hilliard, M.R., Webb, E., Busch I., J. Hess R., Roni M.S., Hilbert J., Handler R.M., Bittencourt R., Valente A., Laitinen T., “Opportunities and Challenges in the Design and Analysis of Biomass Supply Chains” *Environmental Management* 56(2015) 1397.
- [158] Boukis I., Vassilakos N., Kontopoulos G., Karellas S., “Policy plan for the use of biomass and biofuels in Greece: part II: logistics and economic investigation”, *Renew. Sustain Energy Rev.*, 13 (2009) 703-720.
- [159] Hamelinck C.N., Suurs R.A.A, Faaij A.P.C., “International bioenergy transport costs and energy balance”, *Biomass Bioenergy*, 29 (2005) 114-134.
- [160] Gustavsson L., Borjesson P., “Biomass utilisation and transportation demands”, *Renew Energy*, 9 (1996) 1037-1040.
- [161] H. M. Abdelmotalib, M.A.M. Youssef, A.A, Hassan, S.B. Youn, I. Im, “Heat transfer process in gas–solid fluidized bed combustors: A review”, *International Journal of Heat and Mass Transfer*, 89 (2015) 567–575.
- [162] J.P. Smart, R. Patel, G.S. Riley, “Oxy-fuel combustion of coal and biomass, the effect on radiative and convective heat transfer and burnout”, *Combustion and Flame*, 157 (2010) 2230–2240.
- [163] J. Szuhanszki, S. Black, A. Pranzitelli, L. Ma, P.J. Stanger, D.B. Ingham, M. Pourkashanian, “Evaluation of the performance of a power plant boiler firing coal, biomass and a blend under oxy-fuel conditions as a CO<sub>2</sub> capture technique”, *Energy Procedia*, 37 (2013) 1413 – 1422.

- [164] G. Krishnamoorthy, C. Wolf, “Assessing the Role of Particles in Radiative Heat Transfer during Oxy-Combustion of Coal and Biomass Blends”, *Journal of Combustion* vol. 2015 (2015) 1-15.
- [165] S. Black, J. Szuhanski, A. Pranzitelli, L. Ma, P.J. Stanger., D.B. Ingham, M. Pourkashanian, “Effects of firing coal and biomass under oxy-fuel conditions in a power plant boiler using CFD modelling”, *Fuel* 113 (2013) 780–786.
- [166] N. Jurado, H.G. Darabkhani., E.J. Anthony, J.E. Oakey, “Oxy-combustion studies into the co –firing of coal and biomass blends: effects on heat transfer, gas and ash compositions”, *Energy Procedia* 63 (2014) 440 – 452.
- [167] L.G. Blevins, T.H. Cauley, “Fine Particulate Formation During Switchgrass/Coal Cofiring”, *Journal of Engineering for Gas Turbines and Power*, 127 (2005) 457-463.
- [168] P. Sun, S. Hui, Z. Gao, Q. Zhou, H. Tan, Q. Zhao, T. Xu, “Experimental investigation on the combustion and heat transfer characteristics of wide size biomass co-firing in 0.2 MW circulating fluidized bed”, *Applied Thermal Engineering*, 52 (2013) 284-292.
- [169] B. Andersson, B. Leckner, L.E. Amand, “Fluidized Bed Combustion of Coals and Alternative Fuels”, *8<sup>th</sup> International Conference on Fluidized Bed Combustion*, DOE/METC-85/6021, 2 (1985) 1019-1029.
- [170] D.E. Alagoz, G. Kulah, N. Selçuk “A Comprehensive Fluidized Bed Combustion Model Coupled with a Radiation Model”, *Combustion Science and Technology*, 180:5 (2008) 910-926.
- [171] E. D. Palik, “Handbook of Optical Constants of Solids”, Elsevier Inc., 1997.
- [172] P. Perez , M. El Hafi , P. J. Coelho, R. Fournier, “Accurate Solutions for Radiative Heat Transfer in Two-Dimensional Axisymmetric Enclosures with Gas Radiation and Reflective Surfaces”, *Numerical Heat Transfer, Part B: Fundamentals*, 47:1 (2004) 39-63.
- [173] V.P. Solovjov, B.W. Webb, “An Efficient Method for Modeling Radiative Transfer in Multicomponent Gas Mixtures with Soot”, *Journal of Heat Transfer*, 123 (201), pp.450-456.

[174] M.F. Modest, R. J. Riazzi, “Assembly of Full-spectrum k-distributions from a Narrow-band database; effects of mixing gases, gases and nongray absorbing particles, and mixtures with nongray scatterers in nongray enclosures”, *J. Quant. Spectrosc. Radiat. Transfer*, 90 (2005) 169–189.

[175] S. H. Kim, K. Y. Huh, “A New Angular Discretization Scheme of the Finite Volume Method for 3-D Radiative Heat Transfer in Absorbing, Emitting and Anisotropically Scattering Media”, *Int. J. Heat Mass Transfer*, 43 (2000) 1233- 1242.

[176] L. S. Rothman, R. R. Gamache, R. H. Tipping, , C. P. Rinsland, , M. A. H. Smith, D. Chris Benner, V. Malathy Devi, J. M. Flaud, C. Camy-Peyret, A. Perrin, A. Goldman, S.T. Massie, L.R: Brown, 1992, “The HITRAN Molecular Database: Editions of 1991 and 1992a,” *Journal of Quantitative Spectroscopy and Radiative Transfer*, 48 (1992) 469-507.

[177] L.S. Rothman, I.E. Gordon, R.J. Barber, H. Dothe, R.R. Gamache, A. Goldman, V.I. Perevalov, S.A. Tashkun, J. Tennyson, “HITEMP, the high-temperature molecular spectroscopic database”, *Journal of Quantitative Spectroscopy & Radiative Transfer*, 111 (2010) 2139–2150.



## APPENDIX A

### ORDINATES AND WEIGHTS FOR $S_N$ APPROXIMATION

Order of Approximation	Ordinates			Weights
	$\mu$	$\eta$	$\xi$	w
$S_2$	0.5000000	0.7071068	0.5000000	3.1415927
$S_4$	0.2958759	0.2958759	0.9082483	1.0471976
	0.2958759	0.9082483	0.2958759	1.0471976
	0.9082483	0.2958759	0.2958759	1.0471976
$S_6$	0.1838670	0.1838670	0.9656013	0.3219034
	0.1838670	0.6950514	0.6950514	0.7252938
	0.6950514	0.1838670	0.6950514	0.7252938
	0.1838670	0.9656013	0.1838670	0.3219034
	0.6950514	0.6950514	0.1838670	0.7252938
	0.9656013	0.1838670	0.1838670	0.3219034
$S_8$	0.1422555	0.1422555	0.9795543	0.3424718
	0.1422555	0.5773503	0.8040087	0.1984568
	0.5773503	0.1422555	0.8040087	0.1984568
	0.1422555	0.8040087	0.5773503	0.1984568
	0.5773503	0.5773503	0.5773503	0.9234358
	0.8040087	0.1422555	0.5773503	0.1984568
	0.1422555	0.9795543	0.1422555	0.3424718
	0.5773503	0.8040087	0.1422555	0.1984568
	0.8040087	0.5773503	0.1422555	0.1984568
	0.9795543	0.1422555	0.1422555	0.3424718

Order of Approximation	Ordinates			Weights
	$\mu$	$\eta$	$\xi$	w
S <sub>10</sub>	0.9809754	0.1372719	0.1372719	0.0944411
	0.8523177	0.1372719	0.5046889	0.1483950
	0.8523177	0.1372719	0.5046889	0.1483950
	0.7004129	0.1372719	0.7004129	0.0173700
	0.7004129	0.5046889	0.5046889	0.1149972
	0.7004129	0.7004129	0.1372719	0.0173701
	0.5046889	0.1372719	0.8523177	0.1483950
	0.5046889	0.5046889	0.7004129	0.1149972
	0.5046889	0.7004129	0.5046889	0.1149972
	0.5046889	0.8523177	0.1372719	0.1483950
	0.1372719	0.1372719	0.9809754	0.0944411
	0.1372719	0.5046889	0.8523177	0.1483950
	0.1372719	0.7004129	0.7004129	0.0173701
	0.1372719	0.8523177	0.5046889	0.1483950
	0.1372719	0.9809754	0.1372719	0.0944411

## APPENDIX B

### BANDED SLW PARAMETERS

**$b_{lmn}$  Coefficients used in Equation 3.42 for H<sub>2</sub>O**

		n			
		0	1	2	3
m	$i = 1, \eta = 400 \text{ cm}^{-1}$				
0	1.03488	-3.20532	5.23391	-2.44424	
1	0.1625176	1.05783	-1.89812	1.00031	
2	6.23E-02	-0.438688	0.523441	-0.168893	
3	-4.47E-03	5.47E-02	-3.02E-02	-1.19E-02	
m	$i = 2, \eta = 800 \text{ cm}^{-1}$				
0	4.69881	-13.6462	18.48558	-8.0758	
1	0.7013564	-1.04909	0.767759	-0.119224	
2	1.24E-02	0.2343079	-0.47488	0.2488919	
3	-3.38E-03	4.20E-02	-6.04E-02	2.60E-02	
m	$i = 3, \eta = 1200 \text{ cm}^{-1}$				
0	2.7936	-6.65072	8.67361	-3.88429	
1	0.5387762	-0.512367	0.835504	-0.296496	
2	1.75E-02	0.3302229	-0.79243	0.5047118	
3	-3.59E-03	6.20E-02	-0.12934	7.82E-02	
m	$i = 4, \eta = 1600 \text{ cm}^{-1}$				
0	0.6615483	0.2395768	-0.34537	0.2786642	
1	0.352983	0.2928606	-0.15918	6.82E-02	
2	-2.77E-02	0.2001896	-0.32512	0.2052319	
3	1.02E-02	-3.00E-02	7.90E-02	-3.21E-02	
m	$i = 5, \eta = 2000 \text{ cm}^{-1}$				
0	2.27017	-3.14322	4.17413	-1.72313	
1	0.3971992	0.258657	-0.24302	0.1551463	
2	1.26E-02	0.2452768	-0.46875	0.2777312	
3	-2.90E-03	5.57E-02	-8.86E-02	4.80E-02	

**$b_{lmn}$  Coefficients used in Equation 3.42 for H<sub>2</sub>O (cont'd)**

		n			
		0	1	2	3
m	i = 6, $\eta = 2400 \text{ cm}^{-1}$				
0	1.71293	11.87195	-25.3632	16.15517	
1	-1.56307	12.65764	-22.5869	13.13224	
2	-0.319807	2.09791	-3.862	2.33382	
3	-1.60E-02	0.1030389	-0.19408	0.1243171	
m	i = 7, $\eta = 2800 \text{ cm}^{-1}$				
0	4.4159	1.29733	-6.91015	6.34496	
1	0.1491786	4.51358	-9.10281	6.36933	
2	-7.06E-02	0.8717525	-1.88024	1.34793	
3	-4.95E-03	4.61E-02	-0.10447	8.01E-02	
m	i = 8, $\eta = 3200 \text{ cm}^{-1}$				
0	5.8876	-14.45	17.20371	-7.01927	
1	2.23259	-6.8922	9.58736	-4.25281	
2	0.3579812	-1.31045	1.97187	-0.934688	
3	2.30E-02	-8.34E-02	0.154301	-7.49E-02	
m	i = 9, $\eta = 3600 \text{ cm}^{-1}$				
0	1.09098	-0.667602	1.19697	-0.478035	
1	0.4536091	-0.392997	0.989952	-0.480344	
2	-1.14E-02	0.232239	-0.52828	0.3277193	
3	-1.38E-02	0.1383609	-0.19727	0.1001742	
m	i = 10, $\eta = 4000 \text{ cm}^{-1}$				
0	1.28504	-0.354062	1.04285	-0.535162	
1	0.3378185	0.2212536	0.221063	-0.209401	
2	3.13E-02	1.68E-02	2.43E-02	-7.91E-03	
3	1.41E-03	1.02E-02	-1.42E-02	8.10E-03	
m	i = 11, $\eta = 4400 \text{ cm}^{-1}$				
0	3.97338	-1.31E-02	-2.72889	2.23012	
1	7.99E-02	2.30826	-4.12312	2.11729	
2	-2.21E-02	0.191051	-0.32346	0.1484448	
3	0	0	0	0	
m	i = 12, $\eta = 4800 \text{ cm}^{-1}$				
0	10.72517	-20.8689	17.10614	-3.42195	
1	1.80942	-2.15199	-0.5687	2.1685	
2	0.1061922	0.110237	-0.80414	0.7618767	
3	2.07E-03	1.82E-02	-6.81E-02	6.17E-02	

**b<sub>lmn</sub> Coefficients used in Equation 3.42 for H<sub>2</sub>O (cont'd)**

m	n			
	0	1	2	3
m	i = 13, $\eta = 5200 \text{ cm}^{-1}$			
0	2.05883	-0.428569	2.44014	-1.64767
1	0.3975633	0.300877	2.02134	-1.7171
2	-4.11E-02	0.3046176	0.427193	-0.490756
3	-7.51E-03	4.24E-02	6.64E-02	-6.82E-02
m	i = 14, $\eta = 5600 \text{ cm}^{-1}$			
0	2.1058	1.24095	-2.25157	1.49862
1	0.2958509	1.77627	-2.9417	1.69086
2	-1.58E-02	0.4320648	-0.76344	0.4484763
3	-3.03E-03	3.86E-02	-6.41E-02	3.61E-02
m	i = 15, $\eta = 6000 \text{ cm}^{-1}$			
0	2.08129	32.43989	-66.2961	41.88874
1	-1.06563	15.13963	-29.3362	18.25687
2	-0.177146	1.80877	-3.58766	2.28947
3	-6.74E-03	6.82E-02	-0.14095	9.46E-02
m	i = 16, $\eta = 6400 \text{ cm}^{-1}$			
0	5.0824	4.61629	-11.998	9.54621
1	-0.29326	4.8422	-7.90777	6.28887
2	-0.118469	0.6704229	-1.439	1.35239
3	-5.97E-03	3.35E-02	-9.67E-02	0.1016853
m	i = 17, $\eta = 6800 \text{ cm}^{-1}$			
0	3.78073	1.43388	-5.65167	4.42455
1	0.4037876	4.34835	-8.0583	5.20287
2	-5.90E-02	1.17914	-2.15149	1.46167
3	-5.62E-03	8.25E-02	-0.13266	0.1068784
m	i = 18, $\eta = 7200 \text{ cm}^{-1}$			
0	2.04482	-0.615712	3.88566	-1.87036
1	0.8049103	-1.34236	3.70058	-1.77727
2	0.1146259	-0.20045	0.608866	-0.293221
3	1.04E-02	1.83E-02	-9.36E-03	2.29E-03
m	i = 19, $\eta = 7600 \text{ cm}^{-1}$			
0	4.05534	-4.446	5.38251	-1.94098
1	0.3911651	1.449	-2.91808	1.65826
2	-2.83E-02	0.4606226	-0.82508	0.4531455
3	-2.59E-03	3.02E-02	-5.40E-02	3.08E-02

**$b_{lmn}$  Coefficients used in Equation 3.42 for H<sub>2</sub>O (cont'd)**

		n			
		0	1	2	3
m	i = 20, $\eta = 8000 \text{ cm}^{-1}$				
0	1.3666	47.31528	-77.6847	34.65779	
1	-0.566972	10.61622	-16.1337	6.7969	
2	-5.69E-02	0.5877169	-0.88086	0.3485547	
3	0	0	0	0	
m	i = 21, $\eta = 8400 \text{ cm}^{-1}$				
0	7.73261	-9.43582	4.20441	6.97274	
1	0.9386401	0.8873606	-5.46215	7.1544	
2	-1.59E-03	0.4178969	-1.25337	1.36091	
3	-1.28E-03	1.85E-02	-4.98E-02	6.40E-02	
m	i = 22, $\eta = 8800 \text{ cm}^{-1}$				
0	7.53802	-15.0285	34.83388	-19.0212	
1	3.11639	-8.27622	17.5147	-9.46823	
2	0.4969846	-1.36621	2.7339	-1.47653	
3	2.93E-02	-7.21E-02	0.140141	-7.69E-02	
m	i = 23, $\eta = 9200 \text{ cm}^{-1}$				
0	10.93284	-31.2926	45.38196	-21.1143	
1	1.85853	-6.24774	8.76805	-4.10597	
2	8.25E-02	-0.330505	0.461993	-0.223626	
3	0	0	0	0	
m	i = 24, $\eta = 9600 \text{ cm}^{-1}$				
0	60.37538	-161.185	179.4196	-70.2446	
1	10.8268	-32.3926	38.98925	-16.1849	
2	0.4982083	-1.56252	1.91765	-0.816269	
3	0	0	0	0	
m	i = 25, $\eta = 10000 \text{ cm}^{-1}$				
0	7.42494	-9.19223	29.90838	-15.8349	
1	1.28346	-5.60371	15.74417	-7.81315	
2	0.1423836	-1.104	2.53814	-1.16418	
3	7.63E-03	-6.32E-02	0.132586	-5.79E-02	
m	i = 26, $\eta = 10400 \text{ cm}^{-1}$				
0	4.20597	5.80168	2.0771	-2.29606	
1	0.3902882	4.6389	-2.72277	0.6941512	
2	-5.23E-02	0.9777681	-0.87226	0.3134598	
3	-4.58E-03	6.12E-02	-6.05E-02	2.20E-02	

**$b_{mn}$  Coefficients used in Equation 3.42 for H<sub>2</sub>O (cont'd)**

		n			
		0	1	2	3
m	i = 27, $\eta = 10800 \text{ cm}^{-1}$				
0	5.54022	-6.55996	14.1469	-8.0968	
1	1.25037	-2.77726	5.21509	-3.00288	
2	0.1141942	-0.410314	0.716019	-0.402913	
3	5.30E-03	-2.09E-02	3.43E-02	-1.87E-02	
m	i = 28, $\eta = 11200 \text{ cm}^{-1}$				
0	24.53812	-95.26	153.3482	-71.4101	
1	7.9318	-36.0494	57.34011	-27.1841	
2	0.9083312	-4.40888	6.9924	-3.35854	
3	3.56E-02	-0.175753	0.277693	-0.134244	
m	i = 29, $\eta = 11600 \text{ cm}^{-1}$				
0	204.1396	-858.38	1221.677	-526.127	
1	57.36587	-264.126	386.5144	-168.827	
2	5.64894	-27.7973	41.40002	-18.2485	
3	0.1900102	-0.983824	1.4837	-0.658178	
m	i = 30, $\eta = 12000 \text{ cm}^{-1}$				
0	12.68037	6.37427	-25.0873	34.22428	
1	3.38372	0.8476225	-7.94033	11.38799	
2	0.3586564	-5.52E-02	-0.79988	1.23767	
3	1.41E-02	-7.45E-03	-2.51E-02	4.35E-02	

**c<sub>lmn</sub> Coefficients used in Equation 3.45 for H<sub>2</sub>O**

		n			
		0	1	2	3
m	i = 1, $\eta = 400 \text{ cm}^{-1}$				
0	6.01249	-0.983854	4.89E-03	-1.82E-02	
1	-11.0529	2.57271	-0.574373	5.73E-02	
2	1.15E+01	-3.68484	1.28155	-0.134567	
3	-4.50E+00	1.80E+00	-7.44E-01	8.35E-02	
m	i = 2, $\eta = 800 \text{ cm}^{-1}$				
0	4.9625	-1.56299	-0.321975	-2.56E-02	
2	-11.628	2.31118	0.6434991	7.41E-02	
2	1.28E+01	-2.18203	-0.817465	-0.114893	
3	-5.18E+00	7.90E-01	3.67E-01	5.73E-02	
m	i = 3, $\eta = 1200 \text{ cm}^{-1}$				
0	2.43967	-1.38987	-0.233354	-1.74E-02	
1	-5.64583	1.1359	-6.77E-03	-1.78E-04	
2	6.58E+00	1.03E-02	0.3402566	2.13E-02	
3	-2.78E+00	-3.72E-01	-0.265149	-2.05E-02	
m	i = 4, $\eta = 1600 \text{ cm}^{-1}$				
0	1.7483	-1.07315	-0.10533	9.54E-04	
1	-2.47287	1.62921	-9.40E-02	-6.29E-03	
2	2.47E+00	-1.96467	9.55E-02	-6.73E-03	
3	-1.01E+00	9.45E-01	-2.40E-02	1.05E-03	
m	i = 5, $\eta = 2000 \text{ cm}^{-1}$				
0	1.83348	-1.25217	-0.246067	-2.15E-02	
1	-3.67734	2.45767	0.761219	9.60E-02	
2	3.64E+00	-3.6376	-1.59045	-0.224196	
3	-1.40E+00	1.82E+00	9.15E-01	1.34E-01	
m	i = 6, $\eta = 2400 \text{ cm}^{-1}$				
0	-4.90269	-2.48241	-0.207389	-8.28E-03	
1	5.50034	3.20344	0.305713	2.27E-02	
2	-21.5761	-12.5508	-2.0592	-0.128794	
3	1.28E+01	7.24703	1.20532	7.21E-02	
m	i = 7, $\eta = 2800 \text{ cm}^{-1}$				
0	-8.36756	-3.41993	-0.26149	-6.17E-03	
1	-3.69488	-1.60283	-0.506064	-2.21E-02	
2	-7.64E+00	-5.54079	-0.881401	-6.36E-02	
3	9.46E+00	5.86E+00	1.01087	6.31E-02	



**c<sub>l,m,n</sub> Coefficients used in Equation 3.45 for H<sub>2</sub>O (cont'd)**

		n			
		0	1	2	3
m	i = 8, $\eta = 3200 \text{ cm}^{-1}$				
0	-0.293299	-1.20615	-0.122646	-1.24E-02	
1	1.67504	5.27839	1.42079	0.151646	
2	-10.0927	-15.2154	-4.59322	-0.462659	
3	8.39E+00	1.08E+01	3.30463	3.26E-01	
m	i = 9, $\eta = 3600 \text{ cm}^{-1}$				
0	1.69469	-0.431034	-0.200718	-0.113743	
1	-3.31931	-0.74188	0.6714234	0.4541327	
2	3.94E+00	1.72716	-1.37757	-0.826218	
3	-1.77E+00	-0.96043	0.8461514	0.4732806	
m	i = 10, $\eta = 4000 \text{ cm}^{-1}$				
0	1.70276	-1.38757	-0.18765	-9.69E-03	
1	-3.2541	2.98873	0.5821874	4.82E-02	
2	3.44E+00	-3.88E+00	-1.04E+00	-1.03E-01	
3	-1.39E+00	1.75E+00	5.37E-01	5.56E-02	
m	i = 11, $\eta = 4400 \text{ cm}^{-1}$				
0	-16.9684	-8.45E+00	-1.13848	-5.20E-02	
1	3.85E+01	21.71089	3.46576	0.1841887	
2	-6.21E+01	-33.4257	-5.3488	-0.281705	
3	31.15406	16.25876	2.58159	0.1346302	
m	i = 12, $\eta = 4800 \text{ cm}^{-1}$				
0	-3.33365	-1.3537	-9.12E-03	4.31E-03	
1	-5.29116	-1.40511	-0.296025	-4.16E-03	
2	4.0574	-0.913207	-0.40728	-5.23E-02	
3	-9.91E-01	1.05E+00	3.61E-01	3.62E-02	
m	i = 13, $\eta = 5200 \text{ cm}^{-1}$				
0	-1.64925	-2.26031	-0.517058	-5.84E-02	
1	-8.80E-02	2.61952	1.1375	0.1723197	
2	2.30E+00	-0.664808	-0.793314	-0.164811	
3	-2.02E+00	-9.34E-01	-1.97E-02	3.77E-02	
m	i = 14, $\eta = 5600 \text{ cm}^{-1}$				
0	-3.33794	-3.7234	-0.549166	-2.59E-02	
1	7.356	9.23427	1.57472	8.39E-02	
2	-1.12E+01	-14.9245	-2.98062	-0.179267	
3	4.85E+00	7.33E+00	1.58E+00	9.93E-02	

**$c_{mn}$  Coefficients used in Equation 3.45 for H<sub>2</sub>O (cont'd)**

		n			
		0	1	2	3
m	i = 15, $\eta = 6000 \text{ cm}^{-1}$				
0	-13.879	-3.01159	-0.106739	0	
1	-37.192	-10.3616	-0.788729	0	
2	70.46981	19.114	1.35109	0	
3	-3.40E+01	-9.16E+00	-0.635453	0.00E+00	
m	i = 16, $\eta = 6400 \text{ cm}^{-1}$				
0	-37.2783	-14.3524	-1.80192	-7.94E-02	
1	149.382	64.24343	9.00516	0.4230659	
2	-199.686	-87.3695	-12.4422	-0.589144	
3	7.86E+01	3.48E+01	5.00E+00	0.2391663	
m	i = 17, $\eta = 6800 \text{ cm}^{-1}$				
0	-16.4668	-10.229	-1.94622	-0.130937	
1	59.44704	41.38283	9.00038	0.6492674	
2	-9.05E+01	-66.419	-15.28	-1.14427	
3	4.48E+01	3.38E+01	7.99426	0.6100925	
m	i = 18, $\eta = 7200 \text{ cm}^{-1}$				
0	-0.400976	-0.111904	0.1522728	0	
1	-2.82798	-2.65246	-0.769741	0	
2	4.61914	4.37431	1.1612	0	
3	-1.91E+00	-1.92E+00	-5.30E-01	0.00E+00	
m	i = 19, $\eta = 7600 \text{ cm}^{-1}$				
0	-1.82783	-2.54278	-0.432174	-2.39E-02	
1	-7.54732	-3.06294	-0.881314	-6.93E-02	
2	1.20E+01	7.14753	1.92226	0.1478565	
3	-6.35E+00	-4.56E+00	1.23E+00	-9.46E-02	
m	i = 20, $\eta = 8000 \text{ cm}^{-1}$				
0	6.92E-02	0.681132	8.87E-02	0	
1	-189.364	-42.4375	-2.38711	0	
2	4.49E+02	100.8311	5.65117	0	
3	-260.113	-58.5695	-3.28445	0	
m	i = 21, $\eta = 8400 \text{ cm}^{-1}$				
0	-3.66112	-1.37637	-0.176879	-1.25E-02	
1	-6.9631	-1.69081	2.14E-02	2.36E-02	
2	-2.83E+01	-15.9225	-2.89556	-0.176382	
3	2.94E+01	1.49E+01	2.49E+00	1.38E-01	

**c<sub>lmn</sub> Coefficients used in Equation 3.45 for H<sub>2</sub>O (cont'd)**

		n			
		0	1	2	3
m	i = 22, $\eta = 8800 \text{ cm}^{-1}$				
0	-13.5751	-7.12409	-1.20554	-7.41E-02	
1	34.15462	22.09339	4.49261	0.3004772	
2	-67.9313	-43.4154	-8.81561	-0.581553	
3	3.96E+01	2.51E+01	5.06353	3.31E-01	
m	i = 23, $\eta = 9200 \text{ cm}^{-1}$				
0	-16.1306	-8.25034	-1.23575	-6.08E-02	
1	-71.0008	-29.9685	-4.19718	-0.188165	
2	1.06E+02	44.67879	6.10504	0.2654607	
3	-50.0572	-20.4972	-2.70191	-0.112441	
m	i = 24, $\eta = 9600 \text{ cm}^{-1}$				
0	0	0	0	0	
1	0	0	0	0	
2	0	0	0	0	
3	0	0	0	0	
m	i = 25, $\eta = 10000 \text{ cm}^{-1}$				
0	-29.731	-6.26625	-0.305489	0	
1	79.49421	17.48574	0.9204174	0	
2	-89.4159	-19.3126	-0.998899	0	
3	2.59E+01	5.18E+00	0.2390553	0.00E+00	
m	i = 26, $\eta = 10400 \text{ cm}^{-1}$				
0	-17.7075	-7.96598	-1.19151	-6.40E-02	
1	99.64907	49.2126	7.8364	0.4103868	
2	-1.74E+02	-86.5249	-13.8921	-0.727189	
3	9.02E+01	4.53E+01	7.33E+00	3.85E-01	
m	i = 27, $\eta = 10800 \text{ cm}^{-1}$				
0	1.37817	1.36084	0.3117555	1.58E-02	
1	-58.0904	-25.7893	-3.69006	-0.165159	
2	107.8955	47.28263	6.67477	0.3013131	
3	-6.11E+01	-2.68E+01	-3.78E+00	-1.73E-01	
m	i = 28, $\eta = 11200 \text{ cm}^{-1}$				
0	-36.2252	-13.956	-1.80831	-8.11E-02	
1	241.1333	103.1054	14.4299	0.6647685	
2	-1154.19	-462.464	-61.3303	-2.6928	
3	8.41E+02	334.1098	43.97779	1.91748	

**$c_{lmn}$  Coefficients used in Equation 3.45 for H<sub>2</sub>O (cont'd)**

		n			
		0	1	2	3
m	$i = 29, \eta = 11600 \text{ cm}^{-1}$				
0	0	0	0	0	0
1	0	0	0	0	0
2	0	0	0	0	0
3	0	0	0	0	0
m	$i = 30, \eta = 12000 \text{ cm}^{-1}$				
0	-23.4075	-4.77289	-0.21987	0	
1	38.40742	8.31828	0.4140962	0	
2	-35.0421	-7.18E+00	-0.327761	0	
3	1.59E+01	3.26E+00	1.51E-01	0.00E+00	

**$d_{lmn}$  Coefficients used in Equation 3.47 for CO<sub>2</sub>**

		n			
		0	1	2	3
m	i = 1, $\eta = 300 \text{ cm}^{-1}$				
0	14.0921	-45.0083	76.58615	-38.507	
1	3.58714	-16.3422	32.33776	-17.444	
2	5484479	-3.15321	6.03382	-3.2201	
3	3.00E-02	-0.1817	0.334136	-0.1754	
4	0	0	0	0	
m	i = 2, $\eta = 600 \text{ cm}^{-1}$				
0	1.15158	-3.26518	2.59753	-0.3652	
1	0.163145	1.43612	-2.04598	1.10266	
2	2.65E-02	-3.52E-02	0.805636	-0.5708	
3	2.07E-02	-0.19222	0.492278	-0.2908	
4	1.14E-03	-5.45E-03	-1.52E-02	1.19E-02	
m	i = 3, $\eta = 900 \text{ cm}^{-1}$				
0	5.9862	-18.0877	20.66159	-7.7611	
1	0.304536	3.32031	-6.21269	3.4235	
2	-7.76E-02	0.914673	-0.81071	0.19843	
3	-8.46E-03	4.26E-02	0.232125	-0.2133	
4	0	0	0	0	
m	i = 4, $\eta = 1200 \text{ cm}^{-1}$				
0	-8.54365	85.96118	-138.22	67.8633	
1	-10.6996	73.40007	-110.148	51.7057	
2	-2.88148	17.96319	-25.6151	11.5679	
3	-0.29364	1.73138	-2.33409	1.0061	
4	-1.02E-02	5.74E-02	-7.27E-02	2.95E-02	
m	i = 5, $\eta = 1500 \text{ cm}^{-1}$				
0	6.4705	-0.57989	0	0	
1	0.432575	1.08E-02	0	0	
2	0	0	0	0	
3	0	0	0	0	
4	0	0	0	0	
m	i = 6, $\eta = 1800 \text{ cm}^{-1}$				
0	-22.6409	175.1414	-211.511	86.9663	
1	-9.237	60.50893	-74.2377	31.3632	
2	-1.09788	6.57929	-8.05278	3.45055	
3	-4.14E-02	0.233599	-0.27951	0.12002	
4	0	0	0	0	

**$d_{lmn}$  Coefficients used in Equation 3.47 for CO<sub>2</sub> (cont'd)**

		n			
		0	1	2	3
m	i = 7, $\eta = 2100 \text{ cm}^{-1}$				
0	5.19158	-18.1762	23.11375	-10.0175	
1	0.295888	0.169255	-1.13653	0.894114	
2	-8.14E-02	0.775819	-1.32523	0.683492	
3	-1.45E-02	0.152943	-0.246466	0.117372	
4	-5.76E-04	6.63E-03	-1.11E-02	4.71E-03	
m	i = 8a, $\eta = 2400 \text{ cm}^{-1}$				
0	3.71251	-9.29926	68.20571	-41.9071	
1	1.59233	-12.6548	46.65398	-26.5327	
2	0.385473	-3.35629	9.16992	-4.8462	
3	2.45E-02	-0.20647	0.5086159	-0.25443	
4	0	0	0	0	
m	i = 8b, $\eta = 2400 \text{ cm}^{-1}$				
0	2.43525	-23.4269	36.06301	-16.6106	
1	-0.60682	6.65931	-10.3374	4.72869	
2	-4.34E-02	0.440435	-1.30056	0.73577	
3	2.60E-02	-0.18921	0.4550245	-0.22424	
4	0	0	0	0	
m	i = 9, $\eta = 2700 \text{ cm}^{-1}$				
0	19.53294	6.88267	-27.5395	13.01214	
1	2.53874	4.13532	-8.25867	3.51868	
2	0.119748	0.142277	-0.295336	0.114518	
3	0	0	0	0	
4	0	0	0	0	
m	i = 10, $\eta = 3000 \text{ cm}^{-1}$				
0	57.10882	-89.4966	53.8838	-6.56494	
1	8.01819	-7.49078	-1.53514	3.55053	
2	0.303043	-8.55E-02	-0.406005	0.301169	
3	0	0	0	0	
4	0	0	0	0	
m	i = 11, $\eta = 3300 \text{ cm}^{-1}$				
0	15.70242	-38.6012	41.13481	-15.3492	
1	5.58877	-14.0059	16.22966	-6.68418	
2	1.18327	-3.27645	3.90966	-1.65808	
3	0.10818	-0.26276	0.2593289	-9.55E-02	
4	3.22E-03	-4.87E-03	3.99E-04	1.19E-03	

**d<sub>lmn</sub> Coefficients used in Equation 3.47 for CO<sub>2</sub> (cont'd)**

		n			
		0	1	2	3
m	i = 12, $\eta = 3600 \text{ cm}^{-1}$				
0	1.05772	-1.12297	1.48552	-0.29435	
1	0.225422	2.11191	-1.0328	0.582535	
2	-3.78E-02	1.04045	-2.65059	2.30773	
3	1.69E-03	-1.11E-02	0.178781	1.46E-02	
4	0	0	0	0	
m	i = 13, $\eta = 3900 \text{ cm}^{-1}$				
0	2.21539	1.57039	-2.64837	1.48911	
1	-0.86373	6.42893	-5.78834	1.56506	
2	-0.12249	0.513625	0.351379	-0.52336	
3	-3.15E-03	1.90E-03	8.20E-02	-6.62E-02	
4	0	0	0	0	
m	i = 14, $\eta = 4200 \text{ cm}^{-1}$				
0	37.1305	-97.3515	144.7474	-72.9772	
1	11.33407	-36.4884	57.95252	-30.0663	
2	1.36608	-5.05091	8.12622	-4.20333	
3	5.61E-02	-0.22263	0.358408	-0.18429	
4	0	0	0	0	
m	i = 15, $\eta = 4500 \text{ cm}^{-1}$				
0	17.60564	16.58984	-28.2868	15.67965	
1	0.754699	17.70807	-22.6973	10.31991	
2	-0.22332	2.60383	-3.17603	1.38881	
3	-1.55E-02	0.111595	-0.13376	5.77E-02	
4	0	0	0	0	
m	i = 16, $\eta = 4800 \text{ cm}^{-1}$				
0	5.23098	0.412313	8.75E-02	-0.85075	
1	0.596114	2.86911	2.36629	-3.6757	
2	2.26E-02	-0.10376	2.23556	-1.80705	
3	2.34E-03	-4.62E-02	0.243823	-0.1755	
4	0	0	0	0	
m	i = 17, $\eta = 5100 \text{ cm}^{-1}$				
0	3.43948	14.24252	-33.7441	20.07414	
1	0.823179	7.01401	-15.1667	8.68	
2	7.82E-02	1.02703	-2.04541	1.13408	
3	-2.21E-03	9.49E-02	-0.14343	6.78E-02	
4	0	0	0	0	

**$d_{lmn}$  Coefficients used in Equation 3.47 for CO<sub>2</sub> (cont'd)**

m	n			
	0	1	2	3
m	i = 18, $\eta = 5400 \text{ cm}^{-1}$			
0	4.69596	2.17386	-10.4688	7.5745
1	0.844226	1.3615	-3.33406	1.97178
2	0.490874	-2.41059	3.79997	-1.88068
3	8.88E-02	-0.50739	0.8075786	-0.39906
4	4.44E-03	-2.59E-02	4.10E-02	-2.01E-02
m	i = 19, $\eta = 5700 \text{ cm}^{-1}$			
0	14.73215	-38.1016	56.02793	-23.1993
1	1.00773	-2.49233	3.8112	-1.58693
2	0	0	0	0
3	0	0	0	0
4	0	0	0	0
m	i = 20, $\eta = 6000 \text{ cm}^{-1}$			
0	88.60791	-212.17	699.7952	30.42419
1	18.01877	-6.09152	166.0792	86.83708
2	-4.20E-02	13.49606	3.06221	27.00287
3	-0.214	2.09582	-1.66169	2.95871
4	-1.16E-02	8.87E-02	-9.91E-02	0.108894
m	i = 21, $\eta = 6300 \text{ cm}^{-1}$			
0	17.0485	-55.6963	180.4821	-127.229
1	4.65814	-21.9752	93.66551	-70.2865
2	0.693567	-4.4651	20.00938	-15.1547
3	5.83E-02	-0.40984	1.85272	-1.40874
4	1.89E-03	-1.33E-02	6.16E-02	-4.73E-02
m	i = 22, $\eta = 6600 \text{ cm}^{-1}$			
0	-38.7333	334.7941	-582.748	293.5895
1	-21.8232	177.2234	-308.523	154.9974
2	-4.11296	33.78847	-59.144	29.7639
3	-0.33499	2.83098	-4.99356	2.52504
4	-1.02E-02	8.83E-02	-0.157415	8.02E-02
m	i = 23, $\eta = 6700 \text{ cm}^{-1}$			
0	24.08093	-142.762	401.2463	-237.612
1	10.96572	-72.7851	184.0839	-106.488
2	2.0021	-13.2476	30.76956	-17.3918
3	0.16197	-1.02068	2.21961	-1.22962
4	4.86E-03	-2.88E-02	5.92E-02	-3.22E-02



## APPENDIX C

### COMPLEX INDEX OF REFRACTIONS MODELS FOR ASH PARTICLES

#### C1. Complex Index of Refraction Model Proposed by Liu

Wavelength Range ( $\mu\text{m}$ )	Refractive index (n)
0.5-6.0	1.5
6.0-8.0	$1.5-0.35(\lambda-6.0)$
8.0-11.0	$0.8+0.5(\lambda-8.0)$
11.0-12.0	$2.3-0.5(\lambda-11.0)$
Wavelength Range ( $\mu\text{m}$ )	Absorption index (k)
0.5-1.0	$10^{-4.6+2.2(\lambda-0.5)}$
1.0-4.0	$10^{-3.5}$
4.0-5.0	$10^{-3.5+(\lambda-4.0)}$
5.0-7.5	$10^{-2.5+0.24(\lambda-5.0)}$
7.5-8.5	$10^{-1.9+1.8(\lambda-7.5)}$
8.5-10.5	$10^{-4.6+2.2(\lambda-0.5)}$
10.5-12.0	$10^{-0.1-0.733(\lambda-10.5)}$

*F. Liu, J. Swithenbank, "The effects of particle size distribution and refractive index on fly-ash radiative properties using a simplified approach", Int. J. Heat Mass Transfer, 36 (1993) 1905–1912.*

## C2. Complex Index of Refraction Model Proposed by Marakis

Wavelength Range ( $\mu\text{m}$ )	Refractive index (n)
0.5-6.0	1.5
6.0-8.0	$1.5-0.4(\lambda-6)$
8.0-11.0	$0.8+0.5(\lambda-8)$
11.0-12.0	$2.3-0.5(\lambda-11)$
Wavelength Range ( $\mu\text{m}$ )	Absorption index (k)
0.5-1.0	$10^{-4.6+2.2(\lambda-0.5)}$
1.0-4.0	$10^{-3.5}$
4.0-5.0	$10^{-3.5+(\lambda-4.0)}$
5.0-5.5	$10^{-2.5+0.3(\lambda-5.0)}$
5.5-7.8	$10^{-2.2+0.4(\lambda-5.5)}$
7.8-8.5	$10^{-1.4+1.8(\lambda-7.8)}$
8.5-12.0	$10^{-0.1-0.7(\lambda-10.5)}$

*J.G. Marakis, C. Papapavlou, E. Kakaras, "A Parametric Study of Radiative Heat Transfer in Pulverised Coal Furnaces" Int. J. Heat Mass Transfer, 43(16) (2000) 2961–2971.*

### C3. Complex Index of Refraction Model Proposed by Bahador

Wavelength Range ( $\mu\text{m}$ )	Refractive index (n)
0.5-3.4	1.5
3.4-7.2	$1.5-0.074(\lambda-3.4)$
7.2-8.2	$1.22-0.46(\lambda-7.2)$
8.2-11.0	$0.76+0.57(\lambda-8.2)$
11.0-	$2.3-0.56(\lambda-11)$
Wavelength Range ( $\mu\text{m}$ )	Absorption index (k)
0.2-0.5	$10^{-2.96-4.6(\lambda-0.22)}$
0.5-1.0	$10^{-4.48+1.96(\lambda-0.5)}$
1.0-4.0	$10^{-3.5}$
4.0-5.0	$10^{-3.5+1.0(\lambda-4)}$
5.0-7.5	$10^{-2.5+0.26(\lambda-5)}$
7.5-8.5	$10^{-1.86+1.76(\lambda-7.5)}$
8.5-10.5	$10^{-0.1}$
10.5-	$10^{-0.1-1.0(\lambda-10.5)}$

*M. Bahador, B. Sunden, "Investigation on the effects of fly ash particles on the thermal radiation in biomass fired boilers", Int. J. Heat Mass Transfer, 51 (2008) 2411–2417.*

#### C4. Complex Index of Refraction Model Proposed by Johansson

##### C4.1. Ash Particles containing Iron Oxide

Wavelength Range ( $\mu\text{m}$ )	Refractive index (n)
0.0-6.0	1.5
6.0-8.0	$1.5-0.35(\lambda-6)$
8.0-11.0	$0.8+0.5(\lambda-8)$
11.0-12.0	$2.3-0.5(\lambda-11)$
12.0-	1.8
Wavelength Range ( $\mu\text{m}$ )	Absorption index (k)
0.0-0.5	$1.0 \times 10^{-3} - 1.86 \times 10^{-3} \lambda$
0.5-1.5	$-2.45 \times 10^{-4} + 6.3 \times 10^{-4} \lambda$
1.5-4.0	$7.0 \times 10^{-4}$
4.0-7.0	$-9.02 \times 10^{-3} + 2.43 \times 10^{-3} \lambda$
7.0-9.0	$-3.46 + 0.496 \lambda$
9.0-11.0	1.0
11.0-12.0	$8.7 - 0.7 \lambda$
12.0-	0.3

#### C5. Complex Index of Refraction Model Proposed by Johansson

##### C4.2. Ash Particles containing Carbon Residue

Wavelength Range ( $\mu\text{m}$ )	Refractive index (n)
0.0-6.0	1.5
6.0-8.0	$1.5-0.35(\lambda-6)$
8.0-11.0	$0.8+0.5(\lambda-8)$
11.0-12.0	$2.3-0.5(\lambda-11)$
12.0-	1.8
Wavelength Range ( $\mu\text{m}$ )	Absorption index (k)
0.0-2.6	$-1.5 \times 10^{-3} + 7.5 \times 10^{-3} \lambda$
2.6-5.0	$0.0119 + 2.33 \times 10^{-3} \lambda$
5.0-9.0	$-1.19 + 0.244 \lambda$
9.0-11.0	1.0
11.0-12.0	$8.7 - 0.7 \lambda$
12.0-	0.3

*R. Johansson, B. Leckner, K. Andersson, F. Johnsson, "Influence of particle and gas radiation in oxy-fuel combustion", Int. J. Heat Mass Transfer, 65 (2013) 143–152.*

**C5. Complex Index of Refraction Model Proposed by Johansson (II) for Ash Particles containing High Carbon Residue**

<b>Wavelength Range (<math>\mu\text{m}</math>)</b>	<b>Refractive index (n)</b>
0.0-6.0	1.5
6.0-8.0	$1.5-0.35(\lambda-6)$
8.0-11.0	$0.8+0.5(\lambda-8)$
11.0-12.0	$2.3-0.5(\lambda-11)$
12.0-	1.8
<b>Wavelength Range (<math>\mu\text{m}</math>)</b>	<b>Absorption index (k)</b>
0.0-2.6	$-1.5 \times 10^{-3} + 7.5 \times 10^{-3} \lambda$
2.6-7.0	$0.0119 + 2.33 \times 10^{-3} \lambda$
7.0-9.0	$-3.39 + 0.488 \lambda$
9.0-11.0	1
11.0-12.0	$8.7 - 0.7 \lambda$
12.0-	0.3

*R. Johansson, T. Gronarz, R. Kneer, "Influence of index of refraction and particle size distribution on radiative heat transfer in a pulverized coal combustion furnace" J. Heat Transfer, 139 (2017) 042702-1-8.*

## C6. Complex Index of Refraction Model Proposed by Goodwin

### C6.1 Calculation of Spectral Refractive Indices (n) between 1-8 μm

Goodwin developed a mixture rule to allow calculation of  $n$  as a function of composition in the wavelength range of 1-8 of μm. The mixture rule for  $n$  assumes that the refractivity is a linear function of composition, with two empirical adjustments. After these modifications, mixture rule for  $n$  was given as follows,

$$\frac{n^2 - 1}{n^2 + 2} = \rho \sum_i X_{m,i} F_i(\lambda) \quad (\text{C. 1})$$

$$n(\lambda) = \left( \frac{1 + 2\rho \sum_i X_{m,i} F_i(\lambda)}{1 - \sum_i X_{m,i} F_i(\lambda)} \right)^{0.5} \quad (\text{C. 2})$$

where  $\rho$  is the sample density (in g/cm<sup>3</sup>) and  $F_i(\lambda)$  is the fitting function for component  $i$ , which is defined as,

$$F_i(\lambda) = \frac{(a_i \lambda^2 - b_i)}{(c_i \lambda^2 - d_i)} \quad (\text{C. 3})$$

Fitting parameters for the function  $F_i(\lambda)$  is given in Table C1.

Table C1. Fitting parameters for the mixture rule

	<b>F(SiO<sub>2</sub>)</b>	<b>F(Al<sub>2</sub>O<sub>3</sub>)</b>	<b>F(CaO)</b>	<b>F(Fe<sub>2</sub>O<sub>3</sub>)</b>	<b>F(MgO)</b>	<b>F(TiO<sub>2</sub>)</b>
a	0.9389	1.914	4.250	1.647	1.278	2.72
b	53	174	827.7	0.00	136.9	260.0
c	5.001	10.36	16.63	11.36	7.433	15.80
d	420	1633.8	6102.3	0.00	1200.9	1954.4

The mixture rule includes only the six oxides given in Table C1. It should be noted that these oxides account for roughly 95% - 97% by weight of typical coal ashes. The oxides not included in the mixture rule were excluded by Goodwin due to the lack of refractive index data for these components. Nevertheless, he suggested that mixture rule can be extended to include other components with two different approaches.

- (i) Use Eq. (C.2) directly, ignoring the other components. This is equivalent to assuming the excluded components have zero refractivity ( $n \ll 1$ ).
- (ii) Normalize the weight fractions of the six oxides included in the mixture rule to 1.0 before employing Eq. (C.2). This is essentially equivalent to setting the refractivity of the excluded components equal to the average refractivity of the included components.

Goodwin showed that both procedures give similar results, where the agreement is slightly better for the normalized results. Nevertheless, it should be noted that if the excluded components constitute a large fraction of the total mass, these approximate procedures cannot be expected to be accurate.

### C6.2 Calculation of Spectral Absorption Indices (k) between 1-4 $\mu\text{m}$

The predominant absorber in the infrared for wavelengths below about 4  $\mu\text{m}$  is iron oxide. Goodwin provided a simple expression which represents two different Fe absorption mechanisms in the infrared region. This equation allows to calculate spectral absorption indices as a function of wavelength, Fe content, and oxidation state of Fe,

$$k(\lambda) = a_1 e^{b/\lambda} + a_2 g(\lambda) \quad (\text{C. 4})$$

where the exponent  $b$  and the function  $g(\lambda)$  are independent of composition. Composition dependency comes from the variables  $a_1$  and  $a_2$ . Goodwin expressed composition dependency of  $k$  through  $a_1$  and  $a_2$  by fitting experimental measurements of various ash samples with weight percent of  $\text{Fe}_2\text{O}_3$  and the ferrous ratio ( $r$ ), which gives the following expression,

$$k(\lambda) = 3.61 \times 10^{-7} \rho^2 (1 - r) (\text{Fe}_2\text{O}_3)^2 e^{\frac{1.75}{\lambda}} + \rho r (\text{Fe}_2\text{O}_3) [0.0963 + 0.0011 \rho r (\text{Fe}_2\text{O}_3)] g(\lambda) \quad (\text{C. 5})$$

where

$\rho$  is the sample density ( $\text{g}/\text{cm}^3$ ) and  $(\text{Fe}_2\text{O}_3)$  is the  $\text{Fe}_2\text{O}_3$  weight percent,  $r$  is the ferrous ratio,

$$r = \frac{Fe^{2+}}{Fe^{2+} + Fe^{3+}} \quad (C. 6)$$

$g(\lambda)$  characterizes the  $Fe^{2+}$  absorption spectrum and  $g(\lambda)$  values derived by Goodwin are given in Table C2.

Table C2. Data for the function  $g(\lambda)$

$\lambda$	$g(\lambda)$	$\lambda$	$g(\lambda)$
0.7	0.304	2.4	2.002
0.8	0.727	2.5	1.941
0.9	1.355	2.6	1.898
1.0	2.025	2.7	1.891
1.1	2.488	2.8	1.892
1.2	2.641	2.9	1.904
1.3	2.521	3.0	1.919
1.4	2.318	3.1	1.928
1.5	2.202	3.2	1.94
1.6	2.213	3.3	1.948
1.7	2.32	3.4	1.97
1.8	2.422	3.5	1.994
1.9	2.463	3.6	2.015
2	2.424	3.7	2.048
2.1	2.332	3.8	2.077
2.2	2.213	3.9	2.115
2.3	2.094	4.0	2.153

### C6.3 Calculation of Spectral Absorption Indices (k) between 4-8 $\mu\text{m}$

Absorption in the 4-8  $\mu\text{m}$  region is mainly originated from the silica content of the ash by means of vibrational absorption mechanisms. Measurements of Goodwin indicated that absorption in this wavelength region is not significantly affected by the presence of the other oxides. Therefore, he expressed the absorption index (k) by a simple scaling law with respect to  $\text{SiO}_2$  content of the ash,

$$k(\lambda) = \frac{\rho}{\rho_{\text{SiO}_2}} X_{\text{SiO}_2} k_0(\lambda) \quad (C. 7)$$

where is the  $\text{SiO}_2$  absorption index data. Goodwin's measurements on spectral silica absorption indices are given in Table C3.



Table C3. SiO<sub>2</sub> absorption index data

$\lambda$	$k_0(\lambda)$	$\lambda$	$k_0(\lambda)$
4	0.0000579	5.405	0.00572
4.082	0.0000799	5.556	0.00563
4.167	0.000107	5.882	0.00594
4.255	0.000132	6.061	0.00632
4.348	0.000213	6.154	0.00646
4.396	0.000265	6.25	0.00652
4.444	0.000284	6.452	0.00657
4.494	0.000284	6.667	0.00716
4.545	0.000256	6.897	0.00851
4.651	0.000262	7.143	0.0106
4.762	0.000485	7.407	0.0148
4.878	0.00182	7.692	0.0372
5	0.00398	7.752	0.0474
5.063	0.00512	7.813	0.0768
5.128	0.00518	7.874	0.132
5.263	0.00549	7.937	0.216
5.333	0.00569	8	0.323

In the calculations, this experimental data is fitted to polynomial functions (Eq. C.8). A visual comparison of the fitting function and measurements is presented in Figure C1.

for  $4 \leq \lambda \leq 4.4$ :

$$k_0(\lambda) = -0.0705119\lambda + 0.0514052\lambda^2 - 0.0125009\lambda^3 + 0.0010144\lambda^4 \quad (\text{C. 8.1})$$

for  $4.4 < \lambda \leq 4.8$ :

$$k_0(\lambda) = -0.4879839\lambda + 0.3234942\lambda^2 - 0.0714526\lambda^3 + 0.0052591\lambda^4 \quad (\text{C. 8.2})$$

for  $4.8 < \lambda \leq 5.4$ :

$$k_0(\lambda) = 219.3123 - 173.6359\lambda + 51.49852\lambda^2 - 6.781594\lambda^3 + 0.3345718\lambda^4 \quad (\text{C. 8.3})$$

for  $5.4 < \lambda \leq 6.4$ :

$$k_0(\lambda) = -0.9501931\lambda + 0.6835954\lambda^2 - 0.1834775\lambda^3 + 0.0218031\lambda^4 - 0.0009681\lambda^5 \quad (\text{C. 8.4})$$

for  $6.4 < \lambda \leq 7.7$ :

$$k_0(\lambda) = 20.66834\lambda - 12.00397\lambda^2 + 2.613003\lambda^3 - 0.2526626\lambda^4 + 0.0091574\lambda^5 \quad (\text{C. 8.5})$$

for  $7.7 < \lambda \leq 8.0$ :

$$k_0(\lambda) = 146.2145\lambda - 52.81511\lambda^2 + 6.32314\lambda^3 - 0.2506528\lambda^4 \quad (\text{C. 8.6})$$

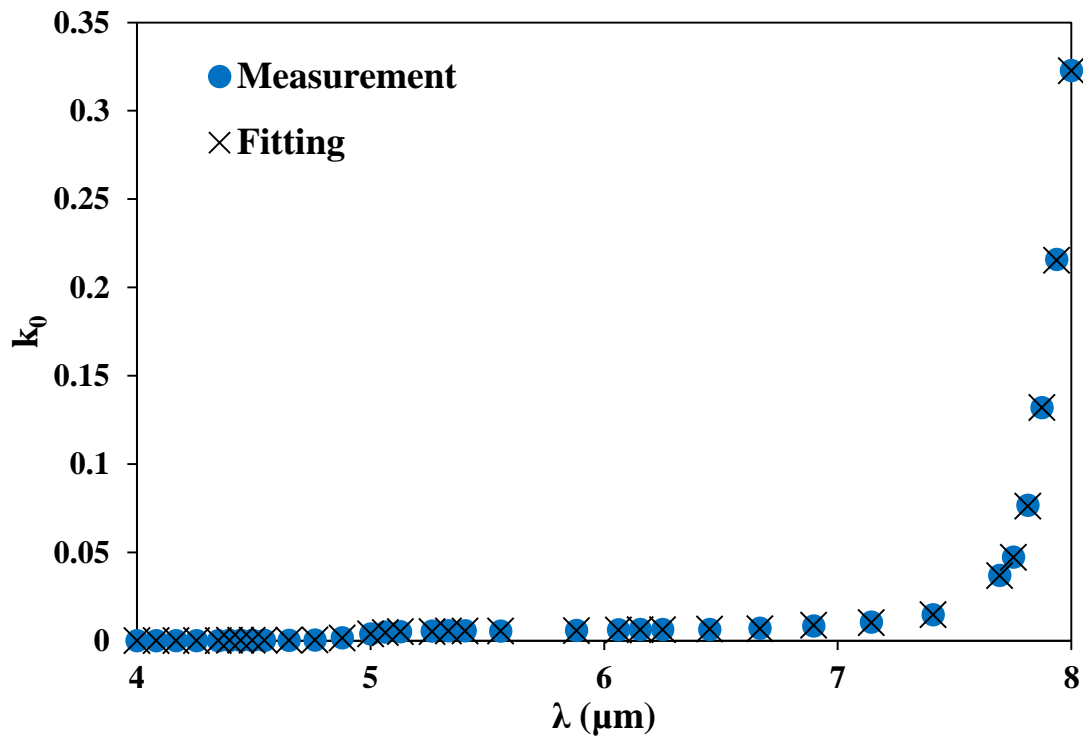


Figure C1. Comparison of silica absorption index measurements and fitted polynomial utilized in the study

#### C6.4 Calculation of Spectral Refractive (n) and Absorption (k) Indices between 8-13 $\mu\text{m}$

Absorption band in 8-13  $\mu\text{m}$  region is due to vibrational absorption by Si-O-Si and Si-O<sup>-</sup> bonds. In this region, optical constants were described by a multiple oscillator model which gives m rather than giving n and k separately,

$$m^2 = n_{\infty}^2 + \sum_j \frac{\omega_{pj}^2}{\omega_{0j}^2 - \omega^2 - i\gamma_j\omega} \quad (\text{C. 9})$$

Where  $\omega = 1/\lambda$ ,  $\omega_{pj}$ ,  $\omega_{0j}$  and  $\gamma_j$  are the strength, position and width of the j<sup>th</sup> oscillator, respectively.

If m in Eq. (C.9) is explicitly expressed, two equations are obtained:

$$n^2 - k^2 = n_{\infty}^2 + \sum_j \frac{\omega_{pj}^2(\omega_j^2 - \omega^2)}{(\omega_j^2 - \omega^2)^2 + \gamma_j^2\omega^2} \quad (\text{C. 10})$$

$$-2nk = \sum_j \frac{\omega_{pj}^2\gamma_j\omega}{(\omega_j^2 - \omega^2)^2 + \gamma_j^2\omega^2} \quad (\text{C. 11})$$

Goodwin found that two oscillators are sufficient to describe the 8-12  $\mu\text{m}$  region and a third was added to account for the rise near 13  $\mu\text{m}$ .

These three oscillation peaks are defined as follows,

$$\left(\frac{\omega_{p1}}{\omega_{0,1}}\right)^2 = (0.425 - 0.60X_{\text{Fe2O3}}) \left(\frac{X_{\text{SiO2}}}{0.52}\right) \quad (\text{C. 12})$$

$$\left(\frac{\omega_{p2}}{\omega_{0,2}}\right)^2 = (0.175 + 0.75X_{\text{Fe2O3}}) \left(\frac{X_{\text{SiO2}}}{0.52}\right) \quad (\text{C. 13})$$

$$\left(\frac{\omega_{p3}}{\omega_{0,3}}\right)^2 = (0.053) \left(\frac{X_{\text{SiO}}}{0.52}\right) \quad (\text{C. 14})$$

Fitting parameters for these three oscillations are given in Table C4.

Table C4. Fitting parameters for the multiple oscillator model

	$n_{\infty}^2$	$\omega_{0,j}$	$\gamma_j$
1 <sup>st</sup> oscillation	2.15	1062.8	164.7
2 <sup>nd</sup> oscillation		955.8	79.1
3 <sup>rd</sup> oscillation		762	27.5

In this study, n and k parameters are solved analytically from the oscillator model and separate solutions are obtained as shown below:

$$n^2 - k^2 = n_{\infty}^2 + \sum_j \frac{\omega_{pj}^2(\omega_j^2 - \omega^2)}{(\omega_j^2 - \omega^2)^2 + \gamma_j^2\omega^2} = A \quad (C. 15)$$

$$2nk = \sum_j \frac{\omega_{pj}^2\gamma_j\omega}{(\omega_j^2 - \omega^2)^2 + \gamma_j^2\omega^2} = B \quad (C. 16)$$

$$n = \sqrt{\frac{A}{2} + \frac{\sqrt{A^2 + B^2}}{2}} \quad (C. 17)$$

$$k = \frac{B}{2\sqrt{\frac{A}{2} + \frac{\sqrt{A^2 + B^2}}{2}}} \quad (C. 18)$$

### C6.5 Calculation of Spectral Refractive (n) and Absorption (k) Indices between 13-20 $\mu\text{m}$

No experimental data are reported for the long wavelength region  $\lambda > 13 \mu\text{m}$ . Following the suggestion of Goodwin, the optical constants in this range are assumed to be dominated by the Reststrahlen bands of  $\text{Al}_2\text{O}_3$  and  $\text{MgO}$ . Therefore, a simple summation rule is deployed based on based on the mass fractions of  $\text{Al}_2\text{O}_3$  and  $\text{MgO}$ ,

$$n(\lambda) = \sum x_i n_i(\lambda) \quad (C. 19)$$

$$k(\lambda) = \sum x_i k_i(\lambda) \quad (C. 20)$$

Complex index of refraction data of Al<sub>2</sub>O<sub>3</sub> and MgO is taken from the literature, which is also shown in Table C5.

Table C5. Spectral refractive (n) and absorption (k) indices for Al<sub>2</sub>O<sub>3</sub> and MgO

Wavelength ( $\mu\text{m}$ )	Al <sub>2</sub> O <sub>3</sub>		MgO	
	n	k	n	k
13.33	0.121	1.637	0.503	0.0475
13.51	0.122	1.736	0.393	0.0913
13.7	0.122	1.836	0.267	0.172
13.89	0.124	1.947	0.156	0.317
14.09	0.126	2.058	0.139	0.478
14.29	0.129	2.169	0.132	0.595
14.49	0.131	2.296	0.134	0.692
14.71	0.142	2.441	0.136	0.787
14.93	0.167	2.585	0.143	0.877
15.15	0.192	2.811	0.154	0.955
15.39	0.251	3.175	0.155	1.03
15.63	0.807	3.642	0.151	1.09
15.87	0.502	3.04	0.135	1.17
16.13	0.361	3.479	0.116	1.26
16.39	0.377	4.082	0.108	1.35
16.67	0.516	4.784	0.098	1.45
16.95	2.155	5.601	0.086	1.56
17.24	4.935	7.345	0.087	1.67
17.54	6.703	5.552	0.086	1.78
17.86	7.407	0.816	0.088	1.9
18.18	5.406	0.487	0.089	2.03
18.52	4.391	0.378	0.091	2.16
18.87	3.526	0.35	0.093	2.31
19.23	2.722	0.357	0.097	2.47
19.61	2.089	0.584	0.102	2.64
20	1.674	1.002	0.109	2.84
Complex index of refraction data is taken from: E. D. Palik, Handbook of Optical Constants of Solids, Elsevier Inc., 1997.				

*D.G. Goodwin, "Infrared Optical Constants of Coal Slags", PhD Thesis, Stanford University, Stanford, USA, 1986.*

## C7. Complex Index of Refraction Model Proposed by Ebert

### C7.1 Density Calculation

If the sample density (skeletal density) is not known, it can be calculated from a simple summation rule based on effective densities of each oxide as follows,

$$\frac{1}{\rho} = \sum x_i / \rho_i \quad (\text{C. 21})$$

where  $x_i$  is the weight fraction of oxide  $i$ , and  $\rho_i$  is the density of oxide  $i$  in glass. It should be noted that using free oxide densities leads to over-prediction of the samples while densities in glass (i.e. effective densities) were shown to lead to errors less than 3% for various samples. These effective densities are given in Table C6. It should also be noted that silicate glasses have low thermal expansion coefficients (for Aluminosilicate, it is  $3.3 \times 10^{-6} / ^\circ\text{C}$ ).

Table C5. Oxide densities in glass at room temperature

Oxide	Oxide density in glass (g/cm <sup>3</sup> )
SiO <sub>2</sub>	2.28
Al <sub>2</sub> O <sub>3</sub>	2.5
CaO	3.9
Fe <sub>2</sub> O <sub>3</sub>	5.24
MgO	3.3
TiO <sub>2</sub>	3.8
Na <sub>2</sub> O	3.1
K <sub>2</sub> O	2.8
BaO	7

### C7.2 Calculation of Spectral Refractive Indices (n) between 1-8 μm

In Ebert's model, refractive index  $n$  is also calculated by using a summation rule in the wavelength region between 1-8 μm.

$$\frac{n^2 - 1}{n^2 + 2} = \rho \sum_i \frac{X_{m,i}}{\rho_i} \frac{n_i^2 - 1}{n_i^2 + 2} \quad (\text{C. 22})$$

where  $X_{m,i}$  is the mass fraction of the species  $i$ ,  $\rho_i$  is its density and  $n_i$  is its refractive index.  $n_i$  is found for each specie as follows,

$$n_i^2 = 1 + C_i - \frac{B_i \lambda^2}{\lambda_{0,i}^2 - \lambda^2} \quad (\text{C.23})$$

$C_i$ ,  $B_i$  and  $\lambda_{0,i}$  values are given in Table C6.

Table C6. Dispersion equation (C.23) parameters for oxides

	SiO <sub>2</sub>	Al <sub>2</sub> O <sub>3</sub>	CaO	Fe <sub>2</sub> O <sub>3</sub>	TiO <sub>2</sub>	MgO
$\rho_i$	2.20	3.97	3.31	5.24	4.86	3.58
$C_i$	1.104	2.082	2.31	8.3636	5.031	1.9625
$B_i$	0.8975	5.281	11.32	0	7.764	2.47
$\lambda_{0,i}$	9.896	17.93	33.9	0	15.6	15.56

Ebert also modified Eq. (C.23) to account for the shift in  $\lambda_0$  with decreasing silica content,

$$n_{SiO_2}^2 = 1 + C_{SiO_2} - \frac{B_{SiO_2} \lambda^2}{(\lambda_{0,SiO_2} + \delta \lambda_{0,SiO_2})^2 - \lambda^2} \quad (\text{C.24})$$

$$\delta \lambda_{0,SiO_2} = 2.82 - 2.90 \hat{x}_{SiO_2} \quad (\text{C.25})$$

where  $\hat{x}_{SiO_2}$  is the mole fraction of SiO<sub>2</sub>.

In the calculations,  $n$  is found explicitly from the following equation,

$$\frac{n^2 - 1}{n^2 + 2} = \rho \sum_i \frac{X_{m,i}}{\rho_i} \frac{n_i^2 - 1}{n_i^2 + 2} = \alpha \quad (\text{C.26})$$

$$n = \left| \frac{\sqrt{\alpha + 1 - 2\alpha^2}}{\alpha - 1} \right| \quad (\text{C.27})$$

### C7.3 Calculation of Absorption Indices (k) between 1-4 μm

Ebert proposed a very simple equation for the absorption index (k) in this wavelength region. He correlated absorption index (k) with iron oxide content by using 16 different samples and formulated the following relationship,

$$k(\text{Fe}) = (4.02X_{\text{Fe}_2\text{O}_3} + 16.9X_{\text{Fe}_2\text{O}_3}^2)10^{-3} \quad (\text{C. 28})$$

where  $X_{\text{Fe}_2\text{O}_3}$  is the iron oxide mass fraction.

### C7.4 Calculation of Absorption Indices (k) between 4-8 μm

In this region, absorption index k is described by two-phonon model,

$$k = k_0 + k_b \left[ 1 + \frac{2}{\exp\left(\frac{C_2}{2\lambda T}\right) - 1} \right] \quad (\text{C. 29})$$

$$k_b = \frac{A_0}{\omega} \exp\left(-\frac{\omega}{B_0}\right), \quad \omega < \omega^* \quad (\text{C. 30})$$

$$k_b = \frac{A_1}{\omega} \exp\left(-\frac{\omega}{B_1}\right), \quad \omega > \omega^* \quad (\text{C. 31})$$

$$\omega^* = \frac{\ln(A_1/A_0)}{\frac{1}{B_1} - \frac{1}{B_0}} \quad (\text{C. 32})$$

$$k_0 = A_{k_0} \exp\left[-\left(\frac{\omega - B_{k_0}}{C_{k_0}}\right)^2\right] \quad (\text{C. 33})$$

where  $C_2$  is the second blackbody emissive power constant. All constants used in Eqs. 29-33 are given in Table C7.



Table C7. Parameters used in the evaluation of absorption index (k) between 4-8  $\mu\text{m}$

$A_0$ ( $\text{cm}^{-1}$ )	295
$B_0$ ( $\text{cm}^{-1}$ )	443
$A_1$ ( $\text{cm}^{-1}$ )	51370
$B_1$ ( $\text{cm}^{-1}$ )	200
$A_{k0}$	0.0015
$B_{k0}$ ( $\text{cm}^{-1}$ )	1800
$C_{k0}$ ( $\text{cm}^{-1}$ )	110
$C_2$ ( $\mu\text{mK}$ )	14388

It should be noted that frequency  $\omega$  in Eqs. 29-33 should be modified to account for the shifts in oscillations according to the silica content of the sample;

$$\omega = \omega + \delta\omega = \omega + 355(0.678 - \hat{x}_{\text{SiO}_2}) \quad (\text{C. 34})$$

where  $\hat{x}_{\text{SiO}_2}$  is mole fraction of silica in the sample.

### C7.5 Calculation of Spectral Refractive (n) and Absorption (k) Indices between 8-13 $\mu\text{m}$

Ebert developed a single Lorentz harmonic oscillator model equation for the spectral range of 8-13  $\mu\text{m}$ . Nevertheless, he stated that previous multiple oscillatory model can also be used. In this study, multiple oscillations are used based on his suggestion.

Absorption band in 8-13  $\mu\text{m}$  region is due to vibrational absorption by Si-O-Si and Si-O bonds. In this region, optical constants were described by a multiple oscillator model which gives m rather than giving n and k separately,

$$m^2 = n_\infty^2 + \sum_j \frac{\omega_{pj}^2}{\omega_{0j}^2 - \omega^2 - i\gamma_j\omega} \quad (\text{C. 35})$$

Where  $\omega = 1/\lambda$ ,  $\omega_{pj}$ ,  $\omega_{0j}$  and  $\gamma_j$  are the strength, position and width of the  $j^{\text{th}}$  oscillator, respectively.

If m in Eq. (C.9) is explicitly expressed, two equations are obtained:

$$n^2 - k^2 = n_\infty^2 + \sum_j \frac{\omega_{pj}^2(\omega_j^2 - \omega^2)}{(\omega_j^2 - \omega^2)^2 + \gamma_j^2\omega^2} \quad (\text{C. 36})$$

$$-2nk = \sum_j \frac{\omega_{pj}^2 \gamma_j \omega}{(\omega_j^2 - \omega^2)^2 + \gamma_j^2 \omega^2} \quad (\text{C. 37})$$

Goodwin found that two oscillators are sufficient to describe the 8-12  $\mu\text{m}$  region and a third was added to account for the rise near 13  $\mu\text{m}$ .

These three oscillation peaks are defined as follows,

$$\left(\frac{\omega_{p1}}{\omega_{0,1}}\right)^2 = (0.425 - 0.60X_{\text{Fe2O3}}) \left(\frac{X_{\text{SiO2}}}{0.52}\right) \quad (\text{C. 38})$$

$$\left(\frac{\omega_{p2}}{\omega_{0,2}}\right)^2 = (0.175 + 0.75X_{\text{Fe2O3}}) \left(\frac{X_{\text{SiO2}}}{0.52}\right) \quad (\text{C. 39})$$

$$\left(\frac{\omega_{p3}}{\omega_{0,3}}\right)^2 = (0.053) \left(\frac{X_{\text{SiO}}}{0.52}\right) \quad (\text{C. 40})$$

Fitting parameters for these three oscillations are given in Table C8.

Table C8. Fitting parameters for the multiple oscillator model

	$n_{\infty}^2$	$\omega_{0,j}$	$\gamma_j$
1 <sup>st</sup> oscillation	2.15	1062.8	164.7
2 <sup>nd</sup> oscillation		955.8	79.1
3 <sup>rd</sup> oscillation		762	27.5

In this study, n and k parameters are solved analytically from the oscillator model and separate solutions are obtained as shown below:

$$n^2 - k^2 = n_{\infty}^2 + \sum_j \frac{\omega_{pj}^2 (\omega_j^2 - \omega^2)}{(\omega_j^2 - \omega^2)^2 + \gamma_j^2 \omega^2} = A \quad (\text{C. 41})$$

$$2nk = \sum_j \frac{\omega_{pj}^2 \gamma_j \omega}{(\omega_j^2 - \omega^2)^2 + \gamma_j^2 \omega^2} = B \quad (\text{C. 42})$$

$$n = \sqrt{\frac{A}{2} + \frac{\sqrt{A^2 + B^2}}{2}} \quad (\text{C. 43})$$

$$k = \frac{B}{2\sqrt{\frac{A}{2} + \frac{\sqrt{A^2 + B^2}}{2}}} \quad (\text{C. 44})$$

### C6.5 Calculation of Spectral Refractive (n) and Absorption (k) Indices between 13-20 $\mu\text{m}$

No experimental data are reported for the long wavelength region  $\lambda > 13 \mu\text{m}$  in Ebert's work. Following the previous suggestion of Goodwin, the optical constants in this range are assumed to be dominated by the Reststrahlen bands of  $\text{Al}_2\text{O}_3$  and  $\text{MgO}$ . Therefore, a simple summation rule is deployed based on based on the mass fractions of  $\text{Al}_2\text{O}_3$  and  $\text{MgO}$ ,

$$n(\lambda) = \sum x_i n_i(\lambda) \quad (\text{C. 45})$$

$$k(\lambda) = \sum x_i k_i(\lambda) \quad (\text{C. 46})$$

Complex index of refraction data of  $\text{Al}_2\text{O}_3$  and  $\text{MgO}$  is taken from the literature, which is also shown in Table C9.

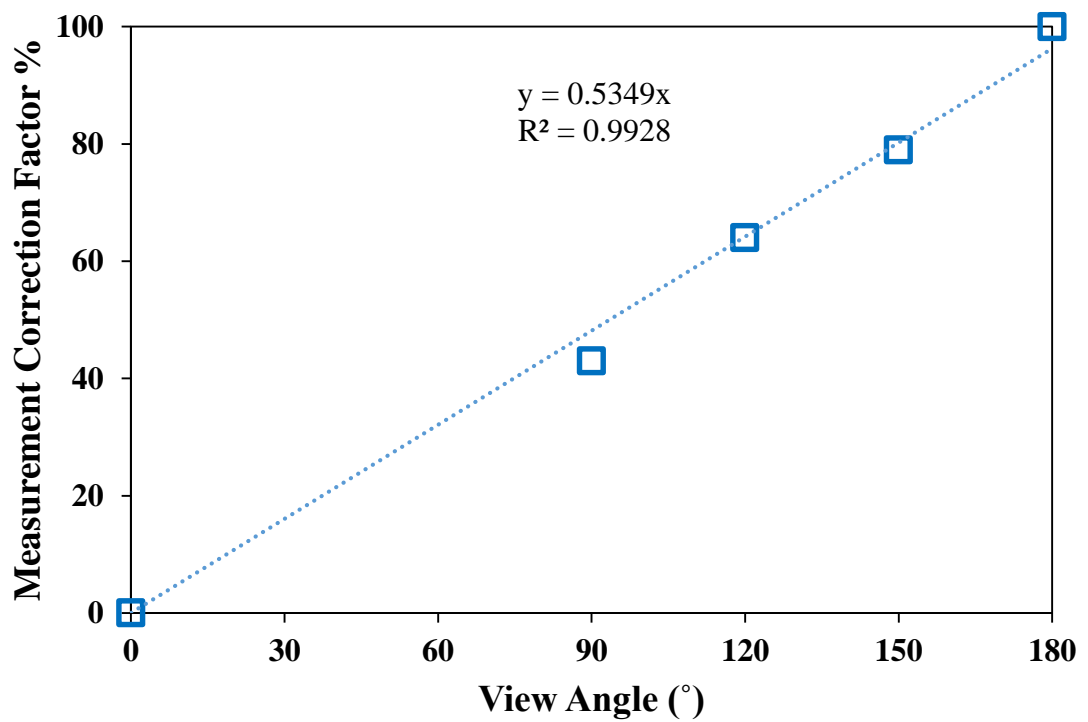
Table C9. Spectral refractive (n) and absorption (k) indices for Al<sub>2</sub>O<sub>3</sub> and MgO

Wavelength ( $\mu\text{m}$ )	Al <sub>2</sub> O <sub>3</sub>		MgO	
	n	k	n	k
13.33	0.121	1.637	0.503	0.0475
13.51	0.122	1.736	0.393	0.0913
13.7	0.122	1.836	0.267	0.172
13.89	0.124	1.947	0.156	0.317
14.09	0.126	2.058	0.139	0.478
14.29	0.129	2.169	0.132	0.595
14.49	0.131	2.296	0.134	0.692
14.71	0.142	2.441	0.136	0.787
14.93	0.167	2.585	0.143	0.877
15.15	0.192	2.811	0.154	0.955
15.39	0.251	3.175	0.155	1.03
15.63	0.807	3.642	0.151	1.09
15.87	0.502	3.04	0.135	1.17
16.13	0.361	3.479	0.116	1.26
16.39	0.377	4.082	0.108	1.35
16.67	0.516	4.784	0.098	1.45
16.95	2.155	5.601	0.086	1.56
17.24	4.935	7.345	0.087	1.67
17.54	6.703	5.552	0.086	1.78
17.86	7.407	0.816	0.088	1.9
18.18	5.406	0.487	0.089	2.03
18.52	4.391	0.378	0.091	2.16
18.87	3.526	0.35	0.093	2.31
19.23	2.722	0.357	0.097	2.47
19.61	2.089	0.584	0.102	2.64
20	1.674	1.002	0.109	2.84
Complex index of refraction data is taken from: E. D. Palik, Handbook of Optical Constants of Solids, Elsevier Inc., 1997.				

*J. L. Ebert, "Infrared Optical Properties of Coal Slag at High Temperatures" PhD Thesis (1994), Stanford University, Stanford, USA.*

## APPENDIX D

### RADIOMETER CALIBRATION CURVE



View of the Medtherm 48P (ZnSe)-20-22K used in radiative heat flux measurements was 150°. Accordingly, a correction factor of 0.79 was utilized to calculate actual incident radiative heat fluxes.



## APPENDIX E

### PSD MEASUREMENTS FOR THE COMBUSTION TESTS

#### E1. Coal Combustion Tests in 300 kWt ABFBC

Table E1. Size distribution of cyclone ash of Test 1

SIEVE OPENING, mm	DIFFERENTIAL WEIGHT, %	CUMULATIVE WEIGHT, %
1.7000	0.00	0.00
1.4000	0.00	0.00
1.1800	0.00	0.00
1.0000	0.00	0.00
0.8500	0.00	0.00
0.7100	0.37	0.37
0.6000	0.64	1.01
0.4925	5.21	6.21
0.4042	3.37	9.58
0.3318	2.05	11.63
0.2723	1.64	13.27
0.2235	2.17	15.44
0.1834	3.44	18.88
0.1506	4.95	23.83
0.1236	6.20	30.02
0.1014	7.03	37.05
0.0833	7.40	44.46
0.0683	7.33	51.78
0.0561	6.84	58.62
0.0460	6.18	64.80

Table E1. Size distribution of cyclone ash of Test 1 (cont'd)

SIEVE OPENING, mm	DIFFERENTIAL WEIGHT, %	CUMULATIVE WEIGHT, %
0.0378	5.50	70.30
0.0310	4.91	75.21
0.0255	4.41	79.62
0.0209	3.92	83.54
0.0172	3.43	86.97
0.0141	2.93	89.90
0.0116	2.44	92.34
0.0095	1.95	94.29
0.0078	1.50	95.79
0.0064	1.11	96.90
0.0052	0.76	97.66
0.0043	0.49	98.16
0.0035	0.35	98.51
0.0029	0.30	98.80
0.0024	0.30	99.10
0.0020	0.32	99.42
0.0016	0.30	99.71
0.0013	0.21	99.92
0.0005	0.08	100.00



Table E2. Size distribution of cyclone ash of Test 2

SIEVE OPENING, mm	DIFFERENTIAL WEIGHT, %	CUMULATIVE WEIGHT, %
1.7000	0.00	0.00
1.4000	0.00	0.00
1.1800	0.00	0.00
1.0000	0.00	0.00
0.8500	0.00	0.00
0.7100	0.53	0.53
0.6000	0.65	1.18
0.4925	6.24	7.41
0.4042	3.81	11.23
0.3318	2.12	13.35
0.2723	1.53	14.89
0.2235	2.04	16.92
0.1834	3.43	20.35
0.1506	5.20	25.55
0.1236	6.76	32.31
0.1014	7.93	40.23
0.0833	8.62	48.85
0.0683	8.75	57.60
0.0561	8.25	65.85
0.0460	7.36	73.21
0.0378	6.30	79.51
0.0310	5.19	84.70
0.0255	4.12	88.82
0.0209	3.15	91.98
0.0172	2.30	94.28
0.0141	1.61	95.89
0.0116	1.10	96.99
0.0095	0.72	97.71
0.0078	0.46	98.17
0.0064	0.31	98.48
0.0052	0.21	98.69
0.0043	0.16	98.84
0.0035	0.15	98.99
0.0029	0.17	99.16
0.0024	0.21	99.37
0.0020	0.23	99.59
0.0016	0.21	99.80
0.0013	0.15	99.95
0.0005	0.05	100.00

Table E3. Size distribution of baghouse filter ash of Test 1

SIEVE OPENING, mm	DIFFERENTIAL WEIGHT, %	CUMULATIVE WEIGHT, %
0.4925	0.00	0.00
0.4042	0.00	0.00
0.3318	0.00	0.00
0.2723	0.00	0.00
0.2235	0.00	0.00
0.1834	0.00	0.00
0.1506	0.00	0.00
0.1236	0.00	0.00
0.1014	0.02	0.02
0.0833	0.07	0.09
0.0683	0.15	0.24
0.0561	0.26	0.50
0.0460	0.37	0.87
0.0378	0.47	1.34
0.0310	0.62	1.96
0.0255	0.85	2.81
0.0209	1.21	4.02
0.0172	1.71	5.73
0.0141	2.35	8.08
0.0116	3.20	11.28
0.0095	4.30	15.58
0.0078	5.60	21.18
0.0064	6.97	28.15
0.0052	8.18	36.33
0.0043	9.12	45.45
0.0035	9.91	55.36
0.0029	10.48	65.84
0.0024	10.58	76.42
0.0020	9.83	86.25
0.0016	7.91	94.16
0.0013	4.84	99.00
0.0005	1.00	100.00

Table E4. Size distribution of baghouse filter ash of Test 2

SIEVE OPENING, mm	DIFFERENTIAL WEIGHT, %	CUMULATIVE WEIGHT, %
0.4925	0.00	0.00
0.4042	0.00	0.00
0.3318	0.00	0.00
0.2723	0.00	0.00
0.2235	0.00	0.00
0.1834	0.00	0.00
0.1506	0.00	0.00
0.1236	0.00	0.00
0.1014	0.00	0.00
0.0833	0.00	0.00
0.0683	0.00	0.00
0.0561	0.12	0.12
0.0460	0.45	0.57
0.0378	1.01	1.58
0.0310	1.87	3.45
0.0255	3.05	6.50
0.0209	4.43	10.93
0.0172	5.87	16.80
0.0141	7.07	23.87
0.0116	7.95	31.82
0.0095	8.42	40.24
0.0078	8.49	48.73
0.0064	8.22	56.95
0.0052	7.60	64.55
0.0043	6.84	71.39
0.0035	6.20	77.59
0.0029	5.74	83.33
0.0024	5.34	88.67
0.0020	4.76	93.43
0.0016	3.77	97.20
0.0013	2.31	99.51
0.0005	0.49	100.00

**E2. Coal Combustion Tests with Limestone and Biomass Addition in 300 kWt  
ABFBC**

Table E5. Size distribution of cyclone ash of Test 1

SIZE, µm	CUMULATIVE WEIGHT, %	SIZE, µm	CUMULATIVE WEIGHT, %
1261.915	0.000	28.251	86.920
1124.683	0.110	25.179	87.730
1002.374	0.410	22.440	88.490
893.367	1.130	20.000	89.210
796.214	2.390	17.825	89.900
709.627	4.510	15.887	90.560
632.456	7.510	14.159	91.200
563.667	11.310	12.619	91.830
502.377	15.770	11.247	92.440
447.744	20.720	10.024	93.030
399.052	25.980	8.934	93.610
355.656	31.370	7.962	94.180
316.979	36.710	7.096	94.730
282.508	41.860	6.325	95.270
251.785	46.710	5.637	95.780
224.404	51.200	5.024	96.270
200.000	55.290	4.477	96.730
178.250	58.960	3.991	97.150
158.866	62.240	3.557	97.520
141.589	65.160	3.170	97.850
126.191	67.760	2.825	98.100
112.468	70.090	2.518	98.310
100.237	72.210	2.244	98.530
89.337	74.130	2.000	98.750
79.621	75.910	1.783	98.970
70.963	77.550	1.589	99.170
63.246	79.070	1.416	99.370
56.368	80.480	1.262	99.550
50.238	81.780	1.125	99.710
44.774	82.980	1.002	99.830
39.905	84.090	0.893	99.930
35.566	85.110	0.796	99.990
31.698	86.050	0.710	100.000

Table E6. Size distribution of cyclone ash of Test 2

SIZE, µm	CUMULATIVE WEIGHT, %	SIZE, µm	CUMULATIVE WEIGHT, %
1002.374	0.000	22.440	78.370
893.367	0.030	20.000	80.030
796.214	0.150	17.825	81.640
709.627	0.380	15.887	83.190
632.456	0.860	14.159	84.700
563.667	1.780	12.619	86.150
502.377	3.200	11.247	87.540
447.744	5.050	10.024	88.840
399.052	7.280	8.934	90.060
355.656	9.870	7.962	91.190
316.979	12.770	7.096	92.210
282.508	15.930	6.325	93.120
251.785	19.310	5.637	93.920
224.404	22.860	5.024	94.630
200.000	26.520	4.477	95.250
178.250	30.230	3.991	95.790
158.866	33.940	3.557	96.270
141.589	37.610	3.170	96.700
126.191	41.190	2.825	97.100
112.468	44.650	2.518	97.470
100.237	47.960	2.244	97.820
89.337	51.130	2.000	98.160
79.621	54.130	1.783	98.480
70.963	56.980	1.589	98.780
63.246	59.670	1.416	99.070
56.368	62.200	1.262	99.330
50.238	64.600	1.125	99.560
44.774	66.860	1.002	99.750
39.905	69.010	0.893	99.890
35.566	71.050	0.796	99.980
31.698	72.990	0.710	100.000
28.251	74.860		
25.179	76.640		

Table E7. Size distribution of cyclone ash of Test 3

SIZE, μm	CUMULATIVE WEIGHT, %	SIZE, μm	CUMULATIVE WEIGHT, %
893.367	0.000	20.000	86.900
796.214	0.010	17.825	87.850
709.627	0.450	15.887	88.780
632.456	1.700	14.159	89.690
563.667	3.760	12.619	90.580
502.377	6.620	11.247	91.440
447.744	10.230	10.024	92.280
399.052	14.520	8.934	93.070
355.656	19.350	7.962	93.810
316.979	24.560	7.096	94.510
282.508	29.970	6.325	95.150
251.785	35.400	5.637	95.740
224.404	40.680	5.024	96.270
200.000	45.680	4.477	96.750
178.250	50.300	3.991	97.190
158.866	54.480	3.557	97.580
141.589	58.210	3.170	97.930
126.191	61.500	2.825	98.250
112.468	64.400	2.518	98.540
100.237	66.950	2.244	98.800
89.337	69.220	2.000	99.030
79.621	71.240	1.783	99.240
70.963	73.080	1.589	99.420
63.246	74.770	1.416	99.590
56.368	76.320	1.262	99.720
50.238	77.770	1.125	99.840
44.774	79.130	1.002	99.930
39.905	80.420	0.893	100.000
35.566	81.630		
31.698	82.770		
28.251	83.870		
25.179	84.920		
22.440	85.920		

Table E8. Size distribution of cyclone ash of Test 4

SIZE, µm	CUMULATIVE WEIGHT, %	SIZE, µm	CUMULATIVE WEIGHT, %
893.367	0.000	20.000	87.470
796.214	0.020	17.825	88.380
709.627	0.630	15.887	89.270
632.456	2.050	14.159	90.140
563.667	4.230	12.619	90.980
502.377	7.210	11.247	91.790
447.744	10.950	10.024	92.580
399.052	15.380	8.934	93.320
355.656	20.380	7.962	94.020
316.979	25.760	7.096	94.680
282.508	31.330	6.325	95.280
251.785	36.890	5.637	95.840
224.404	42.270	5.024	96.350
200.000	47.310	4.477	96.820
178.250	51.920	3.991	97.240
158.866	56.040	3.557	97.630
141.589	59.670	3.170	97.970
126.191	62.830	2.825	98.290
112.468	65.590	2.518	98.570
100.237	68.010	2.244	98.830
89.337	70.160	2.000	99.060
79.621	72.090	1.783	99.260
70.963	73.860	1.589	99.440
63.246	75.500	1.416	99.600
56.368	77.020	1.262	99.740
50.238	78.460	1.125	99.850
44.774	79.810	1.002	99.930
39.905	81.080	0.893	100.000
35.566	82.290		
31.698	83.430		
28.251	84.510		
25.179	85.540		
22.440	86.520		

Table E9. Size distribution of cyclone ash of Test 5

SIZE, μm	CUMULATIVE WEIGHT, %	SIZE, μm	CUMULATIVE WEIGHT, %
893.367	0.000	20.000	87.380
796.214	0.020	17.825	88.290
709.627	0.760	15.887	89.180
632.456	2.290	14.159	90.030
563.667	4.540	12.619	90.870
502.377	7.590	11.247	91.680
447.744	11.390	10.024	92.460
399.052	15.890	8.934	93.200
355.656	20.940	7.962	93.910
316.979	26.370	7.096	94.570
282.508	31.970	6.325	95.190
251.785	37.530	5.637	95.760
224.404	42.870	5.024	96.290
200.000	47.850	4.477	96.770
178.250	52.370	3.991	97.210
158.866	56.390	3.557	97.600
141.589	59.920	3.170	97.960
126.191	62.980	2.825	98.290
112.468	65.650	2.518	98.580
100.237	67.980	2.244	98.840
89.337	70.060	2.000	99.070
79.621	71.940	1.783	99.280
70.963	73.670	1.589	99.460
63.246	75.280	1.416	99.610
56.368	76.800	1.262	99.740
50.238	78.240	1.125	99.850
44.774	79.600	1.002	99.940
39.905	80.900	0.893	100.000
35.566	82.130		
31.698	83.290		
28.251	84.390		
25.179	85.440		
22.440	86.430		



Table E10. Size distribution of cyclone ash of Test 6

SIZE, µm	CUMULATIVE WEIGHT, %	SIZE, µm	CUMULATIVE WEIGHT, %
2000.000	0.000	35.566	68.770
1782.502	0.050	31.698	70.760
1588.656	0.130	28.251	72.650
1415.892	0.230	25.179	74.450
1261.915	0.350	22.440	76.180
1124.683	0.480	20.000	77.860
1002.374	0.590	17.825	79.490
893.367	0.700	15.887	81.080
796.214	0.810	14.159	82.640
709.627	0.930	12.619	84.160
632.456	1.080	11.247	85.640
563.667	1.450	10.024	87.050
502.377	2.150	8.934	88.390
447.744	3.180	7.962	89.640
399.052	4.590	7.096	90.790
355.656	6.430	6.325	91.830
316.979	8.690	5.637	92.750
282.508	11.370	5.024	93.580
251.785	14.410	4.477	94.310
224.404	17.770	3.991	94.950
200.000	21.360	3.557	95.530
178.250	25.120	3.170	96.050
158.866	28.970	2.825	96.530
141.589	32.850	2.518	96.980
126.191	36.690	2.244	97.400
112.468	40.440	2.000	97.800
100.237	44.060	1.783	98.190
89.337	47.520	1.589	98.550
79.621	50.810	1.416	98.890
70.963	53.910	1.262	99.200
63.246	56.820	1.125	99.470
56.368	59.530	1.002	99.700
50.238	62.070	0.893	99.870
44.774	64.450	0.796	99.980

Table E11. Size distribution of cyclone ash of Test 7

SIZE, µm	CUMULATIVE WEIGHT, %	SIZE, µm	CUMULATIVE WEIGHT, %
2000.000	0.000	35.566	64.820
1782.502	0.180	31.698	67.020
1588.656	0.470	28.251	69.170
1415.892	0.850	25.179	71.270
1261.915	1.250	22.440	73.330
1124.683	1.640	20.000	75.340
1002.374	1.990	17.825	77.320
893.367	2.300	15.887	79.240
796.214	2.590	14.159	81.120
709.627	2.940	12.619	82.940
632.456	3.400	11.247	84.680
563.667	4.060	10.024	86.330
502.377	4.990	8.934	87.870
447.744	6.240	7.962	89.280
399.052	7.830	7.096	90.560
355.656	9.770	6.325	91.710
316.979	12.030	5.637	92.720
282.508	14.580	5.024	93.610
251.785	17.340	4.477	94.380
224.404	20.270	3.991	95.050
200.000	23.310	3.557	95.630
178.250	26.420	3.170	96.150
158.866	29.550	2.825	96.630
141.589	32.670	2.518	97.060
126.191	35.760	2.244	97.470
112.468	38.800	2.000	97.860
100.237	41.780	1.783	98.230
89.337	44.680	1.589	98.580
79.621	47.490	1.416	98.910
70.963	50.220	1.262	99.210
63.246	52.860	1.125	99.480
56.368	55.400	1.002	99.700
50.238	57.860	0.893	99.870
44.774	60.250	0.796	99.980

Table E12. Size distribution of cyclone ash of Test 8

SIZE, µm	CUMULATIVE WEIGHT, %	SIZE, µm	CUMULATIVE WEIGHT, %
1124.683	0.000	25.179	87.850
1002.374	0.060	22.440	88.790
893.367	0.490	20.000	89.670
796.214	1.490	17.825	90.500
709.627	3.030	15.887	91.290
632.456	5.270	14.159	92.040
563.667	8.260	12.619	92.760
502.377	12.010	11.247	93.450
447.744	16.440	10.024	94.110
399.052	21.420	8.934	94.740
355.656	26.790	7.962	95.340
316.979	32.310	7.096	95.930
282.508	37.790	6.325	96.490
251.785	43.040	5.637	97.040
224.404	47.910	5.024	97.570
200.000	52.330	4.477	98.070
178.250	56.240	3.991	98.540
158.866	59.670	3.557	98.960
141.589	62.670	3.170	99.330
126.191	65.280	2.825	99.640
112.468	67.610	2.518	99.850
100.237	69.730	2.244	99.990
89.337	71.690	2.000	100.000
79.621	73.550		
70.963	75.340		
63.246	77.080		
56.368	78.740		
50.238	80.340		
44.774	81.840		
39.905	83.250		
35.566	84.550		
31.698	85.740		
28.251	86.840		

Table E13. Size distribution of baghouse filter ash of Test 1

SIZE, µm	CUMULATIVE WEIGHT, %	SIZE, µm	CUMULATIVE WEIGHT, %
14.159	0.000	1.002	84.720
12.619	0.050	0.893	86.990
11.247	0.490	0.796	89.020
10.024	1.580	0.710	90.860
8.934	3.270	0.632	92.510
7.962	5.590	0.564	94.000
7.096	8.560	0.502	95.320
6.325	12.170	0.448	96.480
5.637	16.380	0.399	97.460
5.024	21.130	0.356	98.250
4.477	26.320	0.317	98.860
3.991	31.820	0.283	99.320
3.557	37.500	0.252	99.650
3.170	43.220	0.224	99.880
2.825	48.860	0.200	100.000
2.518	54.290		
2.244	59.440		
2.000	64.220		
1.783	68.610		
1.589	72.580		
1.416	76.150		
1.262	79.350		
1.125	82.190		

Table E14. Size distribution of baghouse filter ash of Test 2

SIZE, µm	CUMULATIVE WEIGHT, %	SIZE, µm	CUMULATIVE WEIGHT, %
14.159	0.000	1.002	86.470
12.619	0.070	0.893	88.420
11.247	0.600	0.796	90.170
10.024	1.810	0.710	91.750
8.934	3.670	0.632	93.180
7.962	6.210	0.564	94.490
7.096	9.440	0.502	95.670
6.325	13.360	0.448	96.710
5.637	17.930	0.399	97.610
5.024	23.060	0.356	98.350
4.477	28.620	0.317	98.910
3.991	34.480	0.283	99.350
3.557	40.480	0.252	99.660
3.170	46.460	0.224	99.880
2.825	52.270	0.200	100.000
2.518	57.800		
2.244	62.940		
2.000	67.640		
1.783	71.860		
1.589	75.600		
1.416	78.890		
1.262	81.760		
1.125	84.270		

Table E15. Size distribution of baghouse filter ash of Test 3

SIZE, μm	CUMULATIVE WEIGHT, %	SIZE, μm	CUMULATIVE WEIGHT, %
14.159	0.000	1.002	86.950
12.619	0.050	0.893	88.910
11.247	0.320	0.796	90.650
10.024	1.440	0.710	92.210
8.934	3.220	0.632	93.600
7.962	5.650	0.564	94.860
7.096	8.800	0.502	95.980
6.325	12.650	0.448	96.960
5.637	17.170	0.399	97.800
5.024	22.270	0.356	98.490
4.477	27.840	0.317	99.010
3.991	33.730	0.283	99.410
3.557	39.800	0.252	99.700
3.170	45.870	0.224	99.890
2.825	51.800	0.200	100.000
2.518	57.460		
2.244	62.740		
2.000	67.580		
1.783	71.930		
1.589	75.800		
1.416	79.180		
1.262	82.140		
1.125	84.710		

Table E16. Size distribution of baghouse filter ash of Test 4

SIZE, µm	CUMULATIVE WEIGHT, %	SIZE, µm	CUMULATIVE WEIGHT, %
15.887	0.000	1.125	85.550
14.159	0.380	1.002	87.560
12.619	1.370	0.893	89.350
11.247	2.880	0.796	90.960
10.024	4.970	0.710	92.410
8.934	7.670	0.632	93.740
7.962	10.950	0.564	94.940
7.096	14.810	0.502	96.030
6.325	19.190	0.448	96.990
5.637	24.030	0.399	97.820
5.024	29.240	0.356	98.490
4.477	34.710	0.317	99.010
3.991	40.320	0.283	99.410
3.557	45.940	0.252	99.690
3.170	51.450	0.224	99.890
2.825	56.750	0.200	100.000
2.518	61.750		
2.244	66.370		
2.000	70.580		
1.783	74.360		
1.589	77.720		
1.416	80.680		
1.262	83.280		

Table E17. Size distribution of baghouse filter ash of Test 5

SIZE, μm	CUMULATIVE WEIGHT, %	SIZE, μm	CUMULATIVE WEIGHT, %
14.159	0.000	1.002	86.930
12.619	0.210	0.893	88.840
11.247	1.120	0.796	90.550
10.024	2.590	0.710	92.090
8.934	4.690	0.632	93.480
7.962	7.430	0.564	94.740
7.096	10.830	0.502	95.870
6.325	14.870	0.448	96.870
5.637	19.480	0.399	97.730
5.024	24.600	0.356	98.430
4.477	30.120	0.317	98.970
3.991	35.890	0.283	99.380
3.557	41.770	0.252	99.680
3.170	47.630	0.224	99.880
2.825	53.320	0.200	100.000
2.518	58.730		
2.244	63.770		
2.000	68.370		
1.783	72.520		
1.589	76.210		
1.416	79.450		
1.262	82.290		
1.125	84.760		



Table E18. Size distribution of baghouse filter ash of Test 6

SIZE, µm	CUMULATIVE WEIGHT, %	SIZE, µm	CUMULATIVE WEIGHT, %
12.619	0.000	0.893	88.030
11.247	0.070	0.796	89.900
10.024	0.900	0.710	91.570
8.934	2.350	0.632	93.070
7.962	4.430	0.564	94.420
7.096	7.230	0.502	95.630
6.325	10.730	0.448	96.690
5.637	14.930	0.399	97.600
5.024	19.760	0.356	98.340
4.477	25.120	0.317	98.910
3.991	30.890	0.283	99.350
3.557	36.900	0.252	99.660
3.170	42.990	0.224	99.880
2.825	49.010	0.200	100.000
2.518	54.820		
2.244	60.280		
2.000	65.330		
1.783	69.900		
1.589	73.990		
1.416	77.600		
1.262	80.760		
1.125	83.510		
1.002	85.910		

Table E19. Size distribution of baghouse filter ash of Test 7

SIZE, μm	CUMULATIVE WEIGHT, %	SIZE, μm	CUMULATIVE WEIGHT, %
14.159	0.000	1.002	86.160
12.619	0.080	0.893	88.210
11.247	0.080	0.796	90.030
10.024	0.970	0.710	91.660
8.934	2.470	0.632	93.120
7.962	4.600	0.564	94.450
7.096	7.460	0.502	95.640
6.325	11.020	0.448	96.700
5.637	15.280	0.399	97.600
5.024	20.170	0.356	98.340
4.477	25.600	0.317	98.910
3.991	31.420	0.283	99.340
3.557	37.480	0.252	99.660
3.170	43.610	0.224	99.880
2.825	49.650	0.200	100.000
2.518	55.450		
2.244	60.910		
2.000	65.920		
1.783	70.460		
1.589	74.490		
1.416	78.030		
1.262	81.130		
1.125	83.810		

Table E20. Size distribution of baghouse filter ash of Test 8

SIZE, µm	CUMULATIVE WEIGHT, %	SIZE, µm	CUMULATIVE WEIGHT, %
14.159	0.000	1.002	86.860
12.619	0.050	0.893	88.800
11.247	0.320	0.796	90.520
10.024	1.410	0.710	92.060
8.934	3.140	0.632	93.450
7.962	5.520	0.564	94.710
7.096	8.620	0.502	95.840
6.325	12.420	0.448	96.840
5.637	16.900	0.399	97.710
5.024	21.970	0.356	98.410
4.477	27.530	0.317	98.960
3.991	33.440	0.283	99.370
3.557	39.530	0.252	99.670
3.170	45.640	0.224	99.880
2.825	51.620	0.200	100.000
2.518	57.320		
2.244	62.640		
2.000	67.510		
1.783	71.890		
1.589	75.760		
1.416	79.150		
1.262	82.090		
1.125	84.640		

### E3. Coal Combustion Tests in 150 kWt CFBC

Table E21. Size distribution of cyclone ash

SIZE, $\mu\text{m}$	DIFFERENTIAL WEIGHT, %	CUMULATIVE WEIGHT, %
1000.000	0.000	0.000
850.000	0.000	0.000
600.000	17.029	17.029
430.000	33.088	50.117
360.000	13.638	63.755
180.000	24.655	88.410
110.000	7.114	95.524
0.365	4.476	100.000

Table E22. Size distribution of baghouse filter ash

SIZE, µm	CUMULATIVE WEIGHT, %	SIZE, µm	CUMULATIVE WEIGHT, %
282.508	0.000	6.325	85.140
251.785	0.040	5.637	86.630
224.404	0.110	5.024	87.990
200.000	0.310	4.477	89.250
178.250	0.760	3.991	90.400
158.866	1.550	3.557	91.460
141.589	2.700	3.170	92.430
126.191	4.230	2.825	93.320
112.468	6.200	2.518	94.130
100.237	8.620	2.244	94.860
89.337	11.490	2.000	95.500
79.621	14.780	1.783	96.060
70.963	18.440	1.589	96.600
63.246	22.390	1.416	96.970
56.368	26.550	1.262	97.330
50.238	30.820	1.125	97.670
44.774	35.130	1.002	97.990
39.905	39.400	0.893	98.310
35.566	43.570	0.796	98.640
31.698	47.600	0.710	98.950
28.251	51.450	0.632	99.260
25.179	55.120	0.564	99.530
22.440	58.590	0.502	99.770
20.000	61.860	0.448	99.930
17.825	64.940	0.399	100.000
15.887	67.840		
14.159	70.560		
12.619	73.120		
11.247	75.510		
10.024	77.740		
8.934	79.820		
7.962	81.740		
7.096	83.510		



## APPENDIX F

### CALCULATION OF PLANCK MEAN PROPERTIES

Radiative energy emitted from a surface is called emissive power. Spectral emissive power is defined as the emitted energy per unit time per unit surface area per frequency from which total emissive power is found from,

$$E = \int_0^{\infty} E_{\lambda}(T, \lambda) d\lambda \quad (\text{F. 1})$$

As can be seen from the above statement, emitted energy is a function of wavelength and temperature. Distribution of spectral blackbody emissive power as a function of wavelength and temperature was first formulated by Max Planck in 1901, which is usually referred as Planck's law,

$$E_b(T, \eta) = \frac{2\pi hc_0 \eta^3}{n^2 \left[ \exp\left(\frac{hc_0 \eta}{nkT}\right) - 1 \right]} = \frac{3.7419 \times 10^{-8} \eta (cm^{-1})^3}{\exp\left(\frac{1.4388 \eta}{T}\right) - 1} \quad (\text{F. 2})$$

where  $\eta$  denotes the wavenumber ( $cm^{-1}$ ). In Figure F1, distribution of blackbody emissive power is demonstrated for a wide range of wavelengths at different temperatures.

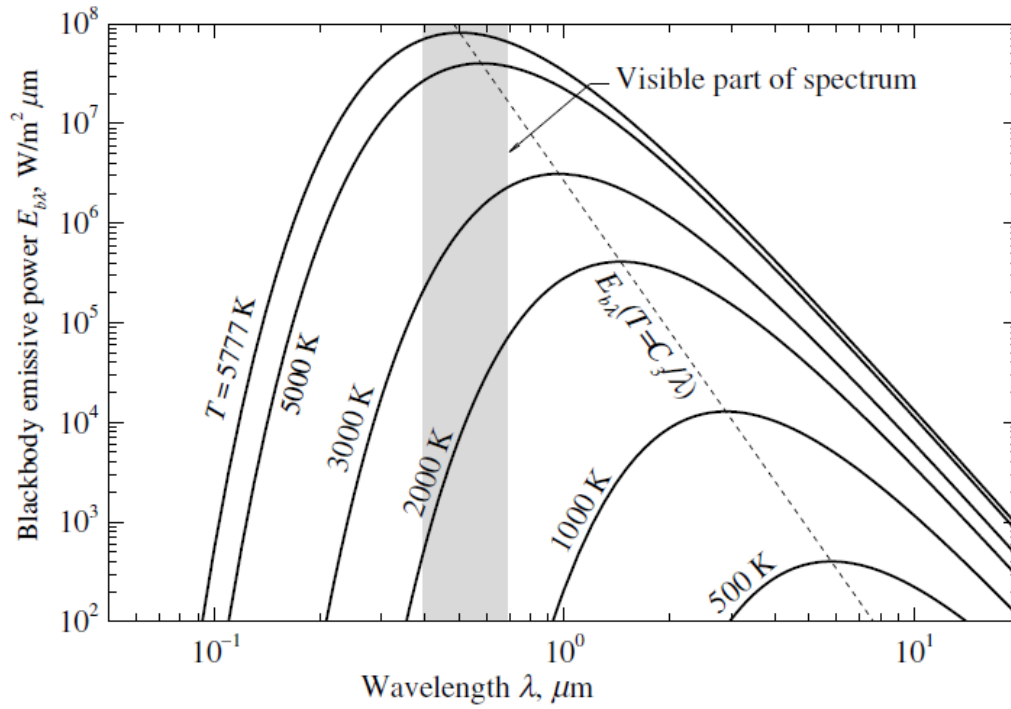


Figure F1. Spectral blackbody emissive power distribution

In radiative heat transfer calculations, spectral properties of participating gases/particles are sometimes simplified by using representative spectrally independent (gray) properties. This is usually achieved by using mean value theorem.

Mean value theorem states that if a function  $f(x)$  is continuous in the interval  $a$ - $b$ , then the value of the integration of  $f(x)$  over an interval  $x = a$  to  $x = b$  is defined as,

$$I = \int_a^b f(x) dx = \langle f \rangle (b - a) \quad (\text{F. 3})$$

Nevertheless, such an approach is not directly suitable for simplification of the spectral radiative properties as the variation of radiant energy with respect to wavelength is highly nonlinear (Figure F1). This is why spectral distribution of radiant energy is used as a weighing factor to calculate a weight-averaged radiative property,  $\bar{\varphi}$ , so that spectral bands with more radiant energy will be more dominant in the spectrally averaged quantities,

$$\bar{\varphi} = \frac{\int_0^\infty w(\lambda)\varphi(\lambda)d\lambda}{\int_0^\infty w(\lambda)d\lambda} \quad (\text{F. 4})$$



In radiative property calculations, fractional emissive power distribution ( $f$ ) is used as the weighing factor,

$$f = \frac{\int_0^\lambda E_{b,\lambda} d\lambda}{\int_0^\infty E_{b,\lambda} d\lambda} \quad (\text{F. 5})$$

which gives the blackbody emissive power fraction between  $\lambda = 0$  and any given wavelength,  $\lambda$ .

Accordingly, fraction of emissive power between the spectral points of  $j'$  and  $j'+1$  can be found from,

$$\Delta f = F_{0-j'+1} - F_{0-j'} \quad (\text{F. 6})$$

where

$$F_{0-j'+1} = \frac{\int_0^{\lambda_{j'+1}} E_{b,\lambda} d\lambda}{\int_0^\infty E_{b,\lambda} d\lambda} \quad (\text{F. 7})$$

$$F_{0-j'} = \frac{\int_0^{\lambda_{j'}} E_{b,\lambda} d\lambda}{\int_0^\infty E_{b,\lambda} d\lambda} \quad (\text{F. 8})$$

In this study, spectral radiative properties of combustion gases and particles are evaluated at discrete points between 1-20  $\mu\text{m}$ . Hence, integrals in Eqs. (F.7, 8) are evaluated in series forms,

$$\bar{\varphi} = \frac{\sum_{j'=1}^{NB'} \varphi_{\lambda_{j'}} (F_{0-j'+1} - F_{0-j'})}{\sum_{j'=1}^{NB'} (F_{0-j'+1} - F_{0-j'})} \quad (\text{F. 8})$$

where  $NB'$  represents the total number of spectral points used in the calculations. In particle properties,  $NB'$  is 147, corresponding to a spectral width of 0.1  $\mu\text{m}$  between 1-13  $\mu\text{m}$  and a spectral width of 25  $\text{cm}^{-1}$  between 13-20  $\mu\text{m}$ . The reason behind this variation is the spectral databases used in the calculation of complex index of refraction of ash particles (see Appendix C). In gas property calculations,  $NB'$  is taken as 423, which corresponds to a spectral width of 25  $\text{cm}^{-1}$ .



## APPENDIX G

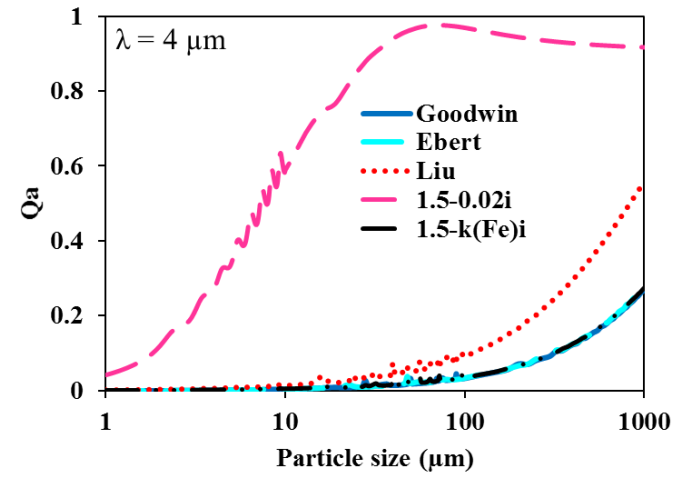
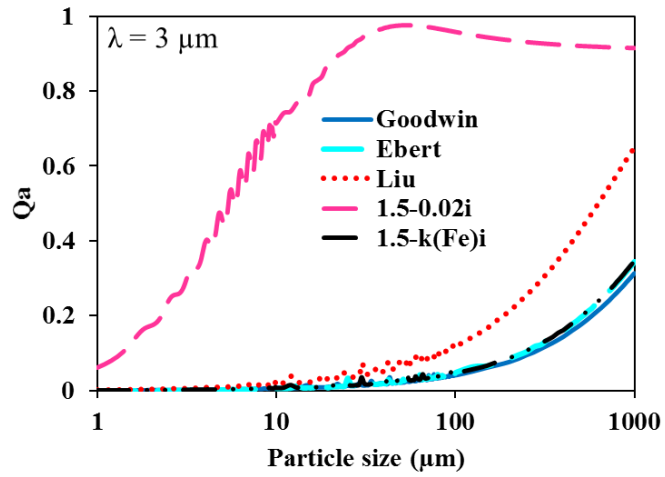
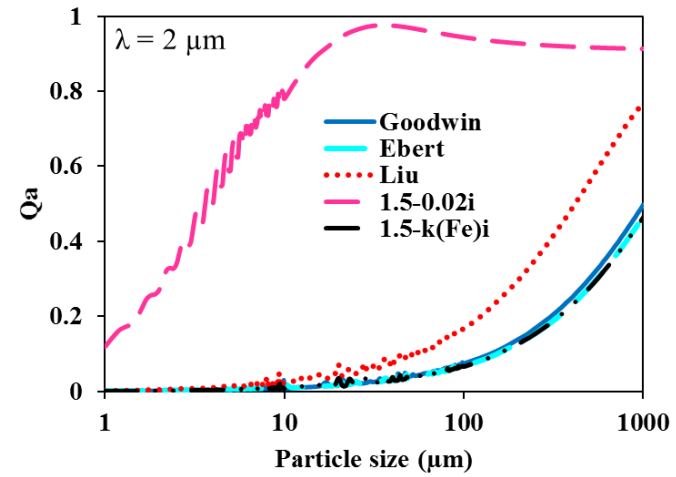
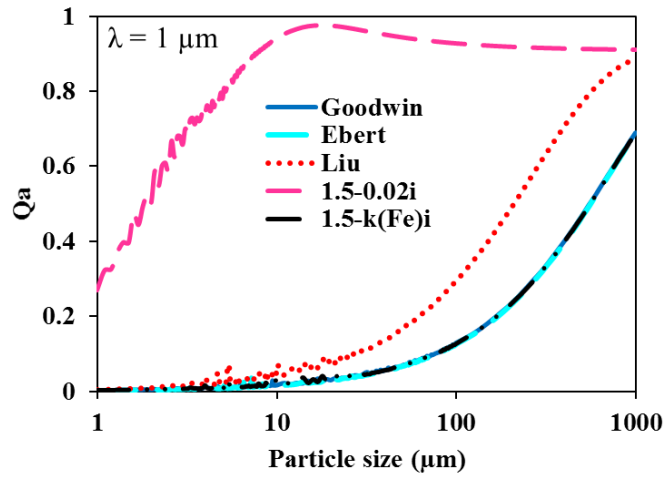
### SPECTRAL MIE SOLUTIONS FOR ASH I-V

This appendix presents the Mie solutions obtained with two chemical-composition-dependent (Ebert (spectral),  $m=1.5-k(\text{Fe})i$  (gray)) and two chemical-composition-independent (Liu (spectral),  $m=1.5-0.02i$  (gray)) RI models with those of Goodwin for increasing wavelengths and particle sizes for five different ash compositions. Discussions of the presented results are given in Section 6.7.2.2. Absorption efficiencies ( $Q_a$ ), scattering efficiencies ( $Q_s$ ) and asymmetry factors ( $g$ ) are demonstrated in order from Ash I to Ash V.

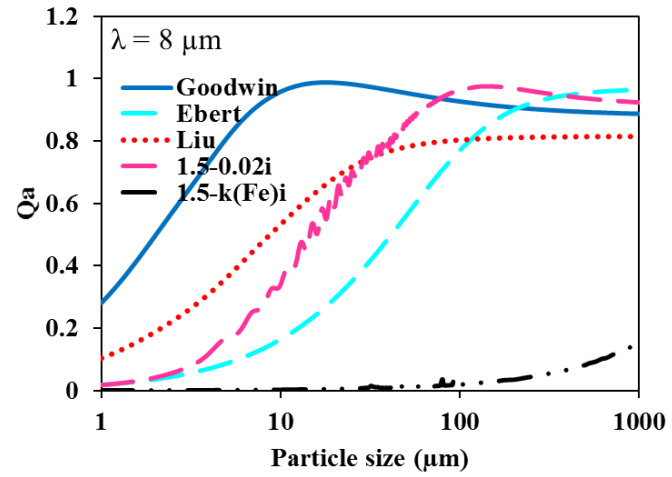
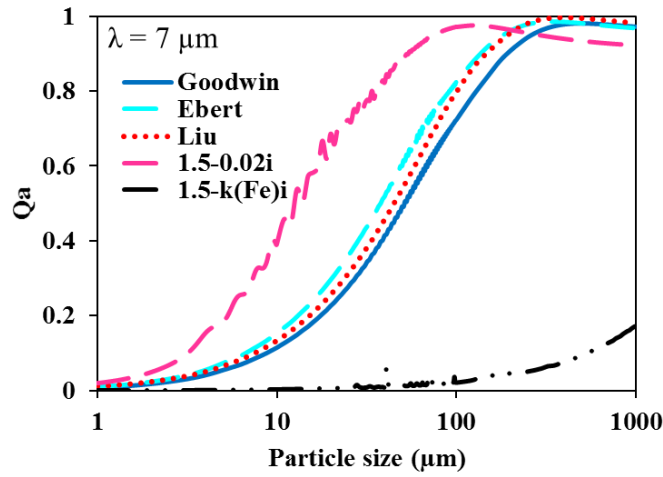
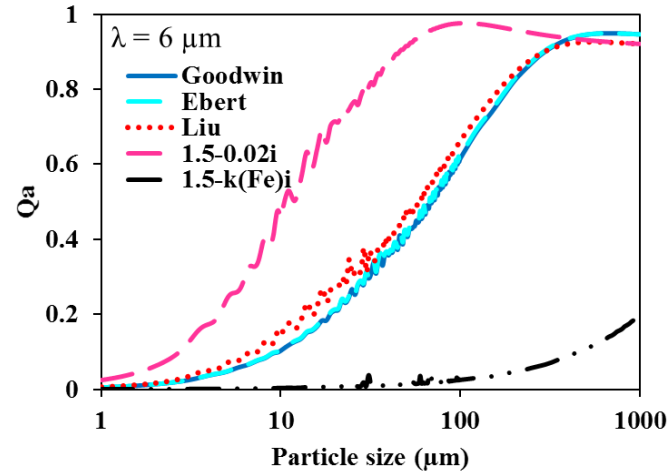
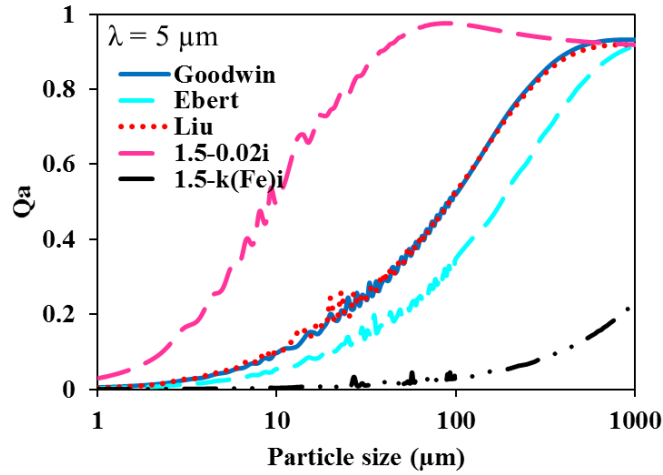
#### Fly ash compositions

	Ash I (Texas)	Ash II (Canada)	Ash III (Çan)	Ash IV (Beypazarı)	Ash V (Pittsburg)
SiO <sub>2</sub> (wt. %)	70.46	51.21	58.08	47.25	39.30
Al <sub>2</sub> O <sub>3</sub> (wt. %)	17.07	20.55	19.48	16.87	20.20
Fe <sub>2</sub> O <sub>3</sub> (wt. %)	2.72	5.37	7.55	14.45	30.50
CaO (wt. %)	4.31	10.04	1.84	0.44	3.00
MgO (wt. %)	0.00	1.82	1.34	1.01	0.80
TiO <sub>2</sub> (wt. %)	1.05	0.94	1.93	3.63	1.17
K <sub>2</sub> O (wt. %)	1.55	1.57	1.48	1.89	1.42
SO <sub>3</sub> (wt. %)	0.74	7.34	6.84	7.44	2.04
Na <sub>2</sub> O (wt. %)	2.10	1.16	1.46	7.02	1.57

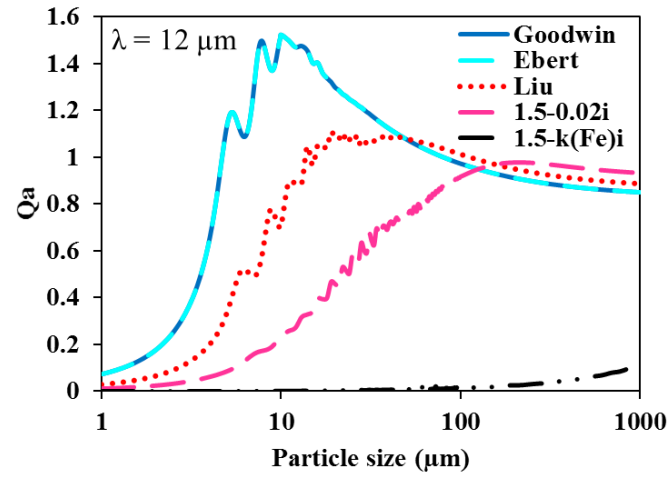
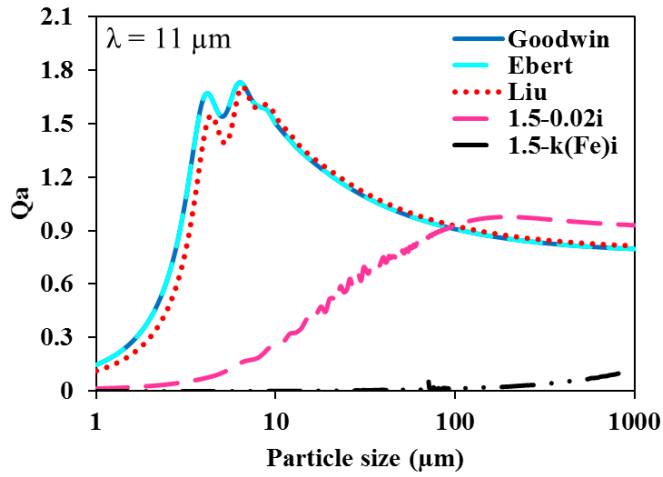
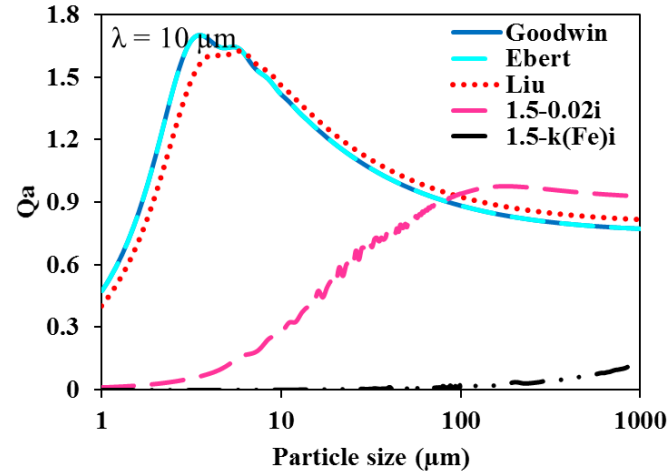
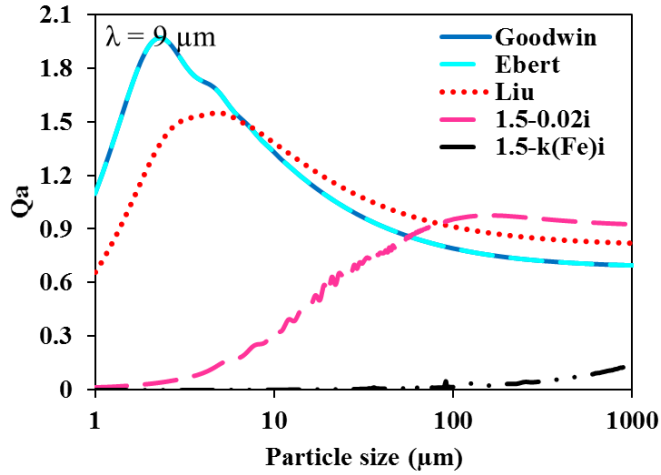
Spectral absorption efficiencies for  $\lambda = 1-4 \mu\text{m}$  (iron oxide absorption band) for Ash I



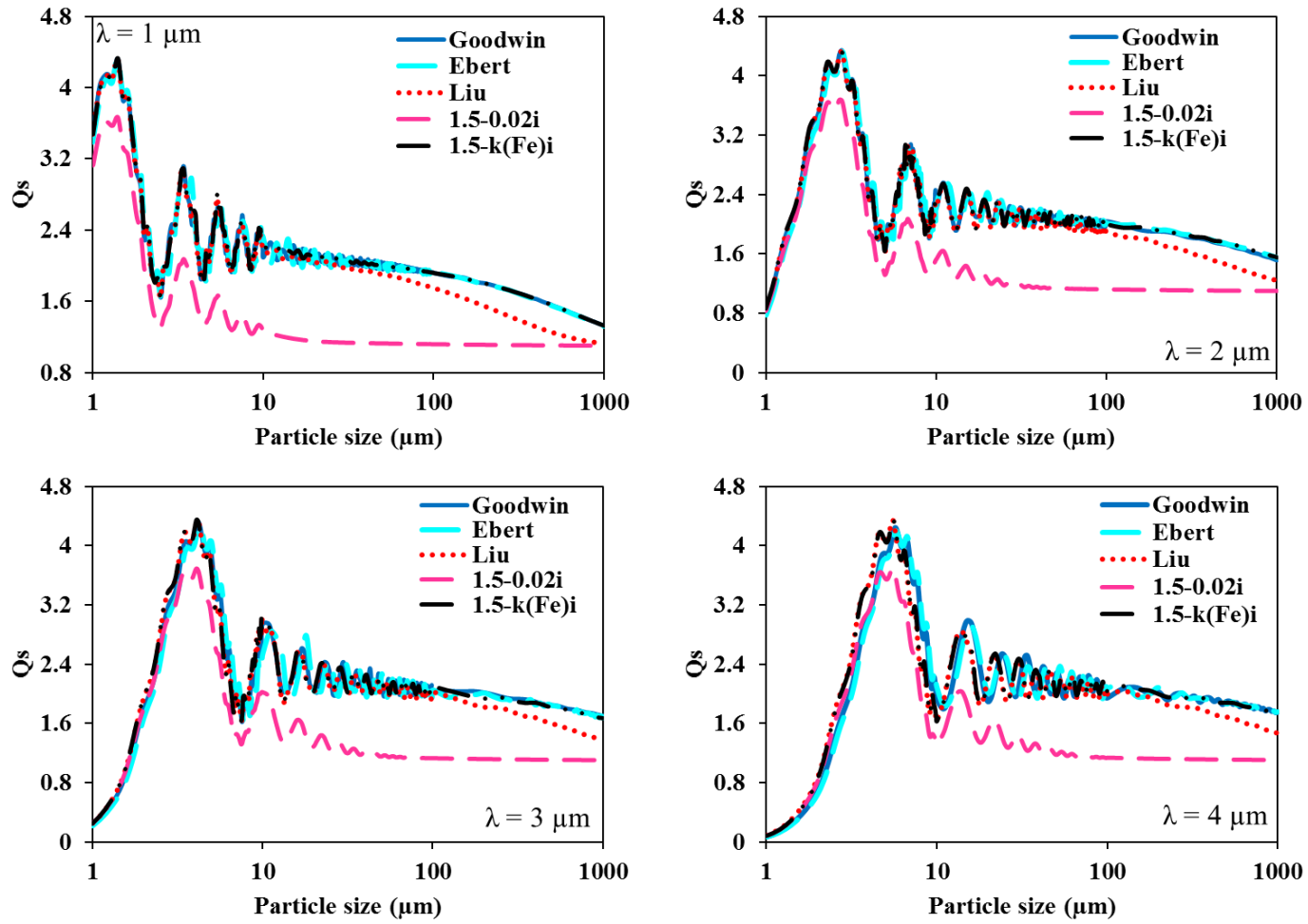
Spectral absorption efficiencies for  $\lambda = 4-8 \mu\text{m}$  (mixed absorption band) for Ash I



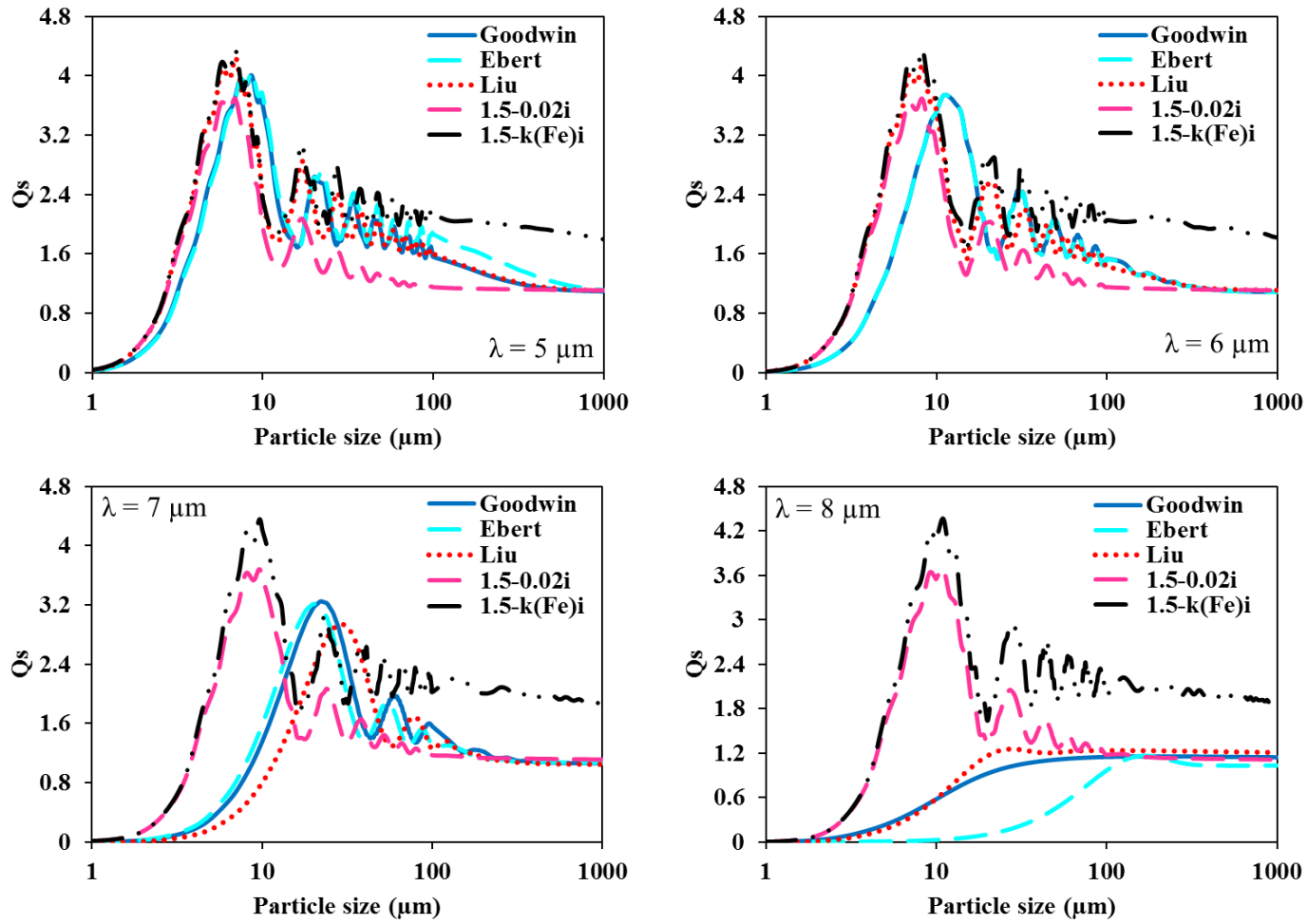
Spectral absorption efficiencies for  $\lambda = 8-12 \mu\text{m}$  (silicon oxide absorption band) for Ash I



Spectral scattering efficiencies for  $\lambda = 1-4 \mu\text{m}$  (iron oxide absorption band) for Ash I

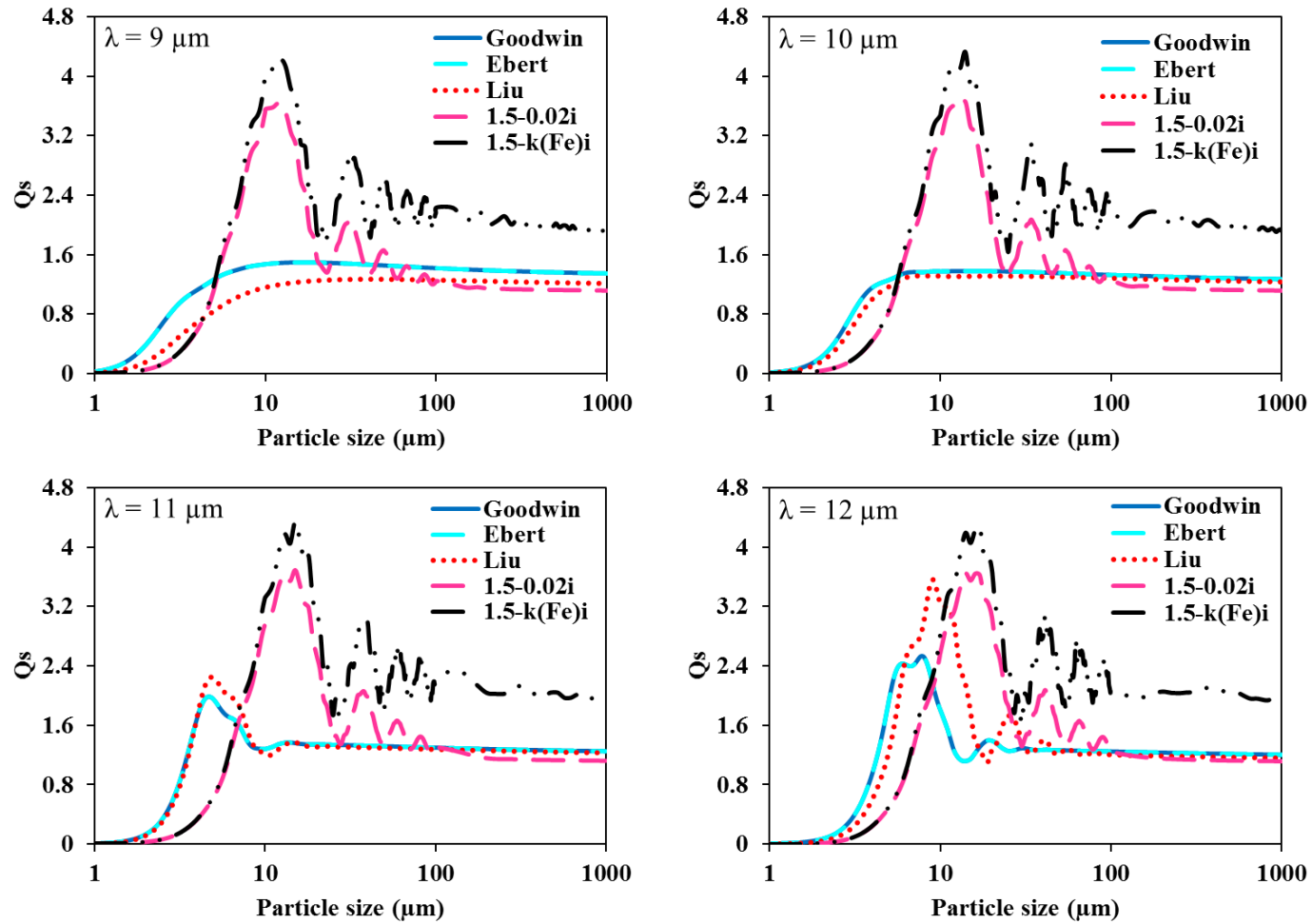


Spectral scattering efficiencies indices for  $\lambda = 4-8 \mu\text{m}$  (mixed absorption band) for Ash I

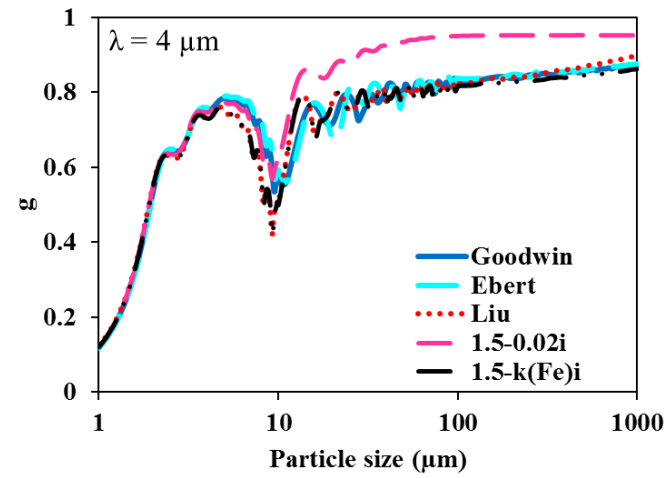
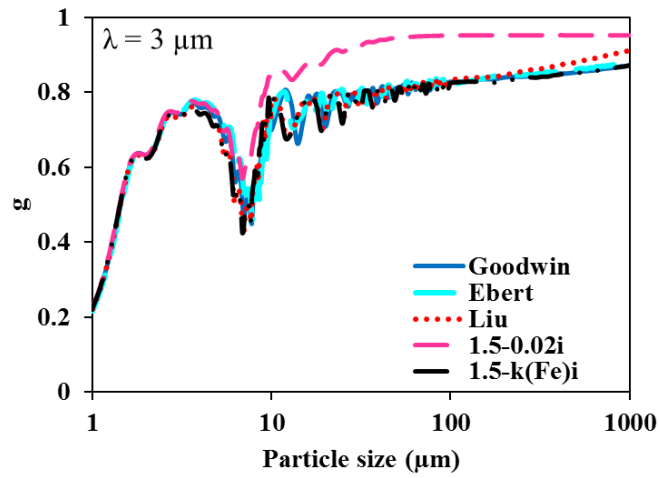
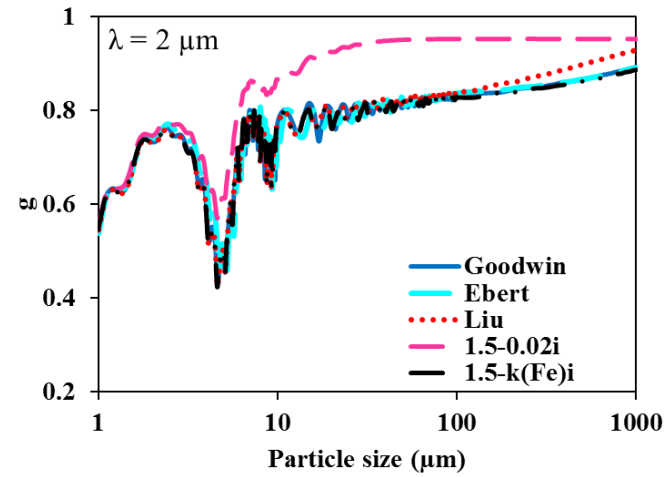
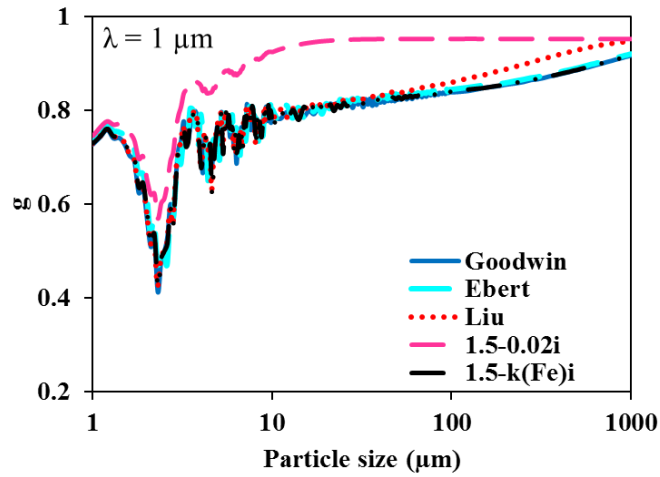




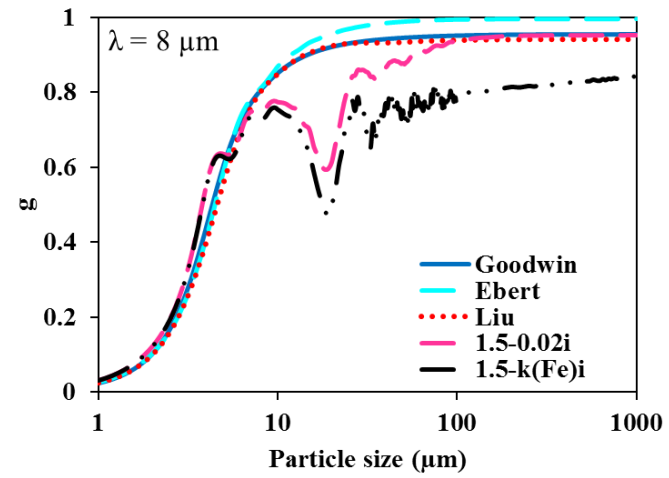
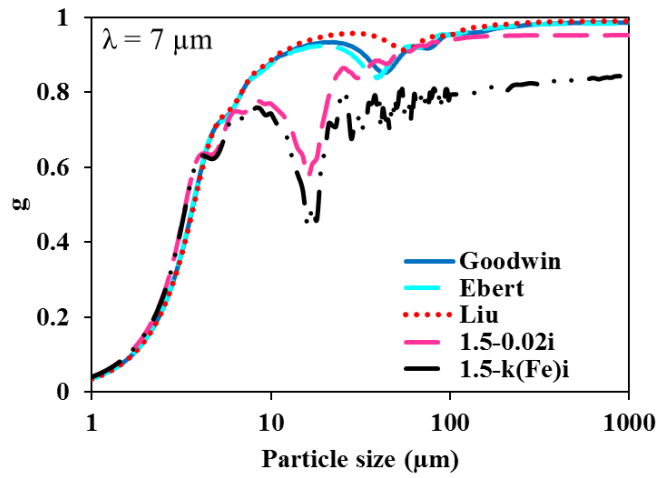
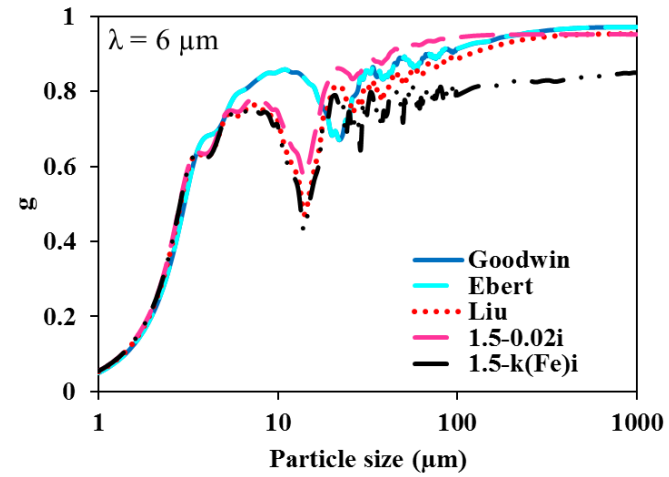
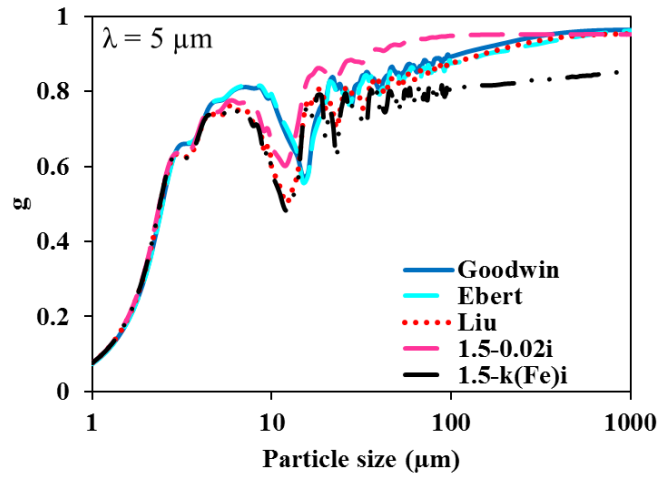
Spectral scattering efficiencies for  $\lambda = 8-12 \mu\text{m}$  (silicon oxide absorption band) for Ash I



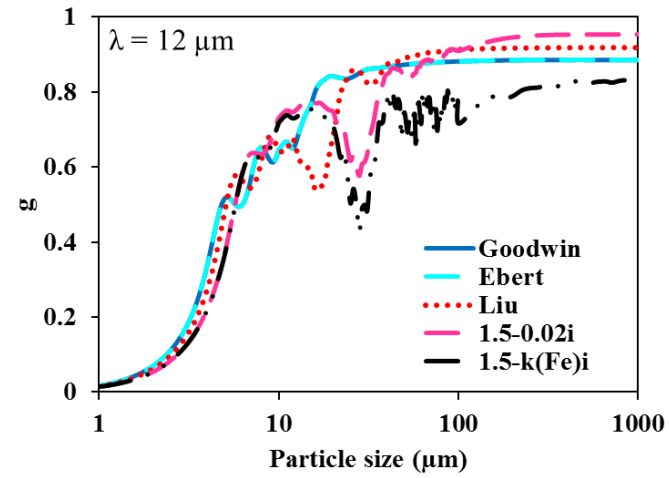
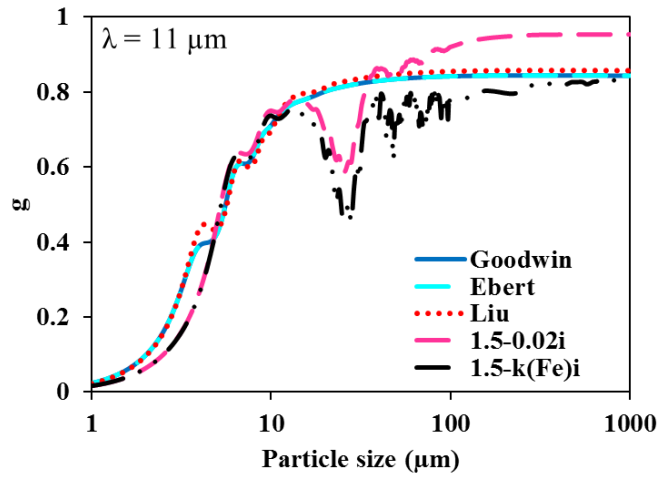
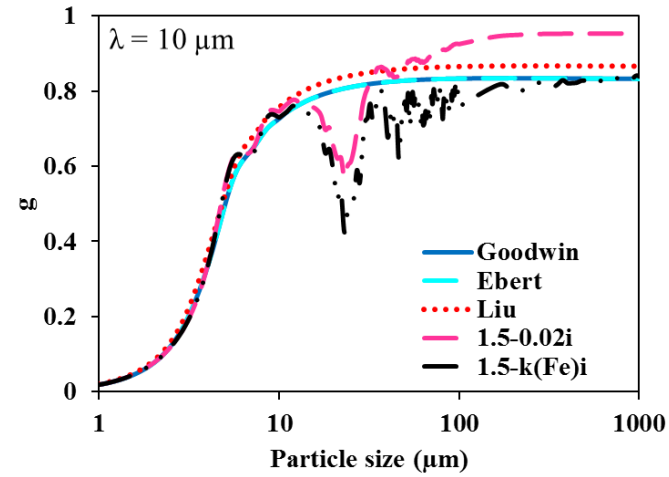
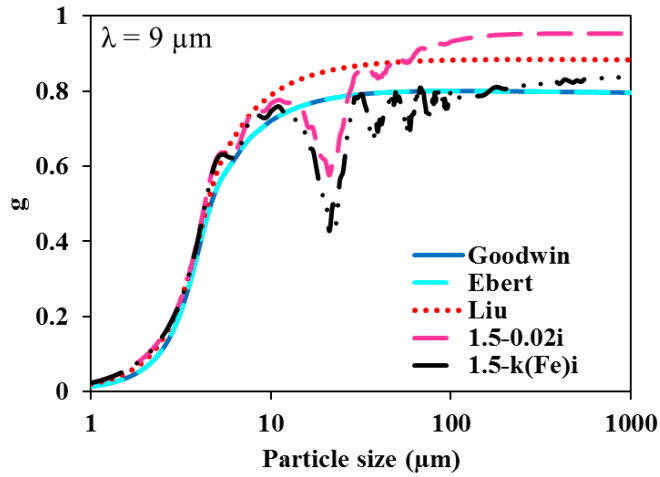
Spectral asymmetry factors for  $\lambda = 1-4 \mu\text{m}$  (iron oxide absorption band) for Ash I



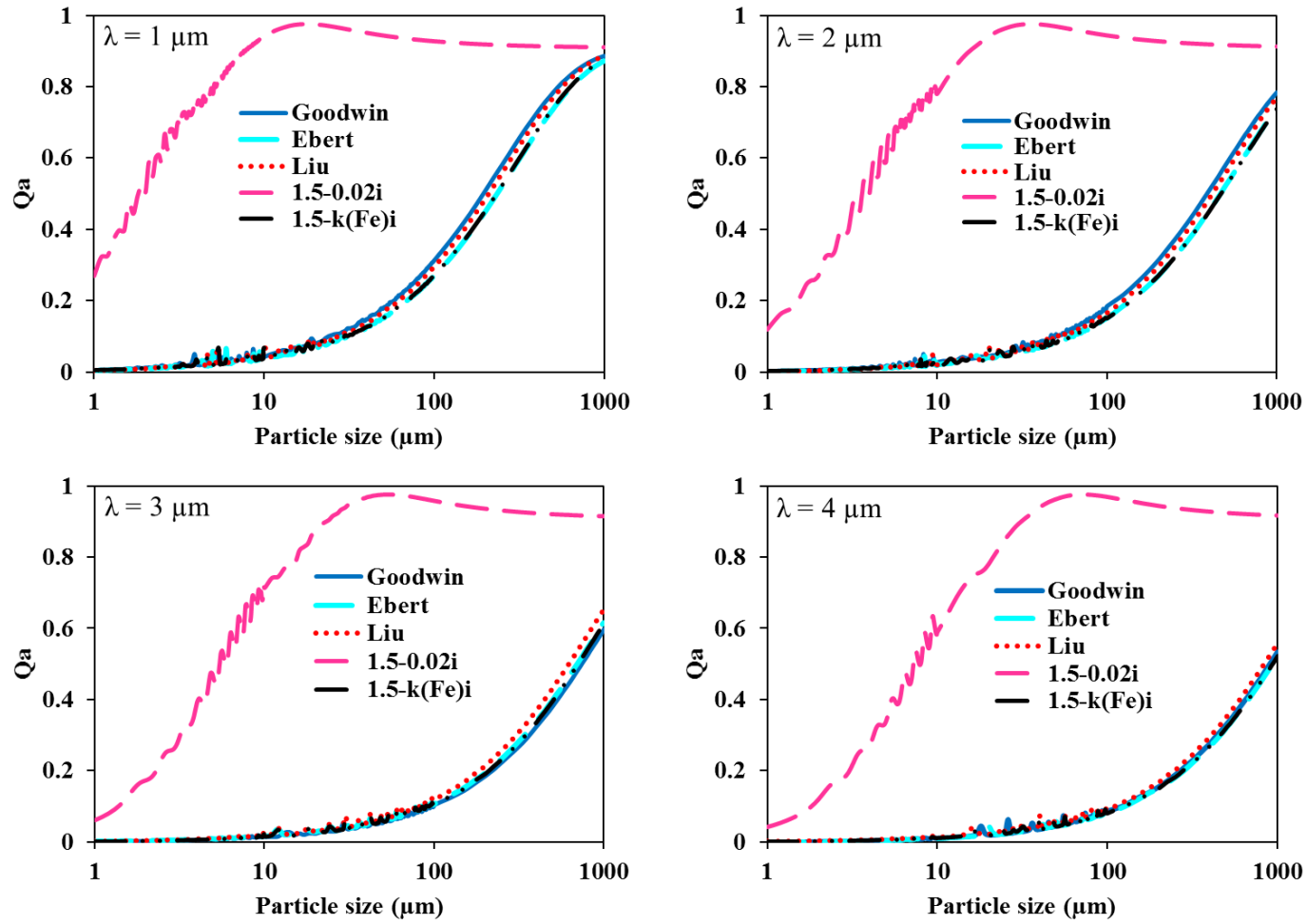
Spectral asymmetry factors for  $\lambda = 4-8 \mu\text{m}$  (mixed absorption band) for Ash I



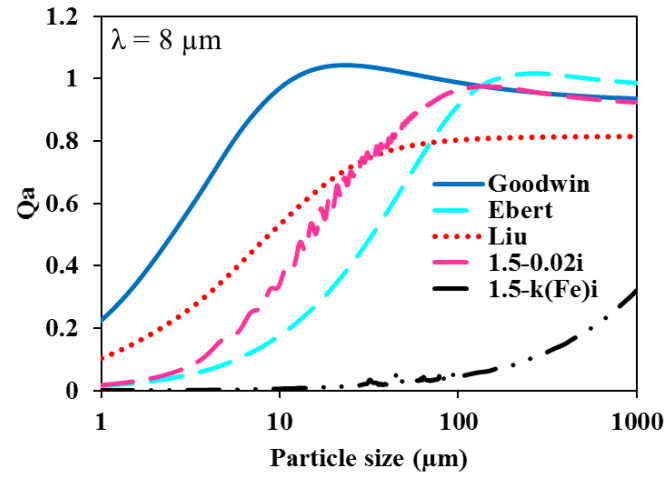
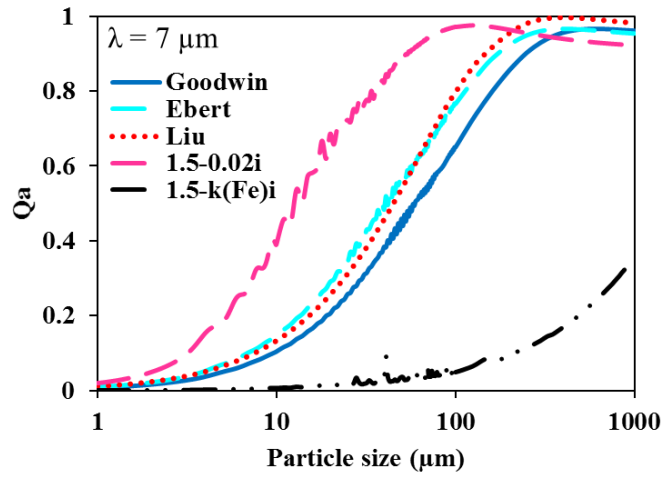
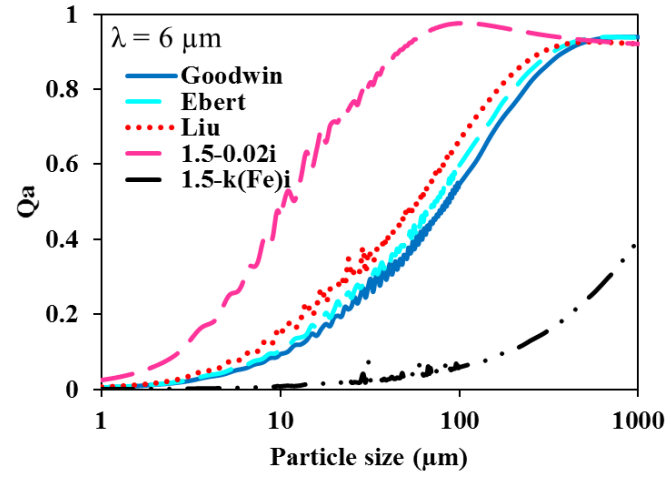
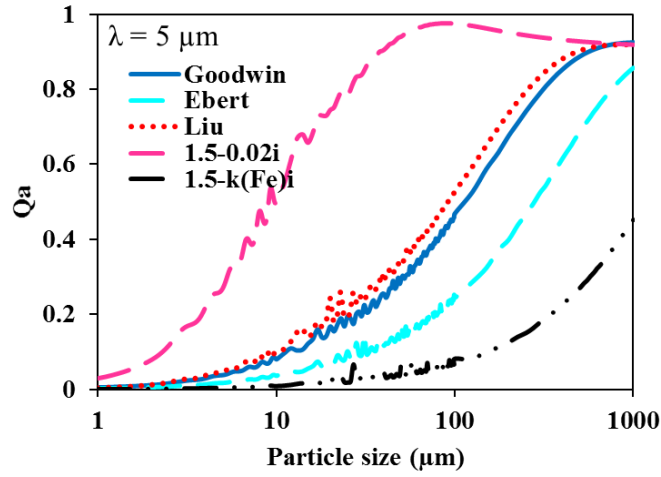
Spectral asymmetry factors for  $\lambda = 8-12 \mu\text{m}$  (silicon oxide absorption band) for Ash I



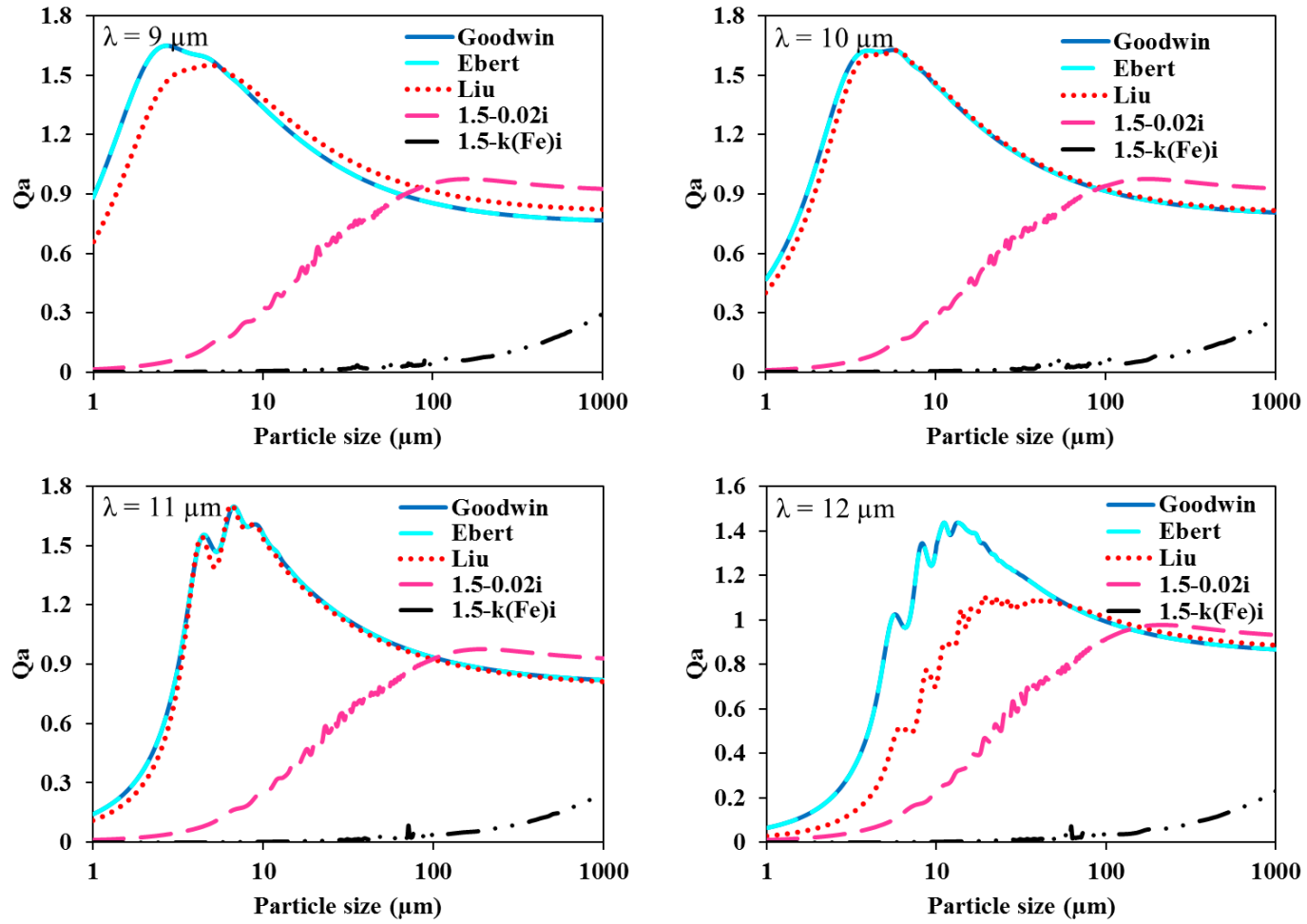
Spectral absorption efficiencies for  $\lambda = 1-4 \mu\text{m}$  (iron oxide absorption band) for Ash II



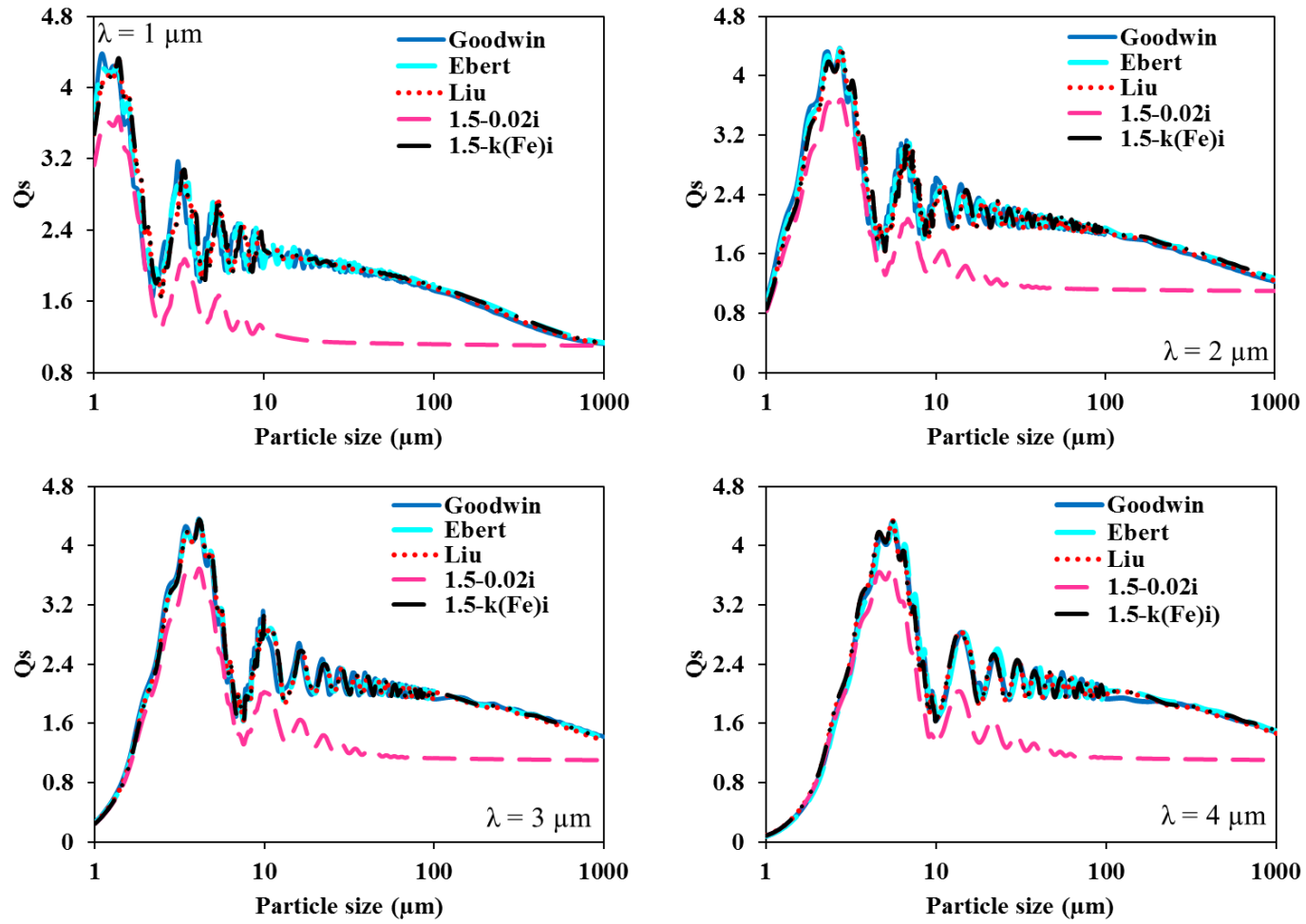
Spectral absorption efficiencies for  $\lambda = 4-8 \mu\text{m}$  (mixed absorption band) for Ash II



Spectral absorption efficiencies for  $\lambda = 8-12 \mu\text{m}$  (silicon oxide absorption band) for Ash II

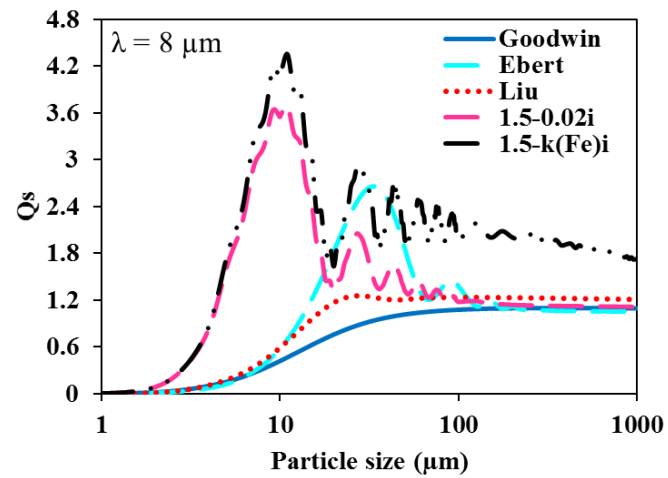
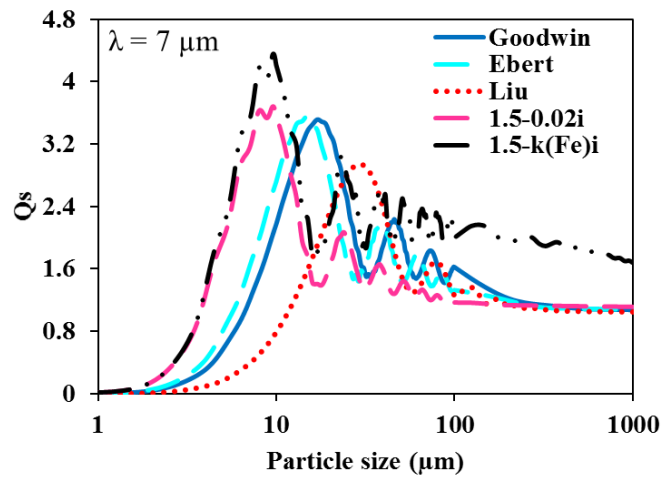
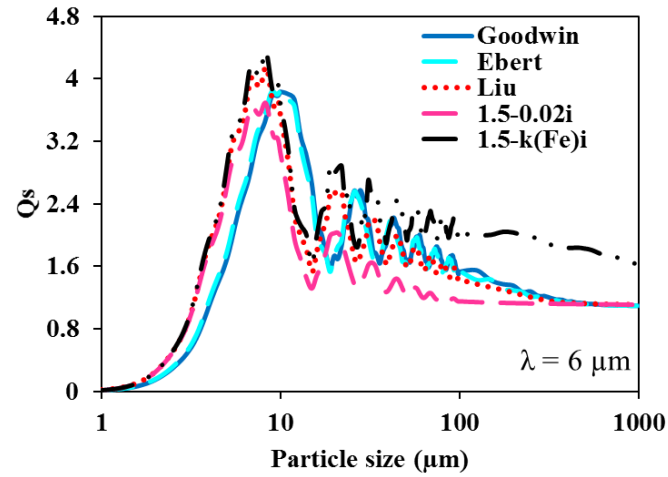
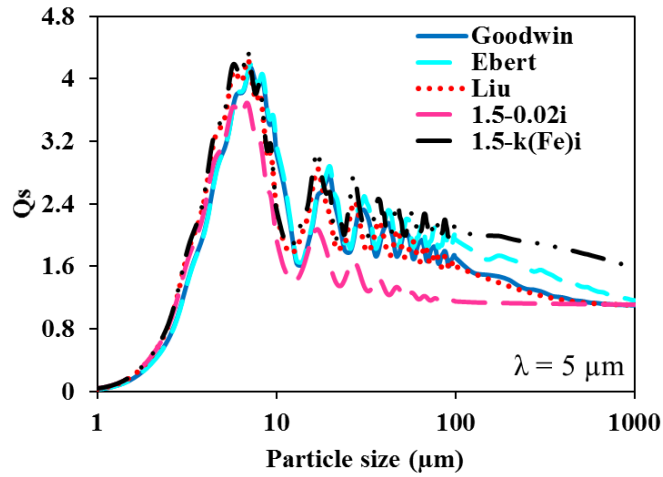


Spectral scattering efficiencies for  $\lambda = 1-4 \mu\text{m}$  (iron oxide absorption band) for Ash II

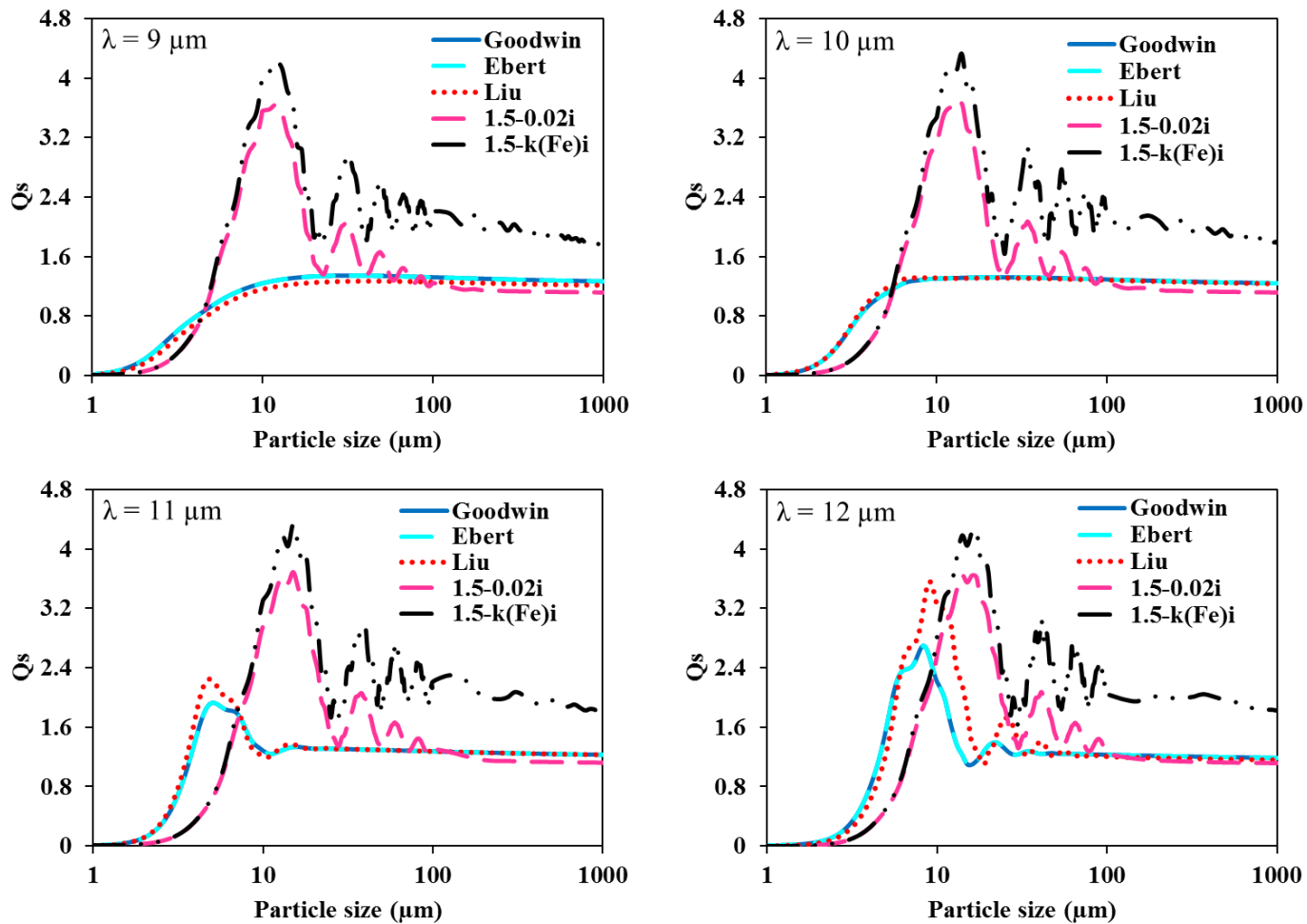




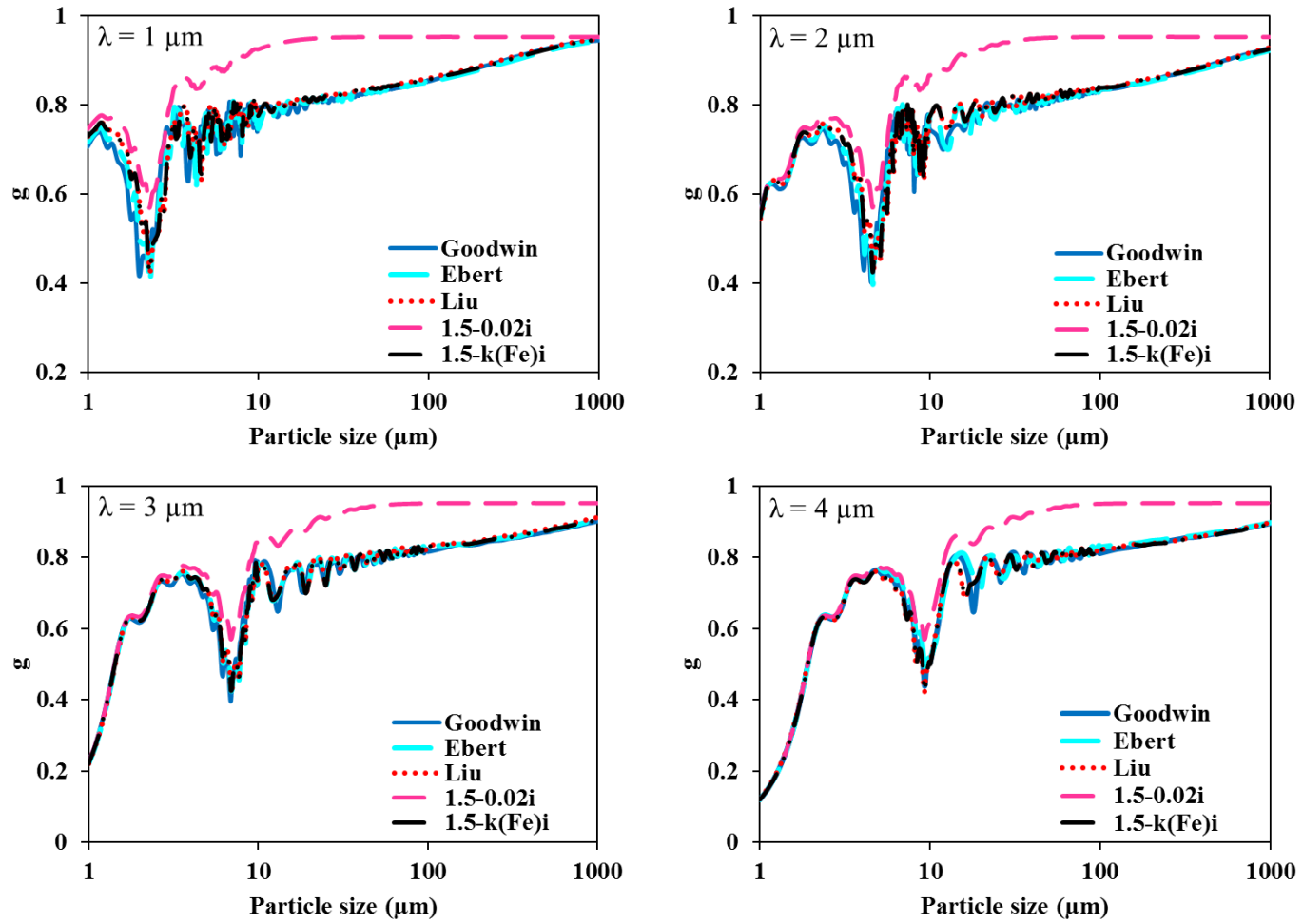
Spectral scattering efficiencies indices for  $\lambda = 4-8 \mu\text{m}$  (mixed absorption band) for Ash II



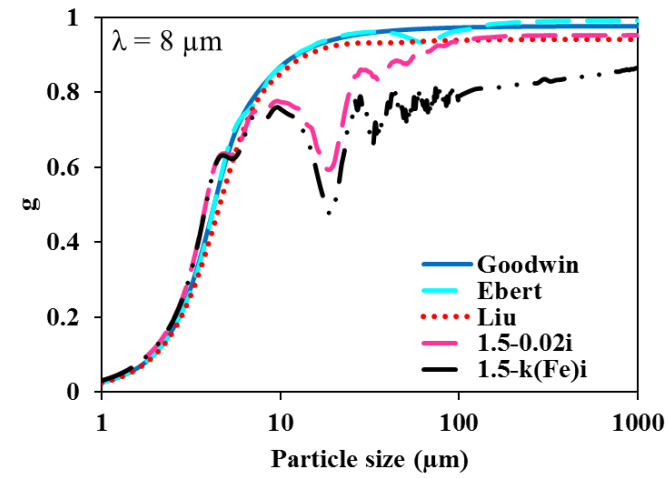
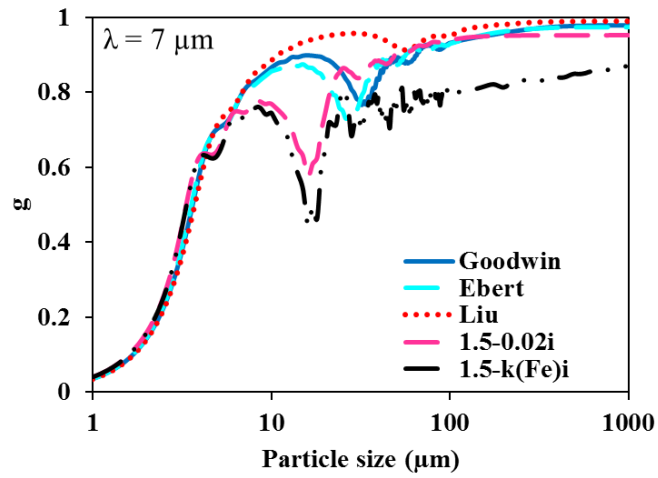
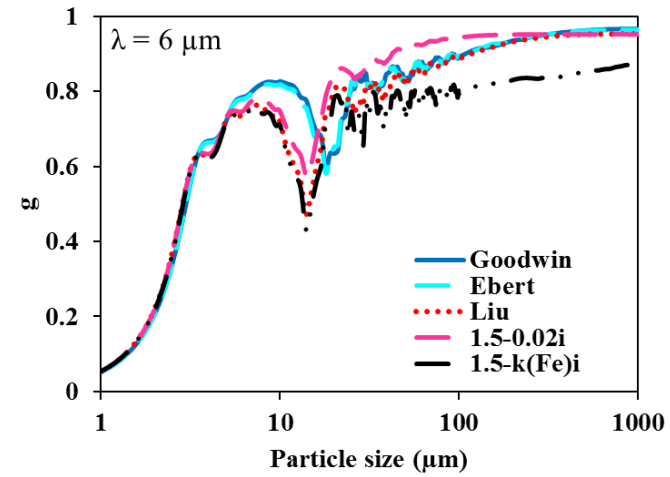
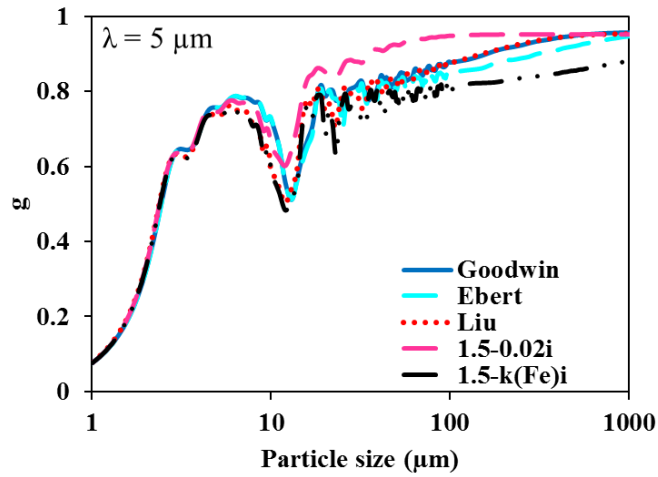
Spectral scattering efficiencies for  $\lambda = 8-12 \mu\text{m}$  (silicon oxide absorption band) for Ash II



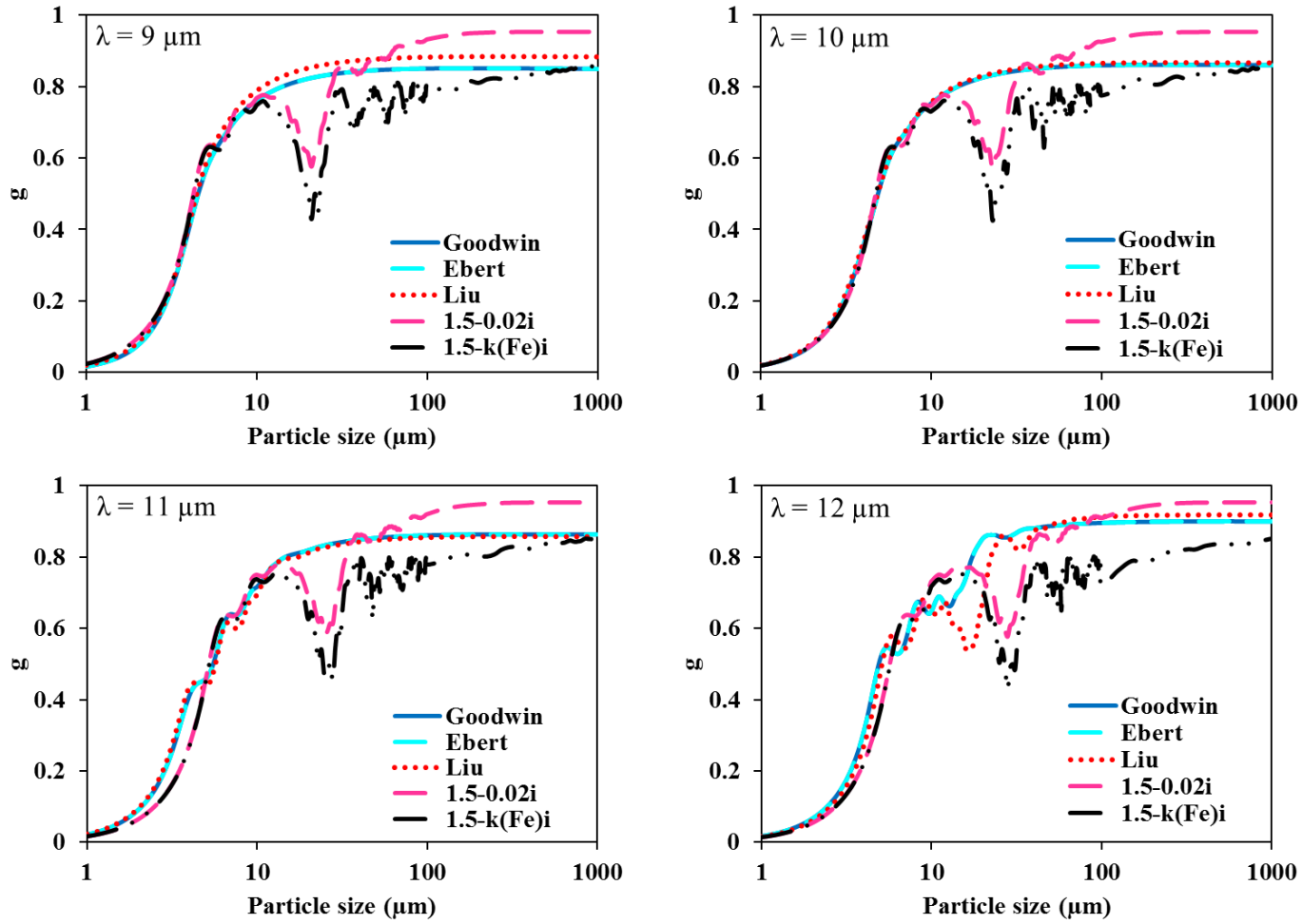
Spectral asymmetry factors for  $\lambda = 1-4 \mu\text{m}$  (iron oxide absorption band) for Ash II



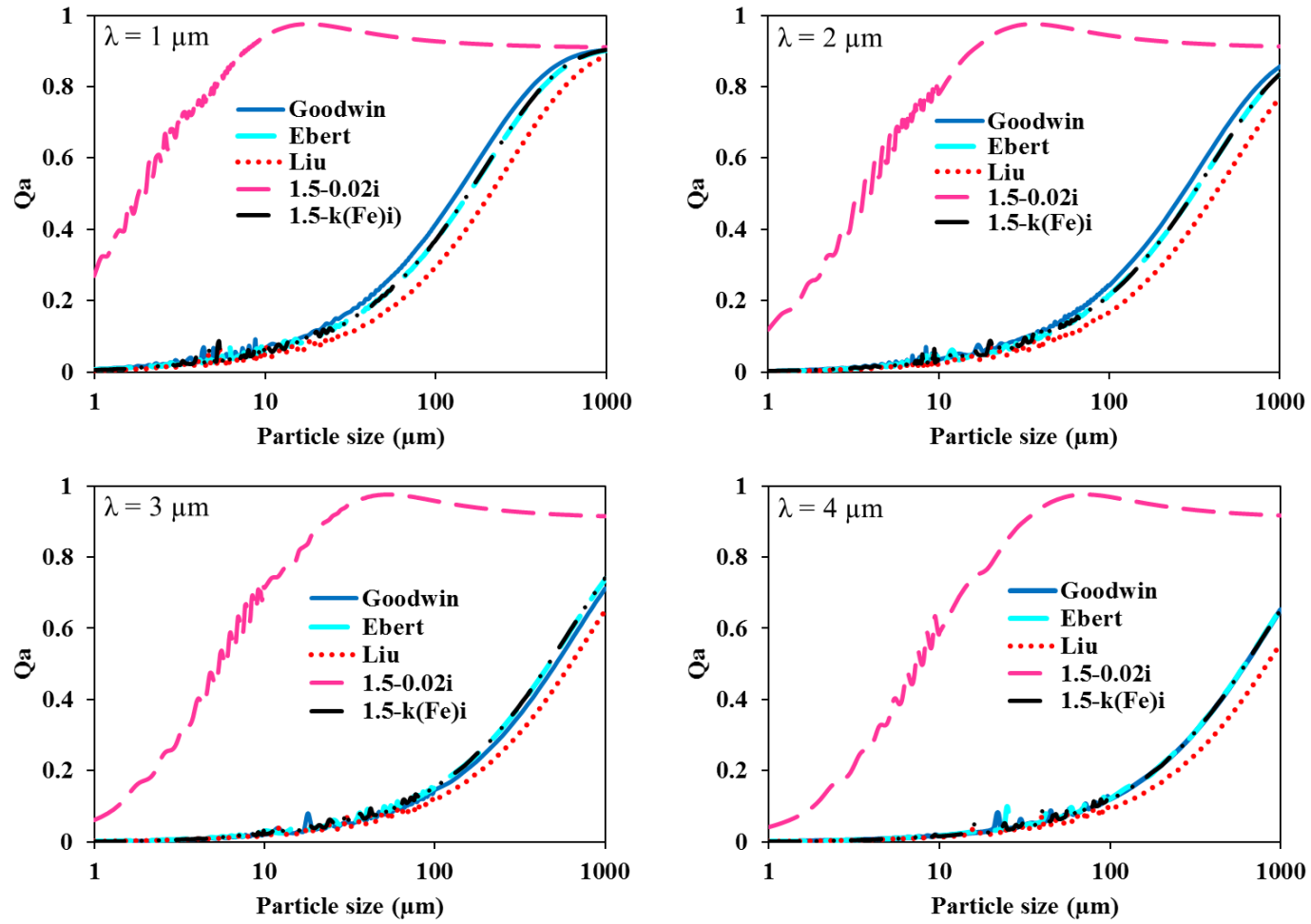
Spectral asymmetry factors for  $\lambda = 4-8 \mu\text{m}$  (mixed absorption band) for Ash II



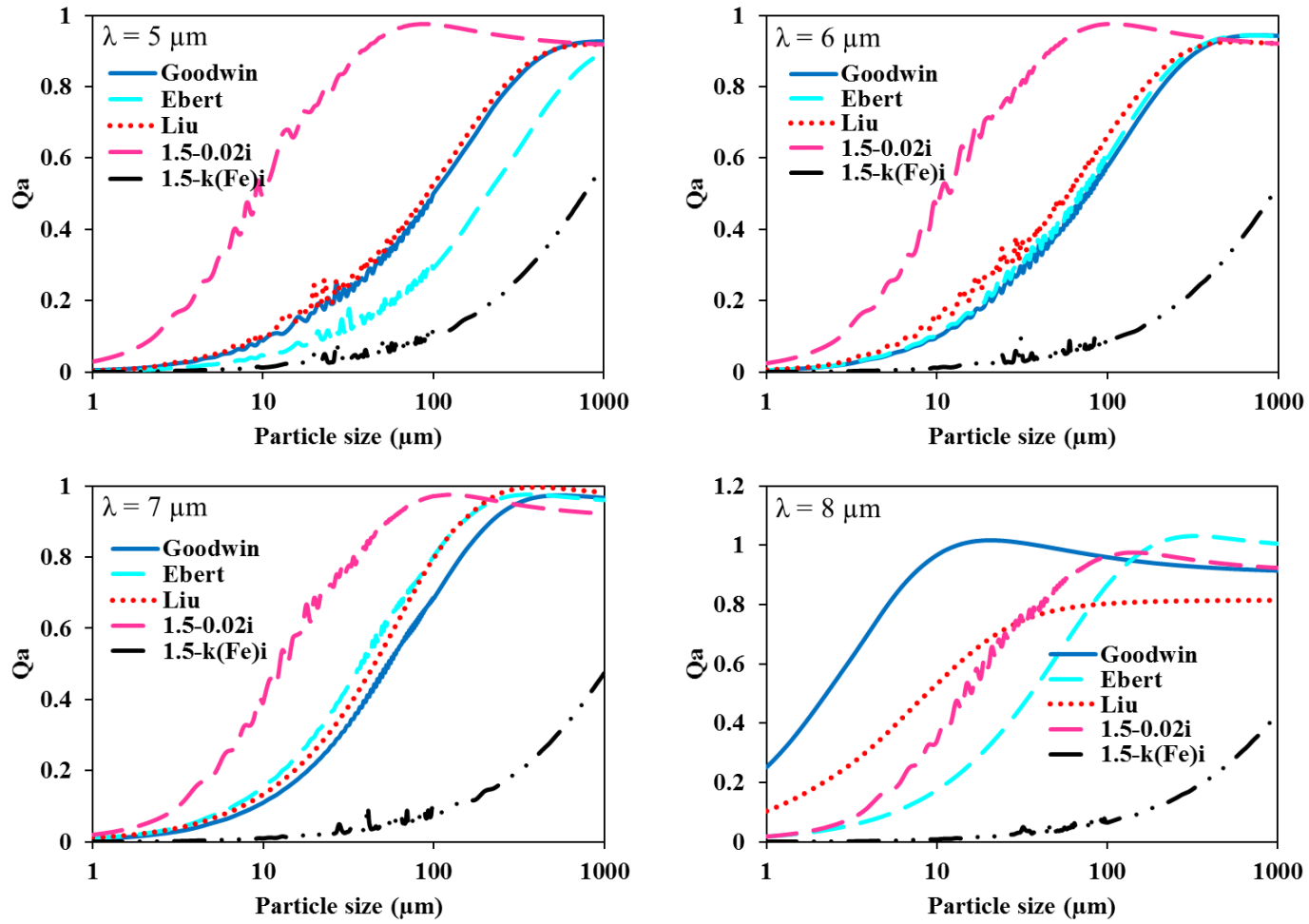
Spectral asymmetry factors for  $\lambda = 8-12 \mu\text{m}$  (silicon oxide absorption band) for Ash II



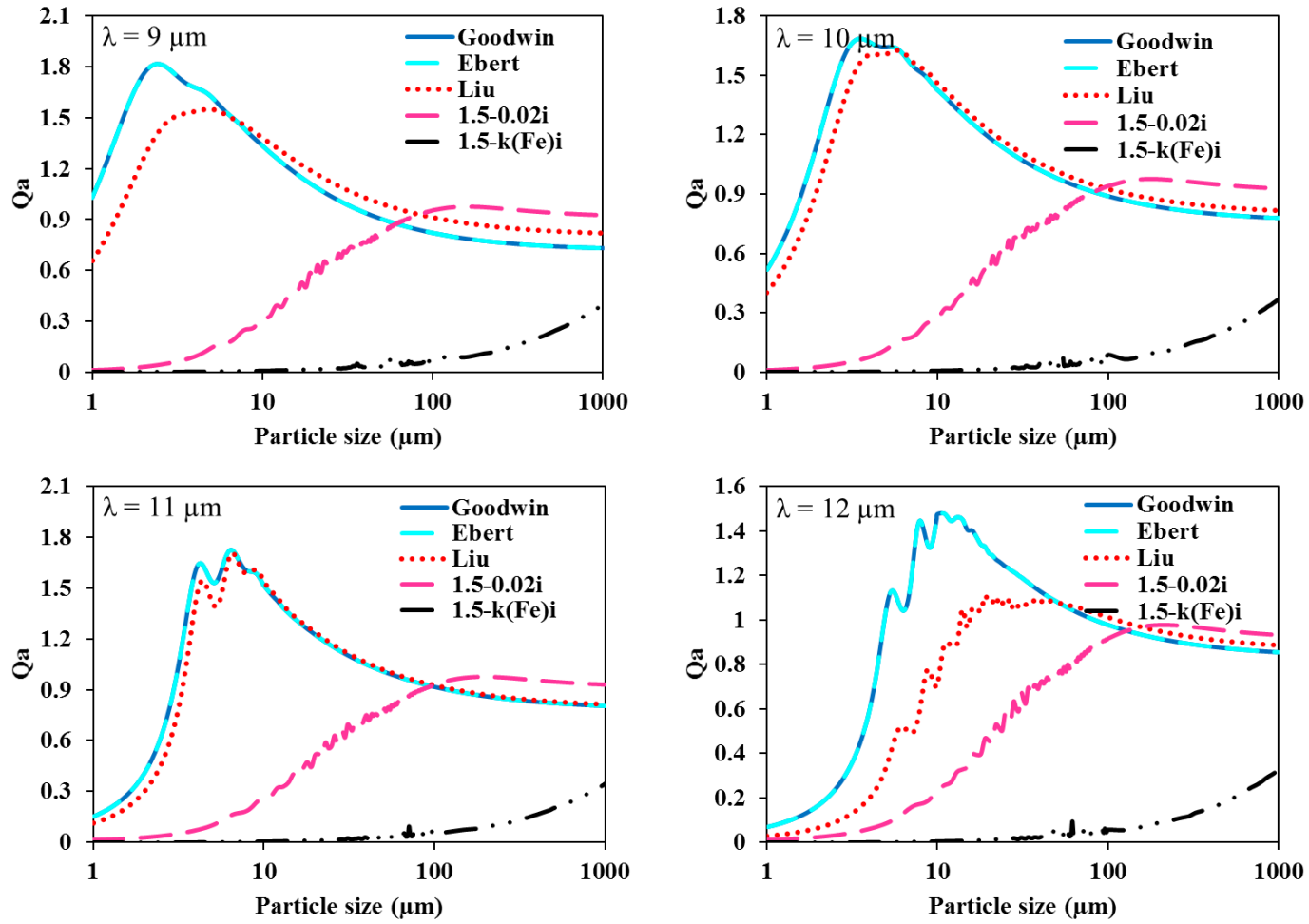
Spectral absorption efficiencies for  $\lambda = 1-4 \mu\text{m}$  (iron oxide absorption band) for Ash III



Spectral absorption efficiencies for  $\lambda = 4-8 \mu\text{m}$  (mixed absorption band) for Ash III

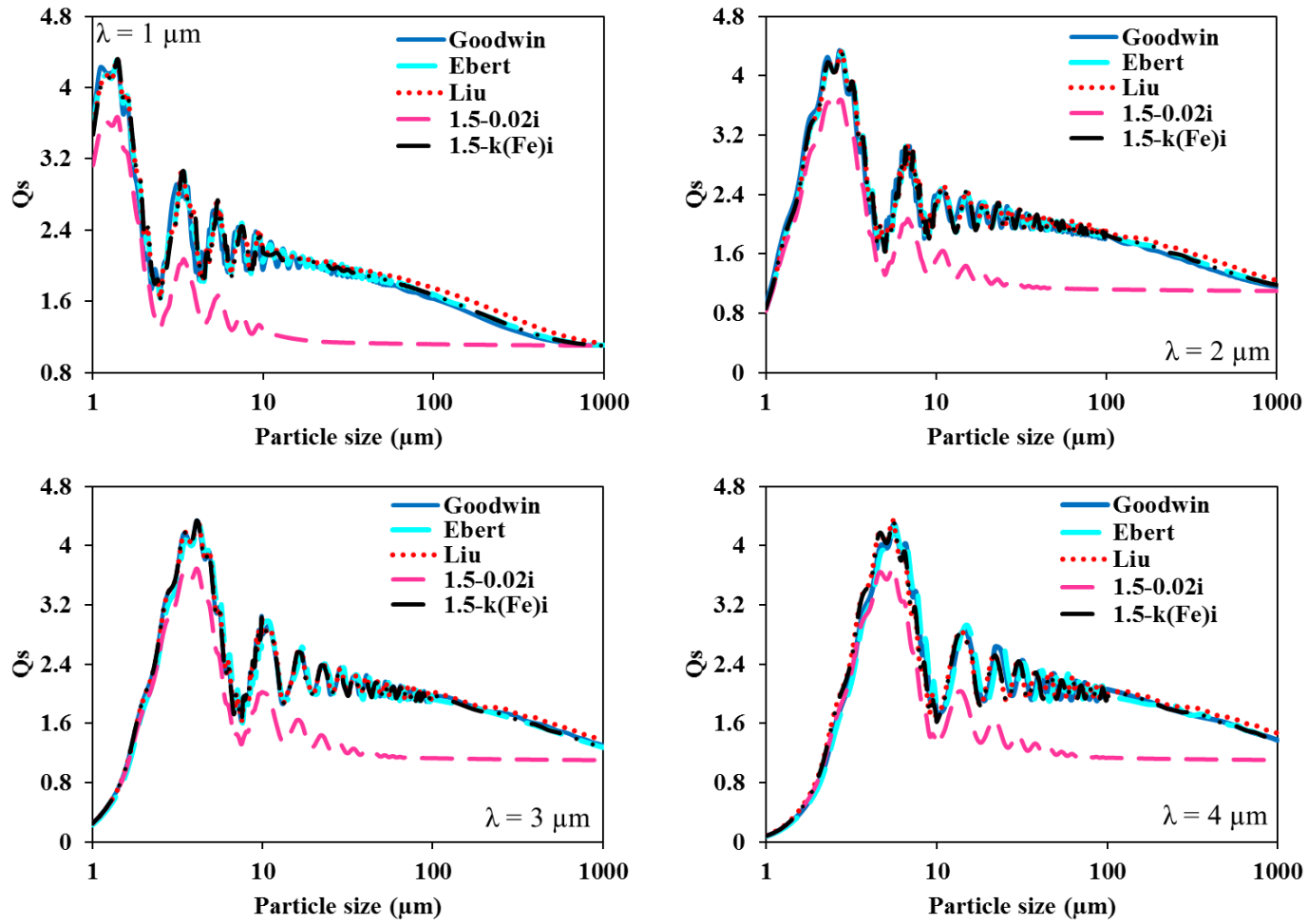


Spectral absorption efficiencies for  $\lambda = 8-12 \mu\text{m}$  (silicon oxide absorption band) for Ash III

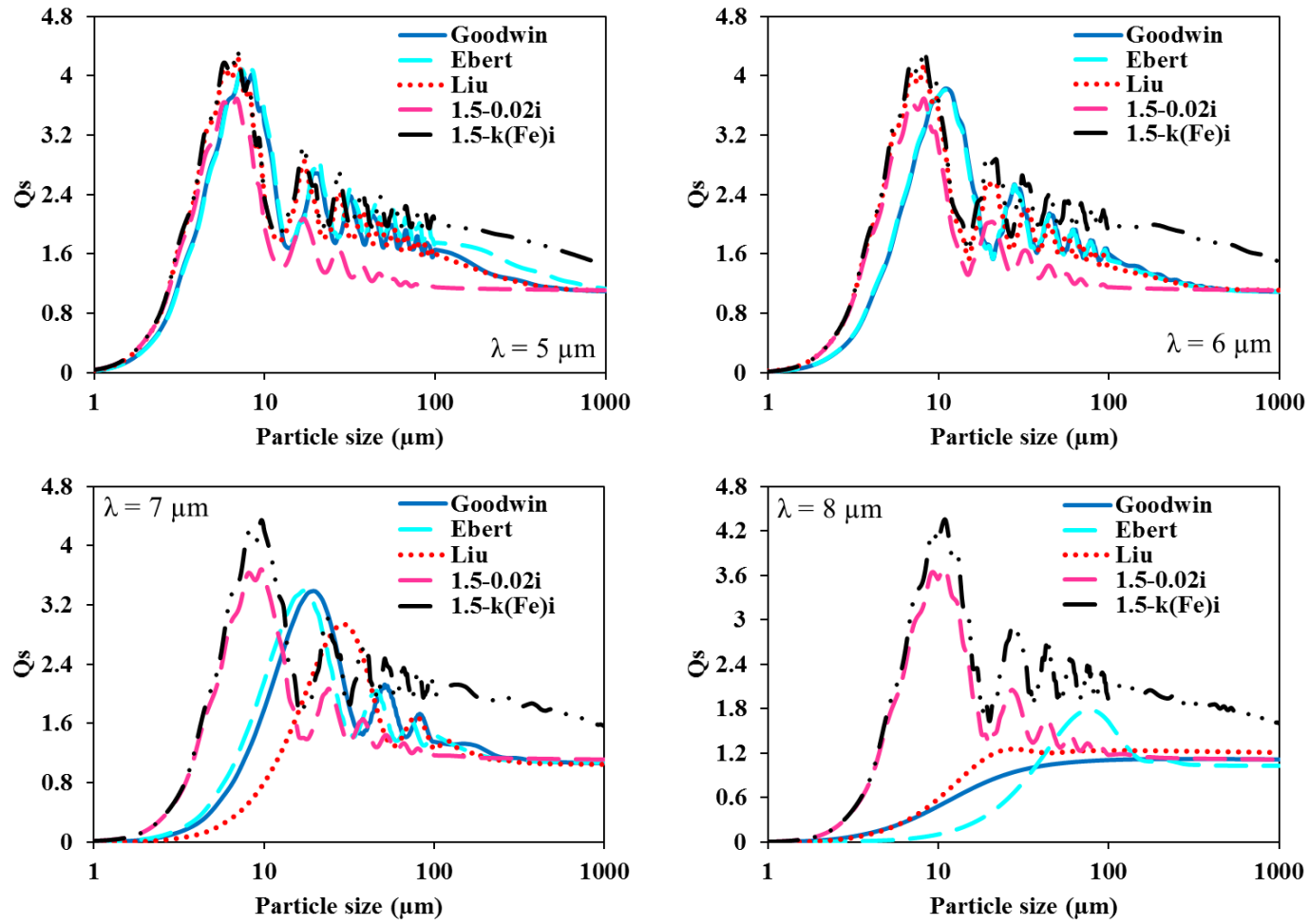




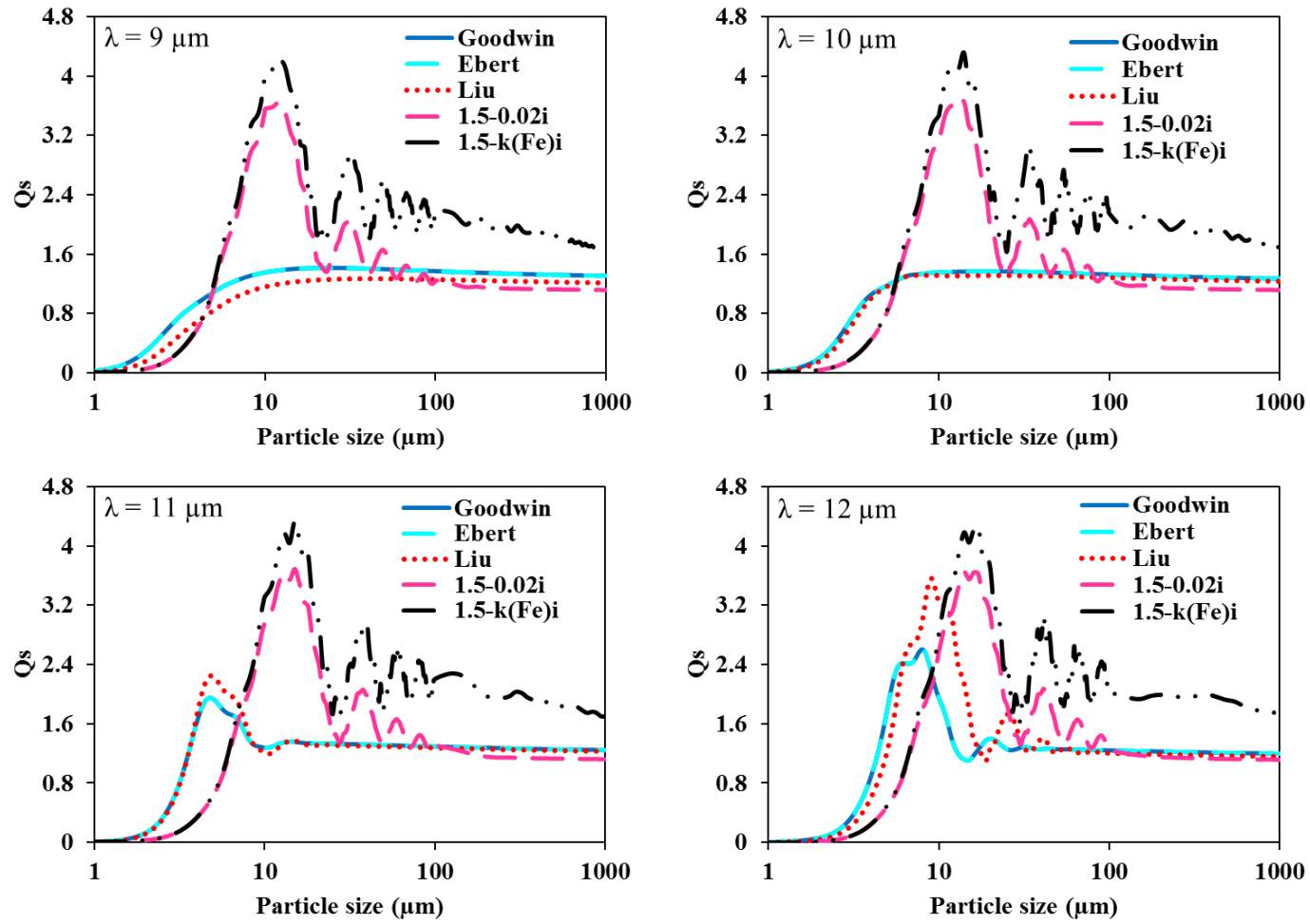
Spectral scattering efficiencies for  $\lambda = 1-4 \mu\text{m}$  (iron oxide absorption band) for Ash III



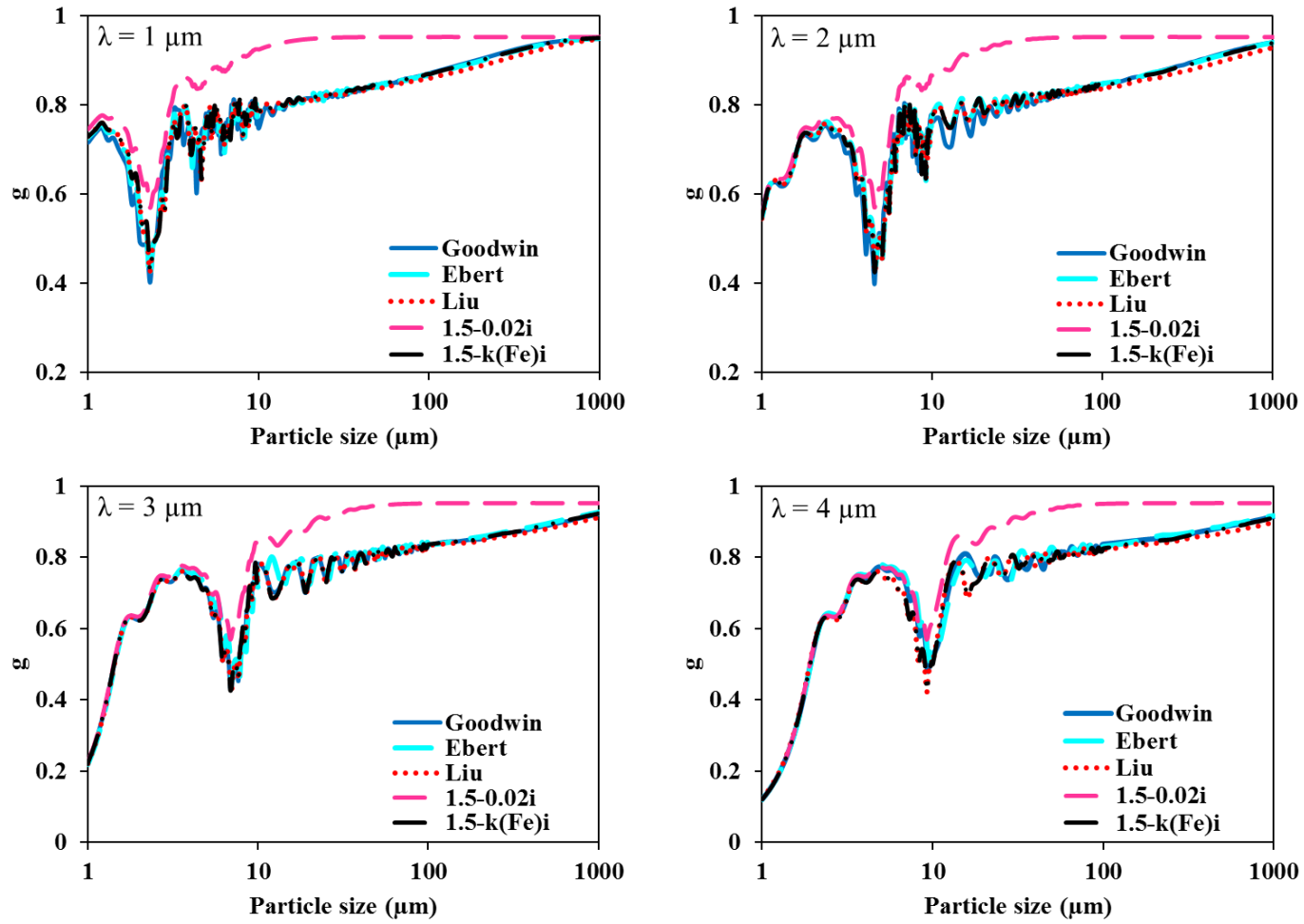
Spectral scattering efficiencies indices for  $\lambda = 4-8 \mu\text{m}$  (mixed absorption band) for Ash III



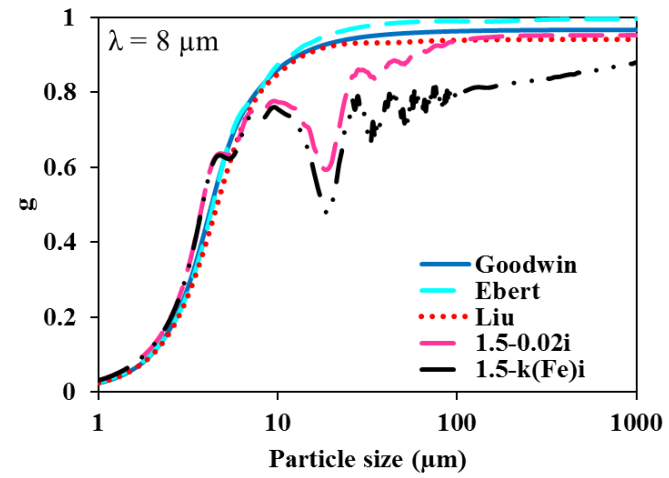
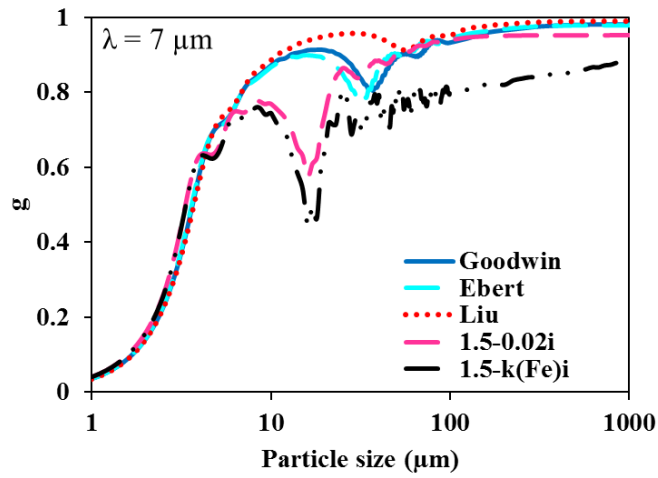
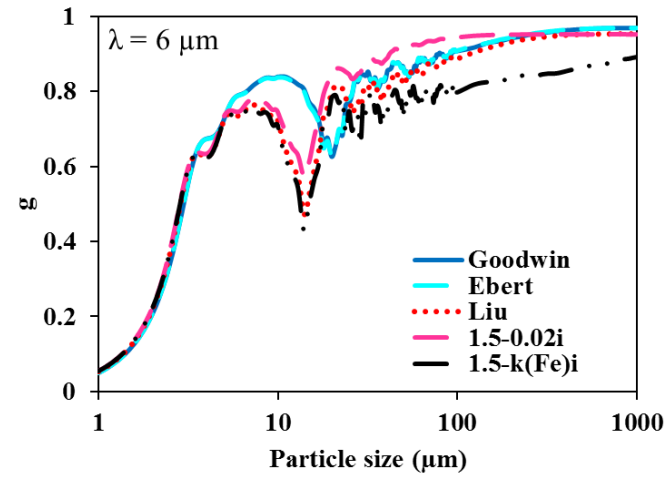
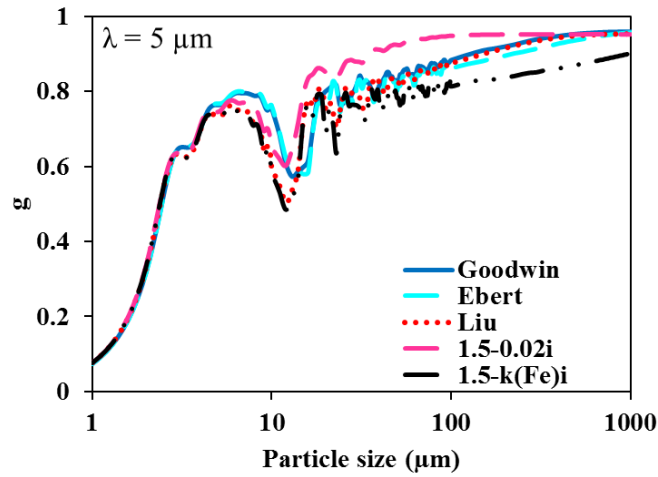
Spectral scattering efficiencies for  $\lambda = 8-12 \mu\text{m}$  (silicon oxide absorption band) for Ash III



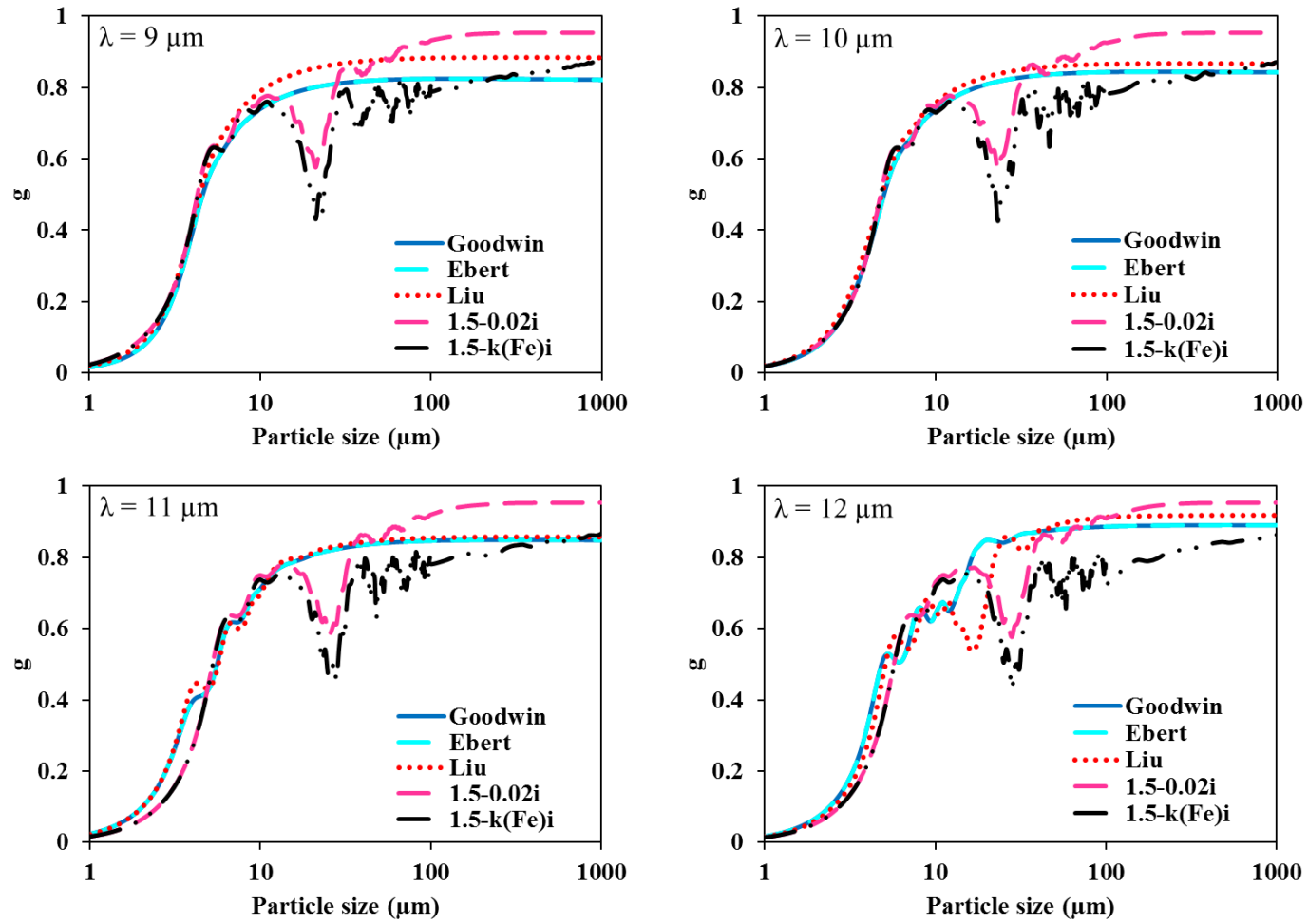
Spectral asymmetry factors for  $\lambda = 1-4 \mu\text{m}$  (iron oxide absorption band) for Ash III



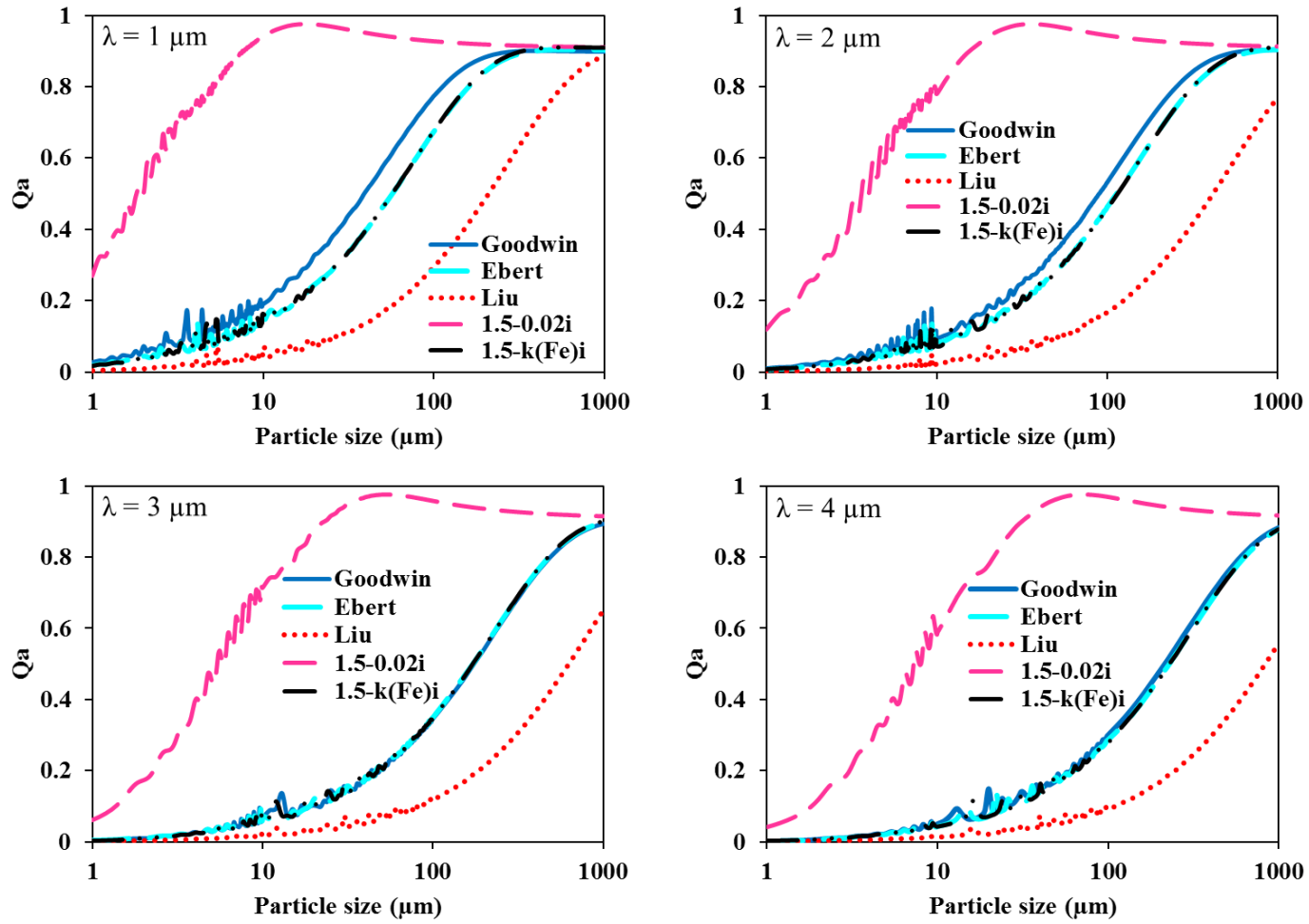
Spectral asymmetry factors for  $\lambda = 4-8 \mu\text{m}$  (mixed absorption band) for Ash III



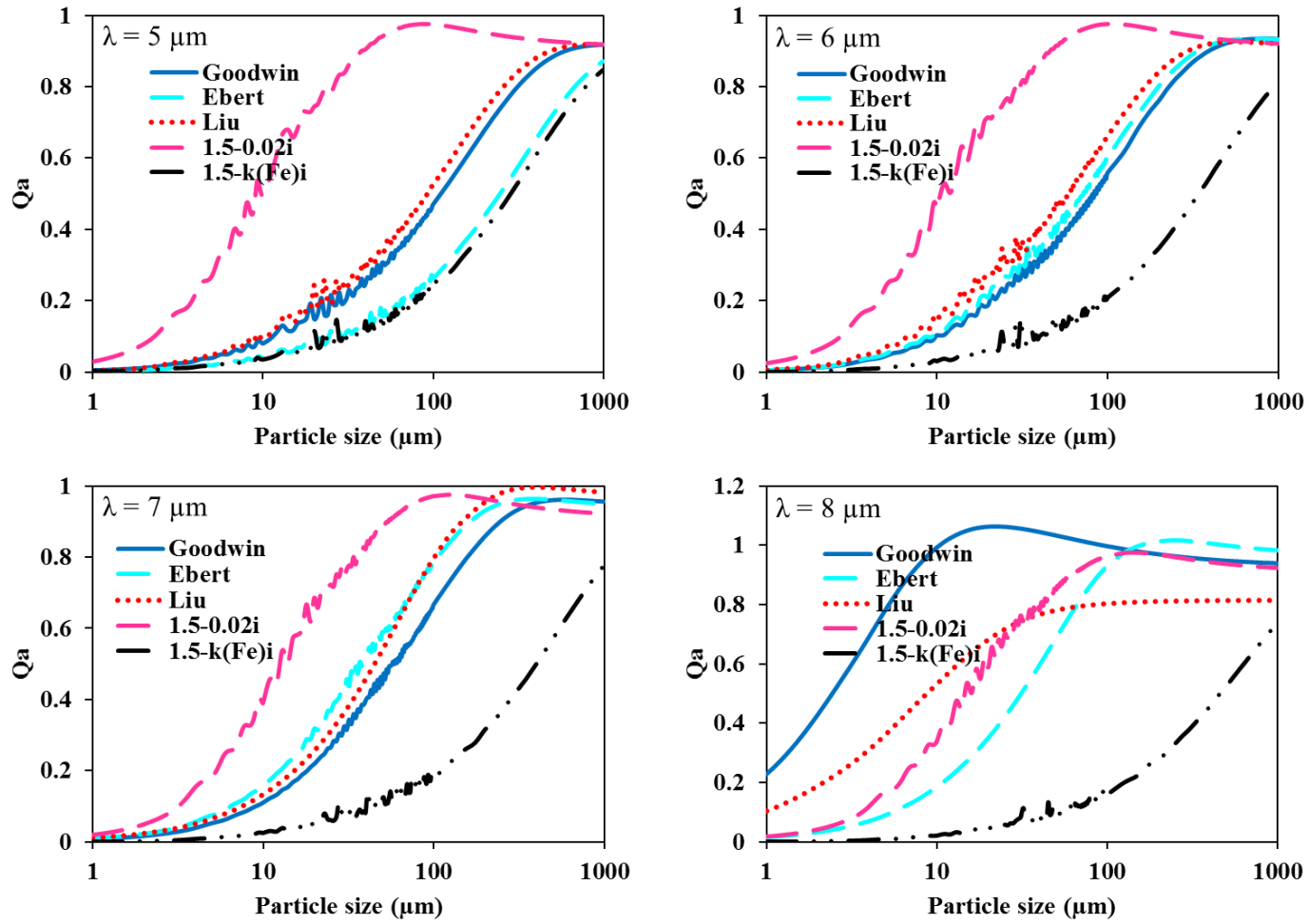
Spectral asymmetry factors for  $\lambda = 8-12 \mu\text{m}$  (silicon oxide absorption band) for Ash III



Spectral absorption efficiencies for  $\lambda = 1-4 \mu\text{m}$  (iron oxide absorption band) for Ash IV

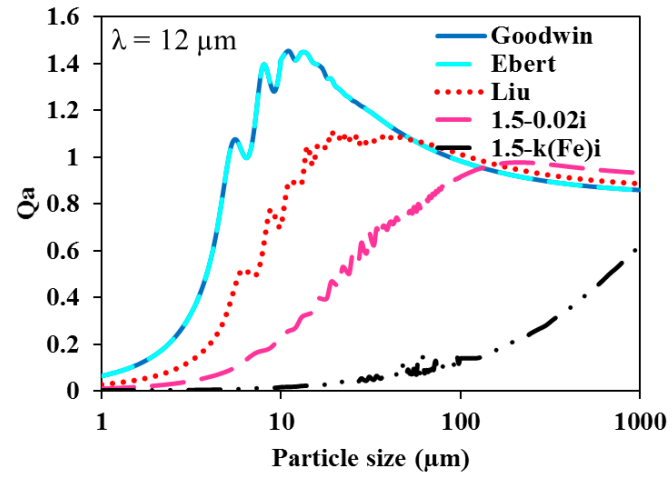
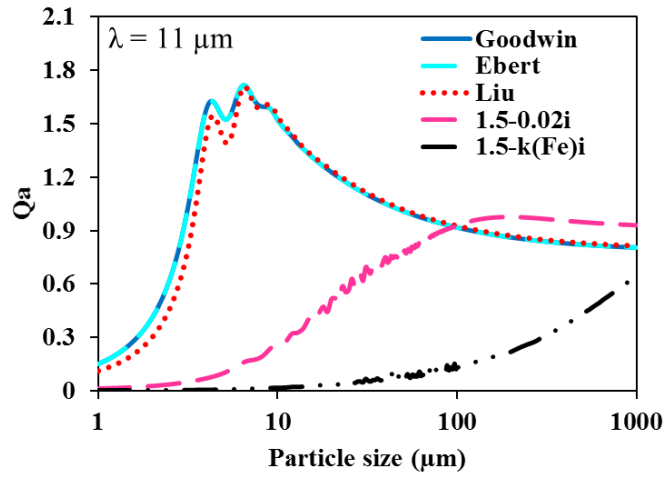
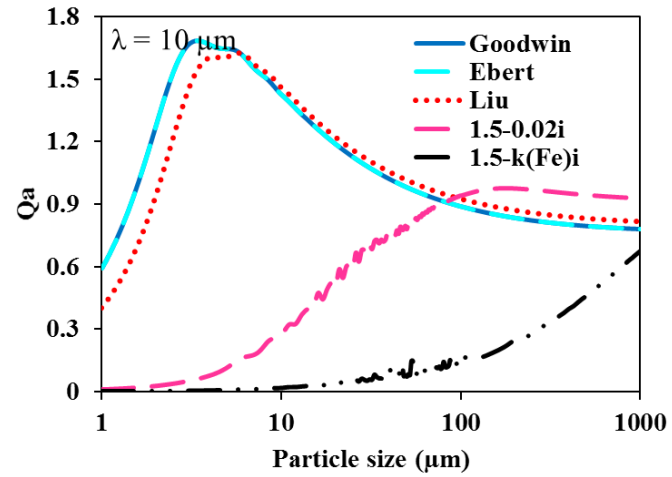
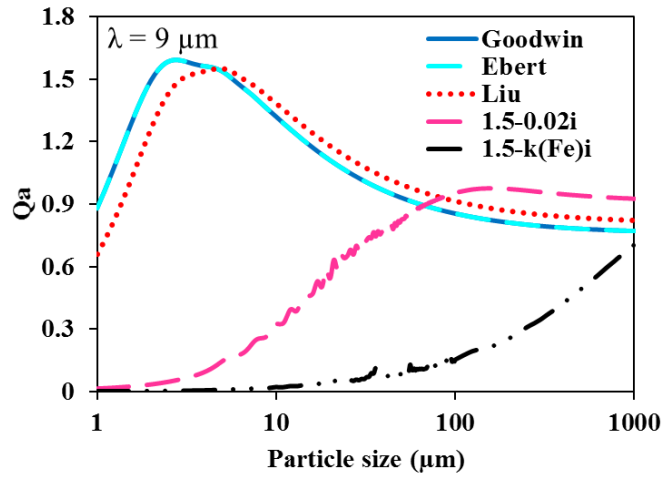


Spectral absorption efficiencies for  $\lambda = 4-8 \mu\text{m}$  (mixed absorption band) for Ash IV

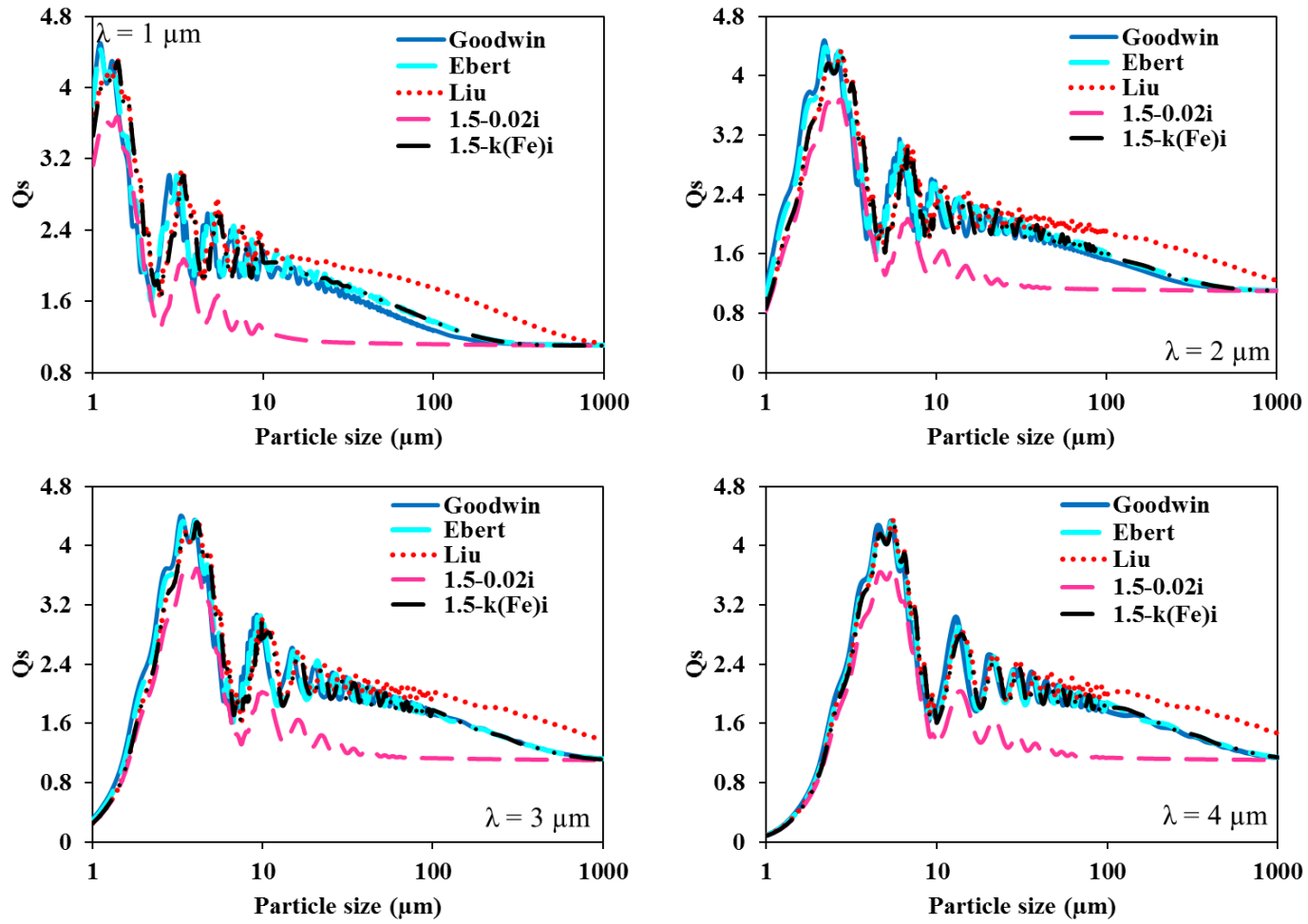




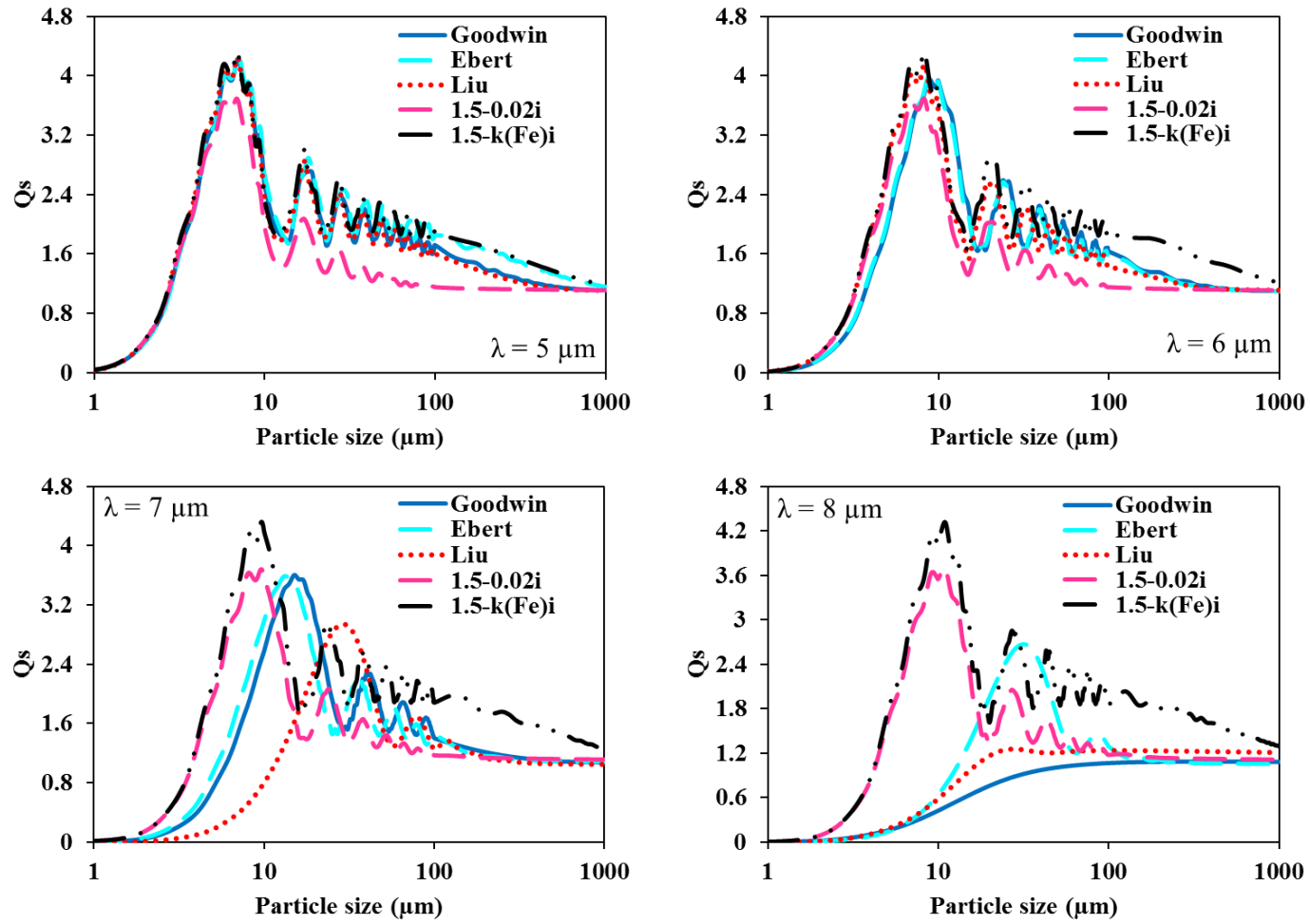
Spectral absorption efficiencies for  $\lambda = 8-12 \mu\text{m}$  (silicon oxide absorption band) for Ash IV



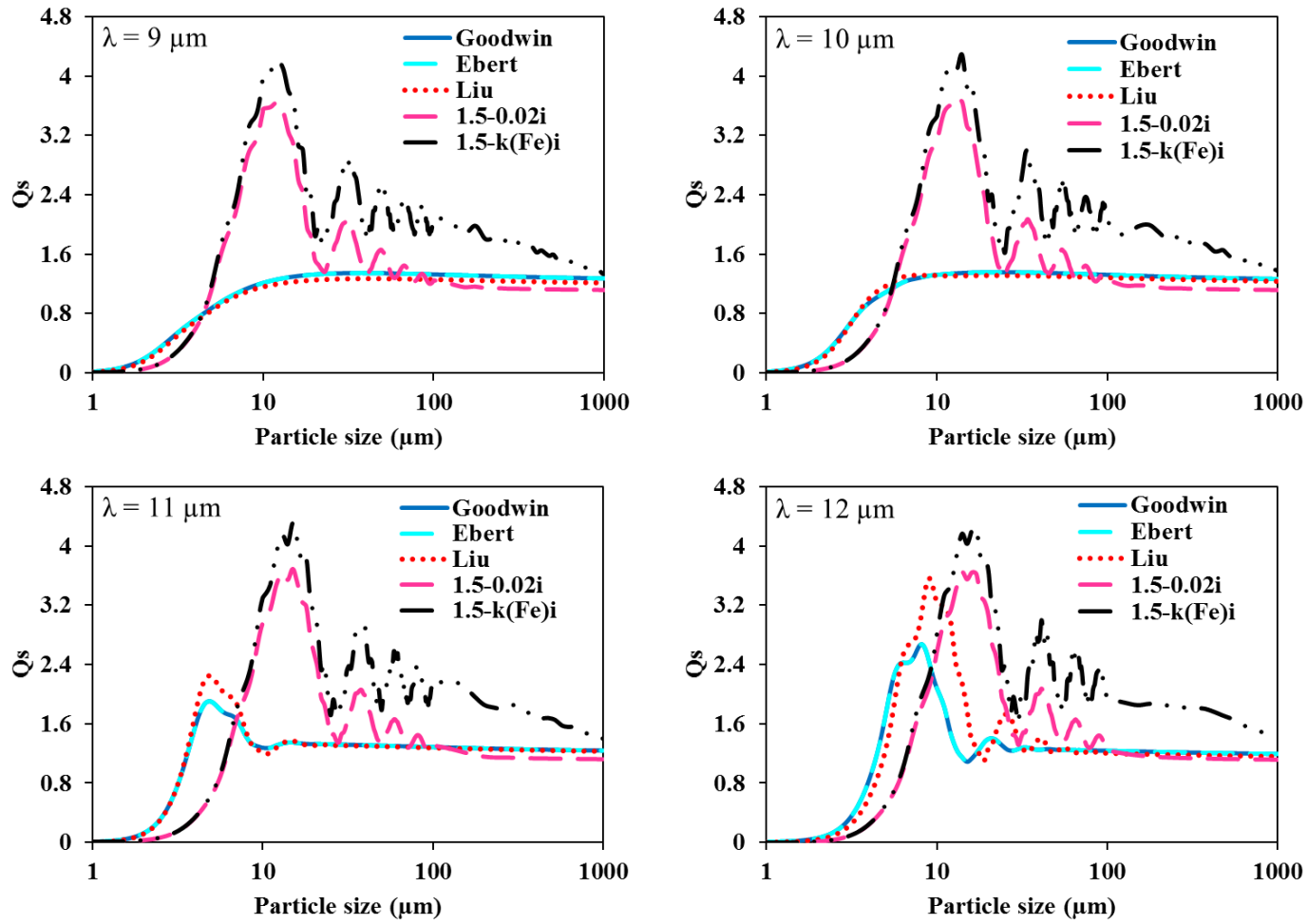
Spectral scattering efficiencies for  $\lambda = 1-4 \mu\text{m}$  (iron oxide absorption band) for Ash IV



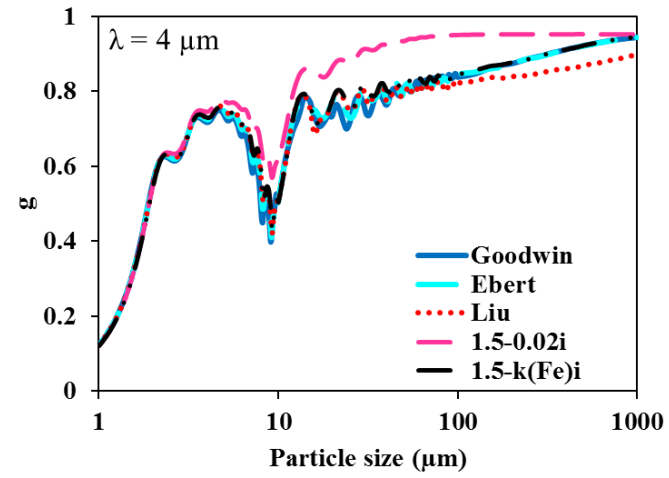
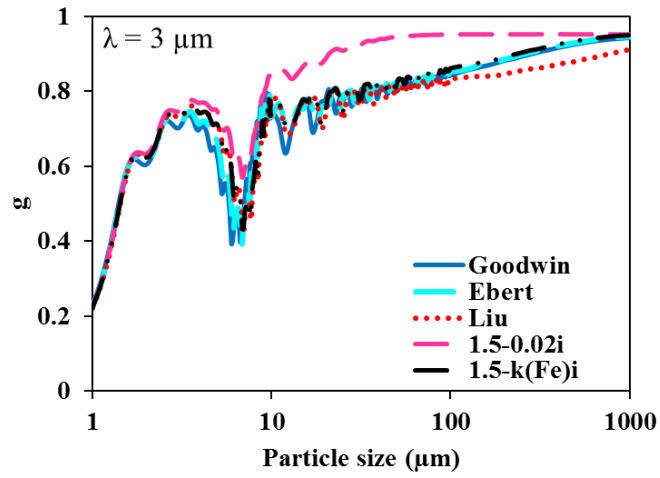
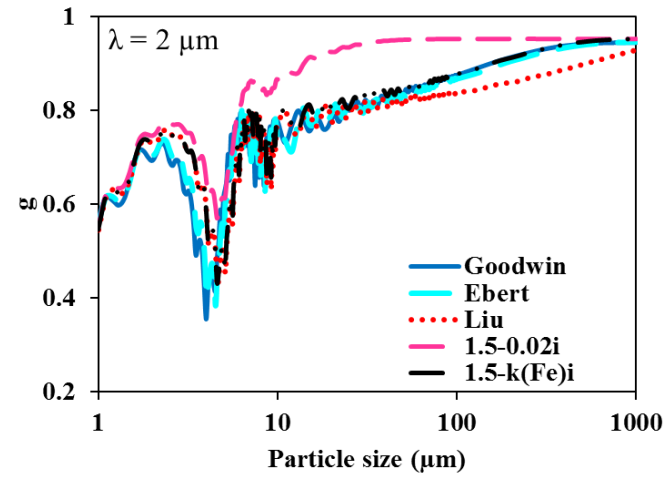
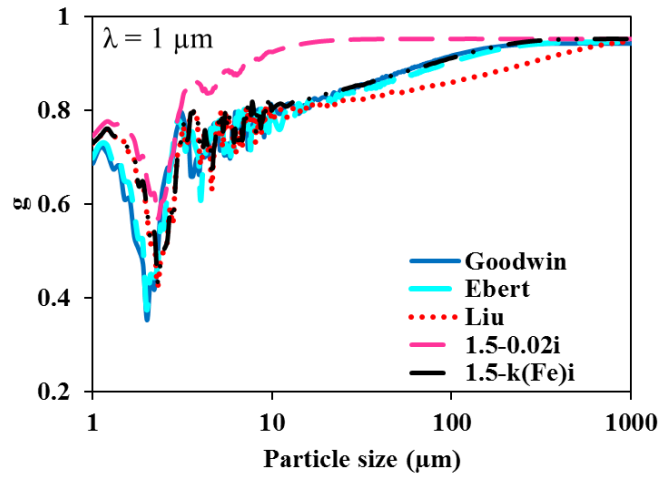
Spectral scattering efficiencies indices for  $\lambda = 4-8 \mu\text{m}$  (mixed absorption band) for Ash IV



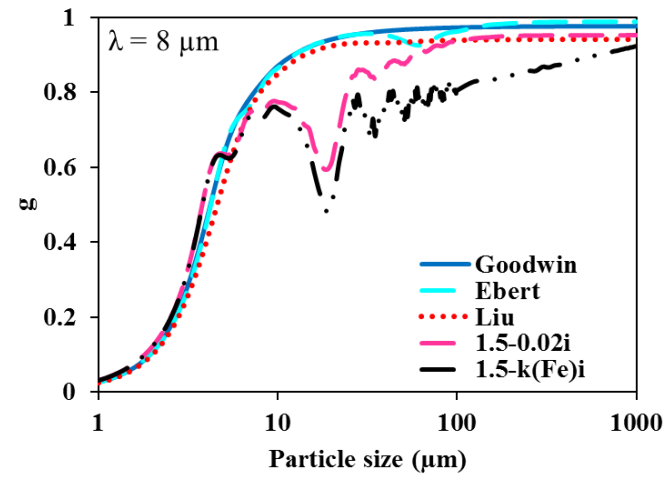
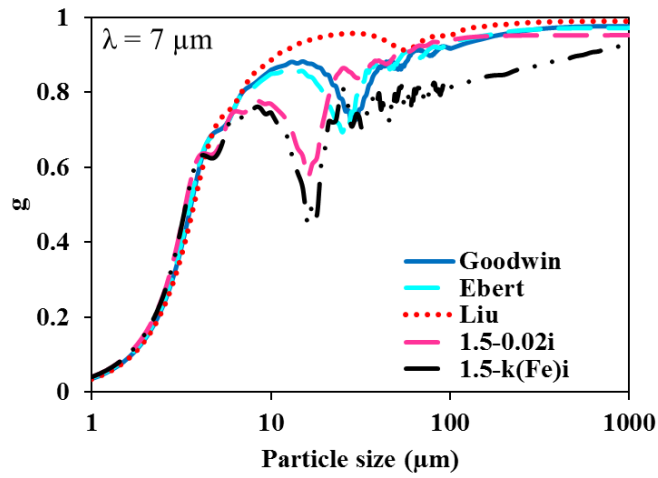
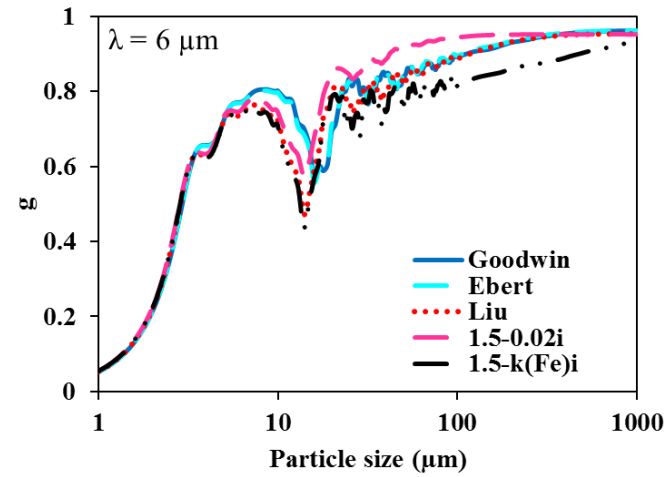
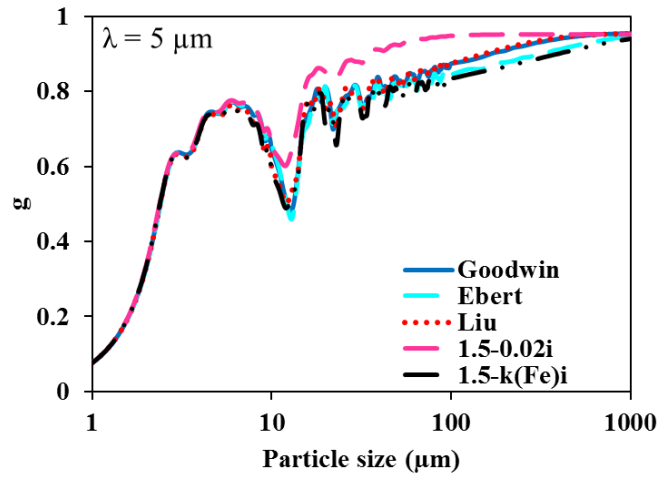
Spectral scattering efficiencies for  $\lambda = 8-12 \mu\text{m}$  (silicon oxide absorption band) for Ash IV



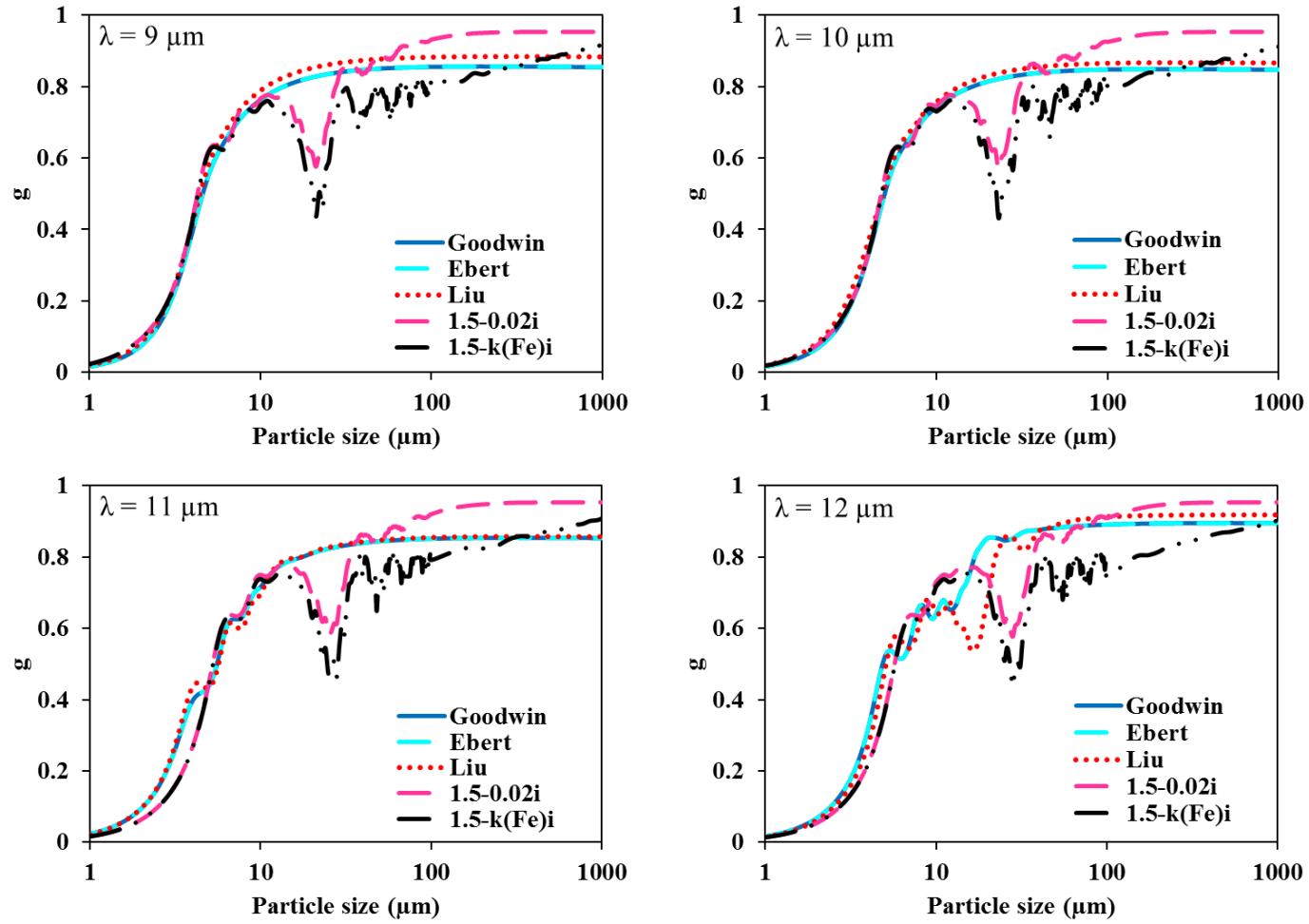
Spectral asymmetry factors for  $\lambda = 1-4 \mu\text{m}$  (iron oxide absorption band) for Ash IV



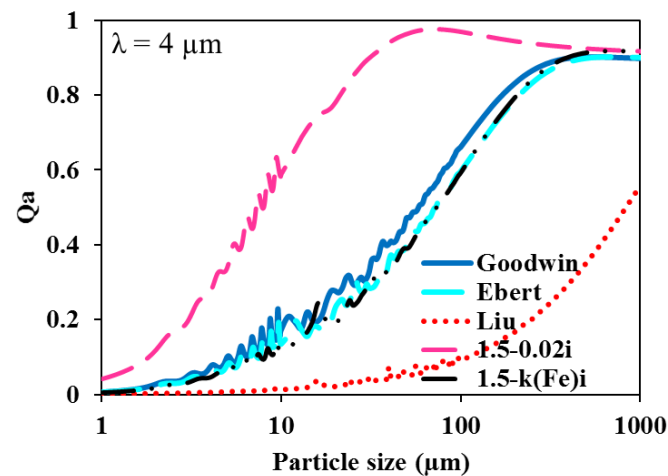
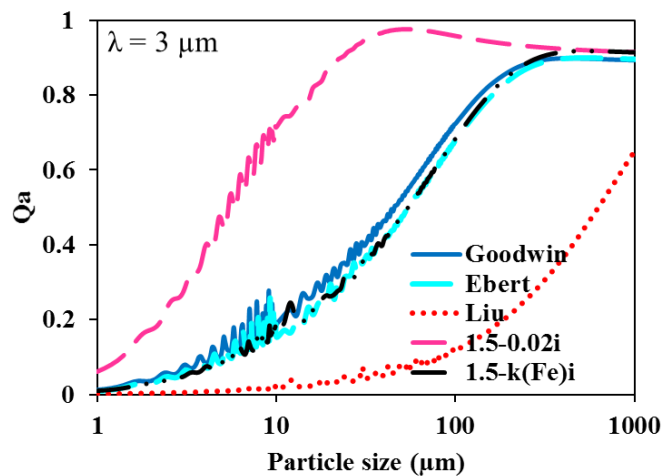
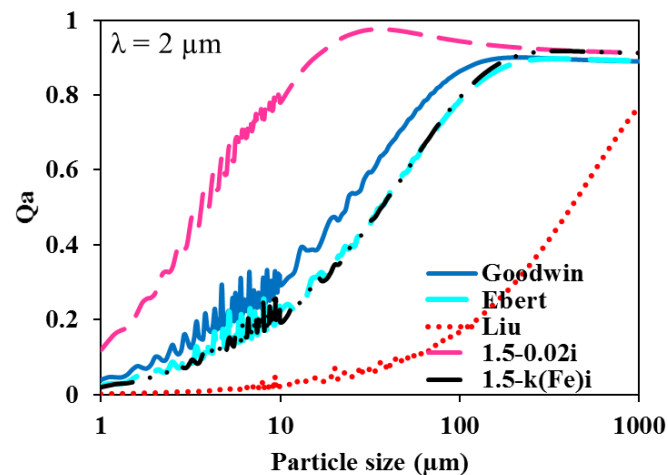
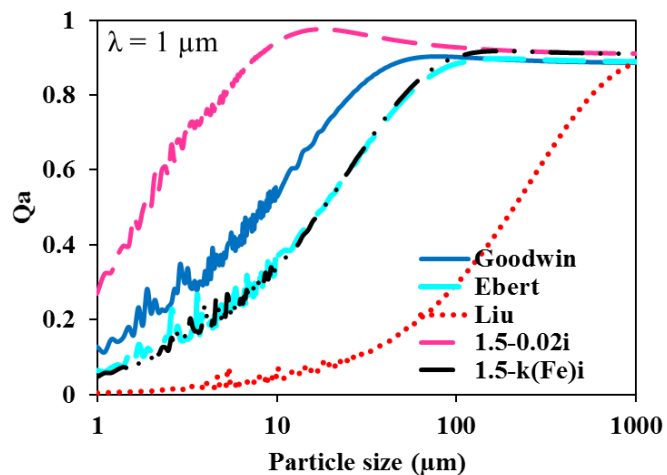
Spectral asymmetry factors for  $\lambda = 4-8 \mu\text{m}$  (mixed absorption band) for Ash IV



Spectral asymmetry factors for  $\lambda = 8-12 \mu\text{m}$  (silicon oxide absorption band) for Ash IV

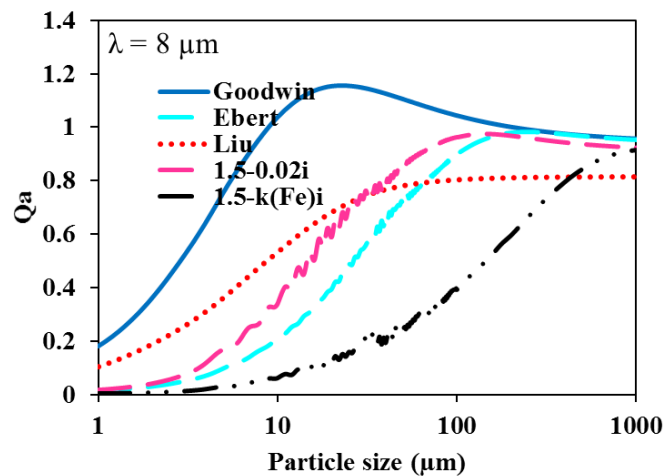
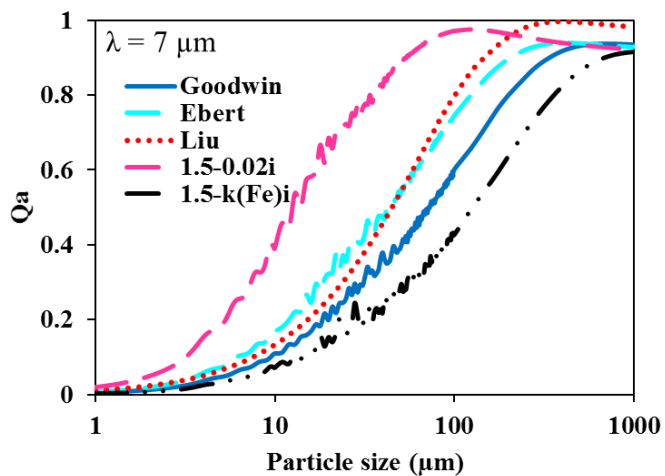
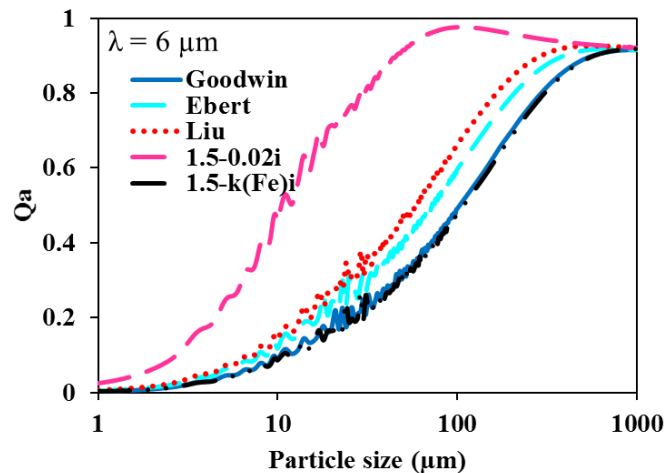
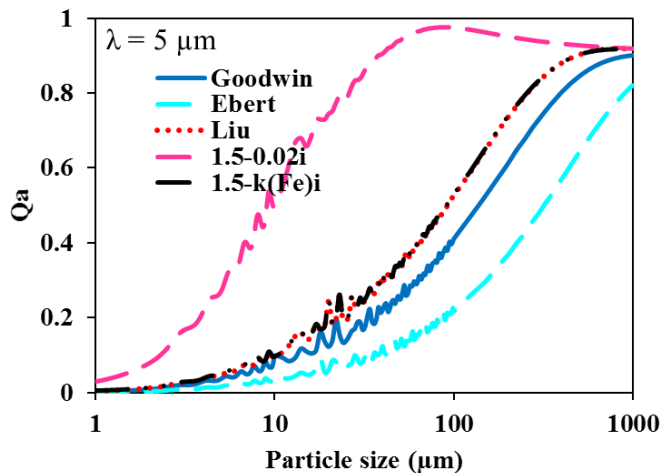


Spectral absorption efficiencies for  $\lambda = 1-4 \mu\text{m}$  (iron oxide absorption band) for Ash V

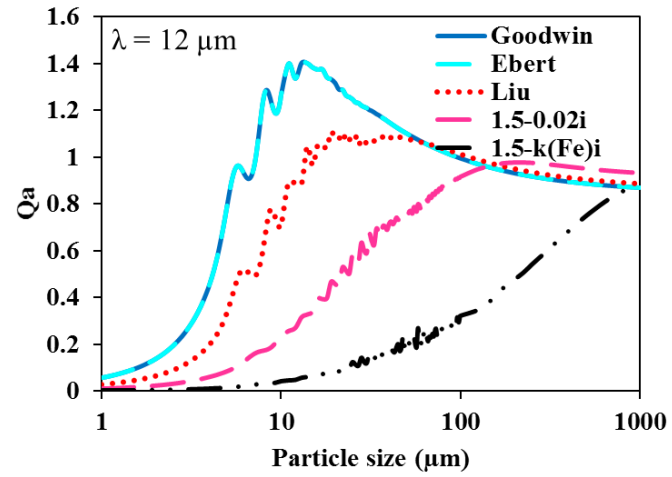
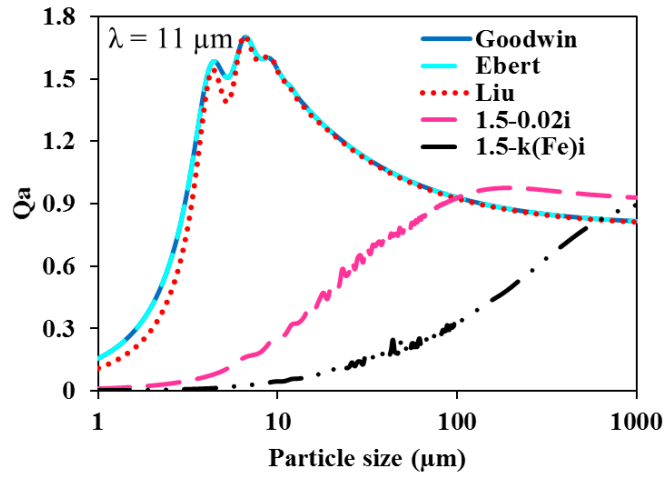
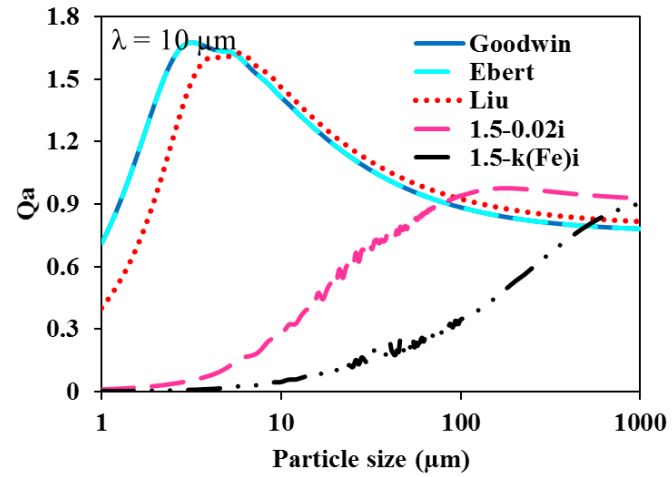
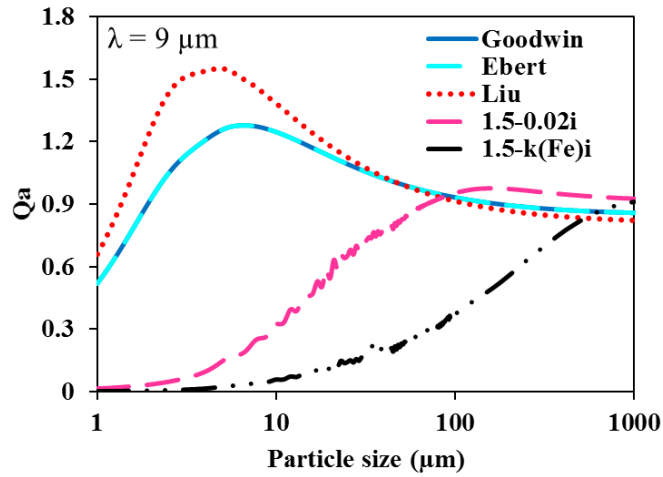




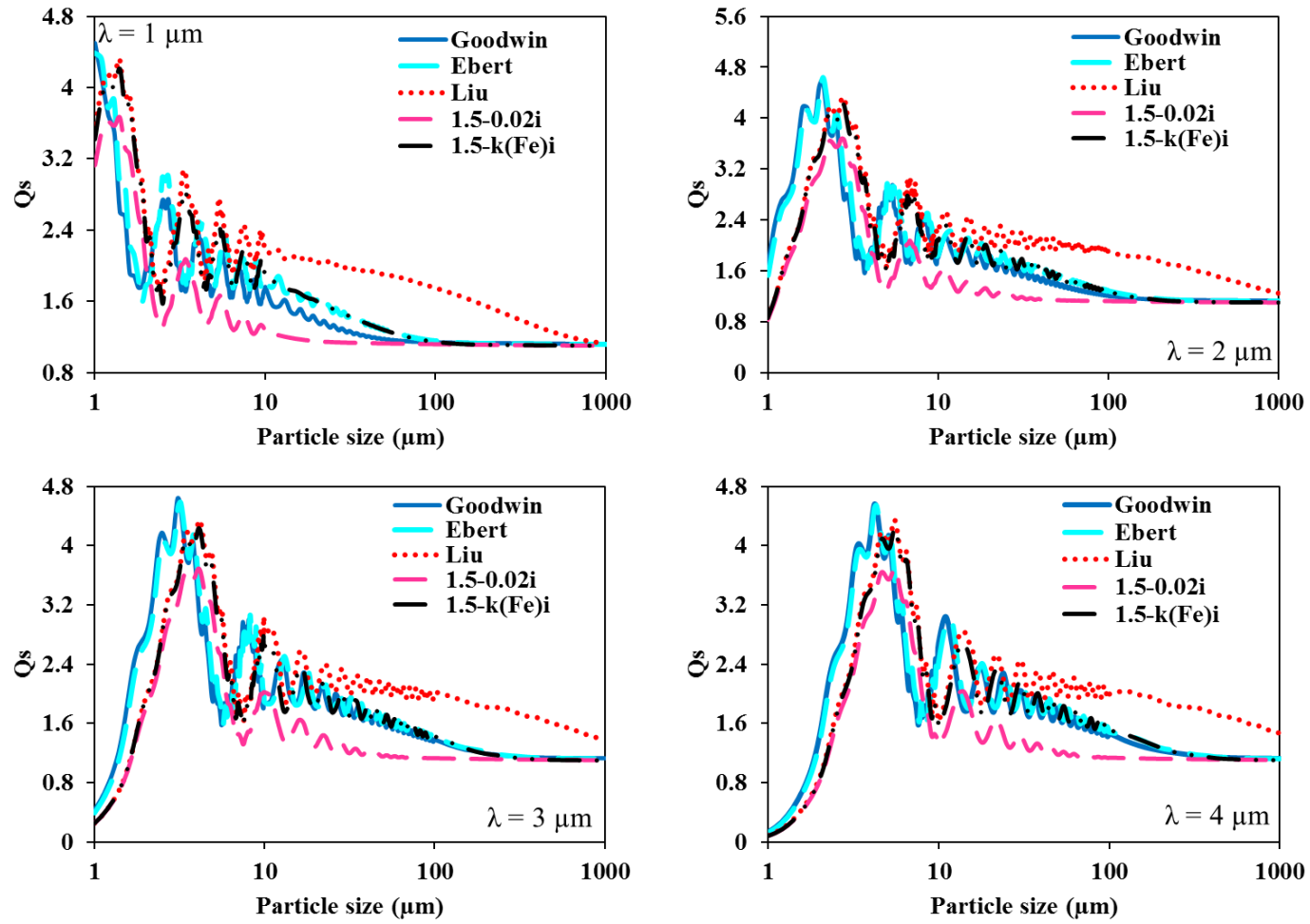
Spectral absorption efficiencies for  $\lambda = 4-8 \mu\text{m}$  (mixed absorption band) for Ash V



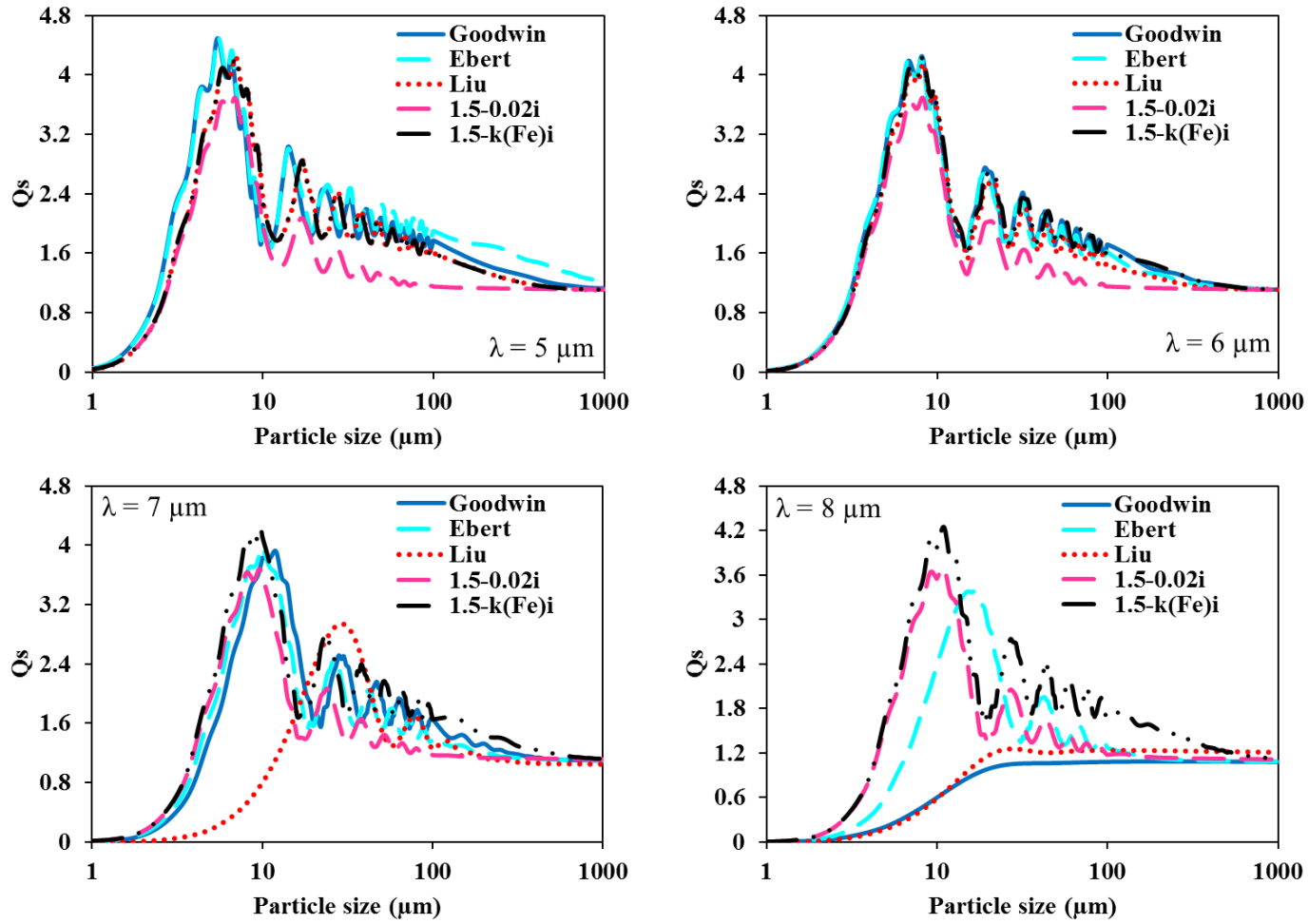
Spectral absorption efficiencies for  $\lambda = 8-12 \mu\text{m}$  (silicon oxide absorption band) for Ash V



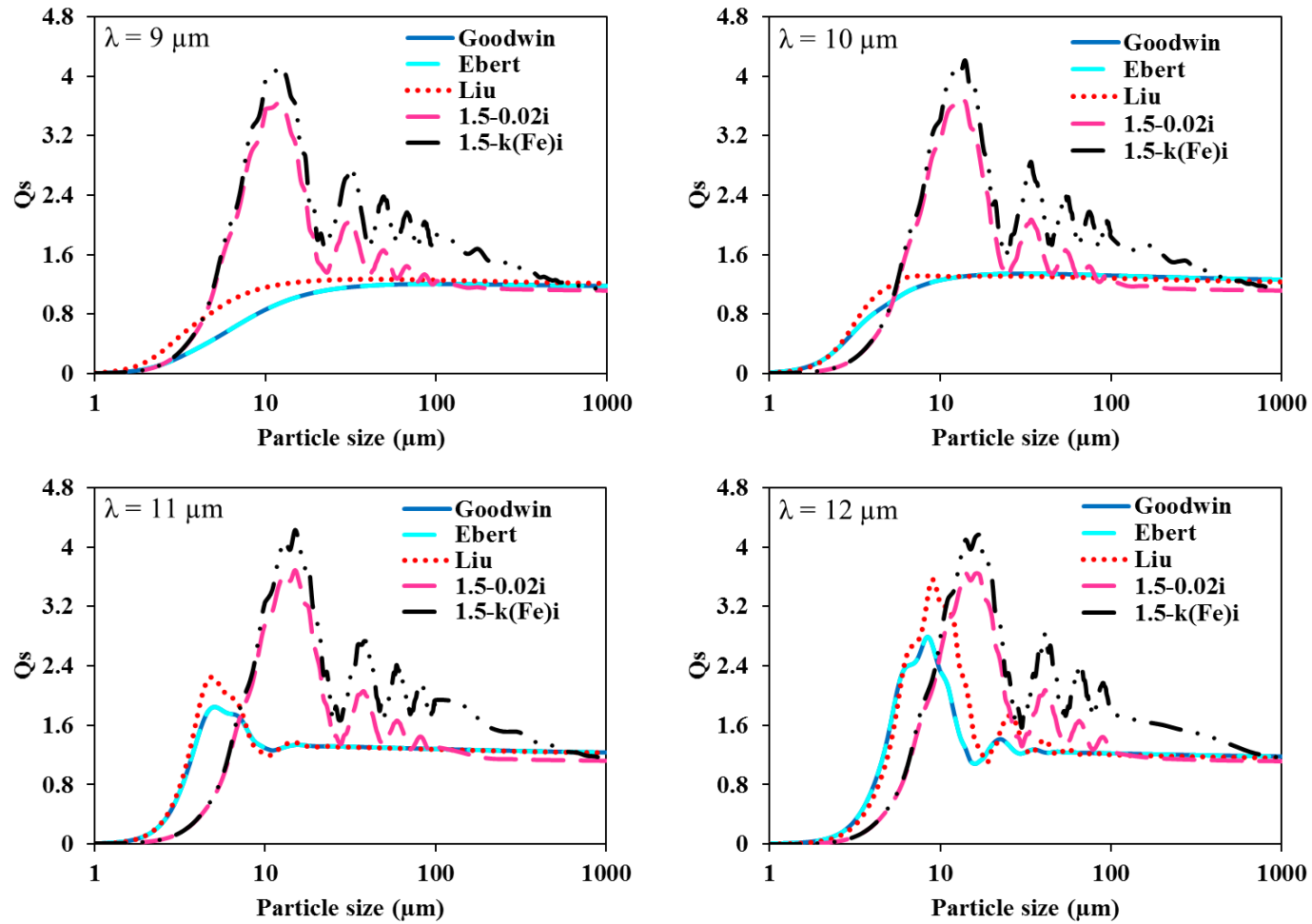
Spectral scattering efficiencies for  $\lambda = 1-4 \mu\text{m}$  (iron oxide absorption band) for Ash V



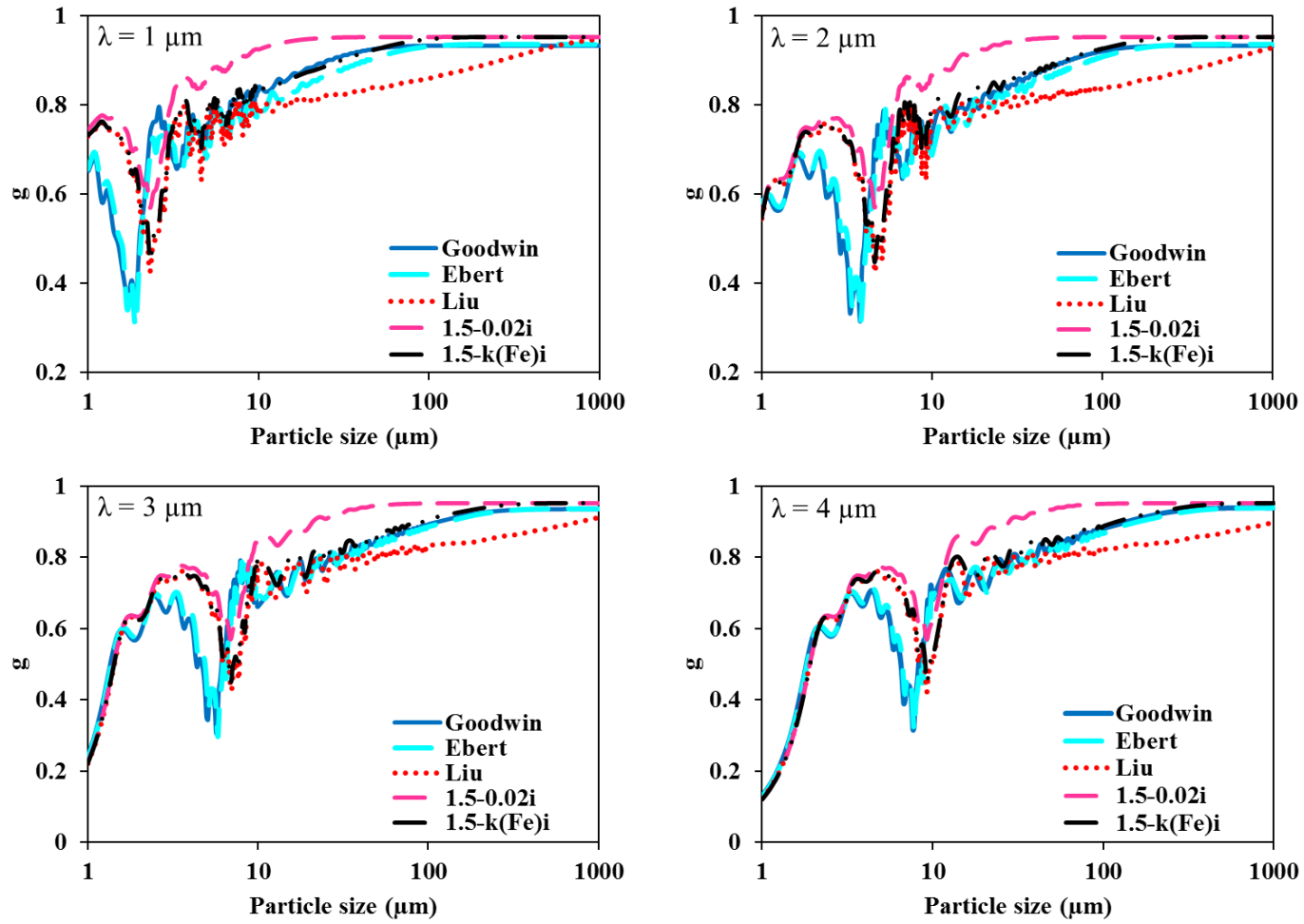
Spectral scattering efficiencies indices for  $\lambda = 4-8 \mu\text{m}$  (mixed absorption band) for Ash V



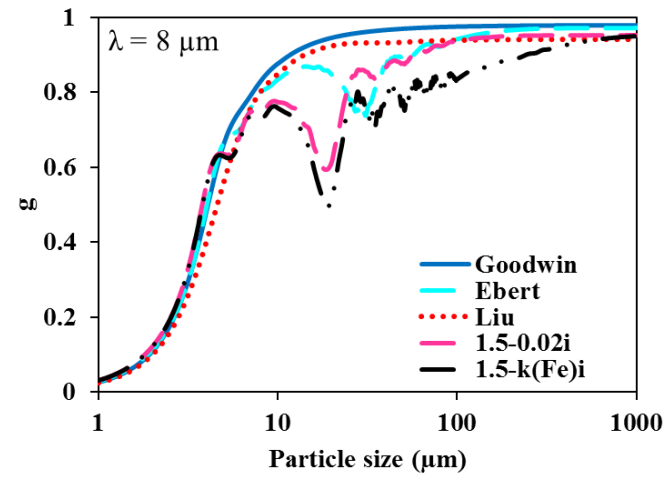
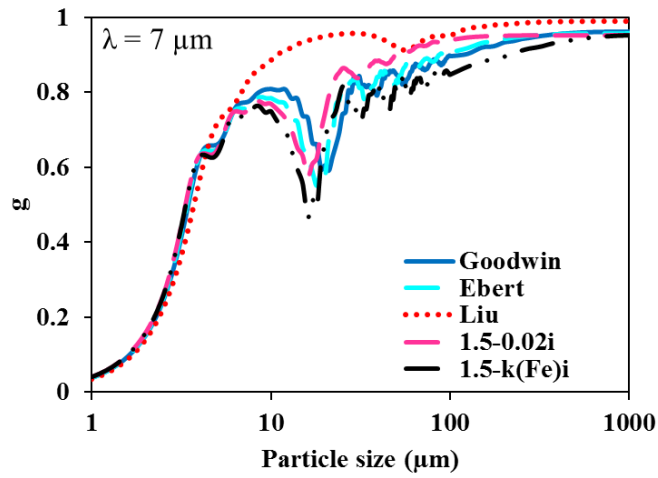
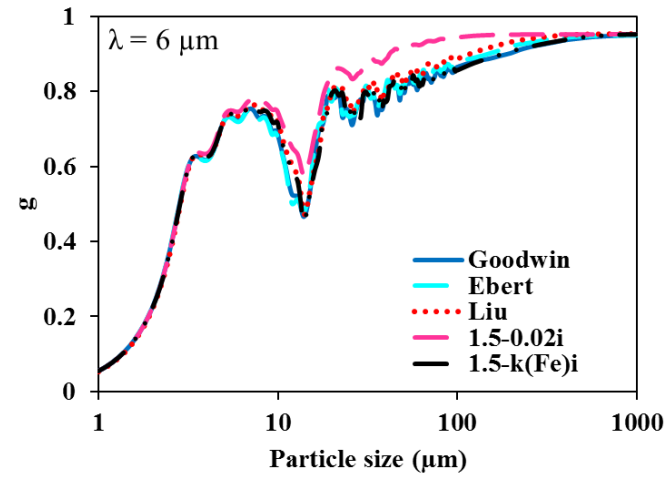
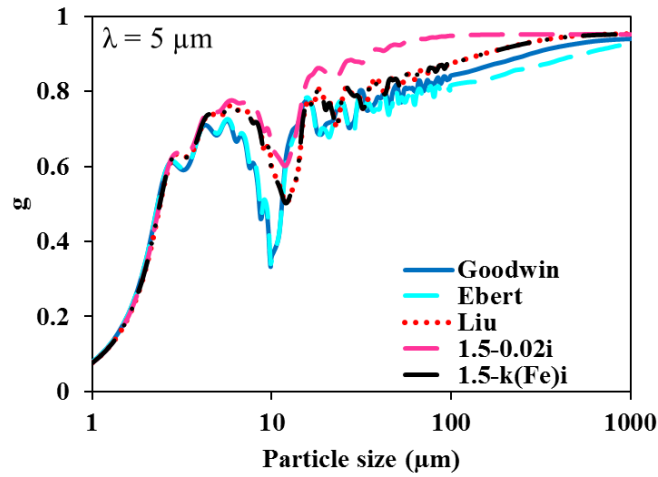
Spectral scattering efficiencies for  $\lambda = 8-12 \mu\text{m}$  (silicon oxide absorption band) for Ash V



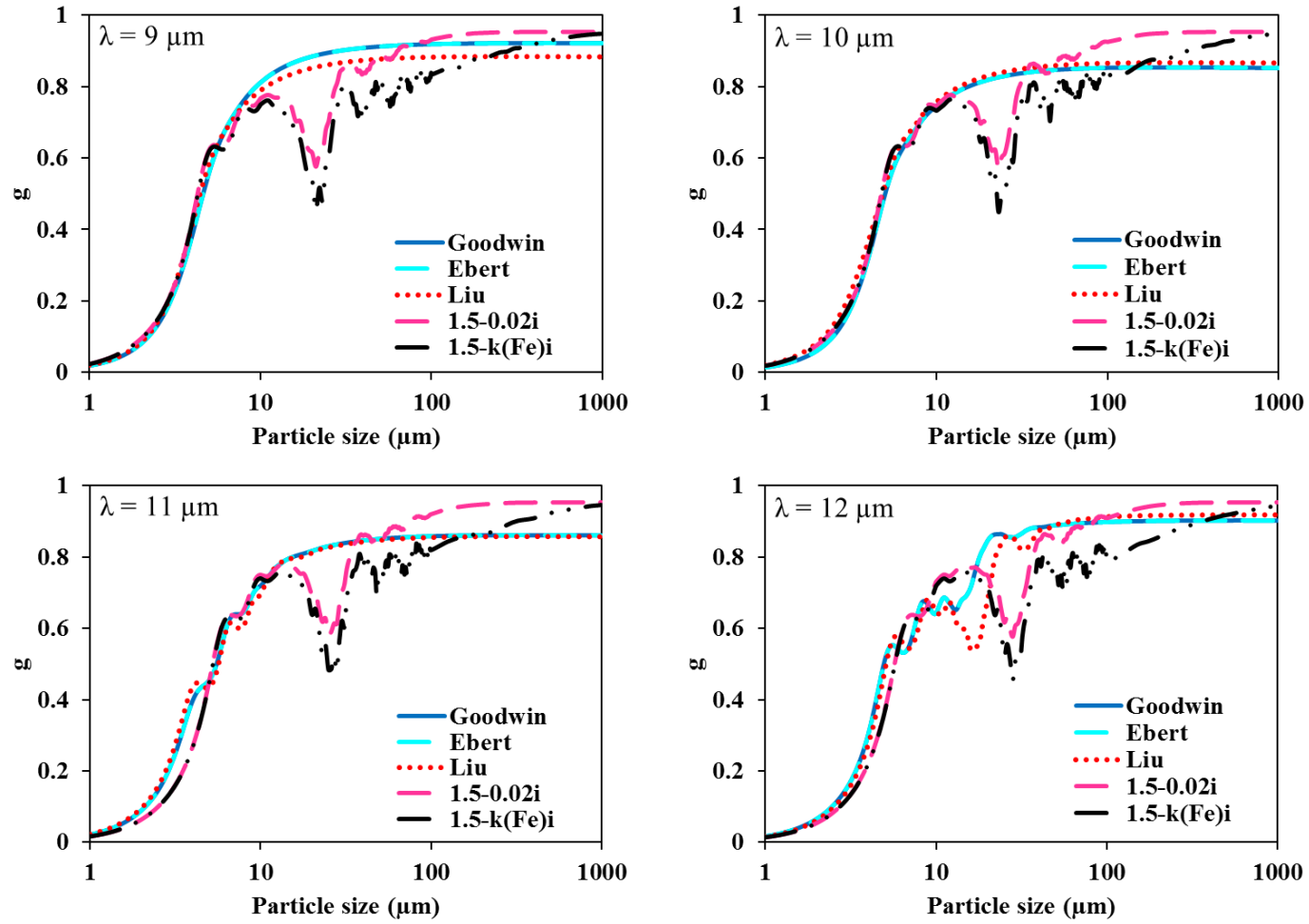
Spectral asymmetry factors for  $\lambda = 1-4 \mu\text{m}$  (iron oxide absorption band) for Ash V



Spectral asymmetry factors for  $\lambda = 4-8 \mu\text{m}$  (mixed absorption band) for Ash V



Spectral asymmetry factors for  $\lambda = 8-12 \mu\text{m}$  (silicon oxide absorption band) for Ash V





# CURRICULUM VITAE

## PERSONAL INFORMATION

**Surname, Name:** ATEŞ, Cihan

**Nationality:** Turkish (TC)

**Date and Place of Birth:** 23-03-1989, Bursa

**Marital Status:** Married

## EDUCATION

Degree	Institution	Year of Graduation
M.Sc.	Chemical Engineering, METU	2015
B.Sc.	Chemical Engineering, METU	2012

## PUBLICATIONS

### Journal Articles

1. G. Ozen, C. Ates, N. Selçuk, G. Kulah, “Assessment of SLW-1 Model in the Presence of Gray and Non-Gray Particles”, *International Journal of Thermal Sciences*, under review, 2018.
2. C. Ates, N. Selçuk, G. Kulah, “Influence of Gray Particle Assumption on the Predictive Accuracy of Gas Property Approximations”, *J. Quant. Spectrosc. Radiat. Transfer*, under review, 2018.

3. C. Ates, N. Selçuk, G. Kulah, “Influence of Fly Ash Composition on Non-Gray Particle Radiation in Combusting Systems”, *J. Quant. Spectrosc. Radiat. Transfer*, Vol. 215, pp. 25-40, 2018.
4. C. Ates, G. Ozen, N. Selçuk, G. Kulah, “Assessment of Gas Radiative Property Models in the Presence of Non-Gray Particles”, *Numerical Heat Transfer, Part A: Applications*, Vol. 73, pp. 385-407, 2018.
5. C. Ates, N. Selçuk, G. Kulah, Significance of Particle Concentration Distribution on Radiative Heat Transfer in Circulating Fluidized Bed Combustors, *International Journal of Heat and Mass Transfer*, Vol. 117, pp. 58-70, 2018.
6. C. Ates, N. Selçuk, G. Kulah, “Effect of Changing Biomass Source on Radiative Heat Transfer During Co-Firing of High-Sulfur Content Lignite in Fluidized Bed Combustors”, *Applied Thermal Engineering*, vol.128, pp.539–550, 2018.
7. C. Ates, N. Selçuk, G. Kulah, “Effect of Limestone Addition on Radiative Heat Transfer during Co-Firing of High-Sulfur Content Lignite with Biomass in Fluidized Bed Combustors”, *Combustion Science and Technology*, 2018, <https://doi.org/10.1080/00102202.2018.1452122> .
8. C. Ates, O. Sen, N. Selçuk, G. Kulah, “Influence of Spectral Particle Properties on Radiative Heat Transfer in Optically Thin and Thick Media of Fluidized Bed Combustors”, *International Journal of Thermal Sciences*, Vol. 122, pp. 266-280, 2017.
9. C. Ates, N. Selçuk, G. Ozen, G. Kulah, “Benchmarking grey particle approximations against nongrey particle radiation in circulating fluidized bed combustors”, *Numerical Heat Transfer, Part B: Fundamentals*, 71:5, 467-484, 2017.
10. C. Ates, G. Ozen, N. Selçuk, and G. Kulah, “Radiative Heat Transfer in Strongly Forward Scattering Media of Circulating Fluidized Bed Combustors”, *J. Quant. Spectrosc. Radiat. Transfer*, vol. 182, pp. 264–276, 2016.

### **Conference and Symposium Proceedings**

1. C. Ates, N. Selçuk, G. Kulah, “Influence of Spectral Particle Properties on the Predictive Accuracy of Gas Property Approximations”, *Radiative Transfer in Combustion Systems*”, *Proceedings of Computational Thermal Radiation in Participating Media VI*, April 11-13, Lisbon, Portugal, 2018.

2. C. Ates, N. Selçuk, G. Kulah, “Effect of Limestone Addition on Radiative Heat Transfer during Co-Firing of High-Sulfur Content Lignite with Biomass in Fluidized Bed Combustors”, Combustion Diagnostics CD-03, *Proceedings of Tenth Mediterranean Combustion Symposium*, September 17-21, Naples, Italy, 2017.